

nature

PEAK FLOW

How mountains divert the jet stream to form the North American monsoon

Coronavirus
How much protection does vaccination offer against long COVID?

Disordered diamonds
Crushed buckyballs provide route to ultrahard carbon

Agricultural roots
Origin of Transeurasian languages traced to millet farmers in China

Vol. 598 | 25 NOVEMBER 2021 | NATURE.COM

Nature.2021.11.27

[Sat, 27 Nov 2021]

- [This Week](#)
- [News in Focus](#)
- [Books & Arts](#)
- [Opinion](#)
- [Work](#)
- [Research](#)
- [Amendments & Corrections](#)

This Week

- **[US astronomy has ambitious plans — but it needs global partners](#)** [23 November 2021]
Editorial • Ten-year ‘decadal survey’ sets out plans for a ‘super Hubble’, powerful ground-based telescopes and opportunities for international collaboration.
- **[Researchers at risk in Afghanistan need better tools to find help](#)** [24 November 2021]
Editorial • Many organizations are ready to help threatened scholars and professionals — but those in peril often struggle to locate them.
- **[Want research integrity? Stop the blame game](#)** [24 November 2021]
World View • Helping every scientist to improve is more effective than ferreting out a few frauds.
- **[Ancient mud bricks show adobe’s foundations 5,000 years ago](#)** [15 November 2021]
Research Highlight • The oldest known monumental adobe structure in the Americas provides clues to the origins of this versatile material.
- **[This microbe works a toxic metal into a weapon against its foes](#)** [19 November 2021]
Research Highlight • Bacteria that cause hospital infections can process copper into an effective antibiotic.
- **[It’s a snap: the friction-based physics behind a common gesture](#)** [17 November 2021]
Research Highlight • Experiments with various types of glove identify the factors behind a successful finger click.
- **[The art critic in the machine tells forgeries from the real thing](#)** [22 November 2021]
Research Highlight • A neural network can use the surface roughness of a painting to tell one person’s brushstrokes from another’s.
- **[Even organic pesticides spur change in the wildlife next door](#)** [17 November 2021]

Research Highlight • A keystone aquatic species develops resistance to compounds used to treat organic fields near its ponds.

- **High-speed spinning yields some of the toughest spider silk ever found** [16 November 2021]

Research Highlight • The silk that whizzes out of jumping spiders mid-bound is of superior quality.

- **Battery-powered trains offer a cost-effective ride to a cleaner world** [22 November 2021]

Research Highlight • A battery system could power a train for hundreds of kilometres before needing a charge of renewable energy.

- EDITORIAL
- 23 November 2021

US astronomy has ambitious plans — but it needs global partners

Ten-year ‘decadal survey’ sets out plans for a ‘super Hubble’, powerful ground-based telescopes and opportunities for international collaboration.



The Hubble Space Telescope, launched in 1990, was prioritized in the decadal survey released in 1972. Credit: NASA

Astronomers in the United States breathed a collective sigh of relief this month when a long-awaited, COVID-19-delayed, 615-page report finally

landed on their desks. Issued by the National Academies of Sciences, Engineering, and Medicine, the ‘decadal survey’ of astronomy lays out a 10-year plan for the nation’s investments in astronomy and astrophysics, which run to more than US\$2 billion annually.

The United States is the world’s largest funder of astronomy and astrophysics. This report — a massive three-year, grass-roots effort that incorporates hundreds of white papers from thousands of astronomers — is essential reading for astronomers everywhere. That’s because what the United States thinks and does has an impact on scientific priorities for other countries, whose astronomers are often very keen to work with the United States.

The decadal survey is officially a recommendation — but funding agencies generally follow its guidance. It is considered particularly important because, compared with other areas of science, astronomy and astrophysics needs very expensive research infrastructure. Both the Hubble Space Telescope and its successor, the engineering marvel known as the James Webb Space Telescope, were born from recommendations made in previous surveys. Webb’s 6.5-metre-wide mirror will enable astronomers to peer back to when the first stars and galaxies assembled in the Universe, more than 13 billion years ago.



[US astronomy's 10-year plan is super-ambitious](#)

But both missions are the result of extensive international collaboration. Hubble combines the forces of NASA and the European Space Agency (ESA). The \$10-billion Webb is a collaboration between NASA, ESA and the Canadian Space Agency, and is scheduled to launch no earlier than 22 December. The next generation of telescopes will need to be similarly global affairs if they are to succeed.

The latest decadal survey makes it clear that the next decade's priorities will include the search for habitable Earth-like worlds — and will require big facilities to pursue such themes. Those include a 'super Hubble' space telescope — estimated to cost at least \$11 billion — and two enormous, 25–30-metre-wide ground-based telescopes that would be the successors to the current biggest class of telescopes, including the twin 10-metre Keck telescopes in Hawaii. Crucially, the report also identifies opportunities for the United States to coordinate with other nations and space agencies on astronomical exploration. These opportunities must be seized.

Plenty of scope

Collaboration comes in many flavours. Canada, China, India and Japan are partners in one of the next-generation ground-based telescopes, the Thirty Meter Telescope (TMT) project. They are contributing both funds and work on the telescope's hardware. Canada, for example, is building the dome's enclosure, and China is working on polishing mirror segments, in return for a share of future observing time.

Moreover, nations are keen to continue those collaborating roles. Last year, Canada's astronomy community identified technical areas in which Canadian astronomers can complement the work of NASA and other large space agencies. These include the development of scientific instruments and other hardware for future NASA missions, in much the same way as the Canadian Space Agency contributed to Webb.



[NASA won't rename James Webb telescope — and astronomers are angry.](#)

Such collaboration also helps to ensure that research gaps are filled and that projects do not overlap or stray into the territory of others. Europe's astronomers, for example, will be relieved that the proposed 'super Hubble' will operate in ultraviolet, visible and infrared wavelengths. Had the plan been to use X-rays, the telescope would have shouldered uncomfortably into the territory of ESA's Athena X-ray observatory, which is scheduled for launch in the early 2030s. The report does propose an X-ray mission, but it is expected to follow the super Hubble and be designed in ways that would complement rather than compete with Athena. One challenge, however, will be to develop the super Hubble quickly and efficiently enough that it is possible to continue moving down the wish list towards that X-ray mission.

ESA, in turn, has worked hard to not duplicate future NASA missions. Earlier this year, Europe used its Voyage 2050 strategy process to identify science mission themes that stake out its own discovery space, such as exploring the icy moons of the outer Solar System, where life might reside in deep buried oceans. And the pan-European Astronet astronomy road-mapping process is similarly working to identify unique areas for discovery.

Global lifelines

There's also much potential for collaboration with other nations. For instance, addition of an India-based detector to the Laser Interferometer Gravitational-Wave Observatory (LIGO) is currently approved in principle. If India were to grant full approval, then the new detector would work in concert with two existing LIGO detectors in the United States. Likewise, Japan, a world leader in X-ray astronomy, is heading up an X-ray mission that will launch next year, in collaboration with NASA, to keep discoveries flowing until Athena is ready for business.

On the US domestic front, the decadal report does not weigh in on the controversial topic of where to build the TMT. Construction of this facility on the mountain of Maunakea has been halted since 2015 because of concerns that it is being done on lands that many Native Hawaiians consider sacred. If the US federal government became involved, it would further prolong the project approvals process. The report recommends only that the National Science Foundation (NSF) consider funding both the TMT and a similar telescope in the Southern Hemisphere, the Giant Magellan Telescope under construction in Chile by partners in the United States, South Korea, Brazil, Australia and Israel. This arrangement would give US astronomers a chance to apply for a portion of observing time on these ground-breaking facilities, opening up public access to what have thus far been private projects.

Now that the latest decadal survey has been released, the funding agencies that commissioned the report — NASA, the NSF, the Department of Energy and the US Air Force — will begin implementing the recommendations, working with the US Congress, which will allocate the funds. As they do, they should consider how international partners can help with — and build on — the report's powerful vision, so that the world can push the frontiers of discovery together.

Nature **599**, 531-532 (2021)

doi: <https://doi.org/10.1038/d41586-021-03514-2>

| [Section menu](#) | [Main menu](#) |

- EDITORIAL
- 24 November 2021

Researchers at risk in Afghanistan need better tools to find help

Many organizations are ready to help threatened scholars and professionals — but those in peril often struggle to locate them.



Universities such as Khatam Al-Nabieen University in Kabul remain closed more than three months after the Taliban takeover of Afghanistan. Credit: Mohammad Ismail/Reuters

One of the main charities helping scientists to leave countries experiencing conflict has seen a spike in enquiries. Last week, the Council for At-Risk Academics (CARA), which is based in London, said it had received 40

requests from people intent on leaving Afghanistan. It was 98 in the previous week. This is a record for the organization — its highest previous peak was 20 a week in 2016, during the Syria crisis, says CARA's executive director Stephen Wordsworth.

Three months after the Taliban takeover of Afghanistan, the country's educational and research institutions remain closed. The Red Cross says that salaries at government-run hospitals have gone unpaid for months because of economic woes exacerbated by sanctions. Afghanistan's economy is expected to shrink by nearly one-third this year, according to projections from the International Monetary Fund. And the United Nations World Food Programme says that almost 23 million people, out of a population of 40 million, face hunger.

Most academic staff — particularly women and those with international links — are either in hiding or looking to leave the country. One provincial passport office that reopened earlier this month received more than 2,000 applications per day, nearly 10 times its usual daily processing capacity of 250. "The reality is that we are all trying to emigrate," one researcher wrote in an e-mail to *Nature* last week.



[Afghanistan's terrified scientists predict huge research losses](#)

CARA and Scholars at Risk, its US counterpart, connect researchers fleeing conflict with universities in safe countries who need people with specific skills. Both are working flat out to process applications and have been able to find academic jobs for a small number of people, along with safe passage for their families.

But they are just two organizations working manually to help relocate scholars. And although they are well known among university administrators, they are less familiar to research staff and the leaders of research groups, who might have PhD opportunities or vacancies they are looking to fill. What is needed now is a larger and more visible response, coordinated globally — and preferably with a strong digital component — to assist all of those whose lives are in danger. It should be a bold effort, facilitated by everyday digital tools, connecting the growing numbers of people and organizations offering support with the rising number of those at risk.

Just in the past few months, initiatives have been set up to assist women judges, lawyers, musicians and sports professionals who need to leave Afghanistan. In addition to CARA and Scholars at Risk, there's Germany's Philipp Schwartz Initiative, which funds universities to host researchers at risk. The coming weeks and months are likely to see the launch of more such efforts, but these will not be easy for people in Afghanistan to access unless they already know the names of the schemes, or of the people and organizations behind them.



The global research community must not abandon Afghanistan

This problem could be addressed with an organized digital portal or service. It could be a single online space for organizations and individuals to use to display what they are offering in terms of employment, support or advice. It could match them with scholars and other at-risk professionals in Afghanistan (and other countries in conflict, such as Syria and Yemen). And it would need to be built in a way that would allow identities to be verified but simultaneously kept secure. Although limited travel to and from Afghanistan has resumed, anyone with links to people or organizations outside the country is at high risk of persecution.

Academics around the world have generously opened their homes and their institutions to researchers at risk. But more needs to be done to connect those at risk with those ready to provide jobs and other forms of support, not only in universities, but in other types of organization, too.

Researchers applying to CARA to leave Afghanistan are not looking for permanent settlement, Wordsworth says. “This is not brain drain,” he emphasizes. People are frightened, but, when conditions are safe, they are determined to go back and build on the knowledge and infrastructure of higher education and research that has been created in the past 20 years, under the US-led occupation.

Nature **599**, 532 (2021)

doi: <https://doi.org/10.1038/d41586-021-03515-1>

This article was downloaded by **calibre** from <https://www.nature.com/articles/d41586-021-03515-1>

| [Section menu](#) | [Main menu](#) |

- WORLD VIEW
- 24 November 2021

Want research integrity? Stop the blame game



Helping every scientist to improve is more effective than ferreting out a few frauds.

- [Malcolm Macleod](#) ✉

Most scientists reading this probably assume that their research-integrity office has nothing to do with them. It deals with people who cheat, right? Well, it's not that simple: cheaters are relatively rare, but plenty of people produce imperfect, imprecise or uninterpretable results. If the quality of every scientist's work could be made just a little better, then the aggregate impact on research integrity would be enormous.

How institutions can encourage broad, incremental improvements is what I have been working to figure out. Two things are needed: a collective shift in

mindset, and a move towards appropriate measurement.

Over the past 2 years, some 20 institutions in the United Kingdom have joined the UK Reproducibility Network (UKRN), a consortium that promotes best practice in research. They have created senior administrative roles to improve research and research integrity. I have taken on this job (on top of my research on evaluating stroke treatments) at the University of Edinburgh. Since then, I've focused on research improvement rather than researcher accountability. Of course, deliberate fraud should be punished, but a focus on investigating individuals will discourage people from acknowledging mistakes, and mean that opportunities for systems to improve are neglected.



[Research integrity: nine ways to move from talk to walk](#)

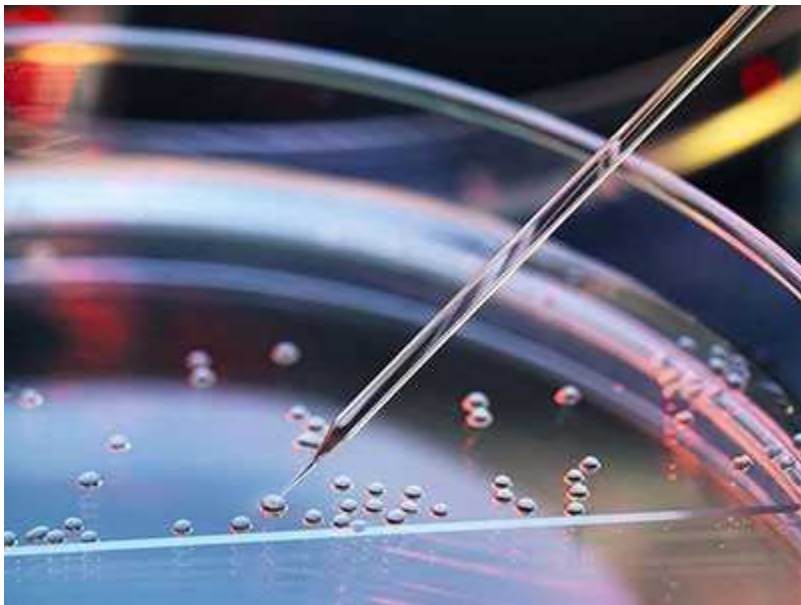
At the University of Edinburgh, we have audits as part of projects to shrink bias in animal research, speed up publication and improve clinical-trial reporting. These are not the metrics that most researchers are used to. Many people are initially wary of yet another ‘external imposition’, but when they see that this is about promoting our own community’s standards — and that there are no extra forms to fill in — they usually welcome this shift in institutional focus.

Here’s what we are learning to look for at my university.

Integrity indicators. Counting papers published in *Science* or *Nature* or prizes received is a poor reflection of performance. Measures should reflect the integrity of research claims: for instance, the proportion of quantitative studies that also publish data and code, and that pre-register their hypothesis, study design and analysis plan. At the University of Edinburgh, we are focusing on the reporting of randomization and blinding in published animal studies that test biomedical hypotheses. Existing tools can be applied to such tasks. The DOIs of publications that match a series of ORCIDs (author IDs) can be identified, the open-access status ascertained through the Unpaywall database, and these details can be linked back to institutions, departments or even individual research groups.

I care more about how my institution is doing compared with last year than about how it performs relative to other organizations. That said, benchmarking can be useful — and working with other organizations can help to develop standard reporting tools without reinventing the wheel.

Evidence of impact. Having data in hand allows an institution to focus on what can be improved, and how. In 2019, only 55% of Edinburgh clinical trials were fully reported on the European Union Clinical Trials Register. Programmes to reach trial organizers (by e-mailing reminders and mentoring them through the process) increased this to 95% in 2021. To build on that, I am working with members of UKRN and others to develop institutional dashboards that will provide real-time data across a range of measures, such as clinical-trial reporting and the quality and timeliness of reporting animal research.



Research integrity is much more than misconduct

Evidence of effectiveness. When a simple, inexpensive intervention improves reporting from 55% to 95%, you don't need a randomized controlled trial. But it's important to make sure that more-involved interventions have the desired effect. The scientific skills needed to establish causality can be applied to assess efforts in and across institutions. For example, at the University of Edinburgh, we offer researchers free consultations on methodology as they write grant applications, and this requires both applicants and consultants to invest much more of their time. We are also designing randomized studies to see whether and how methods and award rates improve.

A culture of trust. Many scientists have been scarred by successive, energy-sapping evaluations. More than one university has based layoffs on counts of faculty members' high-impact papers or high-value grants, a practice that will make researchers sceptical of claims about prioritizing quality. Approaches to improvement need to be open and transparent, and constructive rather than punitive.

Learning from each other. No institution should go this alone. UKRN members are collaborating to ease workloads and encourage standardization, for instance in deploying a common research-culture questionnaire. Creating standards is the best way to change norms,

otherwise early-career researchers will be tempted to concentrate on impressing future employers rather than on their current role.

My goal is that institutions should focus on what they can do to increase research integrity, not on the integrity of their researchers.

Nature **599**, 533 (2021)

doi: <https://doi.org/10.1038/d41586-021-03493-4>

This article was downloaded by **calibre** from <https://www.nature.com/articles/d41586-021-03493-4>

| [Section menu](#) | [Main menu](#) |

- RESEARCH HIGHLIGHT
- 15 November 2021

Ancient mud bricks show adobe's foundations 5,000 years ago

The oldest known monumental adobe structure in the Americas provides clues to the origins of this versatile material.



The Shrine of the Moon in northern Peru was built thousands of years after the construction of adobe walls at the site called Los Morteros. Credit: Kike Calvo/Universal Images Group/Getty

For thousands of years, Andean people have used adobe bricks to build awe-inspiring structures, including towering pyramids that were hundreds of metres wide. The bricks are known to be made from a mixture of clay-rich soil, water and other materials, but researchers understood little about the technology's origins.

Access options

Subscribe to Journal

Get full journal access for 1 year

\$199.00

only \$3.90 per issue

[Subscribe](#)

All prices are NET prices.
VAT will be added later in the checkout.
Tax calculation will be finalised during checkout.

Rent or Buy article

Get time limited or full article access on ReadCube.

from \$8.99

[Rent or Buy](#)

All prices are NET prices.

Additional access options:

- [Log in](#)
- [Learn about institutional subscriptions](#)

Nature **599**, 534 (2021)

doi: <https://doi.org/10.1038/d41586-021-03446-x>

References

1. 1.

Mauricio, A. C. *et al.* *Proc. Natl Acad. Sci. USA* **118**, e2102941118 (2021).

This article was downloaded by **calibre** from <https://www.nature.com/articles/d41586-021-03446-x>

- RESEARCH HIGHLIGHT
- 19 November 2021

This microbe works a toxic metal into a weapon against its foes

Bacteria that cause hospital infections can process copper into an effective antibiotic.

3D illustration of *Pseudomonas aeruginosa* bacteria.

Pseudomonas aeruginosa bacteria (illustration), which can cause deadly infections, use five enzymes to make a compound that kills other bacteria.
Credit: Christoph Burgstedt/Science Photo Library

A bacterium found in soil and water turns copper in its environment into a powerful antibiotic that keeps its rivals at bay¹.

Access options

Subscribe to Journal

Get full journal access for 1 year

\$199.00

only \$3.90 per issue

[Subscribe](#)

All prices are NET prices.

VAT will be added later in the checkout.

Tax calculation will be finalised during checkout.

Rent or Buy article

Get time limited or full article access on ReadCube.

from \$8.99

[Rent or Buy](#)

All prices are NET prices.

Additional access options:

- [Log in](#)
- [Learn about institutional subscriptions](#)

Nature **599**, 534 (2021)

doi: <https://doi.org/10.1038/d41586-021-03477-4>

References

1. 1.

Patteson, J. B. *et al. Science* <http://doi.org/10.1126/science.abj6749> (2021).

This article was downloaded by **calibre** from <https://www.nature.com/articles/d41586-021-03477-4>

- RESEARCH HIGHLIGHT
- 17 November 2021

It's a snap: the friction-based physics behind a common gesture

Experiments with various types of glove identify the factors behind a successful finger click.



Study of the ordinary finger click has shown that it is one of the fastest human motions, at only 7 milliseconds. Credit: Georgia Tech

A simple snap of the fingers boasts some complex physics. The arm loads up energy and then releases it explosively, so that the middle finger hits the palm with a sharp smack. A team has now shown how that process depends on the friction of human skin¹.

Access options

Subscribe to Journal

Get full journal access for 1 year

\$199.00

only \$3.90 per issue

[Subscribe](#)

All prices are NET prices.

VAT will be added later in the checkout.

Tax calculation will be finalised during checkout.

Rent or Buy article

Get time limited or full article access on ReadCube.

from \$8.99

[Rent or Buy](#)

All prices are NET prices.

Additional access options:

- [Log in](#)
- [Learn about institutional subscriptions](#)

Nature **599**, 534 (2021)

doi: <https://doi.org/10.1038/d41586-021-03444-z>

References

1. 1.

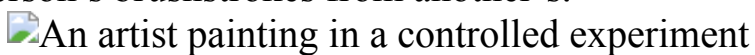
Acharya, R., Challita, E. J., Ilton, M. & Bhamla, M. S. *J. R. Soc. Interface* <https://doi.org/10.1098/rsif.2021.0672> (2021).

This article was downloaded by **calibre** from <https://www.nature.com/articles/d41586-021-03444-z>

- RESEARCH HIGHLIGHT
- 22 November 2021

The art critic in the machine tells forgeries from the real thing

A neural network can use the surface roughness of a painting to tell one person's brushstrokes from another's.



Paintings of flowers honed a neural network's ability to link a work to a specific artist. Credit: F. Ji *et al.*/*Herit. Sci.* ([CC BY 4.0](#)).

Artificial neural networks can tell one artist's work from another's using the 3D topography of the brushstrokes, researchers have found¹. The technique could help to identify forgeries, or to distinguish the hands of various members of an old master's workshop who have contributed to one painting.

Access options

Subscribe to Journal

Get full journal access for 1 year

\$199.00

only \$3.90 per issue

[Subscribe](#)

All prices are NET prices.
VAT will be added later in the checkout.

Tax calculation will be finalised during checkout.

Rent or Buy article

Get time limited or full article access on ReadCube.

from \$8.99

[Rent or Buy](#)

All prices are NET prices.

Additional access options:

- [Log in](#)
- [Learn about institutional subscriptions](#)

Nature **599**, 534 (2021)

doi: <https://doi.org/10.1038/d41586-021-03447-w>

References

1. 1.

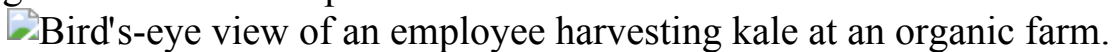
Ji, F. *et al.* *Herit. Sci.* <https://doi.org/10.1186/s40494-021-00618-w> (2021).

This article was downloaded by **calibre** from <https://www.nature.com/articles/d41586-021-03447-w>

- RESEARCH HIGHLIGHT
- 17 November 2021

Even organic pesticides spur change in the wildlife next door

A keystone aquatic species develops resistance to compounds used to treat organic fields near its ponds.



A worker harvests kale on an organic farm. The limited selection of pesticides used on such farms can drive evolution of pesticide resistance in nearby species. Credit: Brendon Thorne/Bloomberg/Getty

Organic farming is touted as a greener alternative to conventional farming. But new research suggests that even the handful of pesticides used on organic fields can affect nearby animals in much the same way that conventional pesticides do¹.

Access options

Subscribe to Journal

Get full journal access for 1 year

\$199.00

only \$3.90 per issue

[Subscribe](#)

All prices are NET prices.
VAT will be added later in the checkout.

Tax calculation will be finalised during checkout.

Rent or Buy article

Get time limited or full article access on ReadCube.

from \$8.99

[Rent or Buy](#)

All prices are NET prices.

Additional access options:

- [Log in](#)
- [Learn about institutional subscriptions](#)

Nature **599**, 535 (2021)

doi: <https://doi.org/10.1038/d41586-021-03445-y>

References

1. 1.

Almeida, R. A., Lemmens, P., De Meester, L. & Brans, K. I. *Proc. R. Soc. B.* <https://doi.org/10.1098/rspb.2021.1903> (2021).

This article was downloaded by **calibre** from <https://www.nature.com/articles/d41586-021-03445-y>.

- RESEARCH HIGHLIGHT
- 16 November 2021

High-speed spinning yields some of the toughest spider silk ever found

The silk that whizzes out of jumping spiders mid-bound is of superior quality.



The zebra jumping spider unfurls silk at up to 7 centimetres per second without sacrificing product quality. Credit: Shutterstock

The thread that a spider hastily spins in mid-jump ranks among the toughest silk known¹.

Access options

Subscribe to Journal

Get full journal access for 1 year

\$199.00

only \$3.90 per issue

[Subscribe](#)

All prices are NET prices.

VAT will be added later in the checkout.

Tax calculation will be finalised during checkout.

Rent or Buy article

Get time limited or full article access on ReadCube.

from \$8.99

[Rent or Buy](#)

All prices are NET prices.

Additional access options:

- [Log in](#)
- [Learn about institutional subscriptions](#)

Nature **599**, 535 (2021)

doi: <https://doi.org/10.1038/d41586-021-03443-0>

References

1. 1.

Chen, A., Kim, K. & Shamble, P. S. *Curr. Biol.* **31**, R1422–R1423 (2021).

This article was downloaded by **calibre** from <https://www.nature.com/articles/d41586-021-03443-0>

| [Section menu](#) | [Main menu](#) |

- RESEARCH HIGHLIGHT
- 22 November 2021

Battery-powered trains offer a cost-effective ride to a cleaner world

A battery system could power a train for hundreds of kilometres before needing a charge of renewable energy.



Diesel-electric locomotives, which are widely used to pull US freight trains, emit greenhouse gases and toxic pollution that could be eliminated by battery-powered versions. Credit: Bruce Leighty/Alamy

Once the domain of toys for toddlers, battery-powered electric trains could enable zero-emission cargo transport at prices that are competitive with existing diesel-powered locomotives¹.

Access options

Subscribe to Journal

Get full journal access for 1 year

\$199.00

only \$3.90 per issue

[Subscribe](#)

All prices are NET prices.

VAT will be added later in the checkout.

Tax calculation will be finalised during checkout.

Rent or Buy article

Get time limited or full article access on ReadCube.

from \$8.99

[Rent or Buy](#)

All prices are NET prices.

Additional access options:

- [Log in](#)
- [Learn about institutional subscriptions](#)

Nature **599**, 535 (2021)

doi: <https://doi.org/10.1038/d41586-021-03448-9>

References

1. 1.

Popovich, N. D., Rajagopal, D., Tasar, E. & Phadke, A. *Nature Energy* **6**, 1017–1025 (2021).

This article was downloaded by **calibre** from <https://www.nature.com/articles/d41586-021-03448-9>

News in Focus

- **[COVID deaths, gravitational waves and pandemic PhD supervision](#)** [24 November 2021]
News Round-Up • The latest science news, in brief.
- **[Homicide is a top cause of maternal death in the United States](#)** [12 November 2021]
News • Evaluation of death certificates from national database paints grim picture for pregnant women.
- **[Do childhood colds help the body respond to COVID?](#)** [18 November 2021]
News • A mechanism known as ‘original antigenic sin’ protects some people from flu; whether it helps immune reactions to coronaviruses is still unclear.
- **[First quantum computer to pack 100 qubits enters crowded race](#)** [19 November 2021]
News • But IBM’s latest quantum chip and its competitors face a long path towards making the machines useful.
- **[How do people resist COVID infections? Hospital workers offer a hint](#)** [11 November 2021]
News • Immune cells might ‘abort’ SARS-CoV-2 infection, forestalling a positive PCR or antibody test.
- **[More Alzheimer’s drugs head for FDA review: what scientists are watching](#)** [15 November 2021]
News Explainer • Eli Lilly and other pharma firms have begun submitting their anti-amyloid drug hopefuls for approval. But questions linger over the controversial precedent set by Biogen’s aducanumab.
- **[Do vaccines protect against long COVID? What the data say](#)** [23 November 2021]
News Feature • Vaccines reduce the risk of developing COVID-19 — but studies disagree on their protective effect against long COVID.
- **[How record wildfires are harming human health](#)** [24 November 2021]

News Feature • As fires get bigger and rage for more of the year, scientists are racing to understand the lingering impacts.

| [Next section](#) | [Main menu](#) | [Previous section](#) |

- NEWS ROUND-UP
- 24 November 2021

COVID deaths, gravitational waves and pandemic PhD supervision

The latest science news, in brief.



Elisabeth Steubesand, 105, receives an inoculation against COVID-19 in Germany, which has a large population of people vulnerable to the disease because they are older and have neither caught the virus nor received a vaccine
Credit: Andreas Rentz/Getty

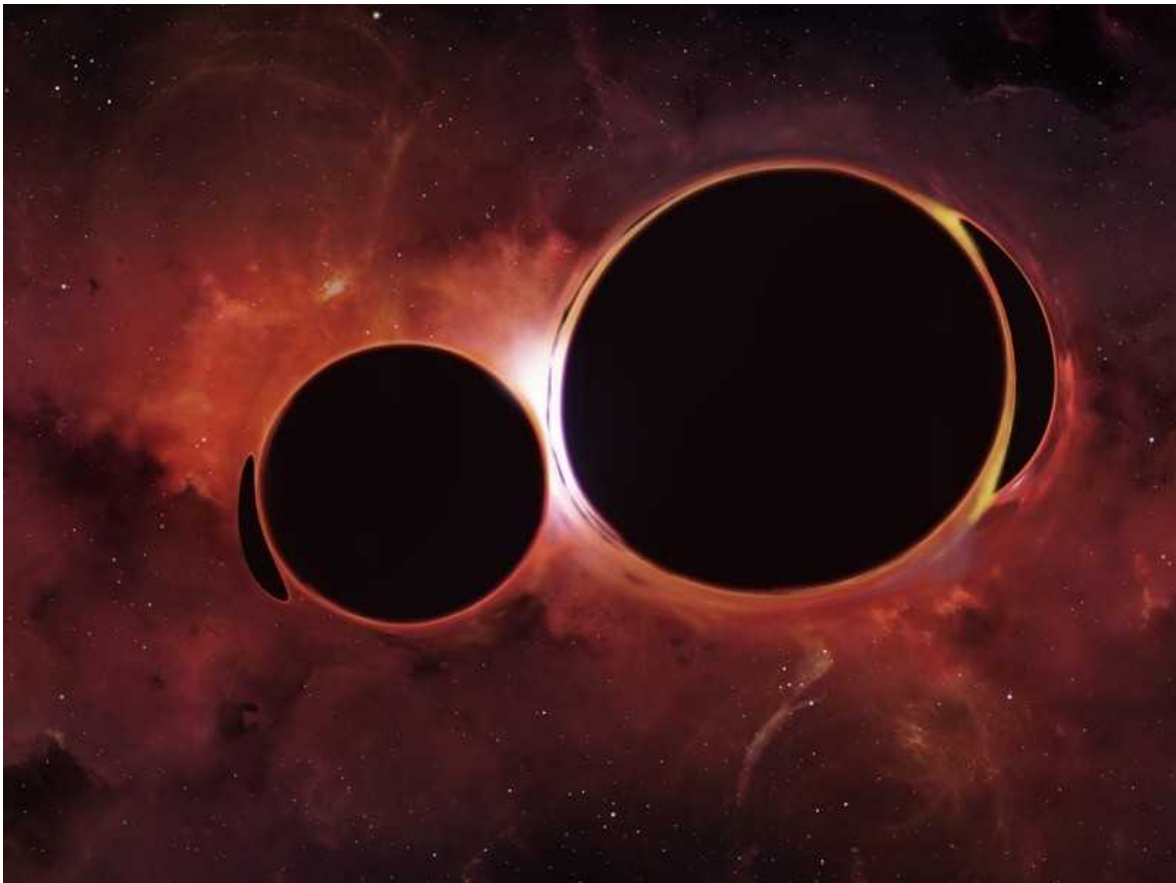
Europe's COVID deaths could rise sharply

The COVID-19 pandemic [could cost an extra 300,000 lives in Europe](#), according to a study of the number of people who have not been infected or vaccinated.

The work also predicts that the pandemic could lead to roughly one million hospitalizations in Europe, some of which would contribute to the death toll. But the authors note that their estimates are maximums that assume, for example, that all anti-infection restrictions are lifted ([L. A. C. Chapman et al. Preprint at medRxiv https://doi.org/g6rt; 2021](https://doi.org/g6rt)). The study has not yet been peer reviewed.

Researchers at the London School of Hygiene & Tropical Medicine collected data on COVID-19 deaths in a range of age groups in 19 countries, and estimated the total number of people who had been infected in each country by early November 2021. This figure was used with data on vaccination rates to calculate the share of the population that had not acquired immunity to SARS-CoV-2 — and so was still at increased risk of being hospitalized or dying from COVID-19 if all restrictions were lifted. The analysis also accounted for people who could be at risk despite previous exposure or vaccination.

It found large variation: some 8 in 1,000 people in Romania could still be hospitalized, compared with fewer than one per 1,000 in England.



As black holes merge (illustration), they produce gravitational waves that ripple across the Universe.Credit: Mark Garlick/SPL

Gravitational-wave detectors release latest data

Gravitational-wave observatories have released their [latest catalogue of cosmic collisions](#), bringing their total number of detections to 90. The new crop of 35 events includes one featuring the lightest neutron star ever seen, as well as two clashes involving surprisingly large black holes with masses more than 60 times that of the Sun ([R. Abbott *et al.* Preprint at https://arxiv.org/abs/2111.03606; 2021](#)).

The detections come from the two Laser Interferometer Gravitational-Wave Observatory (LIGO) sites, in Louisiana and Washington State, and their sister detector, Virgo, in Italy. They were recorded during 21 weeks of operations, beginning on 1 November 2019, that racked up an average detection rate of one event every 4.2 days.

Gravitational waves are ripples in the fabric of space-time that are produced when large masses accelerate. Like the detections previously reported by LIGO–Virgo, the latest ones are all attributed to pairs of dense stellar remnants spiralling into each other and merging. The collaboration initially released data only on high-confidence detections, but the latest catalogue — as well as the previous one, released in October 2020 — includes any detections that have better-than-even chances of being genuine gravitational waves. The team estimates that around 10–15% of the latest candidates in the catalogue are false alarms, “caused by instrumental noise fluctuations”.

Sleeplessness and anxiety: PhD supervisors on toll of COVID pandemic

One-third of academics who supervise doctoral students say they have lost sleep during the pandemic because of their role, according to a [poll of almost 3,500 supervisors in the United Kingdom](#). Two-thirds said that supervision responsibilities had increased, with many wanting more support to address the well-being and mental health of their PhD students.

Significant changes, affecting both supervisors and students, have been made to the PhD supervision process during the pandemic, says Ronny Gunnarsson, who researches medicine and public health at the University of Gothenburg in Sweden. “Many supervisors and PhD students have suffered emotionally from the lack of on-site meetings,” he says, a problem exacerbated by the loss of informal coffee-break-style chats that can often resolve difficulties.

There are currently about 22,000 PhD supervisors at UK universities, estimates the UK Council for Graduate Education (UKCGE), a charity based in Lichfield. To better understand the pressures and expectations supervisors face, both before and during the pandemic, the UKCGE launched a survey in May 2021 that was partially funded by the biomedical charity Wellcome and by the government agency UK Research and Innovation.

Around 15% of the country’s research supervisors responded, according to the resulting report (see go.nature.com/3ncnk9a). In general, they enjoyed and valued their role, with more than 80% saying it increased the quality of

their research, and three-quarters saying they were satisfied with their effectiveness in the position.

But respondents also revealed the challenges they faced generally as supervisors, and more specifically during the COVID-19 pandemic (see ‘Stresses of supervision’).

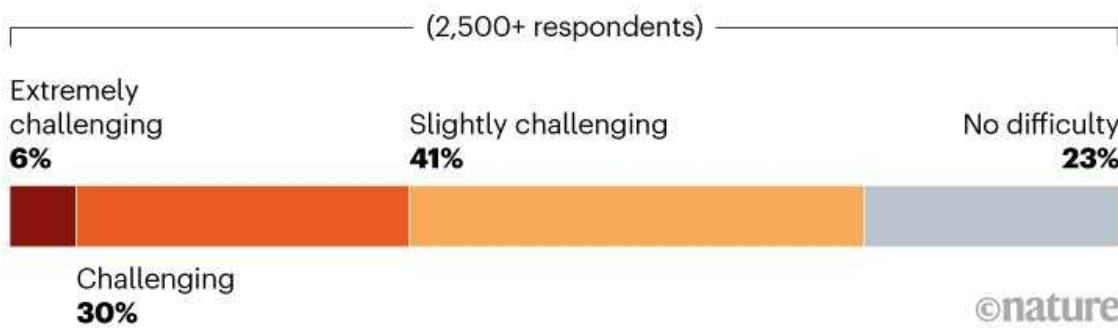
STRESSES OF SUPERVISION

A survey of UK academics finds that the pressures of supervising PhD students have increased over time, particularly during the COVID-19 pandemic.

Do you agree that doctoral supervision has become more demanding over the past five years?



How challenging has helping PhD candidates to refocus their research been during the pandemic?



©nature

Source: UK Research Supervision Survey (UKGCE, 2021)

Half of the respondents said that the pandemic had made the job more challenging. More than one-third agreed with the statement “concerns over supervision have kept me awake at night over the last 12 months”, with a similar proportion agreeing that, over the same period, “supervising doctoral candidates makes me feel anxious”.

Nature **599**, 537 (2021)

doi: <https://doi.org/10.1038/d41586-021-03494-3>

This article was downloaded by **calibre** from <https://www.nature.com/articles/d41586-021-03494-3>

| [Section menu](#) | [Main menu](#) |

- NEWS
- 12 November 2021

Homicide is a top cause of maternal death in the United States

Evaluation of death certificates from national database paints grim picture for pregnant women.

- [Nidhi Subbaraman](#)



A woman speaks at a protest to demand standards to prevent violence against women. Credit: Nicholas Kamm/AFP via Getty

Pregnant women in the United States die by homicide more often than they die of pregnancy-related causes — and they're frequently killed by a partner, according to a study published last month in *Obstetrics & Gynecology*¹. Researchers revealed this grim statistic by using death certificates to compare homicides and pregnancy-related deaths across the entire country for the first time.



[Why hundreds of scientists are weighing in on a high-stakes US abortion case](#)

Although smaller studies have tracked homicides during pregnancy at the state and local level, confirming the scope of the phenomenon on a national scale is valuable, says Vijay Singh, a physician at the University of Michigan Medical School in Ann Arbor, who studies how health-care workers can monitor abuse by current and former romantic partners. “You can’t understand a problem unless you can measure it.”

The study results, he adds, are “stunning”.

The researchers found that US women who are pregnant or were pregnant in the past 42 days (the post-partum period) die by homicide at more than twice the rate that they die of bleeding or placental disorders — the leading causes of what are usually classified as pregnancy-related deaths. Also, becoming pregnant increases the risk of death by homicide: between the ages of 10 and

44 years, women who are pregnant or had their pregnancy end in the past year are killed at a rate 16% higher than are women who are not pregnant.

“For more than 20 years, researchers have been talking about pregnancy-associated death and homicide of women,” says Phyllis Sharps, a nurse-scientist at the Johns Hopkins School of Nursing in Baltimore, Maryland. The consensus, she says, is that this is happening in large part because of violence by intimate partners.

‘An age and race story’

To arrive at a national snapshot, reproductive epidemiologist Maeve Wallace at Tulane University in New Orleans, Louisiana, and her co-authors analysed data for deaths in all 50 US states from 2018 and 2019, using information in the National Center for Health Statistics database, which is hosted by the US Centers for Disease Control and Prevention (CDC).

In 2003, the United States began requiring that death certificates indicate whether a person had died while pregnant, or within either 42 days or 1 year of the end of a pregnancy. By 2010, about 37 states included such an option on their certificates; by 2018, all 50 states required this information. This year, Wallace and coworkers analysed the resulting records. According to their count, across 2018 and 2019, a total of 273 women died by homicide either while pregnant or within a year of the end of their pregnancy.



Millions of black people affected by racial bias in health-care algorithms

When tracking deaths among pregnant women in the United States, the CDC doesn't classify homicide, accidents or suicides as causes of 'maternal mortality'. Wallace and others say homicides should be counted, because there is indeed a connection between homicide and pregnancy.

The overall rate of maternal mortality in the United States is on the rise. And it is particularly high for a wealthy country. Contributing factors include inadequate access to health care, staff who are poorly trained for obstetric emergencies, and subpar care given to Black women because of racism in clinical practice.

On the basis of years of study, specialists in intimate-partner violence expect women who are already in abusive relationships to be at increased risk of homicide if they become pregnant. Wallace and her co-authors say that about two-thirds of the homicides recorded in their data occurred in the person's home, suggesting that the woman was killed by her partner. It's not a perfect indicator, Wallace says, "but it's all we've got in these data".

The team found that Black women in the United States who are pregnant or were recently pregnant have up to nearly three-fold higher risk of dying by homicide than those who are not pregnant — the highest increase reported among any racial or ethnic group. (The team reported rates only among Black, Hispanic and white women, because the sample sizes for other groups — such as Asian American women or Native American women — were too small to publish.)

Black women are similarly at heightened risk of death from obstetric causes. Overall, Black women who are pregnant or were recently pregnant die of pregnancy-related causes 2.5 times as often as non-Hispanic white women, according to the CDC.



What the data say about police brutality and racial bias — and which reforms might work

Age is also a factor in pregnancy-related homicide, the team found: young women between the ages of 10 and 24 are at higher risk of homicide while pregnant than are those who are older, according to the study. “It’s an age and race story,” Wallace says.

What Wallace and coworkers “have done with the data available gives more confidence to the scope of the problem and the work that came before”, says Aaron Kivisto, a clinical psychologist at the University of Indianapolis in Indiana who studies domestic violence and suicide prevention. In a study published in February this year², he and his colleagues showed increased risk of homicide for Black pregnant women, compared with white or Hispanic pregnant women.

Sharps says part of the reason that Black women are at higher risk could be that experiences of racism have led them to be more distrustful of law-enforcement agencies and less likely to bring forward complaints about domestic violence.

Studies such as Wallace’s could be used by policymakers or hospital administrators to improve monitoring of pregnant people and those who have recently given birth, Singh says. It could also build public understanding of harms and risks during pregnancy. “There’s an idea in our

society that pregnancy is a happy time,” Sharps says. “But for a lot of women, that’s just not true, and a lot of women are just not safe in their homes.”

Nature **599**, 539-540 (2021)

doi: <https://doi.org/10.1038/d41586-021-03392-8>

Editor’s note: Nature recognizes that transgender men and non-binary people can become pregnant. We use ‘women’ in this story to reflect the language used in the study, which is based on death certificates that identify people only as men or women.

References

1. 1.

Wallace, M., Gillispie-Bell, V., Cruz, K., Davis, K. & Vilda, D. *Obstet. Gynecol.* **138**, 762–769 (2021).

2. 2.

Kivisto, A. J., Mills, S. & Eastwood, L. S. *J. Interpers. Violence* <https://doi.org/10.1177/0886260521990831> (2021).

This article was downloaded by **calibre** from <https://www.nature.com/articles/d41586-021-03392-8>

- NEWS
- 18 November 2021

Do childhood colds help the body respond to COVID?

A mechanism known as ‘original antigenic sin’ protects some people from flu; whether it helps immune reactions to coronaviruses is still unclear.

- [Rachel Brazil](#)

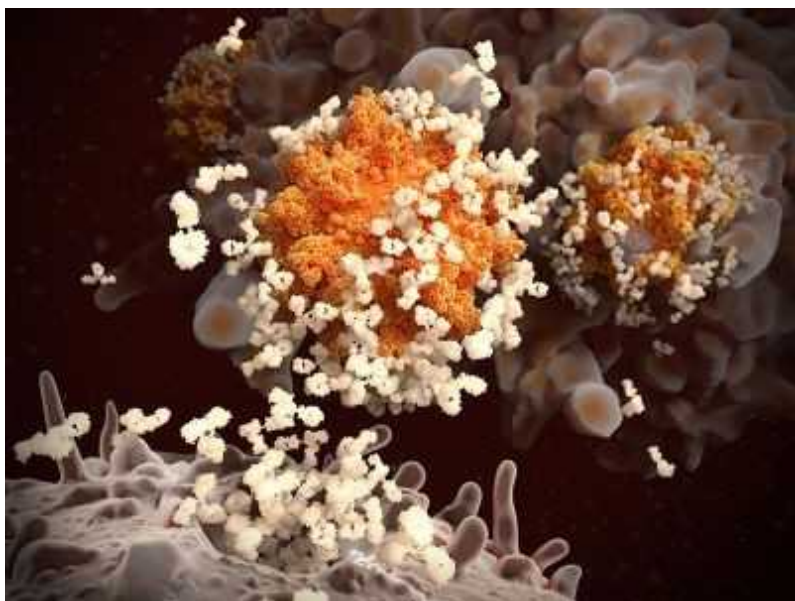


Exposure to other coronaviruses — including those that cause common colds — could affect how the immune system responds to SARS-CoV-

2.Credit: Getty

Some people are better at fighting off seasonal flu when the strain of influenza virus is similar to the first one they encountered in childhood — a phenomenon evocatively dubbed ‘original antigenic sin’, or OAS. Now, there is increasing evidence that people’s immune responses to COVID-19 could be shaped in a similar way by previous infections with common-cold coronaviruses.

The effect could have implications for the design of future COVID-19 vaccines. However, to what extent it affects people with COVID-19 — and whether it provides enhanced protection or, in fact, hampers the immune response — is still unclear. “The debate is quite polarized at the moment,” says Craig Thompson, a virologist at the University of Oxford, UK.



[COVID super-immunity: one of the pandemic's great puzzles](#)

OAS — also called immune imprinting — was first characterized in 1960 by US epidemiologist Thomas Francis Jr, who noticed that the immune system seemed to be permanently programmed to produce antibodies against the first strain of a flu virus that it encountered¹. Immune cells reactivate when the body is infected by a flu virus that shares regions, or ‘epitopes’, with that first strain.

For SARS-CoV-2, there is growing evidence that exposure to other coronaviruses — including those that cause colds and other respiratory illnesses — plays a part in people's immune responses. "Much like flu, most of us are infected with these common coronaviruses by the age of five or six," says Scott Hensley, a microbiologist at the University of Pennsylvania in Philadelphia. His group discovered that blood serum samples taken from people before the pandemic contained antibodies against a common-cold coronavirus called OC43 that could bind to the SARS-CoV-2 spike protein².

Using samples taken before and after SARS-CoV-2 infection, Hensley and his colleagues were able to show that catching SARS-CoV-2 boosted the production of OC43-binding antibodies. Their study, published in April, found that these antibodies bound to the S2 subunit of the SARS-CoV-2 spike protein — which has a similar structure to that in OC43. But the OC43 antibodies did not bind to the S1 region of the SARS-CoV-2 spike and were unable to stop the virus entering cells.

Effects of imprinting

In some cases, imprinting is known to have a positive effect on immunity. Hensley and his colleagues studied the effects of imprinting during the 2009 H1N1 flu pandemic and found that exposure to some historical flu strains provided protection against H1N1 infection³. "There were some epitopes in that virus that were conserved with past seasonal influenza strains," Hensley says. "The recall of antibody responses against those epitopes was actually beneficial."



Why scientists worldwide are watching UK COVID infections

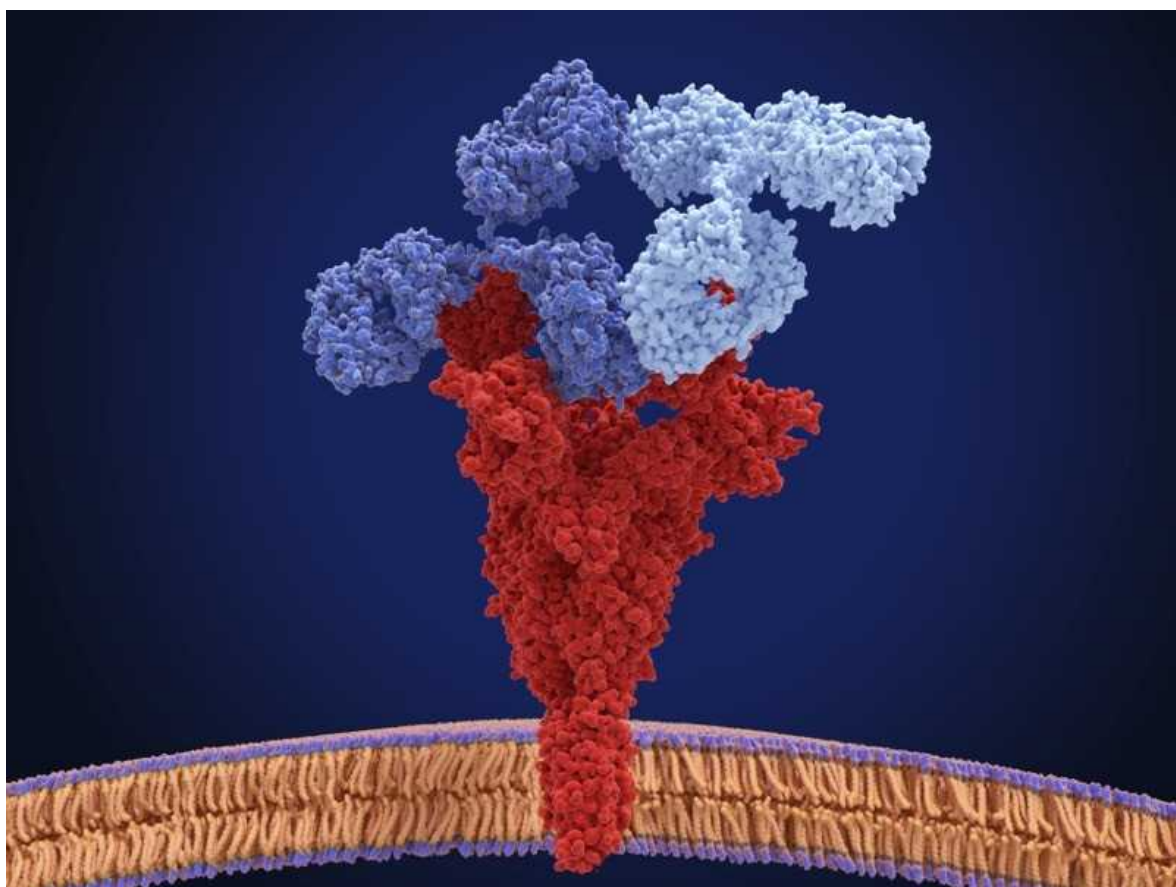
But OAS also has potential downsides. Sometimes, antibodies produced as a result of imprinting are not a very good match to the virus causing an infection, but their production suppresses the activation of naive B cells that would otherwise produce more-protective antibodies. “You get a response that may be skewed towards conserved antigens versus the new antigens,” says Adolfo García-Sastre, director of the Global Health and Emerging Pathogens Institute at the Icahn School of Medicine at Mount Sinai in New York City. This can diminish the immune system’s ability to fight the new infection.

García-Sastre looked at the early immune responses of people hospitalized with COVID-19 in Spain, and observed increased levels of antibodies against both OC43 and another betacoronavirus, called HKU1, that shared epitopes with SARS-CoV-2⁴. “We looked for a correlation between people mounting higher [levels of] antibodies against these conserved epitopes versus having less protective immunity against SARS-CoV-2, and there was a slight correlation,” says García-Sastre.

Signs of OAS negatively affecting people with COVID-19 were also seen by Thompson and his colleagues, in a preprint posted earlier this year⁵. The analysis was based on samples taken in 2020 from people in the United Kingdom who had asymptomatic infections, and from people who were

admitted to hospital with severe COVID-19, half of whom subsequently died. The researchers found that people who died produced fewer antibodies against the SARS-CoV-2 spike protein than did people who survived, but produced the same amount of antibodies to another protein found in the virus — the nucleocapsid protein.

Thompson says these results indicate that imprinted memories of the spike protein from a different coronavirus could be preventing a more effective immune response in those who did not survive. “This is a fingerprint of OAS,” he says. But he adds that it is too early to conclude this definitively.



Antibodies target a coronavirus spike protein (illustration). Some antibodies produced against the common-cold coronavirus OC43 can bind to the S2 subunit of the SARS-CoV-2 spike protein. Credit: Juan Gaertner/SPL

It is difficult to tell from such early results whether OAS is beneficial or detrimental to the immune response against SARS-CoV-2, and the results of preliminary studies are open to interpretation. Hensley warns that just

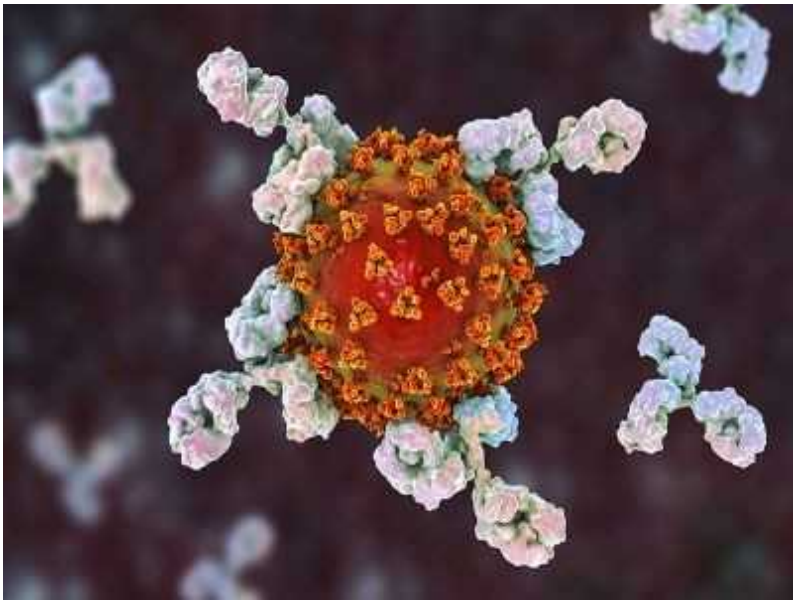
measuring antibody levels does not provide a full picture of a complex immune response. He also thinks the presence of OC43 antibodies in people with COVID-19 could indicate that a recent OC43 infection is helping the immune system to fight the virus. In August, a study of samples from health-care workers showed that individuals with higher OC43 antibody levels, indicating recent OC43 exposure, recovered from a SARS-CoV-2 infection faster⁶ than those with lower levels. Other research has shown similar protective effects.

In a study published in December 2020, George Kassiotis, an immunologist at the Francis Crick Institute in London, also found that pre-existing OC43 antibodies showed reactivity to SARS-CoV-2⁷. At the time, he wasn't sure of the implications, but after reviewing studies published since, he says, "most of the evidence points to a positive overall contribution, not a negative one".

García-Sastre suggests that even if they are not able to stop SARS-CoV-2 entering cells, OC43 antibodies might trigger the immune system to kill infected cells.

Vaccine updates

A key question is whether these observations can help to inform future COVID-19 vaccination strategies. For now, vaccines based on the original version of the coronavirus — first reported in Wuhan, China, in late 2019 — protect against all known variants, says Kassiotis.



COVID vaccine immunity is waning — how much does that matter?

Imprinting sometimes reduces the effectiveness of flu vaccines, according to Sarah Cobey, an evolutionary biologist and flu researcher at the University of Chicago in Illinois. The flu vaccine is updated each year to protect against those strains that researchers think are the most likely to be prevalent. Some people's immune systems are still not seeing the update, says Cobey, and still target parts of the virus that are familiar to them. “It looks like they’re not really mounting a response to the thing that we carefully updated the vaccine for.” It is possible that future COVID-19 vaccines tailored to new variants could experience similar problems.

Hensley does not think this is likely, however. In a study published as a preprint last month, he and his colleagues reported that people do not produce as many OC43 antibodies after receiving a messenger RNA vaccine as they do when infected with SARS-CoV-2 itself⁸. This could be because the mRNA vaccines establish such an efficient immune response that they can bypass any immune-imprinting effect. “Maybe in the context of mRNA vaccines there’s not really going to be as much of a biasing towards conserved epitopes. That’s the hope,” says Hensley.

Thompson says that the problem could also be circumvented in updated COVID-19 vaccines by removing the shared epitopes: “You could easily just chop the S2 domain off... or make a vaccine just targeting the receptor

binding domain of the most recent circulating strain,” he says. “But this is really hypothetical.”

“There likely is a very complicated interplay between seasonal coronavirus infection and disease outcome upon SARS-CoV-2 infection,” says Hensley. “I don’t think anything should be pitched as complete fact at this point.”

Nature **599**, 540-541 (2021)

doi: <https://doi.org/10.1038/d41586-021-03087-0>

References

1. 1.

Francis, T. Jr *Proc. Am. Phil. Soc.* **104**, 572–578 (1960).

2. 2.

Anderson, E. M. *et al.* *Cell* **184**, 1858–1864 (2021).

3. 3.

Li, Y. *et al.* *J. Exp. Med.* **210**, 1493–1500 (2013).

4. 4.

Aydillo, T. *et al.* *Nature Commun.* **12**, 3781 (2021).

5. 5.

McNaughton, A. L. *et al.* Preprint at medRxiv
<https://doi.org/10.1101/2021.05.04.21256571> (2021).

6. 6.

Gouma, S. *et al.* *JCI Insight* **6**, e150449 (2021).

7. 7.

Ng, K. W. *et al.* *Science* **370**, 1339–1343 (2020).

8. 8.

Anderson, E. M. *et al.* Preprint at medRxiv
<https://doi.org/10.1101/2021.09.30.21264363> (2021).

This article was downloaded by **calibre** from <https://www.nature.com/articles/d41586-021-03087-0>

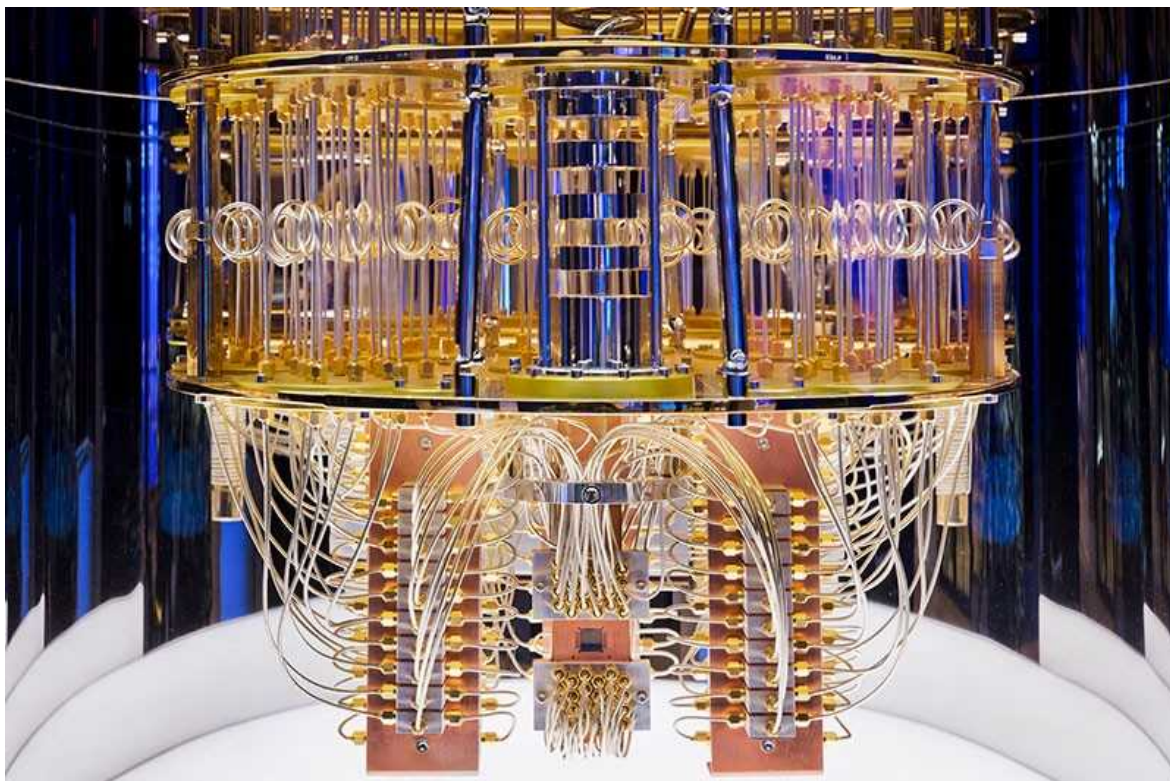
| [Section menu](#) | [Main menu](#) |

- NEWS
- 19 November 2021

First quantum computer to pack 100 qubits enters crowded race

But IBM's latest quantum chip and its competitors face a long path towards making the machines useful.

- [Philip Ball](#)



The innards of an IBM quantum computer show the tangle of cables used to control and read out its qubits. Credit: IBM

IBM's newest quantum-computing chip, revealed on 15 November, established a milestone of sorts: it packs in 127 quantum bits (qubits), making it the first such device to reach 3 digits. But the achievement is only one step in an aggressive agenda boosted by billions of dollars in investments across the industry.

The 'Eagle' chip is a step towards IBM's goal of creating a 433-qubit quantum processor next year, followed by one with 1,121 qubits, named Condor, by 2023. Such targets echo those that for decades the electronics industry has set itself for miniaturizing silicon chips, says Jerry Chow, head of IBM's experimental quantum-computing group at the Thomas J. Watson Research Center in Yorktown Heights, New York.

Other companies — including technology behemoths Google and Honeywell, and a slew of well-funded start-up companies — have similarly ambitious plans. Ultimately, they aim to make quantum computers capable of performing certain tasks that are out of reach of even the largest supercomputers that use classical technology.

"It's good to have ambitious goals, but what matters is whether they can execute their plans," says quantum information theorist John Preskill at the California Institute of Technology in Pasadena.

Quantum advantage

By exploiting the laws of quantum physics to process binary information, quantum-computing circuits such as the Eagle chip can already do calculations that can't easily be simulated on classical supercomputers. Google famously [reported achieving such a 'quantum advantage'](#) in 2019¹, using qubits made, like IBM's, with superconducting loops. A team at the University of Science and Technology of China (USTC) in Hefei last year reported achieving [quantum advantage using optical qubits](#)²; this year, it did the same with superconducting qubits³.

But the tasks these machines were given were artificial, researchers warn. "The current state of the art is that no experiment has demonstrated quantum advantage for practical tasks yet," says physicist Chao-Yang Lu, who co-led

the USTC effort. Solving real-world problems such as simulating drug molecules or materials using quantum chemistry will require quantum computers to get drastically bigger and more powerful.

Quantum engineer Andrew Dzurak at the University of New South Wales in Sydney, Australia, thinks that with 1,000-qubit chips such as IBM's planned Condor, the technology might start to prove its worth. "It's hoped that some useful and even commercially valuable problems can be solved using quantum computers in this thousand-to-million-qubit range," he says. "But to do really paradigm-shifting stuff, you are going to need millions of physical qubits."

Chip challenges

The Eagle chip has almost twice as many qubits as IBM's previous flagship quantum circuit, the 65-qubit Hummingbird. The increase required the team to solve several engineering problems, says Chow. To enable each qubit to interact with several others, the researchers opted for an arrangement in which each is linked to two or three neighbours on a hexagonal grid. And to allow individual control of each qubit without an unmanageable tangle of wires, the team placed wires and other components on several stacked tiers. Chow says that to solve this 'packaging' problem, the researchers drew on experience with 3D architectures in conventional chips. He adds that it was also crucial to find materials that would perform well at the ultralow temperatures needed for superconducting qubits to function.

But the processing power of a quantum circuit isn't just about how many qubits it has. It also depends on how fast they operate and on how resistant they are to errors that could scramble a calculation, due for example to random fluctuations. Chow says that there's still scope for improvement in all these respects for superconducting qubits.

Dealing with errors is particularly difficult, because the laws of physics prevent quantum computers from using the error-correcting methods of classical machines, which typically require keeping multiple copies of each bit.

Instead, researchers aim to build ‘logical qubits’ — in which almost all errors can be identified and corrected — from complicated arrangements of many physical qubits. The procedures so far proposed typically demand that each logical qubit contain around 1,000 physical qubits, although that ratio depends on the intrinsic fidelity — the error-resistance — of the physical qubits, says Dzurak.

Error correction

Some other approaches to building quantum computers hope to benefit from qubits with lower intrinsic error rates. That’s one potential advantage of using trapped ions as the qubits, as is done by the company IonQ, spun out of research at the University of Maryland in College Park, which last month raised more than US\$600 million when it became the first purely quantum-computing company to trade publicly on the New York Stock Exchange — a deal that valued the company at almost \$2 billion. Rigetti Computing, a start-up in Berkeley, California, also went public this year, with a \$1.5-billion valuation.

IonQ co-founder Christopher Monroe, a physicist at the University of Maryland, and his co-workers last month reported a fault-tolerant logical qubit made from just 13 trapped-ion qubits⁴, although Dzurak says that its degree of error-correction was “still quite some way from what is needed for a useful quantum computer, which needs logical error rates well below one in a million”.

The Google team, meanwhile, has achieved similar logical error rates using 21 superconducting qubits⁵: again, “an important result”, says Dzurak, but still far from what is needed to crack the error-correction problem.

But Chow cautions against placing too much emphasis on attaining logical qubits. “We won’t have a situation where we flip a switch and say ‘error-correction is on’”, he says. “Improving qubit performance is a more important story than making logical qubits and dividing everything by 1,000.”

Signal boost

IBM and others are trying to gain a detailed understanding of the error-related noise in a circuit, and then to extract it — rather like noise cancellation to improve the signal-to-noise ratio in acoustics.

Beyond Condor-level devices, Chow says, circuit designs are likely to become modular, with several chips linked through “quantum interconnects”. It’s not yet clear how best to do that — perhaps with the microwave-frequency signals currently used for data input and output to superconducting qubits, or maybe by converting the quantum information to light-based signals. “It’s an entirely new area of research,” says Chow.

Many researchers think the first real-world applications of quantum computers are likely to be in relatively specialized fields, such as simulation of molecules and materials, machine learning and optimization problems in industries including finance. To get to that stage, “I expect we’ll see gradual improvement in performance rather than a sudden leap forward”, says Preskill. “It is likely to be a long slog before we can run useful applications.”

Nature **599**, 542 (2021)

doi: <https://doi.org/10.1038/d41586-021-03476-5>

References

1. 1.

Arute, F. *et al.* *Nature* **574**, 505–510 (2019).

2. 2.

Zhong, H.-S. *et al.* *Science* **370**, 1460–1463 (2020).

3. 3.

Wu, Y. *et al.* *Phys. Rev. Lett.* **127**, 180501 (2021).

4. 4.

Egan, L. *et al.* *Nature* **598**, 281–286 (2021).

5. 5.

Chen, Z. *et al.* *Nature* **595**, 383–387 (2021).

This article was downloaded by **calibre** from <https://www.nature.com/articles/d41586-021-03476-5>

| [Section menu](#) | [Main menu](#) |

- NEWS
- 11 November 2021

How do people resist COVID infections? Hospital workers offer a hint

Immune cells might ‘abort’ SARS-CoV-2 infection, forestalling a positive PCR or antibody test.

- [Max Kozlov](#)



A worker runs COVID-19 tests at a laboratory in Ankara.Credit: Mehmet Ali Ozcan/Anadolu Agency via Getty

Data from dozens of UK health-care workers suggest a tantalizing possibility: that some people can clear a nascent SARS-CoV-2 infection from their bodies so quickly that they never test positive for the virus nor even produce antibodies against it¹. The data also suggest that such resistance is conferred by immune players called memory T cells — possibly those produced after exposure to coronaviruses that cause the common cold.

“I’ve never seen anything like that. It’s really surprising that the T cells might be able to control an infection so quickly,” says Shane Crotty, an immunologist at La Jolla Institute for Immunology in California, who was not involved in the research.

But the study’s authors strongly caution that their results do not show that people who have had the common cold are protected against COVID-19. And the authors also acknowledge that their findings have many caveats, meaning that it’s too early to say with certainty that people can stop an infection in its tracks.



The search for people who never get COVID

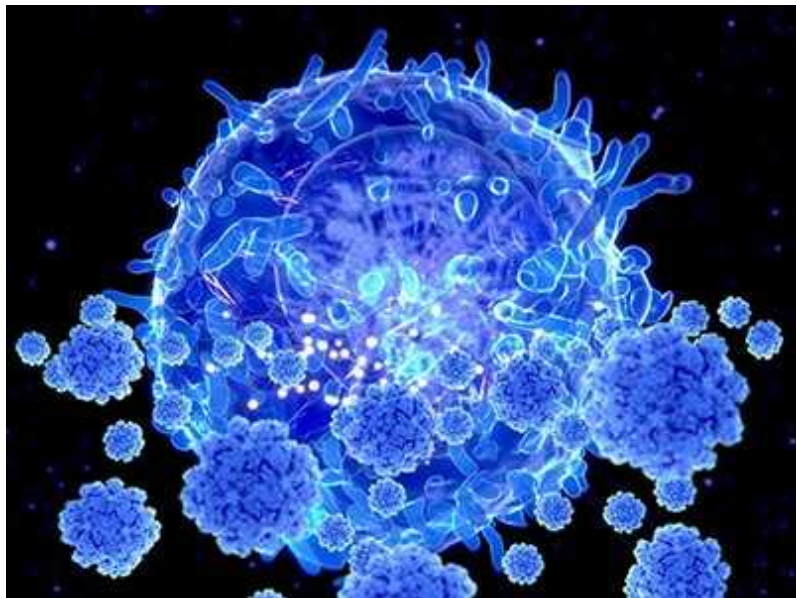
In the study, published on 10 November in *Nature*, the authors examined blood samples collected in the first weeks of the pandemic from nearly 60 UK health-care workers. All worked in hospitals, putting them at high risk

of contracting COVID-19, but never tested positive or produced any antibodies to the virus for four months after enrolling in the study.

The researchers noticed that in 20 of these ‘seronegative’ participants, T cells had multiplied — a sign that the immune system might be gearing up to fight an infection. Nineteen of these individuals also had increased levels of an immune-system protein called IFI27, which the authors say might be an early marker of SARS-CoV-2 infection. The authors say that these data are evidence for ‘abortive infections’, meaning that the virus made an incursion into the body but failed to take hold.

The authors hypothesized that T cells halt SARS-CoV-2 by disabling a cluster of viral proteins called the replication transcription complex, which helps the virus to reproduce. They found evidence to support this theory: a far higher proportion of the seronegative participants had T cells that recognize this complex than did health-care workers who got COVID-19.

The researchers also found that even T cells from blood samples collected before the pandemic could recognize SARS-CoV-2 — and most strongly recognized the replication complex. These T cells could have been generated by infections with coronaviruses that cause common colds, but without direct evidence of how or when the cells originated, it is possible that other triggers contributed to their formation, the authors say.



How ‘killer’ T cells could boost COVID immunity in face of new variants

Most existing COVID-19 vaccines target SARS-CoV-2’s spike protein, which it uses to invade human cells. Spike proteins vary considerably between different coronaviruses. But replication complexes are similar across multiple types of coronavirus, making this part of the virus a promising target for a [‘pan-coronavirus’ vaccine](#) — one that protects against a broad array of such viruses, the authors conclude.

But scientists not involved in the study note that there’s no definitive evidence that the health-care workers who purportedly cleared the virus actually had any SARS-CoV-2 particles in their bodies to begin with. That makes it difficult to draw any conclusions about the role of these T cells, says Donna Farber, an immunologist at Columbia University in New York City.

Study co-author Mala Maini, a viral immunologist at University College London, acknowledges that her team lacks direct confirmation of abortive infections among the study participants. But she notes that the timing of the virus’s uncontrolled early spread in the UK is well documented. As a result, she says, it is probably not a coincidence that the researchers noticed more T cells in participants’ blood around the same time that people with COVID-19 were filling UK hospitals. “The timing is so clear-cut,” she says.

Clearance for all?

Even if some of the study participants did clear the SARS-CoV-2 virus before it could take hold, it’s possible that infections with variants such as [Delta](#) can’t be cleared in the same way, says Marcus Buggert, an immunologist at the Karolinska Institute in Solna, Sweden. He notes that the study documents the phenomenon only in health-care workers, raising the possibility that only people such as hospital staff, who are regularly exposed to a wide variety of respiratory viruses, can mount an abortive response.

The study was also not designed to determine whether the abortive response is driven by T cells or another, unknown immune process. Crotty says it will be important to test the T-cell theory in animals, and Maini says a [human](#)

challenge trial, in which participants are deliberately exposed to SARS-CoV-2, would help to establish whether these T cells are really helping to clear the infection.

Nature **599**, 543 (2021)

doi: <https://doi.org/10.1038/d41586-021-03110-4>

References

1. 1.

Swadling, L. *et al.* *Nature* <https://doi.org/10.1038/s41586-021-04186-8> (2021).

This article was downloaded by **calibre** from <https://www.nature.com/articles/d41586-021-03110-4>

| [Section menu](#) | [Main menu](#) |

- NEWS EXPLAINER
- 15 November 2021

More Alzheimer's drugs head for FDA review: what scientists are watching

Eli Lilly and other pharma firms have begun submitting their anti-amyloid drug hopefuls for approval. But questions linger over the controversial precedent set by Biogen's aducanumab.

- [Asher Mullard](#)



A clinical-trial participant receives an infusion of Biogen's aducanumab in May 2021.Credit: Kayana Szymczak/New York Times/Redux/eyevine

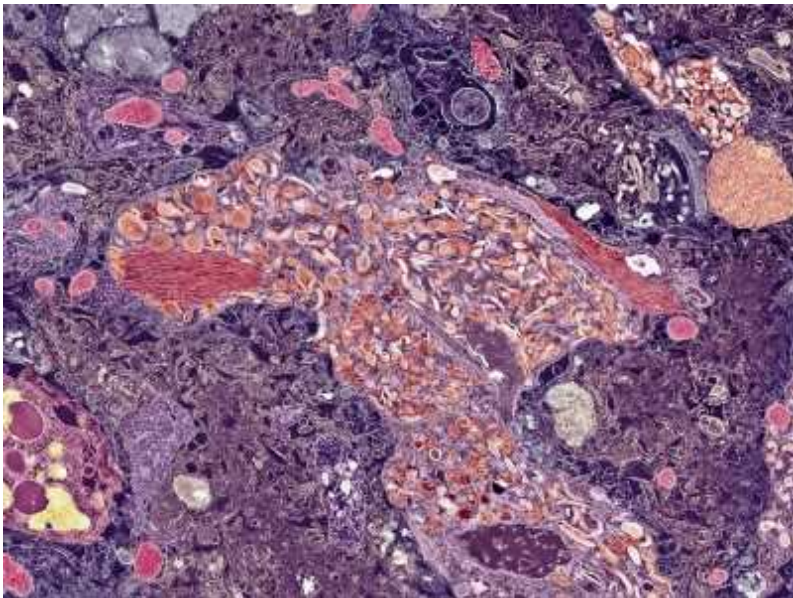
When the US Food and Drug Administration (FDA) approved biotechnology firm Biogen's drug for Alzheimer's disease in June, regulators hoped to usher in a new era of treatment for the neurodegenerative condition. But the decision followed an independent advisory committee's near-unanimous vote to reject the drug, called aducanumab — and [instead divided the community](#). Some researchers think that the approval will bolster the development of drugs for treating brain disease, but others see it as a blemish on the FDA's integrity and an obstacle to progress.

Pharmaceutical company Eli Lilly in Indianapolis hopes that its antibody donanemab, which works in a similar way to aducanumab, will have a better reception. The firm plans to finish submitting its drug candidate for FDA approval in the next few months, paving the way for a decision in the second half of 2022. Meanwhile, Biogen, based in Cambridge, Massachusetts, and its partner Eisai, based in Tokyo, are racing to complete the submission of data for another competitor, lecanemab. The regulatory fate of these therapeutic hopefuls could foretell the future of Alzheimer's and [shape neurodegenerative drug development programmes](#) for years.

Following the Clinical Trials on Alzheimer's Disease (CTAD) conference last week in Boston, where researchers discussed the drug candidates, *Nature* reviews the questions everyone is asking.

Do amyloid-lowering drugs help patients?

According to the 'amyloid hypothesis' of Alzheimer's disease, the build-up of a protein called amyloid- β in the brain causes neurodegeneration. Aducanumab and its would-be competitors clear clumps of amyloid- β from the brain. But clinical trials have not meaningfully demonstrated that these therapeutics slow memory loss or cognitive decline. This is a particular point of contention for aducanumab, an antibody drug that is now on the market for around US\$56,000 per year, despite prematurely halted phase III trials and the messy data set that was submitted for approval.



Landmark Alzheimer's drug approval confounds research community

Some hope that Lilly's donanemab trials will eventually provide proof of benefit. The first of these is an 18-month phase II trial called Trailblazer-Alz that enrolled 257 people. It showed¹ that the cognitive capabilities of people who received the antibody declined more slowly than those of placebo recipients. The average difference was 3.20 points on a 144-point scale.

For Mark Mintun, senior vice-president of neuroscience research and development at Lilly, this signal is promising. Treated patients avoided around six months of cognitive decline over the course of the study, he says. With longer use of donanemab, participants might benefit even more, he speculates.

Rob Howard, a psychiatrist at University College London, is unconvinced, however. The observed 3.20-point difference is “trivial”, he says. Best-case interpretations of aducanumab and lecanemab data point to similarly marginal effects. Generic donepezil — a 25-year-old Alzheimer's drug that treats the symptoms rather than the root cause of the disease — outperforms the antibodies, he adds.

Sharon Sha, a neurologist who oversees neuroscience clinical trials at Stanford University in California, says more data are needed to assess the clinical utility of these drugs. “We really need to make sure that [these

antibodies] are changing the daily lives of patients or keeping them stable,” says Sha, an investigator in trials of all three therapies.

When will solid data be available on whether these therapies improve cognition?

One of the conditions that came with the FDA’s approval of aducanumab was that Biogen run a ‘confirmatory trial’ ensuring that the antibody actually helps people. The biotech firm has yet to launch that trial, and the FDA gave it nine years to collect the results — a long timeline that has contributed to the uproar over the drug’s approval.

For Ezekiel Emanuel, a bioethicist at the University of Pennsylvania in Philadelphia, the data need to come sooner. The accelerated approval pathway should be updated to mandate faster collection of high-quality confirmatory data, he wrote in the journal JAMA².



Controversial Alzheimer’s drug approval could affect other diseases

Assuming that the FDA approves donanemab using the same accelerated approval pathway, Lilly, too, will have to confirm the benefit of its antibody. The pharma firm is running a 1,500-patient phase III trial called Trailblazer-Alz2 of donanemab for people in early stages of Alzheimer’s. Results are

due in the first half of 2023 — after the antibody’s potential approval — and might provide the data needed. Another phase III trial is recruiting 3,300 patients at risk of Alzheimer’s, to test whether earlier use of the antibody delays the onset of dementia. This trial will run until 2027.

The results of these studies might help to heal a divided field. “Could [the approval of aducanumab] have been done better? I think everyone agrees that this could have unfolded more effectively,” Mintun says. “But as the data accumulate, people will get more and more convinced, and the divisions, I think, will disappear.”

Will the FDA approve the anti-amyloid antibodies?

The accelerated approval of aducanumab established a precedent for others to follow. The FDA can approve Alzheimer’s drugs on the basis of their ability to remove amyloid- β from the brain — without clear evidence of cognitive benefit. Pharma watchers therefore think that an accelerated approval for donanemab is likely, barring undisclosed issues regarding efficacy, safety or manufacturing.

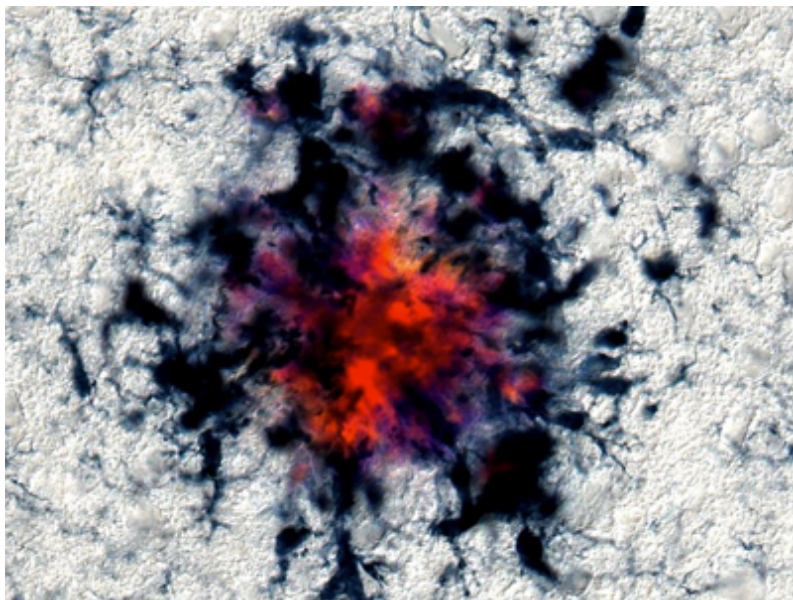
“Of course they’ll approve it,” Howard says. “It’s difficult to see how they can have approved aducanumab and not approve donanemab.”

Donanemab’s amyloid-lowering ability is not in dispute. In Trailblazer-Alz, it lowered amyloid- β levels on average by almost 80%. These data suggest that it outperforms aducanumab on amyloid clearance. Lilly has setup a head-to-head trial of donanemab and aducanumab to directly compare their amyloid-lowering capabilities.

Will the FDA reconvene its outside experts for upcoming approvals?

A flashpoint in the approval of aducanumab was the FDA’s decision to disregard its advisory committee’s concerns about the antibody.

The agency convened this panel of experts one year ago to discuss Biogen's complicated data set. In 2019, the company halted development of aducanumab after interim analyses of two phase III trials showed that the antibody was not helping people. Months later, it reversed course and said it would seek approval on the basis of a fresh analysis of the data that hinted at cognitive benefit.



Is ‘friendly fire’ in the brain provoking Alzheimer’s disease?

One panellist said that Biogen’s statistical interpretation of its data was akin to “firing a shotgun at a barn and then painting a target around the bullet holes”. Ten panellists voted against approval, and one abstained.

After the FDA approved aducanumab, [three members](#) of this committee quit in protest.

High-ranking FDA officials defended their position in prominent journals^{3,4} and [newspapers](#), but the fallout has continued. Off-the-books meetings between the FDA and Biogen might have enabled the approval, [STAT News reported](#) in June. The federal watchdog at the Department of Health and Human Services is now reviewing the steps that led up to the approval, and is due to release a report in 2023. Two congressional committees in the US House of Representatives are also investigating the decision.

If confirmed by the US Senate, Robert Califf, US President Joe Biden's [recent pick to head the FDA](#), will have to handle any repercussions of this decision — and decide how to move forward with accelerated approvals. But with the regulatory precedent established, there is no clear requirement for an independent advisory committee to review donanemab.

For Caleb Alexander, an internist and epidemiologist at the Johns Hopkins Bloomberg School of Public Health in Baltimore, Maryland, the need is instead reputational. "The FDA's credibility has unfortunately taken a significant hit with the management of aducanumab," says Alexander, a member of the committee that advised the FDA not to approve the drug. "If they want to salvage their credibility, they need to be sure that this new product is reviewed by an advisory committee."

Will the FDA limit who can be treated with these therapies?

The FDA initially approved aducanumab for anyone with Alzheimer's — a disease that affects more than six million people in the United States. But Biogen tested the antibody only in a subset of these patients.

After the backlash, the agency narrowed the specification to people with "mild cognitive impairment or mild dementia stage", to better match the group tested in Biogen's trials. But the drug's label, which specifies who should use it, does not stipulate that people must have evidence of amyloid build-up in their brain — a key requirement for inclusion in Alzheimer's trials.



Frustrated Alzheimer's researchers seek better lab mice

One concern is that the FDA's guidelines put people at risk of potentially fatal side effects, for little or no chance of benefit. Aducanumab can cause brain swelling. Most patients don't experience any symptoms from this swelling, but they need regular brain scans — which are onerous and expensive — to avoid possible complications.

Lilly tested donanemab, which also causes brain swelling, in people at early stages of the disease. It measured amyloid- β , as well as levels of another protein marker of disease, called tau, to limit trial enrolment to the patients who are most likely to benefit. Mintun declined to comment on Lilly's vision for treatment eligibility. "This is a conversation I would love to have with the FDA," he says.

Howard expects another broad approval from the FDA. "It doesn't make any sense to punish Lilly and treat them differently from Biogen," he says. The onus then falls on doctors to work out how and when to use the antibody safely.

But Emanuel argues that the FDA should narrow eligibility for all anti-amyloid therapies — and ensure that real-world usage of any drugs approved under accelerated approval are closely aligned with clinical-trial

designs. “If a court develops a bad precedent, you don’t continue the bad precedent. You revise the precedent,” he says.

Nature **599**, 544–545 (2021)

doi: <https://doi.org/10.1038/d41586-021-03410-9>

References

1. 1.

Mintun, M. A. *et al.* *N. Engl. J. Med.* **384**, 1691–1704 (2021).

2. 2.

Emanuel, E. J. *JAMA* **326**, 1367–1368 (2021).

3. 3.

Dunn, B., Stein, P. & Cavazzoni, P. *JAMA Intern Med.* **181**, 1276–1278 (2021).

4. 4.

Dunn, B., Stein, P., Temple, R. & Cavazzoni, P. *N. Engl. J. Med.* **385**, 856–857 (2021).

This article was downloaded by **calibre** from <https://www.nature.com/articles/d41586-021-03410-9>

- NEWS FEATURE
- 23 November 2021

Do vaccines protect against long COVID? What the data say

Vaccines reduce the risk of developing COVID-19 — but studies disagree on their protective effect against long COVID.

- [Heidi Ledford](#)



Allison Navis (left) assesses Esteban Giron at a clinic for people with post-COVID symptoms at Mount Sinai Hospital in New York City. Credit: Mount Sinai Health System

Physiotherapist David Putrino's neurological rehabilitation clinics used to treat about 50 people each week with conditions such as chronic pain, Parkinson's disease and sports injuries. Then came long COVID.

Now, Mount Sinai Hospital's Abilities Research Center in New York City, one of three clinics that Putrino directs, treats another 50–100 people each week who are coping with issues such as extreme fatigue, breathlessness, difficulty concentrating or any of the many other symptoms of long COVID — the long-lasting, poorly understood syndrome that can occur after infection with the SARS-CoV-2 coronavirus. He has 1,600 clients with long COVID, and more on a waiting list.

Putrino has noticed that even being fully vaccinated doesn't necessarily protect against long COVID. Many of his clients were infected before vaccines were rolled out, and had been coping with symptoms for a year or more before they were referred to him. But he has seen about a dozen people who experienced long COVID from 'breakthrough' infections — in which vaccinated people catch the coronavirus. "It is noticeably less common than in unvaccinated people, but it's still there," he says. He thinks that clinics could see more such cases as the months tick by.



[The four most urgent questions about long COVID](#)

Vaccines reduce the risk of long COVID by lowering the chances of contracting COVID-19 in the first place. But for those who do experience a breakthrough infection, studies suggest that vaccination might only halve the risk of long COVID — or have no effect on it at all^{[1,2](#)}. Understanding the prevalence of long COVID among vaccinated people has urgent public-health implications as restrictions that limited viral spread are eased in some countries. It could also offer clues about what causes lingering COVID-19 symptoms long after the acute infection has cleared.

At present, public-health officials are flying blind when it comes to long COVID and vaccination. Although vaccines greatly reduce the rates of serious illness and death caused by COVID-19, they are not as effective at completely preventing the disease, and long COVID can arise even after a mild or asymptomatic coronavirus infection. Countries with high infection rates could still end up with many cases of long COVID, even if nations have high rates of vaccination. “That is hard to predict,” says Nisreen Alwan, an epidemiologist at the University of Southampton, UK, who has had long COVID. “We still need to see how much long COVID there is and how long it lasts after vaccination.”

Determining the risk of long COVID from breakthrough infections is challenging. Many people with mild or asymptomatic infections might not be tested for COVID-19, says immunologist Petter Brodin at the Karolinska Institute in Stockholm. “Doing any kind of assessment of how many people develop long-term symptoms after they are vaccinated is going to be incredibly difficult,” he says. “We will miss so many people.”



People waiting to receive the COVID-19 vaccine in Dhaka, Bangladesh. Credit: Anadolu Agency via Getty

More data should arrive as countries continue to roll out vaccines, including booster shots, and as research funding for studying long COVID is deployed — including more than US\$1.1 billion from the US National Institutes of Health (NIH). Long COVID is still a poorly defined syndrome with a wide range of symptoms. A UK study estimates that between 7% and 18% of people who had COVID-19 went on to develop some symptoms of long COVID that lingered for at least 5 weeks³.

For some individuals, long-COVID symptoms are mild; for others, they are life-changing. Nearly one-third of the people with long COVID at Putrino's clinic have severe cognitive difficulties that can affect their ability to concentrate, speak and remember, and which were not present before their illness. About 60% of Putrino's patients have had to change jobs or stop working as a result of their illness. "If you're young and healthy, death from COVID may be highly unlikely," Putrino says. "But severe debilitation is not."

The cause of long COVID — also known as the post-acute sequelae of a SARS-CoV-2 infection — is as unclear as its definition. One possibility is that a reservoir of the coronavirus lingers after the acute infection, lurking in various tissues — such as the intestine, liver or brain — and continues to cause damage. Another possibility is that the broad immune response triggered by the initial infection can generate antibodies and other immunological reactions against the body's own tissues. That could continue to cause complications after the infection has been cleared.



[Long COVID and kids: scientists race to find answers](#)

Vaccination could reduce the likelihood of these scenarios. If a vaccine induces high levels of antibodies and T cells capable of recognizing SARS-CoV-2, the immune system could stop the virus during its first few replications before it can establish hidden reservoirs in the body, says Akiko Iwasaki, an immunologist at Yale University in New Haven, Connecticut.

And vaccination allows the body to launch a more-targeted immune response from the moment a coronavirus infiltrates the body, reducing the chance that nonspecific immune reactions will target normal tissue. “The immune system is already sort of pointed in the right direction,” says Brodin. “You’re calling in these very specific cells to attack this specific virus.”

Both anecdotes and data suggest that such protection against long COVID is partial at best, but it is difficult to tease out exactly how common long COVID is in breakthrough infections. One Facebook poll of about 1,950 fully vaccinated people found 44 breakthrough cases, 24 of whom reported long-COVID symptoms. The survey was done by the long-COVID patient-advocacy group Survivor Corps, and the results are reported in a preprint⁴. But because the poll was not a random sampling of people, the findings cannot be used to estimate the rate of long COVID after vaccination — they show only that such cases exist.

Another study in Israel, of around 1,500 vaccinated health-care workers, found that 7 (19%) of the 39 breakthrough infections produced symptoms that lingered for more than 6 weeks⁵. However, the numbers of infections studied are too small for firm conclusions to be drawn about the absolute risk.

One of the largest studies so far has gathered data from 1.2 million people who received at least one dose of a COVID-19 vaccine and logged their experience in the COVID Symptom Study app, which was developed by the London-based data-science company ZOE and King's College London¹. The team found that a full two-dose regimen of vaccination reduced the risk of long COVID — as defined by persistent symptoms for at least 28 days after infection — by about half among those who had breakthrough infections. But the study contained disproportionately more women than men and fewer people from lower-income areas.

Still, the message is clear, says Claire Steves, a geriatrician at King's College London and lead author of the study. Vaccination considerably reduces infection rates and the severity of symptoms: even with waning immunity and the emergence of the more-infectious Delta variant. One study of US veterans found that the COVID-19 vaccines for that group offered about 50% protection against coronavirus infection, even during the Delta surge⁶. Steves and her colleagues found that vaccination then further reduces the risk of long COVID in those who develop a breakthrough infection by another half: about 11% in the unvaccinated group had persistent symptoms for at least 28 days compared with about 5% in the vaccinated group of breakthrough infections¹. Even so, the number of people who developed

long COVID from breakthrough infections is significant, she says. “It does still exist — we do still have to be aware that’s the case.”



A COVID-19 vaccination centre inside a department store in Moscow, Russia.Credit: Andrey Rudakov/Bloomberg via Getty

Another large study² — which has not yet been peer reviewed — suggests that the situation could be worse: a retrospective analysis of electronic health records from about 10,000 people with breakthrough infections found vaccination did not protect against several conditions associated with long COVID. That group was compared with a control group of people with confirmed SARS-CoV-2 infections who had not been vaccinated against COVID-19, but who had received an influenza vaccine. Differences in how the two studies were designed could account for the different results generated by this work and the COVID Symptom Study, says Maxime Taquet, a psychiatrist and researcher at the University of Oxford, UK, who is first author of the health-records analysis². For example, Taquet’s study tried to account for potential lifestyle differences between those who received the COVID-19 vaccine and those who did not by including the control group.

However, because his study relied on health records, it might not include data for people with milder symptoms that would not have warranted a consultation with a physician.

Overall, Iwasaki has found the results of these studies disappointing. “I honestly thought the vaccine would protect against long COVID much more extensively,” she says. Iwasaki proposes that Delta — which is more transmissible than other variants are — might have weakened the vaccines’ protection against long COVID. If people infected with Delta breathe out a great number of infectious particles, as is thought, the infections that they pass on will have higher initial amounts of virus. That could allow Delta to replicate more readily than other variants, even in fully vaccinated people, says Iwasaki. This higher dose could give the virus a better opportunity to establish a reservoir or provoke an overactive immune response, either of which might then lead to long COVID, she suggests.

As vaccination programmes continue, researchers will gain a better sense of how vaccines and variants affect long-COVID rates and severity. It’s also possible that vaccination might help to reduce long COVID in those who already have the condition. In October, the UK Office for National Statistics, which is collecting data on long COVID, reported that the first dose of a COVID-19 vaccine was associated with a 13% decrease in self-reported long-COVID symptoms among those who already had the condition. The second dose yielded a further 9% drop relative to the first⁷.



COVID vaccines cut the risk of transmitting Delta — but not for long

The study followed people for only about two months, so it's unclear how long the effects will last, says Iwasaki, who has been studying how vaccination affects long-COVID symptoms. But it is largely in line with other findings, she adds. One survey conducted by Survivor Corps found that about 40% of respondents with long COVID reported an improvement in their symptoms after vaccination. Another 14%, however, said that their symptoms got worse.⁸

The US Centers for Disease Control and Prevention is not tracking mild COVID-19 breakthrough illnesses, and so might miss many cases that lead to long COVID. However, last December, the US Congress allocated the NIH \$1.15 billion over 4 years to study the long-term health consequences of SARS-CoV-2 infections; in June, the NIH granted the first awards for a long-COVID research programme called RECOVER. This aims to enrol tens of thousands of people — including those with or without long COVID after acute coronavirus infection, and those who have not been infected — and track their symptoms. One of the main goals is to learn more about the pathology of long COVID and to better define the condition.

Over the course of that study, the RECOVER team should also be able to generate data on rates of long COVID among those who are vaccinated. Other useful information should include the severity, duration and nature of a person's symptoms and, when possible, the coronavirus variant responsible for their illness, says cardiologist Stuart Katz at New York University, a lead investigator on the programme who has also experienced long COVID. "We are enrolling people and recording the history of vaccination," says Katz. "But, of course, a big challenge for any research in this space is that we don't yet really have a definition of what long COVID is."

The team hopes to finish enrolment in the programme's first year — a speedy pace for such a large initiative, but still painfully slow given the pressing need to improve treatments for long COVID, says Iwasaki.

RECOVER will also collect data on vaccinated children and adolescents — an important gap in currently published studies, and one that will be easier to fill as vaccines are rolled out to young people in several countries. One

study⁹ of more than 6,700 adolescents found that about 30% of those who tested positive for SARS-CoV-2 had 3 or more symptoms 3 months after diagnosis, compared with 16% of those in a control group that tested negative. The findings from the control group, a factor not included in most other such studies in this age group, bring the rate of long COVID down below some other estimates for adolescents, but means that it is still comparable to the rate seen in adults, says paediatrician Terence Stephenson at University College London. “It’s not the tsunami that perhaps was envisaged,” he says. “But neither is it trivial.”

And while the data trickle in, Alwan worries that countries with high vaccine coverage will put COVID-19 testing on the back burner as concerns about hospitalizations and deaths decrease and as more people receive boosters. That not only hurts efforts to determine the influence of vaccination on long COVID, but also means that those with long COVID after a mild or asymptomatic infection might not have the documentation they need for treatment. “It’s important to get that lab confirmation for care,” she says. “Otherwise, people struggle a lot.”

Nature **599**, 546-548 (2021)

doi: <https://doi.org/10.1038/d41586-021-03495-2>

References

1. 1.

Antonelli, M. *et al. Lancet Infect. Dis.* [https://doi.org/10.1016/S1473-3099\(21\)00460-6](https://doi.org/10.1016/S1473-3099(21)00460-6) (2021).

2. 2.

Taquet, M., Dercon, Q. & Harrison, P. J. Preprint at medRxiv <https://doi.org/10.1101/2021.10.26.21265508> (2021).

3. 3.

Office for National Statistics. *Updated estimates of the prevalence of post-acute symptoms among people with coronavirus (COVID-19) in the UK: 16 September 2021* (ONS, 2021).

4. 4.

Massey, D., Berrent, D. & Krumholz, H. Preprint at medRxiv
<https://doi.org/10.1101/2021.07.23.21261030> (2021).

5. 5.

Bergwerk, M. *et al.* *N. Engl. J. Med.* **385**, 1474–1484 (2021).

6. 6.

Cohn, B. A., Cirillo, P. M., Murphy, C. C., Krigbaum, N. Y. & Wallace, A. W. *Science* <https://doi.org/10.1126/science.abm0620> (2021).

7. 7.

Office for National Statistics. *Coronavirus (COVID-19) vaccination and self-reported long COVID in the UK: 25 October 2021* (ONS, 2021).

8. 8.

Massey, D. *et al.* Preprint at medRxiv
<https://doi.org/10.1101/2021.07.21.21260391> (2021).

9. 9.

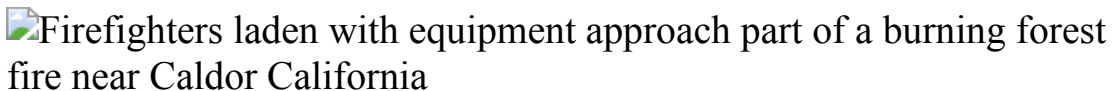
Stephenson, T. *et al.* Preprint at Research Square
<https://doi.org/10.21203/rs.3.rs-798316/v1> (2021).

- NEWS FEATURE
- 24 November 2021

How record wildfires are harming human health

As fires get bigger and rage for more of the year, scientists are racing to understand the lingering impacts.

- [Max Kozlov](#)



Firefighters battle the Caldor wildfire in California in August. Credit: Michael Nigro/Pacific Press/ZUMA/eyevine

On a cool September morning in San Francisco, a group of firefighters packed their gear into a bright red van. The sickly sweet odour of pine resin from a distant blaze hung in the air as the crew prepared to battle the rapidly growing Dixie fire, on its way towards becoming the largest single wildfire in California's history. Sweeping across the Sierra Nevada mountains, it would come to scorch more than 3,900 square kilometres before crews fully contained it in late October.

The firefighters had one more stop before they joined the thousands of other people working to control the blaze. In a small classroom inside the San Francisco Fire Department's training building in the Mission District, Mary Prunicki and a team of researchers collected questionnaires and blood samples from each firefighter.

Prunicki, a pollution biologist at nearby Stanford University, will use the samples as a baseline to compare with ones taken when the firefighters

return. She'll be looking for signs of their bodies' reaction to the smoke, including inflammation and changes to immune and heart function.

Smoke from wildfires is responsible for tens to hundreds of thousands of premature deaths around the world each year. And Prunicki is one of hundreds of researchers trying to understand the health effects of smoke exposure. Scientists want to know what it is in wildfire smoke that makes it more harmful to humans than other forms of pollution. They are looking at short-term and long-term effects; who is most vulnerable to the pollutants; and how best to keep people safe and healthy in smoke plumes that can stretch for thousands of kilometres from a blaze such as the Dixie fire.



Australian bush fires belched out immense quantity of carbon

The work has taken on fresh urgency in recent years. Climate change has been exacerbating droughts and heatwaves around the world, nearly doubling the total area where the right spark could set dry vegetation ablaze and trigger an inferno. As a result, wildfires are increasing in frequency, size and intensity around the world, and smoke seasons are getting longer.

Wildfires have ravaged the western United States in the past decade, but other countries have also faced their worst blazes in generations. Fires in the Siberia region of Russia this year burnt a bigger area than all the world's other blazes combined. And Australia is still reeling from its devastating 2019–20 bush-fire season — colloquially called the 'black summer' —

which destroyed thousands of homes and killed at least 30 people and hundreds of millions of animals.

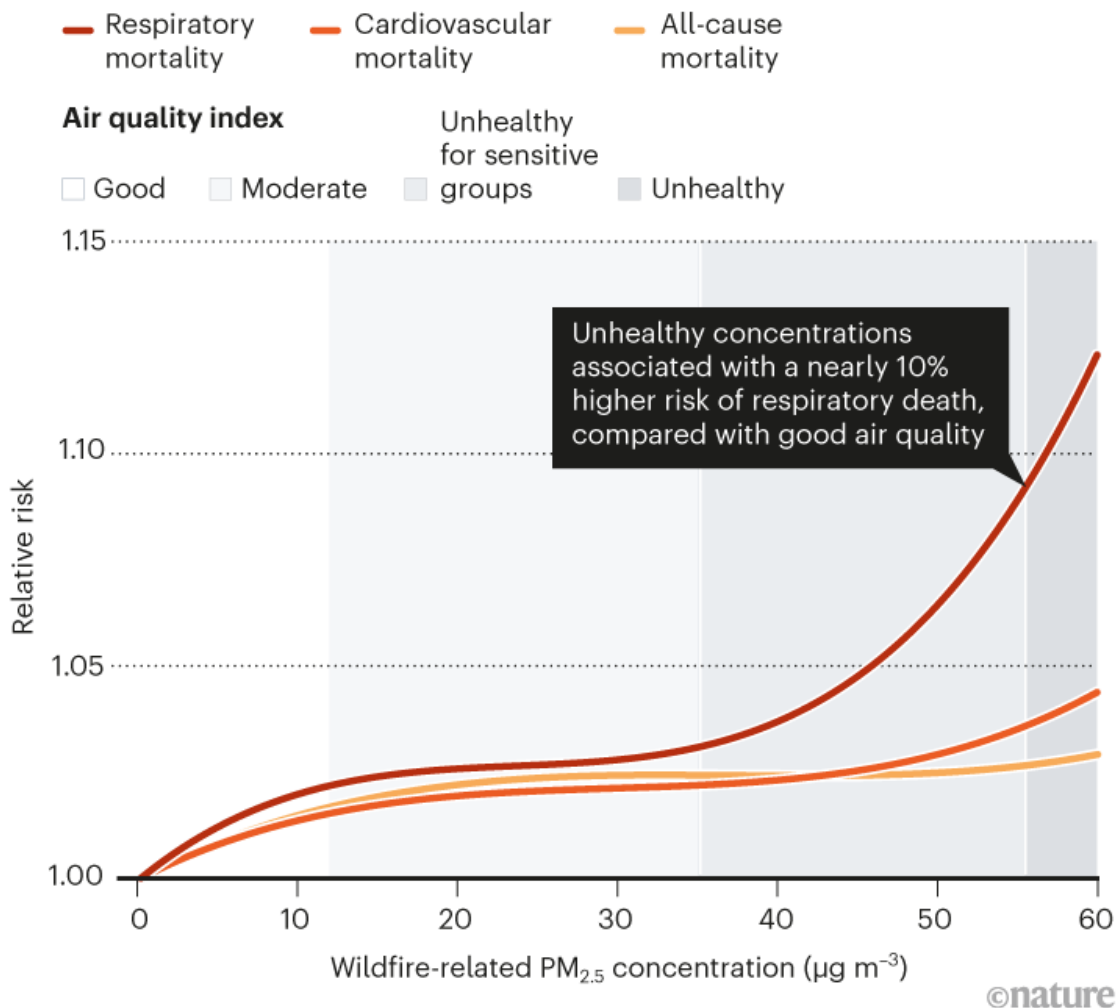
“If you compare the last 5 years to the 10 to 15 years before that, it’s just not really comparable,” says Sam Heft-Neal, an environmental economist at Stanford University who studies the health risks of wildfires. “It’s like a totally different fire regime.”

A toxic mix

Wildfire smoke contains dozens of different particles, such as soot, and chemicals, such as carbon monoxide, but one of the main concerns for air-quality specialists are the tiniest particles in smoke that measure 2.5 micrometres or less across (on average 1/40th the width of a human hair). The firefighters working with Prunicki will encounter copious amounts of this PM_{2.5}, as it is known. But according to Francesca Dominici, a biostatistician at the Harvard T. H. Chan School of Public Health in Boston, Massachusetts, there is no amount of fine particulate matter that is safe to breathe because it is known to penetrate deep into the smallest crevices of the lungs and enter the bloodstream (see ‘Risky exposures’).

RISKY EXPOSURES

An analysis of more than 65 million deaths in 43 countries found an increased risk of death from all causes soon after exposure to particulates ($\text{PM}_{2.5}$) from wildfire smoke.



Source: G. Chen *et al. Lancet Planet. Health* **5**, E579–E587 (2021).

When smoke enters the airway, the body reacts “like there’s germs and infection in there”, says Fay Johnston, an environmental epidemiologist at the University of Tasmania in Hobart, Australia. That comes with a whole suite of physiological changes: the hormone cortisol and blood glucose spike, which in turn makes heart rhythms less stable and blood more likely to clot. The lining of the lungs becomes inflamed, making it more difficult to breathe.

Prunicki hopes to understand these physiological changes by measuring certain biomarkers — molecules in the blood — that can give a snapshot of immune, respiratory and cardiovascular function. She has turned to firefighters, people who face high occupational exposure to smoke, to see whether she can detect any changes in their biomarkers after direct exposure — and whether the changes are long-lasting or similar to those seen in people who don't fight fires but are still subjected to smoke. Close to a fire, PM_{2.5} can sometimes reach levels more than 15 times greater than the 24-hour exposure standard of 35 micrograms per cubic metre set by the US Environmental Protection Agency (EPA). But many firefighters don't wear respirators when they are battling blazes because they can be cumbersome, says Prunicki. "This level is outrageously high," says Dominici. "At that point, you're just breathing a toxic soup."



'Apocalyptic' fires are ravaging the world's largest tropical wetland

But even lower levels might pose a severe health risk, she says, because in such conditions people are less likely to take protective measures such as wearing a respirator. Prunicki has shown that, even in areas more than 100 km away from wildfires, smoke exposure is linked to a slew of changes in biomarkers that might be a sign of immune and cardiovascular dysfunction¹.

Wildfires don't happen in a bubble, either, says Dominici. Smoke can predispose people to infectious diseases or exacerbate the symptoms of other

respiratory conditions, including COVID-19 and influenza. Dominici and her colleagues estimate that increased PM_{2.5} levels during the 2020 fire season in Washington, California and Oregon correlated with about an extra 19,700 COVID-19 cases and 750 deaths².

The leading hypothesis for the cause of the excess cases is that PM_{2.5} compromises the immune system and causes inflammation, which could make people more susceptible to infection or exacerbate the effects of disease, leading to a rise in positive diagnoses. A more controversial take, says Dominici, is that some respiratory viruses might hitch a ride on fine particulate matter when entering lung tissue.

Underlying health conditions pose another problem, says Johnston, especially if smoke is affecting millions of people at once, as it did during Australia's black summer. Her team reported that those fires led to an excess of thousands of hospitalizations and hundreds of deaths from heart and respiratory problems stemming from the smoke, which blanketed nearly 80% of the country's population³.



Smoke from Australian bushfires during the summer of 2019–20 led to thousands of additional hospitalizations and hundreds of excess deaths. Credit Matthew Abbott/Panos

On high-smoke days, hospital-admissions data show an increase in the number of people being admitted with cardiovascular and respiratory problems and diabetes, particularly children and older people. Pregnant people might also be at higher risk of having gestational diabetes, high blood pressure or giving birth to low-weight babies: Heft-Neal's research estimates that nearly 7,000 excess premature births in California between 2007 and 2012 can be attributed to wildfire smoke exposure during pregnancy⁴.

Socio-economic status, too, cannot be overlooked, says Dominici. People in under-resourced communities are more likely to have outdoor occupations, such as farming or landscaping, higher rates of accompanying diseases and conditions and less access to adequate health care and air purifiers — all of which make wildfires an even greater burden for communities of colour and low-income communities, she says.

Long-term effects

Studying the long-term health effects of smoke on humans has proved difficult. Longitudinal studies to track people's health after exposure would need to span decades and distinguish between the effects of many different environmental exposures.

In 2008, Lisa Miller, a respiratory immunologist at the University of California, Davis, had a useful, if unfortunate, opportunity to observe long-term effects in a controlled population. She had been working with a troop of rhesus macaques (*Macaca mulatta*) to study allergies and asthma when a bad fire season hit northern California. Twenty-five newborn macaques, housed outside, were exposed to ten days of ambient PM_{2.5} levels above federal guidelines. Miller has been monitoring their health — and that of their offspring — ever since.



Bush-fire smoke linked to hundreds of deaths

Compared with macaques born the following year, the 2008 group had a reduced immune response and decreased lung capacity. In a study that is not yet published, Miller and her colleagues scanned the lungs of these monkeys and found that the tissue had stiffened in a way that might change how the animals move around and breathe to compensate for the reduced respiratory function.

Miller says these data offer some tantalizing hints about the long-term toxicity of wildfire smoke on respiratory and immunological function in humans: “We know it’s bad,” she says.

Still, the work has caveats, Miller says. The experiment is controlled because the researchers know the whereabouts of the animals at all times, but most people do not experience round-the-clock outdoor exposure, and humans might react to smoke differently from macaques.

Indoors or outdoors

Scientists are still trying to pin down the extent of people’s wildfire smoke exposure in different settings. Only in the past few years have researchers applied machine-learning techniques to meteorological models and high-

quality satellite data to try to predict how smoke moves through the atmosphere. And household air-quality sensors offer researchers a deluge of real-time data with which to track PM_{2.5} levels more precisely.

But scientists are running out of comparator groups, says Miller. Because poor air quality is so ubiquitous today — more than 90% of children around the world breathe air laden with PM_{2.5} levels above World Health Organization guidelines — the number of unexposed humans or other primates in long-term studies is dwindling, making research all the more pressing, she says.

The next key area of research, Miller says, will be to understand exactly which chemicals in wildfire smoke make it more dangerous to respiratory health than other types of pollution, and how those interact with and harm human cells. “We’ve been burning wood in our fireplaces since the dawn of time,” she says. “It’s not just the combustion of biomass, it’s the combustion of man-made materials with that biomass.”



Fog and smoke from nearby wildfires lent an eerie hue to the San Francisco skyline in September 2020.Credit: David Paul Morris/Bloomberg/Getty

Other important questions involve how well smoke infiltrates indoor spaces, says Heft-Neal. Public-health officials generally recommend that high-risk groups stay indoors and shut all doors and windows during days with poor air quality. But these recommendations are “very generic and not nuanced”, says Johnston, who adds that the advice isn’t especially helpful in Australia, where housing doesn’t tend to be very well insulated.

Preliminary research in California households with indoor air monitors shows that, although indoor air contained less than half the concentration of fine particulates found outdoors, indoor PM_{2.5} levels nearly triple during wildfire events, often surpassing the EPA’s 24-hour PM_{2.5} exposure standard⁵. Still, infiltration rates are likely to differ from house to house, and Heft-Neal says it will be crucial to understand the types of housing structure best suited to protecting against air pollution.

Colleen Reid, a health geographer at the University of Colorado Boulder, is investigating air quality in schools. These are crucial sites, given that children generally seem to be more vulnerable to wildfire smoke than adults. She and her colleagues plan to study the air quality inside and outside school buildings in Colorado and compare it with that at pupils’ homes.



Climate change made North America's deadly heatwave 150 times more likely

The current public-health guidance in the United States leaves it up to individual school districts to determine whether to stay open during air-pollution events, depending on whether the air quality is better in the schools or at home, Reid says. “But nobody actually has any of that data,” she adds.

She says this research could help local authorities to determine whether to establish ‘clean air shelters’, where people could access purified air. Schools could provide clean air to pupils during the day and to the community when classes aren’t in session, Reid says.

More indoor and community-level air-quality sensors will help with these public-health recommendations. So, too, will personal monitoring, Prunicki says, particularly for those who, like her firefighter volunteers, are being heavily exposed. Using her research on cardiovascular and immunological biomarkers, Prunicki envisages a day when firefighters and other vulnerable populations could take a simple blood test to see whether they’ve reached a dangerous level of lifetime smoke exposure, and should take extra precautions to avoid continued contact. “Just like X-ray technicians wear the X-ray badges to see how much cumulative exposure they’ve had, why can’t we do that with smoke?” she says.

But, Johnston says, however essential it is to understand the intricacies of how smoke harms the human body and people’s risk levels, that research doesn’t address the root of the problem — climate change.

“We could have all the research in the world that tells you to take an anti-inflammatory or use a subsidized HEPA filter, but we’re gonna be going backwards until we actually address the fundamental underlying problem,” she says of climate change. “We’re on a terrible trajectory right now.”

Climate modellers predict that the [kinds of fire that charred California](#) and Russia this year are just the beginning. The area burnt in California each year, for example, will increase by 77% by the end of the century if greenhouse-gas emissions continue to rise, according to the state’s 2018

climate-change assessment. Researchers and policymakers alike are scrambling to avert these nightmare scenarios.

Current predictions show that rising emissions would be linked to an enormous health-care burden, with potentially millions of people having reduced respiratory, cardiovascular and immunological function — especially in high-risk communities. The health cost associated with premature death and hospital admission from Australia's black summer, for example, is estimated at Aus\$2 billion (US\$1.47 billion) — about 10 times higher than that of previous years, says Johnston.

In the meantime, scientists are continuing to piece together the risks of exposure. Front-line workers are willing to take part in the research, but they worry about learning the answers. As the firefighters pack into the van bound for the Dixie fire, the driver, lieutenant Ken Smith, is opening his door and starting to climb inside when he stops.

"We don't think about what's in the smoke," he says. "If we knew what we breathe in while we work, we couldn't do it."

Nature **599**, 550–552 (2021)

doi: <https://doi.org/10.1038/d41586-021-03496-1>

References

1. 1.

Prunicki, M. M. *et al. Allergy* **74**, 1989–1991 (2019).

2. 2.

Zhou, X. *et al. Sci. Adv.* **7**, eabi8789 (2021).

3. 3.

Borchers Arriagada, N. *et al. Med. J. Aust.*
<https://doi.org/10.5694/mja2.50545> (2020).

4. 4.

Heft-Neal, S. *et al. Environ. Res.* **203**, 111872 (2022).

5. 5.

Liang, Y. *et al. Proc. Natl Acad. Sci. USA* **118**, e2106478118 (2021).

This article was downloaded by **calibre** from <https://www.nature.com/articles/d41586-021-03496-1>

| [Section menu](#) | [Main menu](#) |

Books & Arts

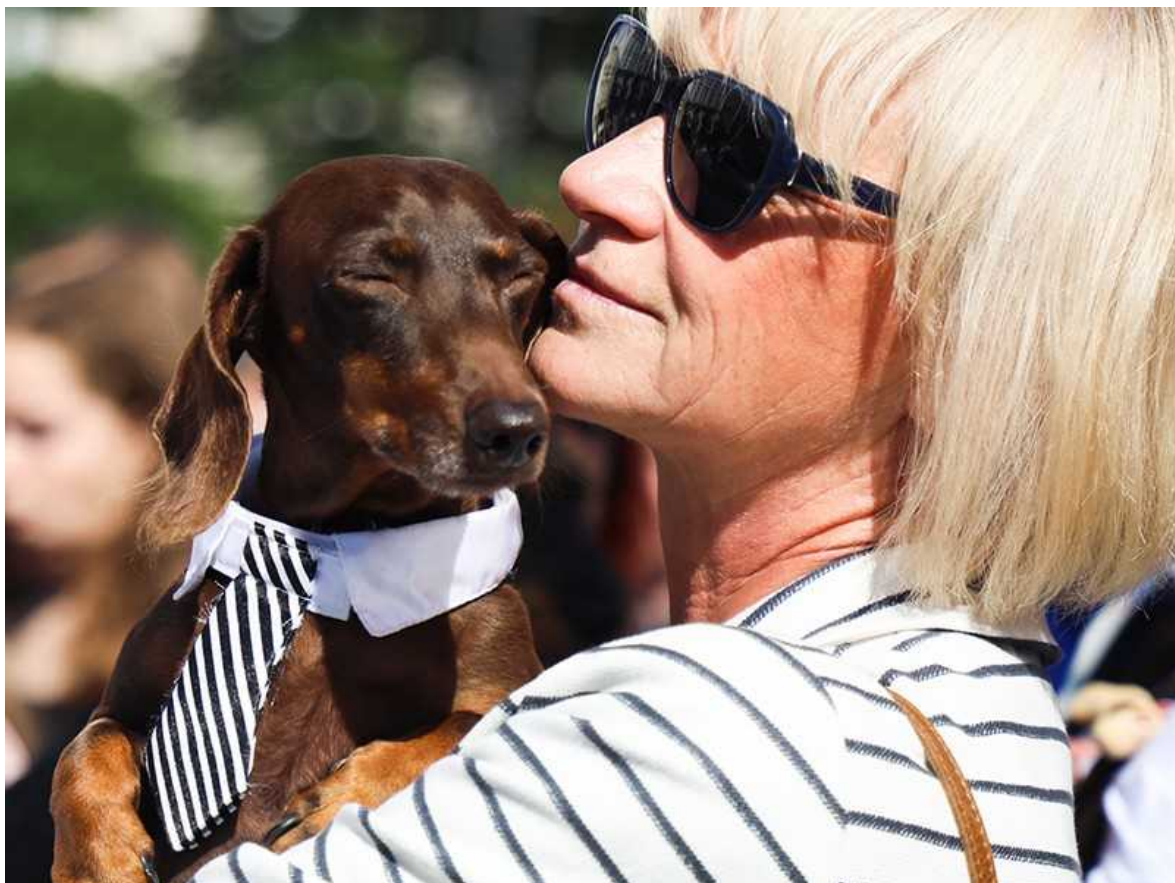
- **[How dogs became humans' best friends: from Neanderthals to now](#)** [22 November 2021]
Book Review • A lively tale of evolution, domestication, migration and fellowship.
- **[The power of poo, and what to expect from robots: Books in brief](#)** [05 November 2021]
Book Review • Andrew Robinson reviews five of the week's best science picks.

- BOOK REVIEW
- 22 November 2021

How dogs became humans' best friends: from Neanderthals to now

A lively tale of evolution, domestication, migration and fellowship.

- [Josie Glausiusz](#) 0



Dogs and humans: a partnership tens of thousands of years in the making. Credit: Beata Zawrzela/NurPhoto/Getty

Our Oldest Companions: The Story of the First Dogs *Pat Shipman* Belknap (2021)

Several years ago, strolling through Washington Square Park in New York City, I found myself surrounded by hundreds of dachshunds with their human partners. Some were even dressed as hot dogs. I had stumbled on Dachshund Day, an annual event.

Short-legged and long-bodied, the dachshund seems eons away in shape and lifestyle from its ancestor, the grey wolf (*Canis lupus*). Yet domestic dogs differ from their wild forebears by, at most, 0.2% of their mitochondrial DNA sequence. So relates palaeoanthropologist Pat Shipman in her lively tale of dog domestication and migration, *Our Oldest Companions*.

Unlike wolves, dachshunds — originally bred in Germany to hunt badgers — are keen to be part of, and communicate with, a group that includes humans. All domesticated dogs exhibit such traits: they are our companions, protectors, playmates, herders, blankets and hunting aids, Shipman writes.



[Horse eyeballs and bone hammers: surprising lives of Neanderthals](#)

Dogs were the earliest animal to be domesticated. But when and why did they become our fellow travellers? That question is at the heart of Shipman's narrative, a round-the-world and back-in-time journey to the era when *Homo*

sapiens first encountered Neanderthals in ice-age Europe, one of the most likely locales for early dog domestication. Neanderthals never domesticated dogs, but they did hunt the same animals as European wolves, mostly medium- to large-sized herbivores, including deer.

When *Homo sapiens*, travelling out of Africa, reached Europe between 50,000 and 40,000 years ago, they encountered — and bred with — Neanderthals. *Homo sapiens* gained the advantage, Shipman claims, by forging a “long-term, mutually beneficial partnership with canids” to hunt bigger prey, which might have helped to drive the extinction of Neanderthals. She concedes that not everyone agrees with this hypothesis.

Skill share

By cooperating with dogs, and living intimately with them, humans were able to capitalize on the animals’ abilities, “such as a keen sense of smell, the stamina to run swiftly and nearly tirelessly after potential prey, and good eyesight”, Shipman writes. She hypothesizes that, perhaps 36,000 years ago, animals that she calls wolf-dogs — not yet fully resembling modern dogs, but no longer wolves — became our companions. The collaboration offered mutual benefits: wolf-dogs could find, surround and hold a mammoth until humans could spear it; humans could protect wolf-dogs from local, wild wolf packs.

Mietje Germonpré, an archaeozoologist at the Royal Belgian Institute of Natural Sciences in Brussels, has found skulls, jaws and sharp teeth of canids at archaeological sites in Belgium, the Czech Republic and Russia that date to as far back as 36,000 years ago. But such dates for domestication are highly contested, and these “protodogs” might represent subspecies of the grey wolf. A period around 16,000 years ago is the more widely accepted time frame for dog domestication. However, “there is no single anatomical trait that can distinguish a dog from a wolf with certainty”, Shipman writes.



Marauding elephants, menacing macaques and epicurean bears

Instead, researchers rely on subtle variations in mitochondrial DNA, dietary changes (detected in ancient bones) and cultural shifts, such as the burial of dogs alongside humans, most famously at the 14,000-year-old site of Bonn-Oberkassel in Germany. In 2018, analysis of a tooth found in the grave indicated that humans had cared for a sick puppy for weeks before it died ([L. Janssens et al. *J. Archaeol. Sci.* 92, 126–138; 2018](#)).

There are some mysterious gaps in the narrative. By at least 55,000 years ago, the first Australians had navigated open seas in boats to reach the super-continent of Sahul, or Greater Australia (comprising Australia, New Guinea and Tasmania, which were one land mass when sea levels were lower).

These travellers were dogless. Instead of partnering with canids to pursue prey, Shipman posits, they fished and gathered shellfish, or hunted small marsupial animals and birds so fearless of humans that they were easy to capture. Dingoes were brought to Australia by boat about 5,000 years ago, after which Indigenous Australians did form bonds with them. They raised dingo pups as pets and treated them as companions and guardians against humans or supernatural beings.

Global range

None of the earliest Americans, who migrated to North America from Siberia across the land mass of Beringia, were associated with canids, either. An 18,000-year-old puppy, dubbed Dogor ('friend' in the Yakut language), that emerged from melting Siberian permafrost in 2018 could have been an ancestor of dogs or wolves. But the earliest trace of a dog in North America, a fragment of femur from Alaska, is just 10,000 years old.

The Mexican Chihuahua might be descended directly from dogs that lived in the region before the arrival of Europeans, but in South America, wild canines such as the rare bush dog (*Speothos venaticus*) remained untamed. Horrifyingly, conquistadors trained Spanish mastiffs to chase and kill Indigenous peoples of South America. Yet Shipman writes that Indigenous peoples later eagerly adopted European dogs and formed close bonds with them.

As I followed Shipman on her journey, I began to understand why the fellowship of dachshunds — or poodles or pugs or chihuahuas — is one of partnership, not ownership. The companionship of dogs has been shown to ameliorate mental and physical disabilities, and reduce anxiety associated with ageing, loneliness, autism and post-traumatic stress disorder. Perhaps, as Shipman concludes, that is because dogs' friendship and protection have helped us to survive and thrive, together, for millennia.

Nature **599**, 553-554 (2021)

doi: <https://doi.org/10.1038/d41586-021-03497-0>

This article was downloaded by **calibre** from <https://www.nature.com/articles/d41586-021-03497-0>

- BOOK REVIEW
- 05 November 2021

The power of poo, and what to expect from robots: Books in brief

Andrew Robinson reviews five of the week's best science picks.

- [Andrew Robinson](#) 0

THE OTHER DARK MATTER

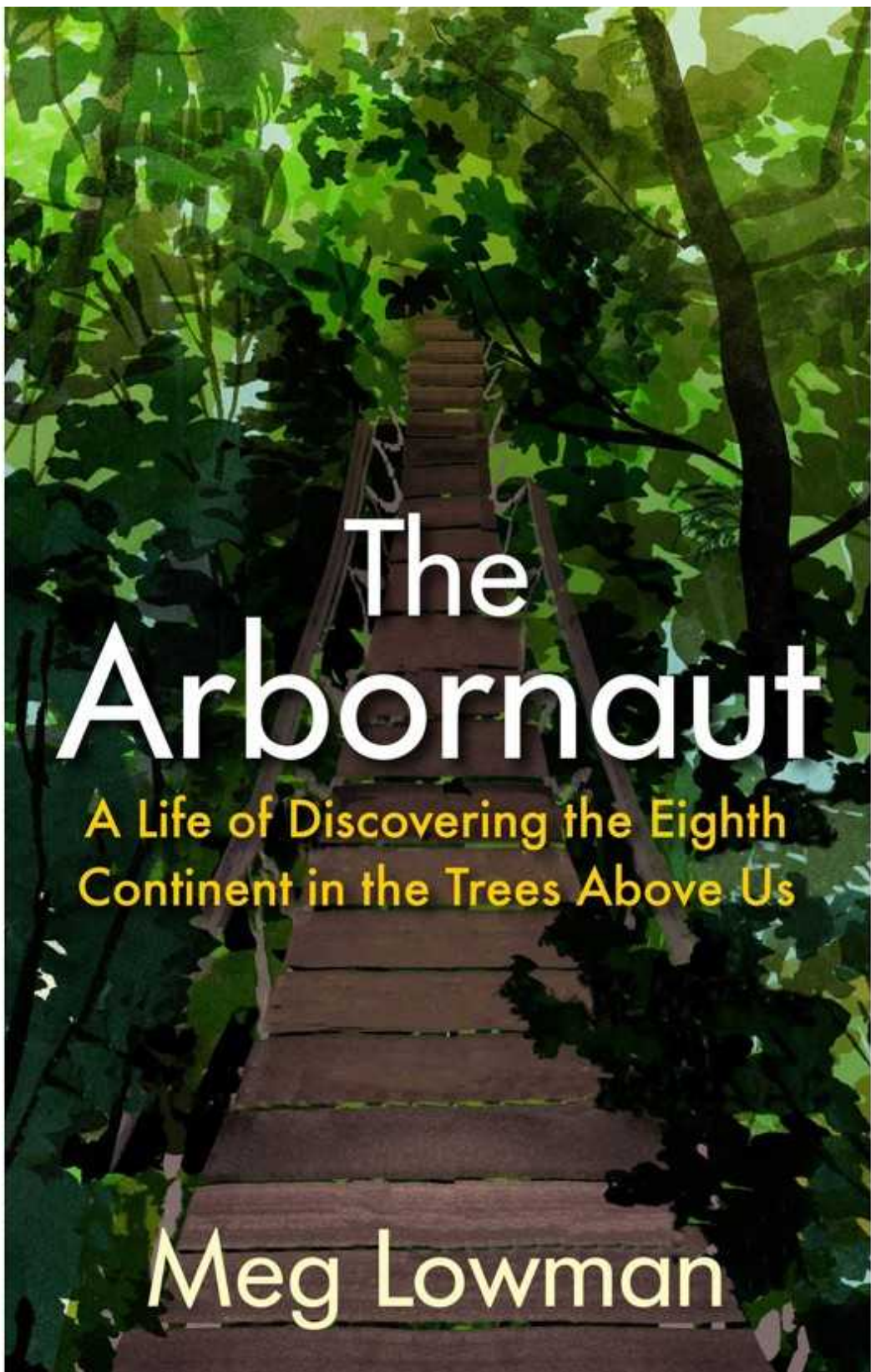
THE SCIENCE
AND BUSINESS
OF TURNING
WASTE INTO
WEALTH AND
HEALTH

LINA ZELDOVICH

The Other Dark Matter

Lina Zeldovich *Univ. Chicago Press* (2021)

Sewage is the subject of this original, necessary book, which several publishing houses rejected because of the “yuck factor”, notes journalist Lina Zeldovich. Her lifelong interest stems from her scientifically trained Russian grandfather, who annually recycled the family’s septic tank onto their farm, treating the contents as *dobró* — ‘rich’. Zeldovich describes a growing global awareness of how human waste can become sustainable energy source, organic fertilizer and medical therapy.



The Arbornaut

Meg Lowman *Allen & Unwin* (2021)

For centuries, the health of trees — even the tallest — was assessed at eye level. Today, more than half of terrestrial creatures are known to live 30 metres or more above our heads, notes tree-climbing biologist Meg Lowman, an “arbornaut” since the 1970s. Her wonderfully informative and evocative memoir explores the “eighth continent” of tree canopies from ropes and walkways, cherry pickers, hot-air balloons, cranes and drones. Her project Mission Green aims to conserve high-biodiversity canopies through local forest stewardship.

RULE OF THE ROBOTS

HOW ARTIFICIAL
INTELLIGENCE
WILL TRANSFORM
EVERYTHING

MARTIN FORD

AUTHOR OF THE NEW YORK TIMES
BESTSELLER *RISE OF THE ROBOTS*

Rule of the Robots

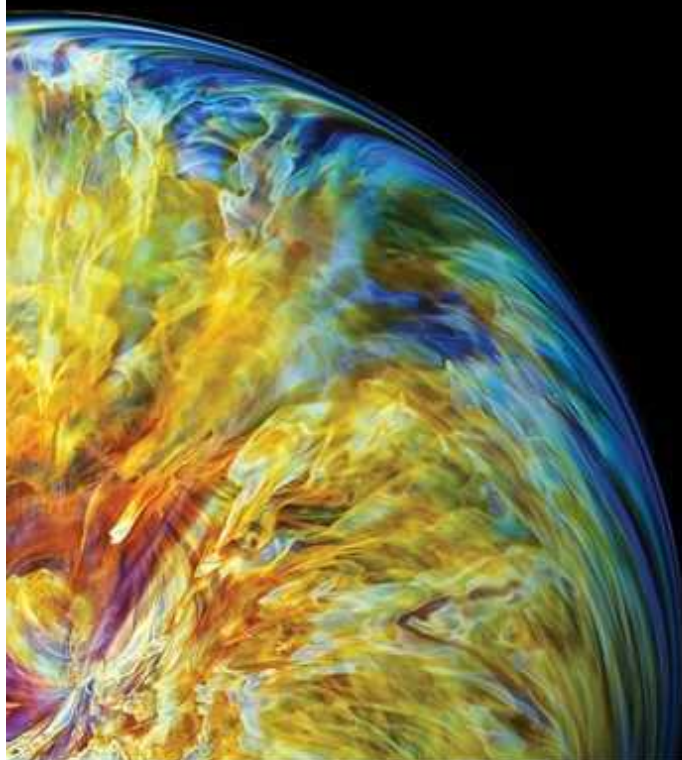
Martin Ford *Basic* (2021)

According to software developer Martin Ford, artificial intelligence (AI) will probably transform society faster than electricity did, but with unpredictable effects. His well-informed study notes a 2016 forecast that within five years, radiologists would be overtaken by advances in AI. But that hasn't happened: AI cannot currently integrate key information from sources such as clinical notes. AI's future, Ford concludes, lies somewhere between the science-fictional extremes of utopian *Star Trek* and dystopian *The Matrix*.

Into the Anthropocosmos

A Whole Space Catalog from the
MIT Space Exploration Initiative

Ariel Ekblaw
Foreword by Cady Coleman



Into the Anthropocosmos

Ariel Ekblaw (Ed.) *MIT Press* (2021)

This lavishly illustrated book chronicles the MIT Space Exploration Initiative, founded by Ariel Ekblaw, which develops tools and projects “to truly make space for everyone” says astronaut Cady Coleman’s foreword. Ekblaw says the project is “grounded” in the *Earthrise* image taken by Apollo 8, reinforcing humanity’s responsibilities as citizens of the planet. The space experiments depicted range from biology and engineering to cookery and music, including social robots to relieve astronauts’ isolation.

THE MAN FROM THE FUTURE



The
Life of

Visionary

John von
Neumann

By ANANYO

BHATTACHARYA

allen lane

The Man from the Future

Ananyo Bhattacharya *Allen Lane* (2021)

Hungarian-born mathematician John von Neumann influenced many fields. In 1927–32, he helped to found quantum mechanics. During the Second World War, he was key to the atomic-bomb effort. Later, he co-designed the first programmable electronic digital computer, was an AI visionary and introduced game theory into political science, military strategy, psychology and evolutionary biology. Excellent on the science, Ananyo Bhattacharya's ambitious biography struggles to portray the conflicted human.

Nature **599**, 554 (2021)

doi: <https://doi.org/10.1038/d41586-021-03067-4>

This article was downloaded by **calibre** from <https://www.nature.com/articles/d41586-021-03067-4>

| [Section menu](#) | [Main menu](#) |

Opinion

- **[Michael Rutter \(1933–2021\)](#)** [22 November 2021]
Obituary • Child psychiatrist who transformed understanding of autism.
- **[Science community steps up to reform open access](#)** [23 November 2021]
Correspondence •
- **[Ahmedabad: local data beat the heat](#)** [23 November 2021]
Correspondence •
- **[Support deaf participants at virtual conferences](#)** [23 November 2021]
Correspondence •
- **[Ditch gendered terminology for cell division](#)** [23 November 2021]
Correspondence •

- OBITUARY
- 22 November 2021

Michael Rutter (1933–2021)

Child psychiatrist who transformed understanding of autism.

- [Uta Frith](#) ⁰ &
- [Francesca Happé](#) ¹



Credit: Corbin O'Grady Studio/SPL

Michael (Mike) Rutter turned child psychiatry from an incoherent set of theories and practices into a rigorous and humane discipline. His work provided the first evidence that autism, now one of the most active areas of research in neurodevelopmental disorders, had a genetic basis. The discovery created the momentum for large-scale population studies using genetically sensitive designs, and for constant improvements in methodology and technology. His 1972 book, *Maternal Deprivation Reassessed*, countered prevailing views that inadequate mothering was the principal cause of psychiatric problems in children and thereby effectively liberated future generations of working mothers.

During the 1990s, thousands of orphans who had experienced extreme deprivation in Romanian institutions were adopted into UK family homes, giving Rutter an opportunity to address the nature-or-nurture question. He personally interviewed the children as they grew up; many showed a remarkable recovery. This supported his theory and previous work on resilience without downplaying the long-term consequences of early neglect in childhood.

Michael Llewellyn Rutter was born in 1933 in Lebanon, where his father was a doctor. Having moved to England, in 1940 his parents sent the seven-year-old Mike and his sister to live with foster families in North America for four years, fearing a German invasion. Rutter spoke fondly about his foster family and denied any link between being fostered and his work on maternal attachment. He trained in medicine at the University of Birmingham, UK, and at the Maudsley Hospital in London.



Seeing the spectrum entire

At what was then the hospital's Institute of Psychiatry, Rutter's interest in child psychology and psychiatry was encouraged. He began to question some of the vague ideas about child development that had been largely influenced by psychoanalysis. Unlike most clinicians at the time, he adopted rigorous empirical methods and compared groups of children to probe possible causes of behavioural and educational problems. This anticipated his later search for genetic and other biological causes of developmental and psychiatric disorders. His interests spanned a variety of conditions, including dyslexia, attention deficit hyperactivity disorder and autism. The diagnostic criteria and interview protocols now used to diagnose autism were developed under Rutter's authoritative guidance.

In the 1960s and 1970s, mothers were widely blamed for causing their child's autism. Rutter had the idea of studying autism in twins to establish the role of genetic and environmental factors. To collect evidence, Susan Folstein, then a trainee US psychiatrist, visited 21 twin pairs across the United Kingdom, in which at least one twin had been diagnosed with autism. Symptoms of autism and cognitive abilities showed a stunning degree of concordance (82%) in the identical twin pairs, which was not seen in those who were non-identical ([S. Folstein and M. Rutter *J. Child Psychol. Psychiatry* 18, 297–321; 1977](#)).

This remarkable finding — which Rutter had not expected — made him optimistic that he could find the ‘handful’ of genes he thought might be implicated in causing autism. Always ready to be proved wrong, he quickly recognized that hundreds of genes are likely to be involved, and that the causal paths from gene to brain, mind and behaviour are too entangled to arrive at a single, definitive explanation. His discovery of a genetic basis for autism, published in 1977, transformed understanding and launched a new era of research.



Are mothers too easy to blame?

During this period, Rutter and his collaborators also conducted long-term population studies of educational attainments and mental health, in inner London and on the Isle of Wight, UK, focusing on children aged 9–11. These were among the first to identify specific problems with reading — relative to age and intellectual level — in a whole population. The studies gave a first estimate of the prevalence of these and other differences, and the findings led to policy changes in UK clinical services and in education.

In 1973, Rutter became the first professor of child psychiatry in the United Kingdom, at the Institute of Psychiatry. There, he established the Medical Research Council (MRC) Child Psychiatry Research Unit in 1984, and, a decade later, the MRC Social, Genetic and Developmental Psychiatry Centre. The centre attracted a formidable team to study the interplay of

genetics and environment in typical and atypical development. Its work included psychologist Robert Plomin's Twins Early Development Study.

After 55 years at what is now the Institute of Psychiatry, Psychology and Neuroscience at King's College London, Rutter retired, only months before his death. His office was next to that of one of us (F.H.) for many years. He was an inspirational leader and mentor, and had recently donated one of his many prizes to support the work of younger colleagues. He was knighted in 1992.

His legacy includes a continuously revised textbook of child and adolescent psychiatry, around 400 research papers, and his influence on generations of child psychiatrists and psychologists, us among them. When one of us (U.F.) trained in the 1960s, it was the rigour of his ward rounds that sparked a lifelong career in autism research. Although he was a formidable authority in the medical establishment, and a feared critic, he was accessible and encouraging to students.

Competitive in his academic work, as in his much-loved tennis, Mike could be daunting in debate. He worked incredibly hard — supported by and occasionally co-authoring with his wife Marjorie Rutter — and he sometimes overlooked the personal demands that kept others from meeting his strict standards. However, he was famously gentle with his patients, and notably kind and avuncular in his later years.

Nature **599**, 555 (2021)

doi: <https://doi.org/10.1038/d41586-021-03498-z>

This article was downloaded by **calibre** from <https://www.nature.com/articles/d41586-021-03498-z>

- CORRESPONDENCE
- 23 November 2021

Science community steps up to reform open access

- [Geoffrey Boulton](#) ORCID: <http://orcid.org/0000-0001-9535-0684>⁰,
- [Ahmed C. Bawa](#) ORCID: <http://orcid.org/0000-0002-5889-5295>¹,
- [Dominique Babini](#) ORCID: <http://orcid.org/0000-0002-5752-7060>² &
- [Luke Drury](#) ORCID: <http://orcid.org/0000-0002-9257-2270>³

The International Science Council (ISC) and ALLEA (All European Academies) last month drew the attention of the scientific community to the inadequacies of open access to research papers as currently implemented by publishers (see go.nature.com/3otps2d and go.nature.com/3cfp6bq). Open access to the record of science is essential for an equitable and inclusive global scientific enterprise and to the scientific self-correction that is crucial for rigour and public trust. The ISC statement sets out eight fundamental principles of publishing that need to be upheld in serving the needs of science, including mandating access to all evidential data and removing restrictive copyright.

Publishing, making ideas and data public on increasingly diverse and sophisticated platforms, accompanied by critical peer evaluation, is central to how science works. Its governance should therefore be accountable to the science community — the principal producer, validator and consumer of scientific publications.

The science community is raising its voice; funders, governments, universities and research institutions must now step up to reform open access to the scientific record according to the framework outlined in the ISC and ALLEA statements.

Nature **599**, 556 (2021)

doi: <https://doi.org/10.1038/d41586-021-03485-4>

This article was downloaded by **calibre** from <https://www.nature.com/articles/d41586-021-03485-4>

| [Section menu](#) | [Main menu](#) |

- CORRESPONDENCE
- 23 November 2021

Ahmedabad: local data beat the heat

- [Priya Dutta](#)⁰,
- [Jeremy J. Hess](#)¹ &
- [Polash Mukerjee](#)²

The Indian city of Ahmedabad, population around 6 million, aims to assess the effectiveness of its Heat Action Plan annually (see [L. Keith et al. *Nature* 598, 29–31; 2021](#)). The results so far are encouraging. The city's coordinated research and policy efforts are testament to the power of collecting local data.

Access options

Subscribe to Journal

Get full journal access for 1 year

\$199.00

only \$3.90 per issue

[Subscribe](#)

All prices are NET prices.

VAT will be added later in the checkout.

Tax calculation will be finalised during checkout.

Rent or Buy article

Get time limited or full article access on ReadCube.

from \$8.99

[Rent or Buy](#)

All prices are NET prices.

Additional access options:

- [Log in](#)
- [Learn about institutional subscriptions](#)

Nature **599**, 556 (2021)

doi: <https://doi.org/10.1038/d41586-021-03486-3>

This article was downloaded by **calibre** from <https://www.nature.com/articles/d41586-021-03486-3>

| [Section menu](#) | [Main menu](#) |

- CORRESPONDENCE
- 23 November 2021

Support deaf participants at virtual conferences

- [Denis Meuthen](#) [ORCID: http://orcid.org/0000-0002-3373-5383](http://orcid.org/0000-0002-3373-5383) ⁰

Virtual meetings are often considered to be a more inclusive alternative to in-person scientific conferences (see [R. Joo *Nature* 598, 257 \(2021\)](#) and [Nature](#) 598, 221–223; 2021). They might indeed benefit some disabled participants, such as those who use wheelchairs. But in my experience as a legally deaf researcher, too many conference organizers overlook the needs of people with impaired hearing who must rely on lip-reading, signing or subtitles for comprehension.

Access options

Subscribe to Journal

Get full journal access for 1 year

\$199.00

only \$3.90 per issue

[Subscribe](#)

All prices are NET prices.

VAT will be added later in the checkout.

Tax calculation will be finalised during checkout.

Rent or Buy article

Get time limited or full article access on ReadCube.

from \$8.99

[Rent or Buy](#)

All prices are NET prices.

Additional access options:

- [Log in](#)
- [Learn about institutional subscriptions](#)

Nature **599**, 556 (2021)

doi: <https://doi.org/10.1038/d41586-021-03487-2>

This article was downloaded by **calibre** from <https://www.nature.com/articles/d41586-021-03487-2>

| [Section menu](#) | [Main menu](#) |

- CORRESPONDENCE
- 23 November 2021

Ditch gendered terminology for cell division

- [Peter White ORCID: http://orcid.org/0000-0002-1784-3990](#)⁰,
- [Shahnaz Masani](#)¹,
- [Stef Shuster ORCID: http://orcid.org/0000-0003-1970-5257](#)² &
- [Nicole Wonderlin](#)³

The cell-division processes of mitosis and meiosis are still described in gendered language that was established in the early 1900s. So-called sister chromatids — the two copies formed by a replicating chromosome — separate in a mother cell, which then divides into daughter cells. In our view, this outdated anthropomorphization is neither accurate nor necessary. We think it also reinforces stereotypes and non-inclusive, gender-binary thinking.

Access options

Subscribe to Journal

Get full journal access for 1 year

\$199.00

only \$3.90 per issue

[Subscribe](#)

All prices are NET prices.
VAT will be added later in the checkout.

Tax calculation will be finalised during checkout.

Rent or Buy article

Get time limited or full article access on ReadCube.

from \$8.99

[Rent or Buy](#)

All prices are NET prices.

Additional access options:

- [Log in](#)
- [Learn about institutional subscriptions](#)

Nature **599**, 556 (2021)

doi: <https://doi.org/10.1038/d41586-021-03490-7>

This article was downloaded by **calibre** from <https://www.nature.com/articles/d41586-021-03490-7>

| [Section menu](#) | [Main menu](#) |

Work

- **[How burnout and imposter syndrome blight scientific careers](#)** [23 November 2021]

Career Feature • Most scientists love what they do, but job satisfaction levels hit a new low, Nature's survey finds.

- **[Artificial intelligence powers protein-folding predictions](#)** [23 November 2021]

Technology Feature • Deep-learning algorithms such as AlphaFold2 and RoseTTAFold can now predict a protein's 3D shape from its linear sequence — a huge boon to structural biologists.

- **[All-nighter: staying up to fight malaria](#)** [22 November 2021]

Where I Work • Victor Chaumeau collects mosquitoes in Myanmar to better understand how to control malaria.

- CAREER FEATURE
- 23 November 2021

How burnout and imposter syndrome blight scientific careers

Most scientists love what they do, but job satisfaction levels hit a new low, *Nature*'s survey finds.

- [Chris Woolston](#) ✉

[Find a new job](#)



Illustration by Antonio Rodríguez

Scientists around the world could learn something from the cautionary tale of John Henry, a US folk hero who literally worked himself to death, says Tiffany Rolle, a science education and engagement fellow at the National Human Genome Research Institute in Bethesda, Maryland. Rolle co-wrote a 2021 paper about stress, burnout and ‘John Henryism’ in the STEM workforce.

Science tends to attract people who want to get to the bottom of important questions, but few things in science are ever fully solved, says Rolle. “That level of curiosity can keep you on a hamster wheel,” she says. “The finish line isn’t strongly defined unless you define it for yourself.”

John Henryism is a term that particularly applies to under-represented groups, who feel an especially intense pressure to perform, she adds. “You are in a competitive field, but you’re constantly getting these messages that you aren’t good enough, that you shouldn’t be here, that you barely made the cut. There’s a chip on your shoulder to prove yourself.”

Stress, burnout, impostor syndrome and the mental-health problems they can trigger are strongly tied to job satisfaction, a key focus of *Nature*’s 2021 careers survey (see ‘*Nature*’s salary and job survey’).

Nature’s salary and job survey

This article is the third of four linked to *Nature*’s global salary and job satisfaction survey. A final article is scheduled for next week, and will explore experiences of diversity, equity and inclusion in the scientific workplace.

The salary survey runs every three years and [last took place in 2018](#). It was created together with Shift Learning, a market-research company in London, and was advertised on nature.com, in Springer Nature digital products and through e-mail campaigns. It was offered in English, Mandarin Chinese, Spanish, French and Portuguese. The full survey data sets are available at go.nature.com/3eqcpk9.

Less than 60% of respondents to the sixth Salary and Job Satisfaction survey reported being satisfied with their positions. That’s about 10 percentage

points less than in earlier satisfaction surveys, including the previous one, which ran in 2018.

As satisfaction wanes, mental health seems to be a growing concern. Forty-two per cent of respondents said they had sought help or wanted to seek help for job-related anxiety or depression, a rise of six percentage points from 2018.

This year's survey ran in June and July and drew responses from more than 3,200 self-selected scientists at various stages of their careers. It included a series of questions that illuminate the realities of working life. Through survey answers and free-text comments, the respondents shared the upsides and downsides of scientific careers. Follow-up interviews with selected respondents provided a glimpse of the real-life stories behind the numbers. All in all, the survey suggests a growing uneasiness with a career path that still manages to challenge and inspire.

A low point for satisfaction

The 58% of respondents who said they were either somewhat or very satisfied with their positions marks an all-time low in the ten-year history of annual *Nature* surveys. Our 2020 survey of postdoctoral researchers, a group particularly prone to overwork and stress, found a satisfaction rate of 61%. In the 2019 survey of PhD students, 71% of respondents said they were satisfied with their PhD experience. Our 2018 survey, the most recent survey of the general scientific population, found a satisfaction rate of 68%.



Scientists count the career costs of COVID

In this year's survey, more than half (54%) of respondents said that their job satisfaction had worsened in the past year. That period was marked by widespread COVID-related slowdowns and disruptions, but the pandemic wasn't the only factor darkening the moods of scientists. Fiona Simpson, a cancer researcher at the University of Queensland in Brisbane, Australia, says that her satisfaction significantly worsened as demands of the job steadily increased. "I love the work I do. I love the science," she says. "The problem is the conditions that we work under." She continues: "As a profession we've gotten into a position where we work every night, we read theses, we review for journals, we sit on grant panels, all for free. I basically have two full-time jobs."

For many, long hours are a fact of life in science. Nearly one-third (31%) of respondents reported working more than 50 hours a week, even though only 2% indicated that such long hours were written into a contract. Working weeks of 50 hours or more were twice as common in academia (36%) as in industry (18%). Overall, 59% of respondents said they were satisfied with their work-life balance, down from 70% in 2018.

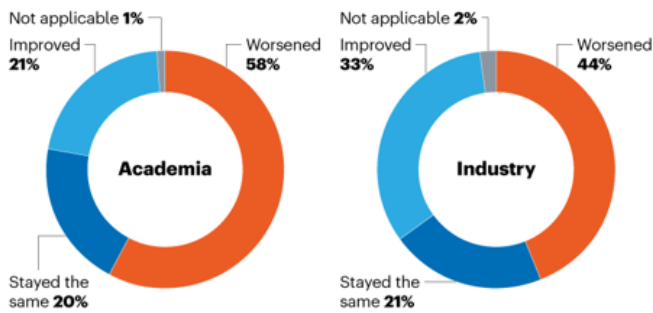
Burnt out on science

Signs of burnout were common. Forty-five per cent of respondents said they frequently or always felt that they couldn't keep up with the demands of the job (see 'Satisfaction and strain'). Fifty-one per cent of female researchers, and 39% of their male counterparts, said that they felt that way. A woman who is now president of her own health-care company in the United States said that, earlier in her career, she was forced to invest more "time, effort and personal resources" than her male colleagues to achieve similar levels of funding and respect. Thirty-nine per cent of all respondents said that they frequently or always felt drained of emotional and physical energy. Forty-five per cent of respondents felt that they weren't achieving as much as they should.

SATISFACTION AND STRAIN

Most respondents felt job satisfaction levels wane over the past year. Stress and burnout have taken a toll on mental health, but a slight majority would still recommend a scientific research career to students.

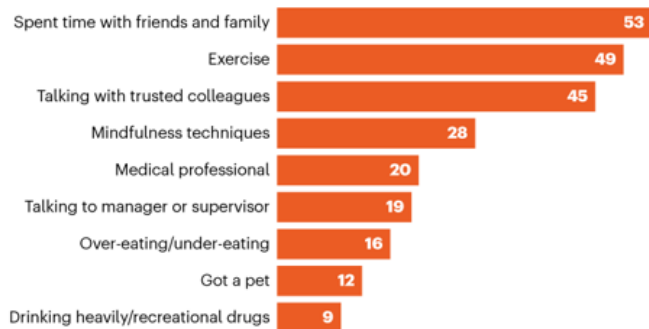
In the past year, how would you say your level of satisfaction has changed?



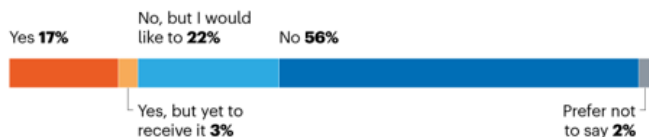
Have you experienced any of the following symptoms of burnout in the past 12 months?



Have you sought help or support for these feelings in any of the following ways?



Have you sought or received professional help for depression or anxiety?



Would you recommend to students that they pursue a career in scientific research?



All that stress exacts a mental toll. In this survey, one in five said that they had sought help for depression or anxiety caused by their work, and 22% that they had not sought help but wished they had. That's a notable increase since 2018, when 16% said they had received help and 17% that they had wanted help but had not yet sought it out.

A tenure-track biomedical professor in the United States who said that he had not sought professional help but would like to do so added this comment: "It is amazing to me how we can be in seminars about the impact of stress and sleep disruption on cancer outcomes, for example, and then we are all stressed and under-slept. We rarely recognize how much selection there is in academia for those willing to sacrifice health and family for their career."

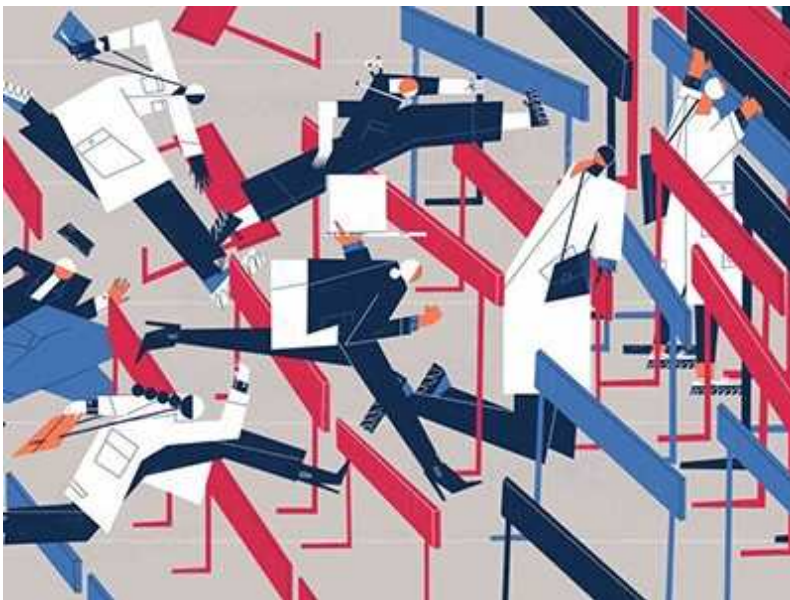
Rolle says that the high number of respondents reporting mental-health issues and burnout is hardly surprising. Not only is scientific work becoming more stressful, but the stigma surrounding mental health is fading away, she says. "People are more willing to talk about burnout and pressure because it's such a common thing," she says. "You see it on social media. Everyone is frazzled."

Industry strengths

Sometimes, a change of role can be good for a person's mental health. Ana Rakonjac says that she felt extreme strain as a postdoctoral physics researcher at Durham University, UK. She spent more than five years working on a series of short-term contracts that lacked stability or security. Over that time, she accumulated managerial and supervisory tasks that greatly added to her workload without changing her job title or salary. "I learnt a lot, and it was good for my career, but it was quite stressful because the responsibilities and the work hours kept piling up," she says. "I got massive migraine headaches that ramped up around that time."

Rakonjac says that, as a postdoc, she also frequently experienced 'impostor syndrome', the feeling that a person isn't worthy or doesn't belong. "At a university, everyone around you knows more than you do," she says.

“Professors have been doing this for decades, so it’s easy to think that you know very little.”



[Stagnating salaries present hurdles to career satisfaction](#)

The impostor syndrome disappeared when Rakonjac took an industry job at Atomionics, an atomic physics company in Singapore, a position she started in September 2019. “Everyone’s skills are really valued,” she says. Much of the stress vanished, too. She says that the working hours were similar to those she’d had as a postdoc, but she didn’t feel so overextended. “[In industry], I wasn’t spread between three or four tasks in a given day,” she says. In October, Rakonjac started a new job working for a government laboratory in New Zealand.

Rakonjac’s story illustrates a trend: satisfaction is generally easier to find in industry than in academia. Two-thirds (66%) of respondents in industry said they were somewhat or very satisfied with their work, compared with 56% of respondents in academia. At the other end of the spectrum, 5% of respondents in industry, and 11% in academia, said they were extremely dissatisfied with their positions.

When conditions are right, a position in academia can be extremely rewarding. Ingo Fetzer, an ecologist at the Stockholm Resilience Centre at Stockholm University, says he’s very happy with his job. He explains that

the centre brings together researchers from different disciplines to tackle issues in sustainability. “Collaborations between disciplines make scientific work extremely creative and fruitful,” he says. “The work here is a group effort.”

Likewise, Sudha Sourav, an electrical engineer at the University of Hamburg in Germany, marked himself as “extremely satisfied” with his position as a research engineer. The job, which mainly involves designing devices to study visual areas of the brain, combines research with hands-on tinkering. “I get to see projects from the very abstract theoretical part to the nitty gritty details,” he says. “I always wanted to have a job where you could develop something and then prove whether it works or not. The fact that someone pays me to do that is very satisfying.”



Pandemic burnout is rampant in academia

Sourav says he’s especially grateful for the job security that comes with a permanent position. “I’m very fortunate,” he says. “I don’t need to worry if my job will run out in six months.” He adds that he could be a victim of burnout if he didn’t have the comfort of knowing that his position was secure and stable. “I’m a happy and mentally healthy scientist, but that’s not because I’m special.”

Sourav thinks that institutions could improve the working lives of researchers by creating more positions like his: permanent, well-paid jobs for scientists who don't want to run their own labs. Such positions have been dubbed 'super postdocs' or 'superdocs'. "Not everyone needs to be a professor," he says. "Not everyone can be."

Security means different things in different places. Sunday Akomoledé, a biology lecturer at the Federal College of Education in Potiskum, Nigeria, says that he can keep his job as long as he likes. Still, he counted himself as "somewhat dissatisfied" with his job, largely because of the struggles of life in northern Nigeria. He says his pay doesn't come close to matching his efforts. Like other educators, he worries about attacks from Boko Haram, a terrorist group with a history of kidnapping or killing students and teachers. In 2014, a suicide bomber disguised as a student killed more than 40 students at a Potiskum secondary school. "Whenever we go to work, we pray to God to keep us safe. These people can attack at any time."

Akomoledé says that his dream is to be accepted at a university in the United States where he can eventually obtain a PhD degree and become a professor. "I am looking for greener pastures," he says.

Scientific rewards

Science will always have its appeals. Seventy-nine per cent of respondents said that they were satisfied with their level of interest in their work, and 75% said they appreciate the meaningfulness of the job. Heather Richbourg, a bioinformatician at Ultragenyx, a pharmaceutical company in Novato, California, is one researcher who knows that her work matters. The company specializes in developing biological drugs for rare diseases, including Duchenne muscular dystrophy. "Everything we do is directly linked to patients in need," she says. She adds: "I love the diversity of things I'm working on."

Despite everything that science has to offer, respondents had mixed feelings overall about a scientific career (see 'Sounding off: respondents share frustrations with scientific life'). Fifty-four per cent said they would

recommend a research career to students, a marked drop from the 75% who endorsed such a path in our 2018 survey.

A government staff scientist in the United States who reported making more than US\$200,000 a year declined to advocate a science career despite her personal success. “The culture of science today is fundamentally inhuman and demoralizing,” she wrote. “Improve the culture, the job security, stabilize funding and then people with talent will flock to science since it is fundamentally rewarding and offers great joy.”

Sounding off: respondents share frustrations with scientific life

Free-text comments in *Nature*'s salary and job satisfaction survey highlight many of the tensions facing scientists. Comments have been edited for length and clarity and, when necessary, translated into English.

- There is a deep-rooted culture of having one set of rules on the surface (rules that promote work/life balance or diversity, for instance), but everyone breaks them because of the rat race and the never-ending workload. I stay because I love science and believe in the cause for higher education. But the system is becoming very unviable. *Postdoc in biomedicine, United Kingdom.*
- Elite academic institutions are borderline abusive. People are stuck with low-paying jobs for long hours because they don't know of anywhere else they can go. The shift in my mental health, job prospects, salary, and lack of harassment/abuse when I moved from academia to industry has been night to day. *Project manager in biomedicine, United States.*
- People with the level of talent and intelligence that most scientists have are better off in another profession for overall satisfaction, quality of life, and a chance for happiness. Why study for 12 years and then end up part of the gig economy? *Government staff scientist in chemistry, United States.*
- Young researchers are under too much pressure. Family obligations, scientific research, teaching, and administrative tasks add up to a heavy load. *Staff scientist in engineering, China. (Translated from Chinese.)*

- I love my job. I get to help the most vulnerable populations. I'm not sure I would encourage anyone to plan on a pharma career, though, with all of the other options open to smart young people. *Staff scientist in pharmaceutical industry, United States.*
- In Mexico, science has been forgotten by the government. This makes it extremely difficult to train people who are dedicated to science. Coupled with the pandemic, this will cause a setback in science. *Associate professor in biomedical field, Mexico. (Translated from Spanish.)*

Nature **599**, 703-705 (2021)

doi: <https://doi.org/10.1038/d41586-021-03042-z>

This article was downloaded by **calibre** from <https://www.nature.com/articles/d41586-021-03042-z>

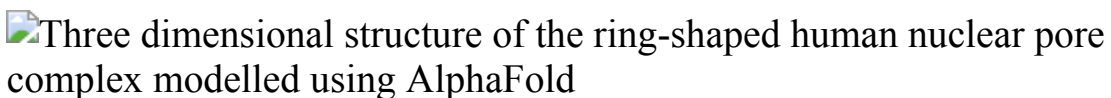
| [Section menu](#) | [Main menu](#) |

- TECHNOLOGY FEATURE
- 23 November 2021

Artificial intelligence powers protein-folding predictions

Deep-learning algorithms such as AlphaFold2 and RoseTTAFold can now predict a protein’s 3D shape from its linear sequence — a huge boon to structural biologists.

- [Michael Eisenstein](#) 0



A model of the human nuclear pore complex, built using AlphaFold2 and structural data. Credit: Agnieszka Obarska-Kosinska

Rarely does scientific software spark such sensational headlines. “One of biology’s biggest mysteries ‘largely solved’ by AI”, declared the BBC. *Forbes* called it “the most important achievement in AI — ever”. The buzz over the November 2020 debut of AlphaFold2, Google DeepMind’s artificial-intelligence (AI) system for predicting the 3D structure of proteins, has only intensified since the tool was made freely available in July.

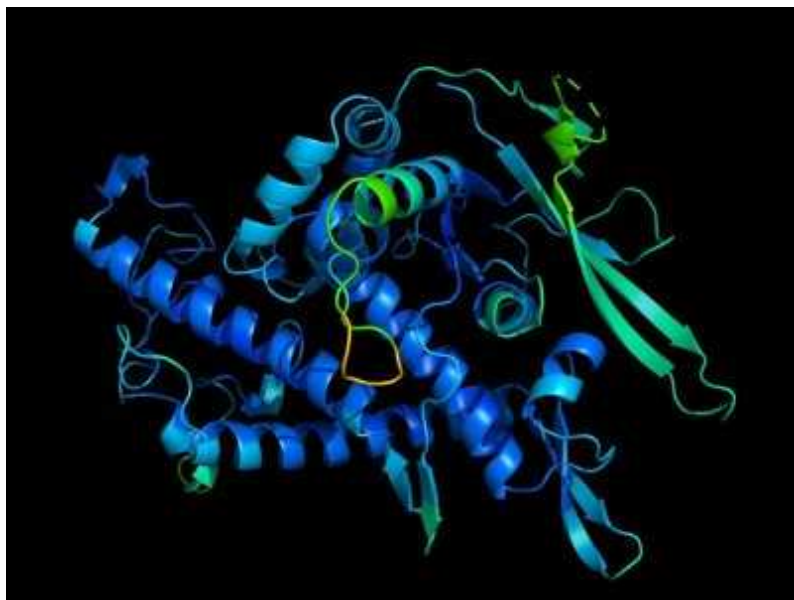
The excitement relates to the software’s potential to solve one of biology’s thorniest problems — predicting the functional, folded structure of a protein molecule from its linear amino-acid sequence, right down to the position of each atom in 3D space. The underlying physicochemical rules for how proteins form their 3D structures remain too complicated for humans to parse, so this ‘protein-folding problem’ has remained unsolved for decades.

Researchers have worked out the structures of around 160,000 proteins from all kingdoms of life. They have been using experimental techniques, such as

X-ray crystallography and cryo-electron microscopy (cryo-EM), and then depositing their 3D information in the [Protein Data Bank](#). Computational biologists have made steady gains in developing software that complements these methods, and have correctly predicted the 3D shapes of some molecules from well-studied protein families.

Despite these advances, researchers still lacked structural information for around 4,800 human proteins. But AlphaFold2 has taken structure-prediction strategies to the next level. For instance, an independent analysis by researchers in Spain showed¹ that the algorithm's predictions had reduced the number of human proteins for which no structural data was available to just 29.

AlphaFold2 was revealed last November at CASP14, the 14th critical assessment of protein structure prediction (CASP), a biennial competition that challenges computational biologists to test their algorithms against proteins for which structures have been experimentally solved, but not publicly released. DeepMind's software — which uses the sophisticated machine-learning technique known as deep learning — blew the competition out of the water.



['It will change everything': DeepMind's AI makes gigantic leap in solving protein structures](#)

“Based on CASP14 [results], they could get about two-thirds of the proteins with experimental accuracy overall, and even for hard targets, they can fold about one-third of the proteins with experimental accuracy,” says Yang Zhang, a biological chemist at the University of Michigan in Ann Arbor, whose algorithm was among CASP14’s runners-up. “That’s a very amazing result.” Two subsequent *Nature* papers^{2,3} and dozens of preprints have further demonstrated AlphaFold2’s predictive power.

Zhang considers AlphaFold2 to be a striking demonstration of the power of deep learning, but only a partial solution to the protein-folding problem. The algorithm can deliver highly accurate results for many proteins — and some multi-protein complexes — even in the absence of structural information. This could drastically accelerate experimental structural biology and help to guide research in protein engineering and drug discovery.

But many essential details remain out of reach for some proteins. Chris Sander, a computational biologist at the Dana-Farber Cancer Institute in Boston, Massachusetts, notes that algorithms still struggle with complicated protein targets that have multiple functional domains or highly dynamic structures. “It’s great what they’ve done,” says Sander. “But the flexibility of proteins and how they change is not touched by that, and just having a single snapshot doesn’t solve the problem of biological function.”

Progress in deep learning — and a growing community of AlphaFold2 users — could bring some of these challenges to heel, but a comprehensive understanding of protein biology will require a much broader computational and experimental toolbox.

Higher education

Deep learning incorporates machine-learning strategies in which computational neural networks are trained to recognize and interpret patterns in data. “These models don’t try to predict the structure all in one go,” says David Baker, a computational biologist at the University of Washington in Seattle. “They’re more like a physical simulation where the models are learning how to make good moves to improve the structure.” By training these algorithms with vast amounts of annotated experimental data, they can

begin identifying links between sequence and structure that inform predictions for new proteins.

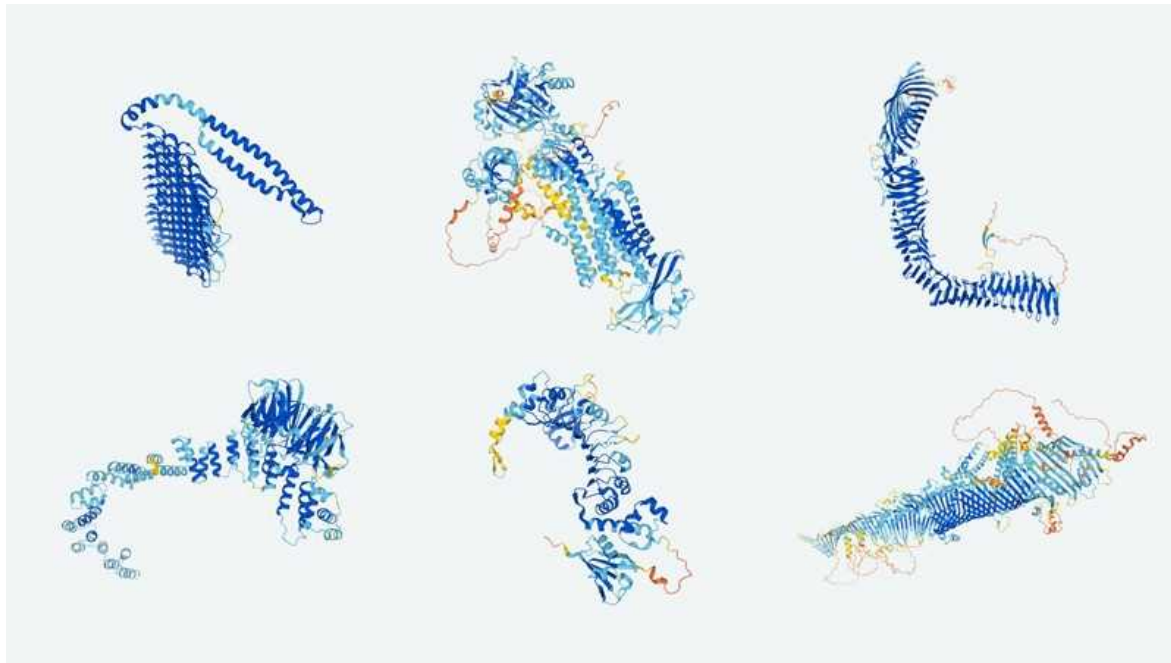
Over the past five years, multiple teams have made headway in applying deep learning to structure prediction. The first iteration of AlphaFold won CASP13 in 2018, but its performance was nowhere near the stand-out victory seen last year. Several academic laboratories subsequently developed deep-learning-based algorithms that outperformed the first generation of AlphaFold, including the Zhang lab's D-I-TASSER⁴, the Baker lab's trRosetta⁵ and RaptorX⁶, developed by Jinbo Xu and his team at the Toyota Technological Institute in Chicago, Illinois.

But these algorithms were generally applied as parts of a larger software pipeline, creating the potential for error and inefficiency. "You often had different components miscommunicating or not communicating optimally with one another because they were built piecemeal," says Mohammed AlQuraishi, a systems biologist at Columbia University in New York City. These limitations have fuelled interest in end-to-end algorithms that manage the entire process from sequence to structure. DeepMind senior research scientist John Jumper, who is based in London, says that after CASP13, his team essentially discarded the first-generation AlphaFold and began to develop such a solution — AlphaFold2.

Several aspects of AlphaFold2 build on established techniques. For example, the algorithm begins by generating multi-sequence alignments (MSAs), in which a new protein with unknown structure is compared against related sequences from other species. By identifying co-evolving amino acids that change in parallel, algorithms can hone in on those that are most likely to associate with each other in the folded protein — places where one change in the sequence requires compensatory mutations to preserve the overall structure.

Sander and his collaborator, computational biologist Debora Marks at Harvard University in Cambridge, Massachusetts, and their team developed this co-evolution-based technique in 2011⁷. "It was the first solution that worked across the board for many proteins, using evolution to get the correct fold and the basic shape," says Sander. "And now machine learning makes it even better."

AlphaFold2's developers drew on an unprecedented amount of information to build their MSAs, using billions of protein sequences from a data set compiled by computational biologist Martin Steinegger at Seoul National University in South Korea and Johannes Söding at the Max Planck Institute for Biophysical Chemistry in Göttingen, Germany. "They wanted me to turn that into a searchable database," Steinegger says.



These predictions generated by AlphaFold2 highlight the structural variety of proteins.Credit: DeepMind

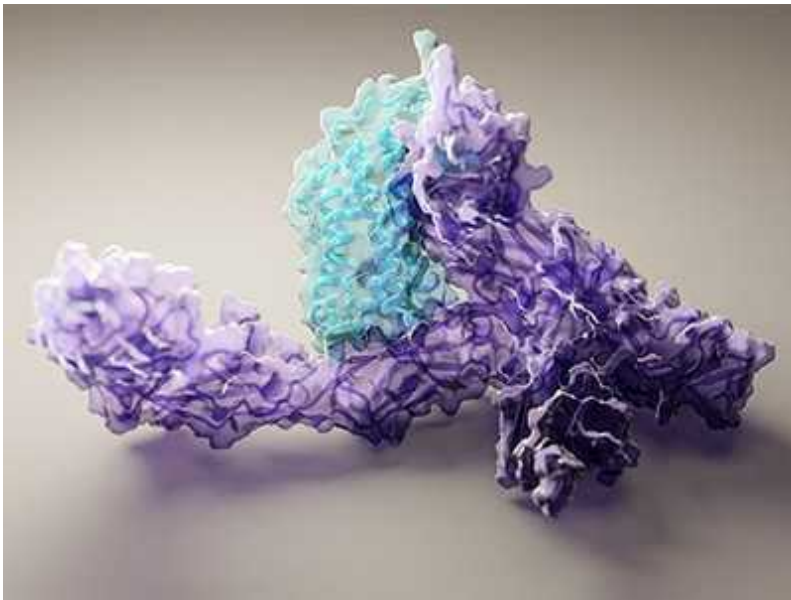
The DeepMind team also devised innovative solutions to the protein-folding problem. One is the use of pattern-recognition tools known as transformers, which are commonly used in image analysis and natural-language processing. Transformers are designed to recognize local patterns — strings of words or adjacent visual elements, for instance — that might guide interpretation of the data. DeepMind adapted them to work in the more challenging terrain of protein structure, building transformers that identify and focus on long-range protein interactions that are likely to be important in the final folded form. "In the final protein structure, you'll make connections between quite distant things — like maybe residue 10 will talk to residue 350," says Jumper.

The AlphaFold2 process simultaneously tackles protein folding from multiple angles, and generates multiple representations of the predicted structure in parallel. These are then compared, and the resulting insights help to refine the modelling process in subsequent iterations. Jumper and his colleagues enabled this by designing a neural-network architecture that allows fluid and efficient information exchange between components of the software. “I think the biggest thing that made this what it is was that very well-engineered communication system,” says AlQuraishi.

Prediction for the people

Because of the lag between AlphaFold2’s debut and the papers being published, and uncertainty among academics over whether full details would be made available, Baker and his postdoc Minkyung Baek worked from sparse information on the software’s architecture to develop their own version, RoseTTAFold⁸. This uses many of the same strategies as AlphaFold2, but with a few distinctive twists.

“At the time we made it available, it was far and away the best such structure-prediction method that you could use — but not as good as AlphaFold2,” says Baker. He points out that, by contrast with most academic labs, DeepMind is a private entity with huge resources and a long-standing team of multidisciplinary experts. The broadest explanation for AlphaFold2’s success “is just that this is Google money”, says Amelie Stein, a computational biologist at the University of Copenhagen. “But it’s also bringing together the expertise of software engineers and people who know proteins and understand protein structures.”



DeepMind's AI for protein structure is coming to the masses

Since AlphaFold2's July release², labs have clamoured to work with the software and its structure predictions, which are available through a [database hosted by the European Bioinformatics Institute](#).

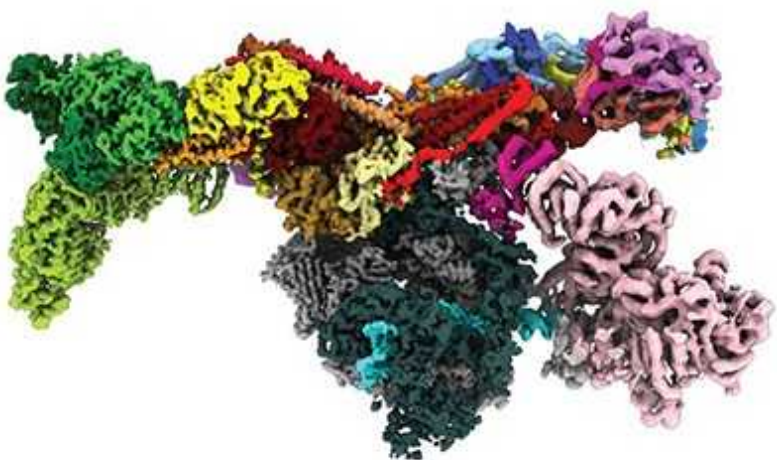
Users generally find the software straightforward to use, although they need several terabytes of disk space to download the databases and multiple graphic processing units (GPUs) to handle the analysis. "Single-structure computations are not that bad — we run it for a couple of hours," says bioinformatician Arne Elofsson at Stockholm University. But because of their scale and the resources required, analyses of the full complement of an organism's proteins, or proteome, are likely to be out of reach for most academic labs for the time being.

For researchers who wish to test-drive the software, Steinegger and his colleagues developed ColabFold, a cloud-based system that runs both AlphaFold2 and RoseTTAFold using remote databases and computing power provided by Google⁹. The web-based interface is relatively simple: "You can plug in your sequence and then just push a button and it predicts the structure for you," says Steinegger. But it also allows users to tinker with settings and optimize their experiments — such as by changing the number of iterations of structure prediction.

Finding the fold

Even the DeepMind team was taken aback by how well AlphaFold2 performed at CASP14. “We obviously had internal benchmarking that suggested that we were going to do very well,” says Jumper. “But at the end of the day, there was still a feeling in the back of my mind: is this really, really true?”

CASP14 assuaged those concerns, and the past few months have seen numerous demonstrations of the capabilities and limits of AlphaFold2. In a study³ published alongside the paper describing the algorithm, the DeepMind team applied AlphaFold2 to a data set comprising 98.5% of the human proteome. The algorithm uses a metric called a predicted local distance difference test (pLDDT) to indicate its confidence that a particular amino acid’s position and orientation accurately reflects its real-world structure. In this way, 36% of all residues in the proteome could be resolved with very high confidence³.



[DeepMind’s AI predicts structures for a vast trove of proteins](#)

In August, researchers led by bioinformatician Alfonso Valencia at the Barcelona Supercomputing Center in Spain independently concluded¹ that

AlphaFold2 boosted the proportion of amino acids in human proteins that can be accurately mapped from 31% to 50%.

Zhang expects the software will make short work of the proteome's low-hanging fruit. "They can probably fold all the single-domain proteins," he says. But many proteins remain a challenge, such as those comprising multiple, independent, functional units joined by relatively flexible linker elements. In these cases, individual domains might fall in line, but their orientation relative to one another might not.

Even more challenging are protein segments that are intrinsically disordered in their natural state, which could represent more than one-third of all amino acids in the human proteome³. No algorithm can currently predict how these fold, but Jumper notes that extremely low pLDDT scores can at least demarcate these segments in a structure. "A totally unconfident prediction is quite a strong indicator of disorder," he says.

One unexpected feature of both AlphaFold2 and RoseTTAFold is their ability to predict accurate structures from pairs of protein chains that form complexes called homodimers (if formed of two identical proteins) or heterodimers (formed of two different proteins) — something they were not initially trained to do.

Elofsson and his team have reported that they successfully modelled up to 59% of the two-protein complexes¹⁰ that they analysed using AlphaFold2. This process becomes more computationally challenging when attempting to identify likely complexes from scratch than when modelling known interacting pairs. But Baker and his team showed¹¹ that, by applying multiple deep-learning algorithms in tandem, they were able to both identify and model hundreds of multi-protein complexes from millions of possible interacting pairs in the proteome of the yeast *Saccharomyces cerevisiae*. "RoseTTAFold was about 100 times faster [than AlphaFold2], and so we could run it on all pairs and then use it to filter out the ones that were most likely interacting," says Baker. "Then we ran AlphaFold2 on that much smaller subset."

Sensing the enthusiasm for this application, in October, DeepMind released AlphaFold-Multimer, which is specifically trained to tackle complexes of

proteins that are formed by assemblies of multiple chains¹². AlphaFold-Multimer generated high-accuracy predictions of interactions for 34% of the homodimeric complexes tested, and for 23% of heterodimeric complexes.

Functional frontiers

Still, many questions remain out of reach, notes Marks. “If your technology is bent on really learning to copy crystallography very well, then that’s great,” she says. But such static structural snapshots will not be suitable for exploring questions that relate to the manipulation or inherent dynamic behaviour of a given protein, she points out.

For example, AlphaFold2 typically produces a single ‘correct’ answer for each sequence. But many proteins have multiple conformational states that are all relevant to function — determining, for example, whether an enzyme is active or inhibited. “You can try to tweak AlphaFold to get at one or the other, but often you just generate one [conformation] no matter what you do,” says Elofsson. The algorithm is simply not designed to simulate complex molecular physics, even if it captures the influence of these forces while generating predictions. Getting at such problems will probably require experimental techniques that show the structure of the actual protein in multiple states, such as cryo-EM.



NatureTech hub

AlphaFold2 is also generally not suitable for predicting how individual amino acid changes alter protein structure — a crucial factor in understanding how mutations contribute to disease. This is in part because the algorithm uses evolutionary perspectives to converge on a correct solution from many slightly different sequences, says Stein, whose work focuses on characterizing such variants. “If you flip a single residue somewhere, you can’t expect it to suddenly say, ‘this is a disaster’,” she says. However, she and her team have found that they can couple wild-type protein structures generated by deep learning with other mutation-analysis algorithms to achieve more-accurate predictions¹³.

The good news is that structural biologists won’t be out of a job any time soon. In fact, they might now be able to devote more time to other pressing questions in the field. Structural biologist Randy Read at the University of Cambridge, UK, notes, for example, that structure predictions from AlphaFold2 are already helping crystallographers to drastically accelerate their data interpretation by overcoming the tedious ‘phase problem’ — a challenge associated with the interpretation of incomplete data generated in an X-ray diffraction experiment.

Protein designers could also see benefits. Starting from scratch — called de novo protein design — involves models that are generated computationally but tested in the lab. “Now you can just immediately use AlphaFold2 to fold it,” says Zhang. These results can even be used to retrain the design algorithms to produce more-accurate results in future experiments.

For AlQuraishi, these possibilities suggest a new era in structural biology, emphasizing protein function over form. “For the longest time, structural biology was so focused on the individual pieces that it elevated these beautiful ribbon diagrams to being almost like an end to themselves,” he says. “Now I think structural biology is going to earn the ‘biology’ component of its name.”

Nature **599**, 706-708 (2021)

doi: <https://doi.org/10.1038/d41586-021-03499-y>

References

1. 1.
Porta-Pardo, E., Ruiz-Serra, V. & Valencia, A. Preprint at bioRxiv
<https://doi.org/10.1101/2021.08.03.454980> (2021).
2. 2.
Jumper, J. *et al.* *Nature* **596**, 583–589 (2021).
3. 3.
Tunyasuvunakool, K. *et al.* *Nature* **596**, 590–596 (2021).
4. 4.
Zheng, W. *et al.* *Proteins* <https://doi.org/10.1002/prot.26193> (2021).
5. 5.
Yang, J. *et al.* *Proc. Natl Acad. Sci. USA* **117**, 1496–1503 (2020).
6. 6.
Xu, J. *Proc. Natl. Acad. Sci. USA* **116**, 16856–16865 (2019).
7. 7.
Marks, D. S. *et al.* *PLoS ONE* **6**, e28766 (2011).
8. 8.
Baek, M. *et al.* *Science* **373**, 871–876 (2021).
9. 9.
Mirdita, M. *et al.* Preprint at bioRxiv
<https://doi.org/10.1101/2021.08.15.456425> (2021).

10. 10.

Bryant, P., Pozzati, G. & Elofsson, A. Preprint at bioRxiv
<https://doi.org/10.1101/2021.09.15.460468> (2021).

11. 11.

Humphreys, I. R. *et al.* *Science*
<https://doi.org/10.1126/science.abm4805> (2021).

12. 12.

Evans, R. *et al.* Preprint at bioRxiv
<https://doi.org/10.1101/2021.10.04.463034> (2021).

13. 13.

Akdel, M. *et al.* Preprint at bioRxiv
<https://doi.org/10.1101/2021.09.26.461876> (2021).

This article was downloaded by **calibre** from <https://www.nature.com/articles/d41586-021-03499-y>.

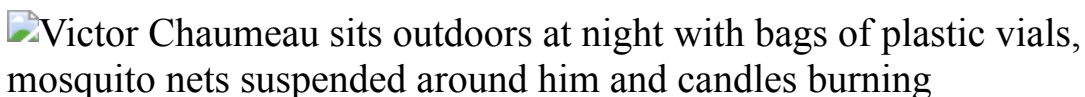
| [Section menu](#) | [Main menu](#) |

- WHERE I WORK
- 22 November 2021

All-nighter: staying up to fight malaria

Victor Chaumeau collects mosquitoes in Myanmar to better understand how to control malaria.

- [Brendan Maher](#)



Victor Chaumeau is head entomologist at the Shoklo Malaria Research Unit, based in Mae Sot, Thailand. Credit: David Högsholt for *Nature*

Every year, my team and I collect mosquitoes at about a dozen villages in Kayin state, Myanmar, a conflict zone near the Thai border. Run by the Shoklo Malaria Research Unit, based in Mae Sot, Thailand, it's one of the largest operations of its kind in the world. It looks like I'm working alone in this picture. In reality, I'm with a team of about 50 people. Most of the collection is done by local villagers, and a lot of work goes into training, coordination and logistics.

We travel by boat, scooter, tractor or car, and sometimes by elephant, to our sites. Htee Kaw Taw, the village in this photo, is accessible by car for only part of the year. Most collections are done between 18:00 and 06:00 for 5 nights, although we occasionally collect mosquitos for 24 hours to observe those that feed in the daytime. We set up five indoor and outdoor collection sites, and often an outdoor site with a 'bait' animal such as a pig or cow, to observe a range of feeding behaviours from the dozens of mosquito species that transmit malaria. Each mosquito goes — alive — into a plastic tube for

transport back to our laboratory in Mae Sot. Through various projects, we've collected probably around 300,000 insects since 2013.

We've learnt a lot from them. Our research, supported by a joint collaboration on tropical medicine by Mahidol University in Bangkok and the University of Oxford, UK, has shown that interventions to control malaria that work well in Africa, such as insecticide-treated bed nets and indoor spraying, are less effective in southeast Asia owing to the variety of mosquitoes there that feed outside or during the day.

We've also shown that providing antimalarial drugs to select populations prophylactically — known as mass drug administration — vastly reduces the number of mosquitoes carrying the parasite. The work supports the idea that people without symptoms are a major reservoir for malaria, and the strategy could go a long way towards eliminating the disease in southeast Asia.

Nature **599**, 710 (2021)

doi: <https://doi.org/10.1038/d41586-021-03500-8>

This article was downloaded by **calibre** from <https://www.nature.com/articles/d41586-021-03500-8>

Research

- **[Tracking the origin of Transeurasian languages](#)** [10 November 2021]

News & Views • A triangulation of linguistic, archaeological and genetic data suggests that the Transeurasian language family originated in a population of grain farmers in China around 9,000 years ago, and that agriculture underpinned its spread.

- **[Mice with disrupted mitochondria used to model Parkinson's disease](#)** [03 November 2021]

News & Views • Mice in which organelles called mitochondria are disrupted in vulnerable neuronal cells provide a new model of Parkinson's disease. The pattern of neurodegeneration challenges long-held ideas about the disease's motor symptoms.

- **[Electrons reveal the need for improved neutrino models](#)**

[24 November 2021]

News & Views • Experiments on electrons interacting with atomic nuclei have shown that the models used to measure neutrino oscillations — and thereby possibly to understand the formation of the Universe — are less accurate than we thought.

- **[A massive effort links protein-coding gene variants to health](#)** [25 October 2021]

News & Views • The protein-coding portions of more than 450,000 individuals' genomes have been sequenced, and analysed together with the individuals' health data, revealing rare and common gene variants linked to various health-related traits.

- **[How to make macroscale non-crystalline diamonds](#)** [24 November 2021]

News & Views

• A diamond shatters easily, despite it being the hardest natural material. Atomically disordered forms of diamond made from buckyballs might not only overcome this problem, but also allow other properties to be optimized.

- **[Electron-beam energy reconstruction for neutrino oscillation measurements](#)** [24 November 2021]

Article • Electron scattering measurements are shown to reproduce only qualitatively state-of-the-art lepton–nucleus energy reconstruction models, indicating that improvements to these particle-interaction models are required to ensure the accuracy of future high-precision neutrino oscillation experiments.

- **[Quantum gas magnifier for sub-lattice-resolved imaging of 3D quantum systems](#)** [24 November 2021]

Article • Existing techniques for high-resolution imaging of trapped quantum gases are limited to two-dimensional systems, but the approach described here works in three dimensions by magnifying the quantum gas with matter wave optics.

- **Colossal angular magnetoresistance in ferrimagnetic nodal-line semiconductors** [24 November 2021]
Article • A study reports a colossal angular magnetoresistance in the topological magnet Mn₃Si₂Te₆, resulting from a metal-to-insulator transition caused by controlled lifting of a topological band degeneracy, and discusses the key parameters involved.
- **Artificial heavy fermions in a van der Waals heterostructure** [24 November 2021]
Article • A study demonstrates the synthesis and characterization of a two-dimensional van der Waals heterostructure hosting artificial heavy fermions, providing a tunable platform for investigations of heavy-fermion physics.
- **On-chip electro-optic frequency shifters and beam splitters**
[24 November 2021]
Article • Engineering of the coupling between optical modes in a lithium niobate chip enables the realization of tunable, bi-directional and low-loss electro-optic frequency shifters controlled using only continuous and single-tone microwaves.
- **Distribution control enables efficient reduced-dimensional perovskite LEDs** [24 November 2021]
Article • The efficiency and operating lifetimes of perovskite light-emitting diodes is improved by using a fluorinated triphenylphosphine oxide additive to control the cation diffusion during film deposition and passivate the surface.
- **Ultrahard bulk amorphous carbon from collapsed fullerene** [24 November 2021]
Article • Preparing amorphous phases of carbon with mostly sp³ bonding in bulk is challenging, but macroscopic samples that are nearly pure sp³ are synthesized here by heating fullerenes at high pressure.
- **Synthesis of paracrystalline diamond** [24 November 2021]
Article • A study describes the synthesis, structural characterization and formation mechanism of a paracrystalline state of diamond, adding an unusual form of diamond to the family of carbon-based materials.
- **Mechanical forcing of the North American monsoon by orography** [24 November 2021]
Article • The core North American monsoon arises through topographic steering of the jet stream, and should be considered as convection-enhanced orographic rainfall produced by a mechanically forced stationary wave.

- [Triangulation supports agricultural spread of the Transeurasian languages](#) [10 November 2021]
Article • A ‘triangulation’ approach combining linguistics, archaeology and genetics suggests that the origin and spread of Transeurasian family of languages can be traced back to early millet farmers in Neolithic North East Asia.
- [A chickpea genetic variation map based on the sequencing of 3,366 genomes](#) [10 November 2021]
Article • Whole-genome sequencing of 3,171 cultivated and 195 wild chickpea accessions is used to construct a chickpea pan-genome, providing insight into chickpea evolution and enabling breeding strategies that could improve crop productivity.
- [Exome sequencing and analysis of 454,787 UK Biobank participants](#) [18 October 2021]
Article • Whole-exome sequencing analysis of 454,787 individuals in the UK Biobank is used to examine the association of protein-coding variants with nearly 4,000 health-related traits, identifying 564 distinct genes with significant trait associations.
- [Neural dynamics underlying birdsong practice and performance](#) [20 October 2021]
Article • In male zebra finches, song practice and courtship song performance are associated with distinct patterns of neural activity in the basal ganglia, resulting in reduced vocal variability during performance.
- [A human-specific modifier of cortical connectivity and circuit function](#) [27 October 2021]
Article • The human-specific gene duplication SRGAP2C is identified as a modifier of structural and functional features of cortical circuits leading to improved behavioural performance that may have allowed the emergence of cognitive properties characterizing the human brain.
- [Striatal indirect pathway mediates exploration via collicular competition](#) [03 November 2021]
Article • Indirect striatal projection neurons in the basal ganglia modulate activity in the superior colliculus, thereby controlling selection and exploration of actions in response to a reward omission.
- [Disruption of mitochondrial complex I induces progressive parkinsonism](#) [03 November 2021]
Article • Dysfunction of mitochondrial complex I in mice is sufficient to cause progressive parkinsonism in which the loss of nigral dopamine release critically contributes to motor dysfunction.

- **Cold-induced *Arabidopsis* FRIGIDA nuclear condensates for FLC repression** [03 November 2021]

Article • In *Arabidopsis thaliana*, downregulation of the floral repressor FLC in response to cold occurs through a mechanism in which the FLC activator FRIGIDA is sequestered into biomolecular condensates away from the FLC promoter.

- **Herpesviruses assimilate kinesin to produce motorized viral particles** [17 November 2021]

Article • Herpes simplex virus type I and pseudorabies virus assimilate kinesin from host epithelial cells and repurpose the motor to traffic to the nuclei of neurons in the peripheral nervous system.

- **Early-life inflammation primes a T helper 2 cell–fibroblast niche in skin** [27 October 2021]

Article • Time-limited skin inflammation in neonatal mice promotes a reciprocal interaction between type 2 helper T cells and fascial fibroblasts that regulates wound repair in later life.

- **Tumour DDR1 promotes collagen fibre alignment to instigate immune exclusion** [03 November 2021]

Article • In mouse models of triple-negative breast cancer, the extracellular domain of the collagen receptor DDR1 has a role in tumour defence against the immune system, by aligning collagen fibres to obstruct immune infiltration.

- **Diverse alterations associated with resistance to KRAS(G12C) inhibition** [10 November 2021]

Article • Multiple treatment-emergent alterations appear in patients with advanced-stage cancer who were treated with a KRAS inhibitor.

- **Cell-type specialization is encoded by specific chromatin topologies** [17 November 2021]

Article • A new technique called immunoGAM, which combines genome architecture mapping (GAM) with immunoselection, enabled the discovery of specialized chromatin conformations linked to gene expression in specific cell populations from mouse brain tissues.

- **Transposon-associated TnpB is a programmable RNA-guided DNA endonuclease** [07 October 2021]

Article • The RNA-directed nuclease TnpB from *Deinococcus radiodurans* can be reprogrammed to cleave DNA target sites in human cells.

- **Few-fs resolution of a photoactive protein traversing a conical intersection** [03 November 2021]

Article • Serial femtosecond crystallography (SFX) has provided significant understanding of time-resolved processes of various systems in biology, for example, rhodopsin, which underlies our vision. The approach involves femtosecond-length X-ray pulses directed at

protein crystals and has been used to study various photoactive proteins. However, the function of proteins such as rhodopsin requires trans–cis isomerization of a chromophore, which involves crossing of a conical intersection—a funne...

- **Spatial scale and the synchrony of ecological disruption** [24 November 2021]
Matters Arising •
- **Reply to: Spatial scale and the synchrony of ecological disruption** [24 November 2021]
Matters Arising •

- NEWS AND VIEWS
- 10 November 2021

Tracking the origin of Transeurasian languages

A triangulation of linguistic, archaeological and genetic data suggests that the Transeurasian language family originated in a population of grain farmers in China around 9,000 years ago, and that agriculture underpinned its spread.

- [Peter Bellwood](#) 0

The Transeurasian language family is one of the most widely distributed language families of the modern world, and one school of thought says that it encompasses the Turkic, Mongolic, Tungusic, Koreanic and Japonic language groups (Tungusic languages are spoken in northeastern China and Siberia). [Writing in Nature](#), Robbeets *et al.*¹ present their use of an innovative approach to resolve the long-standing debate about the origins and spread of this language family.

Access options

Subscribe to Journal

Get full journal access for 1 year

\$199.00

only \$3.90 per issue

[Subscribe](#)

All prices are NET prices.
VAT will be added later in the checkout.
Tax calculation will be finalised during checkout.

Rent or Buy article

Get time limited or full article access on ReadCube.

from \$8.99

[Rent or Buy](#)

All prices are NET prices.

Additional access options:

- [Log in](#)
- [Learn about institutional subscriptions](#)

Nature **599**, 557-558 (2021)

doi: <https://doi.org/10.1038/d41586-021-03037-w>

References

1. 1.

Robbeets, M. *et al.* *Nature* **599**, 616–621 (2021).

2. 2.

Nelson, S., Zhushchikhovskaya, I., Li, T., Hudson, M. & Robbeets, M. *Evol. Hum. Sci.* **2**, e5 (2020).

3. 3.

Wang, J. *et al.* *Archaeol. Anthropol. Sci.* **13**, 156 (2021).

4. 4.

Wang, C.-C. *et al. Nature* **591**, 413–419 (2021).

5. 5.

Bellwood, P. *Science* **361**, 31–32 (2018).

6. 6.

Bellwood, P. *First Farmers* (Blackwell, 2005).

7. 7.

Bellwood, P. & Renfrew, C. (eds) *Examining the Farming/Language Dispersal Hypothesis* (McDonald Inst., 2002).

8. 8.

Bellwood, P. *Evol. Hum. Sci.* **2**, e37 (2020).

9. 9.

Zhang, M., Yan, S., Pan, W. & Jin, L. *Nature* **569**, 112–115 (2019).

10. 10.

Honeychurch, W. *et al. Archaeol. Res. Asia* **26**, 100264 (2021).

11. 11.

Vovin, A. in *The Global Prehistory of Human Migration* (ed. Bellwood, P.) 197–203 (Wiley, 2015).

- NEWS AND VIEWS
- 03 November 2021

Mice with disrupted mitochondria used to model Parkinson's disease

Mice in which organelles called mitochondria are disrupted in vulnerable neuronal cells provide a new model of Parkinson's disease. The pattern of neurodegeneration challenges long-held ideas about the disease's motor symptoms.

- [Zak Doric](#) ⁰ &
- [Ken Nakamura](#) ¹

Mitochondria — the cellular organelles crucial for energy production — have long been thought to be disrupted in the neurodegenerative disorder Parkinson's disease. Mitochondrial function relies on the activity of various enzyme complexes, and dysfunction of complex I in particular has been implicated in Parkinson's disease. [Writing in Nature](#), González-Rodríguez *et al.*¹ report that they genetically engineered mice to lack the gene encoding a complex I subunit called NDUFS2 in neurons that produce the neurotransmitter molecule dopamine. One of the brain regions that has dopamine neurons, the substantia nigra, contains the neurons that die first in individuals with Parkinson's disease. The mice lacking NDUFS2 show neurodegeneration, providing a model of Parkinson's disease (named the MCI-Park model) based on mitochondrial dysfunction. Moreover, the authors' findings challenge the long-held idea that loss of dopamine release in the target structure of substantia nigra dopamine neurons, a brain region called the striatum, is sufficient to elicit the movement deficits associated with Parkinson's disease.

Access options

[Subscribe to Journal](#)

Get full journal access for 1 year

\$199.00

only \$3.90 per issue

[Subscribe](#)

All prices are NET prices.

VAT will be added later in the checkout.

Tax calculation will be finalised during checkout.

Rent or Buy article

Get time limited or full article access on ReadCube.

from \$8.99

[Rent or Buy](#)

All prices are NET prices.

Additional access options:

- [Log in](#)
- [Learn about institutional subscriptions](#)

Nature **599**, 558-560 (2021)

doi: <https://doi.org/10.1038/d41586-021-02955-z>

References

1. 1.

González-Rodríguez, P. *et al.* *Nature* **599**, 650–656 (2021).

2. 2.

Malpartida, A. B., Williamson, M., Narendra, D. P., Wade-Martins, R. & Ryan, B. J. *Trends Biochem. Sci.* **46**, 329–343 (2021).

3. 3.

Ryan, B. J, Hoek, S., Fon, E. A. & Wade-Martins, R. *Trends Biochem Sci.* **40**, 200–210 (2015).

4. 4.

Schapira, A. H. V. *et al.* *Lancet* **333**, 1269 (1989).

5. 5.

Hattori, N., Tanaka, M., Ozawa, T. & Mizuno, Y. *Ann. Neurol.* **30**, 563–571 (1991).

6. 6.

Grünewald, A. *et al.* *Ann. Neurol.* **79**, 366–378 (2016).

7. 7.

Haddad, D. & Nakamura, K. *FEBS Lett.* **589**, 3702–3713 (2015).

8. 8.

Sterky, F. H. *et al.* *Hum. Mol. Genet.* **21**, 1078–1089 (2012).

9. 9.

Kim, H.-W. *et al.* *Neurobiol. Aging* **36**, 2617–2627 (2015).

10. 10.

Quintana, A., Kruse, S. E., Kapur, R. P., Sanz, E. & Palmiter, R. D. *Proc. Natl Acad. Sci. USA* **107**, 10996–11001 (2010).

11. 11.

Betarbet, R. *et al.* *Nature Neurosci.* **3**, 1301–1306 (2000).

12. 12.

Ekstrand, M. I. *et al.* *Proc. Natl Acad. Sci. USA* **104**, 1325–1330 (2007).

13. 13.

Berhet, A. *et al.* *J. Neurosci.* **34**, 14304–14317 (2014).

14. 14.

Mimaki, M., Wang, X., McKenzie, M., Thorburn, D. R. & Ryan, M. T. *Biochim. Biophys. Acta* **1817**, 851–862 (2012).

15. 15.

Tuppen, H. A. L. *et al.* *Brain* **133**, 2952–2963 (2010).

16. 16.

Qian, H. *et al.* *Nature* **582**, 550–556 (2020).

17. 17.

Kordower, J. H. *et al.* *Brain* **136**, 2419–2431 (2013).

This article was downloaded by **calibre** from <https://www.nature.com/articles/d41586-021-02955-z>

- NEWS AND VIEWS
- 24 November 2021

Electrons reveal the need for improved neutrino models

Experiments on electrons interacting with atomic nuclei have shown that the models used to measure neutrino oscillations — and thereby possibly to understand the formation of the Universe — are less accurate than we thought.

- [Noemi Rocco](#) 0

Neutrinos are among the most elusive particles in the Universe — they can pass through sophisticated particle detectors without leaving a trace. And yet precise measurement of neutrinos is one of the highest priorities in particle physics, because it will provide crucial information about the Universe and how it was formed. It might also explain why the Universe seems to be mostly made of matter, even though the Big Bang should have created just as much antimatter. To obtain such measurements, experiments rely on theoretical models that predict how neutrinos interact with the nuclei of atoms. [Writing in Nature](#), Khachatryan *et al.*¹ (members of the CLAS and e4v collaborations) report evidence that these models are not as accurate as expected — suggesting that analysis of current and future experiments designed to characterize the properties of neutrinos might need to be rethought.

Access options

Subscribe to Journal

Get full journal access for 1 year

\$199.00

only \$3.90 per issue

[Subscribe](#)

All prices are NET prices.

VAT will be added later in the checkout.

Tax calculation will be finalised during checkout.

Rent or Buy article

Get time limited or full article access on ReadCube.

from \$8.99

[Rent or Buy](#)

All prices are NET prices.

Additional access options:

- [Log in](#)
- [Learn about institutional subscriptions](#)

Nature **599**, 560-561 (2021)

doi: <https://doi.org/10.1038/d41586-021-03456-9>

References

1. 1.

Khachatryan, M. *et al.* *Nature* **599**, 566–570 (2021).

2. 2.

Fukuda, Y. *et al.* *Phys. Rev. Lett.* **81**, 1562–1567 (1998).

3. 3.

Ahmad, Q. R. *et al. Phys. Rev. Lett.* **89**, 011301 (2002).

4. 4.

DUNE Collaboration. Preprint at <https://arxiv.org/abs/1807.10334> (2018).

5. 5.

Hyper-Kamiokande Proto-Collaboration. Preprint at
<https://arxiv.org/abs/1805.04163> (2018).

This article was downloaded by **calibre** from <https://www.nature.com/articles/d41586-021-03456-9>

| [Section menu](#) | [Main menu](#) |

- NEWS AND VIEWS
- 25 October 2021

A massive effort links protein-coding gene variants to health

The protein-coding portions of more than 450,000 individuals' genomes have been sequenced, and analysed together with the individuals' health data, revealing rare and common gene variants linked to various health-related traits.

- [Yukinori Okada](#) ORCID: [http://orcid.org/0000-0002-0311-8472⁰](http://orcid.org/0000-0002-0311-8472) &
- [Qingbo S. Wang](#) ORCID: [http://orcid.org/0000-0002-9110-5830¹](http://orcid.org/0000-0002-9110-5830)

To link genetic variations to human health, we need to collect genetic data and health-related information from as many individuals, and in as much detail, as possible. The principles of such association testing are long-standing¹, and the field of human genomics has expanded in scale and quality in the past few decades. [Writing in *Nature*](#), Backman *et al.*² report a new milestone. They have analysed the protein-coding parts of the genome — called the exome — of more than 450,000 individuals whose health and genetic data have been collected in the UK Biobank, identifying 12.3 million variants that lead to changes in the encoded protein, which are known as coding variants. The authors then tested these variants for associations with 3,994 health-related traits (health phenotypes) and found 8,865 such associations (Fig. 1). This work is on an unprecedented scale in terms of the number of participants and the quantity of genetic and clinical data gathered.

Access options

Subscribe to Journal

Get full journal access for 1 year

\$199.00

only \$3.90 per issue

[Subscribe](#)

All prices are NET prices.

VAT will be added later in the checkout.

Tax calculation will be finalised during checkout.

Rent or Buy article

Get time limited or full article access on ReadCube.

from \$8.99

[Rent or Buy](#)

All prices are NET prices.

Additional access options:

- [Log in](#)
- [Learn about institutional subscriptions](#)

Nature **599**, 561-563 (2021)

doi: <https://doi.org/10.1038/d41586-021-02873-0>

References

1. 1.

Risch, N. & Merikangas, K. *Science* **273**, 1516–1517 (1996).

2. 2.

Backman, J. D. *et al.* *Nature* **599**, 628–634 (2021).

3. 3.

Bycroft, C. *et al.* *Nature* **562**, 203–209 (2018).

4. 4.

Lek, M. *et al.* *Nature* **536**, 285–291 (2016).

5. 5.

Karczewski, K. J. *et al.* *Nature* **581**, 434–443 (2020).

6. 6.

Dewey, F. E. *et al.* *Science* **354**, aaf6814 (2016).

7. 7.

Taliun, D. *et al.* *Nature* **590**, 290–299 (2021).

8. 8.

Van Hout, C. V. *et al.* *Nature* **586**, 749–756 (2020).

9. 9.

Wang, Q. *et al.* *Nature* **597**, 527–532 (2021).

10. 10.

Reay, W. R. & Cairns, M. J. *Nature Rev. Genet.* **22**, 658–671 (2021).

11. 11.

Choudhury, A. *et al.* *Nature* **586**, 741–748 (2020).

12. 12.

This article was downloaded by **calibre** from <https://www.nature.com/articles/d41586-021-02873-0>

| [Section menu](#) | [Main menu](#) |

- NEWS AND VIEWS
- 24 November 2021

How to make macroscale non-crystalline diamonds

A diamond shatters easily, despite it being the hardest natural material. Atomically disordered forms of diamond made from buckyballs might not only overcome this problem, but also allow other properties to be optimized.

- [Alfonso San-Miguel](#) ✉

The brilliant facets of diamonds have entranced people throughout history and are a result of the ordered atomic structure of these gemstones. But this order comes at a cost: it makes diamonds fragile. In contrast to quartz and many other crystalline materials that produce atomically disordered forms, a disordered — and potentially less fragile — form of diamond has not been available. Writing in *Nature*, [Shang et al.¹](#) and [Tang et al.²](#) report how to produce atomically disordered diamond-like materials with millimetre-scale dimensions, constituting a breakthrough for materials science.

Access options

Subscribe to Journal

Get full journal access for 1 year

\$199.00

only \$3.90 per issue

[Subscribe](#)

All prices are NET prices.
VAT will be added later in the checkout.
Tax calculation will be finalised during checkout.

Rent or Buy article

Get time limited or full article access on ReadCube.

from \$8.99

[Rent or Buy](#)

All prices are NET prices.

Additional access options:

- [Log in](#)
- [Learn about institutional subscriptions](#)

Nature **599**, 563–564 (2021)

doi: <https://doi.org/10.1038/d41586-021-02957-x>

References

1. 1.

Shang, Y. *et al.* *Nature* **599**, 599–604 (2021).

2. 2.

Tang, H. *et al.* *Nature* **599**, 605–610 (2021).

3. 3.

Wisitsorakak, A. & Wolynes, P. G. *Proc. Natl Acad. Sci. USA* **109**, 16068–16072 (2012).

4. 4.

Mélinon, P. *Nanomaterials* **11**, 1694 (2021).

5. 5.

Robertson, J. *Surf. Coat. Technol.* **50**, 185–203 (1992).

6. 6.

Hirai, H. & Kondo, K. *Appl. Phys. Lett.* **64**, 1797–1799 (1994).

7. 7.

Zeng, Z. *et al.* *Nature Commun.* **8**, 322 (2017).

8. 8.

Sundqvist, B. *Phys. Rep.* **909**, 1–73 (2021).

9. 9.

Merlen, A. *et al.* *Carbon* **47**, 1643–1651 (2009).

10. 10.

Pande, C. S. & Cooper, K. P. *Prog. Mater. Sci.* **54**, 689–706 (2009).

11. 11.

Naik, S. N. & Walley, S. M. *J. Mater. Sci.* **55**, 2661–2681 (2020).

This article was downloaded by **calibre** from <https://www.nature.com/articles/d41586-021-02957-x>

- Article
- [Published: 24 November 2021](#)

Electron-beam energy reconstruction for neutrino oscillation measurements

- [M. Khachatryan¹](#)^{na1},
- [A. Papadopoulou²](#)^{na1},
- [A. Ashkenazi²](#),
- [F. Hauenstein^{1,2}](#),
- [A. Nambrath²](#),
- [A. Hrnjic²](#),
- [L. B. Weinstein¹](#),
- [O. Hen](#) [ORCID: orcid.org/0000-0002-4890-6544²](#),
- [E. Piasetzky³](#),
- [M. Betancourt⁴](#),
- [S. Dytman⁵](#),
- [K. Mahn⁶](#),
- [P. Coloma^{7,8}](#),
- [the CLAS Collaboration &](#)
- [e4v Collaboration*](#)

[Nature](#) volume **599**, pages 565–570 (2021)

- 844 Accesses
- 106 Altmetric
- [Metrics details](#)

Subjects

- [Experimental nuclear physics](#)
- [Experimental particle physics](#)

This article has been [updated](#)

Abstract

Neutrinos exist in one of three types or ‘flavours’—electron, muon and tau neutrinos—and oscillate from one flavour to another when propagating through space. This phenomena is one of the few that cannot be described using the standard model of particle physics (reviewed in ref. [1](#)), and so its experimental study can provide new insight into the nature of our Universe (reviewed in ref. [2](#)). Neutrinos oscillate as a function of their propagation distance (L) divided by their energy (E). Therefore, experiments extract oscillation parameters by measuring their energy distribution at different locations. As accelerator-based oscillation experiments cannot directly measure E , the interpretation of these experiments relies heavily on phenomenological models of neutrino–nucleus interactions to infer E . Here we exploit the similarity of electron–nucleus and neutrino–nucleus interactions, and use electron scattering data with known beam energies to test energy reconstruction methods and interaction models. We find that even in simple interactions where no pions are detected, only a small fraction of events reconstruct to the correct incident energy. More importantly, widely used interaction models reproduce the reconstructed energy distribution only qualitatively and the quality of the reproduction varies strongly with beam energy. This shows both the need and the pathway to improve current models to meet the requirements of next-generation, high-precision experiments such as Hyper-Kamiokande (Japan)[3](#) and DUNE (USA)[4](#).

Access options

[Subscribe to Journal](#)

Get full journal access for 1 year

\$199.00

only \$3.90 per issue

[Subscribe](#)

All prices are NET prices.

VAT will be added later in the checkout.

Tax calculation will be finalised during checkout.

Rent or Buy article

Get time limited or full article access on ReadCube.

from \$8.99

[Rent or Buy](#)

All prices are NET prices.

Additional access options:

- [Log in](#)
- [Access through your institution](#)
- [Learn about institutional subscriptions](#)

Fig. 1: Neutrino oscillations and energy spectra measurements.

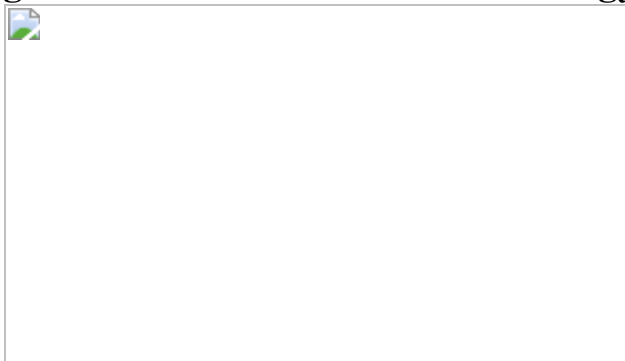


Fig. 2: Quasi-elastic reconstructed energy.



Fig. 3: Calorimetric reconstructed energy.

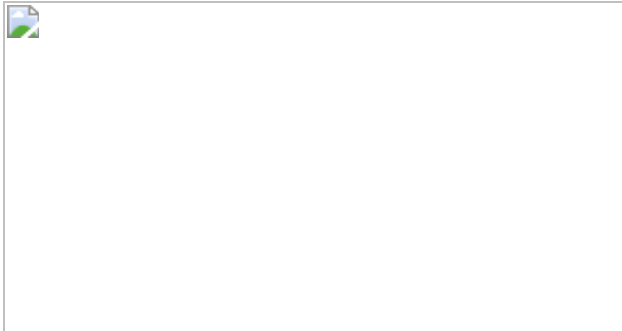
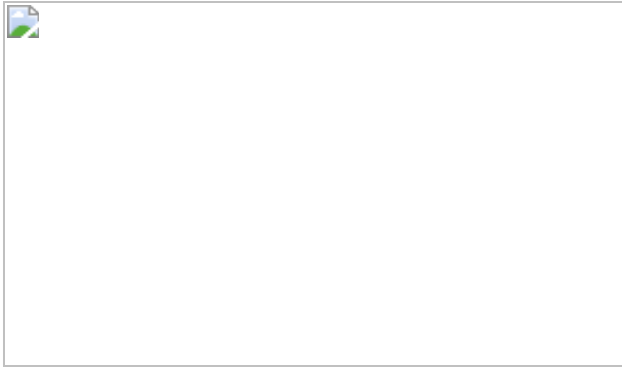


Fig. 4: Reconstructed energies and perpendicular momenta.



Data availability

The raw data from this experiment are archived in the Jefferson Lab's mass storage silo under the CLAS E2 run-period dataset. Access to these data can be facilitated by contacting either the corresponding authors or the Jefferson Lab computing centre at helpdesk@jlab.org.

Change history

- **25 November 2021**

The linking to some of the Source Data files was originally incorrect and has now been amended.

References

1. 1.
Particle Data Group. Review of particle physics. *Phys. Rev. D* **98**, 030001 (2018).
2. 2.
Mohapatra, R. N. et al. Theory of neutrinos: a white paper. *Rep. Prog. Phys.* **70**, 1757–1867 (2007).
3. 3.
Hyper-Kamiokande Proto-Collaboration. Hyper-Kamiokande design report. Preprint at <https://arxiv.org/abs/1805.04163> (2018).
4. 4.
DUNE Collaboration. The DUNE Far Detector interim design report. Volume 1: physics, technology and strategies. Preprint at <https://arxiv.org/abs/1807.10334> (2018).
5. 5.
Gonzalez-Garcia, M. C. & Nir, Y. Neutrino masses and mixing: evidence and implications. *Rev. Mod. Phys.* **75**, 345–402 (2003).
6. 6.
Fukugita, M. & Yanagida, T. Baryogenesis without grand unification. *Phys. Lett. B* **174**, 45–47 (1986).

7. 7.

The T2K Collaboration. Constraint on the matter–antimatter symmetry-violating phase in neutrino oscillations. *Nature* **580**, 339–344 (2020).

8. 8.

T2K Collaboration. Search for CP violation in neutrino and antineutrino oscillations by the T2K Experiment with 2.2×10^{21} protons on target. *Phys. Rev. Lett.* **121**, 171802 (2018).

9. 9.

Alvarez-Ruso, L. et al. NuSTEC White Paper: status and challenges of neutrino nucleus scattering. *Prog. Part. Nucl. Phys.* **100**, 1–68 (2018).

10. 10.

NOvA Collaboration. New constraints on oscillation parameters from ν_e appearance and ν_μ disappearance in the NOvA experiment. *Phys. Rev. D* **98**, 032012 (2018).

11. 11.

Ankowski, A. et al. Missing energy and the measurement of the CP-violating phase in neutrino oscillations. *Phys. Rev. D* **92**, 091301 (2015).

12. 12.

Rocco, N. Ab initio calculations of lepton–nucleus scattering. *Front. Phys.* **8**, 00116 (2020).

13. 13.

Dolan, S., Megias, G. D. & Bolognesi, S. Implementation of the SuSAv2-meson exchange current 1p1h and 2p2h models in GENIE

and analysis of nuclear effects in T2K measurements. *Phys. Rev. D* **101**, 033003 (2020).

14. 14.

Rocco, N., Lovato, A. & Benhar, O. Unified description of electron–nucleus scattering within the spectral function formalism. *Phys. Rev. Lett.* **116**, 192501 (2016).

15. 15.

MINERvA Collaboration. Neutrino flux predictions for the NuMI beam. *Phys. Rev. D* **94**, 092005 (2016).

16. 16.

Maan, K. K. on behalf of the NOvA Collaboration. Constraints on the neutrino flux in NOvA using the near-detector data. In *Proc. Sci. 38th Intl Conf. High Energy Physics (ICHEP2016)* Vol. 282 931 (Sissa, 2016).

17. 17.

T2K Collaboration. T2K near detector constraints for oscillation results. In *18th Intl Workshop on Neutrino Factories and Future Neutrino Facilities Search 2* (2017); <https://arxiv.org/abs/1701.02559>

18. 18.

Ankowski, A. & Friedland, A. Assessing the accuracy of the GENIE event generator with electron-scattering data. *Phys. Rev. D* **102**, 053001 (2020).

19. 19.

Papadopoulou, A. et al. Inclusive electron scattering and the GENIE neutrino event generator. *Phys. Rev. D* **103**, 113003 (2021).

20. 20.

Mecking, B. A. et al. The CEBAF large acceptance spectrometer (CLAS). *Nucl. Instrum. Meth. A* **503**, 513–553 (2003).

21. 21.

MINERvA Collaboration. Direct measurement of nuclear dependence of charged current quasielastic-like neutrino interactions using MINERvA *Phys. Rev. Lett.* **119**, 082001 (2017).

22. 22.

Aliaga, L. et al. Design, calibration, and performance of the MINERvA detector. *Nucl. Instrum. Meth. A* **743** 130–159 (2014).

23. 23.

Acciarri, R. et al. Design and construction of the MicroBooNE detector. *J. Instrum.* **12**, P02017 (2017).

24. 24.

The ICARUS-WA104 Collaboration, The LAr1-ND Collaboration, The MicroBooNE Collaboration & additional Fermilab contributors. A proposal for a three detector short-baseline neutrino oscillation program in the Fermilab Booster Neutrino Beam. Preprint at <https://arxiv.org/abs/1503.01520>

25. 25.

The DUNE Collaboration. Long-Baseline Neutrino Facility (LBNF) and Deep Underground Neutrino Experiment (DUNE) conceptual design report. Volume 2: The physics program for DUNE at LBNF. Preprint at <https://arxiv.org/abs/1512.06148> (2016).

26. 26.

Katori, T. & Martini, M. Neutrino–nucleus cross sections for oscillation experiments. *J. Phys. G* **45**, 013001 (2018).

27. 27.

Andreopoulos, C. et al. The GENIE neutrino Monte Carlo generator. *Nucl. Instrum. Meth. A* **614**, 87–104 (2010).

28. 28.

MicroBooNE Collaboration. First measurement of inclusive muon neutrino charged current differential cross sections on argon at $E_\nu \sim 0.8$ GeV with the MicroBooNE detector. *Phys. Rev. Lett.* **123**, 131801 (2019).

29. 29.

Lu, X.-G. et al. Measurement of nuclear effects in neutrino interactions with minimal dependence on neutrino energy. *Phys. Rev. C* **94**, 015503 (2016).

30. 30.

The T2K Collaboration. Characterization of nuclear effects in muon–neutrino scattering on hydrocarbon with a measurement of final-state kinematics and correlations in charged-current pionless interactions at T2K. *Phys. Rev. D* **98**, 032003 (2018).

31. 31.

MINERvA Collaboration. Measurement of final-state correlations in neutrino muon–proton mesonless production on hydrocarbon at $\langle E_\nu \rangle = 3$ GeV. *Phys. Rev. Lett.* **121**, 022504 (2018).

32. 32.

Freund, M. Analytic approximations for three neutrino oscillation parameters and probabilities in matter. *Phys. Rev. D* **64**, 053003 (2001).

33. 33.

Cervera, A. et al. Golden measurements at a neutrino factory. *Nucl. Phys. B* **579**, 17–55 (2000).

34. 34.

Cervera, A. et al. Erratum to: “Golden measurements at a neutrino factory”: [Nucl. Phys. B 579 (2000) 17]. *Nucl. Phys. B* **593**, 731–732 (2001).

35. 35.

Osipenko, M. et al. Measurement of the nucleon structure function F_2 in the nuclear medium and evaluation of its moments. *Nucl. Phys. A* **845**, 1–32 (2010).

36. 36.

CLAS Collaboration. Measurement of two- and three-nucleon short-range correlation probabilities in nuclei. *Phys. Rev. Lett.* **96**, 082501 (2006).

37. 37.

CLAS Collaboration. Survey of A_{LT} asymmetries in semi-exclusive electron scattering on ${}^4\text{He}$ and ${}^{12}\text{C}$. *Nucl. Phys. A* **748**, 357–373 (2005).

38. 38.

CLAS Collaboration. Proton source size measurements in the $eA \rightarrow e'ppX$ reaction. *Phys. Rev. Lett.* **93**, 192301 (2004).

39. 39.

CLAS Collaboration. Two-nucleon momentum distributions measured in ${}^3\text{He}(e, e'pp)n$. *Phys. Rev. Lett.* **92**, 052303 (2004).

40. 40.

CLAS Collaboration. Observation of nuclear scaling in the $A(e, e')$ reaction at $x_B > 1$. *Phys. Rev. C* **68**, 014313 (2003).

41. 41.

Hen, O. et al. Momentum sharing in imbalanced Fermi systems. *Science* **346**, 614–617 (2014).

42. 42.

Sealock, R. M. et al. Electroexcitation of the $\Delta(1232)$ in nuclei. *Phys. Rev. Lett.* **62**, 1350–1353 (1989).

43. 43.

González-Jiménez, R. et al. Extensions of superscaling from relativistic mean field theory: the SuSAv2 model. *Phys. Rev. C* **90**, 035501 (2014).

44. 44.

Megias, G. D. et al. Inclusive electron scattering within the SuSAv2 meson-exchange current approach. *Phys. Rev. D* **94**, 013012 (2016).

45. 45.

De Pace, A., Nardi, M., Alberico, W. M., Donnelly, T.W. & Molinaria, A. The 2p–2h electromagnetic response in the quasielastic peak and beyond. *Nucl. Phys. A* **726**, 303–326 (2003).

46. 46.

Katori, T. Meson exchange current (MEC) models in neutrino interaction generators. In *NuINT12: 8th Intl Workshop On Neutrino–Nucleus Interactions in the Few-GeV Region* (eds. Da Motta, H. et al.) <https://doi.org/10.1063/1.4919465> (AIP, 2015).

47. 47.

GENIE Collaboration. Neutrino–nucleon cross-section model tuning in GENIE v3. *Phys. Rev. D* **104**, 072009 (2021).

48. 48.

Berger, Ch. & Sehgal, L. M. Lepton mass effects in single pion production by neutrinos. *Phys. Rev. D* **76**, 113004 (2007).

49. 49.

Feynman, R. P., Kislinger, M. & Ravndal, F. Current matrix elements from a relativistic quark model. *Phys. Rev. D* **3**, 2706 (1971).

50. 50.

Bodek, A. & Yang, U. K. Higher twist, ζ_w scaling, and effective LO PDFs for lepton scattering in the few GeV region. *J. Phys. G* **29**, 1899–1905 (2003).

51. 51.

Yang, T., Andreopoulos, C., Gallagher, H., Hofmann, K. & Kehayias, P. A hadronization model for few-GeV neutrino interactions. *Eur. Phys. J. C* **63**, 1–10 (2009).

52. 52.

Sjostrand, T., Mrenna, S. & Skands, P. Z. PYTHIA 6.4 physics and manual. *J. High Energy Phys.* **2006**, 026 (2006).

53. 53.

Andreopoulos, C. et al. The GENIE neutrino Monte Carlo generator: physics and user manual. Preprint at <https://arxiv.org/abs/1510.05494> (2015).

54. 54.

Dytman, S. A. & Meyer, A. S. Final state interactions in GENIE. *AIP Conf. Proc.* **1405**, 213 (2011).

55. 55.

Merenyi, R. et al. Determination of pion intranuclear rescattering rates in ν_μ -Ne versus ν_μ -D interactions for the atmospheric ν flux. *Phys. Rev. D* **45**, 743–751 (1992).

56. 56.

Mashnik, S. G., Sierk, A. J., Gudima, K. K. & Baznat, M. I. CEM03 and LAQGSM03—new modeling tools for nuclear applications. *Phys. Conf. Ser.* **41**, <https://doi.org/10.1088/1742-6596/41/1/037> (2006).

57. 57.

Mo, L. W. & Tsai, Y.-S. Radiative corrections to elastic and inelastic $e p$ and μp scattering. *Rev. Mod. Phys.* **41**, 205–235 (1969).

58. 58.

The T2K Collaboration. Measurement of the muon neutrino charged-current single π^+ production on hydrocarbon using the T2K off-axis near detector ND280. *Phys. Rev. D* **101**, 012007 (2020).

59. 59.

The T2K Collaboration. Exclusive $\pi^0 p$ electroproduction off protons in the resonance region at photon virtualities $0.4 \text{ GeV}^2 \leq Q^2 \leq 1 \text{ GeV}^2$. *Phys. Rev. C* **101**, 015208 (2020).

60. 60.

Osipenko, M. *A Kinematically Complete Measurement of the Proton Structure Function F2 in the Resonance Region and Evaluation of its Moments*. PhD thesis, Moscow State Univ. (2002);
https://www.jlab.org/Hall-B/general/thesis/Osipenko_thesis.ps.gz

61. 61.

The T2K Collaboration. Improved constraints on neutrino mixing from the T2K experiment with 3.13×10^{21} protons on target. *Phys. Rev. D* **103**, 112008 (2021).

62. 62.

DUNE Collaboration. Long-baseline neutrino oscillation physics potential of the DUNE experiment. *Eur. Phys. J. C* **80**, 978 (2020).

Acknowledgements

We acknowledge the efforts of the staff of the Accelerator and Physics Divisions at Jefferson Lab that made this experiment possible. We thank L. Pickering for useful discussions. The analysis presented here was carried out as part of the Jefferson Lab Hall B Data-Mining project supported by the US Department of Energy (DOE). The research was supported also by DOE, the US National Science Foundation, the Israel Science Foundation, the Chilean Comisión Nacional de Investigación Científica y Tecnológica, the French Centre national de la recherche scientifique and Commissariat à l'Energie Atomique et aux Energies Alternatives, the French–American Cultural Exchange, the Italian Istituto Nazionale di Fisica Nucleare, the National Research Foundation of Korea, and the UK Science and Technology Facilities Council. P. Coloma acknowledges support from project PROMETEO/2019/083. This project has been supported by the European Union Horizon 2020 research and innovation programme under the Marie Skłodowska-Curie grant agreement no. 674896 (Elusives, H2020-MSCA-ITN- 2015-674896). G.D.M. acknowledges support from the Spanish Ministerio de Economía y Competitividad and ERDF (European Regional Development Fund) under contract FIS2017-88410-P, by the University of Tokyo ICRRs Inter-University Research Program FY2020 & 2021, refs no. A07 and A06; by the Junta de Andalucía (grant no. FQM160); and by the European Union Horizon 2020 research and innovation programme under the Marie Skłodowska-Curie grant agreement no. 839481. This document was prepared by the *e4v* Collaboration using the resources of the Fermi National Accelerator Laboratory (Fermilab), a US

Department of Energy, Office of Science, HEP User Facility. Fermilab is managed by Fermi Research Alliance, LLC (FRA), acting under contract no. DE-AC02-07CH11359. Jefferson Science Associates operates the Thomas Jefferson National Accelerator Facility for the DOE, Office of Science, Office of Nuclear Physics under contract DE-AC05-06OR23177. The raw data from this experiment are archived in Jefferson Lab's mass storage silo.

Author information

Author notes

1. These authors contributed equally: M. Khachatryan and A. Papadopoulou

Affiliations

1. Old Dominion University, Norfolk, VA, USA

M. Khachatryan, F. Hauenstein, L. B. Weinstein, M. J. Amaryan, D. Bulumulla, M. Hattawy, S. E. Kuhn, J. Poudel, Y. Prok & S. Stepanyan

2. Massachusetts Institute of Technology, Cambridge, MA, USA

A. Papadopoulou, A. Ashkenazi, F. Hauenstein, A. Nambrath, A. Hrnjic, O. Hen, A. Beck, R. Cruz-Torres, A. Denniston, I. Korover, S. May-Tal Beck, J. Pybus & E. P. Segarra

3. Tel Aviv University, Tel Aviv, Israel

E. Piasetzky, E. O. Cohen & M. Duer

4. Fermi National Accelerator Laboratory, Batavia, IL, USA

M. Betancourt

5. University of Pittsburgh, Pittsburgh, PA, USA

S. Dytman

6. Michigan State University, East Lansing, MI, USA

K. Mahn

7. Instituto de Física Corpuscular, Universidad de Valencia and CSIC,
Valencia, Spain

P. Coloma

8. Universidad Autonoma de Madrid, Madrid, Spain

P. Coloma

9. Florida International University, Miami, Florida, USA

S. Adhikari, J. C. Carvajal, L. Guo, A. Khanal & B. Raue

10. The George Washington University, Washington, DC, USA

Giovanni Angelini, W. J. Briscoe, Y. Ilieva, C. W. Kim, A. Schmidt, I.
I. Strakovsky & S. Strauch

11. Temple University, Philadelphia, PA, USA

H. Atac, M. Paolone & N. Sparveris

12. INFN, Ferrara, Italy

L. Barion, G. Ciullo, M. Contalbrigo, P. Lenisa, A. Movsisyan & L. L.
Pappalardo

13. Thomas Jefferson National Accelerator Facility, Newport News, VA,
USA

M. Battaglieri, S. Boiarinov, W. K. Brooks, V. D. Burkert, D. S.
Carman, A. Deur, H. Egiyan, L. Elouadrhiri, G. Gavalian, F. X.
Girod, L. Guo, D. Heddle, V. Kubarovskiy, N. Markov, V. Mokeev, P.

Nadel-Turronski, E. Pasyuk, P. Rossi, Y. G. Sharabian, S. Stepanyan, M. Ungaro & X. Wei

14. INFN, Genova, Italy

M. Battaglieri, A. Celentano, R. De Vita, L. Marsicano, M. Osipenko & M. Ripani

15. National Research Centre Kurchatov Institute - ITEP, Moscow, Russia

I. Bedlinskiy & O. Pogorelko

16. Duquesne University, Pittsburgh, PA, USA

F. Benmokhtar

17. Universita degli Studi di Brescia, Brescia, Italy

A. Bianconi, M. Leali, V. Mascagna & L. Venturelli

18. INFN, Pavia, Italy

A. Bianconi, M. Leali & L. Venturelli

19. Fairfield University, Fairfield, CT, USA

A. S. Biselli

20. Carnegie Mellon University, Pittsburgh, PA, USA

A. S. Biselli & R. A. Schumacher

21. University of Paris-Saclay, Gif-sur-Yvette, France

F. Bossu, M. Defurne & F. Sabati

22. Universidad Tecnica Federico Santa Maria, Valpara, Chile

W. K. Brooks, A. El Alaoui, H. Hakobyan & T. Mineeva

23. University Paris-Saclay, Orsay, France

P. Chatagnon, R. Dupre, M. Guidal, A. Hobart, D. Marchand, C. Munoz Camacho, S. Niccolai & E. Voutier

24. Lomonosov Moscow State University, Moscow, Russia

V. Chesnokov, E. Golovatch, B. S. Ishkhanov, E. L. Isupov, V. Mokeev & Iu. Skorodumina

25. Mississippi State University, Mississippi State, MS, USA

T. Chetry & L. El Fassi

26. University di Ferrara, Ferrara, Italy

G. Ciullo, P. Lenisa & L. L. Pappalardo

27. University of Glasgow, Glasgow, United Kingdom

L. Clark, D. I. Glazier, D. G. Ireland, K. Livingston, I. J. D. MacGregor, B. McKinnon, D. Protopopescu, G. Rosner, D. Sokhan & R. Tyson

28. University of Connecticut, Storrs, CT, USA

B. A. Clary, S. Diehl & K. Joo

29. Lamar University, Beaumont, TX, USA

P. L. Cole

30. Idaho State University, Pocatello, ID, USA

P. L. Cole, T. A. Forest & M. Holtrop

31. Florida State University, Tallahassee, FL, USA

V. Crede, P. Eugenio & A. I. Ostrovidov

32. INFN, Rome, Italy

A. D'Angelo, L. Lanza & A. Rizzo

33. Universita di Roma Tor Vergata, Rome, Italy

A. D'Angelo & A. Rizzo

34. Yerevan Physics Institute, Yerevan, Armenia

N. Dashyan, H. Hakobyan & H. Voskanyan

35. Ohio University, Athens, OH, USA

C. Djalali, K. Hicks & U. Shrestha

36. University of South Carolina, Columbia, SC, USA

C. Djalali, R. W. Gothe, Y. Ilieva, K. Neupane, Iu. Skorodumina, S. Strauch, N. Tyler & M. H. Wood

37. Argonne National Laboratory, Argonne, IL, USA

M. Ehrhart

38. Christopher Newport University, Newport News, VA, USA

R. Fersch & D. Heddle

39. INFN, Sezione di Torino, Torino, Italy

A. Filippi

40. University of New Hampshire, Durham, NH, USA

G. Gavalian & R. Paremuzyan

41. University of Richmond, Richmond, VA, USA

G. P. Gilfoyle

42. James Madison University, Harrisonburg, VA, USA

K. L. Giovanetti & G. Niculescu

43. College of William and Mary, Williamsburg, VA, USA

K. A. Griffioen & T. B. Hayward

44. Kyungpook National University, Daegu, Republic of Korea

H. S. Jo, W. Kim & K. Park

45. University of Virginia, Charlottesville, VA, USA

D. Keller, Y. Prok & J. Zhang

46. Norfolk State University, Norfolk, VA, USA

M. Khandaker & C. Salgado

47. Rensselaer Polytechnic Institute, Troy, NY, USA

V. Kubarovský & M. Ungaro

48. INFN, Laboratori Nazionali di Frascati, Frascati, Italy

M. Mirazita, P. Rossi & O. Soto

49. Institute fur Kernphysik (Juelich), Juelich, Germany

J. Ritman

50. University of York, York, UK

D. Watts & N. Zachariou

51. Canisius College, Buffalo, NY, USA

M. H. Wood

52. Duke University, Durham, NC, USA

Z. W. Zhao

53. CERN, European Organization for Nuclear Research, Geneva,
Switzerland

S. Dolan

54. Research Center for Cosmic Neutrinos, Institute for Cosmic Ray
Research, University of Tokyo, Kashiwa, Chiba, Japan

G. D. Megias

55. Fermi National Accelerator Laboratory, Batavia, IL, USA

S. Gardiner

Consortia

the CLAS Collaboration

- M. Khachatryan
- , A. Papadopoulou
- , A. Ashkenazi
- , F. Hauenstein
- , L. B. Weinstein
- , O. Hen
- , E. Piasetzky
- , A. Nambrath
- , A. Hrnjic
- , M. Betancourt
- , S. Dytman
- , K. Mahn
- , P. Coloma
- , S. Adhikari
- , M. J. Amaryan
- , Giovanni Angelini

- , H. Atac
- , L. Barion
- , M. Battaglieri
- , I. Bedlinskiy
- , A. Beck
- , F. Benmokhtar
- , A. Bianconi
- , A. S. Biselli
- , F. Bossu
- , S. Boiarinov
- , W. J. Briscoe
- , W. K. Brooks
- , D. Bulumulla
- , V. D. Burkert
- , D. S. Carman
- , J. C. Carvajal
- , A. Celentano
- , P. Chatagnon
- , V. Chesnokov
- , T. Chetry
- , G. Ciullo
- , L. Clark
- , B. A. Clary
- , E. O. Cohen
- , P. L. Cole
- , M. Contalbrigo
- , V. Crede
- , R. Cruz-Torres
- , A. D'Angelo
- , N. Dashyan
- , R. De Vita
- , M. Defurne
- , A. Denniston
- , A. Deur
- , S. Diehl
- , C. Djalali
- , M. Duer

- , R. Dupre
- , H. Egiyan
- , M. Ehrhart
- , A. El Alaoui
- , L. El Fassi
- , L. Elouadrhiri
- , P. Eugenio
- , R. Fersch
- , A. Filippi
- , T. A. Forest
- , G. Gavalian
- , G. P. Gilfoyle
- , K. L. Giovanetti
- , F. X. Girod
- , D. I. Glazier
- , E. Golovatch
- , R. W. Gothe
- , K. A. Griffioen
- , M. Guidal
- , L. Guo
- , H. Hakobyan
- , M. Hattawy
- , T. B. Hayward
- , D. Heddle
- , K. Hicks
- , A. Hobart
- , M. Holtrop
- , Y. Ilieva
- , D. G. Ireland
- , B. S. Ishkhanov
- , E. L. Isupov
- , H. S. Jo
- , K. Joo
- , D. Keller
- , A. Khanal
- , M. Khandaker
- , C. W. Kim

- , W. Kim
- , I. Korover
- , V. Kubarovsky
- , S. E. Kuhn
- , L. Lanza
- , M. Leali
- , P. Lenisa
- , K. Livingston
- , I. J. D. MacGregor
- , D. Marchand
- , N. Markov
- , L. Marsicano
- , V. Mascagna
- , B. McKinnon
- , S. May-Tal Beck
- , T. Mineeva
- , M. Mirazita
- , V. Mokeev
- , A. Movsisyan
- , C. Munoz Camacho
- , P. Nadel-Turonski
- , K. Neupane
- , S. Niccolai
- , G. Niculescu
- , M. Osipenko
- , A. I. Ostrovidov
- , M. Paolone
- , L. L. Pappalardo
- , R. Paremuzyan
- , K. Park
- , E. Pasyuk
- , O. Pogorelko
- , J. Poudel
- , Y. Prok
- , D. Protopopescu
- , J. Pybus
- , M. Ripani

- , B. Raue
- , J. Ritman
- , A. Rizzo
- , G. Rosner
- , P. Rossi
- , F. Sabati
- , C. Salgado
- , A. Schmidt
- , R. A. Schumacher
- , E. P. Segarra
- , Y. G. Sharabian
- , U. Shrestha
- , Iu. Skorodumina
- , D. Sokhan
- , O. Soto
- , N. Sparveris
- , S. Stepanyan
- , I. I. Strakovsky
- , S. Strauch
- , N. Tyler
- , R. Tyson
- , M. Ungaro
- , L. Venturelli
- , H. Voskanyan
- , E. Voutier
- , D. Watts
- , X. Wei
- , M. H. Wood
- , N. Zachariou
- , J. Zhang
- & Z. W. Zhao

e4v Collaboration*

- M. Khachatryan
- , A. Papadopoulou
- , A. Ashkenazi

- , F. Hauenstein
- , L. B. Weinstein
- , O. Hen
- , E. Piasetzky
- , A. Nambrath
- , A. Hrnjic
- , M. Betancourt
- , S. Dytman
- , K. Mahn
- , P. Coloma
- , S. Dolan
- , G. D. Megias
- , M. Khachtryan
- , A. Papadopoulou
- , A. Ashkenazi
- , F. Hauenstein
- , L. B. Weinstein
- , O. Hen
- , E. Piasetzky
- , A. Nambrath
- , A. Hrnjic
- , M. Betancourt
- , S. Dytman
- , K. Mahn
- , P. Coloma
- , S. Dolan
- , G. D. Megias
- & S. Gardiner

Contributions

The CEBAF Large Acceptance Spectrometer was designed and constructed by the CLAS Collaboration and Jefferson Lab. Data acquisition, processing and calibration, Monte Carlo simulations of the detector and data analyses were performed by a large number of CLAS Collaboration members, who also discussed and approved the scientific results. The analysis presented here was performed by M. Khachtryan, A.P., A.A., A. Hrnjic and A.N.

with guidance from A.A., F.H., O.H., E. Piasetzky and L.B.W., and was reviewed by the CLAS Collaboration. S. Dytman., M. Betancourt and K.M. provided expertise on neutrino scattering. S. Dytman, G.M., S. Dolan and S.G. helped develop *e*-GENIE. P. Coloma performed a simulation of the DUNE sensitivity to the oscillation parameters, and determined the impact of our results on the fit.

Corresponding author

Correspondence to [A. Ashkenazi](#).

Ethics declarations

Competing interests

The authors declare no competing interests.

Additional information

Peer review information *Nature* thanks Tingjun Yang and the other, anonymous, reviewer(s) for their contribution to the peer review of this work. Peer reviewer reports are available.

Publisher's note Springer Nature remains neutral with regard to jurisdictional claims in published maps and institutional affiliations.

Extended data figures and tables

[Extended Data Fig. 1 Energy distributions of different \$\nu_\mu\$ beams.](#)

Left, Before oscillation at the near detector; and right, after oscillation at the far detector^{61,62}. The vertical lines show the three electron beam energies of this measurement. The NOvA far-detector beam flux is calculated using the

near-detector flux and the neutrino oscillation parameters from the Particle Data Group. arb., arbitrary units.

[Extended Data Fig. 2 Peak energy reconstruction fraction and width.](#)

Left, The ratio of e -GENIE to data for the fraction of the weighted cross-section that reconstructs to the correct incident energy, plotted versus incident energy; and right, the e -GENIE–data weighted cross-section ratio for events that reconstruct to the correct incident energy, plotted versus incident energy. The triangles and dashed lines indicate the G2018/data ratios and the squares and solid lines indicate the SuSAv2/data ratios.

SuSAv2 is not intended to model nuclei lighter than ^{12}C . Yellow shows the carbon, blue shows helium and green shows iron. Error bars show the 68% (1σ) confidence limits for the statistical and point-to-point systematic uncertainties added in quadrature. Error bars are not shown when they are smaller than the size of the data point. Normalization uncertainties of 3% not shown.

[Source data.](#)

[Extended Data Fig. 3 Particle multiplicities and include cross-section extraction.](#)

Left, The proton (black) and charged pion (blue) multiplicities for data (points), SuSAv2 (solid histogram) and G2018 (dashed histogram) for 2.257-GeV carbon. Right, Comparison between the inclusive $\text{C}(e, e')$ cross-sections measured at 37.5° for data (points) and SuSAv2 (lines) for the 0.961- and 1.299-GeV SLAC data⁴² and our 1.159-GeV CLAS data. Error bars show the 68% (1σ) confidence limits for the statistical and point-to-point systematic uncertainties added in quadrature. Error bars are not shown when they are smaller than the size of the data point. Normalization uncertainties of 3% not shown.

[Source data.](#)

Extended Data Fig. 4 Energy feed-down cross-sections.

a–d, $(E_{\text{rec}} - E_{\text{true}})/E_{\text{true}}$ for data (points) and SuSAv2 (lines) for 1.159 GeV (red triangles and dotted lines), 2.257 GeV (green squares and solid lines) and 4.453 GeV (blue dots and solid lines) for C E_{cal} (**a**), C E_{QE} (**b**), Fe E_{cal} (**c**), and Fe E_{QE} (**d**). The plots are area-normalized and each bin has been scaled by the bin width. Error bars show the 68% (1σ) confidence limits for the statistical and point-to-point systematic uncertainties added in quadrature. Error bars are not shown when they are smaller than the size of the data point. Normalization uncertainties of 3% not shown.

[Source data.](#)

Extended Data Fig. 5 Transverse missing-momentum-dependent differential cross-section.

The cross-section plotted versus transverse missing momentum P_T for data (black points), SuSAv2 (black solid curve) and G2018 (black dotted curve). Different panels show results for different beam energy and target nucleus combinations: **a–c**, Carbon target at 1.159 GeV (**a**), 2.257 GeV (**b**) and 4.453 GeV (**c**). **d, e**, Iron target at 2.257 GeV (**d**) and 4.453 GeV (**e**). The 4.453-GeV yields have been scaled by four to have the same vertical scale. Coloured lines show the contributions of different processes to the SuSAv2 GENIE simulation: QE (blue), MEC (red), RES (green) and DIS (orange). Error bars show the 68% (1σ) confidence limits for the statistical and point-to-point systematic uncertainties added in quadrature. Error bars are not shown when they are smaller than the size of the data point. Normalization uncertainties of 3% not shown.

[Source data.](#)

Extended Data Fig. 6 $\delta\alpha_T$ -dependent differential cross-section.

a–j, The cross-section plotted versus $\delta\alpha_T$ (**a–e**) and versus $\delta\phi_T$ (**f–j**) for data (black points), SuSAv2 (black solid curve) and G2018 (black dotted curve). Different panels show results for different beam energy and target nucleus

combinations: **a–c**, Carbon target at 1.159 GeV (**a**), 2.257 GeV (**b**) and 4.453 GeV (**c**). **d, e**, Iron target at 2.257 GeV (**d**) and 4.453 GeV (**e**). The 4.453-GeV yields have been scaled by two to have the same vertical scale. Coloured lines show the contributions of different processes to the SuSAv2 GENIE simulation: QE (blue), MEC (red), RES (green) and DIS (orange). Error bars show the 68% (1σ) confidence limits for the statistical and point-to-point systematic uncertainties added in quadrature. Error bars are not shown when they are smaller than the size of the data point. Normalization uncertainties of 3% not shown.

[Source data](#).

[Extended Data Fig. 7 The effect of undetected pion subtraction.](#)

The number of weighted events as a function of reconstructed energy E_{QE} for 4.453-GeV $\text{Fe}(e, e')$ events for: left, events with a detected π^\pm or photon (blue), events with one (red) or two (light brown) undetected π^\pm or photons; and right, all $(e, e'X)$ events with detected or undetected π^\pm or photon (blue), (e, e') events with no detected π^\pm or photon (red), and (e, e') events after subtraction for undetected π^\pm or photon (light brown). The uncertainties are statistical only and are shown at the 1σ or 68% confidence level. Error bars are not shown when they are smaller than the size of the data point.

[Source data](#).

[Extended Data Fig. 8 Acceptance and radiation corrections.](#)

a–c, Acceptance correction factors; **d–f**, acceptance correction factor uncertainties; and **g–i**, electron radiation correction factors plotted versus E_{cal} for the three incident beam energies. Results for carbon are shown in black, helium in green and iron in magenta. The left column (**a, d, g**) shows the 1.159-GeV results, the middle column (**b, e, h**) shows the 2.257-GeV results and the right column (**c, f, i**) shows the 4.453-GeV results.

[Extended Data Fig. 9 CLAS detector and its calibration performance.](#)

a, Cutaway drawing of CLAS showing the sector structure and the different detectors. Yellow, toroidal magnet; blue, drift chambers; magenta, Cherenkov counter; red, scintillation counters (time of flight); green, electromagnetic calorimeter. The beam enters from the upper left and the target is in the center of CLAS. CLAS detector image reproduced with permission of the CLAS Collaboration. **b**, The 2.257-GeV ${}^3\text{He}(e, e'pp)X$ missing mass for data (solid histogram) and simulation (dashed histogram). **c**, The $\text{H}(e, e'\pi^+)X$ missing mass for data (black) and fit to data (red).

Extended Data Table 1 ($e, e'p)_{1p0\pi}$ events reconstructed to the correct beam energy

Supplementary information

[Peer Review File](#)

[Source Data Fig. 2](#)

[Source Data Fig. 3](#)

[Source Data Fig. 4](#)

[Source Data Extended Data Fig. 2](#)

[Source Data Extended Data Fig. 3](#)

[Source Data Extended Data Fig. 4](#)

[Source Data Extended Data Fig. 5](#)

[Source Data Extended Data Fig. 6](#)

[Source Data Extended Data Fig. 7](#)

Rights and permissions

[Reprints and Permissions](#)

About this article

Cite this article

Khachatryan, M., Papadopoulou, A., Ashkenazi, A. *et al.* Electron-beam energy reconstruction for neutrino oscillation measurements. *Nature* **599**, 565–570 (2021). <https://doi.org/10.1038/s41586-021-04046-5>

- Received: 29 June 2020
- Accepted: 22 September 2021
- Published: 24 November 2021
- Issue Date: 25 November 2021
- DOI: <https://doi.org/10.1038/s41586-021-04046-5>

Share this article

Anyone you share the following link with will be able to read this content:

[Get shareable link](#)

Sorry, a shareable link is not currently available for this article.

[Copy to clipboard](#)

Provided by the Springer Nature SharedIt content-sharing initiative

[Electrons reveal the need for improved neutrino models](#)

- Noemi Rocco

News & Views 24 Nov 2021

This article was downloaded by **calibre** from <https://www.nature.com/articles/s41586-021-04046-5>

| [Section menu](#) | [Main menu](#) |

- Article
- Open Access
- [Published: 24 November 2021](#)

Quantum gas magnifier for sub-lattice-resolved imaging of 3D quantum systems

- [Luca Asteria ORCID: orcid.org/0000-0002-7506-4573¹](#),
- [Henrik P. Zahn¹](#),
- [Marcel N. Kosch¹](#),
- [Klaus Sengstock^{1,2,3}](#) &
- [Christof Weitenberg ORCID: orcid.org/0000-0001-9301-2067^{1,2}](#)

Nature volume **599**, pages 571–575 (2021)

- 1562 Accesses
- 42 Altmetric
- [Metrics details](#)

Subjects

- [Bose–Einstein condensates](#)
- [Quantum simulation](#)

Abstract

Imaging is central to gaining microscopic insight into physical systems, and new microscopy methods have always led to the discovery of new phenomena and a deeper understanding of them. Ultracold atoms in optical lattices provide a quantum simulation platform, featuring a variety of advanced detection tools including direct optical imaging while pinning the atoms in the lattice^{1,2}. However, this approach suffers from the diffraction limit, high optical density and small depth of focus, limiting it to two-dimensional (2D) systems. Here we introduce an imaging approach

where matter wave optics magnifies the density distribution before optical imaging, allowing 2D sub-lattice-spacing resolution in three-dimensional (3D) systems. By combining the site-resolved imaging with magnetic resonance techniques for local addressing of individual lattice sites, we demonstrate full accessibility to 2D local information and manipulation in 3D systems. We employ the high-resolution images for precision thermodynamics of Bose–Einstein condensates in optical lattices as well as studies of thermalization dynamics driven by thermal hopping. The sub-lattice resolution is demonstrated via quench dynamics within the lattice sites. The method opens the path for spatially resolved studies of new quantum many-body regimes, including exotic lattice geometries or sub-wavelength lattices^{3,4,5,6}, and paves the way for single-atom-resolved imaging of atomic species, where efficient laser cooling or deep optical traps are not available, but which substantially enrich the toolbox of quantum simulation of many-body systems.

[Download PDF](#)

Main

Experimentally driven understanding of quantum mechanical phenomena depends crucially on the possibility of observing them at the microscopic level. The quantum nature of matter shows itself on small scales, which has triggered tremendous efforts to develop advanced methods with increasing resolution to image the quantum system itself. Here, we introduce the alternative approach based on the idea to first magnify the quantum system itself to more accessible scales, which can then be easily imaged. We demonstrate this approach in a quantum simulator composed of quantum gases in the form of ultracold atoms in optical lattices and realize imaging of 3D systems with 2D sub-lattice resolution.

Direct optically resolved imaging of ultracold atoms in optical lattices, known as quantum gas microscopy^{1,2}, requires very high numerical apertures and is so far restricted to 2D systems due to the fundamental limitation of the depth of focus and to unit lattice site occupation due to light-assisted collisions. The depth of focus can be overcome by using an electron microscope⁷ or an ion microscope⁸, but at the cost of a reduced detection efficiency and a large technological complexity. Recent experiments have reached sub-lattice resolution via super-resolution microscopy using nonlinear atom–light interactions^{9,10}, but relying on scanning techniques. Our quantum gas magnifier does not suffer from these limitations and extends 2D sub-lattice-site-resolved imaging to new 3D regimes such as bosons or fermions in 3D optical lattices or sub-wavelength lattices with drastically enhanced energy scales^{3,4,5,6}. The technique yields full single-shot images, which gives direct access to density correlations and, for example, spontaneous pattern formation such as density waves. Furthermore, the

concept can be applied and adapted to very different physical systems such as exotic atomic species or mixtures.

Our quantum gas magnifier uses matter wave optics in the time domain to magnify the atomic density distribution before the standard optical absorption imaging^{11,12}. To this end, a harmonic potential of trapping frequency $\omega_{\text{pulse}} = 2\pi/T$ is applied for a time $T/4$, mapping the spatial distribution to the momentum distribution^{13,14,15,16}. This is initialized in our case by switching off the lattice, which additionally helps in limiting interaction-driven aberrations due to the fast decrease in local density (see [Supplementary Information](#)). This matter wave lens is followed by free time-of-flight expansion (ToF) of duration t_{ToF} . This combination reproduces the initial spatial distribution with a magnification $M \approx \omega_{\text{pulse}} t_{\text{ToF}}$ (Fig. [1a](#)). Note that more complex pulsed lenses and other time-domain optical elements can be used in this scheme as well. An advantage of combining a $T/4$ pulse with time of flight is that the aberrations introduced by the finite ToF can be perfectly compensated by choosing the evolution time in the harmonic trap slightly above $T/4$ (see [Supplementary Information](#)).

Fig. 1: Working principle of the quantum gas magnifier using matter wave optics.

 **figure1**

a, The density distribution of ultracold atoms in an optical lattice is magnified by matter wave optics composed of a pulsed dynamics in a harmonic trap and a free expansion. Subsequently, it can be imaged with optical absorption imaging of moderate resolution and without restrictions from optical density or depth of focus. **b**,

Sketch of the 2D hexagonal optical lattice. **c**, Images of ultracold bosonic atoms in a 2D triangular lattice for constant system size given by the confinement $\omega_{\text{system}}/2\pi = 225$ Hz, but varying magnification of $M = 43(1), 65(1), 80(1)$ (from left) tuned via tighter magnetic confinements ω_{pulse} during the matter wave optics. **d**, Image of a larger system with confinement $\omega_{\text{system}}/2\pi = 89$ Hz imaged with magnification $M = 43(1)$. **e**, Images of a honeycomb lattice and a boron nitride lattice with a sublattice offset of 4.6 kHz with a magnification of $M = 89(1)$. The scale bars have a length of 1 μm . The atom number is in between 48,000 and 59,000 for the six images.

Figure [1c–e](#) demonstrates the power of this method with the first single-shot site-resolved images of a 3D quantum gases in 2D optical lattices including images of lattices with two-atomic basis. In the following, after describing the concept more closely, we additionally demonstrate high-resolution thermometry across the thermal-to-Bose–Einstein condensate (BEC) phase transition for a 3D quantum gas in a triangular optical lattice as well as full local addressability and precision measurements of thermally activated dynamics in a lattice system. Finally, we also demonstrate sub-wavelength resolution to study local dynamics. The flexibility and adaptability of our concept now allow for very precise locally resolved and locally controlled measurements of higher-dimensional quantum gas systems.

The experiments presented here use ^{87}Rb BECs evaporatively cooled in a magnetic trap. The potential of the magnetic trap is in-plane radially symmetric with a trapping frequency which is ramped within 100 ms to $\omega_{\text{system}} = 2\pi \times [89\text{--}658]$ Hz. We ramp up triangular or honeycomb optical lattices formed by the interference of lattice beams of wavelength $\lambda = 1,064$ nm leading to a lattice constant of $a_{\text{lat}} = 2\lambda/3 = 709$ nm, which sets the energy scale $E_{\text{rec}} = h^2/(2m\lambda^2)$ for the lattice depth, where h is Planck’s constant and m the atomic mass. The harmonic transverse confinement has a trapping frequency ω_z of typically $2\pi \times 29$ Hz, resulting in a Josephson junction array of BECs in the tubes of the 2D lattice. The trap frequency is then ramped to ω_{pulse} for the magnification protocol after freezing the density distribution in a deep optical lattice (see [Supplementary Information](#)). The magnetic trap is suitable for the $T/4$ evolution because of its smoothness, radial symmetry and strong confinement: for typical parameters of $t_{\text{ToF}} \approx 20$ ms and $\omega_{\text{pulse}}/(2\pi)$ up to ~ 700 Hz we measure large magnifications of up to $M = 93(1)$, allowing resolution of the lattice spacing with conventional absorption imaging with magnification 2 on a charge-coupled device (CCD) camera (Fig. [1](#)). The uncertainty in parentheses corresponds to the 68% statistical confidence interval.

The resolution of the quantum gas magnifier can be made very high because the harmonic trap has a large spatial extension corresponding to a large numerical aperture of the matter wave optics. In practice the resolution is mainly limited by the

convolution with our optical imaging resolution (see [Supplementary Information](#)). The effect of interactions during the magnification protocol can be effectively suppressed by working with incoherent systems or by removing the coherence via freezing in a deep lattice (see [Supplementary Information](#)).

As a first benchmark experiment, we study the thermal-to-BEC phase transition in a lattice of tubes, allowing us to confirm the faithful imaging of lattice site occupations. Furthermore, we show how the high-resolution access to real-space profiles via the magnifier provides an excellent approach to optical lattice thermometry, which requires much greater numerical effort from the more common momentum space images^{[17,18,19](#)}.

To study the phase transition, we prepare the system at varying temperature and atom number by adjusting the end point of the evaporation ramp and a varying hold time before ramping up the lattice to the final depth with tunnelling energy $J = \hbar \times 12$ Hz. For the analysis, we start with the extraction of the on-site populations (Fig. [2a,b](#)). The data can be described by a bimodal model consisting of a condensed part and a thermal part including the repulsion of the thermal atoms from the condensate in mean-field approximation (see [Methods](#)). The model is fitted to the 2D distribution and the excellent fit quality can be seen when plotting the data as a function of the radial position (Fig. [2c,d](#)) confirming the exact measurement of the lattice site occupations.

Fig. 2: Thermal-to-BEC phase transition in optical lattices observed via high-resolution density profiles.

 **figure2**

a, b, Spatial density distributions of BECs in triangular optical lattices prepared at different temperatures and atom numbers of 171(1) nK and 37,000(400) atoms (**a**), and 310(1) nK and 106,000(600) atoms (**b**). The densities are shown as atom numbers per lattice site from integration over the Wigner–Seitz cells. **c, d**, Atom number per tube as

a function of the radial position corresponding to **a** and **b**, respectively, with a bimodal fit (orange line) consisting of the condensed part (yellow line) and the thermal part (purple line). **e**, **f**, Condensate fraction (circles) obtained from the bimodal fits as a function of the temperature (**e**) and of the temperature in units of the scaling temperature $\langle T \rangle_{\{\rm rm\{c\}\}}^{\{0\}}$ (**f**). Most error bars are smaller than the symbol size. The light-blue line in **f** shows the power law approximation of the non-interacting theory described in the main text. The purple line is a fit to the data with the same power law. The bandwidth of the lowest band is $k_B \times 5.4$ nK and the gap between the first and second band is $k_B \times 290$ nK. The colour encodes the total atom number of the clouds. All error bars correspond to the 68% confidence interval.

Source data

The fit allows us to extract the temperature T from the thermal component and the condensate fraction f_0 from the atom numbers in the two components with very high precision. Owing to the dependence of the critical temperature T_c on the total atom number, the condensate fraction as a function of temperature does not result in a single curve (Fig. 2e). To describe this dependence we set up an analytic non-interacting model predicting the critical temperature $\langle T \rangle_{\{\rm rm\{c\}\}}^{\{0\}}$ to renormalize the experimental temperatures using $\langle T \rangle_{\{\rm rm\{c\}\}}^{\{0\}}$ as a scaling temperature, resulting in a collapse of the data on a single curve (Fig. 2f). We observe a shift of the critical temperature towards lower values compared to the non-interacting model. To quantify this shift we approximate the non-interacting model by a power law in the density of states, resulting in a description $f_0 = 1 - (T/T_c)^\alpha$ with $\alpha = 2.69(1)$ characterizing the underlying density of states interpolating between a lattice regime and a continuum regime (see [Methods](#)).

Fitting this function to the data satisfying $f_0 > 0.1$ results in $\langle T \rangle_{\{\rm rm\{c\}\}} = 0.901(4) \langle T \rangle_{\{\rm rm\{c\}\}}^{\{0\}}$, where the small statistical error reflects the excellent collapse on a single curve, thus showing the quality of the thermometry. Additionally, we estimate a systematic error of 1% stemming from an uncertainty of the atom number calibration of 3%. A shift of this order of magnitude is expected from interactions and finite size²⁰, but a closed theoretical model for our regime where both trap and lattice are relevant does not exist. With the enhanced interactions in the optical lattice, the shift is larger than those experimentally observed for BECs in 3D harmonic traps for comparable atom numbers^{21,22}. Interestingly, we observe a pronounced smoothing of the phase transition despite the rather large atom number, which might be due to the 2D–3D crossover geometry of an array of tubes. Our precision thermometry measurements thus provide a benchmark for future theoretical studies of phase transitions in such geometries.

In a second set of experiments, we employ magnetic resonance (MR) techniques to realize local addressing of individual lattice sites²³ and thereby demonstrate the full functionality of quantum gas microscopes without the need for large optical access thus making it compatible with other experimental constraints. While site-resolved addressing was previously also realized optically^{24,25} and with an electron beam²⁶, MR techniques are optimally suited for 3D systems by avoiding the depth of focus limitation of optical addressing beams and have, for example, been proposed for wavefunction engineering²⁷.

In the experimental protocol, we freeze the atomic distribution in a deep lattice and shift the magnetic trap ($\omega_{\text{addressing}}/2\pi = 543 \text{ Hz}$) by up to $20 \mu\text{m}$, creating magnetic gradients between 23 and $50 \text{ kHz } \mu\text{m}^{-1}$ at the atom's position. The magnetic gradient spatially splits the radio frequency (RF) transition between the initial stretched $F=2, m_F=2$ state and the target $F=2, m_F=1$ state and we drive spin flips at positions controlled via RF sweeps (Fig. 3a). To empty the addressed lattice sites, we make use of the strongly spin-dependent loss rates driven by hyperfine-changing collisions²⁸, which are suppressed for the stretched initial spin state but empty the addressed lattice sites during the sweep time of 100–400 ms. When choosing F -changing transitions instead, the removal of one state could be achieved via an optical push out. The magnifier approach can also be easily extended to spin dependent imaging (see [Supplementary Information](#)). By choosing the appropriate RF sweeps addressing equipotential surfaces of the magnetic trap, we create very well resolved patterns such as rings of varying radius or—when placing the atoms at the slope of the magnetic trap—single lines or half systems ([Supplementary Information](#)) (Fig. 3b).

Fig. 3: Local addressing and thermalization dynamics.

 figure3

a, Scheme of local addressing via RF transitions in a magnetic field gradient and a sketch of the hyperfine states of ^{87}Rb with the utilized RF transition and the loss channel. **b**, Example images of prepared density distributions. In the upper row, the magnetic trap is shifted approximately two times the system diameter along the x

direction before applying the RF sweeps. In the lower row, the magnetic trap is not shifted. The magnification is 60(1) for the first five images and 77(1) for the last image. **c**, Single-shot density profiles integrated along the y direction for different hold times after removing the left half of the cloud illustrating the thermalization dynamics. The different profiles are offset for clarity. The initial temperature is $T_{\text{init}} = 0.76(2)$ μK . **d**, Time evolution of the imbalance for different initial temperatures. **e**, Density as a function of radial position after 50 ms (blue), shifted upwards for clarity, and 3.2 s (red) hold time with bimodal fits using only lattice site populations with positive x positions larger than the maximally populated line (blue) and all populations (red) respectively. The data are averaged over 27 images (including the top and bottom data from **c**). The fit yields temperatures of 0.68(5) μK and 1.25(4) μK and demonstrates the reached thermal equilibrium. **f**, Dependence of the decay time on the initial temperature modelled by an Arrhenius process for thermal hopping and an offset rate for quantum tunnelling (see text and [Methods](#)). All error bars correspond to the 68% confidence interval.

[Source data](#)

Subsequently, we probe the thermalization dynamics after removal of atoms from one half of the system²⁹ (Fig. 3c). We monitor the thermalization via the imbalance $\mathcal{I} = (\{N\}_{\{\rm R\}} - \{N\}_{\{\rm L\}})/(\{N\}_{\{\rm R\}} + \{N\}_{\{\rm L\}})$ defined as the relative difference of the atom numbers N_R in the right half and N_L in the left half of the trap. The imbalance \mathcal{I} decays to zero (Fig. 3c, d) and we determine the thermalization rate from an exponential fit. We verify that the profiles with no imbalance are indeed in thermal equilibrium (Fig. 3e) by fitting a bimodal model consisting of an inverted parabola and a Gaussian.

The thermalization rate as a function of the initial temperature is almost constant up to temperatures of about 350 nK and then increases steeply with temperature (Fig. 3f). We model this by an Arrhenius law describing thermal hopping combined with an offset rate resulting from quantum tunnelling (see [Methods](#)). We obtain a potential barrier height of $V_B = k_B \times 2.4(6)$ μK , where k_B is the Boltzmann constant, in excellent agreement with the peak-to-peak lattice depth of $k_B \times 2.6$ μK deduced from lattice depth calibration and an offset rate $\Gamma_0 = 0.23(8)$ Hz related to the tunnelling energy $J = h \times 0.1$ Hz of the lowest band. These experiments demonstrate that the quantum gas magnifier allows very precise spatially resolved studies of thermalization dynamics in optical lattices in new parameter regimes, which could be extended to strongly correlated regimes by adding a transverse lattice.

Finally, we demonstrate the capability to resolve density features well below the lattice spacing by observing nanoscale dynamics after a quench of the lattice geometry. We start in a deep honeycomb lattice with large sublattice offset (see [Methods](#)) leading to

an initial population of the A sublattice only and control the geometry by varying the imbalance of the lattice beam intensities I_1 , I_2 and I_3 . By abruptly reducing $I_2 = I_3$ to $0.5I_1$, we create a lattice of dimers with enhanced tunnel coupling within the dimer as well as a displacement of the lattice sites (Fig. 4a), thus exciting both a tunnelling oscillation between the A and B sites and an oscillation within the lattice sites.

Fig. 4: Nanoscale dynamics in a honeycomb optical lattice.



a, The honeycomb lattice with energy offset between the A sites (closed circles) and B sites (open circles) can be tuned into a lattice of dimers with stronger tunnelling bonds along one direction (thicker grey lines). The inset shows cuts of the potential along a dimer before (light blue line) and after the quench (dark blue line) together with the initial density profile (red area). **b**, Experimental images for 10 μ s, 90 μ s after the quench. A lattice vector corresponds to 10.9 pixels with a magnification of $M = 93(1)$. **c**, Time evolution of the density distributions within one dimer after the quench from the simulation (left) and from the experiment (right, cut of 1 pixel width). For a realistic comparison we have broadened the simulation results with a Gauss filter of 76 nm width and added an offset (see [Methods](#)) (middle). The arrows mark the evolution times shown in **b**.

[Source data](#)

The resulting dynamics of the atomic density within the dimer (averaged over all dimers with at least 50% of the signal in the most populated dimer) is shown in (Fig. [4b, c](#)). We capture the dynamics by a non-interacting multi-band simulation including the finite switching time of the laser intensities of about 20 μ s. The quantum gas magnifier on honeycomb optical lattices allows resolving the interplay of tunnelling dynamics between lattice sites with nanoscale dynamics within the lattice sites^{9,10} and opens a real-space approach to studying multi-orbital systems especially for extended 3D systems.

In conclusion, we have introduced a quantum gas magnifier based on matter wave optics and used it to image 3D quantum gases in triangular and honeycomb optical lattices with a resolution below the lattice spacing. Spatially resolved measurements give access to central scientific problems such as transport phenomena²⁹, spontaneous domain formation³⁰, or chiral edge and interface states in interacting topological matter³¹. We estimate that the method can be pushed to a single-atom sensitive regime using free-space fluorescence imaging after the matter wave magnification, when the magnified lattice spacing is larger than the diffusive expansion from photon scattering^{32,33} or using metastable helium and multi-channel plates³⁴ (see [Supplementary Information](#)). This will allow for a direct study of correlations in strongly interacting systems of atomic species, for which laser cooling and very deep optical lattices as in conventional quantum gas microscopes are not available. The magnification approach also circumvents pairwise atom loss during imaging in quantum gas microscopes, allowing measurements of many-body systems with larger occupation number.

Furthermore, the quantum gas magnifier can be employed to access coherence properties with high spatial resolution, for example by applying masks in Fourier space³⁵ or by magnification of interference phenomena like Talbot revivals³⁶

(see [Supplementary Information](#)). We also expect that the sub-lattice spacing resolution would allow band-resolved studies of multi-band systems.

Methods

Optical lattice setup

Our optical lattice setup consists of three running waves of wave vector \mathbf{k}_i with $|\mathbf{k}_i| = 2\pi/\lambda$ intersecting under an angle of 120° . Depending on the polarization of the beams we obtain either a triangular lattice (linear polarization perpendicular to the lattice plane), a honeycomb lattice (linear polarization in plane)^{[37](#)} or a boron nitride lattice (suitable elliptical polarization of the lattice beams^{[38](#)} as in this work or using spin-dependent light shifts^{[39](#)}).

The resulting potential can be written as

```
\begin{array}{c} V_{\rm lat2D}(\mathbf{r}) = \sum_i > \\ j \sqrt{V_{\rm lat}}^i V_{\rm lat}^j \times [\cos^2(\theta) \cos((\mathbf{k}_i - \mathbf{k}_j) \cdot \mathbf{r}) + \alpha_i - \alpha_j] - 2 \sin^2(\theta) \cos((\mathbf{k}_i - \mathbf{k}_j) \cdot \mathbf{r})] \end{array}
```

where the $V_{\rm lat}^i$ are proportional to the intensities of the lattice beams. θ is the angle of the polarization (long half axis) with respect to the lattice plane, α_i is the relative phase between the s and p components of the polarization for beam i . We neglected the phases of the beams with respect to each other because they only result in a global shift of the lattice. If we just name a single lattice depth, then all $V_{\rm lat}^i$ are equal. The boron nitride lattice in Fig. 3 uses $\theta = 9^\circ$ and $\alpha = (0, 120^\circ, 240^\circ)$ yielding an energy offset between the A and B sublattice quantified by the tight-binding parameter Δ_{AB} (ref. [38](#)). Note that the triangular lattice has a much larger barrier between nearest neighbours than the honeycomb or boron nitride lattice for the same laser intensities^{[40](#)}.

Read-out of lattice site populations

For several experiments only the total population of the lattice sites is of interest. We extract these by first fitting a triangular lattice to the data and subsequently summing up the signal in the Wigner–Seitz cells around the individual sites as explained in the following. The lattice constant $a_{\rm lat}$ in pixels is determined by integrating the density of individual images along a real space lattice vector yielding a one-dimensional profile with lattice constant a_{1D} , which is obtained from a fit with the heuristic function $A \exp(-(x - x_0)^2/(2\sigma^2)) (\cos(\pi x/a_{1D} + \phi)^2 + \Delta)$. Finally, the lattice constant is deduced

from the average fit parameter from two different such directions as $\langle\{a\}_z\{\rm{rm}\{lat\}\}\rangle=2\langle a\rangle_1\{\rm{rm}\{D\}\}\}/\sqrt{3}$. Next, the spatial phase of the lattice is determined by multiplying the image with a mask that removes the signal from pixels at a certain radius around the sites of a triangular lattice with the lattice constant determined beforehand. The phase of this mask is varied and the configuration minimizing the remaining density is considered the lattice phase. The final step is to determine the population of each lattice site by summing over the Wigner–Seitz cell around the lattice site. To minimize discretization errors the pixels of the camera are subdivided such that the radius of the cell is about ten subpixels. For an example image with non-discretized Wigner–Seitz masks see Extended Data Fig. 1.

For the lattices with two-atomic basis we slightly adjust the algorithm for lattice phase determination by maximizing the density which is not masked thus locating the centres of the honeycombs.

Lattice phase drifts

For our hexagonal lattice setup composed of three laser beams in two dimensions, phase shifts of the lattice beams only lead to a translation of the whole lattice potential, but not to a change of the lattice geometry⁴¹. We verify that such phase drifts are not a problem on the time scale of the experiments presented here by measuring the position drift of the atomic cloud’s centre of mass in a very deep optical lattice. We find that the cloud position moves and scatters by less than one lattice site peak-to-peak within 6 s hold time. We checked in a previous set of measurements where we deliberately move the lattice, that the lattice is deep enough to be able to drag the atoms along. Shot-to-shot lattice drifts exceed one lattice site (cycle time of 30 s).

Our characterization of the slow phase drifts is compatible with recent direct measurements of triangular lattices using quantum gas microscopes^{42,43}. The drifts can be further reduced to one lattice site per minute in a setup with a single, refolded lattice beam⁴³. In our case, the three beams go through separate optical fibres, a setup in which phase locks have been implemented to stabilize the phase³⁷. From our characterization, we conclude that a phase lock is not necessary for the measurements presented here. The random lattice phase between individual images can be easily taken into account by identifying the phase. For data evaluation in the main text, we determine the lattice position for every experimental image via a fit routine as described above. Note that the envelope of the atomic density is given by the position of the magnetic trap and is therefore not affected by lattice phase drifts.

Bimodal fits of density profiles

The lattice-gas profiles can be described by a bimodal model. Since we are considering the on-site populations only, the presence of the lattice can be included by a renormalization of the interaction constant⁴⁴ $g_{\text{eff}} = g \times A_{\text{WS}} / (2\pi\sigma^2)$ and otherwise using a continuum formalism. Here, A_{WS} is the area of the Wigner–Seitz cell, σ the on-site radial oscillator length and $g = 4\pi\hbar^2 a_{\text{sc}} / m$ the interaction constant, computed from the scattering length $a_{\text{sc}} \approx 100$ Bohr radii and the mass $m = 87$ u. The on-site radial oscillator length is computed as $\sigma = \sqrt{\hbar / (m\omega)}$ from the lattice depth using $\hbar\omega = 3\sqrt{2V_{\text{lat}} / (E_{\text{rec}})}$. The data in Fig. 2 is taken with a lattice depth of $V_{\text{lat}} = 1E_{\text{rec}}$.

The condensed atoms are described by a 3D Thomas–Fermi profile integrated along line of sight,

$$\text{\$}\{n\}_{\text{BEC}}(\text{x},\text{y})=\int \text{d}\text{z} \frac{1}{8\pi} \frac{N_{\text{BEC}}}{\left(1-\frac{\rho(x,y)}{\rho(R_z)}\right)^2} \text{(1)}$$

The fit parameters here are the centre of the cloud x_0, y_0 resulting in $\rho(x, y)^2 = (x - x_0)^2 + (y - y_0)^2$, the in-plane Thomas–Fermi radius R_ρ from which the out-of-plane radius R_z is deduced via a computed aspect ratio, and the number of atoms in the BEC N_{BEC} . In fact, only for the lowest evaporation frequency, where the BEC is very distinct from the thermal part, N_{BEC} and R_ρ are fitted independently. For all other fits we compute the Thomas–Fermi radius from the number of condensed atoms using the expected scaling $R_\rho = \gamma N_{\text{BEC}}^{1/5}$ with γ determined as its mean value from the fits at lowest evaporation frequency. We obtain $\gamma = 0.354 \mu\text{m}$, which agrees excellently with the expected value $\gamma_{\text{theo}} = 0.352 \mu\text{m}$ obtained from⁴⁵

$$\text{\$}\{\gamma_{\text{theo}}\}=\frac{1}{8\pi} \frac{N_{\text{BEC}}}{\left(\frac{g}{m\omega_{\text{system}}} \right)^{1/5}} \text{(2)}$$

supporting the validity of the approximations made. Here $\omega_{\text{system}} = 2\pi \times 305 \text{ Hz}$, $(\bar{\omega}) = (\omega_{\text{system}}^2 \omega_z)^{1/3}$, $\omega_z = 2\pi \times 29 \text{ Hz}$ and $\bar{a} = \sqrt{\hbar / (m\bar{\omega})}$.

The thermal density distribution is described in a semi-ideal approach, that is, as an ideal gas in a potential $V(x) = V_{\text{trap}}(x) + V_{\text{BEC}}(x)$ given by the external trap $V_{\text{trap}}(x)$ and

the repulsion from the condensed atoms $V_{\text{BEC}}(x) = 2 g_{\text{eff}} n_{\text{BEC}}(x)$. In semi-classical approximation the ideal Bose gas density distribution is given by⁴⁵

$$\text{\$}\$\{n\}_{\{\{\text{rm}\{\text{th}\}\}\}}(x)=\{g\}_{\{3/2\}}(\exp(-\beta(V(x)-\mu)))/\{\lambda\}_{\{\{T\}\}^{\{3\}}} \quad (3)$$

with $\langle g \rangle_n(x) = \sum_{i>0} \{x\}^i / \{i\}^n$ and $\langle \lambda(T) \rangle = \hbar / \sqrt{2 \pi / (m k_B T)}$. Additionally, we allow for a small offset that we subtract when determining atom numbers. The fit is performed on the 2D density distribution and both the data and the fit function are subsequently plotted as a function of radial position. Extended Data Fig. 2 shows the data from Fig. 2c,d of the manuscript along with a plot of the logarithm of the density versus the square of the radius, which yields a straight line in the thermal wings. This plot shows the excellent agreement between data and fit and also makes the change of the slope at the onset of the BEC fraction more visible.

Interaction shift and finite size shift

Interactions are known to shift the critical temperature for the BEC transition with a sign depending on the trapping geometry. For a 3D harmonic trap in mean field approximation the shift is negative and given by^{20,45}

$$\text{\$}\$\Delta\{T\}_{\{\{\text{rm}\{c\}\}\}}/\{T\}_{\{\{\text{rm}\{c\}\}\}} \approx -1.33 \frac{\langle g \rangle_{\{\{\text{rm}\{\text{eff}\}\}\}}}{\langle g \rangle \frac{\langle a \rangle_{\{\{\text{rm}\{sc\}\}\}}}{\langle a \rangle} N^{1/6}} \quad (4)$$

predicting a shift of about -0.24 for the typical atom number of the condensed samples of $N = 5 \times 10^4$, which is larger than the measured shift of $-0.099(4)$. However, for interactions of this strength the mean-field approximation overestimates the shift²². Note that we are not aware of a prediction for our 2D–3D crossover geometry of an array of tubes. Our measurements thus set a benchmark for future theoretical studies on the interesting setting of Josephson junction arrays.

We also recall the prediction for the finite size shift of the critical temperature for a 3D harmonic trap. For an anisotropic harmonic trap with trap frequencies $\omega_x, \omega_y, \omega_z$ and their geometric mean $\langle \bar{\omega} \rangle = (\langle \omega_x \rangle \langle \omega_y \rangle \langle \omega_z \rangle)^{1/3}$ and arithmetic mean $\omega_m = (\omega_x + \omega_y + \omega_z)/3$, the shift is given by^{20,45}.

$$\text{\$}\$\Delta\{T\}_{\{\{\text{rm}\{c\}\}\}}/\{T\}_{\{\{\text{rm}\{c\}\}\}} \approx -0.73 \frac{\langle \omega \rangle_{\{\{\text{rm}\{m\}\}\}}}{\langle \bar{\omega} \rangle N^{-1/3}} \quad (5)$$

With our trapping frequencies of $2\pi \times (305, 305, 29)$ Hz, the anisotropy factor is $(\langle \omega \rangle_{\rm rm} / \bar{\omega}) = 1.53$ and the expected shift is -0.03 for our atom number of $N \approx 5 \times 10^4$, that is, much smaller than observed. Note that both interactions and finite size effects can contribute to the shift.

The observed smoothing over a range of almost 0.2 in rescaled temperature is only expected for much smaller atom numbers in the case of a 3D harmonic trap⁴⁶. We therefore conclude that finite size effects are strongly enhanced in our 2D–3D crossover geometry of an array of tubes. We have verified that the small condensate fractions involved in the smoothed transition do not arise from fit artefacts of the bimodal profile to the density profiles. The good agreement with the curve for the visibility shown in Extended Data Fig. 4 is further evidence that the signal is physical and demands for further theoretical studies.

Theoretical description of the density of states

We compare our data of the thermal-to-BEC phase transition to non-interacting calculations based on the density of states. To this end we compute the Hamiltonian matrix for our trap in position basis and diagonalize it. In the numerical spectrum we clearly recognize a crossover between two power laws as a slope change in the log–log plot of Extended Data Fig. 3a. The asymptotes of this crossover can be understood using analytical considerations.

The high energy limit coincides with the well-known spectrum of a 3D harmonic trap resulting in

$$\text{N}(E) = \frac{1}{6} \left(\frac{E}{\hbar \bar{\omega}} \right)^3 \quad (6)$$

states up to energy E . This is due to the fact that the gaps between higher bands are negligible compared to the band widths. So we have to count separately the first band states and harmonic oscillator-like states.

For energies $E < \Delta_g$, where Δ_g is the first bandgap, only states of the first kind are relevant. Here, the tunnel coupling $J = h \times 12$ Hz is negligible compared to the offset introduced by the external trap, which is $\Delta = 1/2m\omega_{\text{syst}}^2 a_{\text{lat}}^2 = h \times 200$ Hz for a site in the centre compared to a nearest neighbour. Hence the spectrum is given by

$$E_{ijk} = \frac{1}{2m} \langle \omega_{\rm rm}(\text{syst}) \rangle^2 r_{ij}^2 + (k+1/2)\hbar \bar{\omega} \quad (7)$$

with r_{ij} being the distance of the lattice site indexed ij from the trap centre and k is the index for the z direction. A lengthy calculation leads to $N(E) = (E/E_0)^2$ with \(\{E\}_0=\sqrt{\hbar A_{\rm WS} m \omega^3 / (2\pi^2)}=h \times 57\text{ Hz}\).

We can therefore find an approximation of the numerical result by the Ansatz

$$\begin{aligned} \text{N}(E) &= \left(\frac{E}{E_0} \right)^2 + \left(\frac{\max(g)}{\Delta_g} \right) \left(\frac{E - \hbar \Delta_g}{\hbar \omega} \right)^3, \end{aligned} \quad (8)$$

where Δ_g is obtained from a simulation without external trap. The crossover between the two power laws appears here at the band gap Δ_g , because the higher bandgaps are small and the lattice can be neglected at higher energies. This analytical model fits very well to the exact diagonalization up to the numerically accessible energies (Extended Data Fig. 3a) while asymptotically reaching the known analytic limit of equation (6) for high energies.

Now we turn to the detailed derivation of the theory curve for a non-interacting system (light-blue line in Fig. 2f). From $N(E)$ we obtain the density of states $g(E) = dN/dE$, which in turn allows to numerically compute the critical temperature \(\{T\}_c(N)\) from

$$\begin{aligned} N &= \int dE g(E) / [\exp(E/\{k\}_B T_c(N)) - 1], \end{aligned} \quad (9)$$

that is, \(\{T\}_c(N)\) is the temperature yielding exactly N excited atoms for chemical potential $\mu = 0$. The fraction of condensed atoms for a given temperature \(\{T\}_c(N)\) can be computed by first evaluating the number of excited atoms as

$$\begin{aligned} N_{\rm exc} &= \int dE g(E) / [\exp(E/\{k\}_B T) - 1] \end{aligned} \quad (10)$$

and then inferring $f_0 = (N - N_{\rm exc})/N$. Following these steps we can compute \(\{T\}_c(N)\) and f_0 for every experimental data point from its measured particle number and temperature. The resulting theoretical values are plotted in Extended Data Fig. 3b. We find that these values can be approximated by \(\{f\}_0 = 1 - \{(T/\{T\}_c(N))^{\alpha}\}^{\alpha}\) as obtained by assuming the density of states \(\{g(E)\} = C \alpha E^{\alpha-1}\) to be a power law⁴⁵. Fitting the theoretical results for \(\{f\}_0(T/\{T\}_c(N))^\alpha\) with α as the fit

parameter yields $\alpha = 2.69(1)$. The corresponding fit shown in Extended Data Fig. 3b is the same line as the light-blue line in Fig. 2f (Extended Data Fig. 3b).

Comparison to ToF data

For comparison, we also take momentum space images from ToF expansion at the same parameters and evaluate their visibility⁴⁷, which is a measure of coherence in the system. We use circular masks around the Bragg peaks (Extended Data Fig. 4a). The radius is determined by fitting the ToF data by a central bimodal distribution

$$\begin{aligned} \$\$n(\{\bf{k}\};\sigma,\{k\}_{\rm R},\{n\}_0,\{G\},\{n\}_0,\{P\}), \\ \{\bf{k}\}_0=\{n\}_0,\{G\}\exp(-\{\bf{k}\}- \\ \{\bf{k}\}_0)^2/(2\sigma^2)+\{n\}_0,\{P\}),\max(1- \\ (\{\bf{k}\}-\{\bf{k}\}_0)^2/\{k\}_{\rm R}^2,0) \\ (11) \end{aligned}$$

and a set of six inverse parabola $n(k; k_{\rm R}, n_{0,P}, k_0) = n_{0,P} \max(1 - (k - k_0)2/k_{\rm R}^2, 0)$ spaced by a reciprocal lattice vector from the centre, resulting in the complete fit function reading

$$\begin{aligned} \$\$\\begin{array}{c} n(\{\bf{k}\};\sigma,\{k\}_{\rm R},\{k\}_{\rm Bragg}, \\ \{n\}_0,\{G\},\{n\}_0,\{P\},\{n\}_0,\{P\}, \\ \{k\}_{\rm Bragg},\{\bf{k}\}_0,\{k\}_{\rm reci}) \\ =n(\{\bf{k}\};\sigma, \\ \{k\}_{\rm R},\{c\},\{n\}_0,\{G\},\{n\}_0,\{P\},\{k\}_{\rm Bragg}, \\ \{n\}_0,\{P\},\{k\}_{\rm Bragg},\{\bf{k}\}_0) \\ +\sum_{j=1}^6 n(\{\bf{k}\};\{k\}_{\rm R}, \\ \{k\}_{\rm Bragg},\{n\}_0,\{P\},\{k\}_{\rm reci}) (\cos j\pi/3, \sin j\pi/3) \\ \\ (12) \end{array} \\ \$\$ \end{aligned}$$

where the variables separated by a semicolon are the fit parameters, the parameter $k_{\rm R,Bragg}$ is used for the radius and the parameters k_0 and $k_{\rm reci}$ for the position of the circular masks. We plot the visibility as a function of $(T/T_0)^{\alpha}$ as obtained from the corresponding real space data (Extended Data Fig. 4b). We plot the theory curve for the condensate fraction as a guide to the eye. This comparison shows that the real-space and momentum-space images give a compatible description of the system.

The visibility and the condensate fraction vanish for the same temperatures (see Fig. 2f and Extended Data Fig. 4). This is in contrast to 3D optical lattices around unit filling, where a finite visibility also for the case of vanishing condensate fraction is observed^{18,19}. In these experiments the critical temperatures are much smaller, of the order of a few tunnelling energies, and thus low-energy states that are not the ground

state but still have short range phase-coherence are substantially populated yielding a finite visibility above the critical temperature. For our experimental temperatures of a few hundred tunnelling energies no other state than the ground state gets substantially populated.

Details on magnetic resonance addressing

In order to engineer the density distributions shown in Fig. 3, we used a trap frequency of $\omega_{\text{addressing}}/2\pi = 543$ Hz for the first five images, of $\omega_{\text{addressing}}/2\pi = 658$ Hz for the last image and different trap shifts and RF sequences. By shifting the magnetic trap perpendicularly to a real-space lattice vector by around $14 \mu\text{m}$, corresponding to approximately twice the system diameter, the curvature of the equipotential lines becomes negligible and the density patterns created by addressing exhibit straight edges. In Fig. 3 the trap centre resonance frequency is $\omega_c/2\pi = 108$ kHz for all images, except the last one of panel b where it is $\omega_c/2\pi = 67$ kHz. The trap is shifted by $14.1 \mu\text{m}$ for the first and third image, by $15.7 \mu\text{m}$ for the second image and not shifted for the fourth to sixth image, but always shifted back to the position of the atoms before imaging. For the third image a constant RF pulse of 360 kHz is turned on for 200 ms. For the first image, an RF ramp from 360 to 290 kHz is used, leading to the depletion of all lattice sites from the centre of the cloud towards the centre of the shifted magnetic trap. Here, for the same RF ramp time (200 ms) we ramp over a wider range and therefore have to compensate the reduced time by which the resonance condition is met at each position by increasing the RF amplitude. In all protocols, Fourier broadening is negligible. Lattice phase fluctuations from shot to shot lead to one or two partially depleted rows in most images. The second image in Fig. 3 is created by applying two RF ramps. In this case the trap was shifted further to the side resulting in a higher energy difference to the target $F=2, m_F=1$ state and thus we used ramps from 420 to 486 kHz and from 494 to 540 kHz with 200 ms each to target all sites except for the centre line. For the fourth to sixth image 100 ms were used as the RF duration. In the fourth image the outer wings of the distribution are cut via a RF ramp from 150 to 110 kHz. In the following images only a single frequency very close to the respective ω_c , 108.5 and 67.2 kHz, is used to address a ring or a single lattice site. The third and fifth image also visualize the second difference between addressing with and without shifting the magnetic trap: the slope grows linearly from the centre, which leads to sharper resonances for shifted systems.

Modelling of thermal hopping

The Arrhenius law is often used to describe chemical reaction rates, but also to model thermal hopping of continuously laser-cooled atoms in very deep optical lattices⁴⁸. Here we use it to model the thermal hopping of ultracold atoms in our two-

dimensional lattice. In contrast to quantum mechanical tunnelling through the barrier between two lattice sites, thermal hopping refers to motion that is activated thermally when the thermal energy allows to overcome the barrier. To good approximation, the activation energy for a hopping event can be identified with the potential barrier in the lattice, which is $V_B = 9V_{\text{lat}}$ in our triangular lattice convention.

The Arrhenius law describes the hopping rate Γ_h as the product of an attempt rate Γ_a and the probability $P(E > V_B)$ to sample an energy E above the barrier V_B in the thermal distribution. The hopping rate can then be written as

$$\begin{aligned} \text{\$}\{\{\text{Gamma}\}\}_{\{\{\text{rm}\{h\}\}\}}\text{\approx}\{\{\text{Gamma}\}\}_{\{\{\text{rm}\{a\}\}\}}P(E > \\ \{V\}_{\{\{\text{rm}\{B\}\}\}}=\{\{\text{Gamma}\}\}_{\{\{\text{rm}\{a\}\}\}}(\{\int \\ \}_{\{V\}_{\{\{\text{rm}\{B\}\}\}}}^{\{\{\text{rm}\{\infty\}\}\}}\exp(-E/\{k\}_{\{\{\text{rm}\{B\}\}\}}T) \\ \{\text{rm}\{d\}\}E)/(\{k\}_{\{\{\text{rm}\{B\}\}\}}T).\$\$ \\ (13) \end{aligned}$$

To include quantum tunnelling, we add an offset rate, resulting in

$$\begin{aligned} \text{\$}\{\{\text{Gamma}\}\}_{\{\{\text{rm}\{h\}\}\}}\text{\approx}\{\{\text{Gamma}\}\}_{\{\{\text{rm}\{a\}\}\}}\backslash\exp(- \\ \{V\}_{\{\{\text{rm}\{B\}\}\}}/\{k\}_{\{\{\text{rm}\{B\}\}\}}T)+\{\{\text{Gamma}\}\}_{\{0\}}.\$\$ \\ (14) \end{aligned}$$

In Fig. 3, we model the temperature-dependent thermalization rate by the modified Arrhenius law of equation (14) and extract an activation barrier of $V_B = k_B \times 2.4(6) \mu\text{K}$ and an attempt rate of $\Gamma_a = 52(44) \text{ Hz}$ as well as an offset rate of $\Gamma_0 = 0.23(8) \text{ Hz}$, which we attribute to quantum tunnelling in higher bands. The barrier height for the calibrated lattice depth of $V_{\text{lat}} = 3E_r$ is $V_B/k_B = 2.6 \mu\text{K}$. We note that in contrast to quantum tunnelling, for thermal hopping the atoms can move over long distances in single hopping events. This enables the large-scale mass transport in Fig. 3 within few hopping events.

Modelling of nanoscale dynamics

We describe here the numerical simulations shown in Fig. 4c. The simulations start with the ground state of the periodic potential with initial optical lattice beam intensities $I_2, I_3 = I_1$. At time $t = 0$, I_2 and I_3 are set to $0.5I_1$; the intensities change on the intensity lock time scale of about $20 \mu\text{s}$. For every time step ($5 \mu\text{s}$) we diagonalize the Hamiltonian in plane-wave basis of the instantaneous periodic potential and let the state evolve according to the instantaneous eigenstates and eigenvalues. Because the dimers are decoupled from each other, the bands are completely flat and all quasi-momenta are equivalent and we perform the calculations at the Γ point in the Brillouin zone. After the quench, 99.5% of the probability distribution of the time-evolved state

is found to lie in the lowest six bands, demonstrating that the dynamics features interference between the two s bands and four p bands, the latter being the smallest in-plane excitations within a lattice site.

The extracted atomic distribution in a cut of 65 nm width is plotted in Fig. 4c (left). In Fig. 4c (middle) the distribution is convoluted with a Gauss filter of 76 nm width, and summed with an offset, for comparison with the experimental data in Fig. 4c (right). The lattice depth used in the theory ($32E_{\text{rec}}$; note that the tunnel barriers are much smaller in a honeycomb lattice compared to a triangular lattice of the same total depth) is calibrated from the comparison with the experiment. The external trap is not included in the analysis, because experimentally we don't see any dependence of the dynamics on the position of the dimer with respect to the trap centre.

Data availability

All data files are available from the corresponding author on request. [Source data](#) are provided with this paper.

References

1. 1.

Bakr, W. S. et al. Probing the superfluid-to-Mott insulator transition at the single-atom level. *Science* **329**, 547–550 (2010).

2. 2.

Sherson, J. F. et al. Single-atom-resolved fluorescence imaging of an atomic Mott insulator. *Nature* **467**, 68–72 (2010).

3. 3.

Ritt, G., Geckeler, C., Salger, T., Cennini, G. & Weitz, M. Fourier synthesis of optical potentials for atomic quantum gases. *Phys. Rev. A* **74**, 063622 (2006).

4. 4.

Nascimbene, S., Goldman, N., Cooper, N. R. & Dalibard, J. Dynamic optical lattices of subwavelength spacing for ultracold atoms. *Phys. Rev. Lett.* **115**, 140401 (2015).

5. 5.

Wang, Y. et al. Dark state optical lattice with a subwavelength spatial structure. *Phys. Rev. Lett.* **120**, 083601 (2018).

6. 6.

Anderson, R. P. et al. Realization of a deeply subwavelength adiabatic optical lattice. *Phys. Rev. Res.* **2**, 013149 (2020).

7. 7.

Gericke, T., Würtz, P., Reitz, D., Langen, T. & Ott, H. High-resolution scanning electron microscopy of an ultracold quantum gas. *Nat. Phys.* **4**, 949–953 (2008).

8. 8.

Veit, C. et al. Pulsed ion microscope to probe quantum gases. *Phys. Rev. X* **11**, 011036 (2021).

9. 9.

McDonald, M., Trisnadi, J., Yao, K. X. & Chin, C. Superresolution microscopy of cold atoms in an optical lattice. *Phys. Rev. X* **9**, 021001 (2019).

10. 10.

Subhankar, S., Wang, Y., Tsui, T. C., Rolston, S. L. & Porto, J. V. Nanoscale atomic density microscopy. *Phys. Rev. X* **9**, 021002 (2019).

11. 11.

Anderson, B. P. & Meystre, P. Nonlinear atom optics. *Contemp. Phys.* **44**, 473–483 (2003).

12. 12.

Bongs, K. & Sengstock, K. Physics with coherent matter waves. *Rep. Prog. Phys.* **67**, 907–963 (2004).

13. 13.

Shvarchuck, I. et al. Bose-Einstein condensation into nonequilibrium states studied by condensate focusing. *Phys. Rev. Lett.* **89**, 270404 (2002).

14. 14.

Van Amerongen, A. H., Van Es, J. J., Wicke, P., Kheruntsyan, K. V. & Van Druten, N. J. Yang-Yang thermodynamics on an atom chip. *Phys. Rev. Lett.* **100**, 090402 (2008).

15. 15.

Tung, S., Lamporesi, G., Lobser, D., Xia, L. & Cornell, E. A. Observation of the presuperfluid regime in a two-dimensional Bose gas. *Phys. Rev. Lett.* **105**, 230408 (2010).

16. 16.

Murthy, P. A. et al. Matter-wave Fourier optics with a strongly interacting two-dimensional Fermi gas. *Phys. Rev. A* **90**, 043611 (2014).

17. 17.

McKay, D., White, M. & DeMarco, B. Lattice thermodynamics for ultracold atoms. *Phys. Rev. A* **79**, 063605 (2009).

18. 18.

Trotzky, S. et al. Suppression of the critical temperature for superfluidity near the Mott transition. *Nat. Phys.* **6**, 998–1004 (2010).

19. 19.

Cayla, H. et al. Single-atom-resolved probing of lattice gases in momentum space. *Phys. Rev. A* **97**, 061609 (2018).

20. 20.

Giorgini, S., Pitaevskii, L. P. & Stringari, S. Condensate fraction and critical temperature of a trapped interacting Bose gas. *Phys. Rev. A* **54**, R4633–R4636 (1996).

21. 21.

Ensher, J. R., Jin, D. S., Matthews, M. R., Wieman, C. E. & Cornell, E. A. Bose-Einstein condensation in a dilute gas: measurement of energy and ground-state occupation. *Phys. Rev. Lett.* **77**, 4984–4987 (1996).

22. 22.

Smith, R. P., Campbell, R. L. D., Tammuz, N. & Hadzibabic, Z. Effects of interactions on the critical temperature of a trapped Bose gas. *Phys. Rev. Lett.* **106**, 250403 (2011).

23. 23.

Karski, M. et al. Imprinting patterns of neutral atoms in an optical lattice using magnetic resonance techniques. *New J. Phys.* **12**, 065027 (2010).

24. 24.

Weitenberg, C. et al. Single-spin addressing in an atomic Mott insulator. *Nature* **471**, 319–324 (2011).

25. 25.

Preiss, P. M. et al. Strongly correlated quantum walks in optical lattices. *Science* **347**, 1229–1233 (2015).

26. 26.

Würtz, P., Langen, T., Gericke, T., Koglbauer, A. & Ott, H. Experimental demonstration of single-site addressability in a two-dimensional optical lattice. *Phys. Rev. Lett.* **103**, 080404 (2009).

27. 27.

Wigley, P. B. et al. Precise wave-function engineering with magnetic resonance. *Phys. Rev. A* **96**, 013612 (2017).

28. 28.

Schmaljohann, H. et al. Dynamics of $F=2$ spinor Bose-Einstein condensates. *Phys. Rev. Lett.* **92**, 040402 (2004).

29. 29.

Choi, J.-y. et al. Exploring the many-body localization transition in two dimensions. *Science* **352**, 1547–1552 (2016).

30. 30.

Parker, C. V., Ha, L. C. & Chin, C. Direct observation of effective ferromagnetic domains of cold atoms in a shaken optical lattice. *Nat. Phys.* **9**, 769–774 (2013).

31. 31.

Irsigler, B., Zheng, J.-H. & Hofstetter, W. Interacting Hofstadter interface. *Phys. Rev. Lett.* **122**, 010406 (2019).

32. 32.

Bücker, R. et al. Single-particle-sensitive imaging of freely propagating ultracold atoms. *New J. Phys.* **11**, 103039 (2009).

33. 33.

Bergschneider, A. et al. Spin-resolved single-atom imaging of ${}^6\text{Li}$ in free space. *Phys. Rev. A* **97**, 063613 (2018).

34. 34.

Lawall, J. et al. Three-dimensional laser cooling of helium beyond the single-photon recoil limit. *Phys. Rev. Lett.* **75**, 4194–4197 (1995).

35. 35.

Murthy, P. A. & Jochim, S. Direct imaging of the order parameter of an atomic superfluid using matterwave optics. Preprint at <https://arxiv.org/abs/1911.10824> (2019).

36. 36.

Santra, B. et al. Measuring finite-range phase coherence in an optical lattice using Talbot interferometry. *Nat. Commun.* **8**, 15601 (2017).

37. 37.

Becker, C. et al. Ultracold quantum gases in triangular optical lattices. *New J. Phys.* **12**, 065025 (2010).

38. 38.

Fläschner, N. et al. Experimental reconstruction of the Berry curvature in a Floquet Bloch band. *Science* **352**, 1091–1094 (2016).

39. 39.

Soltan-Panahi, P. et al. Multi-component quantum gases in spin-dependent hexagonal lattices. *Nat. Phys.* **7**, 434–440 (2011).

40. 40.

Windpassinger, P. & Sengstock, K. Engineering novel optical lattices. *Rep. Prog. Phys.* **76**, 086401 (2013).

41. 41.

Petsas, K. I., Coates, A. B. & Grynberg, G. Crystallography of optical lattices. *Phys. Rev. A* **50**, 5173–5189 (1994).

42. 42.

Yamamoto, R., Ozawa, H., Nak, D. C., Nakamura, I. & Fukuhara, T. Single-site-resolved imaging of ultracold atoms in a triangular optical lattice. *New J. Phys.* **22**, 123028 (2020).

43. 43.

Yang, J., Liu, L., Mongkolkiattichai, J. & Schauss, P. Site-resolved imaging of ultracold fermions in a triangular-lattice quantum gas microscope. *PRX Quantum* **2**, 020344 (2021).

44. 44.

Pitaevskii, L. & Stringari, S. *Bose-Einstein Condensation and Superfluidity* (Oxford Univ. Press, 2016).

45. 45.

Pethick, C. J. & Smith, H. *Bose-Einstein Condensation in Dilute Gases* (Cambridge Univ. Press, 2002).

46. 46.

Ketterle, W. & van Druten, N. J. Bose-Einstein condensation of a finite number of particles trapped in one or three dimensions. *Phys. Rev. A* **54**, 656–660 (1996).

47. 47.

Gerbier, F. et al. Expansion of a quantum gas released from an optical lattice. *Phys. Rev. Lett.* **101**, 155303 (2008).

48. 48.

Nelson, K. D., Li, X. & Weiss, D. S. Imaging single atoms in a three-dimensional array. *Nat. Phys.* **3**, 556–560 (2007).

Acknowledgements

The work is funded by the Cluster of Excellence ‘CUI: Advanced Imaging of Matter’ of the Deutsche Forschungsgemeinschaft (DFG)—EXC 2056—project ID 390715994 and by the DFG Research Unit FOR 2414, project ID 277974659. C.W. acknowledges funding by the European Research Council (ERC) under the European Union’s Horizon 2020 research and innovation programme under grant agreement no. 802701.

Funding

Open access funding provided by Universität Hamburg.

Author information

Affiliations

1. Institut für Laserphysik, Universität Hamburg, Hamburg, Germany

Luca Asteria, Henrik P. Zahn, Marcel N. Kosch, Klaus Sengstock & Christof Weitenberg

2. The Hamburg Centre for Ultrafast Imaging, Hamburg, Germany

Klaus Sengstock & Christof Weitenberg

3. Zentrum für Optische Quantentechnologien, Universität Hamburg, Hamburg, Germany

Klaus Sengstock

Contributions

L.A., H.P.Z. and M.N.K. took and analysed the experimental data and performed numerical simulations under the supervision of K.S. and C.W. All authors contributed to the interpretation of the results and to the writing of the manuscript.

Corresponding author

Correspondence to [Klaus Sengstock](#).

Ethics declarations

Competing interests

The authors declare no competing interests.

Additional information

Peer review information *Nature* thanks Philipp Preiss and the other, anonymous, reviewer(s) for their contribution to the peer review of this work.

Publisher's note Springer Nature remains neutral with regard to jurisdictional claims in published maps and institutional affiliations.

Extended data figures and tables

[Extended Data Fig. 1 On-site population computation.](#)

a, Raw density distribution of a typical image. **b**, On-site populations determined from the image in **a** using the Wigner-Seitz masks plotted as solid lines in **a**.

[Extended Data Fig. 2 Density as a function of radial position.](#)

a, b, Density of partially condensed BECs in a lattice as function of radial position as shown in Fig. [2c,d](#). The examples are prepared by end points of the radio frequency evaporation of 85 kHz (**a**) and 105 kHz (**b**) and a hold time at the final evaporation frequency of 1 ms. **c, d**, Same data as in **a** and **b** plotted with natural logarithmic y axis and quadratic x axis resulting in the Gaussian wings appearing as a straight line.

[Source data](#)

[Extended Data Fig. 3 Numerical evaluation of the density of states.](#)

a, Number of states $N(E)$ up to energy E for a triangular lattice of tubes with tight external confinement: the analytical approximation of equation (8) (black curve) reproduces the numerical diagonalization of the system (red points). The crossover

between $\alpha = 2$ and $\alpha = 3$ in the relevant energy range can be seen in the slope change in the log–log plot. **b**, Theoretical values of f_0 for the experimentally accessed parameters computed using the analytical approximation (symbols). The orange curve is a fit of the form $\langle f \rangle_0 = 1 - \left(\frac{T}{T_c} \right)^{\alpha}$ as explained in the main text.

[Source data](#)

Extended Data Fig. 4 Visibility across the BEC phase transition.

a, Density after time of flight for the parameters of Fig. 2a in the main text showing the momentum space density with Bragg peaks reflecting the coherence in the system. The visibility is computed as the difference of the density in the blue circles and red circles compared to their sum. **b**, Visibility of the time-of-flight images of the lattice gas as a function of the reduced temperature $(T/T_c)^{\alpha}$ where T_c is the scaling temperature computed from the corresponding real space images in Fig. 2. The line is the fit to the experimental condensate fractions f_0 from the main text for reference.

[Source data](#)

Supplementary information

Supplementary Information

Supplementary sections (I)–(III), including Supplementary Figs. 1–5, and additional references.

Source data

[Source Data Fig. 2](#)

[Source Data Fig. 3](#)

[Source Data Fig. 4](#)

[Source Data Extended Data Fig. 2](#)

[Source Data Extended Data Fig. 3](#)

Source Data Extended Data Fig. 4

Rights and permissions

Open Access This article is licensed under a Creative Commons Attribution 4.0 International License, which permits use, sharing, adaptation, distribution and reproduction in any medium or format, as long as you give appropriate credit to the original author(s) and the source, provide a link to the Creative Commons license, and indicate if changes were made. The images or other third party material in this article are included in the article's Creative Commons license, unless indicated otherwise in a credit line to the material. If material is not included in the article's Creative Commons license and your intended use is not permitted by statutory regulation or exceeds the permitted use, you will need to obtain permission directly from the copyright holder. To view a copy of this license, visit <http://creativecommons.org/licenses/by/4.0/>.

Reprints and Permissions

About this article

Cite this article

Asteria, L., Zahn, H.P., Kosch, M.N. *et al.* Quantum gas magnifier for sub-lattice-resolved imaging of 3D quantum systems. *Nature* **599**, 571–575 (2021).
<https://doi.org/10.1038/s41586-021-04011-2>

- Received: 06 May 2021
- Accepted: 09 September 2021
- Published: 24 November 2021
- Issue Date: 25 November 2021
- DOI: <https://doi.org/10.1038/s41586-021-04011-2>

Share this article

Anyone you share the following link with will be able to read this content:

[Get shareable link](#)

Sorry, a shareable link is not currently available for this article.

[Copy to clipboard](#)

Provided by the Springer Nature SharedIt content-sharing initiative

This article was downloaded by **calibre** from <https://www.nature.com/articles/s41586-021-04011-2>

| [Section menu](#) | [Main menu](#) |

- Article
- [Published: 24 November 2021](#)

Colossal angular magnetoresistance in ferrimagnetic nodal-line semiconductors

- [Junho Seo^{1,2} na1](#),
- [Chandan De](#) [ORCID: orcid.org/0000-0003-1759-1137](#)^{1,3} na1,
- [Hyunsoo Ha⁴ na1](#),
- [Ji Eun Lee](#) [ORCID: orcid.org/0000-0001-8947-826X](#)⁵ na1,
- [Sungyu Park¹](#),
- [Joonbum Park⁶](#),
- [Yuri Skourski⁶](#),
- [Eun Sang Choi⁷](#),
- [Bongjae Kim](#) [ORCID: orcid.org/0000-0002-3841-2989](#)⁸,
- [Gil Young Cho^{1,2,9}](#),
- [Han Woong Yeom](#) [ORCID: orcid.org/0000-0002-8538-8993](#)^{1,2},
- [Sang-Wook Cheong](#) [ORCID: orcid.org/0000-0001-9905-6175](#)^{3,10},
- [Jae Hoon Kim](#) [ORCID: orcid.org/0000-0002-7840-3630](#)⁵,
- [Bohm-Jung Yang](#) [ORCID: orcid.org/0000-0001-5888-7546](#)^{4,11,12},
- [Kyo Kim](#) [ORCID: orcid.org/0000-0002-7305-8786](#)¹³ &
- [Jun Sung Kim](#) [ORCID: orcid.org/0000-0002-1413-7265](#)^{1,2}

[Nature](#) volume **599**, pages 576–581 (2021)

- 1215 Accesses
- 60 Altmetric
- [Metrics details](#)

Subjects

- [Electronic properties and materials](#)
- [Magnetic properties and materials](#)
- [Topological matter](#)

Abstract

Efficient magnetic control of electronic conduction is at the heart of spintronic functionality for memory and logic applications^{1,2}. Magnets with topological band crossings serve as a good material platform for such control, because their topological band degeneracy can be readily tuned by spin configurations, dramatically modulating electronic conduction^{3,4,5,6,7,8,9,10}. Here we propose that the topological nodal-line degeneracy of spin-polarized bands in magnetic semiconductors induces an extremely large angular response of magnetotransport. Taking a layered ferrimagnet, $\text{Mn}_3\text{Si}_2\text{Te}_6$, and its derived compounds as a model system, we show that the topological band degeneracy, driven by chiral molecular orbital states, is lifted depending on spin orientation, which leads to a metal–insulator transition in the same ferrimagnetic phase. The resulting variation of angular magnetoresistance with rotating magnetization exceeds a trillion per cent per radian, which we call colossal angular magnetoresistance. Our findings demonstrate that magnetic nodal-line semiconductors are a promising platform for realizing extremely sensitive spin- and orbital-dependent functionalities.

Access options

Subscribe to Journal

Get full journal access for 1 year

\$199.00

only \$3.90 per issue

[Subscribe](#)

All prices are NET prices.

VAT will be added later in the checkout.

Tax calculation will be finalised during checkout.

Rent or Buy article

Get time limited or full article access on ReadCube.

from \$8.99

[Rent or Buy](#)

All prices are NET prices.

Additional access options:

- [Log in](#)
- [Access through your institution](#)
- [Learn about institutional subscriptions](#)

Fig. 1: Magnetic nodal-line semimetal and semiconductor.

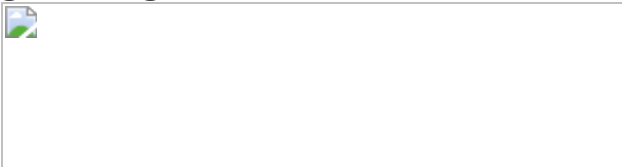


Fig. 2: Nodal-line band degeneracy of the chiral orbital states in $\text{Mn}_3\text{Si}_2\text{Te}_6$.

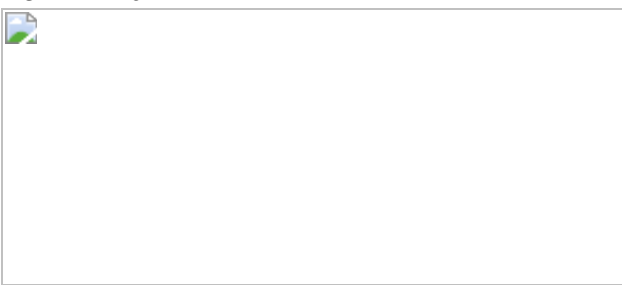


Fig. 3: Metal–insulator transition by spin orientation.

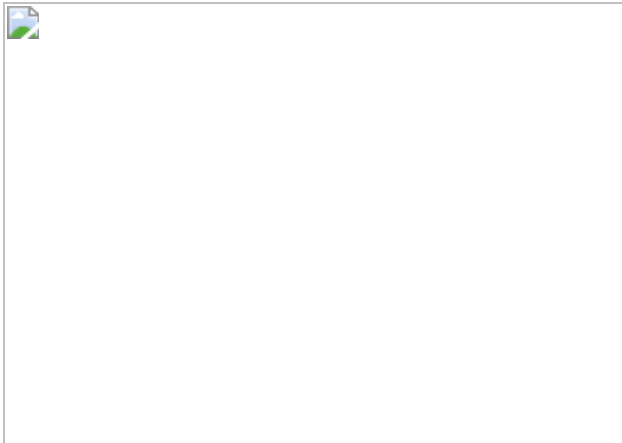
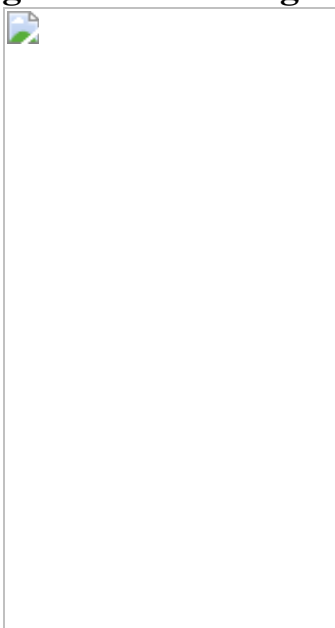


Fig. 4: Colossal angular MR.



Data availability

The data that support the findings of this study are available from the corresponding authors on request.

References

1. 1.

Žutić, I., Fabian, J. & Das Sarma, S. Spintronics: fundamentals and applications. *Rev. Mod. Phys.* **76**, 323–410 (2004).

2. 2.

Fert, A. Nobel lecture: Origin, development, and future of spintronics. *Rev. Mod. Phys.* **80**, 1517–1530 (2008).

3. 3.

Hasan, M. Z. & Kane, C. L. Colloquium: Topological insulators. *Rev. Mod. Phys.* **82**, 3045–3067 (2010).

4. 4.

Qi, X.-L. & Zhang, S.-C. Topological insulators and superconductors. *Rev. Mod. Phys.* **83**, 1057–1110 (2011).

5. 5.

Wang, J. & Zhang, S. C. Topological states of condensed matter. *Nat. Mater.* **16**, 1062–1067 (2017).

6. 6.

Armitage, N. P., Mele, E. J. & Vishwanath, A. Weyl and Dirac semimetals in three-dimensional solids. *Rev. Mod. Phys.* **90**, 015001 (2018).

7. 7.

Manna, K., Sun, Y., Muechler, L., Kübler, J. & Felser, C. Heusler, Weyl and Berry. *Nat. Rev. Mater.* **3**, 244–256 (2018).

8. 8.

Nagaosa, N., Morimoto, T. & Tokura, Y. Transport, magnetic and optical properties of Weyl materials. *Nat. Rev. Mater.* **5**, 621–636 (2020).

9. 9.

Kumar, N., Guin, S. N., Manna, K., Shekhar, C. & Felser, C.
Topological quantum materials from the viewpoint of chemistry.
Chem. Rev. **121**, 2780–2815 (2021).

10. 10.

Narang, P., Garcia, C. A. & Felser, C. The topology of electronic band structures. *Nat. Mater.* **20**, 293–300 (2021).

11. 11.

Liu, E. et al. Giant anomalous Hall effect in a ferromagnetic kagome-lattice semimetal. *Nat. Phys.* **14**, 1125–1131 (2018).

12. 12.

Okamura, Y. et al. Giant magneto-optical responses in magnetic Weyl semimetal $\text{Co}_3\text{Sn}_2\text{S}_2$. *Nat. Commun.* **11**, 4619 (2020).

13. 13.

Ding, L. et al. Intrinsic anomalous Nernst effect amplified by disorder in a half-metallic semimetal. *Phys. Rev. X* **91**, 041061 (2019).

14. 14.

Sakai, A. et al. Giant anomalous Nernst effect and quantum-critical scaling in a ferromagnetic semimetal. *Nat. Phys.* **14**, 1119–1124 (2018).

15. 15.

Xu, L. et al. Anomalous transverse response of Co_2MnGa and universality of the room-temperature $(\{\alpha\}_{ij}^A/\{\sigma\}_{ij}^A)$ ratio across topological magnets. *Phys. Rev. B* **101**, 180404 (2020).

16. 16.

Li, P. et al. Giant room temperature anomalous Hall effect and tunable topology in a ferromagnetic topological semimetal Co₂MnAl. *Nat. Commun.* **11**, 3476 (2020).

17. 17.

Ye, L. et al. Massive Dirac fermions in a ferromagnetic kagome metal. *Nature* **555**, 638–642 (2018).

18. 18.

Kim, K. et al. Large anomalous Hall current induced by topological nodal lines in a ferromagnetic van der Waals semimetal. *Nat. Mater.* **17**, 794–799 (2018).

19. 19.

Suzuki, T. et al. Singular angular magnetoresistance in a magnetic nodal semimetal. *Science* **365**, 377–381 (2019).

20. 20.

Sakai, A. et al. Iron-based binary ferromagnets for transverse thermoelectric conversion. *Nature* **581**, 53–57 (2020).

21. 21.

Chang, C. Z. et al. Experimental observation of the quantum anomalous Hall effect in a magnetic topological insulator. *Science* **340**, 167–170 (2013).

22. 22.

Checkelsky, J. G. et al. Trajectory of the anomalous Hall effect towards the quantized state in a ferromagnetic topological insulator. *Nat. Phys.* **10**, 731–736 (2014).

23. 23.

Yasuda, K. et al. Quantized chiral edge conduction on domain walls of a magnetic topological insulator. *Science* **358**, 1311–1314 (2017).

24. 24.

Yasuda, K. et al. Large non-reciprocal charge transport mediated by quantum anomalous Hall edge states. *Nat. Nanotechnol.* **15**, 831–835 (2020).

25. 25.

Chang, C. Z. et al. High-precision realization of robust quantum anomalous Hall state in a hard ferromagnetic topological insulator. *Nat. Mater.* **14**, 473–477 (2015).

26. 26.

Deng, Y. et al. Quantum anomalous Hall effect in intrinsic magnetic topological insulator MnBi_2Te_4 . *Science* **367**, 895–900 (2020).

27. 27.

Rimet, R., Schlenker, C. & Vincent, H. A new semiconducting ferrimagnet: a silicon manganese telluride. *J. Magn. Magn. Mater.* **25**, 7–10 (1981).

28. 28.

Vincent, H., Leroux, D., Bijaoui, D., Rimet, R. & Schlenker, C. Crystal structure of $\text{Mn}_3\text{Si}_2\text{Te}_6$. *J. Solid State Chem.* **63**, 349–352 (1986).

29. 29.

May, A. F. et al. Magnetic order and interactions in ferrimagnetic $\text{Mn}_3\text{Si}_2\text{Te}_6$. *Phys. Rev. B* **95**, 174440 (2017).

30. 30.

Kanamori, J. & Terakura, K. A general mechanism underlying ferromagnetism in transition metal compounds. *J. Phys. Soc. Jpn* **70**, 1433–1434 (2001).

31. 31.

Jungwirth, T., Sinova, J., Mašek, J., Kučera, J. & MacDonald, A. H. Theory of ferromagnetic (III,Mn)V semiconductors. *Rev. Mod. Phys.* **78**, 809–864 (2006).

32. 32.

Yu, P. Y. & Cardona, M. *Fundamentals of Semiconductors* (Springer, 2005).

33. 33.

Sharma, S. K., Sagar, P., Gupta, H., Kumar, R. & Mehra, R. M. Meyer–Neldel rule in Se and S-doped hydrogenated amorphous silicon. *Solid State Electron.* **51**, 1124–1128 (2007).

34. 34.

Durá, O. J. et al. Transport, electronic, and structural properties of nanocrystalline CuAlO₂ delafossites. *Phys. Rev. B* **83**, 045202 (2011).

35. 35.

Hauser, A. J. et al. Electronic and magnetic tunability of Sr₂CrReO₆ films by growth-mediated oxygen modulation. *Appl. Phys. Lett.* **102**, 032403 (2013).

36. 36.

Kokado, S., Tsunoda, M., Harigaya, K. & Sakuma, A. Anisotropic magnetoresistance effects in Fe, Co, Ni, Fe₄N, and half-metallic ferromagnet: a systematic analysis. *J. Phys. Soc. Jpn* **81**, 024705 (2012).

37. 37.

Wang, H. et al. Giant anisotropic magnetoresistance and nonvolatile memory in canted antiferromagnet Sr_2IrO_4 . *Nat. Commun.* **10**, 2280 (2019).

38. 38.

Endo, T., Kubota, H. & Miyazaki, T. Magnetoresistance of $\text{Co}_2\text{MnAl}_{1-x}\text{Si}_x$ Heusler alloys. *J. Magn. Soc. Jpn* **23**, 1129–1132 (1999).

39. 39.

Eckstein, J. N., Bozovic, I., O'Donnell, J., Onellion, M. & Rzchowski, M. S. Anisotropic magnetoresistance in tetragonal $\text{La}_{1-x}\text{Ca}_x\text{MnO}_3$ thin films. *Appl. Phys. Lett.* **69**, 1312 (1996).

40. 40.

Li, R.-W. et al. Anomalously large anisotropic magnetoresistance in a perovskite manganite. *Proc. Natl Acad. Sci. USA* **106**, 14224–14229 (2009).

41. 41.

Wang, Z.-C. et al. Colossal magnetoresistance without mixed valence in a layered phosphide crystal. *Adv. Mater.* **33**, 2005755 (2021).

42. 42.

Soh, J.-R. et al. Magnetic and electronic structure of Dirac semimetal candidate EuMnSb_2 . *Phys. Rev. B* **100**, 174406 (2019).

43. 43.

Yin, J. et al. Large negative magnetoresistance in the antiferromagnetic rare-earth dichalcogenide EuTe_2 . *Phys. Rev. Mater.* **4**, 013405 (2020).

44. 44.

Yang, H. et al. Observation of an unusual colossal anisotropic magnetoresistance effect in an antiferromagnetic semiconductor. Preprint at <https://arxiv.org/abs/2103.02818> (2021).

45. 45.

Ni, Y. et al. Colossal magnetoresistance via avoiding fully polarized magnetization in the ferrimagnetic insulator $\text{Mn}_3\text{Si}_2\text{Te}_6$. *Phys. Rev. B* **103**, L161105 (2021).

46. 46.

Manyala, N. et al. Magnetoresistance from quantum interference effects in ferromagnets. *Nature* **404**, 581–584 (2000).

47. 47.

Tsuji, N., Nishide, A., Hayakawa, J. & Mori, T. Observation of enhanced thermopower due to spin fluctuation in weak itinerant ferromagnet. *Sci. Adv.* **5**, eaat5935 (2019).

48. 48.

Lu, C. et al. Crossover of conduction mechanism in Sr_2IrO_4 epitaxial thin films. *Appl. Phys. Lett.* **105**, 082407 (2014).

49. 49.

Yildiz, A., Serin, N., Serin, T. & Kasap, M. Crossover from nearest-neighbor hopping conduction to Efros–Shklovskii variable-range hopping conduction in hydrogenated amorphous silicon films. *Jpn. J. Appl. Phys.* **48**, 111203 (2009).

50. 50.

Li, Z. et al. Transition between Efros–Shklovskii and Mott variable-range hopping conduction in polycrystalline germanium thin films. *Semicond. Sci. Technol.* **32**, 035010 (2017).

51. 51.

Koepernik, K. & Eschrig, H. Full-potential nonorthogonal local-orbital minimum-basis band-structure scheme. *Phys. Rev. B* **59**, 1743–1757 (1999).

52. 52.

Giannozzi, P. et al. QUANTUM ESPRESSO: a modular and open-source software project for quantum simulations of materials. *J. Phys. Condens. Matter* **21**, 395502 (2009).

53. 53.

Mostofi, A. A. et al. An updated version of wannier90: a tool for obtaining maximally-localised Wannier functions. *Comput. Phys. Commun.* **185**, 2309–2310 (2014).

54. 54.

Tsirkin, S. S. High performance Wannier interpolation of Berry curvature and related quantities with WannierBerri code. *npj Comput. Mater.* **7**, 33 (2021).

Acknowledgements

We thank H. W. Lee and J. Y. Kim for productive discussion. We also thank H. G. Kim from the Pohang Accelerator Laboratory (PAL) for technical support. This work was supported by the Institute for Basic Science (IBS) through the Center for Artificial Low Dimensional Electronic Systems (no. IBS-R014-D1), and by the National Research Foundation of Korea (NRF) through the SRC (grant no. 2018R1A5A6075964), and the Max Planck-POSTECH Center for Complex Phase Materials (grant no. 2016K1A4A4A01922028). H.H. was supported by Samsung Science and

Technology Foundation under project number SSTF-BA2002-06. The pulsed field work was supported by the HLD at HZDR, member of the European Magnetic Field Laboratory (EMFL). K.K. was supported by the NRF (grant no. 2016R1D1A1B02008461), and the internal R&D programme at KAERI (no. 524460-21). B.-J.Y. was supported by the Institute for Basic Science in Korea (grant no. IBS-R009-D1), Samsung Science and Technology Foundation under project number SSTF-BA2002-06, and NRF grants funded by the Korea government (MSIT; no. 2021R1A2C4002773 and no. NRF-2021R1A5A1032996). J.H.K. acknowledges financial support from the NRF through grant no. NRF-2021R1A2C3004989 and grant no. 2017R1A5A1014862 (vdWMRC SRC Program). B.K. acknowledges support by the NRF through grant no. 2021R1C1C1007017. S.-W.C. was partially supported by the Center for Quantum Materials Synthesis (cQMS), funded by the Gordon and Betty Moore Foundation's EPiQS initiative through grant GBMF10104, and by Rutgers University. A portion of this work was performed at the National High Magnetic Field Laboratory, which is supported by the National Science Foundation Cooperative agreement no. DMR-1644779 and the State of Florida.

Author information

Author notes

1. These authors contributed equally: Junho Seo, Chandan De, Hyunsoo Ha, Ji Eun Lee

Affiliations

1. Center for Artificial Low Dimensional Electronic Systems, Institute for Basic Science (IBS), Pohang, Korea

Junho Seo, Chandan De, Sungyu Park, Gil Young Cho, Han Woong Yeom & Jun Sung Kim

2. Department of Physics, Pohang University of Science and Technology (POSTECH), Pohang, Korea

Junho Seo, Gil Young Cho, Han Woong Yeom & Jun Sung Kim

3. Laboratory of Pohang Emergent Materials, Pohang Accelerator Laboratory, Pohang, Korea

Chandan De & Sang-Wook Cheong

4. Department of Physics and Astronomy, Seoul National University, Seoul, Korea

Hyunsoo Ha & Bohm-Jung Yang

5. Department of Physics, Yonsei University, Seoul, Korea

Ji Eun Lee & Jae Hoon Kim

6. Hochfeld-Magnetlabor Dresden (HLD-EMFL), Helmholtz-Zentrum Dresden-Rossendorf, Dresden, Germany

Joonbum Park & Yurii Skourski

7. National High Magnetic Field Laboratory, Florida State University, Tallahassee, FL, USA

Eun Sang Choi

8. Department of Physics, Kunsan National University, Gunsan, Korea

Bongjae Kim

9. Asia Pacific Center for Theoretical Physics, Pohang, Korea

Gil Young Cho

10. Rutgers Center for Emergent Materials and Department of Physics & Astronomy, Rutgers University, Piscataway, NJ, USA

Sang-Wook Cheong

11. Center for Correlated Electron Systems, Institute for Basic Science (IBS), Seoul, Korea

Bohm-Jung Yang

12. Center for Theoretical Physics (CTP), Seoul National University, Seoul, Korea

Bohm-Jung Yang

13. Korea Atomic Energy Research Institute (KAERI), Daejeon, Korea

Kyoo Kim

Contributions

J.S.K., J.S. and C.D. conceived the projects. J.S. and S.P. performed the transport measurements on bulk crystals. C.D., under the guidance of S.W.-C., synthesized the bulk crystals. H.H., B.K., K.K., G.Y.C. and B.-J.Y. performed the electronic-structure calculations and the band analysis. J.E.L. and J.H.K. conducted terahertz spectroscopy measurements and spectral analysis. J.P., Y.S. and E.S.C. conducted high-field experiments. G.Y.C. and H.W.Y. contributed to the data analysis. J.S., C.D., H.H., J.H.K., B.-J.Y., K.K. and J.S.K. co-wrote the manuscript. All authors discussed the results and commented on the paper.

Corresponding authors

Correspondence to [Jae Hoon Kim](#), [Bohm-Jung Yang](#), [Kyoo Kim](#) or [Jun Sung Kim](#).

Ethics declarations

Competing interests

The authors declare no competing interests.

Additional information

Peer review information *Nature* thanks Yong Xu and the other, anonymous, reviewer(s) for their contribution to the peer review of this work. Peer reviewer reports are available.

Publisher's note Springer Nature remains neutral with regard to jurisdictional claims in published maps and institutional affiliations.

Extended data figures and tables

Extended Data Fig. 1 Single crystal growth.

a, X-ray diffraction pattern of the undoped, Ge- and Se-doped $\text{Mn}_3\text{Si}_2\text{Te}_6$ crystals recorded on (0 0 L) plane at room temperature. The insets show a typical crystal image and a magnified X-ray diffraction data for Bragg peak (004). **b–d**, The energy dispersive spectroscopy images on a selected area of $\text{Mn}_3\text{Si}_2\text{Te}_6$ crystal, taken at Mn $(\text{K}\alpha 1)$ (**b**), Si $(\text{K}\alpha 1)$ (**c**) and Te $(\text{L}\alpha 1)$ (**d**) edges. **e**, Combined Mn, Si and Te EDS image, showing a spatially uniform stoichiometry of $\text{Mn}_3\text{Si}_2\text{Te}_6$ crystal.

Extended Data Fig. 2 Magnetic properties of $\text{Mn}_3\text{Si}_2\text{Te}_6$.

a–c, Temperature dependent magnetic susceptibility $(\chi(T))$ of undoped, Ge-doped and Se-doped $\text{Mn}_3\text{Si}_2\text{Te}_6$ single crystals for $(H \parallel c)$ (green) and $(H \parallel ab)$ (red) at $H = 1$ kOe. **d–f**, Magnetic field-dependent magnetization $(M(H))$ of undoped, Ge-doped and Se-doped $\text{Mn}_3\text{Si}_2\text{Te}_6$ single crystals for $(H \parallel c)$ (green) and $(H \parallel ab)$ (red) taken at $T = 2$ or 5 K.

Extended Data Fig. 3 Electronic conduction of $\text{Mn}_3\text{Si}_2\text{Te}_6$ at zero magnetic field.

a–c, In-plane resistivity (ρ_{ab}) as a function of the inverse temperature for undoped (**a**), Ge-doped (**b**) and Se-doped (**c**) $\text{Mn}_3\text{Si}_2\text{Te}_6$ single crystals. Above and below T_c , $(\rho_{ab}(T))$ follows the thermally activated semiconducting behaviour, described by $(\rho_{ab}(T)) \propto (\exp(\Delta/k_B T))$ (red line), with different transport gap Δ (Extended Data Table 1). **d–f**, Variable-range hopping (VRH) conduction at low temperatures for undoped (**d**), Ge-doped (**e**) and Se-doped (**f**) $\text{Mn}_3\text{Si}_2\text{Te}_6$ single crystals. The in-plane resistivity $(\rho_{ab}(T))$ is plotted as a function of $1/(T^p)$ with exponents $p = 1/4$ (left), $1/3$ (middle), and $1/2$ (right), corresponding to the Mott-VRH models with three- and two-dimensions and the Efros-Shklovskii (ES) VRH model, respectively.

Extended Data Fig. 4 Electronic conduction of $\text{Mn}_3\text{Si}_2\text{Te}_6$ under magnetic fields.

a–f, Temperature dependent in-plane resistivity $(\rho_{ab}(T))$ (left panel) and its first derivative $(d\rho_{ab}(T)/dT)$ (right panel) for undoped (upper), Ge-doped (middle) and Se-doped (lower) $\text{Mn}_3\text{Si}_2\text{Te}_6$ at different magnetic fields and orientations, $(H \parallel ab)$ (**a–c**) and $(H \parallel c)$ (**d–f**). The estimated T_c is indicated by the arrows. **g–i**, Magnetic field dependent T_c for $(H \parallel ab)$ and $(H \parallel c)$. The errors in the experimental data are smaller than the size of the points.

Extended Data Fig. 5 Magnetic field dependent semiconducting conduction in $\text{Mn}_3\text{Si}_2\text{Te}_6$.

a–c, Arrhenius plot of $(\rho_{ab}(T))$ for $(H \parallel ab)$ (left panel) and $(H \parallel c)$ (right panel) at various magnetic fields for the undoped (**a**), Ge-doped (**b**) and Se-doped (**c**) $\text{Mn}_3\text{Si}_2\text{Te}_6$. **d–f**, Magnetic field dependent activation gap $(\Delta(H))$, extracted from the Arrhenius plot of $(\rho_{ab}(T))$, for $(H \parallel c)$ (solid symbols) and $(H \parallel ab)$ (open symbols). The errors in the experimental data are smaller than the size of the points.

Extended Data Fig. 6 Magnetic and magnetotransport properties of $\text{Mn}_3\text{Si}_2\text{Te}_6$ at high magnetic fields.

a, Magnetic field dependent torque magnetometry $(\tau(H))$ for different field angle θ with respect to the ab -plane. No signature of the ferrimagnetic-to-ferromagnetic transition is observed up to $H \sim 70$ T. **b**, Magnetic field dependent magnetization $(M(\{H\}))$, taken under pulsed magnetic fields at $T = 4.2$ K (black line). Magnetization $M(H)$ under static magnetic fields is also plotted for comparison (orange symbol). **c**, Magnetic field dependent in-plane resistivity $(\{\rho\}_{ab}(H))$ for $(H \parallel ab)$ and $(H \parallel c)$. For $(H \parallel ab)$, the resistivity $(\{\rho\}_{ab}(H))$ exhibits a relatively slow decrease with magnetic fields up to ~ 30 T, while rapid reduction of $(\{\rho\}_{ab}(H))$ for $(H \parallel c)$ induces the insulator-to metal-transition at $H \sim 4$ T.

Extended Data Fig. 7 Temperature- and magnetic field-dependent angular magnetoresistance.

a–i, Angle dependent resistivity $(\{\rho\}_{ab}(\theta))$ at various temperatures and magnetic fields for undoped (**a–c**), Ge-doped (**d–f**) and Se-doped (**h, i**) samples. The tilting angle of the external magnetic field (θ) with respect to the ab -plane and its azimuthal angle ϕ against the current direction are illustrated in **g**. For the undoped sample, $(\{\rho\}_{ab}(\theta))$ taken for two different azimuthal angle $\phi = 0^\circ$ ($(M \parallel J)$, open symbol) and 90° ($(M \perp J)$, solid symbol) are almost identical. **j**, Angular magnetoresistance (MR) $((1/\{\rho\}_{\min})/(d\rho/\theta))$ as a function of temperature under $H = 5$ T (undoped), 6 T (Ge-doped) and 10 T (Se-doped). The arrows indicate T_c at zero magnetic field. **k**, Angular MR of the undoped and doped $\text{Mn}_3\text{Si}_2\text{Te}_6$ as a function of magnetic field. Angular MR of Eu-based antiferromagnets and topological magnet candidate CeAlGe are also plotted for comparison^{19,41,42,44}.

Extended Data Fig. 8 Terahertz absorption spectroscopy.

a–i, Absorption coefficient as a function of energy under zero magnetic field for undoped, Ge-doped and Se-doped $\text{Mn}_3\text{Si}_2\text{Te}_6$ taken at various temperatures. **j–o**, Absorption coefficient as a function of energy for the undoped (upper panel), Ge-doped (middle panel) and Se-doped (lower panel) $\text{Mn}_3\text{Si}_2\text{Te}_6$ taken at $T = 1.5$ K for $\langle H \parallel ab \rangle$ (**j–l**) and $\langle H \parallel c \rangle$ (**m–o**). The peaks that appear in the case of the doped samples are infrared-active transverse optical (TO) phonon modes.

Extended Data Table 1 Characteristic parameters of the undoped, Ge-doped and Se-doped $\text{Mn}_3\text{Si}_2\text{Te}_6$ including the ferrimagnetic transition temperature (T_c), the saturated magnetization $\langle M \rangle_{\rm sat}$) and fields $\langle H \rangle_{\rm sat}$ along the c -axis and the ab -plane, the magnetocrystalline anisotropy energy (K), the activation gap above T_c ($\Delta_{\rm P} M$) and below T_c (Δ), and the temperature scale T_θ of the ES-VRH model

Extended Data Table 2 Magnetoresistance (MR) and angular MR of various magnetic materials. For each case, the magnetic phase, the magnetic ordering temperature (T_c or T_N), the MR, the angular MR, and the corresponding temperature (T) and magnetic field (H) are listed

Supplementary information

[Supplementary Information](#)

This file contains Supplementary Notes 1–5, Figs. 1–6 and References.

[Peer Review File](#)

Rights and permissions

[Reprints and Permissions](#)

About this article

Cite this article

Seo, J., De, C., Ha, H. *et al.* Colossal angular magnetoresistance in ferrimagnetic nodal-line semiconductors. *Nature* **599**, 576–581 (2021). <https://doi.org/10.1038/s41586-021-04028-7>

- Received: 07 April 2021
- Accepted: 15 September 2021
- Published: 24 November 2021
- Issue Date: 25 November 2021
- DOI: <https://doi.org/10.1038/s41586-021-04028-7>

Share this article

Anyone you share the following link with will be able to read this content:

[Get shareable link](#)

Sorry, a shareable link is not currently available for this article.

[Copy to clipboard](#)

Provided by the Springer Nature SharedIt content-sharing initiative

This article was downloaded by **calibre** from <https://www.nature.com/articles/s41586-021-04028-7>

- Article
- [Published: 24 November 2021](#)

Artificial heavy fermions in a van der Waals heterostructure

- [Viliam Vaňo](#) ORCID: [orcid.org/0000-0003-1050-3931¹](https://orcid.org/0000-0003-1050-3931),
- [Mohammad Amini](#)¹,
- [Somesh C. Ganguli](#)¹,
- [Guangze Chen](#) ORCID: [orcid.org/0000-0002-1956-2519¹](https://orcid.org/0000-0002-1956-2519),
- [Jose L. Lado](#) ORCID: [orcid.org/0000-0002-9916-1589¹](https://orcid.org/0000-0002-9916-1589),
- [Shawulienu Kezilebieke](#) ORCID: [orcid.org/0000-0003-4166-5079¹](https://orcid.org/0000-0003-4166-5079) nAff² &
- [Peter Liljeroth](#) ORCID: [orcid.org/0000-0003-1253-8097¹](https://orcid.org/0000-0003-1253-8097)

[Nature](#) volume **599**, pages 582–586 (2021)

- 2302 Accesses
- 102 Altmetric
- [Metrics details](#)

Subjects

- [Electronic properties and materials](#)
- [Magnetic properties and materials](#)
- [Surfaces, interfaces and thin films](#)
- [Two-dimensional materials](#)

Abstract

Heavy-fermion systems represent one of the paradigmatic strongly correlated states of matter^{1,2,3,4,5}. They have been used as a platform for investigating exotic behaviour ranging from quantum criticality and non-Fermi liquid behaviour to unconventional topological superconductivity^{4,5,6,7,8,9,10,11,12}. The heavy-fermion phenomenon arises from the exchange interaction between localized magnetic moments and conduction electrons leading to Kondo lattice physics, and represents one of the long-standing open problems in quantum materials³. In a Kondo lattice, the exchange interaction gives rise to a band with heavy effective mass. This intriguing phenomenology has so far been realized only in compounds containing rare-earth elements with 4f or 5f electrons^{1,4,13,14}. Here we realize a designer van der Waals heterostructure where artificial heavy fermions emerge from the Kondo coupling between a lattice of localized magnetic moments and itinerant electrons in a 1T/1H-TaS₂ heterostructure. We study the heterostructure using scanning tunnelling microscopy and spectroscopy and show that depending on the stacking order of the monolayers, we can reveal either the localized magnetic moments and the associated Kondo effect, or the conduction electrons with a heavy-fermion hybridization gap. Our experiments realize an ultimately tunable platform for future experiments probing enhanced many-body correlations, dimensional tuning of quantum criticality and unconventional superconductivity in two-dimensional artificial heavy-fermion systems^{15,16,17}.

Access options

Subscribe to Journal

Get full journal access for 1 year

\$199.00

only \$3.90 per issue

[Subscribe](#)

All prices are NET prices.
VAT will be added later in the checkout.
Tax calculation will be finalised during checkout.

Rent or Buy article

Get time limited or full article access on ReadCube.

from \$8.99

[Rent or Buy](#)

All prices are NET prices.

Additional access options:

- [Log in](#)
- [Access through your institution](#)
- [Learn about institutional subscriptions](#)

Fig. 1: Artificial heavy-fermion heterostructure.

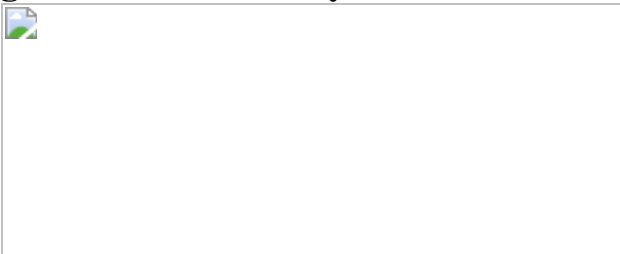


Fig. 2: Kondo resonance in a 1T/1H-TaS₂ vertical heterostructure.

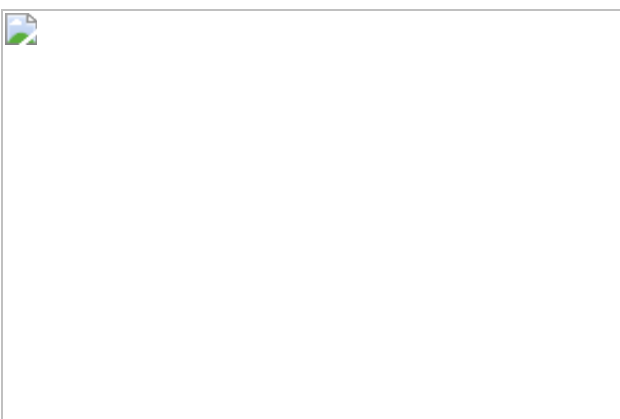
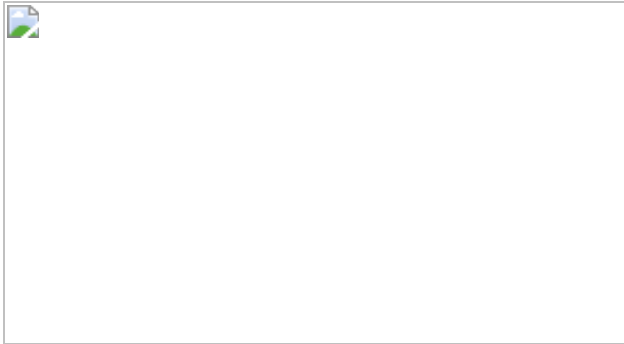


Fig. 3: Heavy-fermion hybridization gap in a 1H/1T-TaS₂ vertical heterostructure.



Data availability

All of the data supporting the findings are available from the corresponding authors upon request.

References

1. 1. Stewart, G. R. Heavy-fermion systems. *Rev. Mod. Phys.* **56**, 755–787 (1984).
2. 2. Yazdani, A., da Silva Neto, E. H. & Aynajian, P. Spectroscopic imaging of strongly correlated electronic states. *Annu. Rev. Condens. Matter Phys.* **7**, 11–33 (2016).
3. 3. Dzero, M., Xia, J., Galitski, V. & Coleman, P. Topological Kondo insulators. *Annu. Rev. Condens. Matter Phys.* **7**, 249–280 (2016).
4. 4.

Wirth, S. & Steglich, F. Exploring heavy fermions from macroscopic to microscopic length scales. *Nat. Rev. Mater.* **1**, 16051 (2016).

5. 5.

Jiao, L. et al. Chiral superconductivity in heavy-fermion metal UTe₂. *Nature* **579**, 523–527 (2020).

6. 6.

Pfleiderer, C. et al. Partial order in the non-Fermi-liquid phase of MnSi. *Nature* **427**, 227–231 (2004).

7. 7.

Stewart, G. R. Non-Fermi-liquid behavior in *d*- and *f*-electron metals. *Rev. Mod. Phys.* **73**, 797–855 (2001).

8. 8.

Löhneysen, H. V., Rosch, A., Vojta, M. & Wölfle, P. Fermi-liquid instabilities at magnetic quantum phase transitions. *Rev. Mod. Phys.* **79**, 1015–1075 (2007).

9. 9.

Gegenwart, P., Si, Q. & Steglich, F. Quantum criticality in heavy-fermion metals. *Nat. Phys.* **4**, 186–197 (2008).

10. 10.

Aynajian, P. et al. Visualizing heavy fermions emerging in a quantum critical Kondo lattice. *Nature* **486**, 201–206 (2012).

11. 11.

Allan, M. P. et al. Imaging Cooper pairing of heavy fermions in CeCoIn₅. *Nat. Phys.* **9**, 468–473 (2013).

12. 12.

Zhou, B. B. et al. Visualizing nodal heavy fermion superconductivity in CeCoIn₅. *Nat. Phys.* **9**, 474–479 (2013).

13. 13.

Chen, C., Sodemann, I. & Lee, P. A. Competition of spinon Fermi surface and heavy Fermi liquid states from the periodic Anderson to the Hubbard model. *Phys. Rev. B* **103**, 085128 (2021).

14. 14.

Ramires, A. & Lado, J. L. Emulating heavy fermions in twisted trilayer graphene. *Phys. Rev. Lett.* **127**, 026401 (2021).

15. 15.

Neumann, M., Nyéki, J., Cowan, B. & Saunders, J. Bilayer ³He: a simple two-dimensional heavy-fermion system with quantum criticality. *Science* **317**, 1356–1359 (2007).

16. 16.

Shishido, H. et al. Tuning the dimensionality of the heavy fermion compound CeIn₃. *Science* **327**, 980–983 (2010).

17. 17.

Mizukami, Y. et al. Extremely strong-coupling superconductivity in artificial two-dimensional Kondo lattices. *Nat. Phys.* **7**, 849–853 (2011).

18. 18.

Geim, A. K. & Grigorieva, I. V. Van der Waals heterostructures. *Nature* **499**, 419–425 (2013).

19. 19.

Liu, Y. et al. Van der Waals heterostructures and devices. *Nat. Rev. Mater.* **1**, 16042 (2016).

20. 20.

Novoselov, K. S., Mishchenko, A., Carvalho, A. & Castro Neto, A. H. 2D materials and van der Waals heterostructures. *Science* **353**, aac9439 (2016).

21. 21.

Kennes, D. M. et al. Moiré heterostructures as a condensed-matter quantum simulator. *Nat. Phys.* **17**, 155–163 (2021).

22. 22.

Andrei, E. Y. et al. The marvels of moiré materials. *Nat. Rev. Mater.* **6**, 201–206 (2021).

23. 23.

Ugeda, M. M. et al. Characterization of collective ground states in single-layer NbSe₂. *Nat. Phys.* **12**, 92–97 (2015).

24. 24.

de la Barrera, S. C. et al. Tuning Ising superconductivity with layer and spin-orbit coupling in two-dimensional transition-metal dichalcogenides. *Nat. Commun.* **9**, 1427 (2018).

25. 25.

Law, K. T. & Lee, P. A. 1T-TaS₂ as a quantum spin liquid. *Proc. Natl Acad. Sci. USA* **114**, 6996–7000 (2017).

26. 26.

Cho, D. et al. Nanoscale manipulation of the Mott insulating state coupled to charge order in 1T-TaS₂. *Nat. Commun.* **7**, 10453 (2016).

27. 27.

Qiao, S. et al. Mottness collapse in 1T-TaS_{2-x}Se_x transition-metal dichalcogenide: an interplay between localized and itinerant orbitals. *Phys. Rev. X* **7**, 041054 (2017).

28. 28.

Chen, Y. et al. Strong correlations and orbital texture in single-layer 1T-TaSe₂. *Nat. Phys.* **16**, 218–224 (2020).

29. 29.

Ruan, W. et al. Evidence for quantum spin liquid behaviour in single-layer 1T-TaSe₂ from scanning tunnelling microscopy. *Nat. Phys.* **17**, 1154–1161 (2021).

30. 30.

Kratochvilova, M. et al. The low-temperature highly correlated quantum phase in the charge-density-wave 1T-TaS₂ compound. *npj Quant. Mater.* **2**, 42 (2017).

31. 31.

Coqblin, B. & Schrieffer, J. R. Exchange interaction in alloys with cerium impurities. *Phys. Rev.* **185**, 847–853 (1969).

32. 32.

Wen, C. et al. Roles of the narrow electronic band near the Fermi level in 1T-TaS₂-related layered materials. *Phys. Rev. Lett.* **126**, 256402 (2021).

33. 33.

Zhang, Y.-H. et al. Temperature and magnetic field dependence of a Kondo system in the weak coupling regime. *Nat. Commun.* **4**, 2110 (2013).

34. 34.

Ryu, H. et al. Persistent charge-density-wave order in single-layer TaSe₂. *Nano Lett.* **18**, 689–694 (2018).

35. 35.

McMillan, W. L. & Mochel, J. Electron tunneling experiments on amorphous Ge_{1-x}Au_x. *Phys. Rev. Lett.* **46**, 556–557 (1981).

36. 36.

Ernst, S. et al. Emerging local Kondo screening and spatial coherence in the heavy-fermion metal YbRh₂Si₂. *Nature* **474**, 362–366 (2011).

37. 37.

Rößler, S. et al. Hybridization gap and Fano resonance in SmB₆. *Proc. Natl Acad. Sci. USA* **111**, 4798–4802 (2014).

38. 38.

Bose, S. & Ayyub, P. A review of finite size effects in quasi-zero dimensional superconductors. *Rep. Prog. Phys.* **77**, 116503 (2014).

39. 39.

Ganguli, S. C., Vaňo, V., Kezilebieke, S., Lado, J. L. & Liljeroth, P. Controlling correlations in NbSe₂ via quantum confinement. Preprint at <https://arxiv.org/abs/2009.13422> (2020).

40. 40.

Kouwenhoven, L. P., Austing, D. G. & Tarucha, S. Few-electron quantum dots. *Rep. Prog. Phys.* **64**, 701–736 (2001).

41. 41.

She, J.-H., Kim, C. H., Fennie, C. J., Lawler, M. J. & Kim, E.-A. Topological superconductivity in metal/quantum-spin-ice heterostructures. *npj Quant. Mater.* **2**, 64 (2017).

42. 42.

Ribak, A. et al. Chiral superconductivity in the alternate stacking compound 4Hb-TaS₂. *Sci. Adv.* **6**, eaax9480 (2020).

43. 43.

Seiro, S. et al. Evolution of the Kondo lattice and non-Fermi liquid excitations in a heavy-fermion metal. *Nat. Commun.* **9**, 3324 (2018).

44. 44.

Hall, J. et al. Molecular beam epitaxy of quasi-freestanding transition metal disulphide monolayers on van der Waals substrates: a growth study. *2D Mater.* **5**, 025005 (2018).

45. 45.

Lin, H. et al. Growth of atomically thick transition metal sulfide films on graphene/6H-SiC(0001) by molecular beam epitaxy. *Nano Res.* **11**, 4722–4727 (2018).

Acknowledgements

This research made use of the Aalto Nanomicroscopy Center (Aalto NMC) facilities and was supported by the European Research Council (ERC-2017-AdG no. 788185 “Artificial Designer Materials”), the Academy of Finland (Academy professor funding nos. 318995 and 320555, Academy postdoctoral researcher no. 309975, Academy research fellow nos. 331342

and 336243) and the Jane and Aatos Erkko Foundation. We acknowledge the computational resources provided by the Aalto Science-IT project.

Author information

Author notes

1. Shawulienu Kezilebieke

Present address: Department of Physics, Department of Chemistry and Nanoscience Center, University of Jyväskylä, Jyväskylä, Finland

Affiliations

1. Department of Applied Physics, Aalto University, Espoo, Finland

Viliam Vaňo, Mohammad Amini, Somesh C. Ganguli, Guangze Chen, Jose L. Lado, Shawulienu Kezilebieke & Peter Liljeroth

Contributions

V.V., J.L.L., S.K. and P.L. conceived the experiment, V.V., M.A., S.C.G. and S.K. carried out the sample growth and the low-temperature STM experiments. V.V. analysed the STM data. G.C. and J.L.L. developed the theoretical model. V.V., J.L.L. and P.L. wrote the manuscript with input from all co-authors.

Corresponding authors

Correspondence to [Jose L. Lado](#) or [Peter Liljeroth](#).

Ethics declarations

Competing interests

The authors declare no competing interests.

Additional information

Peer review information *Nature* thanks Milan Allan, Stefan Kirchner and the other, anonymous, reviewer(s) for their contribution to the peer review of this work. Peer reviewer reports are available.

Publisher's note Springer Nature remains neutral with regard to jurisdictional claims in published maps and institutional affiliations.

Extended data figures and tables

[Extended Data Fig. 1 Grid spectroscopy measurement of a 1T-TaS₂/1H-TaS₂ heterostructure.](#)

a, STM image of a 1T/1H-TaS₂ heterostructure ($V = 200$ mV and $I = 10$ pA). **b**, Tunneling spectra across the red line shown in (a), starting from top left. We observe a Kondo peak located on each of the CDW centers. **c**, dI/dV map at $V = 0$ mV measured on the area shown in (a) showing the Kondo lattice. Due to a Kondo peak, there is a higher dI/dV intensity on each of the CDW centers. Middle and bottom rows: dI/dV maps at given bias voltages, all measured on the area shown in (a) and using the same colour scale as in (c). Each of the dI/dV curves was normalized by dividing it by its mean value. Single tunneling spectra on different CDW centers and on a different area are shown in Extended Data Fig. 2.

[Extended Data Fig. 2 Single tunneling spectra in the centre of different CDW unit cells.](#)

Left: STM image of a 1T-TaS₂/1H-TaS₂ heterostructure ($V = 200$ mV and $I = 20$ pA). Right: tunneling spectra measured at locations highlighted by the same-coloured dots on the STM image, spectra are vertically offset for clarity.

[Extended Data Fig. 3 Fitting of the Kondo resonances.](#)

Left: Temperature dependence of a Kondo resonance in tunneling spectroscopy (black lines), and their respective fits to the Fano lineshape (red lines). The spectra are vertically offset for clarity. Right: Table of the fit parameters.

Extended Data Fig. 4 Thermal broadening of the Kondo resonance.

Tunneling spectroscopy of a Kondo resonance at 300 mK (blue), 18 K (green), and a simulated tunneling spectrum at 18 K (red), where the 300 mK spectrum was taken as the density of states.

Extended Data Fig. 5 Tunneling spectra of 1H-TaS₂ on different substrates.

Tunneling spectroscopy of 1H-TaS₂ on HOPG (purple line), bilayer 1H-TaS₂ (blue line) and 1H-TaS₂ on monolayer 1T-TaS₂ (green line). The spectra are measured on positions highlighted by the same-coloured dots in the STM image on the left. The spectra exhibit a dip around the Fermi level, but while 1H-TaS₂ on HOPG (purple line) and bilayer 1H-TaS₂ (blue line) have finite zero-bias conductance, only the spectroscopy of 1H/1T-TaS₂ (green line) exhibits a heavy-fermion gap with zero conductance at zero bias.

Extended Data Fig. 6 Examples of different 1H/1T-TaS₂ heterostructures.

STM images (left) and corresponding tunneling spectra measured on top of a heterostructure (right). Purple dots highlight the positions, where the tunneling spectra were taken. All the heterostructures exhibit a heavy-fermion gap with zero conductance at zero bias and approximately the same gap width, regardless of the island size.

Extended Data Fig. 7 Tunneling spectroscopy across middle of the 1H/1T-TaS₂ island.

a, STM image of a 1H/1T-TaS₂ vertical heterostructure ($V = 900$ mV and $I = 20$ pA). **b**, Tunneling spectra across the red line shown in (a). **c**, Average tunneling spectrum from the spectra across line in (b).

Extended Data Fig. 8 Spatial dependence of the heavy-fermion gap.

a, STM image of a 1H-TaS₂/1T-TaS₂ heterostructure ($V = 50$ mV and $I = 500$ pA). Larger scale topographic image is shown in Extended Data Fig. [9e](#). **b**, Tunneling spectra across the red line shown in (a). **c**, dI/dV map at $V = 0$ mV measured on the area shown in (a). Middle and bottom rows: dI/dV maps at given bias voltages, all measured on the area shown in (a) and using the same colour scale as in (c).

Extended Data Fig. 9 High-resolution STM images of different heterostructures.

a, c, e, g, Large area STM images. **b**, STM image of a 1H-TaS₂ on HOPG ($V = 50$ mV and $I = 500$ pA). Inset shows fast Fourier transform of the image. **d**, STM image of a monolayer 1T-TaS₂ on HOPG ($V = 1$ V and $I = 20$ pA). **f**, STM image of a 1H/1T-TaS₂ vertical heterostructure ($V = 50$ V and $I = 500$ pA). Inset shows fast Fourier transform of the image. **h**, STM image of a 1T/1H-TaS₂ vertical heterostructure ($V = 0.3$ V and $I = 50$ pA). 1H-TaS₂ on HOPG exhibits a strong 3×3 CDW, while 1H-TaS₂ on 1T-TaS₂ shows no signs of CDW. Both 1T-TaS₂ on HOPG and 1T-TaS₂ on 1H-TaS₂ exhibit a strong $\sqrt{13} \times \sqrt{13}$ CDW.

Extended Data Fig. 10 Magnetic field dependence of a heavy-fermion gap.

Tunneling spectroscopy of a heavy-fermion gap measured on a 1H/1T-TaS₂ vertical heterostructure at different applied magnetic fields, the spectra are vertically offset for clarity.

Supplementary information

Supplementary Information

This file contains Supplementary Sections 1–3: detailed description of the theoretical model; discussion on the comparison with the magnetic field dependence of natural heavy-fermion compounds; discussion on the potential further probes of the heavy-fermion regime.

Peer Review File

Rights and permissions

Reprints and Permissions

About this article

Cite this article

Vaňo, V., Amini, M., Ganguli, S.C. *et al.* Artificial heavy fermions in a van der Waals heterostructure. *Nature* **599**, 582–586 (2021).
<https://doi.org/10.1038/s41586-021-04021-0>

- Received: 26 March 2021
- Accepted: 14 September 2021
- Published: 24 November 2021
- Issue Date: 25 November 2021
- DOI: <https://doi.org/10.1038/s41586-021-04021-0>

Share this article

Anyone you share the following link with will be able to read this content:

[Get shareable link](#)

Sorry, a shareable link is not currently available for this article.

[Copy to clipboard](#)

Provided by the Springer Nature SharedIt content-sharing initiative

This article was downloaded by **calibre** from <https://www.nature.com/articles/s41586-021-04021-0>

| [Section menu](#) | [Main menu](#) |

- Article
- [Published: 24 November 2021](#)

On-chip electro-optic frequency shifters and beam splitters

- [Yaowen Hu](#) [ORCID: orcid.org/0000-0002-0127-1959^{1,2}](#),
- [Mengjie Yu¹](#),
- [Di Zhu](#) [ORCID: orcid.org/0000-0003-0210-1860¹](#),
- [Neil Sinclair^{1,3,4}](#),
- [Amirhassan Shams-Ansari¹](#),
- [Linbo Shao](#) [ORCID: orcid.org/0000-0002-0615-7848¹](#),
- [Jeffrey Holzgrafe¹](#),
- [Eric Puma¹](#),
- [Mian Zhang](#) [ORCID: orcid.org/0000-0001-9838-3895⁵](#) &
- [Marko Lončar](#) [ORCID: orcid.org/0000-0002-5029-5017¹](#)

[Nature](#) volume 599, pages 587–593 (2021)

- 1315 Accesses
- 27 Altmetric
- [Metrics details](#)

Subjects

- [Integrated optics](#)
- [Nanophotonics and plasmonics](#)
- [Nonlinear optics](#)

Abstract

Efficient frequency shifting and beam splitting are important for a wide range of applications, including atomic physics^{1,2}, microwave photonics^{3,4,5,6}, optical communication^{7,8} and photonic quantum computing^{9,10,11,12,13,14}. However, realizing gigahertz-scale frequency shifts with high efficiency, low loss and tunability—in particular using a miniature and scalable device—is challenging because it requires efficient and controllable nonlinear processes. Existing approaches based on acousto-optics^{6,15,16,17}, all-optical wave mixing^{10,13,18,19,20,21,22} and electro-optics^{23,24,25,26,27} are either limited to low efficiencies or frequencies, or are bulky. Furthermore, most approaches are not bi-directional, which renders them unsuitable for frequency beam splitters. Here we demonstrate electro-optic frequency shifters that are controlled using only continuous and single-tone microwaves. This is accomplished by engineering the density of states of, and coupling between, optical modes in ultralow-loss waveguides and resonators in lithium niobate nanophotonics²⁸. Our devices, consisting of two coupled ring-resonators, provide frequency shifts as high as 28 gigahertz with an on-chip conversion efficiency of approximately 90 per cent. Importantly, the devices can be reconfigured as tunable frequency-domain beam splitters. We also demonstrate a non-blocking and efficient swap of information between two frequency channels with one of the devices. Finally, we propose and demonstrate a scheme for cascaded frequency shifting that allows shifts of 119.2 gigahertz using a 29.8 gigahertz continuous and single-tone microwave signal. Our devices could become building blocks for future high-speed and large-scale classical information processors^{7,29} as well as emerging frequency-domain photonic quantum computers^{9,11,14}.

Access options

Subscribe to Journal

Get full journal access for 1 year

\$199.00

only \$3.90 per issue

[Subscribe](#)

All prices are NET prices.

VAT will be added later in the checkout.

Tax calculation will be finalised during checkout.

Rent or Buy article

Get time limited or full article access on ReadCube.

from \$8.99

[Rent or Buy](#)

All prices are NET prices.

Additional access options:

- [Log in](#)
- [Access through your institution](#)
- [Learn about institutional subscriptions](#)

Fig. 1: Concept of the electro-optic frequency shifter and beam splitter.

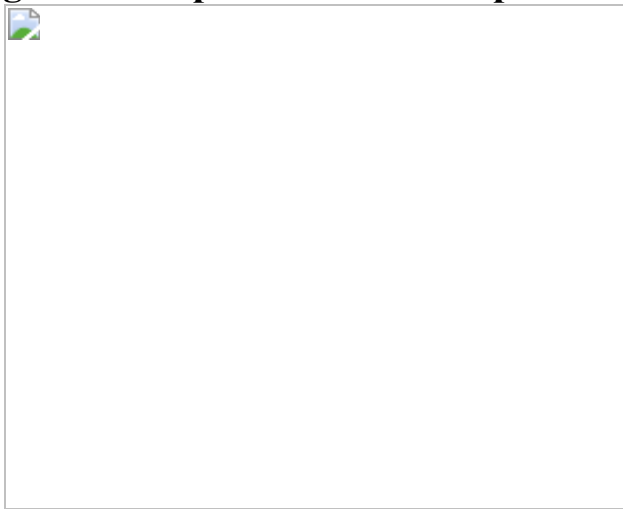


Fig. 2: Electro-optic frequency shifter and beam splitter.



Fig. 3: Information swapping between two frequency channels.

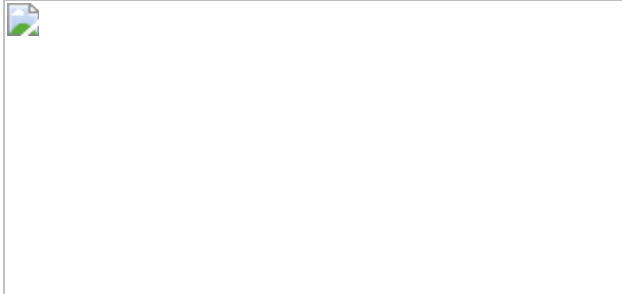
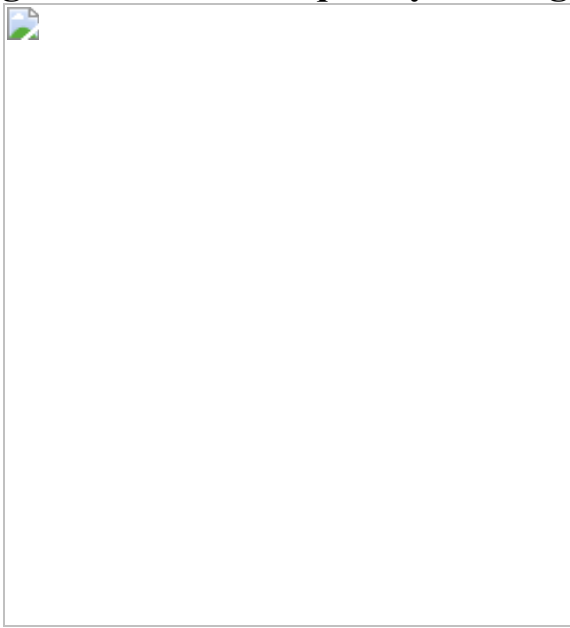


Fig. 4: Cascaded frequency shifting.



Data availability

The datasets generated and analysed during the current study are available from the corresponding author on reasonable request.

References

1. 1.

Greiner, M., Mandel, O., Esslinger, T., Hänsch, T. W. & Bloch, I. Quantum phase transition from a superfluid to a Mott insulator in a gas of ultracold atoms. *Nature* **415**, 39–44 (2002).

2. 2.

Hu, J. et al. Creation of a Bose-condensed gas of ^{87}Rb by laser cooling. *Science*. **358**, 1078–1080 (2017).

3. 3.

Supradeepa, V. R. et al. Comb-based radiofrequency photonic filters with rapid tunability and high selectivity. *Nat. Photon.* **6**, 186–194 (2012).

4. 4.

Marpaung, D., Yao, J. & Capmany, J. Integrated microwave photonics. *Nat. Photon.* **13**, 80–90 (2019).

5. 5.

Fandiño, J. S., Muñoz, P., Doménech, D. & Capmany, J. A monolithic integrated photonic microwave filter. *Nat. Photon.* **11**, 124–129 (2016).

6. 6.

Eggleton, B. J., Poulton, C. G., Rakich, P. T., Steel, M. J. & Bahl, G. Brillouin integrated photonics. *Nat. Photon.* **13**, 664–677 (2019).

7. 7.

Yoo, S. J. B. Wavelength conversion technologies for WDM network applications. *J. Light. Technol.* **14**, 955–966 (1996).

8. 8.

Lukens, J. M. et al. All-optical frequency processor for networking applications. *J. Light. Technol.* **38**, 1678–1687 (2020).

9. 9.

Kues, M. et al. On-chip generation of high-dimensional entangled quantum states and their coherent control. *Nature* **546**, 622–626 (2017).

10. 10.

Kobayashi, T. et al. Frequency-domain Hong–Ou–Mandel interference. *Nat. Photon.* **10**, 441–444 (2016).

11. 11.

Lukens, J. M. & Lougovski, P. Frequency-encoded photonic qubits for scalable quantum information processing. *Optica* **4**, 8–16 (2016).

12. 12.

Lu, H. H. et al. Electro-optic frequency beam splitters and tritters for high-fidelity photonic quantum information processing. *Phys. Rev. Lett.* **120**, 30502 (2018).

13. 13.

Joshi, C. et al. Frequency-domain quantum interference with correlated photons from an integrated microresonator. *Phys. Rev. Lett.* **124**, 143601 (2020).

14. 14.

Kues, M. et al. Quantum optical microcombs. *Nat. Photon.* **13**, 170–179 (2019).

15. 15.

Kittlaus, E. A., Otterstrom, N. T., Kharel, P., Gertler, S. & Rakich, P. T. Non-reciprocal interband Brillouin modulation. *Nat. Photon.* **12**, 613–619 (2018).

16. 16.

Sohn, D. B., Kim, S. & Bahl, G. Time-reversal symmetry breaking with acoustic pumping of nanophotonic circuits. *Nat. Photon.* **12**, 91–97 (2018).

17. 17.

Liu, Q., Li, H. & Li, M. Electromechanical Brillouin scattering in integrated optomechanical waveguides. *Optica* **6**, 778–785 (2019).

18. 18.

Huang, J. & Kumar, P. Observation of quantum frequency conversion. *Phys. Rev. Lett.* **68**, 2153–2156 (1992).

19. 19.

Li, Q., Davanço, M. & Srinivasan, K. Efficient and low-noise single-photon-level frequency conversion interfaces using silicon nanophotonics. *Nat. Photon.* **10**, 406–414 (2016).

20. 20.

Heuck, M. et al. Unidirectional frequency conversion in microring resonators for on-chip frequency-multiplexed single-photon sources. *New J. Phys.* **21**, 33037 (2019).

21. 21.

Raymer, M. G., van Enk, S. J., McKinstry, C. J. & McGuinness, H. J. Interference of two photons of different colour. *Opt. Commun.* **283**, 747–752 (2010).

22. 22.

Pelc, J. S. et al. Dual-channel, single-photon upconversion detector at 13 μm . *Opt. Express* **20**, 19075–19087 (2012).

23. 23.

Preble, S. F., Xu, Q. & Lipson, M. Changing the colour of light in a silicon resonator. *Nat. Photon.* **1**, 293–296 (2007).

24. 24.

Johnson, L. M. & Cox, C. H. Serrodyne optical frequency translation with high sideband suppression. *J. Light. Technol.* **6**, 109–112 (1988).

25. 25.

Izutsu, M., Shikama, S. & Sueta, T. Integrated optical SSB modulator/frequency shifter. *IEEE J. Quantum Electron.* **17**, 2225–2227 (1981).

26. 26.

Wright, L. J., Karpiński, M., Söller, C. & Smith, B. J. Spectral shearing of quantum light pulses by electro-optic phase modulation. *Phys. Rev. Lett.* **118**, 23601 (2017).

27. 27.

Savchenkov, A. A. et al. Tunable optical single-sideband modulator with complete sideband suppression. *Opt. Lett.* **34**, 1300–1302 (2009).

28. 28.

Zhang, M., Wang, C., Cheng, R., Shams-Ansari, A. & Lončar, M. Monolithic ultra-high- Q lithium niobate microring resonator. *Optica* **4**, 1536–1537 (2017).

29. 29.

Frankel, M. Y. & Esman, R. D. Optical single-sideband suppressed-carrier modulator for wide-band signal processing. *J. Light. Technol.* **16**, 859–863 (1998).

30. 30.

Lo, H.-P. & Takesue, H. Precise tuning of single-photon frequency using an optical single sideband modulator. *Optica* **4**, 919–923 (2017).

31. 31.

Xu, M. et al. High-performance coherent optical modulators based on thin-film lithium niobate platform. *Nat. Commun.* **11**, 3911 (2020).

32. 32.

Fan, L. et al. Integrated optomechanical single-photon frequency shifter. *Nat. Photon.* **10**, 766–770 (2016).

33. 33.

Zhang, M. et al. Electronically programmable photonic molecule. *Nat. Photon.* **13**, 36–40 (2019).

34. 34.

He, L. et al. Low-loss fibre-to-chip interface for lithium niobate photonic integrated circuits. *Opt. Lett.* **44**, 2314–2317 (2019).

35. 35.

Khan, S. et al. Low-loss, high-bandwidth fibre-to-chip coupling using capped adiabatic tapered fibers. *APL Photonics* **5**, 056101 (2020).

36. 36.

Yuan, L., Lin, Q., Xiao, M. & Fan, S. Synthetic dimension in photonics. *Optica* **5**, 1396–1405 (2018).

37. 37.

Hu, Y., Reimer, C., Shams-Ansari, A., Zhang, M. & Loncar, M. Realization of high-dimensional frequency crystals in electro-optic microcombs. *Optica* **7**, 1189–1194 (2020).

38. 38.

Wang, C. et al. Integrated lithium niobate electro-optic modulators operating at CMOS-compatible voltages. *Nature* **562**, 101–104 (2018).

39. 39.

Soltani, M. et al. Efficient quantum microwave-to-optical conversion using electro-optic nanophotonic coupled resonators. *Phys. Rev. A* **96**, 043808 (2017).

40. 40.

Sinclair, N. et al. Spectral multiplexing for scalable quantum photonics using an atomic frequency comb quantum memory and feed-forward control. *Phys. Rev. Lett.* **113**, 053603 (2014).

41. 41.

Joshi, C., Farsi, A., Clemmen, S., Ramelow, S. & Gaeta, A. L. Frequency multiplexing for quasi-deterministic heralded single-photon sources. *Nat. Commun.* **9**, 847 (2018).

42. 42.

Grimau Puigibert, M. et al. Heralded single photons based on spectral multiplexing and feed-forward control. *Phys. Rev. Lett.* **119**, 083601 (2017).

43. 43.

Ghelfi, P. et al. A fully photonics-based coherent radar system. *Nature* **507**, 341–345 (2014).

44. 44.

Demtröder, W. *Laser Spectroscopy. Volume 2: Experimental Techniques* (Springer, 2008).

45. 45.

Kohlhaas, R. et al. Robust laser frequency stabilization by serrodyne modulation. *Opt. Lett.* **37**, 1005–1007 (2012).

46. 46.

Wang, C. et al. Monolithic lithium niobate photonic circuits for Kerr frequency comb generation and modulation. *Nat. Commun.* **10**, 978 (2019).

Acknowledgements

We thank C. Wang, C. Reimer, J. Lukens and P. Lougovski for helpful discussions. This work is supported by the US Office of Naval Research (QOMAND N00014-15-1-2761), Air Force Office of Scientific Research (FA9550-19-1-0310 and FA9550-20-1-0105), National Science Foundation (ECCS-1839197, ECCS-1541959 and PFI-TT IIP-1827720), Army Research Office (W911NF2010248), and Department of Energy (HEADS-QON DE-SC0020376). Device fabrication was performed at the Harvard University Center for Nanoscale Systems. D.Z. acknowledges support by the Harvard Quantum Initiative post-doctoral fellowship. N.S. acknowledges support by the Natural Sciences and Engineering Research Council of Canada (NSERC) and the AQT Intelligent Quantum Networks and Technologies (INQNET) research programme. E.P. acknowledges support by a Draper Fellowship.

Author information

Affiliations

1. John A. Paulson School of Engineering and Applied Sciences, Harvard University, Cambridge, MA, USA

Yaowen Hu, Mengjie Yu, Di Zhu, Neil Sinclair, Amirhassan Shams-Ansari, Linbo Shao, Jeffrey Holzgrafe, Eric Puma & Marko Lončar

2. Department of Physics, Harvard University, Cambridge, MA, USA

Yaowen Hu

3. Division of Physics, Mathematics and Astronomy, California Institute of Technology, Pasadena, CA, USA

Neil Sinclair

4. Alliance for Quantum Technologies (AQT), Pasadena, CA, USA

Neil Sinclair

5. HyperLight Corporation, Cambridge, MA, USA

Mian Zhang

Contributions

Y.H. and M.Z. conceived the idea. Y.H. developed the theory, performed numerical simulations and fabricated the devices. Y.H., M.Y. and D.Z. carried out the measurements with N.S. assisting. Y.H., N.S., D.Z., M.Y., M.Z. and M.L. wrote the manuscript. A.S.-A., L.S., J.H. and E.P. helped with the project. M.L. supervised the project.

Corresponding author

Correspondence to [Marko Lončar](#).

Ethics declarations

Competing interests

M.Z. and M.L. are involved in developing lithium niobate technologies at HyperLight Corporation.

Additional information

Peer review information *Nature* thanks Andrew Weiner and the other, anonymous, reviewer(s) for their contribution to the peer review of this work. Peer reviewer reports are available.

Publisher's note Springer Nature remains neutral with regard to jurisdictional claims in published maps and institutional affiliations.

Extended data figures and tables

[Extended Data Fig. 1 Illustration of the cross-section of one of the two-resonator devices, set-up of frequency shift measurements, and optical transmission spectra.](#)

a, Cross-section of one of the two-resonator devices. The parameters labelled in the cross-section are $w=1.2\text{ }\mu\text{m}$, $h=350\text{ nm}$, $t=250\text{ nm}$, $d_1=300\text{ nm}$, $d_2=500\text{ nm}$, and $h_1=h_2=800\text{ nm}$.

b, Set-up for measuring frequency up- and down-shifts. PC, polarization controller; OSA, optical spectrum analyser; PD, photodetector. **c**, Measured transmission spectrum of the 12.5-GHz two-resonator device (Fig. 2b,c) when the microwave drive is turned off (left panel) and on (right panel). **d**, Simulation of the transmission and phase spectra of the 12.5-GHz two-resonator device in the presence and absence of the microwave drive. MW, microwave.

[Extended Data Fig. 2 Polarization of the frequency shifter output.](#)

This measurement is performed on a two-resonator device with $\backslash(11.0\backslash, \{\rm{GHz}\})$ doublet splitting. The TE and TM components of the output light are measured using an optical spectrum analyser after passing a polarizer. Here the power is normalized by the summation of TE and TM output powers.

Extended Data Fig. 3 Modulation bandwidth and frequency channel shifting with pseudorandom bit sequences.

a, Experimental set-ups. The input laser beam is modulated by either a sinusoidal signal from the port 1 of a vector network analyser (VNA) (bandwidth measurement) or an actual data stream that is generated by an arbitrary waveform generator (AWG) (eye diagram measurement). The input light is up-shifted and detected by a photodetector (PD) followed by either port 2 of the VNA (bandwidth measurement) or an oscilloscope (eye diagram measurement). The measurements are performed at a wavelength of 1,560 nm on the two-resonator device in Fig. [2b,c](#), in which the doublet splitting is 11.3 GHz due to optical dispersion (doublet splitting is 12.5 GHz at 1,601 nm). **b**, Measured modulation bandwidth of the device. The 3-dB modulation bandwidth is 2.2 GHz, corresponding to an optical bandwidth of 4.4 GHz. The modulation bandwidth is broadened to 4.1 GHz by increasing the microwave driving power from 126 mW to 398 mW. **c**, Measured eye diagrams when using actual data streams to modulate the input laser beam. The eye diagrams before shift are measured by setting the input laser beam off-resonance with the filter window centered to the input wavelength (filter bandwidth unchanged). By comparing the amplitude of the eye diagrams before and after swap, we found the loss is ~ 1 dB which is consistent with the on-chip loss (0.92 dB).

Extended Data Fig. 4 Simulated shift ratio as a function of the detuning of the laser.

The simulated two-resonator device is optimized for high optical bandwidth. Design parameters: $\backslash(\gamma = \backslash,2\{\pi\}\times 20\backslash, \{\rm{GHz}\})$ (leads to a $\backslash(\kappa_e = \backslash,2\{\pi\}\times 10\backslash, \{\rm{GHz}\})$), $\backslash(\kappa_{int} = \backslash,2\{\pi\}\times 170\backslash,$

$\text{MHz})$, $\{\omega\}_{\text{m}} = 2\pi \times 28.2 \text{ GHz}$. A 3-dB optical bandwidth of $\sim 14 \text{ GHz}$ can be achieved using a critical-drive microwave power of 1.35 mW with a 26.7 dB suppression of parasitic sidebands and 0.13 dB on-chip loss. The microwave power for a 50–50 split on such a device is expected to be 238 mW .

Extended Data Fig. 5 Crosstalk measurement for channel swapping.

a, Experimental set-ups for the crosstalk measurement. Two input laser beams are each independently modulated by a sinusoidal signal to define two distinct frequency channels, sent into a two-resonator device, and detected by an OSA and a PD followed by an RSA. The sinusoidal signal applied to the input beam of channel 1 (matching the S resonance) is swept from 200 MHz to 2.8 GHz while the sinusoidal signal on the input beam of channel 2 (matching the AS resonance) is kept at 1 GHz. Each channel is selected by a tunable filter. **b**, Radio-frequency spectrum for channel 1 and channel 2 after the swap when the modulation frequency in channel 1 is set to 2.6 GHz depicts low crosstalk in the swap measurements. The crosstalk is defined as the ratio between the shifted frequency and the residual frequency. The frequency component of 1.6 GHz that appears in channel 1 is the beat note between the shifted frequency and the residual frequency. The 2 GHz component is the second harmonic signal that is generated by the amplitude modulator, which is verified beforehand. **c**, Measured crosstalk for two channels when sweeping the modulation frequency in channel 1 from 200 MHz to 2.8 GHz . We find the crosstalk to be approximately -35 dB at low frequency (several hundreds of MHz) and approximately -25 dB at 2.8 GHz . PC, polarization controller; AM, amplitude modulator; EDFA, erbium-doped fibre amplifier; OSA, optical spectrum analyser; PD, photodetector; RSA, real-time spectrum analyser.

Extended Data Fig. 6 Varying the shift frequency with d.c. voltage.

Each of the resonators in a 12.5-GHz two-resonator device (Fig. 2b,c) are detuned from each other using a d.c. voltage to provide a variation of the frequency difference between the two hybrid modes. For each frequency difference between two modes, the microwave frequency is changed to match this difference, while the powers of the microwave signals are kept constant and equal to that used when the resonances of each ring are degenerate (Fig. 2b,c). The shift ratio remains >0.9 when the shift frequency is detuned ($> 20\text{ GHz}$).

Extended Data Fig. 7 Limitation of the on-chip loss and parasitic sidebands.

a, Predicted two-resonator on-chip loss with varied $\langle Q \rangle_{intrinsic}$ for different waveguide–ring couplings γ . The theoretical curve of on-chip loss is calculated under the optimal condition of both pump and microwave detunings are zero. The measured on-chip loss of the (11.0, 12.5, and 28.2, GHz) devices used in this work are labelled with a triangle, square, and diamond, respectively. **b**, Simulation of the normalized power of the parasitic sidebands as a function of the shift frequency. The waveguide–cavity coupling rate (γ) is varied from (2π) to $(2\pi \times 7)$. Waveguide–cavity coupling rates that are as high as $(2\pi \times 7)$ can still keep the parasitic sidebands suppressed below (20 dB) for shift frequencies ($> 10\text{ GHz}$) and below (30 dB) for shifts that are ($> 30\text{ GHz}$). In this work, the parasitic sidebands are lower than (25 dB) in devices at shift frequencies of $(10\text{--}30\text{ GHz})$.

Extended Data Fig. 8 Simulated electrode performance for varied microwave frequencies.

a, The relative voltage delivered to the capacitor V_C and probe ($\langle V \rangle_0$) for varied microwave frequencies. **b**, Power required at the probe ((50Ω)) for a maximal shift ratio as a function of microwave frequency. Our current (28.2, GHz) two-resonator device requires

\(188\text{ mW}\) of theoretical microwave power (\(4.34\text{ V}\)) microwave peak voltage). We assume that the voltage V_C delivered to the capacitor is kept identical to the peak-voltage on capacitor ($V_C = 7.46$ V) of our \(28.2\text{ GHz}\) device when reaching \((0.987)\) shift ratio. MW, microwave.

Extended Data Fig. 9 Simulation of the cascaded frequency shifter.

a, Simulated optical spectrum shows a cascaded frequency shift when the GCC condition is satisfied. A single microwave tone at \(30\text{ GHz}\) (equal to the FSR of ring 2) generates a five-mode cascaded frequency shift of \(120\text{ GHz}\) with an on-chip loss of \(1.1\text{ dB}\). The inset illustrates the energy flow in the coupled cavities system. The frequency of mode 1 in the x axis of the inset is denoted by $\{\omega\}_1$. **b**, The shift can be scaled to a larger number of modes, with an incremental on-chip loss of \(0.15\text{ dB}\) per mode.

Extended Data Table 1 Parameters of the two-resonator devices
Extended Data Table 2 Parameters of the cascaded frequency shifter

Supplementary information

Supplementary Audio File

Two different and repeated sounds are chosen to be the left channel and the right channel of the audio file. In the experiment, the left channel and the right channel of the audio file are used to drive the two different amplitude modulators for laser beam 1 and laser beam 2, respectively.

Peer Review File

Rights and permissions

Reprints and Permissions

About this article

Cite this article

Hu, Y., Yu, M., Zhu, D. *et al.* On-chip electro-optic frequency shifters and beam splitters. *Nature* **599**, 587–593 (2021).
<https://doi.org/10.1038/s41586-021-03999-x>

- Received: 12 May 2020
- Accepted: 07 September 2021
- Published: 24 November 2021
- Issue Date: 25 November 2021
- DOI: <https://doi.org/10.1038/s41586-021-03999-x>

Share this article

Anyone you share the following link with will be able to read this content:

[Get shareable link](#)

Sorry, a shareable link is not currently available for this article.

[Copy to clipboard](#)

Provided by the Springer Nature SharedIt content-sharing initiative

This article was downloaded by **calibre** from <https://www.nature.com/articles/s41586-021-03999-x>

- Article
- [Published: 24 November 2021](#)

Distribution control enables efficient reduced-dimensional perovskite LEDs

- [Dongxin Ma](#) [ORCID: orcid.org/0000-0002-9790-5951¹](#),
- [Kebin Lin²](#),
- [Yitong Dong¹](#),
- [Hitarth Choubisa¹](#),
- [Andrew H. Proppe¹](#),
- [Dan Wu³](#),
- [Ya-Kun Wang](#) [ORCID: orcid.org/0000-0002-8970-6856¹](#),
- [Bin Chen](#) [ORCID: orcid.org/0000-0002-2106-7664¹](#),
- [Peicheng Li⁴](#),
- [James Z. Fan¹](#),
- [Fanglong Yuan^{1,4}](#),
- [Andrew Johnston](#) [ORCID: orcid.org/0000-0002-4545-532X¹](#),
- [Yuan Liu](#) [ORCID: orcid.org/0000-0001-8611-1673¹](#),
- [Yuetong Kang](#) [ORCID: orcid.org/0000-0001-8354-0392^{5 nAff6}](#),
- [Zheng-Hong Lu](#) [ORCID: orcid.org/0000-0003-2050-0822⁴](#),
- [Zhanhua Wei](#) [ORCID: orcid.org/0000-0003-2687-0293²](#) &
- [Edward H. Sargent](#) [ORCID: orcid.org/0000-0003-0396-6495¹](#)

[Nature](#) volume 599, pages 594–598 (2021)

- 2633 Accesses
- 24 Altmetric

- [Metrics details](#)

Subjects

- [Lasers, LEDs and light sources](#)
- [Nanoscale materials](#)

Abstract

Light-emitting diodes (LEDs) based on perovskite quantum dots have shown external quantum efficiencies (EQEs) of over 23% and narrowband emission, but suffer from limited operating stability¹. Reduced-dimensional perovskites (RDPs) consisting of quantum wells (QWs) separated by organic intercalating cations show high exciton binding energies and have the potential to increase the stability and the photoluminescence quantum yield^{2,3}. However, until now, RDP-based LEDs have exhibited lower EQEs and inferior colour purities^{4,5,6}. We posit that the presence of variably confined QWs may contribute to non-radiative recombination losses and broadened emission. Here we report bright RDPs with a more monodispersed QW thickness distribution, achieved through the use of a bifunctional molecular additive that simultaneously controls the RDP polydispersity while passivating the perovskite QW surfaces. We synthesize a fluorinated triphenylphosphine oxide additive that hydrogen bonds with the organic cations, controlling their diffusion during RDP film deposition and suppressing the formation of low-thickness QWs. The phosphine oxide moiety passivates the perovskite grain boundaries via coordination bonding with unsaturated sites, which suppresses defect formation. This results in compact, smooth and uniform RDP thin films with narrowband emission and high photoluminescence quantum yield. This enables LEDs with an EQE of 25.6% with an average of $22.1 \pm 1.2\%$ over 40 devices, and an operating half-life of two hours at an initial luminance of 7,200 candela per metre squared, indicating tenfold-enhanced operating stability relative to the best-known perovskite LEDs with an EQE exceeding 20%^{1,4,5,6}.

Access options

[Subscribe to Journal](#)

Get full journal access for 1 year

\$199.00

only \$3.90 per issue

[Subscribe](#)

All prices are NET prices.

VAT will be added later in the checkout.

Tax calculation will be finalised during checkout.

Rent or Buy article

Get time limited or full article access on ReadCube.

from \$8.99

[Rent or Buy](#)

All prices are NET prices.

Additional access options:

- [Log in](#)
- [Access through your institution](#)
- [Learn about institutional subscriptions](#)

Fig. 1: Distribution control strategy.

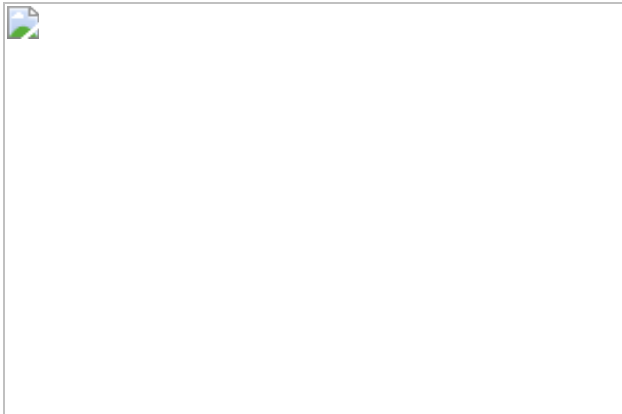


Fig. 2: Optical characteristics.

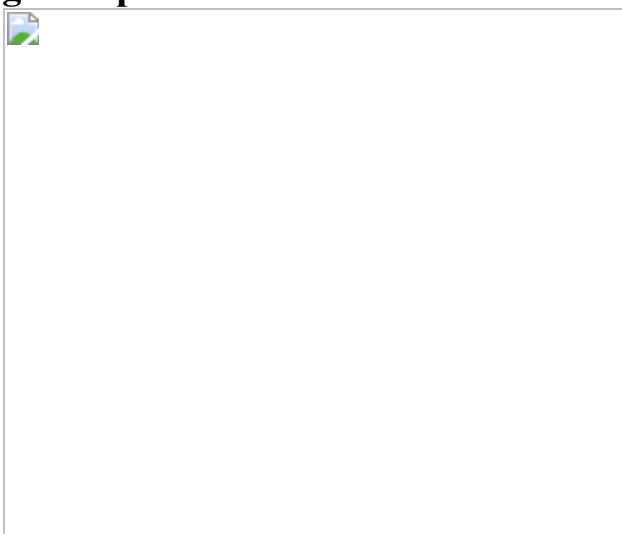


Fig. 3: NMR, XPS and FTIR studies.

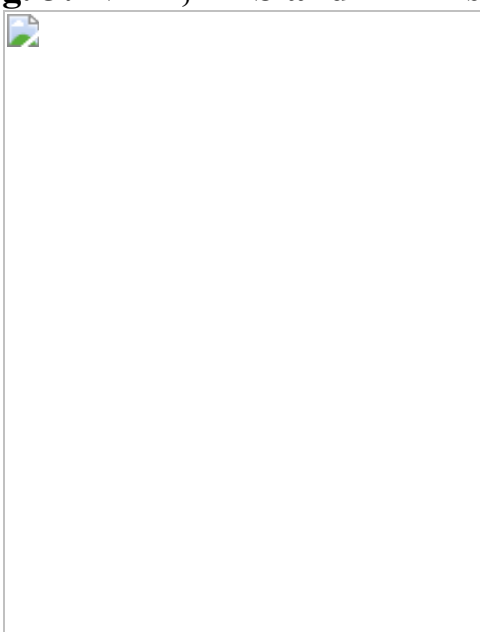
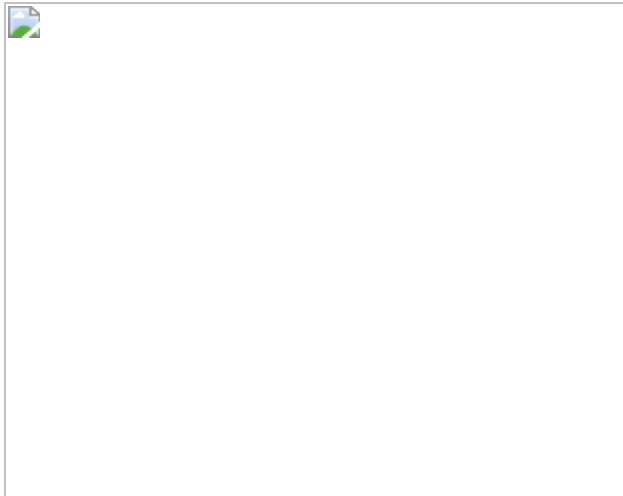


Fig. 4: LED performance.



Data availability

The data that support the findings of this study are available from the corresponding authors.

References

1. 1. Kim, Y.-H. et al. Comprehensive defect suppression in perovskite nanocrystals for high-efficiency light-emitting diodes. *Nat. Photon.* **15**, 148–155 (2021).
2. 2. Hong, K., Le, Q. V., Kim, S. Y. & Jang, H. W. Low-dimensional halide perovskites: review and issues. *J. Mater. Chem. C* **6**, 2189 (2018).
3. 3. Gao, X. et al. Ruddlesden–Popper perovskites: synthesis and optical properties for optoelectronic applications. *Adv. Sci.* **6**, 1900941 (2019).
4. 4.

Jiang, Y. et al. Reducing the impact of Auger recombination in quasi-2D perovskite light-emitting diodes. *Nat. Commun.* **12**, 336 (2021).

5. 5.

Kong, L. et al. Smoothing the energy transfer pathway in quasi-2D perovskite films using methanesulfonate leads to highly efficient light-emitting devices. *Nat. Commun.* **12**, 1246 (2021).

6. 6.

Sun, C. et al. High-performance large-area quasi-2D perovskite light-emitting diodes. *Nat. Commun.* **12**, 2207 (2021)

7. 7.

Jena, A. K., Kulkarni, A. & Miyasaka, T. Halide perovskite photovoltaics: background, status, and future prospects. *Chem. Rev.* **119**, 3036 (2019).

8. 8.

Xing, G. et al. Low-temperature solution-processed wavelength-tunable perovskites for lasing. *Nat. Mater.* **13**, 476–480 (2014).

9. 9.

Dou, L. et al. Solution-processed hybrid perovskite photodetectors with high detectivity. *Nat. Commun.* **5**, 5404 (2014).

10. 10.

Quan, L. N., Arquer, F. P. G., Sabatini, R. P. & Sargent, E. H. Perovskites for light emission. *Adv. Mater.* **30**, 1801996 (2018).

11. 11.

Shen, H. et al. Visible quantum dot light-emitting diodes with simultaneous high brightness and efficiency. *Nat. Photon.* **13**, 192–197

(2019).

12. 12.

Won, Y.-H. et al. Highly efficient and stable InP/ZnSe/ZnS quantum dot light-emitting diodes. *Nature* **575**, 634–638 (2019).

13. 13.

Ly, K. T. et al. Near-infrared organic light-emitting diodes with very high external quantum efficiency and radiance. *Nat. Photon.* **11**, 63–68 (2017).

14. 14.

Wu, T.-L. et al. Diboron compound-based organic light-emitting diodes with high efficiency and reduced efficiency roll-off. *Nat. Photon.* **12**, 235–240 (2018).

15. 15.

Cho, H. et al. Overcoming the electroluminescence efficiency limitations of perovskite light-emitting diodes. *Science* **350**, 1222 (2015).

16. 16.

Richter, J. M. et al. Enhancing photoluminescence yields in lead halide perovskites by photon recycling and light out-coupling. *Nat. Commun.* **7**, 13941 (2016).

17. 17.

Xing, G. et al. Transcending the slow bimolecular recombination in lead-halide perovskites for electroluminescence. *Nat. Commun.* **8**, 14558 (2017).

18. 18.

Miyata, A. et al. Direct measurement of the exciton binding energy and effective masses for charge carriers in organic-inorganic tri-halide perovskites. *Nat. Phys.* **11**, 582–587 (2015).

19. 19.

Quintero-Bermudez, R. et al. Compositional and orientational control in metal halide perovskites of reduced dimensionality. *Nat. Mater.* **17**, 900–907 (2018).

20. 20.

Ma, D. et al. Chloride insertion-immobilization enables bright, narrowband, and stable blue-emitting perovskite diodes. *J. Am. Chem. Soc.* **142**, 5126 (2020).

21. 21.

deQuilettes, D. W. et al. Photoluminescence lifetimes exceeding $8\ \mu s$ and quantum yields exceeding 30% in hybrid perovskite thin films by ligand passivation. *ACS Energy Lett.* **1**, 438 (2016).

22. 22.

Braly, I. L. et al. Hybrid perovskite films approaching the radiative limit with over 90% photoluminescence quantum efficiency. *Nat. Photon.* **12**, 355–361 (2018).

23. 23.

Lin-Vien, D., Colthup, N. B., Fateley, W. G. & Grasselli, J. G. in *The Handbook of Infrared and Raman Characteristic Frequencies of Organic Molecules* Ch. 16 (Academic Press, 1991).

24. 24.

Lin-Vien, D., Colthup, N. B., Fateley, W. G. & Grasselli, J. G. in *The Handbook of Infrared and Raman Characteristic Frequencies of Organic Molecules* Ch. 6 (Academic Press, 1991).

25. 25.

Lin-Vien, D., Colthup, N. B., Fateley, W. G. & Grasselli, J. G. in *The Handbook of Infrared and Raman Characteristic Frequencies of Organic Molecules* Ch. 3 (Academic Press, 1991).

26. 26.

Wang, H. et al. A multi-functional molecular modifier enabling efficient large-area perovskite light-emitting diodes. *Joule* **4**, 1977 (2020).

27. 27.

Dong, Y., et al. Bipolar-shell resurfacing for blue LEDs based on strongly confined perovskite quantum dots. *Nat. Nanotechnol.* **15**, 668–674 (2020).

28. 28.

Lin, K. et al. Perovskite light-emitting diodes with external quantum efficiency exceeding 20 per cent. *Nature* **562**, 245–248 (2018).

29. 29.

Shen, Y. et al. High-efficiency perovskite light-emitting diodes with synergetic outcoupling enhancement. *Adv. Mater.* **31**, 1901517 (2019).

30. 30.

Ilavsky, J. Nika: software for two-dimensional data reduction. *J. Appl. Cryst.* **45**, 324 (2012).

31. 31.

Jiang, Z. GIXGUI: a MATLAB toolbox for grazing-incidence X-ray scattering data visualization and reduction, and indexing of buried three-dimensional periodic nanostructured films. *J. Appl. Cryst.* **48**, 917 (2015).

32. 32.

Kresse, G. & Furthmüller, J. Vienna Ab-Initio Simulation Package (VASP) (Vienna Univ., 2001).

33. 33.

Perdew, J. P.; Burke, K., Ernzerhof, M. Perdew, Burke, and Ernzerhof reply. *Phys. Rev. Lett.* **80**, 891 (1998).

34. 34.

Kresse, G. & Joubert, D. From ultrasoft pseudopotentials to the projector augmented-wave method. *Phys. Rev. B* **59**, 1758 (1999).

35. 35.

Blöchl, P. E. Projector augmented-wave method. *Phys. Rev. B* **50**, 17953 (1994).

36. 36.

Forrest, S. R., Bradley, D. D. C. & Thompson, M. E. Measuring the efficiency of organic light-emitting devices. *Adv. Mater.* **15**, 1043 (2003).

37. 37.

Li, H. et al. A review of characterization of perovskite film in solar cells by spectroscopic ellipsometry. *Sol. Energy* **212**, 48 (2020).

38. 38.

Jellison, G. E. Jr Data analysis for spectroscopic ellipsometry. *Thin Solid Films* **234**, 416 (1993).

39. 39.

Zhao, B. et al. High-efficiency perovskite-polymer bulk heterostructure light-emitting diodes. *Nat. Photon.* **12**, 783–789 (2018).

40. 40.

Meng, S.-S., Li, Y.-Q. & Tang, J.-X. Theoretical perspective to light outcoupling and management in perovskite light-emitting diodes. *Org. Electron.* **61**, 351 (2018).

41. 41.

Zhu, R., Luo, Z. & Wu, S.-T. Light extraction analysis and enhancement in a quantum dot light emitting diode. *Opt. Express* **22**, A1783 (2014).

42. 42.

Cho, C. et al. The role of photon recycling in perovskite light-emitting diodes. *Nat. Commun.* **11**, 611 (2020).

Acknowledgements

This publication is based in part on work supported by the Natural Sciences and Engineering Research Council of Canada (NSERC, number 537463-18), the National Natural Science Foundation of China (numbers 51802102, 21805101, 51902110 and 61905107), the Natural Science Foundation of Fujian Province (numbers 2020J06021 and 2019J01057) and the National Key R&D Program of China (number 2019YFB1704600). We also acknowledge Huawei Canada for financial support and thank C. Zhu of the Advanced Light Source for assistance with GIWAXS measurements; G. Xing and J. Guo at University of Macau for LED light distribution measurements; C. Cui, S. Bian and J. Lu at Huaqiao University for optical constant measurements; and the National Institute of Metrology (NIM) of China for cross-checking LED measurements.

Author information

Author notes

1. Yuetong Kang

Present address: State Key Laboratory for Advanced Metals and Materials, School of Materials Science and Engineering, University of Science and Technology Beijing, Beijing, People's Republic of China

Affiliations

1. Department of Electrical and Computer Engineering, University of Toronto, Toronto, Ontario, Canada

Dongxin Ma, Yitong Dong, Hitarth Choubisa, Andrew H. Proppe, Ya-Kun Wang, Bin Chen, James Z. Fan, Fanglong Yuan, Andrew Johnston, Yuan Liu & Edward H. Sargent

2. Xiamen Key Laboratory of Optoelectronic Materials and Advanced Manufacturing, Institute of Luminescent Materials and Information Displays, College of Materials Science and Engineering, Huaqiao University, Xiamen, People's Republic of China

Kebin Lin & Zhanhua Wei

3. College of New Materials and New Energies, Shenzhen Technology University, Shenzhen, People's Republic of China

Dan Wu

4. Department of Materials Science and Engineering, University of Toronto, Toronto, Ontario, Canada

Peicheng Li, Fanglong Yuan & Zheng-Hong Lu

5. Department of Chemistry, University of Victoria, Victoria, British Columbia, Canada

Yuetong Kang

Contributions

E.H.S. and Z.W. supervised the project. D.M. and E.H.S. conceived the idea, designed the experiments and wrote the manuscript. D.M. and Y.K. synthesized and purified TFPPO. D.M. and K.L. prepared the RDP thin films, performed XPS and PL characterization, and fabricated LEDs. D.M., Y.D. and Y.L. performed TA measurements. H.C. performed DFT calculations. A.H.P. and A.J. performed GIWAXS measurements. D.W. performed optical modelling. Y.-K.W. performed XRD and AFM measurements. K.L. and B.C. performed SEM and TEM measurements. D.M., K.L., F.Y., Z.-H.L. and Z.W. performed LED measurements. P.L. performed ultraviolet photoelectron spectroscopy measurements. J.Z.F. performed FTIR measurements. Y.K. analysed the NMR data. All authors discussed the results and commented on the paper.

Corresponding authors

Correspondence to [Zhanhua Wei](#) or [Edward H. Sargent](#).

Ethics declarations

Competing interests

The authors declare no competing interests.

Additional information

Peer review information *Nature* thanks Tae-Woo Lee, Henry Snaith and the other, anonymous, reviewer(s) for their contribution to the peer review of this work.

Publisher's note Springer Nature remains neutral with regard to jurisdictional claims in published maps and institutional affiliations.

Extended data figures and tables

Extended Data Fig. 1 Characteristics of control, TPPO-treated and TFPPO-treated RDPs.

a–c, GIWAXS profiles. **d–f**, Excitation power-dependent PLQY of control, TPPO-treated and TFPPO-treated RDPs with and without PMMA additives. **g**, Time-resolved PL decay curves. **h**, Photostability under continuous excitation using a laser diode (365 nm, about 180 mW cm⁻²) in a nitrogen-filled glovebox. The half-lives are 6 nm, 13 nm and 65 min, respectively. **i**, XRD profiles. The crystallite sizes calculated using the Scherrer equation are 11.4 nm, 7.5 nm and 6.5 nm, respectively.

Extended Data Fig. 2 Optical characteristics of TPP-treated and TFPP-treated RDPs.

a, TA spectra at a delay time ranging from 0 ps to 50 ps. **b**, TA spectra at delay times of 1 ps, 2 ps, 5 ps, 10 ps and 50 ps. **c**, PL spectra. The inset shows the chemical structure of TPP and TFPP, respectively.

Extended Data Fig. 3 Film morphology.

Top-view SEM and AFM images of control, TPPO-treated and TFPPO-treated RDP thin films with and without PMMA additives.

Extended Data Fig. 4 Density functional theory simulations.

a, TFPPO binding with the unsaturated lead dangling bonds at the perovskite edge through P=O:Pb and forming hydrogen bonds with the ammonium tails of the PEA organic cations (N-H···F) shows a binding energy of 1.88 eV. **b**, TFPP with only P=O:Pb (no N-H···F) shows a binding energy of 1.23 eV.

Extended Data Fig. 5 Ultraviolet photoelectron spectroscopy characteristics.

a, Second electron cut-off. **b**, Valence band spectra of control, TPPO-treated and TFPPO-treated RDPs (from left to right).

Extended Data Fig. 6 Supplementary LED characteristics.

a, Luminance versus current density curves; **b**, EL spectra of LEDs based on control, TPPO-treated and TFPPO-treated RDPs. **c**, Box plot of 40 devices based on TFPPO-treated RDPs (made across four batches). **d, e**, Angle-dependent EL intensity and spectra of LEDs based on TFPPO-treated RDPs. **f**, EQE versus current density curves of commercial OLEDs measured in our lab at Huaqiao University (HQU) and at the National Institute of Metrology (NIM) of China.

Extended Data Fig. 7 Optical modelling.

a, TEM image of LEDs based on TFPPO-treated RDPs, top-view SEM and AFM images of the PEDOT:PSS:PFI layer on ITO substrates. **b**, Refractive indices of the HTL, RDP and ETL layers for numerical simulations. **c**, Power dissipation channels for planar LEDs (left), outcoupling efficiency of planar LEDs as a functional of ERCL (middle) and power dissipation channels for LEDs with a randomly-nanostructured interface between HTL and RDPs (right).

Extended Data Table 1 Performance of reported green perovskite LEDs having EQE exceeding 20%

Rights and permissions

Reprints and Permissions

About this article

Cite this article

Ma, D., Lin, K., Dong, Y. *et al.* Distribution control enables efficient reduced-dimensional perovskite LEDs. *Nature* **599**, 594–598 (2021). <https://doi.org/10.1038/s41586-021-03997-z>

- Received: 22 April 2020

- Accepted: 05 September 2021
- Published: 24 November 2021
- Issue Date: 25 November 2021
- DOI: <https://doi.org/10.1038/s41586-021-03997-z>

Share this article

Anyone you share the following link with will be able to read this content:

[Get shareable link](#)

Sorry, a shareable link is not currently available for this article.

[Copy to clipboard](#)

Provided by the Springer Nature SharedIt content-sharing initiative

This article was downloaded by **calibre** from <https://www.nature.com/articles/s41586-021-03997-z>

| [Section menu](#) | [Main menu](#) |

- Article
- [Published: 24 November 2021](#)

Ultrahard bulk amorphous carbon from collapsed fullerene

- [Yuchen Shang](#) [ORCID: orcid.org/0000-0001-5709-0914](#)^{1 na1},
- [Zhaodong Liu](#)^{1,2 na1},
- [Jiajun Dong](#)^{1 na1},
- [Mingguang Yao](#) [ORCID: orcid.org/0000-0002-1297-5679](#)¹,
- [Zhenxing Yang](#)¹,
- [Quanjun Li](#)¹,
- [Chunguang Zhai](#) [ORCID: orcid.org/0000-0002-6707-0359](#)¹,
- [Fangren Shen](#)¹,
- [Xuyuan Hou](#)¹,
- [Lin Wang](#)^{3,4},
- [Nianqiang Zhang](#)⁵,
- [Wei Zhang](#) [ORCID: orcid.org/0000-0002-6414-7015](#)⁶,
- [Rong Fu](#)⁷,
- [Jianfeng Ji](#)⁸,
- [Xingmin Zhang](#)⁸,
- [He Lin](#) [ORCID: orcid.org/0000-0002-9907-8494](#)⁸,
- [Yingwei Fei](#) [ORCID: orcid.org/0000-0001-9955-5353](#)³,
- [Bertil Sundqvist](#)^{1,9},
- [Weihua Wang](#)¹⁰ &
- [Bingbing Liu](#) [ORCID: orcid.org/0000-0003-3989-0891](#)^{1,2}

[Nature](#) volume **599**, pages 599–604 (2021)

- 3266 Accesses

- 222 Altmetric
- [Metrics details](#)

Subjects

- [Carbon nanotubes and fullerenes](#)
- [Mechanical properties](#)
- [Phase transitions and critical phenomena](#)
- [Structure of solids and liquids](#)

Abstract

Amorphous materials inherit short- and medium-range order from the corresponding crystal and thus preserve some of its properties while still exhibiting novel properties^{1,2}. Due to its important applications in technology, amorphous carbon with sp^2 or mixed sp^2 – sp^3 hybridization has been explored and prepared^{3,4}, but synthesis of bulk amorphous carbon with sp^3 concentration close to 100% remains a challenge. Such materials inherit the short-/medium-range order of diamond and should also inherit its superior properties⁵. Here, we successfully synthesized millimetre-sized samples—with volumes 10^3 – 10^4 times as large as produced in earlier studies—of transparent, nearly pure sp^3 amorphous carbon by heating fullerenes at pressures close to the cage collapse boundary. The material synthesized consists of many randomly oriented clusters with diamond-like short-/medium-range order and possesses the highest hardness (101.9 ± 2.3 GPa), elastic modulus ($1,182 \pm 40$ GPa) and thermal conductivity (26.0 ± 1.3 W m⁻¹ K⁻¹) observed in any known amorphous material. It also exhibits optical bandgaps tunable from 1.85 eV to 2.79 eV. These discoveries contribute to our knowledge about advanced amorphous materials and the synthesis of bulk amorphous materials by high-pressure and high-temperature techniques and may enable new applications for amorphous solids.

Access options

Subscribe to Journal

Get full journal access for 1 year

\$199.00

only \$3.90 per issue

[Subscribe](#)

All prices are NET prices.

VAT will be added later in the checkout.

Tax calculation will be finalised during checkout.

Rent or Buy article

Get time limited or full article access on ReadCube.

from \$8.99

[Rent or Buy](#)

All prices are NET prices.

Additional access options:

- [Log in](#)
- [Access through your institution](#)
- [Learn about institutional subscriptions](#)

Fig. 1: Optical photographs of the recovered samples from different HPHT conditions.

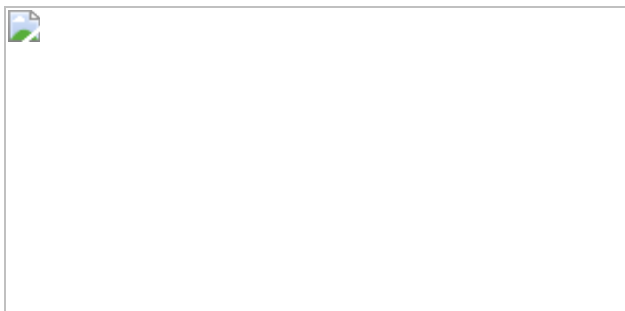


Fig. 2: XRD patterns, EELS, UV-visible absorption spectra and atomic configuration of samples recovered from different HPHT conditions.

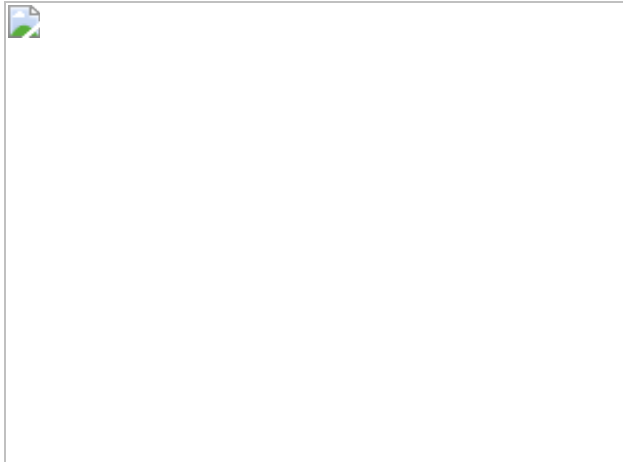


Fig. 3: TEM studies of the AC-3 sample.

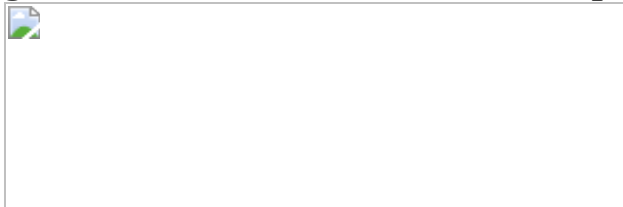
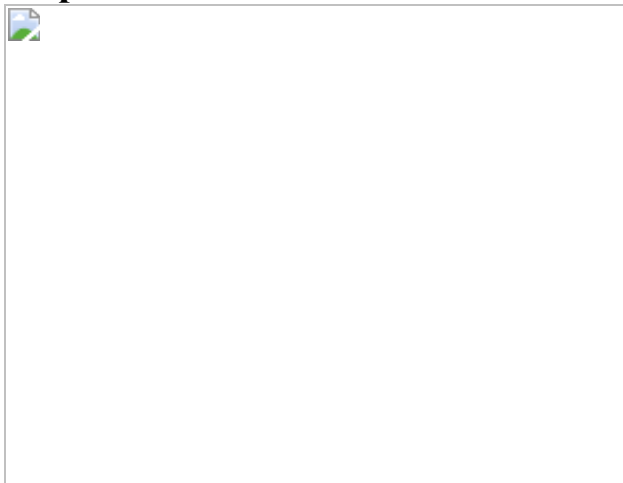


Fig. 4: Mechanical and thermal conductivity properties of sp^3 amorphous carbon.



Data availability

The authors declare that the data supporting the findings of this study are available within the article. [Source data](#) are provided with this paper.

References

1. 1. Wang, W. H. The elastic properties, elastic models and elastic perspectives of metallic glasses. *Prog. Mater Sci.* **57**, 487–656 (2012).
2. 2. Treacy, M. M. J. & Borisenko, K. B. The local structure of amorphous silicon. *Science* **335**, 950–953 (2012).
3. 3. Harris, P. J. F. Fullerene-related structure of commercial glassy carbons. *Philos. Mag.* **84**, 3159–3167 (2004).
4. 4. Hu, M. et al. Compressed glassy carbon: an ultrastrong and elastic interpenetrating graphene network. *Sci. Adv.* **3**, e1603213 (2017).
5. 5. Yue, Y. et al. Hierarchically structured diamond composite with exceptional toughness. *Nature* **582**, 370–374 (2020).
6. 6. McMillan, P. F. et al. Amorphous and nanocrystalline luminescent Si and Ge obtained via a solid-state chemical metathesis synthesis route. *J. Solid State Chem.* **178**, 937–949 (2005).
7. 7. To, T. et al. Fracture toughness of a metal–organic framework glass. *Nat. Commun.* **11**, 2593 (2020).

8. 8.

Blank, V. D. et al. Structures and physical properties of superhard and ultrahard 3D polymerized fullerites created from solid C₆₀ by high pressure high temperature treatment. *Carbon* **36**, 665–670 (1998).

9. 9.

Blank, V. D., Buga, S. G., Ivlev, A. N. & Mavrin, B. N. Ultrahard and superhard carbon phases produced from C₆₀ by heating at high pressure: structural and Raman studies. *Phys. Lett. A* **205**, 208–216 (1995).

10. 10.

Brazhkin, V. V. & Lyapin, A. G. Hard and superhard carbon phases synthesized from fullerites under pressure. *J. Superhard Mater.* **34**, 400–423 (2012).

11. 11.

Robertson, J. Diamond-like amorphous carbon. *Mater. Sci. Eng. R-Rep.* **37**, 129–281 (2002).

12. 12.

Zeng, Z. et al. Synthesis of quenchable amorphous diamond. *Nat. Commun.* **8**, 322 (2017).

13. 13.

Hirai, H., Kondo, K., Yoshizawa, N. & Shiraishi, M. Amorphous diamond from C₆₀ fullerene. *Appl. Phys. Lett.* **64**, 1797–1799 (1994).

14. 14.

Hirai, H., Terauchi, M., Tanaka, M. & Kondo, K. Band gap of essentially fourfold-coordinated amorphous diamond synthesized from

C_{60} fullerene. *Phys. Rev. B* **60**, 6357–6361 (1999).

15. 15.

Bundy, F. P. et al. The pressure-temperature phase and transformation diagram for carbon; updated through 1994. *Carbon* **34**, 141–153 (1996).

16. 16.

Sundqvist, B. Fullerenes under high pressures. *Adv. Phys.* **48**, 1–134 (1999).

17. 17.

Yoo, C. S. & Nellis, W. J. Phase transition from C_{60} molecules to strongly interacting C_{60} agglomerates at hydrostatic high pressures. *Chem. Phys. Lett.* **198**, 379–382 (1992).

18. 18.

Wang, L. et al. Long-range ordered carbon clusters: a crystalline material with amorphous building blocks. *Science* **337**, 825–828 (2012).

19. 19.

Yao, M. et al. Tailoring building blocks and their boundary interaction for the creation of new, potentially superhard, carbon materials. *Adv. Mater.* **27**, 3962–3968 (2015).

20. 20.

Su, Y. F. et al. Characterization at atomic resolution of carbon nanotube/resin interface in nanocomposites by mapping sp^2 -bonding states using electron energy-loss spectroscopy. *Microsc. Microanal.* **22**, 666–672 (2016).

21. 21.

Mochalin, V. N., Shenderova, O., Ho, D. & Gogotsi, Y. The properties and applications of nanodiamonds. *Nat. Nanotechnol.* **7**, 11–23 (2012).

22. 22.

LiBassi, A. et al. Density, sp^3 content and internal layering of DLC films by X-ray reflectivity and electron energy loss spectroscopy. *Diam. Relat. Mater.* **9**, 771–776 (2000).

23. 23.

Gaskell, P. H. & Wallis, D. J. Medium-range order in silica, the canonical network glass. *Phys. Rev. Lett.* **76**, 66–69 (1996).

24. 24.

Ramamurty, U. & Jang, J. Nanoindentation for probing the mechanical behavior of molecular crystals—a review of the technique and how to use it. *CrystEngComm* **16**, 12–23 (2014).

25. 25.

Blase, X., Gillet, P., San Miguel, A. & Mélinon, P. Exceptional ideal strength of carbon clathrates. *Phys. Rev. Lett.* **92**, 215505 (2004).

26. 26.

Ghorbal, G. B., Tricoteaux, A., Thuault, A., Louis, G. & Chicot, D. Comparison of conventional Knoop and Vickers hardness of ceramic materials. *J. Eur. Ceram. Soc.* **37**, 2531–2535 (2017).

27. 27.

Zhu, J., Wu, X., Lattery, D. M., Zheng, W. & Wang, X. The ultrafast laser pump-probe technique for thermal characterization of materials with micro/nanostructures. *Nanoscale Microscale Thermophys. Eng.* **21**, 177–198 (2017).

28. 28.

Balandin, A. A. Thermal properties of graphene and nanostructured carbon materials. *Nat. Mater.* **10**, 569–581 (2011).

29. 29.

Tauc, J., Grigorovici, R. & Vancu, A. Optical properties and electronic structure of amorphous germanium. *Phys. Status Solidi b* **15**, 627–637 (1966).

30. 30.

Shi, Y. et al. Ring size distribution in silicate glasses revealed by neutron scattering first sharp diffraction peak analysis. *J. Non-Cryst. Solids* **516**, 71–81 (2019).

31. 31.

Liu, X. et al. High thermal conductivity of a hydrogenated amorphous silicon film. *Phys. Rev. Lett.* **102**, 035901 (2009).

32. 32.

Hashemi, A., Babaei, H. & Lee, S. Effects of medium range order on propagon thermal conductivity in amorphous silicon. *J. Appl. Phys.* **127**, 045109 (2020).

33. 33.

Choy, C. L., Tong, K. W., Wong, H. K. & Leung, W. P. Thermal conductivity of amorphous alloys above room temperature. *J. Appl. Phys.* **70**, 4919–4925 (1991).

34. 34.

Shang, Y. C. et al. Pressure generation above 35 GPa in a Walker-type large-volume press. *Chin. Phys. Lett.* **37**, 080701 (2020).

35. 35.

Ishii, T. et al. Sharp 660-km discontinuity controlled by extremely narrow binary post-spinel transition. *Nat. Geosci.* **12**, 869–872 (2019).

36. 36.

Ishii, T. et al. Generation of pressures over 40 GPa using Kawai-type multi-anvil press with tungsten carbide anvils. *Rev. Sci. Instrum.* **87**, 024501 (2016).

37. 37.

Liu, Z. et al. Phase relations in the system MgSiO₃-Al₂O₃ up to 2,300 K at lower mantle pressures. *J. Geophys. Res.* **122**, 7775–7788 (2017).

38. 38.

Chupas, P. J. et al. Rapid-acquisition pair distribution function (RA-PDF) analysis. *J. Appl. Crystallogr.* **36**, 1342–1347 (2003).

39. 39.

Prescher, C. & Prakapenka, V. B. DIOPTAS: a program for reduction of two-dimensional X-ray diffraction data and data exploration. *High Press. Res.* **35**, 223–230 (2015).

40. 40.

Qiu, X., Thompson, J. W. & Billinge, S. J. L. PDFgetX2: a GUI-driven program to obtain the pair distribution function from X-ray powder diffraction data. *J. Appl. Crystallogr.* **37**, 678–678 (2004).

41. 41.

Ditmars, D. A., Plint, C. A. & Shukla, R. C. Aluminum. I. Measurement of the relative enthalpy from 273 to 929 K and derivation of thermodynamic functions for Al(s) from 0 K to its melting point. *Int. J. Thermophys.* **6**, 499–515 (1985).

42. 42.

Cadot, G. B. J., Billingham, J. & Axinte, D. A. A study of surface swelling caused by graphitisation during pulsed laser ablation of carbon allotrope with high content of sp^3 bounds. *J. Phys. Appl. Phys.* **50**, 245301 (2017).

43. 43.

Bruley, J., Williams, D. B., Cuomo, J. J. & Pappas, D. P. Quantitative near-edge structure analysis of diamond-like carbon in the electron microscope using a two-window method. *J. Microsc.* **180**, 22–32 (1995).

Acknowledgements

We thank the help from beamline scientists at BL13HB for doing the PDF experiments, and the beamline scientists at BL02U for doing preliminary PDF scattering measurements. We thank R. Tai and W. Wen for their help about the PDF measurements. We thank M. Dove and G. Zhang for discussion on the PDF data processing. M.Y. would like to thank Y. Liu from the Chinese Academy of Sciences, Institute of Physics, M. Wen from Jilin University, S. Lan from Nanjing University of Science and Technology, L. Zhang and B. Yang from the Chinese Academy of Sciences, Institute of Metal Research, and G. Liu from the Shanghai Synchrotron Radiation Facility for their fruitful discussion on the structures and deformation mechanism of amorphous materials. We thank Y. Wang from the Electron Microscopy Center, Jilin University for help with HRTEM and EELS measurements. We also thank Z. Zhang for help with TDTR measurements and data analysis. This work was supported financially by the National Key R&D Program of China (2018YFA0305900, 2018YFA0703400 and 2017YFA0403801), the National Natural Science Foundation of China (51822204, 51320105007, 11634004, 41902034 and U1732120), the China Postdoctoral Science Foundation (2020TQ0121).

Author information

Author notes

1. These authors contributed equally: Yuchen Shang, Zhaodong Liu and Jiajun Dong

Affiliations

1. State Key Laboratory of Superhard Materials, College of Physics, Jilin University, Changchun, China

Yuchen Shang, Zhaodong Liu, Jiajun Dong, Mingguang Yao, Zhenxing Yang, Quanjun Li, Chunguang Zhai, Fangren Shen, Xuyuan Hou, Bertil Sundqvist & Bingbing Liu

2. Synergetic Extreme Condition User Facility, Jilin University, Changchun, China

Zhaodong Liu & Bingbing Liu

3. Earth and Planets Laboratory, Carnegie Institution for Science, Washington DC, USA

Lin Wang & Yingwei Fei

4. Bayerisches Geoinstitut, University of Bayreuth, Bayreuth, Germany

Lin Wang

5. Key Laboratory of Structures Dynamic Behavior and Control of Ministry of Education, Harbin Institute of Technology, Harbin, China

Nianqiang Zhang

6. Key Laboratory of Automobile Materials MOE, School of Materials Science and Engineering, Electron Microscopy Center, and

International Center of Future Science, Jilin University, Changchun,
China

Wei Zhang

7. School of Materials Science and Engineering, State Key Laboratory of
Advanced Special Steel, Shanghai University, Shanghai, China

Rong Fu

8. Shanghai Institute of Applied Physics, Chinese Academy of Sciences,
Shanghai, China

Jianfeng Ji, Xingmin Zhang & He Lin

9. Department of Physics, Umeå University, Umeå, Sweden

Bertil Sundqvist

10. Institute of Physics, Chinese Academy of Sciences, Beijing, China

Weihua Wang

Contributions

B.L. and M.Y. conceived and designed the study. Y.S., Z.L., M.Y., Z.Y., F.S., X.H., L.W. and Y.F. synthesized the materials. Y.S., Z.Y., J.D., F.S. and C.Z. performed the XRD, Raman, UV-vis absorption measurements. Y.S., J.D., W.Z. and M.Y. performed the TEM characterization and analysis. Z.L., Y.S., F.S. and N.Z. performed the nanoindentation measurements. Y.S. performed Vickers, Knoop hardness measurements and TDTR measurements. J.D., Y.S., Q.L., H.L., X.H., R.F., M.Y., J.J. and X.Z. performed the synchrotron XRD measurements and data analysis. Y.S. and C.Z. draw the pictures. Y.S., M.Y., B.L., W.W., Z.L., J.D., F.S., B.S. and Y.F. analysed the results of data. M.Y., Y.S., B.S. and B.L. wrote the manuscript. All authors discussed the results and contributed to the final manuscript.

Corresponding authors

Correspondence to [Mingguang Yao](#) or [Bingbing Liu](#).

Ethics declarations

Competing interests

The authors declare no competing interests.

Additional information

Peer review information *Nature* thanks Alfonso San Miguel, Yogesh Vohra and the other, anonymous, reviewer(s) for their contribution to the peer review of this work.

Publisher's note Springer Nature remains neutral with regard to jurisdictional claims in published maps and institutional affiliations.

Extended data figures and tables

[Extended Data Fig. 1 Optical image of thin slices of bulk \$sp^3\$ amorphous carbon samples.](#)

The thin slices were cut from the bulk samples recovered from different HPHT conditions. The colour difference of these samples can be observed.

[Extended Data Fig. 2 P-T phase diagram of C₆₀.](#)

Results for pressure below 20 GPa and temperature below 2,000 K are from ref. [10](#). Solid symbols denote different samples obtained in this study: blue hexagon, dual-coloured hexagon, red circle and dual-coloured circle represent nanocrystalline diamonds, bulk sp^3 amorphous carbon containing nanocrystalline diamonds (NCD), nearly fully sp^3 -bonded amorphous

carbon, and amorphous carbon with a small amount of sp^2 carbons, respectively. Abbreviations Gra and Dia represent graphite and diamond, respectively. The ‘collapse’ line represents the fullerene will collapse at 27~28 GPa at room temperature

[Source data.](#)

Extended Data Fig. 3 EELS spectra of AC-1, AC-2, AC-3 and AC-6 samples.

The black line is EELS of standard sp^2 glassy carbon, the green line is amorphous diamond obtained from ref. ¹² and the yellow line is sp^3 -rich tetrahedral amorphous carbon (ta-C) from ref. ¹⁴. The boxes indicate the energy windows for intensity integration used in two-windows method. The lines 284 and 291 correspond to the energy channels at which the intensities, used in peak-ratio method, were taken

[Source data.](#)

Extended Data Fig. 4 Peak-ratio method used for determining the sp^3 concentration of different sp^3 amorphous carbon samples.

a–h, The sp^3 concentration of standard sp^2 glassy carbon and samples AC-1, AC-2, AC-3, AC-4, AC-5 and AC-6, plus a sample recovered from 27 GPa and 700 °C, respectively

[Source data.](#)

Extended Data Fig. 5 Photoluminescence and Raman spectra of sp^3 amorphous carbon.

a, Photoluminescence spectra of AC-1 and AC-3 samples at room temperature. **b**, Raman spectra of AC-1 and AC-3 samples excited by

visible (514.5 nm) and UV (325 nm) laser. **c, d**, The corresponding UV Raman spectra after PL background subtraction

[Source data.](#)

Extended Data Fig. 6 TEM images of the samples recovered from 20 GPa 1,000 °C and 37 GPa 1,000 °C.

a, HRTEM image of AC-1 sample in which disordered sp^2 carbon was clearly observed. **b**, HRTEM image of diamond nanocrystals existing in the sp^3 amorphous carbon sample obtained at 37 GPa and 1,000 °C.

Extended Data Fig. 7 Nanoindentation measurements of sp^3 amorphous carbon samples and single crystalline diamond.

The indentation force versus depth ($P-h$) curves of AC-1, AC-3 and of the (100) face of single crystal diamond during loading and unloading with the maximum loads ranging from 100 to 500 mN

[Source data.](#)

Extended Data Fig. 8 Knoop hardness measurements of sp^3 amorphous carbon samples and the SEM image of the indentation in our amorphous carbon and single crystal diamond after Vickers hardness measurement.

a, H_K of AC-1 and AC-3 samples as a function of applied load (F). The inserts are optical images of the indentation at a load of 4.9 N. Error bars indicate five different measurement points, standard deviations. **b, c**, SEM images of the indentation in our amorphous carbon and in single crystal diamond after Vickers hardness measurement. The fracture of our sp^3 amorphous carbon shows irregular, tooth-like cracks/edges, while that of single crystal diamond shows a regular fracture along some crystal planes. The different fracture behaviour compared with crystalline diamond should be due to the amorphous structure of our materials, in which the

fracture/crack propagation behaves different from that in anisotropic crystals, leading to the irregular fracture surface

[Source data.](#)

Extended Data Fig. 9 TDTR measurements on sp^3 amorphous carbon and standard samples.

a, c, The ratio signals of in-phase and out-of-phase, $-V_{in}/V_{out}$ (open circles) for amorphous carbon samples (**a**) and standard Si, Al₂O₃, and SiO₂ (**c**) samples, as a function of delay time. The solid lines represent the best fit to the thermal model. **b**, The measured thermal conductivities of standard materials (Si, Al₂O₃ and SiO₂) compared with literature data

[Source data.](#)

Extended Data Fig. 10 The Tauc bandgap of sp^3 amorphous carbon samples determined from plots of $(ahv)^{1/2}$ versus photon-energy.

a–f, The obtained Tauc bandgap of samples recovered from 37 GPa and 450 °C (**a**), 20 GPa and 1,000 °C (**b**), 25 GPa and 1,000 °C (**c**), 27 GPa and 700 °C (**d**), 27 GPa and 900 °C (**e**), and 27 GPa and 1,000 °C (**f**)

[Source data.](#)

Source data

Source Data Fig. 2

Source Data Fig. 3

Source Data Extended Data Fig. 2

[**Source Data Extended Data Fig. 3**](#)

[**Source Data Extended Data Fig. 4**](#)

[**Source Data Extended Data Fig. 5**](#)

[**Source Data Extended Data Fig. 7**](#)

[**Source Data Extended Data Fig. 8**](#)

[**Source Data Extended Data Fig. 9**](#)

[**Source Data Extended Data Fig. 10**](#)

Rights and permissions

[Reprints and Permissions](#)

About this article

Cite this article

Shang, Y., Liu, Z., Dong, J. *et al.* Ultrahard bulk amorphous carbon from collapsed fullerene. *Nature* **599**, 599–604 (2021).
<https://doi.org/10.1038/s41586-021-03882-9>

- Received: 29 January 2021
- Accepted: 05 August 2021
- Published: 24 November 2021
- Issue Date: 25 November 2021
- DOI: <https://doi.org/10.1038/s41586-021-03882-9>

Share this article

Anyone you share the following link with will be able to read this content:

[Get shareable link](#)

Sorry, a shareable link is not currently available for this article.

[Copy to clipboard](#)

Provided by the Springer Nature SharedIt content-sharing initiative

How to make macroscale non-crystalline diamonds

- Alfonso San-Miguel

News & Views 24 Nov 2021

This article was downloaded by **calibre** from <https://www.nature.com/articles/s41586-021-03882-9>

| [Section menu](#) | [Main menu](#) |

- Article
- [Published: 24 November 2021](#)

Synthesis of paracrystalline diamond

- [Hu Tang](#) ORCID: [orcid.org/0000-0003-1571-8843¹](https://orcid.org/0000-0003-1571-8843),
- [Xiaohong Yuan¹](#),
- [Yong Cheng²](#),
- [Hongzhan Fei](#) ORCID: [orcid.org/0000-0003-3143-7363³](https://orcid.org/0000-0003-3143-7363),
- [Fuyang Liu¹](#),
- [Tao Liang¹](#),
- [Zhidan Zeng](#) ORCID: [orcid.org/0000-0003-4283-2393¹](https://orcid.org/0000-0003-4283-2393),
- [Takayuki Ishii](#) ORCID: [orcid.org/0000-0002-1494-2141^{1,3}](https://orcid.org/0000-0002-1494-2141),
- [Ming-Sheng Wang](#) ORCID: [orcid.org/0000-0003-3754-2850²](https://orcid.org/0000-0003-3754-2850),
- [Tomoo Katsura](#) ORCID: [orcid.org/0000-0001-7857-5101³](https://orcid.org/0000-0001-7857-5101),
- [Howard Sheng](#) ORCID: [orcid.org/0000-0002-6134-0354⁴](https://orcid.org/0000-0002-6134-0354) &
- [Huiyang Gou](#) ORCID: [orcid.org/0000-0002-2612-4314^{1,5}](https://orcid.org/0000-0002-2612-4314)

Nature volume 599, pages 605–610 (2021)

- 2462 Accesses
- 88 Altmetric
- [Metrics details](#)

Subjects

- [Atomistic models](#)
- [Structure of solids and liquids](#)

Abstract

Solids in nature can be generally classified into crystalline and non-crystalline states^{1,2,3,4,5,6,7}, depending on whether long-range lattice periodicity is present in the material. The differentiation of the two states, however, could face fundamental challenges if the degree of long-range order in crystals is significantly reduced. Here we report a paracrystalline state of diamond that is distinct from either crystalline or amorphous diamond^{8,9,10}. The paracrystalline diamond reported in this work, consisting of sub-nanometre-sized paracrystallites that possess a well-defined crystalline medium-range order up to a few atomic shells^{4,5,11,12,13}, was synthesized in high-pressure high-temperature conditions (for example, 30 GPa and 1,600 K) employing face-centred cubic C₆₀ as a precursor. The structural characteristics of the paracrystalline diamond were identified through a combination of X-ray diffraction, high-resolution transmission microscopy and advanced molecular dynamics simulation. The formation of paracrystalline diamond is a result of densely distributed nucleation sites developed in compressed C₆₀ as well as pronounced second-nearest-neighbour short-range order in amorphous diamond due to strong sp³ bonding. The discovery of paracrystalline diamond adds an unusual diamond form to the enriched carbon family^{14,15,16}, which exhibits distinguishing physical properties and can be furthered exploited to develop new materials. Furthermore, this work reveals the missing link in the length scale between amorphous and crystalline states across the structural landscape, having profound implications for recognizing complex structures arising from amorphous materials.

Access options

Subscribe to Journal

Get full journal access for 1 year

\$199.00

only \$3.90 per issue

Subscribe

All prices are NET prices.

VAT will be added later in the checkout.

Tax calculation will be finalised during checkout.

Rent or Buy article

Get time limited or full article access on ReadCube.

from \$8.99

Rent or Buy

All prices are NET prices.

Additional access options:

- [Log in](#)
- [Access through your institution](#)
- [Learn about institutional subscriptions](#)

Fig. 1: Synthesizing fully sp^3 -bonded carbon samples at 30 GPa and 1,200–1,600 K for 10 min.

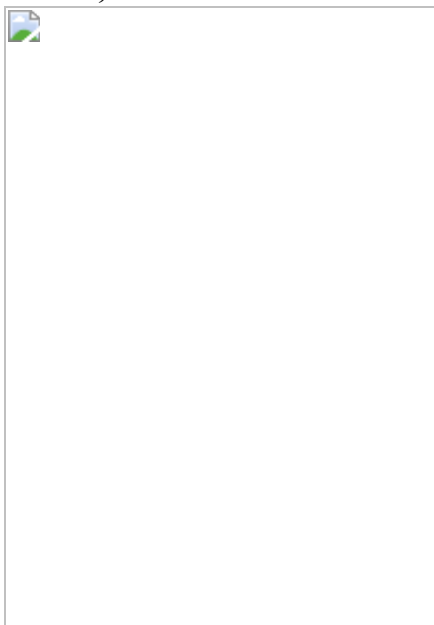


Fig. 2: HRTEM characterization of samples recovered from 30 GPa and 1,200–1,600 K.



Fig. 3: Identification of p-D.

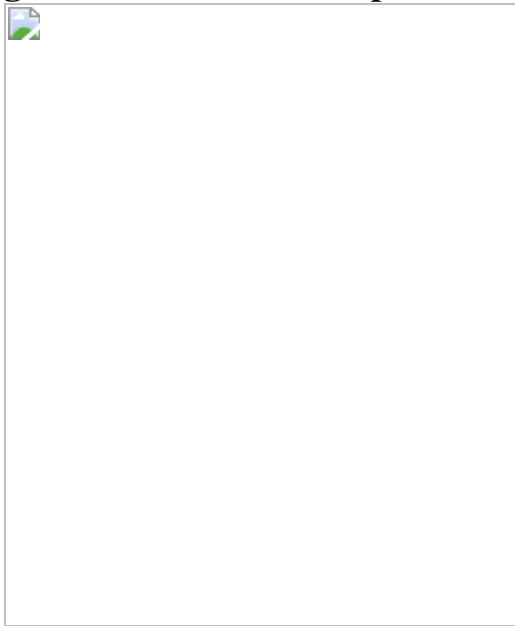


Fig. 4: Distinguishing p-D from a-D.



Data availability

The data that support the findings of this study are available from the corresponding authors upon request.

Code availability

The software used for data analysis is available from H.S. upon request.

References

1. 1.

Zallen, R. *The Physics of Amorphous Solids* (Wiley, 1983).

2. 2.

Zachariasen, W. H. The atomic arrangement in glass. *J. Am. Chem. Soc.* **54**, 3841–3851 (1932).

3. 3.

Elliott, S. R. A continuous random network approach to the structure of vitreous boron trioxide. *Philos. Mag. B* **37**, 435–446 (1978).

4. 4.

Elliott, S. R. Medium-range structural order in covalent amorphous solids. *Nature* **354**, 445–452 (1991).

5. 5.

Sheng, H. W., Luo, W. K., Alamgir, F. M., Bai, J. M. & Ma, E. Atomic packing and short-to-medium-range order in metallic glasses. *Nature* **439**, 419–425 (2006).

6. 6.

Miracle, D. B. A structural model for metallic glasses. *Nat. Mater.* **3**, 697–702 (2004).

7. 7.

Hirata, A. et al. Direct observation of local atomic order in a metallic glass. *Nat. Mater.* **10**, 28–33 (2011).

8. 8.

Hirai, H., Kondo, K., Yoshizawa, N. & Shiraishi, M. Amorphous diamond from C₆₀ fullerene. *Appl. Phys. Lett.* **64**, 1797–1799 (1994).

9. 9.

Zeng, Z. et al. Synthesis of quenchable amorphous diamond. *Nat. Commun.* **8**, 322 (2017).

10. 10.

Lin, Y. et al. Amorphous diamond: a high-pressure superhard carbon allotrope. *Phys. Rev. Lett.* **107**, 175504 (2011).

11. 11.

Treacy, M. M. J. & Borisenko, K. B. The local structure of amorphous silicon. *Science* **335**, 950–953 (2012).

12. 12.

Leocmach, M. & Tanaka, H. Roles of icosahedral and crystal-like order in the hard spheres glass transition. *Nat. Commun.* **3** (2012).

13. 13.

Gibson, J. M., Treacy, M. M. J., Sun, T. & Zaluzec, N. J. Substantial crystalline topology in amorphous silicon. *Phys. Rev. Lett.* **105** (2010).

14. 14.

Oganov, A. R., Hemley, R. J., Hazen, R. M. & Jones, A. P. Structure, bonding, and mineralogy of carbon at extreme conditions. *Rev. Mineral. Geochem.* **75**, 47–77 (2013).

15. 15.

Georgakilas, V., Perman, J. A., Tucek, J. & Zboril, R. Broad family of carbon nanoallotropes: classification, chemistry, and applications of fullerenes, carbon dots, nanotubes, graphene, nanodiamonds, and combined superstructures. *Chem. Rev.* **115**, 4744–4822 (2015).

16. 16.

Németh, P. et al. Complex nanostructures in diamond. *Nat. Mater.* **19**, 1126–1131 (2020).

17. 17.

Sarac, B. et al. Origin of large plasticity and multiscale effects in iron-based metallic glasses. *Nat. Commun.* **9** (2018).

18. 18.

Hwang, J. et al. Nanoscale structure and structural relaxation in $\text{Zr}_{50}\text{Cu}_{45}\text{Al}_5$ bulk metallic glass. *Phys. Rev. Lett.* **108** (2012).

19. 19.

Voyles, P. M. et al. Structure and physical properties of paracrystalline atomistic models of amorphous silicon. *J. Appl. Phys.* **90**, 4437–4451 (2001).

20. 20.

Robertson, J. Diamond-like amorphous carbon. *Mater. Sci. Eng. R Rep.* **37**, 129–281 (2002).

21. 21.

Ishii, T., Liu, Z. & Katsura, T. A breakthrough in pressure generation by a Kawai-type multi-anvil apparatus with tungsten carbide anvils. *Engineering* **5**, 434–440 (2019).

22. 22.

Iwasa, Y. et al. New phases of C_{60} synthesized at high pressure. *Science* **264**, 1570–1572 (1994).

23. 23.

Blank, V. D. et al. Phase transformations in solid C_{60} at high-pressure-high-temperature treatment and the structure of 3D polymerized fullerites. *Phys. Lett. A* **220**, 149–157 (1996).

24. 24.

Zhang, S. et al. Discovery of carbon-based strongest and hardest amorphous material. Preprint at <https://arxiv.org/abs/2011.14819> (2020).

25. 25.

Yamanaka, S. et al. Electron conductive three-dimensional polymer of cuboidal C₆₀. *Phys. Rev. Lett.* **96**, 076602 (2006).

26. 26.

Sundqvist, B. Carbon under pressure. *Phys. Rep.* **909**, 1–73 (2021).

27. 27.

Ferrari, A. C. & Robertson, J. Raman spectroscopy of amorphous, nanostructured, diamond-like carbon, and nanodiamond. *Philos. Trans. R. Soc. Lond. A Math. Phys. Eng. Sci.* **362**, 2477–2512 (2004).

28. 28.

Daniels, H., Brydson, R., Rand, B. & Brown, A. Investigating carbonization and graphitization using electron energy loss spectroscopy (EELS) in the transmission electron microscope (TEM). *Philos. Mag.* **87**, 4073–4092 (2007).

29. 29.

Chen, L. J. et al. Structural evolution in amorphous silicon and germanium thin films. *Microsc. Microanal.* **8**, 268–273 (2002).

30. 30.

Wang, Q. et al. The atomic-scale mechanism for the enhanced glass-forming-ability of a Cu-Zr based bulk metallic glass with minor element additions. *Sci. Rep.* **4** (2014).

31. 31.

Tang, H. et al. Revealing the formation mechanism of ultrahard nanotwinned diamond from onion carbon. *Carbon* **129**, 159–167 (2018).

32. 32.

Plimpton, S. Fast parallel algorithms for short-range molecular dynamics. *J. Comput. Phys.* **117**, 1–19 (1995).

33. 33.

Zhu, S.-c., Yan, X.-z., Liu, J., Oganov, A. R. & Zhu, Q. A revisited mechanism of the graphite-to-diamond transition at high temperature. *Matter* **3**, 864–878 (2020).

34. 34.

Marchi, M. & Ballone, P. Adiabatic bias molecular dynamics: a method to navigate the conformational space of complex molecular systems. *J. Chem. Phys.* **110**, 3697–3702 (1999).

35. 35.

Lee, L. L. *Molecular Thermodynamics of Electrolyte Solutions* (World Scientific, 2008).

36. 36.

Sheng, H. W. et al. Polyamorphism in a metallic glass. *Nat. Mater.* **6**, 192–197 (2007).

37. 37.

Faken, D. & Jónsson, H. Systematic analysis of local atomic structure combined with 3D computer graphics. *Comput. Mater. Sci.* **2**, 279–286 (1994).

38. 38.

Lechner, W. & Dellago, C. Accurate determination of crystal structures based on averaged local bond order parameters. *J. Chem. Phys.* **129**, 114707 (2008).

39. 39.

Irifune, T., Kurio, A., Sakamoto, S., Inoue, T. & Sumiya, H. Ultrahard polycrystalline diamond from graphite. *Nature* **421**, 599–600 (2003).

40. 40.

Dubrovinskaia, N., Dubrovinsky, L., Langenhorst, F., Jacobsen, S. & Liebske, C. Nanocrystalline diamond synthesized from C₆₀. *Diam. Relat. Mater.* **14**, 16–22 (2005).

41. 41.

Sumiya, H. & Irifune, T. Hardness and deformation microstructures of nano-polycrystalline diamonds synthesized from various carbons under high pressure and high temperature. *J. Mater. Res.* **22**, 2345–2351 (2007).

42. 42.

Huang, Q. et al. Nanotwinned diamond with unprecedented hardness and stability. *Nature* **510**, 250–253 (2014).

43. 43.

Tang, H. et al. Synthesis of nano-polycrystalline diamond in proximity to industrial conditions. *Carbon* **108**, 1–6 (2016).

44. 44.

Hujo, W., Shadrack Jubes, B., Rana, V. K., Chakravarty, C. & Molinero, V. The rise and fall of anomalies in tetrahedral liquids. *J. Stat. Phys.* **145**, 293–312 (2011).

45. 45.

Merlen, A. et al. High pressure–high temperature synthesis of diamond from single-wall pristine and iodine doped carbon nanotube bundles. *Carbon* **47**, 1643–1651 (2009).

46. 46.

Teter, D. M. Computational alchemy: the search for new superhard materials. *MRS Bull.* **23**, 22–27 (1998).

47. 47.

Bewilogua, K. & Hofmann, D. History of diamond-like carbon films — from first experiments to worldwide applications. *Surf. Coat. Technol.* **242**, 214–225 (2014).

48. 48.

Osswald, S., Yushin, G., Mochalin, V., Kucheyev, S. O. & Gogotsi, Y. Control of sp^2/sp^3 carbon ratio and surface chemistry of nanodiamond powders by selective oxidation in air. *J. Am. Chem. Soc.* **128**, 11635–11642 (2006).

49. 49.

Pu, J.-C., Wang, S.-F. & Sung, J. C. High-temperature oxidation behaviors of CVD diamond films. *Appl. Surf. Sci.* **256**, 668–673 (2009).

50. 50.

Ishii, T. et al. Generation of pressures over 40 GPa using Kawai-type multi-anvil press with tungsten carbide anvils. *Rev. Sci. Instrum.* **87**, 024501 (2016).

51. 51.

Kubo, A. & Akaogi, M. Post-garnet transitions in the system $Mg_4Si_4O_{12}$ - $Mg_3Al_2Si_3O_{12}$ up to 28 GPa: phase relations of garnet, ilmenite and perovskite. *Phys. Earth Planet. Inter.* **121**, 85–102 (2000).

52. 52.

Oliver, W. C. & Pharr, G. M. An improved technique for determining hardness and elastic modulus using load and displacement sensing

indentation experiments. *J. Mater. Res.* **7**, 1564–1583 (1992).

53. 53.

Kresse, G. & Hafner, J. Ab initio molecular dynamics for liquid metals. *Phys. Rev. B* **47**, 558–561 (1993).

54. 54.

Blöchl, P. E. Projector augmented-wave method. *Phys. Rev. B* **50**, 17953–17979 (1994).

55. 55.

Wooten, F., Winer, K. & Weaire, D. Computer generation of structural models of amorphous Si and Ge. *Phys. Rev. Lett.* **54**, 1392–1395 (1985).

56. 56.

Keating, P. N. Effect of invariance requirements on the elastic strain energy of crystals with application to the diamond structure. *Phys. Rev.* **145**, 637–645 (1966).

57. 57.

Mishin, Y., Mehl, M. J. & Papaconstantopoulos, D. A. Phase stability in the Fe–Ni system: investigation by first-principles calculations and atomistic simulations. *Acta Mater.* **53**, 4029–4041 (2005).

58. 58.

Brommer, P. & Gähler, F. Potfit: effective potentials from ab initio data. *Model. Simul. Mat. Sci. Eng.* **15**, 295–304 (2007).

59. 59.

Cheng, Y. Q., Ma, E. & Sheng, H. W. Atomic level structure in multicomponent bulk metallic glass. *Phys. Rev. Lett.* **102**, 245501

(2009).

60. 60.

Laio, A. & Parrinello, M. Escaping free-energy minima. *Proc. Natl Acad. Sci. USA* **99**, 12562–12566 (2002).

61. 61.

Maragliano, L. & Vanden-Eijnden, E. A temperature accelerated method for sampling free energy and determining reaction pathways in rare events simulations. *Chem. Phys. Lett.* **426**, 168–175 (2006).

62. 62.

Colón-Ramos, D. A., La Riviere, P., Shroff, H. & Oldenbourg, R. Promoting transparency and reproducibility in enhanced molecular simulations. *Nat. Methods* **16**, 670–673 (2019).

63. 63.

Finney, J. L. Random packings and the structure of simple liquids. I. The geometry of random close packing. *Proc. R. Soc. Lond. A Math. Phys. Sci.* **319**, 479–493 (1970).

64. 64.

Steinhardt, P. J., Nelson, D. R. & Ronchetti, M. Bond-orientational order in liquids and glasses. *Phys. Rev. B* **28**, 784–805 (1983).

65. 65.

Stukowski, A. Structure identification methods for atomistic simulations of crystalline materials. *Model. Simul. Mat. Sci. Eng.* **20**, 045021 (2012).

66. 66.

Baxter, R. J. Method of solution of the Percus-Yevick, hypernetted-chain, or similar equations. *Phys. Rev.* **154**, 170–174 (1967).

67. 67.

Dixon, M. & Hutchinson, P. A method for the extrapolation of pair distribution functions. *Mol. Phys.* **33**, 1663–1670 (1977).

68. 68.

Lobato, I., van Aert, S. & Verbeeck, J. Progress and new advances in simulating electron microscopy datasets using MULTEM. *Ultramicroscopy* **168**, 17–27 (2016).

69. 69.

Serebryanaya, N., Blank, V., Ivdenko, V. & Chernozatonskii, L. Pressure-induced superhard phase of C₆₀. *Solid State Commun.* **118**, 183–187 (2001).

70. 70.

Kumar, R. S. et al. X-ray Raman scattering studies on C₆₀ fullerenes and multi-walled carbon nanotubes under pressure. *Diam. Relat. Mater.* **16**, 1250–1253 (2007).

71. 71.

Solozhenko, V. L., Kurakevych, O. O., Andrault, D., Le Godec, Y. & Mezouar, M. Ultimate metastable solubility of boron in diamond: synthesis of superhard diamondlike BC₅. *Phys. Rev. Lett.* **102**, 015506 (2009).

72. 72.

Solozhenko, V. L., Dub, S. N. & Novikov, N. V. Mechanical properties of cubic BC₂N, a new superhard phase. *Diam. Relat. Mater.* **10**, 2228–2231 (2001).

73. 73.

Pan, Z., Sun, H., Zhang, Y. & Chen, C. Harder than diamond: superior indentation strength of wurtzite BN and lonsdaleite. *Phys. Rev. Lett.* **102**, 055503 (2009).

74. 74.

Blase, X., Gillet, P., Miguel, A. S. & Mélinon, P. Exceptional ideal strength of carbon clathrates. *Phys. Rev. Lett.* **92** (2004).

75. 75.

Li, B., Sun, H. & Chen, C. Extreme mechanics of probing the ultimate strength of nanotwinned diamond. *Phys. Rev. Lett.* **117** (2016).

76. 76.

Chang, Y. Y., Jacobsen, S. D., Kimura, M., Irifune, T. & Ohno, I. Elastic properties of transparent nano-polycrystalline diamond measured by GHz-ultrasonic interferometry and resonant sphere methods. *Phys. Earth Planet. Inter.* **228**, 47–55 (2014).

Acknowledgements

We thank H.K. Mao for insightful discussions. This work was supported by the National Natural Science Foundation of China (grant numbers 12075215 and 61471307), the Fundamental Research Funds for the Central Universities (grant number 20720200075) and the European Research Council under the European Union’s Horizon 2020 research and innovation programme (proposal no. 787527). The work at George Mason University was supported by the NSF under grant no. DMR-1611064.

Author information

Affiliations

1. Center for High Pressure Science and Technology Advanced Research,
Beijing, China

Hu Tang, Xiaohong Yuan, Fuyang Liu, Tao Liang, Zhidan
Zeng, Takayuki Ishii & Huiyang Gou

2. State Key Laboratory of Physical Chemistry of Solid Surfaces, College
of Materials, Xiamen University, Xiamen, China

Yong Cheng & Ming-Sheng Wang

3. Bayerisches Geoinstitut, University of Bayreuth, Bayreuth, Germany

Hongzhan Fei, Takayuki Ishii & Tomoo Katsura

4. Department of Physics and Astronomy, George Mason University,
Fairfax, VA, USA

Howard Sheng

5. College of Environmental and Chemical Engineering, Yanshan
University, Qinhuangdao, China

Huiyang Gou

Contributions

H.G. and H.S. proposed and supervised the project; H.T., H.F., T.I. and T.K. synthesized the samples; H.T., X.Y., Y.C., F.L. and M.-S.W. performed the structure characterizations; H.T., X.Y., T. L. and Z.Z. measured the properties; H.S. performed the theoretical calculations; H.T., H.S. and H.G. analysed data and wrote the manuscript with the contributions of all authors.

Corresponding authors

Correspondence to [Howard Sheng](#) or [Huiyang Gou](#).

Ethics declarations

Competing interests

The authors declare no competing interests.

Additional information

Peer review information *Nature* thanks Artem Oganov, Alfonso San Miguel, Yogesh Vohra and the other, anonymous, reviewer(s) for their contribution to the peer review of this work. Peer reviewer reports are available.

Publisher's note Springer Nature remains neutral with regard to jurisdictional claims in published maps and institutional affiliations.

Extended data figures and tables

[Extended Data Fig. 1 XRD patterns, Raman spectra, fluorescence spectra, and EELS in the low-loss region of the recovered samples.](#)

a, XRD patterns of samples synthesized from different precursors: C₆₀ (top), type-1 glassy carbon (middle), and carbon onion (bottom) at 30 GPa and 1400–1800 K, respectively. At 1800 K, the appearance of weak Bragg diffraction peaks indicates nano-crystallization in the non-crystalline diamond formed from C₆₀. At 1600 K, fully *sp*³-bonded p-D was identified. By contrast, in cases of using type-1 glassy carbon and carbon onion as the starting material, crystallization precedes the complete conversion of *sp*² to *sp*³ carbon at 30 GPa and 1400–1600 K, preempting the formation of fully *sp*³-bonded paracrystalline diamond. The experiments demonstrate the importance of the structure of the starting material in the formation pathway of p-D. **b**, Visible Raman (532 nm) spectrum of the sample recovered at 30 GPa and 1400 K, with background removed. The broadened Raman peak

can be fit with a D peak at 1378 cm^{-1} and a G peak at 1556 cm^{-1} . The peak intensity ratio of I_D/I_G is 0.66 and the full width at half maximum (FWHM) of the G peak is 175 cm^{-1} . Similar to our work, the presence of sp^2 bonds results in a wide Raman peak between 1400 cm^{-1} and 1700 cm^{-1} in the visible Raman spectra of diamond-like carbon (DLC) films²⁷. **c**, Ultraviolet (UV) Raman spectra of the samples recovered from 1400 and 1500 K, respectively. The strong peak at 1110 cm^{-1} in the UV Raman spectrum of the sample recovered at 30 GPa and 1400 K is attributed to the T peak caused by sp^3 bonds²⁷. Fitting the Raman profile yields a peak intensity ratio of I_T/I_G 0.91, which is higher than that of DLC films with 88% sp^3 bonds, indicating a higher concentration of sp^3 bonds in the sample²⁷. On the other hand, for the sample recovered from 1500 K, no obvious peaks are discernible in the UV Raman spectrum, indicating the absence of sp^2 bonds in the as-synthesized disordered carbon⁸. **d**, Fluorescence spectra (excitation wavelength of 532 nm) of the sample from 1600 K and type Ia diamond. A main fluorescence peak centered around 702 nm suggests the high background in the Raman spectra is due to a fluorescence effect. **e**, EELS in the low-loss region of diamond crystal, single-crystal graphite, and samples synthesized from C_{60} under 30 GPa and 1400-1500 K. Based on plasmon peak energy derived from low-loss EELS²⁸, the densities of the recovered samples at 1400-1600 K were calculated to be 3.11, 3.20, and 3.25 g/cm^3 , respectively. Due to the presence of ~5.2% sp^2 carbon, the sample recovered from 1400 K has a lower density of 3.11 g/cm^3 .

Extended Data Fig. 2 HRTEM images of samples recovered at 30 GPa and different temperatures.

a–c, Typical HRTEM images of samples synthesized at 30 GPa and 1500, 1600, and 1800 K, respectively. **a–c** and **h–j**, The inverse FFT images and FFT patterns corresponding to the areas marked by the white boxes ($7.0 \times 7.0\text{ nm}^2$) in **(a)**, **(b)**, and **(c)**, respectively. The cyan and yellow circles in **(e)**, **f**) indicate cubic- and hexagonal-like MRO clusters, respectively. In subfigure **g**, the lattice fringes marked with cyan and yellow solid lines indicate that nanosized cubic and hexagonal diamond crystallites are precipitated from the non-crystalline matrix at 1800 K.

Extended Data Fig. 3 Structure factor $S(Q)$, structural models, and simulated HRTEM images of simulated a-D, p-D with different fractions of paracrystallites, and NPD with different grain sizes.

a, $S(Q)$ of simulated a-D and p-D with different fractions of paracrystallites. With increasing ϕ , the intensity of the first peak increases, and the position of the peak shifts to high-Q, which is consistent with the experimental observation that at higher annealing temperatures, the intensity of the first peak increases and the position moves to the right (from 2.89\AA^{-1} at 1200 K to 2.95\AA^{-1} at 1600 K, Fig. 3b in the main text). **b**, $S(Q)$ of simulated NPDs with different grain sizes, juxtaposed with that of the 1800 K sample from our experiment. For the simulated NPD samples, the peak intensity decreases and the peak width broadens as the grain size is refined. Bragg peaks are clearly discernable for the samples with a grain size of 1.2 nm. Experimentally, the protruding diffraction peaks in the 1800 K sample corresponds exactly to the characteristic Bragg peaks of NPD, indicative of crystallization. **c**, In ultrafine NPD, the less-distorted “core” regions of the nanocrystals (blue spheres) are clearly seen. For NPD with $d = 1.56$ nm, ϕ is estimated to be 94%, meaning 6% atoms are located at the interfaces and cannot be properly assigned to any of the crystalline grains.

Extended Data Fig. 4 Short-range ordering of a-D, a-Si, p-D, and NPD.

a, Distributions of tetrahedrality q_t for a-D and a-Si, both of which were obtained from the WWW bond-switching approach and further relaxed with *ab initio* MD. The tetrahedral order parameter q_t is defined as $\langle \{q\}_{\{t\}} = 1 - \frac{1}{8} \sum_{i=1}^3 \sum_{j=i+1}^4 |\cos \theta_{ij}|^{1/3} \rangle^2$, where θ_{ij} is the angle formed by two vectors pointing from the center silicon to two of its neighboring silicon atoms. The summation runs over all the combinations of the four nearest neighbors. The narrow distribution of a-D clearly indicates that a-D has a strong tetrahedral SRO than a-Si. **b**, Bond-angle distribution within the first atomic shell for a-D and a-Si. Compared with a-Si, a-D has a narrower bond-angle

distribution. **c**, Distributions of the second-nearest-neighbour order parameter s of a-D and a-Si. The order parameter s measures the similarity of the local atomic environment (16 atoms) of a central atom with respect to perfect CD or HD lattice arrangements. The higher the s value, the less distortion of the local cluster. Compared with a-Si, the distribution function of s for a-D shifts to high s values with a centroid of 0.42, suggesting much enhanced SRO within the first two atomic shells in a-D. The high similarity of the local atomic environments between a-D and crystalline diamond stems from the strong directional sp^3 bonding of carbon, as evidenced from the narrower bond-angle distribution of a-D in comparison to that of a-Si. **d**, Distributions s of a-D, p-D, and NPD with a grain size of 1.92 nm. The inset atomic clusters illustrate the cluster configurations (red spheres) corresponding to their degree of similarity with the perfect CD lattice arrangement (green spheres). Paracrystalline diamond has a medium s value (0.51) between that of a-D and NPD, revealing crystalline ordering in p-D. It is worth noting that, for NPD with $d = 1.92$ nm, the distribution spike at $s = 0.96$ corresponds to interior atoms in nano-grains that are less distorted. Such atoms are absent in paracrystalline diamond, marking the distinction between p-D and NPD.

Extended Data Fig. 5 Two atomic-shell structures (side and top views) of CD and HD (16 nearest neighbors) atomic packing.

The 12 second nearest neighbors in CD and HD are arranged in the FCC and HCP packing modes, respectively.

Extended Data Fig. 6 Structural evolution of C₆₀ under room-temperature compression.

a, Structure model (Only one layer is shown) of C₆₀ under 30 GPa and room temperature (300 K), obtained by classic and *ab initio* MD. Under high pressure (30 GPa), the inter-molecule distance reduces to 0.86 or 0.87 nm from 1.0 nm. During compression to 30 GPa at room temperature, the buckyballs are deformed and inter-buckyball bonding occurs by formation of four-fold (sp^3) bonds (15%). In this and the following figures, the atoms with sp^3 bonding are colored in blue. The fraction of sp^3 atoms was

approximated by the number of 4-fold coordinated atoms within a cut off distance (in this work, $r_{cut} = 1.85 \text{ \AA}$). We shall point out that, the sp^3 fraction calculated this way is slightly underestimated in comparison to that calculated quantum-mechanically, e.g., with the maximally localized Wannier function (MLWF). **b**, *In situ* Raman spectra of C₆₀ under compression (up to ~ 32 GPa) without pressure transmitting medium, with an excitation wavelength of 532 nm. With increasing pressure, the Raman peaks of the A_g mode corresponding to the breathing of totally symmetric vibrations and the H_g mode are gradually broadened with decreased intensity, suggesting a gradual decline of the symmetric environment of pristine C₆₀, associated with the polymerization of buckyballs⁶⁹ and the formation of sp^3 bonds⁷⁰, consistent with our theoretical results.

Extended Data Fig. 7 MD simulation of fcc-C₆₀ heated to different temperatures at 30 GPa.

a, Classic MD simulation of fcc-C₆₀, heating rate: 10^{10} K/s . The fraction of sp^3 bonds increase with increasing temperature. There is a percolation transition of sp^3 bonds at 500–800 K. Such a percolation transition corresponds to the polymerization of C₆₀ molecules. It should be pointed out that the fractions of sp^3 bonding were determined based on the criterion of 4-fold bonding within 1.85 Å, which may slightly underestimate the real sp^3 fraction of the sample by a few percent. **b**, *Ab initio* MD simulation of fcc-C₆₀ (720 atoms), heating rate: $2 \times 10^{14} \text{ K/s}$. Similar to classic MD simulation, the fraction of sp^3 bonds increases with increasing temperature in *ab initio* MD. The simulation results validate what was observed in classical MD. Note the persistence of parallel sp^3 bonds at 900 K and 1200 K.

Extended Data Fig. 8 Enthalpy and volume as a function of temperature during the heating treatment of C₆₀ at 30 GPa.

The decrease of enthalpy with increasing temperature (500–1250 K) indicates the main sp^2 - sp^3 transition (25% to 70% as shown in Extended

Data Fig. 7a) occurs between 500 K and 1250 K, accompanied by the densification of the material due to the formation of sp^3 bonding. The uprise of the enthalpy at temperatures below 500 K and above 1250 K is mainly due to the thermal effect.

Extended Data Fig. 9 Hidden orientational ordering of sp^3 bonds in compressed C₆₀.

Top: Structure model of a-D obtained from C₆₀ after 30 GPa and 1600 K without long-time isothermal annealing (Extended Data Fig. 7a). Middle: 3D bond-orientation distribution function projected onto the unit sphere surface. Bottom: Two-dimensional stereographic projection of the bond-orientation function showing the pole figure of preferred bond orientations. The lines serve as a guide to the eye. Heterogeneous intensity distributions suggest that the sp^3 bonds in the as-obtained a-D have preferred orientations, inherited from the initial parallel sp^3 bonds in the early stage of polymerization.

Extended Data Fig. 10 Classic MD simulation of the structural evolution of a-D during isothermal annealing at 1600 K and 30 GPa, 6400 atoms, up to 15 ns.

Only the core atoms of the paracrystallites are shown. The paracrystallites marked by turquoise and gold have CD and HD-like structures, respectively. The fraction of paracrystallites increases with the annealing time (**a-o**, at a time interval of 1 ns per image). The last image (**p**) shows a 3D configuration paracrystalline diamond with $\phi = 20\%$ obtained from brute-force classical MD. To further increase the volume fraction of p-D, we resorted to adiabatic-bias molecular dynamics and the final results are given in Fig. 3 of the main text. See [Supplementary Video](#) for the fluctuations of the paracrystallites.

Extended Data Fig. 11 Mechanical properties of recovered samples.

a, Vickers hardness H_V and fracture toughness K_{IC} of the samples recovered at 30 GPa and different temperatures, measured at 4.9 and 9.8 N, respectively. Inset: an optical image of the indentation of p-D recovered from 1600 K. **b**, Side-by-side comparison of the loading/unloading displacement curves of p-D recovered from 1600 K and natural diamond in the nanoindentation experiment. Inset: A table of nanoindentation hardness H_N and elastic modulus E obtained from different test points. **c**, Overview of shear modulus G versus Vickers hardness H_V for typical superhard ceramics^{42,46,71,72}. The shear modulus G (437.9 ± 4.7 GPa) and bulk modulus K (363.3 ± 3.9 GPa) was derived through formulas $G = E/[2(1 + \mu)]$ and $K = E/[3(1-2\mu)]$, where the elastic modulus E (937.2 ± 10.1 GPa) was experimentally measured (shown in b) and μ is the Poisson's ratio (0.07) of diamond. Error bars in **a** and **c** indicate the standard deviations. **d**, Summary for the calculated and experimental hardness of typical sp^3 carbons of p-D, diamond^{42,46}, hexagonal diamond⁷³, carbon clathrates⁷⁴, NPD^{39,41} and nanotwinned diamond (NTD)^{42,75}. **e**, Comparison of theoretical Young's modulus and bulk modulus of p-D and diamond⁷⁶. For the *ab initio* calculations, we used DFT-based *ab initio* modeling stated in the Methods section but with a smaller-sized p-D sample (240 atoms) derived from classical MD.

Extended Data Fig. 12 Thermostability of p-D.

a, Both thermogravimetry (TG) and DSC curves of p-D were measured in air at a heating rate of 5 K/min. **b**, Thermostability of p-D, compared with other superhard carbons^{47,48,49}. Superhard (50-80 GPa) DLC films have a wide range of onset oxidation temperature (673–873 K), depending on the fraction of sp^3 bonds. The thermostability of p-D is superior to that of NPD ($d = \sim 13$ nm)⁴³.

Supplementary information

Peer Review File

Supplementary Video 1

Nucleation and growth of diamond paracrystallites from MD simulation. Adiabatic-bias MD simulation showing the nucleation process of p-D. The morphologies of the p-D nuclei are dynamically changing. The critical nucleus size (20–30 atoms) is found to be ~3.0 Å, suggesting that the paracrystallites belong to supercritical nuclei.

Rights and permissions

[Reprints and Permissions](#)

About this article

Cite this article

Tang, H., Yuan, X., Cheng, Y. *et al.* Synthesis of paracrystalline diamond. *Nature* **599**, 605–610 (2021). <https://doi.org/10.1038/s41586-021-04122-w>

- Received: 18 April 2021
- Accepted: 12 October 2021
- Published: 24 November 2021
- Issue Date: 25 November 2021
- DOI: <https://doi.org/10.1038/s41586-021-04122-w>

Share this article

Anyone you share the following link with will be able to read this content:

[Get shareable link](#)

Sorry, a shareable link is not currently available for this article.

[Copy to clipboard](#)

Provided by the Springer Nature SharedIt content-sharing initiative

How to make macroscale non-crystalline diamonds

- Alfonso San-Miguel

News & Views 24 Nov 2021

This article was downloaded by **calibre** from <https://www.nature.com/articles/s41586-021-04122-w>

| [Section menu](#) | [Main menu](#) |

- Article
- [Published: 24 November 2021](#)

Mechanical forcing of the North American monsoon by orography

- [William R. Boos](#) [ORCID: orcid.org/0000-0001-9076-3551^{1,2}](#) &
- [Salvatore Pascale^{3,4}](#)

[Nature](#) volume **599**, pages 611–615 (2021)

- 623 Accesses
- 85 Altmetric
- [Metrics details](#)

Subjects

- [Atmospheric dynamics](#)
- [Hydrology](#)

Abstract

A band of intense rainfall extends more than 1,000 km along Mexico's west coast during Northern Hemisphere summer, constituting the core of the North American monsoon^{1,2}. As in other tropical monsoons, this rainfall maximum is commonly thought to be thermally forced by emission of heat from land and elevated terrain into the overlying atmosphere^{3,4,5}, but a clear understanding of the fundamental mechanism governing this monsoon is lacking. Here we show that the core North American monsoon is generated when Mexico's Sierra Madre mountains deflect the extratropical jet stream

towards the Equator, mechanically forcing eastward, upslope flow that lifts warm and moist air to produce convective rainfall. These findings are based on analyses of dynamic and thermodynamic structures in observations, global climate model integrations and adiabatic stationary wave solutions. Land surface heat fluxes do precondition the atmosphere for convection, particularly in summer afternoons, but these heat fluxes alone are insufficient for producing the observed rainfall maximum. Our results indicate that the core North American monsoon should be understood as convectively enhanced orographic rainfall in a mechanically forced stationary wave, not as a classic, thermally forced tropical monsoon. This has implications for the response of the North American monsoon to past and future global climate change, making trends in jet stream interactions with orography of central importance.

Access options

Subscribe to Journal

Get full journal access for 1 year

\$199.00

only \$3.90 per issue

[Subscribe](#)

All prices are NET prices.

VAT will be added later in the checkout.

Tax calculation will be finalised during checkout.

Rent or Buy article

Get time limited or full article access on ReadCube.

from \$8.99

[Rent or Buy](#)

All prices are NET prices.

Additional access options:

- [Log in](#)
- [Access through your institution](#)
- [Learn about institutional subscriptions](#)

Fig. 1: Influence of orography on rain and low-level wind.



Fig. 2: Generation of eastward flow across western Mexico by the mechanically forced stationary wave.

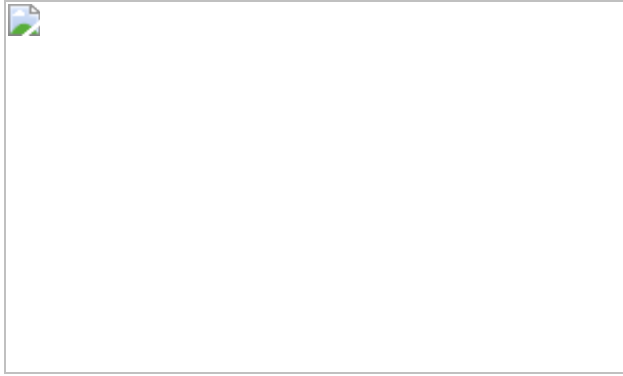


Fig. 3: Diurnal and seasonal cycles in the NAM.

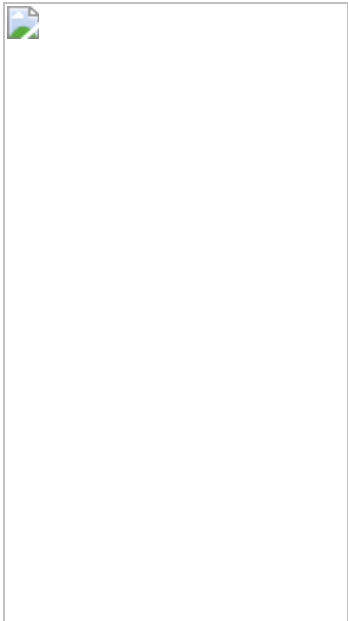
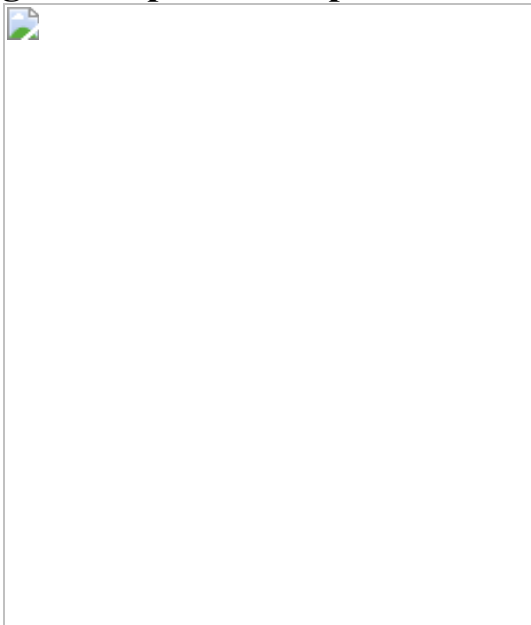


Fig. 4: Response to a pure thermal forcing.



Data availability

The ERA5 monthly averaged data by hour of day were downloaded from the Copernicus Climate Change Service Climate Data Store (identifiers cited in [Methods](#)). MERRA-2 and GPM data were downloaded from the NASA Goddard Earth Sciences Data and Information Services Center (identifiers cited in [Methods](#)). ETOPO1 data were downloaded from the

National Centers for Environmental Information at the National Oceanic and Atmospheric Administration (identifiers cited in [Methods](#)). David K. Adams provided access to GPS Hydromet 2017 data; Trans-boundary, Land and Atmosphere Long-term Observational and Collaborative Network data; and GPS Transect Experiment 2013 data. The time-mean summer climatology from the GCM and time-mean output from the stationary wave model are archived at <https://doi.org/10.5281/zenodo.5076509>.

Code availability

The Community Earth System Model, which is supported primarily by the National Science Foundation, was obtained from <https://www.cesm.ucar.edu>. Isla Simpson provided code for the stationary wave model, the original version of which was written by Mingfang Ting and Linhai Yu.

References

1. 1.
Douglas, M. W., Maddox, R. A., Howard, K. & Reyes, S. The Mexican monsoon. *J. Clim.* **6**, 1665–1677 (1993).
2. 2.
Adams, D. K. & Comrie, A. C. The North American monsoon. *Bull. Am. Meteorol. Soc.* **78**, 2197–2213 (1997).
3. 3.
Tang, M. & Reiter, E. R. Plateau monsoons of the Northern Hemisphere: a comparison between North America and Tibet. *Mon. Weather Rev.* **112**, 617–637 (1984).
4. 4.

Vera, C. et al. Toward a unified view of the American monsoon systems. *J. Clim.* **19**, 4977–5000 (2006).

5. 5.

Mechoso, C. R., Robertson, A. W., Ropelewski, C. F. & Grimm, A. M. in *The Global Monsoon System: Research and Forecast* (eds Chang, C.-P. et al.) Tropical Meteorology Research Programme Report No. 70; 197–206 (No. 1266, WMO/TD, 2005);
<https://doi.org/10.7916/D8ST803T>.

6. 6.

Bryson, R. A. & Lowry, W. P. Synoptic climatology of the Arizona summer precipitation singularity. *Bull. Amer. Meteor. Soc.* **36**, 329–339 (1955).

7. 7.

Krishnamurti, T. N. Tropical east-west circulations during the northern summer. *J. Atmos. Sci.* **28**, 1342–1347 (1971).

8. 8.

Broccoli, A. J. & Manabe, S. The effects of orography on midlatitude Northern Hemisphere dry climates. *J. Clim.* **5**, 1181–1201 (1992).

9. 9.

Stensrud, D., Gall, R., Mullen, S. & Howard, K. Model climatology of the Mexican monsoon. *J. Clim.* **8**, 1775–1794 (1995).

10. 10.

Schmitz, J. T. & Mullen, S. L. Water vapor transport associated with the summertime North American monsoon as depicted by ECMWF analyses. *J. Clim.* **9**, 1621–1634 (1996).

11. 11.

Johnson, R. H., Ciesielski, P. E., McNoldy, B. D., Rogers, P. J. & Taft, R. K. Multiscale variability of the flow during the North American Monsoon Experiment. *J. Clim.* **20**, 1628–1648 (2007).

12. 12.

Berbery, E. H. Mesoscale moisture analysis of the North American monsoon. *J. Clim.* **14**, 121–137 (2001).

13. 13.

Nesbitt, S., Gochis, D. & Lang, T. The diurnal cycle of clouds and precipitation along the Sierra Madre Occidental observed during NAME-2004: implications for warm season precipitation estimation in complex terrain. *J. Hydrometeorol.* **9**, 728–743 (2008).

14. 14.

Ting, M. & Wang, H. The role of the North American topography on the maintenance of the Great Plains summer low-level jet. *J. Atmos. Sci.* **63**, 1056–1068 (2006).

15. 15.

Wexler, H. A boundary layer interpretation of the low-level jet. *Tellus* **13**, 368–378 (1961).

16. 16.

Barlow, M., Nigam, S. & Berbery, E. Evolution of the North American Monsoon System. *J. Clim.* **11**, 2238–2257 (1997).

17. 17.

Collier, J. C. & Zhang, G. J. Effects of increased horizontal resolution on simulation of the North American monsoon in the NCAR CAM3: an evaluation based on surface, satellite, and reanalysis data. *J. Clim.* **20**, 1843–1861 (2007).

18. 18.

Pascale, S. et al. The impact of horizontal resolution on North American monsoon Gulf of California moisture surges in a suite of coupled global climate models. *J. Clim.* **29**, 7911–7936 (2016).

19. 19.

Varuolo-Clarke, A. M., Reed, K. A. & Medeiros, B. Characterizing the North American monsoon in the Community Atmosphere Model: sensitivity to resolution and topography. *J. Climate* **32**, 8355–8372 (2019).

20. 20.

Hu, S. & Boos, W. The physics of orographic elevated heating in radiative–convective equilibrium. *J. Atmos. Sci.* **74**, 2949–2965 (2017).

21. 21.

Gill, A. E. Some simple solutions for heat-induced tropical circulation. *Q. J. R. Meteorol. Soc.* **106**, 447–462 (1980).

22. 22.

Rodwell, M. J. & Hoskins, B. J. Monsoons and the dynamics of deserts. *Q. J. R. Meteorol. Soc.* **122**, 1385–1404 (1996).

23. 23.

Simpson, I. R., Seager, R., Shaw, T. A. & Ting, M. Mediterranean summer climate and the importance of Middle East topography. *J. Clim.* **28**, 1977–1996 (2015).

24. 24.

Simpson, I. R., Seager, R., Ting, M. & Shaw, T. A. Causes of change in Northern Hemisphere winter meridional winds and regional

hydroclimate. *Nat. Clim. Change* **6**, 65–70 (2016).

25. 25.

Rodwell, M. J. & Hoskins, B. J. Subtropical anticyclones and summer monsoons. *J. Clim.* **14**, 3192–3211 (2001).

26. 26.

Emanuel, K. A. *Atmospheric Convection* (Oxford Univ. Press, 1994).

27. 27.

Sobel, A. H. & Bretherton, C. S. Modeling tropical precipitation in a single column. *J. Clim.* **13**, 4378–4392 (2000).

28. 28.

Privé, N. C. & Plumb, R. A. Monsoon dynamics with interactive forcing. Part II: impact of eddies and asymmetric geometries. *J. Atmos. Sci.* **64**, 1431–1442 (2007).

29. 29.

Nie, J., Boos, W. R. & Kuang, Z. Observational evaluation of a convective quasi-equilibrium view of monsoons. *J. Clim.* **23**, 4416–4428 (2010).

30. 30.

Higgins, R. W., Chen, Y. & Douglas, A. V. Interannual variability of the North American warm season precipitation regime. *J. Clim.* **12**, 653–680 (1999).

31. 31.

Hersbach, H. et al. The ERA5 global reanalysis. *Q. J. R. Meteorol. Soc.* **146**, 1999–2049 (2020).

32. 32.

European Centre for Medium-Range Weather Forecasts *ERA5 Reanalysis (0.25 Degree Latitude-Longitude Grid)* (Research Data Archive at the National Center for Atmospheric Research, Computational and Information Systems Laboratory, accessed 30 April 2020); <https://doi.org/10.5065/BH6N-5N20>.

33. 33.

Hersbach, H. et al. *ERA5 Monthly Averaged Data on Single Levels from 1979 to Present* (Copernicus Climate Change Service Climate Data Store, accessed 25 February 2021);
<https://doi.org/10.24381/cds.f17050d7>.

34. 34.

Gelaro, R. et al. The Modern-Era Retrospective Analysis for Research and Applications, Version 2 (MERRA-2). *J. Clim.* **30**, 5419–5454 (2017).

35. 35.

Global Modeling and Assimilation Office *MERRA-2 tavgM_2d_slv_Nx: 2d, Monthly mean, Time-Averaged, Single-Level, Assimilation, Single-Level Diagnostics V5.12.4* (Goddard Earth Sciences Data and Information Services Center, accessed 1 March 2021); <https://doi.org/10.5067/AP1B0BA5PD2K>.

36. 36.

Huffman, G., Stocker, E., Bolvin, D., Nelkin, E. & Tan, J. *GPM IMERG Final Precipitation L3 1 Day 0.1 Degree x 0.1 Degree V06* (ed. Savtchenko, A.) (Goddard Earth Sciences Data and Information Services Center, accessed 3 May 2021);
<https://doi.org/10.5067/GPM/IMERGDF/DAY/06>.

37. 37.

Schneider, U. et al. GPCC's new land surface precipitation climatology based on quality-controlled in situ data and its role in quantifying the global water cycle. *Theor. Appl. Climatol.* **115**, 15–40 (2013).

38. 38.

Schneider, U. et al. *GPCC Full Data Monthly Product Version 7.0 at 0.5°: Monthly Land-Surface Precipitation from Rain-Gauges Built on GTS-Based and Historic Data* (Federal Ministry of Transport and Digital Infrastructure, accessed 1 April 2020);
https://doi.org/10.5676/DWD_GPCC/FD_M_V7_050.

39. 39.

Harris, I., Osborn, T. J., Jones, P. & Lister, D. Version 4 of the CRU TS monthly high-resolution gridded multivariate climate dataset. *Sci. Data* **7**, 109 (2020).

40. 40.

CRU TS4.00: Climatic Research Unit (CRU) Time-Series (TS) Version 4.00 of High-Resolution Gridded Data of Month-by-Month Variation in Climate, Precipitation Monthly Means (The Centre for Environmental Data Analysis UK, accessed 3 April 2020);
<https://doi.org/10.5072/edf8febfdad48abb2cbaf7d7e846a86>.

41. 41.

NOAA National Geophysical Data Center *ETOPO1 1 Arc-Minute Global Relief Model* (NOAA National Centers for Environmental Information, accessed 14 January 2021).

42. 42.

Amante, C. & Eakins, B. *ETOPO1 1 Arc-Minute Global Relief Model: Procedures, Data Sources and Analysis* NOAA Technical Memorandum NESDIS NGDC-24 (National Geophysical Data Center,

NOAA, accessed 14 January 2021);
<https://doi.org/10.7289/V5C8276M>.

43. 43.

Serra, Y. L. et al. The North American Monsoon GPS Transect Experiment 2013. *Bull. Am. Meteorol. Soc.* **97**, 2103–2115 (2016).

44. 44.

Pérez-Ruiz, E. R. et al. Landscape controls on water-energy-carbon fluxes across different ecosystems during the North American monsoon. *J. Geophys. Res. Biogeosci.* **126**, e2020JG005809 (2021).

45. 45.

Cabral-Cano, E. et al. TLALOCNet: a continuous GPS-Met backbone in Mexico for seismotectonic and atmospheric research. *Seismol. Res. Lett.* **89**, 373–381 (2018).

46. 46.

Neale, R. B. et al. *Description of the NCAR Community Atmosphere Model (CAM 5.0)* No. NCAR/TN-464+STR (NCAR, 2012);
<https://doi.org/10.5065/D6N877R0>.

47. 47.

Oleson, K. W. et al. *Technical Description of Version 4.0 of the Community Land Model (CLM)* No. NCAR/TN-478+STR (NCAR, 2010).

48. 48.

Wehner, M. F. et al. Resolution dependence of future tropical cyclone projections of CAM5.1 in the U.S. CLIVAR Hurricane Working Group idealized configuration. *J. Clim.* **28**, 3905–3925 (2015).

49. 49.

Wehner, M. F., Reed, K. A., Loring, B., Stone, D. & Krishnan, H. Changes in tropical cyclones under stabilized 1.5 and 2.0°C global warming scenarios as simulated by the Community Atmospheric Model under the HAPPI protocols. *Earth Syst. Dynam.* **9**, 187–195 (2018).

50. 50.

Mo, K. C., Juang, H. M. H., Higgins, R. W. & Song, Y. Impact of model resolution on the prediction of summer precipitation over the United States and Mexico. *J. Clim.* **18**, 3910–3927 (2005).

51. 51.

Hales, J. E. Surges of maritime tropical air northward over the Gulf of California. *Mon. Weather Rev.* **100**, 298–306 (1972).

52. 52.

Brenner, I. S. A surge of maritime tropical air—Gulf of California to the southwestern United States. *Mon. Weather Rev.* **102**, 375–389 (1974).

53. 53.

Turrent, C. & Cavazos, T. Role of the land-sea thermal contrast in the interannual modulation of the North American Monsoon. *Geophys. Res. Lett.* **36**, L02808 (2009).

54. 54.

Finch, Z. O. & Johnson, R. H. Observational analysis of an upper-level inverted trough during the 2004 North American Monsoon Experiment. *Mon. Weather Rev.* **138**, 3540–3555 (2010).

55. 55.

Liang, X., Zhu, J., Kunkel, K. E., Ting, M. & Wang, J. X. L. Do CGCMs simulate the North American monsoon precipitation seasonal-interannual variability? *J. Clim.* **21**, 4424–4448 (2008).

56. 56.

Geil, K. L., Serra, Y. L. & Zeng, X. Assessment of CMIP5 model simulations of the North American monsoon system. *J. Clim.* **26**, 8787–8801 (2013).

57. 57.

Pascale, S. et al. Weakening of the North American monsoon with global warming. *Nat. Clim. Change* **7**, 806–812 (2017).

58. 58.

Ting, M. & Yu, L. Steady response to tropical heating in wavy linear and nonlinear baroclinic models. *J. Atmos. Sci.* **55**, 3565–3582 (1998).

59. 59.

Ting, M. & Held, I. M. The stationary wave response to a tropical SST anomaly in an idealized GCM. *J. Atmos. Sci.* **47**, 2546–2556 (1990).

60. 60.

Ting, M. The stationary wave response to a tropical SST anomaly in an idealized GCM. *J. Atmos. Sci.* **51**, 3286–3308 (1994).

61. 61.

Held, I. M., Ting, M. & Wang, H. Northern winter stationary waves: theory and modeling. *J. Clim.* **15**, 2125–2144 (2002).

62. 62.

Hoskins, B. J. & Rodwell, M. J. A model of the Asian summer monsoon. Part I: the global scale. *J. Atmos. Sci.* **52**, 1329–1340 (1995).

Acknowledgements

This material is based on work supported by the US Department of Energy, Office of Science, Office of Biological and Environmental Research, Climate and Environmental Sciences Division, Regional and Global Model Analysis Program, under Award DE-SC0019367. It used resources of the National Energy Research Scientific Computing Center, which is a Department of Energy Office of Science User Facility. W.R.B. acknowledges support from the Miller Institute for Basic Research in Science at the University of California, Berkeley. This paper benefited from discussions with D. Adams, Q. Nicolas, I. Fung and J. C. H. Chiang. We thank M. Wehner for advice on running an older configuration of CAM5 at 0.25° resolution.

Author information

Affiliations

1. Department of Earth and Planetary Science, University of California, Berkeley, CA, USA

William R. Boos

2. Climate and Ecosystem Sciences Division, Lawrence Berkeley National Laboratory, Berkeley, CA, USA

William R. Boos

3. Department of Physics and Astronomy, University of Bologna, Bologna, Italy

Salvatore Pascale

4. Centre for Sustainability and Climate Change, Bologna Business School, Bologna, Italy

Salvatore Pascale

Contributions

W.R.B. conceived the study, devised and performed the GCM and stationary wave model integrations, and analysed model output. S.P. assessed the GCM bias. Both authors analysed observations and contributed to writing the manuscript.

Corresponding author

Correspondence to [William R. Boos](#).

Ethics declarations

Competing interests

The authors declare no competing interests.

Additional information

Peer review information *Nature* thanks Jane Baldwin and the other, anonymous, reviewer(s) for their contribution to the peer review of this work. Peer reviewer reports are available.

Publisher's note Springer Nature remains neutral with regard to jurisdictional claims in published maps and institutional affiliations.

Extended data figures and tables

[Extended Data Fig. 1 Main geographic features of the North American monsoon.](#)

The blue line delimits land area used for area-averaging precipitation (NAM domain) in Extended Data Fig. [2a](#), while the dashed black curve outlines the Gulf of California region used for area-averaging the coast-parallel moisture flux in Extended Data Fig. [2b](#). Mapping software: IDL. Adapted from Pascale et al. (2017).

Extended Data Fig. 2 Seasonal cycles of NAM precipitation and along-shore moisture flux in the Gulf of California (GoC) simulated by the high-resolution GCM largely fall within the range of observed interannual variability.

a) Lines show the seasonal cycle of monthly precipitation averaged over the North American monsoon land domain (shown in Extended Data Fig. 1) and over the period 1980–2009 in two observational datasets (CRU in blue and GPCC in purple) and in the Control GCM (CESM; black). Shading bounds the 5th and 95th percentiles of GPCC interannual variability. The GCM lacks the large positive bias in autumn precipitation commonly seen in lower-resolution ocean-atmosphere coupled GCMs. b) Lines show the coast-parallel component of the 10-m moisture flux in the GoC for 1980–2009 in two reanalyses (MERRA2 in blue and ERA5 in purple) and the lowest model-level moisture flux in the Control GCM (CESM; black, about 7 hPa above the surface). Shading bounds the 5th and 95th percentiles of ERA5 interannual variability. The coast-parallel moisture flux is obtained by projecting the vector field along the coast-parallel direction (34° anticlockwise from north), then averaging over the Gulf of California domain shown in Extended Data Fig. 1.

Extended Data Fig. 3 The high-resolution GCM captures the northward low-level wind and the tongue of high moist static energy (MSE) air over the Gulf of California.

Vectors show 10-m horizontal wind from both a) ERA5 and b) MERRA2 (both 1980–2019 means), and c) the lowest model level wind from the Control GCM (CESM; roughly 7 hPa above the surface). Shading in all panels shows 2-m MSE, normalized by the specific heat of dry air to cast this variable in units of K. Mapping software: IDL.

Extended Data Fig. 4 Time-mean winds produce moisture convergence that balances precipitation in the Control GCM.

a) Vertically integrated moisture flux converged by summer-mean winds in the Control GCM, in mm day^{-1} . This has a highly similar spatial pattern to

that of the summer-mean difference between precipitation and surface evaporation (b), which must closely approximate the total vertically integrated moisture flux convergence. The larger magnitude of (a) compared to (b) indicates that transient eddies dry the core NAM precipitation maximum. Convergence of the moisture flux was computed using spherical harmonics truncated at wavenumber 288 to reduce spectral ringing around orography. Mapping software: Cartopy with Natural Earth shapefiles.

Extended Data Fig. 5 Linear stationary wave solution.

Linear solutions were obtained by scaling the Control - FlatMex surface height forcing by 10^{-6} then multiplying the response by 10^6 , thus rendering quadratic terms in the conservation equations a factor of 10^{-6} smaller than linear terms. a) Streamfunction of anomalous 700 hPa horizontal wind (shading, in meters; air flows clockwise around maxima). The thick orange line is the zero contour of the basic-state zonal wind, which near 35°N divides westward trade winds from prevailing eastward extratropical flow. Thin blue lines show 700 hPa potential temperature (in K). b) Anomalous zonal wind at 26°N (shading, in m s^{-1}) with isentropes plotted in blue (5 K contour interval); the total zonal wind (basic state plus response to orography) is contoured in orange, with a contour interval of 2 m s^{-1} , negative contours omitted, and zero contour in bold. Streamfunction in (a) has been normalized by the gravitational acceleration and Coriolis parameter at 45°N . Mapping software: Cartopy with Natural Earth shapefiles.

Extended Data Fig. 6 Basic state isentropes and zonal wind, illustrating how steady, lower-tropospheric adiabatic flow must be deflected southward to avoid being blocked by the ground.

Summer-mean zonal wind (shading, m s^{-1}) and potential temperature (blue contours, interval 5 K) at 103°W in the FlatMex integration. Orography is masked in white.

Extended Data Fig. 7 Low-resolution stationary wave solution.

Fully nonlinear response to the Control - FlatMex surface height forcing obtained with the stationary wave model integrated at R30 horizontal resolution (main text Fig. 2c,d showed solutions at R63 resolution). a) Streamfunction of anomalous 700 hPa horizontal wind (shading, in meters; air flows clockwise around maxima). Surface height of 1.5 km is contoured in green, and thick orange line is zero contour of basic state zonal wind, which near 35°N divides westward trade winds from prevailing eastward extratropical flow. Thin blue lines show 700 hPa potential temperature (in K). b) Anomalous zonal wind at 26°N (shading, in m s^{-1}) with isentropes plotted in blue (5 K contour interval) and orography masked in white; the total zonal wind (basic state plus response to orography) is contoured in orange, with a contour interval of 2 m s^{-1} , negative contours omitted, and the zero contour in bold. Streamfunction in (a) has been normalized by the gravitational acceleration and Coriolis parameter at 45°N. Note that total near-surface flow just west of the SMO is westward, unlike in the high-resolution solutions shown in Fig. 2d. Mapping software: Cartopy with Natural Earth shapefiles.

[Extended Data Fig. 8 Averaging regions for the seasonal cycle of MSE and wind shown in main text Fig. 3c.](#)

Regions over which a) surface air MSE and b) low-level zonal wind were averaged in our seasonal cycle diagnostics. Mapping software: Cartopy with Natural Earth shapefiles.

[Extended Data Fig. 9 Distinct spatial structure of the response to the pure thermal forcing.](#)

Anomalies in summer-mean a) precipitation (mm day^{-1}) and b) surface air MSE (K) in the FlatMexLowAlb model run relative to the FlatMex run. Panels (c) and (d) show the same as (a) and (b) but for the Control run relative to FlatMex. In all panels, only anomalies that are statistically significant at the 5% level by a Student t-test are shown. Mapping software: Cartopy with Natural Earth shapefiles.

Supplementary information

Peer Review File

Rights and permissions

Reprints and Permissions

About this article

Cite this article

Boos, W.R., Pascale, S. Mechanical forcing of the North American monsoon by orography. *Nature* **599**, 611–615 (2021).

<https://doi.org/10.1038/s41586-021-03978-2>

- Received: 10 May 2021
- Accepted: 24 August 2021
- Published: 24 November 2021
- Issue Date: 25 November 2021
- DOI: <https://doi.org/10.1038/s41586-021-03978-2>

Share this article

Anyone you share the following link with will be able to read this content:

[Get shareable link](#)

Sorry, a shareable link is not currently available for this article.

[Copy to clipboard](#)

Provided by the Springer Nature SharedIt content-sharing initiative

This article was downloaded by **calibre** from <https://www.nature.com/articles/s41586-021-03978-2>

| [Section menu](#) | [Main menu](#) |

- Article
- Open Access
- [Published: 10 November 2021](#)

Triangulation supports agricultural spread of the Transeurasian languages

- [Martine Robbeets](#) ORCID: [orcid.org/0000-0002-2860-0230¹](https://orcid.org/0000-0002-2860-0230),
- [Remco Bouckaert](#) ORCID: [orcid.org/0000-0001-6765-3813^{1,2}](https://orcid.org/0000-0001-6765-3813),
- [Matthew Conte³](#),
- [Alexander Savelyev^{1,4}](#),
- [Tao Li^{1,5,6}](#),
- [Deog-Im An⁷](#),
- [Ken-ichi Shinoda⁸](#),
- [Yinqiu Cui](#) ORCID: [orcid.org/0000-0003-3702-5773^{9,10}](https://orcid.org/0000-0003-3702-5773),
- [Takamune Kawashima¹¹](#),
- [Geonyoung Kim³](#),
- [Junzo Uchiyama^{12,13}](#),
- [Joanna Dolińska](#) ORCID: [orcid.org/0000-0002-7855-0454¹](https://orcid.org/0000-0002-7855-0454),
- [Sofia Oskolskaya^{1,14}](#),
- [Ken-Yōjiro Yamano¹⁵](#),
- [Noriko Seguchi](#) ORCID: [orcid.org/0000-0003-0461-6075^{16,17}](https://orcid.org/0000-0003-0461-6075),
- [Hirotaka Tomita^{18,19}](#),
- [Hiroto Takamiya](#) ORCID: [orcid.org/0000-0002-0101-0636²⁰](https://orcid.org/0000-0002-0101-0636),
- [Hideaki Kanzawa-Kiriyama⁸](#),
- [Hiroki Oota²¹](#),
- [Hajime Ishida](#) ORCID: [orcid.org/0000-0002-5781-7914²²](https://orcid.org/0000-0002-5781-7914),
- [Ryosuke Kimura²²](#),
- [Takehiro Sato](#) ORCID: [orcid.org/0000-0001-9866-0346²³](https://orcid.org/0000-0001-9866-0346),
- [Jae-Hyun Kim²⁴](#),
- [Bingcong Deng¹](#),
- [Rasmus Bjørn¹](#),
- [Seongha Rhee](#) ORCID: [orcid.org/0000-0003-0312-0975²⁵](https://orcid.org/0000-0003-0312-0975),
- [Kyou-Dong Ahn²⁵](#),
- [Ilya Gruntov](#) ORCID: [orcid.org/0000-0002-3290-2725^{4,26}](https://orcid.org/0000-0002-3290-2725),

- [Olga Mazo](#) ORCID: [orcid.org/0000-0002-4664-2629^{4,26}](https://orcid.org/0000-0002-4664-2629),
- [John R. Bentley²⁷](#),
- [Ricardo Fernandes^{1,28,29}](#),
- [Patrick Roberts](#) ORCID: [orcid.org/0000-0002-4403-7548¹](https://orcid.org/0000-0002-4403-7548),
- [Ilona R. Bausch^{12,30,31}](#),
- [Linda Gilaizeau¹](#),
- [Minoru Yoneda](#) ORCID: [orcid.org/0000-0003-0129-8921³²](https://orcid.org/0000-0003-0129-8921),
- [Mitsugu Kugai³³](#),
- [Raffaela A. Bianco¹](#),
- [Fan Zhang](#) ORCID: [orcid.org/0000-0001-9259-2223⁹](https://orcid.org/0000-0001-9259-2223),
- [Marie Himmel¹](#),
- [Mark J. Hudson](#) ORCID: [orcid.org/0000-0002-9483-9303^{1,34}](https://orcid.org/0000-0002-9483-9303) &
- [Chao Ning](#) ORCID: [orcid.org/0000-0002-8848-3961^{1,35}](https://orcid.org/0000-0002-8848-3961)

Nature volume 599, pages 616–621 (2021)

- 87k Accesses
- 1 Citations
- 1356 Altmetric
- [Metrics details](#)

Subjects

- [Archaeology](#)
- [Evolution of language](#)

Abstract

The origin and early dispersal of speakers of Transeurasian languages—that is, Japanese, Korean, Tungusic, Mongolic and Turkic—is among the most disputed issues of Eurasian population history^{1,2,3}. A key problem is the relationship between linguistic dispersals, agricultural expansions and population movements^{4,5}. Here we address this question by ‘triangulating’ genetics, archaeology and linguistics in a unified perspective. We report wide-ranging datasets from these disciplines, including a comprehensive Transeurasian agropastoral and basic vocabulary; an archaeological database of 255 Neolithic–Bronze Age sites from Northeast Asia; and a collection of ancient genomes from Korea, the Ryukyu islands and early cereal farmers in Japan, complementing previously published genomes from East Asia. Challenging the

traditional ‘pastoralist hypothesis’^{6,7,8}, we show that the common ancestry and primary dispersals of Transeurasian languages can be traced back to the first farmers moving across Northeast Asia from the Early Neolithic onwards, but that this shared heritage has been masked by extensive cultural interaction since the Bronze Age. As well as marking considerable progress in the three individual disciplines, by combining their converging evidence we show that the early spread of Transeurasian speakers was driven by agriculture.

[Download PDF](#)

Main

Recent breakthroughs in ancient DNA sequencing have made us rethink the connections between human, linguistic and cultural expansions across Eurasia. Compared to western Eurasia^{9,10,11}, however, eastern Eurasia remains poorly understood. Northeast Asia—the vast region encompassing Inner Mongolia, the Yellow, Liao and Amur River basins, the Russian Far East, the Korean peninsula and the Japanese Islands—remains especially under-represented in the recent literature. With a few exceptions that are heavily focused on genetics^{12,13,14} or limited to reviewing existing datasets⁴, truly interdisciplinary approaches to Northeast Asia are scarce.

The linguistic relatedness of the Transeurasian languages—also known as ‘Altaic’—is among the most disputed issues in linguistic prehistory. Transeurasian denotes a large group of geographically adjacent languages stretching across Europe and northern Asia, and includes five uncontroversial linguistic families: Japonic, Koreanic, Tungusic, Mongolic, and Turkic (Fig. 1a). The question of whether these five groups descend from a single common ancestor has been the topic of a long-standing debate between supporters of inheritance and borrowing. Recent assessments show that even if many common properties between these languages are indeed due to borrowing^{15,16,17}, there is nonetheless a core of reliable evidence for the classification of Transeurasian as a valid genealogical group^{1,2,18,19}.

Fig. 1: Distribution of Transeurasian languages in the past and in the present.

 **figure1**

a, Geographical distribution of the 98 Transeurasian language varieties included in this study. Contemporary languages are represented by coloured surfaces, historical varieties by red dots. For legend, see Extended Data Fig. 1. **b**, Reconstructed locations of Transeurasian ancestral languages spoken during the Neolithic (red) and the Bronze Age and later (green). For detailed homeland detection, see Supplementary Data 4.

The estimated time-depth is based on Bayesian inference presented in Supplementary Data [24](#).

Accepting this classification, however, gives rise to new questions about the time depth, location, cultural identity and dispersal routes of ancestral Transeurasian speech communities. Here we challenge the traditional ‘pastoralist hypothesis’ that identifies the primary dispersals of the Transeurasian languages with nomadic expansions starting in the eastern steppe in the fourth millennium before present (bp)[6,7,8](#), by proposing a ‘farming hypothesis’, which places those dispersals within the scope of the ‘farming/language dispersal hypothesis’[5,20,21](#). As these issues reach far beyond linguistics, we address them by integrating archaeology and genetics in a single approach termed ‘triangulation’.

Linguistics

We collected a new dataset of 3,193 cognate sets that represent 254 basic vocabulary concepts for 98 Transeurasian languages, including dialects and historical varieties (Supplementary Data [1](#)). We applied Bayesian methods to infer a dated phylogeny of the Transeurasian languages (Supplementary Data [24](#)). Our results indicate a time-depth of 9181 bp (5595–12793 95% highest probability density (95% HPD)) for the Proto-Transeurasian root of the family; 6811 bp (4404–10166 95% HPD) for Proto-Altaic, the unity of Turkic, Mongolic and Tungusic languages; 4491 bp (2599–6373 95% HPD) for Mongolo-Tungusic; and 5458 bp (3335–8024 95% HPD) for Japano-Koreanic (Fig. [1b](#)). These dates estimate the time-depth of the initial break-up of a given language family into more than one foundational subgroup.

We used our lexical dataset to model the expansion of Transeurasian languages in space (Supplementary Data [3, 4](#)). We applied Bayesian phylogeography to complement classical approaches, such as lexicostatistics, the diversity hotspot principle and cultural reconstruction[1,2,3,8](#).

In contrast to previously proposed homelands, which range from the Altai[6,7,8](#) to the Yellow River[22](#) to the Greater Khingan Mountains[23](#) to the Amur basin[24](#), we find support for a Transeurasian origin in the West Liao River region in the Early Neolithic. After a primary break-up of the family in the Neolithic, further dispersals took place in the Late Neolithic and Bronze Age. The ancestor of the Mongolic languages expanded northwards to the Mongolian Plateau, Proto-Turkic moved westwards over the eastern steppe and the other branches moved eastwards: Proto-Tungusic to the Amur–Ussuri–Khanka region, Proto-Koreanic to the Korean Peninsula and Proto-Japonic over Korea to the Japanese islands (Fig. [1b](#)).

Through a qualitative analysis in which we examined agropastoral words that were revealed in the reconstructed vocabulary of the proto-languages (Supplementary Data 5), we further identified items that are culturally diagnostic for ancestral speech communities in a particular region at a particular time. Common ancestral languages that separated in the Neolithic, such as Proto-Transeurasian, Proto-Altaic, Proto-Mongolo-Tungusic and Proto-Japano-Koreanic, reflect a small core of inherited words that relate to cultivation ('field', 'sow', 'plant', 'grow', 'cultivate', 'spade'); millets but not rice or other crops ('millet seed', 'millet gruel', 'barnyard millet'); food production and preservation ('ferment', 'grind', 'crush to pulp', 'brew'); wild foods suggestive of sedentism ('walnut', 'acorn', 'chestnut'); textile production ('sew', 'weave cloth', 'weave with a loom', 'spin', 'cut cloth', 'ramie', 'hemp'); and pigs and dogs as the only domesticated animals.

By contrast, individual subfamilies that separated in the Bronze Age, such as Turkic, Mongolic, Tungusic, Koreanic and Japonic, inserted new subsistence terms that relate to the cultivation of rice, wheat and barley; dairying; domesticated animals such as cattle, sheep and horses; farming or kitchen tools; and textiles such as silk (Supplementary Data 5). These words are borrowings that result from linguistic interaction between Bronze Age populations speaking various Transeurasian and non-Transeurasian languages.

In summary, the age, homeland, original agricultural vocabulary and contact profile of the Transeurasian family support the farming hypothesis and exclude the pastoralist hypothesis (Supplementary Data 5).

Archaeology

Although Neolithic Northeast Asia was characterized by widespread plant cultivation²⁵, cereal farming expanded from several centres of domestication, the most important of which for Transeurasian was the West Liao basin, where cultivation of broomcorn millet started by 9000 bp^{26,27,28,29}. Extracting data from the published literature, we scored 172 archaeological features for 255 Neolithic and Bronze Age sites (Supplementary Data 6, Fig. 2a) and compiled an inventory of 269 directly carbon-14-dated early crop remains (Supplementary Data 9) in northern China, the Primorye, Korea and Japan.

Fig. 2: Spatiotemporal distribution and clustering of sites included in the archaeological database.

 **figure2**

a, Geographical distribution of 255 sites from the Neolithic (red) and the Bronze Age (green). **b**, Coloured dots cluster the investigated sites according to cultural similarity in line with Bayesian analysis in Supplementary Data [25](#), with indication of the spread of millet and rice in time and space. The distribution of archaeological sites in Fig. [2](#) is smaller than that of contemporary languages in Fig. [1](#) because we focus on the early dispersal of the linguistic subgroups in the Neolithic and the Bronze Age and on the links between the eastward spread of farming and language dispersal.

The main results of our Bayesian analysis (Supplementary Data [25](#)), which clusters the 255 sites according to cultural similarity, are visualized in Fig. [2b](#). We find a cluster of Neolithic cultures in the West Liao basin, from which two branches associated with millet farming separate: a Korean Chulmun branch and a branch of Neolithic cultures covering the Amur, Primorye and Liaodong. This confirms previous findings about the dispersal of millet agriculture to Korea by 5500 bp and via the Amur to the Primorye by 5000 bp^{[30,31](#)}.

Our analysis further clusters Bronze Age sites in the West Liao area with Mumun sites in Korea and Yayoi sites in Japan. This mirrors how during the fourth millennium bp, the agricultural package of the Liaodong–Shandong area was supplemented with rice and wheat. These crops were transmitted to the Korean Peninsula by the Early Bronze Age (3300–2800 bp) and from there to Japan after 3000 bp (Fig. [2b](#)).

Although population movements were not linked with monothetic archaeological cultures, Neolithic farming expansions in Northeast Asia were associated with some diagnostic features, such as stone tools for cultivation and harvesting and textile technology^{[32](#)} (Supplementary Data [7](#)). Domesticated animals and dairying had an important role in the spread of the Neolithic in western Eurasia but, except for dogs and pigs, our database shows little evidence for animal domestication in Northeast

Asia before the Bronze Age (Supplementary Data 6). The link between agriculture and population migrations is especially clear from similarities between ceramics, stone tools, and domestic and burial architecture between Korea and western Japan³³.

Building on previous studies, we provide an overview of demographic changes associated with the introduction of millet farming across the regions in our study (Extended Data Fig. 3). Having invested in elaborate paddy fields, wet rice farmers tended to stay in one place, absorbing population growth through extra labour, whereas millet farmers typically adopted a more expansionary settlement pattern³⁴. Neolithic population densities increased across Northeast Asia before a population crash in the Late Neolithic^{35,36}. The Bronze Age then saw exponential population increases in China, Korea and Japan.

Genetics

We report genomic analyses of 19 authenticated ancient individuals from the Amur, Korea, Kyushu and the Ryukyus and combined them with published genomes that cover the eastern steppe, West Liao, Amur and Yellow River regions, Liaodong, Shandong, the Primorye and Japan between 9500 and 300 bp (Fig. 3a, Extended Data Fig. 4, Supplementary Data 11, 13, 17). We projected them onto a principal component analysis (PCA) of 149 present-day Eurasian populations and 45 East Asian populations (Extended Data Figs. 5–8). Figure 3b models our key ancient populations as an admixture of five genetic components, whereby Jalainur represents Amur, Yangshao the Yellow River and Rokutsu the Jomon genome, whereas Hongshan and Upper Xiajiadian in the West Liao River are composed of Yellow River and Amur genomes (qpAdm admixture of various East Asian genetic components in Supplementary Data 16).

Fig. 3: Spatiotemporal distribution and admixture of ancient genomes.

 **figure3**

a, Ancient genomes located in time and space. For detailed legend, see Extended Data Fig. 4. **b**, QpAdm proximal admixture modelling of 20 key ancient populations from this study. The *x* axis shows ancestry proportion estimates for the target populations in the *y* axis; the error bars represent ± 1 s.e.m. range, estimated by 5-cM block jackknifing.

Contemporary Tungusic as well as Nivkh speakers in the Amur form a tight cluster¹³ (Extended Data Fig. 5). Neolithic hunter-gatherers from Baikal, Primorye and the southeastern steppe, as well as farmers from the West Liao and Amur, all project within this cluster (Extended Data Figs. 8–10).

Late Neolithic Angangxi (Supplementary Data 12) show a high proportion of Amur-like ancestry, whereas West Liao Neolithic millet farmers show a considerable proportion of Amur-like ancestry with a gradual shift towards the Yellow River genome over time¹² (Extended Data Figs. 8–10, Fig. 3b). Although we lack Early Neolithic genomes in the West Liao River, Amur-like ancestry thus is likely to represent the original genetic profile of indigenous pre-Neolithic (or late Palaeolithic) hunter-gatherers covering Baikal, Amur, Primorye, the southeastern steppe and West Liao, continuing in the early farmers from this region. This contradicts a recent genetic study¹³, which concludes that the absence of Yellow River influence in ancient genomes from Mongolia and the Amur does not support the West Liao genetic correlate of the Transeurasian language family.

The PCA (Extended Data Figs. 8–10) shows a general trend for Neolithic individuals from Mongolia to contain high Amur-like ancestry with extensive gene flow from western Eurasia increasing from the Bronze to Middle Ages³⁷. Whereas the Turkic-speaking Xiongnu³⁸, Old Uyghur and Türk are extremely scattered, the Mongolic-speaking³⁹ Iron Age Xianbei fall closer to the Amur cluster than the Shiwei, Rouran, Khitan and Middle Mongolian Khanate from Antiquity and the Middle Ages.

As Amur-related ancestry can be traced down to speakers of Japanese and Korean¹³, it appears to be the original genetic component common to all speakers of Transeurasian languages. By analysing ancient genomes from Korea (Supplementary Data 12), we find that Jomon ancestry was present on the Peninsula by 6000 bp (Fig. 3b, Supplementary Data 13).

The proximal qpAdm modelling (Supplementary Data 13) suggests that Neolithic Ando can be entirely derived from an ancestry related to Hongshan, whereas Yöndaedo and Changhang can be modelled as an admixture of Jomon with a high proportion of Hongshan ancestry, although Yöndaedo has only limited resolution (Supplementary Data 16, Fig. 3b). Yokchido, on the southern coast of Korea, contains nearly 95% Jomon ancestry. Although our genetic analysis cannot itself distinguish between possible East Asian ancestries for Bronze Age Taejungni, given the Bronze Age date it can be best modelled as Upper Xiajiadian; a possible minor Jomon admixture is not statistically significant ($P = 0.228$; Supplementary Data 16). We therefore observe a heterogeneous presence of Jomon ancestry in Neolithic Koreans (0–95%) and its eventual disappearance over time, as shown by a negligible Jomon contribution to present-day Koreans. The lack of a significant Jomon component in

Taejungni indicates that early populations, without detectable Jomon ancestry linked to present-day Koreans, migrated to the Korean peninsula in association with rice farming, and replaced Neolithic populations with some Jomon admixture—although our genetic data currently do not have resolution to test this hypothesis, owing to limited sample size and coverage. We therefore associate the spread of farming to Korea with different waves of Amur and Yellow River gene flow, modelled by Hongshan for the Neolithic introduction of millet farming and by Upper Xiajiadian for the Bronze Age addition of rice agriculture.

Analysing the genomes from Yayoi farmers (Supplementary Data 12), we found that, like Taejungni, they can be modelled as indigenous Jomon ancestry admixed with Bronze Age Upper Xiajiadian ancestry. Our results support massive migration from Korea into Japan in the Bronze Age.

The Nagabaka genomes from Miyako Island (Supplementary Data 12) represent the first—to our knowledge—ancient genome-wide data from the Ryukyus. Contrary to previous findings that Holocene populations reached the southern Ryukyus from Taiwan⁴⁰, our results suggest that the prehistoric Nagabaka population originated in Jomon cultures to the north (Extended Data Fig. 7). The genetic turn-over from Jomon- to Yayoi-like ancestry before the early modern period mirrors the late arrival of agriculture and Ryukyan languages in this region.

Discussion

Triangulation of linguistic, archaeological and genetic evidence shows that the origins of the Transeurasian languages can be traced back to the beginning of millet cultivation and the early Amur gene pool in Neolithic Northeast Asia. The spread of these languages involved two major phases that mirror the dispersal of agriculture and genes (Fig. 4). The first phase, represented by the primary splits in the Transeurasian family, goes back to the Early–Middle Neolithic, when millet farmers associated with Amur-related genes spread from the West Liao River to contiguous regions. The second phase, represented by linguistic contacts between the five daughter branches, goes back to the Late Neolithic, Bronze and Iron Ages, when millet farmers with substantial Amur ancestry gradually admixed with Yellow River, western Eurasian and Jomon populations and added rice, west Eurasian crops and pastoralism to the agricultural package.

Fig. 4: Integration of linguistic, agricultural and genetic expansions in Northeast Asia.

 figure4

Amur ancestry is marked in red, Yellow River ancestry in green and Jomon ancestry in blue. The red arrows show the eastward migrations of millet farmers in the Neolithic, bringing Koreanic and Tungusic languages to the indicated regions. The green arrows mark the integration of rice agriculture in the Late Neolithic and the Bronze Age, bringing the Japonic language over Korea to Japan.

Bringing together the spatiotemporal and subsistence patterns, we find clear links between the three disciplines (Supplementary Data [26](#)). The onset of millet cultivation in the West Liao region around the ninth millennium bp can be associated with substantial Amur-related ancestry and overlaps in time and space with the ancestral Transeurasian speech community. In line with recent associations between the Sino-Tibetan family estimated at 8000 bp^{[41,42](#)} and Neolithic farmers from the Upper and Middle Yellow River^{[13,14](#)}, our results associate the two centres of millet domestication in Northeast Asia with the origins of two major language families: Sino-Tibetan on the Yellow River and Transeurasian on the West Liao River. The lack of evidence for Yellow River influence in the ancestral Transeurasian language and genes is consistent with the multi-centric origins of millet cultivation suggested in archaeobotany^{[28](#)}.

The early stages of millet domestication in the ninth to seventh millennia bp are accompanied by population growth (Extended Data Fig. 3), leading to the formation of environmentally or socially separated subgroups in the West Liao region and broken connectivity between speakers of Altaic and Japano-Koreanic.

Around the mid-sixth millennium bp, some of these farmers started to migrate eastwards, around the Yellow Sea into Korea and northeast into the Primorye, bringing Koreanic and Tungusic languages to these regions and bringing from the West Liao region additional Amur ancestries to the Primorye and mixed Amur–Yellow River ancestries to Korea. Our newly analysed Korean genomes are notable in that they testify to the presence of and admixture with Jomon-related ancestries outside Japan.

The Late Bronze Age saw extensive cultural exchange across the Eurasian steppe, which resulted in the admixture of populations from the West Liao region and the Eastern steppe with western Eurasian genetic lineages. Linguistically, this interaction is mirrored in the borrowing of agropastoral vocabulary by Proto-Mongolic and Proto-Turkic speakers, especially relating to wheat and barley cultivation, herding, dairying and horse exploitation.

Around 3300 bp, farmers from the Liaodong–Shandong area migrated to the Korean peninsula, adding rice, barley and wheat to millet agriculture. This migration aligns with the genetic component modelled as Upper Xiajiadian in our Bronze Age sample from Korea and is reflected in early borrowings between Japonic and Koreanic languages. Archaeologically it can be associated with agriculture in the larger Liaodong–Shandong area without being specifically restricted to Upper Xiajidian material culture.

In the third millennium bp, this agricultural package was transmitted to Kyushu, triggering a transition to full-scale farming, a genetic turn-over from Jomon to Yayoi ancestry and a linguistic shift to Japonic. By adding unique samples from Nagabaka in the southern Ryukyus, we traced the farming/language dispersal to the edge of the Transeurasian world. Demonstrating that Jomon ancestry stretched as far south as Miyako Island, our results contradict previous assumptions of a northward expansion by Austronesian populations from Taiwan. Together with the Jomon profile discovered at Yokchido in Korea, our results show that Jomon genomes and material culture did not always overlap.

By advancing new evidence from ancient DNA, our research thus confirms recent findings that Japanese and Korean populations have West Liao River ancestry, whereas it contradicts previous claims that there is no genetic correlate of the Transeurasian language family¹³.

Although some previous research regarded the Transeurasian zone as beyond the area suitable for farming²⁰, our research confirms that the farming/language dispersal hypothesis remains an important model for understanding Eurasian population dispersals²¹. Triangulation of linguistics, archaeology and genetics resolves the competition between the pastoralist and farming hypotheses and concludes that the early spread of Transeurasian speakers was driven by agriculture.

Methods

Linguistics

Bayesian phylogenetics

Combining dictionary search with fieldwork, we collected a comparative dataset including 3,193 datapoints representing 254 basic vocabulary concepts for 98 Transeurasian languages, including contemporary and historical varieties (Supplementary Data 1). These concepts are based on a merger of the Leipzig–Jakarta 200 (ref. 43) and Jena 200 (ref. 44) lists (Supplementary Data 2). The Turkic and Tungusic basic vocabulary included is based on a revision of recently published datasets^{45,46}. Cognate coding is supported by an inventory of basic vocabulary etymologies and sound correspondences across the Transeurasian languages presented in Supplementary Data 2.

We performed a Bayesian phylogenetic analysis with cognates encoded as binary data⁴⁷. Because the data were collected such that at least one cognate was present, the data were ascertained to not contain any sites having all zeros. Ascertainment correction was applied to cater for this⁴⁷.

We considered the following substitution models, which govern the evolutionary process of cognates along branches of a tree: continuous time Markov chain (CTMC), which assumes a constant rate of mutations; covarion, which assumes a slow and fast rate and the model switching between these two states; and the pseudo Dollo covarion model, which is based on the Dollo principle that a cognate can only appear once, but can be lost many times. Detailed descriptions of the CTMC and covarion models⁴⁷ and the pseudo Dollo covarion model⁴⁸ are available in the literature. For all models, we assume that each meaning class has its own relative rate to capture the variation between rates of evolution of different words.

Although language evolves on average at a constant rate, we find that there can be considerable variation in rates between branches on a tree^{47,48}. Such variation can be

captured using the uncorrelated relaxed clock⁴⁹, assuming rates are log-normally distributed.

A birth death model is used to describe the generative process of language creation. As the data contain ancient languages that may be ancestral to current languages, we allow the tree to have ancestral nodes. A fossilized birth death model⁵⁰, which allows such ancestral nodes, is used as prior on the tree. Language family node ages were informed by age priors (Japonic 2100 bp ± 175, Koreanic 800 bp ± 175, Turkic 2100 bp ± 175, Mongolic 750 bp ± 50, Tungusic 1900 bp ± 275). These calibrations are supported by chronological estimations proposed in linguistic literature (Supplementary Data 18). We found that these node age priors helped to reduce uncertainty slightly in the root age distribution.

We compared the fit of different models by estimating the marginal likelihoods using nested sampling⁵¹ (Supplementary Data 18), and conclude that the pseudo Dollo covarion model with a relaxed clock has the best fit, and covarion with relaxed clock the next best fit. Both models produce compatible time estimates, though covarion estimates tend to have larger uncertainty (that is, have larger 95% HPD intervals). Time estimates of the CTMC model with relaxed clock are still compatible but even wider, and tend to have a higher mean.

All posterior estimates were performed using BEAST v.2.6⁵² using adaptive coupled Markov chain Monte Carlo (MCMC)⁵³. Detailed specification of the models, priors, hyperpriors and settings used to run these models can be found in the BEAST XML files (Supplementary Data 19). The results of our Bayesian analysis are visualized as a dated phylogenetic tree of the Transeurasian languages (Supplementary Data 24).

Bayesian phylogeography

We assumed that the dispersal of people through Eurasia can be described as a random walk, so is best captured by diffusion on a sphere⁵⁴. To get an impression about the uncertainty in locating origins by such model, we performed a post hoc analysis using the posterior tree set from the lexical analysis. We assigned point positions to the tips and randomly sampled trees from the posterior while estimating geographical parameters through MCMC. Even in this relatively restricted set-up, the uncertainty in root location does not allow us to distinguish the different geographical origin hypotheses. The results of our analysis are represented on a map (Supplementary Data 3). As Bayesian phylogeography must contend with a number of limitations^{55,56}, we complemented it with other homeland detection methods such as linguistic palaeontology and the diversity hotspot principle to reach a balanced location for the homelands of the root and nodes of the Transeurasian family (Supplementary Data 4).

Linguistic palaeontology

We compiled comparative agropastoral vocabularies for each Transeurasian subfamily: Turkic (Supplementary Data [5a](#)), Mongolic (Supplementary Data [5b](#)), Tungusic (Supplementary Data [5c](#)), Koreanic (Supplementary Data [5d](#)) and Japonic (Supplementary Data [5e](#)). We applied linguistic reconstruction, a procedure for inferring an unattested ancestral state of a language on the evidence of data that are available from a later period, to corresponding words (Supplementary Data [5](#)).

To distinguish between inherited and borrowed correspondence sets, we used standard criteria based on the phonology, semantics, morphology and distribution of the word involved, as specified in Supplementary Data [5](#). Dividing our dataset into inherited versus borrowed subsistence vocabulary, we determined distinctive spatiotemporal and cultural patterns for each category (Supplementary Data [5](#)).

We applied linguistic palaeontology to our subsistence vocabulary, a historical comparative method that enables us to study human prehistory by correlating our linguistic reconstructions with information from archaeology about the culture of the ancient speech communities that used these words. In this way, we drew inferences about the subsistence strategies available to speakers of the different Transeurasian proto-languages in the Neolithic and Bronze Age (Supplementary Data [5](#)) and identified a plausible location for the homeland of the ancient speech communities involved (Supplementary Data [4](#)).

Diversity hotspot principle

To estimate the location of the ancient speech communities involved, we combined Bayesian phylogeography and linguistic palaeontology with the diversity hotspot principle. The principle is based on the assumption that the homeland is closest to the greatest diversity with regard to the deepest subgroups of the language family. We located these areas on the map and took them as an approximation of the area where a certain proto-language began to diversify (Supplementary Data [4](#)). Although this method must contend with certain limitations (Supplementary Data [4](#)), taken together with the other techniques for homeland location discussed here, it can give us a reasonably robust estimation of the location of an ancient speech community.

Archaeology

Archaeological database

We scored 172 cultural traits for 255 Neolithic–Bronze Age archaeological sites or phases from the West Liao river basin (36), the Amur (Jilin, Heilongjiang and inland

Liaoning) (32), the Primorye (4), the Liaodong peninsula (37), the eastern steppes (1), the Shandong peninsula (4), the Yellow River basin (2), the Korean peninsula (58) and the Japanese islands (85).

Sites with several major cultural phases were scored separately. The sites date from 8400–1700 bp and include the Early Neolithic to Bronze Age in northeast China, the Middle Neolithic Zaisanovka culture in the Primorye, the Middle–Late Neolithic Chulmun and Bronze Age Mumun cultures in Korea, and the Late Neolithic–Bronze Age Final Jomon and Yayoi cultures in western Japan. Categories of cultural traits scored comprised ceramics (70), stone tools (38), buildings (9), plant and animal remains (26), shell and bone artefacts (17) and burials (12). Definitions of scored features are found in Supplementary Data [6](#) (sheet 2) and further discussion of scoring methods can be found in Supplementary Data [7](#). All features were scored as present (1) or absent (0) following published site reports or other literature.

The database was used to analyse changes in the distribution of Neolithic and Bronze Age artefacts over time, especially in relation to the spread of agricultural systems in Northeast Asia (Supplementary Data [7](#)).

In addition, the cultural data in our archaeological database were analysed using Bayesian phylogenetic methods. There is a large amount of phylogenetic work with archaeological data^{[57](#)}, some parsimony-based^{[58](#)}, others distance-based^{[59](#)}. The benefit of Bayesian approaches is that they are model-based, have sound formal mathematical foundations in probability theory allowing us to estimate uncertainty around all estimates, and allow integration of information from various sources in a single analysis (like cognate and geographic data) based on probability theory. BEAST is aimed specifically at inferring rooted time trees, and uncertainty of time estimates, which sets it apart from other Bayesian packages that target unrooted trees. Furthermore, BEAST supports models that are currently not available in other packages, hence the use of this package.

The cultural data are encoded as a binary alignment, and we applied the same substitution and clock models as for the lexical data. The pseudo Dollo model with relaxed clock fits the data best (Supplementary Data [20](#)). Because the coefficient of variation of the relaxed clock exceeded 1, which indicates a considerable amount of variation, we also ran the analysis with the standard deviation capped at 1, which only slightly affected time estimates.

The large number of sampling dates and uncertainty on number of missing cultures made it hard to apply the fossilized birth death prior, so we opted for the flexible Bayesian skyline plot instead^{[60](#)}. Timing information is based on sampling dates of archaeological finds. As there is uncertainty in dating these findings, tip dates were uniformly sampled in these intervals during the MCMC. In line with previous

archaeological studies^{61,62,63}, we constrained the clades ‘Xinglongwa–Zhabaogou–Hongshan’ and ‘Yabuli–Primorye’ to be monophyletic (Supplementary Data 8). All analyses were performed in BEAST v.2.6⁵² using adaptive coupled MCMC⁵³. Details on models, priors, hyperpriors and settings can be found in the BEAST XML (Supplementary Data 21). The results of our Bayesian analysis are visualized as a phylogenetic tree of archaeological cultures in Northeast Asia (Supplementary Data 25) and interpreted in Supplementary Data 8.

Archaeobotanical database

In addition to the database of archaeological features, we compiled a list of the earliest crop remains from each region of Northeast Asia directly dated by radiocarbon (Supplementary Data 9). This list comprises 269 samples (China, 82; Primorye, 12; Korea, 31; Japan (excluding Ryukyus), 120; Ryukyu Islands, 24). Radiocarbon dates in this database were re-calibrated using OxCal v.4.4. We used kernel density mapping to plot the spread of cereals in this database over time (Supplementary Data 7). Our databases were supplemented by published datasets for faunal remains^{64,65}, dolmens⁶⁶ and spindle whorls⁶⁷.

Genetics

Laboratory procedures

Ancient DNA wet laboratory work, including DNA extraction and library preparation, was performed in a dedicated ancient DNA clean room facility at the Max Planck Institute for the Science of Human History (MPI-SHH) and in an ancient DNA laboratory at Jilin University following established protocols⁶⁸. A double-stranded library was built with 8-mer index sequences at both P5 and P7 Illumina adapters. Four individuals from China characterized in Jilin were directly shotgun-sequenced on the Illumina HiSeq X10 instrument in the 150-bp paired-end sequencing design to obtain an adequate coverage. Eighty-three double-stranded libraries for 33 individuals from Korea and Japan were generated and characterized in the MPI-SHH either by shotgun sequencing or by insolution capture at approximately 1.2 million informative nuclear single-nucleotide polymorphisms (SNPs). After initial screening of the preservation of those libraries, a further 108 single-stranded libraries were built aiming at retrieving more endogenous DNA from the samples, and again, those libraries were directly shotgun-sequenced and in-solution-captured at around 1.2 million SNPs (Supplementary Data 17) and sequenced on the Illumina HiSeq 4000 platform following the manufacturer’s protocols.

Sequence data processing

Raw sequencing reads were processed by an automated workflow with the EAGER v.1.92.55 programme⁶⁹. Illumina adapter sequences were trimmed from the sequencing data and overlapping pairs were merged with AdapterRemoval v.2.2.0⁷⁰. We mapped the merged reads with a minimum of 30 bp to the human reference genome (hs37d5; GRCh37 with decoy sequences) using BWA v.0.7.12⁷¹. We removed PCR duplicates by DeDup v.0.12.2⁶⁰. To minimize the effect of post-mortem DNA damage on genotyping, we masked 2 bp for nonUDG libraries and 10 bp for half-UDG libraries on both ends per read using the trimbam function on bamUtils v.1.0.13⁷². The cleaned reads with both base quality (Phred-scale quality) and mapping quality (Phred-scale mapping quality) over 30 were piled up by SAMtools 1.3⁶⁰ with the mpileup function. We called pseudo-diploid genotypes using the pileupCaller program (<https://github.com/stschiff/sequenceTools>) against SNPs in the ‘1240k’ panel^{73,74} under the random haploid calling mode. For C/T and G/A SNPs, we used the masked BAM files; for the rest we used the original unmasked BAM files.

Reference datasets

We compared our ancient individuals to three sets of world-wide genotype panels, one based on the Affymetrix HumanOrigins Axiom Genome-wide Human Origins 1 array (‘HumanOrigins’; 593,124 autosomal SNPs)⁷⁵, the ‘1240k’ panel⁷³, and the ‘Illumina’ dataset⁷⁶. We augmented these datasets by adding the Simons Genome Diversity Panel⁷⁷ and published ancient genomes (Supplementary Data 11).

Ancient DNA authentication

We applied multiple criteria to confirm the authentication of the newly published ancient genomes from Korea and Japan. First, we characterized the post-mortem chemical modifications characteristic for ancient DNA using mapDamage v.2.0.6⁷⁸. Second, we estimated mitochondrial contamination rates for all individuals using Schmutzi v.1.5.1⁷⁹. Third, we measured the nuclear genome contamination rate in males on the basis of X chromosome data as implemented in ANGSD v.0.910⁸⁰. As males have only a single copy of the X chromosome, mismatches between bases, aligned to the same polymorphic position, beyond the level of sequencing error are considered as evidence of contamination. Fourth, we assessed the potential West Eurasian contamination with all reads available and the damage-restricted reads on single-stranded libraries implemented in the PMDtools⁸¹ with a PMD score of at least 3 and compared their positions in a Eurasia PCA with all reads and damaged reads alone. Fifth, we applied qpAdm⁷⁴ per individual to further characterize the West Eurasian contamination with West Eurasian characteristic groups such as Sintashta_MLBA or LBK_EN as sources (see Supplementary Data 17, 22 for details).

Population structure analysis

We performed a PCA with the smartpca v.16000⁸² using a set of 2,077 present-day Eurasian individuals from the ‘HumanOrigins’ dataset and the ‘1240kIllumina’ dataset with the option ‘lsqproject: YES’ and ‘shrinkmode: YES’. We used outgroup- f_3 statistics^{83,84} to obtain a measurement of genetic affinity between two populations since their divergence from an African outgroup. We calculated f_4 statistics with the ‘f4mode: YES’ function in admixtools³¹. Both f_3 and f_4 statistics were calculated using qp3Pop v.435 and qpDstat v.755 in the admixtools package.

Genetic sexing and uniparental haplogroup assignment

We determined the molecular sex of our ancient samples by comparing the ratio of X and Y chromosome coverages to autosomes⁸⁵. For women, we would expect an approximately even ratio of X to autosome coverage and a Y ratio of 0. For men we would expect roughly half of the coverage on X and Y than autosomes.

Admixture modelling with qpAdm

We modelled the ancient individuals in this study using the qpWave/qpAdm framework (qpWave v.410 and qpAdm v.810) in the admixtools v.5.1 package⁷⁴. We used the following 7 populations in ‘1240k’ datasets as outgroup (‘OG’): Mbuti, Onge, Iran_N, Villabruna, Karitiana, Naxi and Funadomari Jomon. This set includes an African outgroup (Mbuti), Andamanese islanders (Onge), early Neolithic Iranians from the Tepe Ganj Dareh site (Iran_N), late Pleistocene European hunter-gatherers (Villabruna), indigenous Karitiana from Brazil, a Tibetan-Burman speaking group from southern China (Naxi) and ancient hunter-gatherers from Japan (Funadomari Jomon) (Supplementary Data [13](#), [16](#)).

Triangulation

The term ‘triangulation’ is borrowed from a navigational technique that determines a single point in space with the convergence of measurements taken from two other distinct points. In qualitative research it designates a method used to capture different dimensions of the same phenomenon by using evidence from three distinct scientific disciplines. To avoid circularity in the argumentation, data collection, analyses and results are performed or reached within the limits of each individual discipline, independently from the other two. Only in the final phase of the triangulation process are the inferences drawn by the three disciplines mapped on each other by comparing a number of variables describing the phenomenon. The purpose of triangulation is to

increase the credibility and validity of the results by evaluating the extent to which the evidence from the three disciplines converges and by identifying correlations, inconsistencies, uncertainties and potential biases across the different perspectives on the investigated phenomena.

Building on previous applications of triangulation in anthropology⁸⁶, we applied the method to the dispersal of the Transeurasian languages, integrating linguistics, archaeology and genetics to contribute a better understanding of the phenomenon. We collected different datasets and applied the methods described above to draw independent inferences with regard to a number of variables such as location, chronology, migratory dynamics, continuity versus diffusion, and subsistence (Supplementary Data 26). Each discipline inferred the most parsimonious model involving these variables on the basis of the application of tools internal to its own field, whether qualitative or quantitative, based on direct or indirect evidence. Taken by itself, a single discipline alone cannot conclusively resolve the question about farming/language dispersals, but taken together the three disciplines increase the credibility and validity of this scenario. Aligning the evidence offered by the three disciplines, we gained a more balanced and richer understanding of Transeurasian migration than each of the three disciplines could provide us with individually.

Reporting summary

Further information on research design is available in the [Nature Research Reporting Summary](#) linked to this paper.

Data availability

Linguistic and archaeological datasets are available through the [Supplementary Information](#). Files that require applications were uploaded to FigShare. The links to FigShare are as follows: Supplementary Data 3: Bayesian phylogeographic analysis modelling the spatiotemporal expansion of the Transeurasian languages (<https://figshare.com/s/b9c67ca3ea47faf51d48>); Supplementary Data 19: BEAST XML files specifying the models, priors, hyperpriors and settings used to run the analyses of the linguistic database (<https://figshare.com/s/748bf751fe3ba7752046>); Supplementary Data 21: BEAST XML files specifying the models, priors, hyperpriors and settings used to run the analyses of the archaeological database (<https://figshare.com/s/99f5aab9a2e43eb2ffd4>); Supplementary Data 24: dated Bayesian phylogeny of the Transeurasian languages (<https://figshare.com/s/709f239fa45982911b87>); and Supplementary Data 25: Bayesian phylogenetic analysis of the archaeological database (<https://figshare.com/s/65615dddc0817bc0184f>). The link to the figtree application is: <https://github.com/rambaut/figtree/releases/tag/v1.4.3> For our genetic datasets, the

DNA sequences reported in this paper have been deposited in the European Nucleotide Archive (ENA) under accession [PRJEB46162](#). Haploid genotype data of ancient individuals in this study on the ‘1240k’ panel are available in the EIGENSTRAT format from the following link:

<https://edmond.mpdl.mpg.de/imeji/collection/59JGAaOpSxRb96Vh>.

Code availability

Readers can access the code that underlies our Bayesian analyses of linguistic and cultural datasets through the [Supplementary Information](#). The files in Supplementary Data [19](#) relate to languages and those in Supplementary Data [21](#) to cultures. The web-links are: Supplementary Data [19](#): BEAST XML files specifying the models, priors, hyperpriors and settings used to run the analyses of the linguistic database (<https://figshare.com/s/748bf751fe3ba7752046>); Supplementary Data [21](#): BEAST XML files specifying the models, priors, hyperpriors and settings used to run the analyses of the archaeological database (<https://figshare.com/s/99f5aab9a2e43eb2ffd4>).

References

1. 1.

Starostin, S., Dybo, A. & Mudrak, O. *Etymological Dictionary of the Altaic Languages* Vol. I– III (Brill, 2003).

2. 2.

Blažek, V. *Altaic Languages. History of Research, Survey, Classification and a Sketch of Comparative Grammar* (Masaryk Univ. Press, 2019).

3. 3.

Robbeets, M. in *The Oxford Guide to the Transeurasian Languages* (eds Robbeets, M. & Savelyev, A.) 772–783 (Oxford Univ. Press, 2020).

4. 4.

Mallory, J., Dybo, A. & Balanovsky, O. The impact of genetics research on archaeology and linguistics in Eurasia. *Russ. J. Genet.* **55**, 1472–1487 (2019).

5. 5.

Bellwood, P. & Renfrew, C. (eds) *Examining the Farming/Language Dispersal Hypothesis* (McDonald Institute for Archaeological Research, 2002).

6. 6.

Menges, K. Dravidian and Altaic. *Anthropos* **72**, 129–179 (1977).

7. 7.

Miller, R. A. Archaeological light on Japanese linguistic origins. *Asian Pac. Quart. Soc. Cult. Affairs* **22**, 1–26 (1990).

8. 8.

Dybo, A. Language and archeology: some methodological problems. 1. Indo-European and Altaic landscapes. *J. Language Relationship* **9**, 69–92 (2013).

9. 9.

Haak, W. et al. Massive migration from the steppe was a source for Indo-European languages in Europe. *Nature* **522**, 207–211 (2015).

10. 10.

Allentoft, M. et al. Population genomics of Bronze Age Eurasia. *Nature* **522**, 167–172 (2015).

11. 11.

Damgaard, P. et al. The first horse herders and the impact of early Bronze Age steppe expansions into Asia. *Science* **360**, eaar7711 (2018).

12. 12.

Ning, C. et al. Ancient genomes from northern China suggest links between subsistence changes and human migration. *Nat. Commun.* **11**, 2700 (2020).

13. 13.

Wang, C. C. et al. Genomic insights into the formation of human populations in East Asia. *Nature* **591**, 413–419 (2021).

14. 14.

Yang, M. A. et al. Ancient DNA indicates human population shifts and admixture in northern and southern China. *Science* **369**, 282–288 (2020).

15. 15.

Francis-Ratte, A. & Unger, J. M. in *The Oxford Guide to the Transeurasian Languages* (eds Robbeets, M. & Saveliev, A.) 705–714 (Oxford Univ. Press, 2020).

16. 16.

Anderson, G. in *The Oxford Guide to the Transeurasian Languages* (eds Robbeets, M. & Saveliev, A.) 715–725 (Oxford Univ. Press, 2020).

17. 17.

Vajda, E. in *The Oxford Guide to the Transeurasian Languages* (eds Robbeets, M. & Saveliev, A.) 726–734 (Oxford Univ. Press, 2020).

18. 18.

Robbeets, M. *Is Japanese related to Korean, Tungusic, Mongolic and Turkic?* (Harrassowitz, 2005).

19. 19.

Robbeets, M. *Diachrony of Verb Morphology: Japanese and the Transeurasian languages* (Vol. 291 in *Trends in Linguistics. Studies and Monographs*) (Mouton de Gruyter, 2015).

20. 20.

Heggarty, P. & Beresford-Jones, D. in *Encyclopedia of Global Archaeology* (ed. Smith, C.) 1–9 (Springer, 2014).

21. 21.

Bellwood, P. *First Farmers: The Origins of Agricultural Societies* (Blackwell, 2005).

22. 22.

Starostin, S. in *Past Human Migrations in East Asia: Matching Archaeology, Linguistics and Genetics* (eds Sanchez-Mazas, A. et al.) 254–262 (Routledge,

2008).

23. 23.

Ramstedt, G. J. A Comparison of the Altaic Languages with Japanese. *Trans. Asiatic Soc. Japan Second Ser.* **7**, 41–54 (1924).

24. 24.

Kæmpfer, E. *De Beschryving van Japan, benevens eene Beschryving van het Koningryk Siam* (Balthasar Lakeman, 1729).

25. 25.

Crawford, G. W. in *Handbook of East and Southeast Asian Archaeology* (eds Habu, J., Lape, P.V. & Olsen, J.W.) 421–435 (Springer, 2018).

26. 26.

Stevens, C. & Fuller, D. The spread of agriculture in eastern Asia: archaeological bases for hypothetical farmer/language dispersals. *Lang. Dyn. Chang.* **7**, 152–186 (2017).

27. 27.

Leipe, C. et al. Discontinuous spread of millet agriculture in eastern Asia and prehistoric population dynamics. *Sci. Adv.* **5**, eaax6225 (2019).

28. 28.

Stevens, C. et al. A model for the domestication of *Panicum miliaceum* (common, proso or broomcorn millet) in China. *Veget. Hist. Archaeobot.* **30**, 21–33 (2021).

29. 29.

Shelach-Lavi, G. et al. Sedentism and plant cultivation in northeast China emerged during affluent conditions. *PLoS ONE* **14**, e0218751 (2019).

30. 30.

Lee, G. A. in *Handbook of East and Southeast Asian Archaeology* (eds Habu, J., Lape, P. & Olsen, J.) 451–481 (Springer, 2017).

31. 31.

Li, T. et al. Millet agriculture dispersed from Northeast China to the Russian Far East: integrating archaeology, genetics and linguistics. *Archaeol. Res. Asia* **22**, 100177 (2020).

32. 32.

Nelson, S. M. et al. Tracing population movements in ancient East Asia through the linguistics and archaeology of textile production. *Evol. Hum. Sci.* **2**, e5 (2020).

33. 33.

Hudson, M. J. *Ruins of Identity: Ethnogenesis in the Japanese Islands* (Univ. Hawai‘i Press, 1999).

34. 34.

Qin, L. & Fuller D. Q. in *Prehistoric Maritime Cultures and Seafaring* (eds Wu, C. & Rolett, B.) 159–191 (Springer, 2019).

35. 35.

Hosner, D. et al. Spatiotemporal distribution patterns of archaeological sites in China during the Neolithic and Bronze Age: an overview. *Holocene* **26**, 1576–1593 (2016).

36. 36.

Hudson, M. J. & Robbeets, M. Archaeolinguistic evidence for the farming/language dispersal of Koreanic. *Evol. Hum. Sci.* **2**, e52 (2020).

37. 37.

Jeong, C. et al. A dynamic 6,000-year genetic history of Eurasia’s Eastern Steppe. *Cell* **183**, 890–904 (2020).

38. 38.

Savelyev, A. & Jeong, C. Early nomads of the Eastern Steppe and their tentative connections in the West. *Evol. Human Sci.* **2**, e20 (2020).

39. 39.

Janhunen, J. in *The Mongolic languages* (ed. Janhunen, J.) 1–29 (Routledge, 2003).

40. 40.

Hudson, M. J. in *New Perspectives in Southeast Asian and Pacific Prehistory* (eds Piper, P., H. Matsumura, H. & Bulbeck, D.) 189–199 (ANU Press, 2017).

41. 41.

Sagart, L. et al. Dated language phylogenies shed light on the ancestry of Sino-Tibetan. *Proc. Natl Acad. Sci. USA* **116**, 10317–10322 (2019).

42. 42.

Zhang, H. et al. Dated phylogeny suggests early Neolithic origin of Sino-Tibetan languages. *Sci. Rep.* **10**, 20792 (2020).

43. 43.

Haspelmath, M. & Tadmor, U. *Loanwords in the World's Languages: a Comparative Handbook* (Mouton de Gruyter, 2009).

44. 44.

Heggarty, P. & Anderson, C. *Cognacy in Basic Lexicon (CoBL)*, <https://www.shh.mpg.de/dlce-research-projects/ie-cor-database> (Max Planck Institute for the Science of Human History, 2015).

45. 45.

Savelyev, A. & Robbeets, M. Bayesian phylolinguistics infers the internal structure and the time-depth of the Turkic language family. *J. Lang. Evol.* 39–53 (2019).

46. 46.

Oskolskaya, S., Koile, E. & Robbeets, M. A Bayesian approach to the classification of Tungusic languages. *Diachronica* <https://doi.org/10.1075/dia.20010.osk> (2021).

47. 47.

Bouckaert, R., Bowern, C. & Atkinson, Q. D. The origin and expansion of Pama–Nyungan languages across Australia. *Nat. Ecol. Evol.* **2**, 741–749 (2018).

48. 48.

Bouckaert, R. & Robbeets, M. Pseudo Dollo models for the evolution of binary characters along a tree. Preprint at <https://doi.org/10.1101/207571> (2018).

49. 49.

Drummond, A. J. et al. Relaxed phylogenetics and dating with confidence. *PLoS Biol.* **4**, e88 (2006).

50. 50.

Gavryushkina, A. et al. Bayesian inference of sampled ancestor trees for epidemiology and fossil calibration. *PLoS Comput. Biol.* **10**, e1003919 (2014).

51. 51.

Maturana, P. M. et al. Model selection and parameter inference in phylogenetics using nested sampling. *Syst. Biol.* **68**, 219–233 (2019).

52. 52.

Bouckaert, R. et al. BEAST 2.5: an advanced software platform for Bayesian evolutionary analysis. *PLoS Comput. Biol.*, **15**, e1006650 (2019).

53. 53.

Mueller, N. F. & Bouckaert, R. Adaptive parallel tempering for BEAST 2. Preprint at <https://doi.org/10.1101/603514> (2020).

54. 54.

Bouckaert, R. Phylogeography by diffusion on a sphere: whole world phylogeography. *PeerJ*, **4**, e2406 (2016).

55. 55.

Wichmann, S. & Rama, T. Testing methods of linguistic homeland detection using synthetic data. Preprint at <https://doi.org/10.1101/2020.09.03.280826> (2020).

56. 56.
Neureiter, N., Ranacher, P., van Gijn, R., Bickel, B. & Weibel, R. 2021 Can Bayesian phylogeography reconstruct migrations and expansions in linguistic evolution? *R. Soc. Open Sci.* **8**, 201079 (2021).
57. 57.
Mace, R., Holden, C. & Shennan, S. *The Evolution of Cultural Diversity—a Phylogenetic Approach* (UCL Press, 2005).
58. 58.
O'Brien, M. J. & Lyman, R. L. Evolutionary archeology: current status and future prospects. *Evol. Anthropol.* **11**, 26–36 (2002).
59. 59.
Allaby, R. G., Fuller, D. Q. & Brown, T. A. The genetic expectations of a protracted model for the origins of domesticated crops. *Proc. Natl Acad. Sci. USA* **105**, 13982–13986 (2008).
60. 60.
Drummond, A. J. et al. Bayesian coalescent inference of past population dynamics from molecular sequences. *Mol. Biol. Evol.* **22**, 1185–1192 (2005).
61. 61.
Shelach, G. & Teng, M. in *A Companion to Chinese Archaeology* (ed. Underhill, A.) 37–54 (Wiley–Blackwell, 2013).
62. 62.
Miyamoto, K. The initial spread of early agriculture into Northeast Asia. *Asian Archaeol.* **3**, 11–26 (2014).
63. 63.
Li, T., Ning, C., Zhushchikhovskaya, I. S., Hudson, M. J. & Robbeets, M. Millet agriculture dispersed from Northeast China to the Russian Far East: integrating archaeology, genetics and linguistics. *Archaeol. Res. Asia* **22**, e100177 (2020).
64. 64.

Kōmoto, M. in *A Study on the Environmental Change and Adaptation System in Prehistoric Northeast Asia* (ed. Kōmoto, M.) 8–34 (Kumamoto Univ., 2007).

65. 65.

An, S. (ed.) *Nongōbūi kogohak* (Sahoep'yōngnon, 2013).

66. 66.

Nishitani, T. (ed.) *Higashi Aja ni okeru shisekibo no sōgōteki kenkyū* (Kyushu Univ., 1997).

67. 67.

Furusawa, Y. in *A Study on the Environmental Change and Adaptation System in Prehistoric Northeast Asia* (ed. Kōmoto, M.) 86–109 (Kumamoto Univ., 2007).

68. 68.

Dabney, J. et al. Complete mitochondrial genome sequence of a Middle Pleistocene cave bear reconstructed from ultrashort DNA fragments. *Proc. Natl Acad. Sci. USA* **110**, 15758–15763 (2013).

69. 69.

Peltzer, A., Herbig, A. & Krause, J. EAGER: efficient ancient genome reconstruction. *Genome Biol.* **17**, 60 (2016).

70. 70.

Schubert, M., Lindgreen, S. & Orlando, L. AdapterRemoval v2: rapid adapter trimming, identification, and read merging. *BMC Res. Notes* **9**, 88 (2016).

71. 71.

Li, H. et al. The Sequence Alignment/Map format and SAMtools. *Bioinformatics* **25**, 2078–2079 (2009).

72. 72.

Jun, G. et al. An efficient and scalable analysis framework for variant extraction and refinement from population-scale DNA sequence data. *Genome Res.* **25**, 918–925 (2015).

73. 73.
Mathieson, I. et al. Genome-wide patterns of selection in 230 ancient Eurasians. *Nature* **528**, 499–503 (2015).
74. 74.
Haak, W. et al. Massive migration from the steppe was a source for Indo-European languages in Europe. *Nature* **522**, 207–211 (2015).
75. 75.
Jeong, C. et al. The genetic history of admixture across inner Eurasia. *Nat. Ecol. Evol.* **3**, 966–976 (2019).
76. 76.
Jeong, C. et al. Bronze Age population dynamics and the rise of dairy pastoralism on the eastern Eurasian steppe. *Proc. Natl Acad. Sci. USA* **115**, E11248–E11255 (2018).
77. 77.
Mallick, S. et al. The Simons Genome Diversity Project: 300 genomes from 142 diverse populations. *Nature* **538**, 201–206 (2016).
78. 78.
Jónsson, H., Ginolhac, A., Schubert, M., Johnson, P. L. F. & Orlando, L. mapDamage2.0: fast approximate Bayesian estimates of ancient DNA damage parameters. *Bioinformatics* **29**, 1682–1684 (2013).
79. 79.
Renaud, G., Slon, V., Duggan, A. T. & Kelso, J. Schmutzi: estimation of contamination and endogenous mitochondrial consensus calling for ancient DNA. *Genome Biol.* **16**, 224 (2015).
80. 80.
Korneliussen, T. S., Albrechtsen, A. & Nielsen, R. ANGSD: analysis of next generation sequencing data. *BMC Bioinformatics* **15**, 356 (2014).
81. 81.

Skoglund, P. et al. Separating endogenous ancient DNA from modern day contamination in a Siberian Neandertal. *Proc. Natl Acad. Sci. USA* **111**, 2229–2234 (2014).

82. 82.

Patterson, N., Price, A. L. & Reich, D. Population structure and eigen analysis. *PLoS Genet.* **2**, e190 (2006).

83. 83.

Raghavan, M. et al. Upper Palaeolithic Siberian genome reveals dual ancestry of Native Americans. *Nature* **505**, 87–91 (2014).

84. 84.

Patterson, N. et al. Ancient admixture in human history. *Genetics* **192**, 1065–1093 (2012).

85. 85.

Fu, Q. et al. An early modern human from Romania with a recent Neanderthal ancestor. *Nature* **524**, 216–219 (2015).

86. 86.

Kirch, P. V. & Green, R. *Hawaiki, Ancestral Polynesia: An Essay in Historical Anthropology* (Cambridge Univ. Press, 2001).

87. 87.

Oh, Y., Conte, M., Kang, S., Kim, J. & Hwang, J. Population fluctuation and the adoption of food production in prehistoric Korea: using radiocarbon dates as a proxy for population change. *Radiocarbon* **59**, 1761–1770 (2017).

88. 88.

Hosner, D., Wagner, M., Tarasov, P. E., Chen, X. & Leipe, C. Spatiotemporal distribution patterns of archaeological sites in China during the Neolithic and Bronze Age: an overview. *Holocene* **26**, 1576–1593 (2016).

89. 89.

Koyama, S. Jomon subsistence and population. *SENRI Ethnol. Stud.* **2**, 1–65 (1978).

Acknowledgements

The research leading to these results has received funding from the European Research Council under the European Union’s Horizon 2020 research and innovation programme (grant agreement no. 646612) granted to M.R. R.B. was supported by a Marsden grant 18-UOA-096 from the Royal Society of New Zealand. We thank N. Adachi, T. Kakuda, E. Savelyeva, W. Lawrence, S. Wichmann, C. Wang, M. Burri, N. Klyuev, I. Zhushchikhovskaya, M. Byington, H. Miyagi, Y. Vostretsov, A. Jarosz, J.-O. Svantesson, M. Levy, J. Lefort, M. Miller, K. Mishchenkova, E. Perekhvalskaya, I. Nikolaeva, P. Czerwinski, N. Aralova, A. Francis-Ratte, I. Joo, R. Máté, T. Pellard and the Korean National Museum for helping to compile, analyse or interpret data.

Funding

Open access funding provided by Max Planck Society.

Author information

Affiliations

1. Max Planck Institute for the Science of Human History, Jena, Germany

Martine Robbeets, Remco Bouckaert, Alexander Savelyev, Tao Li, Joanna Dolińska, Sofia Oskolskaya, Bingcong Deng, Rasmus Bjørn, Ricardo Fernandes, Patrick Roberts, Linda Gilaizeau, Raffaela A. Bianco, Marie Himmel, Mark J. Hudson & Chao Ning

2. Centre of Computational Evolution, University of Auckland, Auckland, New Zealand

Remco Bouckaert

3. Department of Archaeology and Art History, Seoul National University, Seoul, South Korea

Matthew Conte & Geonyoung Kim

4. Institute of Linguistics, Russian Academy of Sciences, Moscow, Russia

Alexander Savelyev, Ilya Gruntov & Olga Mazo

5. Department of Archaeology, Wuhan University, Wuhan, China

Tao Li

6. Archaeological Institute for Yangtze Civilization (AIYC), Wuhan University, Wuhan, China

Tao Li

7. Department of Conservation of Cultural Heritage, Hanseo University, Seosan, Korea

Deog-Im An

8. Department of Anthropology, National Museum of Nature and Science, Tsukuba, Japan

Ken-ichi Shinoda & Hideaki Kanzawa-Kiriyama

9. School of Life Sciences, Jilin University, Changchun, China

Yinqiu Cui & Fan Zhang

10. Research Center for Chinese Frontier Archaeology of Jilin University, Jilin University, Changchun, China

Yinqiu Cui

11. Hiroshima University Museum, Higashi-Hiroshima, Japan

Takamune Kawashima

12. Sainsbury Institute for the Study of Japanese Arts and Cultures, Norwich, UK

Junzo Uchiyama & Ilona R. Bausch

13. Center for Cultural Resource Studies, Kanazawa University, Kanazawa, Japan

Junzo Uchiyama

14. Institute for Linguistic Studies, Russian Academy of Sciences, Saint Petersburg, Russia

Sofia Oskolskaya

15. Research Center for Buried Cultural Properties, Kumamoto University,
Kumamoto, Japan

Ken-Yōjiro Yamano

16. Department of Environmental Changes, Faculty of Social and Cultural Studies,
Kyushu University, Fukuoka, Japan

Noriko Seguchi

17. Department of Anthropology, The University of Montana, Missoula, MT, USA

Noriko Seguchi

18. Hokkaido Government Board of Education, Sapporo, Japan

Hirotaka Tomita

19. Graduate School of Integrated Sciences of Global Society, Kyushu University,
Fukuoka, Japan

Hirotaka Tomita

20. Research Center for the Pacific Islands, Kagoshima University, Kagoshima,
Japan

Hiroto Takamiya

21. Department of Biological Sciences, Graduate School of Science, The University
of Tokyo, Tokyo, Japan

Hiroki Oota

22. Graduate School of Medicine, University of the Ryukyus, Nishihara, Japan

Hajime Ishida & Ryosuke Kimura

23. Department of Bioinformatics and Genomics, Graduate School of Medical
Sciences, Kanazawa University, Kanazawa, Japan

Takehiro Sato

24. Department of Archaeology and Art History, Donga University, Busan, South Korea

Jae-Hyun Kim

25. Hankuk University of Foreign Studies, Seoul, South Korea

Seongha Rhee & Kyou-Dong Ahn

26. National Research University Higher School of Economics, Moscow, Russia

Ilya Gruntov & Olga Mazo

27. Department of World Languages and Cultures, Northern Illinois University, DeKalb, IL, USA

John R. Bentley

28. Faculty of Arts, Masaryk University, Brno, Czech Republic

Ricardo Fernandes

29. School of Archaeology, University of Oxford, Oxford, UK

Ricardo Fernandes

30. Leiden University Institute of Area Studies, Leiden, The Netherlands

Ilona R. Bausch

31. Kokugakuin University Museum, Tokyo, Japan

Ilona R. Bausch

32. University Museum, University of Tokyo, Tokyo, Japan

Minoru Yoneda

33. Miyakojima City Board of Education, Miyakojima, Japan

Mitsugu Kugai

34. Institut d'Asie Orientale, ENS de Lyon, Lyon, France

Mark J. Hudson

35. School of Archaeology and Museology, Peking University, Beijing, China

Chao Ning

Contributions

The research was conceptualized by M.R. Linguistic datasets were collected by A.S., J.D., S.O., B.D., R. Bjørn, S.R., K.-D.A., I.G., O.M., J.R.B. and M.R. The linguistic database was scored by M.R. and analysed by M.R. and R. Bouckaert. Etymologies were established by M.R. The archaeology database was scored by T.L., M.C., T.K., G.K., J.U. and L.G., and analysed by M.J.H., R. Bouckaert, M.R., M.C. and I.R.B. The Nagabaka site was excavated by T.K. and K.-Y.Y. under the direction of M.J.H. with advice from M.K. and H.I. Post-excavation analyses of materials from Nagabaka were analysed by K.-Y.Y., T.K., N.S., H. Tomita, H. Takamiya, J.U., P.R., R.F. and M.Y. Y.C. shared the Angangxi data, D.I.-A. and J.-H.K. the ancient Korean data, K.i.S. the Yayoi data and H.I., R.K., T.S. and H.O. the modern Ryukyu data. Wet laboratory works for ancient DNA data from Korea and Japan were carried out by R.A.B. and M.H. Genetic data analyses were carried out by C.N. with input from H.K.-K. and F.Z. The writing was done by M.R., M.J.H. and C.N.

Corresponding authors

Correspondence to [Martine Robbeets](#), [Mark J. Hudson](#) or [Chao Ning](#).

Ethics declarations

Competing interests

The authors declare no competing interests.

Additional information

Peer review information *Nature* thanks Peter Bellwood, Václav Blažek, Dorian Fuller, Carles Lalueza-Fox and the other, anonymous, reviewer(s) for their contribution to the peer review of this work. Peer reviewer reports are available.

Publisher's note Springer Nature remains neutral with regard to jurisdictional claims in published maps and institutional affiliations.

Extended data figures and tables

[Extended Data Fig. 1 Legend for Fig. 1.](#)

Detailed legend to accompany main Fig. 1.

[Extended Data Fig. 2 Legend for Fig. 2.](#)

Detailed legend to accompany main Fig. 2.

[Extended Data Fig. 3 Demographic changes with agriculture in Neolithic and Bronze Age. Northeast Asia.](#)

A1 shows changes following the adoption of millet farming ca. 8000–4000 BP, using quantity of pottery for the West Liao²⁹ and B2 shows these changes using radiocarbon proxy dates for Korea⁸⁷. Figures A to E show long-term dynamics ca. 8000–2000 BP following the integration of millet with rice, barley and wheat in the Bronze Age and based on site numbers for NE China⁸⁸, radiocarbon dates for Korea⁸⁷ and site numbers for Japan⁸⁹. For references and methods used to derive demographic information from the proxies, see Supplementary Data [7](#).

[Extended Data Fig. 4 Ancient genomes located in time and space.](#)

Includes detailed legend to accompany main Fig. 3 and Extended Data Figs. 7–10.

[Extended Data Fig. 5 PCA displaying the genetic structure of present-day Eurasians.](#)

PC1 separates Western and Eastern Eurasian populations, PC2 Southern and Northern Eurasian populations. Transeurasian populations are coloured according to subfamily (Turkic in grey, Mongolic in orange, Tungusic in yellow, Koreanic in pink, Japonic in light grey). Non-Transeurasian populations are coloured according to families. Populations are labelled with three letters, for a list of abbreviations, see Supplementary Data [10](#).

[Extended Data Fig. 6 PCA displaying the genetic structure of present-day East Asians.](#)

Populations are labelled with three letters, for a list of abbreviations, see Supplementary Data [10](#).

[Extended Data Fig. 7 Ancient genomes plotted on PCA displaying the genetic structure of present-day East Asians.](#)

For a detailed legend, see Extended Data Fig. 4.

[Extended Data Fig. 8 Ancient genomes plotted on PCA displaying the genetic structure of present-day Eurasians.](#)

For a detailed legend, see Extended Data Fig. 4.

[Extended Data Fig. 9 Ancient genomes from Bronze Age, Iron Age, West Liao and Amur plotted on PCA displaying the genetic structure of present-day Eurasians.](#)

For a detailed legend, see Extended Data Fig. 4.

[Extended Data Fig. 10 Ancient genomes from Primorye, eastern steppe and Yellow River plotted on PCA displaying the genetic structure of present-day Eurasians.](#)

For a detailed legend, see Extended Data Fig. 4.

Supplementary information

[Supplementary Information](#)

This file contains a full guide to Supplementary Data Files 1–26. Note that Supplementary Data Files 3 and 21 are hosted externally; please refer to the links within this Supplementary Guide file for details.

[Reporting Summary](#)

[Supplementary Data](#)

This zipped file contains Supplementary Data Files 1, 2 and 4–6; see Supplementary Information file for full descriptions (Supplementary Data File 3 is hosted externally; see Supplementary Information file for links).

[Supplementary Data](#)

This zipped file contains Supplementary Data Files 7–11; see Supplementary Information file for full descriptions.

Supplementary Data

This zipped file contains Supplementary Data Files 12–16; see Supplementary Information file for full descriptions.

Supplementary Data

This zipped file contains Supplementary Data Files 17–20 and 22; see Supplementary Information file for full descriptions (Supplementary Data File 21 is hosted externally; see Supplementary Information file for links).

Supplementary Data

This zipped file contains Supplementary Data Files 23–26; see Supplementary Information file for full descriptions.

Peer Review File

Rights and permissions

Open Access This article is licensed under a Creative Commons Attribution 4.0 International License, which permits use, sharing, adaptation, distribution and reproduction in any medium or format, as long as you give appropriate credit to the original author(s) and the source, provide a link to the Creative Commons license, and indicate if changes were made. The images or other third party material in this article are included in the article's Creative Commons license, unless indicated otherwise in a credit line to the material. If material is not included in the article's Creative Commons license and your intended use is not permitted by statutory regulation or exceeds the permitted use, you will need to obtain permission directly from the copyright holder. To view a copy of this license, visit <http://creativecommons.org/licenses/by/4.0/>.

Reprints and Permissions

About this article

Cite this article

Robbeets, M., Bouckaert, R., Conte, M. *et al.* Triangulation supports agricultural spread of the Transeurasian languages. *Nature* **599**, 616–621 (2021).
<https://doi.org/10.1038/s41586-021-04108-8>

- Received: 18 February 2021
- Accepted: 07 October 2021
- Published: 10 November 2021
- Issue Date: 25 November 2021
- DOI: <https://doi.org/10.1038/s41586-021-04108-8>

Share this article

Anyone you share the following link with will be able to read this content:

[Get shareable link](#)

Sorry, a shareable link is not currently available for this article.

[Copy to clipboard](#)

Provided by the Springer Nature SharedIt content-sharing initiative

Further reading

- [**Tracking the origin of Transeurasian languages**](#)

- Peter Bellwood

Nature (2021)

[**Tracking the origin of Transeurasian languages**](#)

- Peter Bellwood

News & Views 10 Nov 2021

This article was downloaded by **calibre** from <https://www.nature.com/articles/s41586-021-04108-8>

- Article
- Open Access
- [Published: 10 November 2021](#)

A chickpea genetic variation map based on the sequencing of 3,366 genomes

- [Rajeev K. Varshney](#) [ORCID: orcid.org/0000-0002-4562-9131](#)^{1,2},
- [Manish Roorkiwal](#) [ORCID: orcid.org/0000-0001-6595-281X](#)¹,
- [Shuai Sun](#) [ORCID: orcid.org/0000-0003-1092-3186](#)^{3,4,5},
- [Prasad Bajaj](#) [ORCID: orcid.org/0000-0002-3282-9441](#)¹,
- [Annapurna Chitikineni](#)¹,
- [Mahendar Thudi](#) [ORCID: orcid.org/0000-0003-2851-6837](#)^{1,6},
- [Narendra P. Singh](#)⁷,
- [Xiao Du](#)^{3,4},
- [Hari D. Upadhyaya](#)^{8,9},
- [Aamir W. Khan](#) [ORCID: orcid.org/0000-0001-9734-8123](#)¹,
- [Yue Wang](#) [ORCID: orcid.org/0000-0003-2103-4237](#)^{3,4},
- [Vanika Garg](#) [ORCID: orcid.org/0000-0001-6446-4603](#)¹,
- [Guangyi Fan](#)^{3,4,10,11},
- [Wallace A. Cowling](#) [ORCID: orcid.org/0000-0002-3101-7695](#)¹²,
- [José Crossa](#)¹³,
- [Laurent Gentzbittel](#) [ORCID: orcid.org/0000-0001-7851-0332](#)¹⁴,
- [Kai Peter Voss-Fels](#) [ORCID: orcid.org/0000-0003-0782-366X](#)¹⁵,
- [Vinod Kumar Valluri](#)¹,
- [Pallavi Sinha](#)^{1,16},
- [Vikas K. Singh](#)^{1,16},
- [Cécile Ben](#)^{14,17},
- [Abhishek Rathore](#) [ORCID: orcid.org/0000-0001-6887-4095](#)¹,
- [Ramu Punna](#) [ORCID: orcid.org/0000-0003-3998-568X](#)¹⁸,
- [Muneendra K. Singh](#)¹,
- [Bunyamin Tar'an](#)¹⁹,
- [Chellapilla Bharadwaj](#)²⁰,
- [Mohammad Yasin](#)²¹,
- [Motisagar S. Pithia](#)²²,

- [Servejeet Singh](#)²³,
- [Khela Ram Soren](#)⁷,
- [Himabindu Kudapa](#) [ORCID: orcid.org/0000-0003-0778-9959](#)¹,
- [Diego Jarquín](#) [ORCID: orcid.org/0000-0002-5098-2060](#)²⁴,
- [Philippe Cubry](#)²⁵,
- [Lee T. Hickey](#) [ORCID: orcid.org/0000-0001-6909-7101](#)¹⁵,
- [Girish Prasad Dixit](#)⁷,
- [Anne-Céline Thuillet](#)²⁵,
- [Aladdin Hamwieh](#) [ORCID: orcid.org/0000-0001-6060-5560](#)²⁶,
- [Shiv Kumar](#)²⁷,
- [Amit A. Deokar](#)¹⁹,
- [Sushil K. Chaturvedi](#)²⁸,
- [Aleena Francis](#)²⁹,
- [Réka Howard](#)³⁰,
- [Debasis Chattopadhyay](#)²⁹,
- [David Edwards](#) [ORCID: orcid.org/0000-0001-7599-6760](#)¹²,
- [Eric Lyons](#)³¹,
- [Yves Vigouroux](#) [ORCID: orcid.org/0000-0002-8361-6040](#)²⁵,
- [Ben J. Hayes](#) [ORCID: orcid.org/0000-0002-5606-3970](#)¹⁵,
- [Eric von Wettberg](#) [ORCID: orcid.org/0000-0002-2724-0317](#)³²,
- [Swapan K. Datta](#)³³,
- [Huanming Yang](#)^{10,11,34,36},
- [Henry T. Nguyen](#) [ORCID: orcid.org/0000-0002-7597-1800](#)³⁵,
- [Jian Wang](#)^{11,36},
- [Kadambot H. M. Siddique](#) [ORCID: orcid.org/0000-0001-6097-4235](#)¹²,
- [Trilochan Mohapatra](#)³⁷,
- [Jeffrey L. Bennetzen](#) [ORCID: orcid.org/0000-0003-1762-8307](#)³⁸,
- [Xun Xu](#) [ORCID: orcid.org/0000-0002-5338-5173](#)^{10,39} &
- [Xin Liu](#) [ORCID: orcid.org/0000-0003-3256-2940](#)^{10,11,40,41}

Nature volume 599, pages 622–627 (2021)

- 16k Accesses
- 523 Altmetric
- [Metrics details](#)

Subjects

- [Agricultural genetics](#)
- [Natural variation in plants](#)
- [Plant breeding](#)
- [Structural variation](#)

Abstract

Zero hunger and good health could be realized by 2030 through effective conservation, characterization and utilization of germplasm resources¹. So far, few chickpea (*Cicer arietinum*) germplasm accessions have been characterized at the genome sequence level². Here we present a detailed map of variation in 3,171 cultivated and 195 wild accessions to provide publicly available resources for chickpea genomics research and breeding. We constructed a chickpea pan-genome to describe genomic diversity across cultivated chickpea and its wild progenitor accessions. A divergence tree using genes present in around 80% of individuals in one species allowed us to estimate the divergence of *Cicer* over the last 21 million years. Our analysis found chromosomal segments and genes that show signatures of selection during domestication, migration and improvement. The chromosomal locations of deleterious mutations responsible for limited genetic diversity and decreased fitness were identified in elite germplasm. We identified superior haplotypes for improvement-related traits in landraces that can be introgressed into elite breeding lines through haplotype-based breeding, and found targets for purging deleterious alleles through genomics-assisted breeding and/or gene editing. Finally, we propose three crop breeding strategies based on genomic prediction to enhance crop productivity for 16 traits while avoiding the erosion of genetic diversity through optimal contribution selection (OCS)-based pre-breeding. The predicted performance for 100-seed weight, an important yield-related trait, increased by up to 23% and 12% with OCS- and haplotype-based genomic approaches, respectively.

[Download PDF](#)

Main

Pulses are an important crop commodity providing protein for human health. Worldwide pulse productivity has been stagnant for the last five decades, contributing to low per-capita availability of these foods and high levels of malnutrition in developing countries³. Chickpea (*Cicer arietinum* L.) production ranks third among pulses, and chickpea is cultivated in more than 50 countries, especially in South Asia and sub-Saharan Africa. As it is an important source of protein, dietary fibre and micronutrients, chickpea is key to nutritional security. More than 80,000 chickpea

germplasm accessions are being conserved in 30 genebanks across the world⁴, but only a few have been used for chickpea improvement².

Germplasm sequencing efforts in some crop plants have provided insights into the global distribution of genetic variation⁵; how this diversity has been shaped by the genetic bottlenecks associated with domestication⁶ and by the effects of selective breeding⁷; and, finally, how we can link this genetic variation to phenotypic diversity² for breeding applications. Haplotype maps developed using whole-genome sequencing (WGS) data have helped to determine the percentage of the constrained genome and detect deleterious mutations that can be purged for accelerated breeding^{8,9}. Furthermore, sequencing and genotyping of a germplasm collection allows better conservation and management in genebanks^{5,10}.

On the basis of WGS of 3,366 chickpea germplasm accessions, we report here a rich map of the genetic variation in chickpea. We provide a chickpea pan-genome and offer insights into species divergence, the migration of the cultigen (*C. arietinum*), rare allele burden and fitness loss in chickpea. We propose three genomic breeding approaches—haplotype-based breeding, genomic prediction and OCS—for developing tailor-made high-yielding and climate-resilient chickpea varieties.

We sequenced 3,366 chickpea germplasm lines, including 3,171 cultivated and 195 wild accessions at an average coverage of around 12× ([Methods](#), Extended Data Fig. 1, Supplementary Data 1 Tables 1, 2). Alignment of WGS data to the CDC Frontier reference genome¹¹ identified 3.94 million and 19.57 million single-nucleotide polymorphisms (SNPs) in 3,171 cultivated and 195 wild accessions, respectively (Extended Data Table 1, Supplementary Data 1 Tables 3–7, [Supplementary Notes](#)). This SNP dataset was used to assess linkage disequilibrium (LD) decay (Supplementary Data 2 Tables 1, 2, Extended Data Fig. 2, [Supplementary Notes](#)) and identify private and population-enriched SNPs (Supplementary Data 3 Tables 1–4, [Supplementary Notes](#)). These private and population-enriched SNPs suggest rapid adaptation and can enhance the genetic foundation in the elite gene pool.

Pan-genome

We developed a chickpea pan-genome (592.58 Mb) using an iterative mapping and assembly approach by combining the CDC Frontier reference genome, an additional 2.93 Mb from a desi genome (ICC 4958)¹², 3.70 Mb from a *Cicer reticulatum* genome¹³ and 53.66 Mb from de-novo-assembled sequences from cultivated (48.38 Mb; 3,171) and *C. reticulatum* (5.28 Mb; 28) accessions (Supplementary Data 4 Table 1). Although similar pan-genome studies have been conducted in other crops,

including rice^{5,14}, soybean¹⁵ and *Brassica oleracea*¹⁶, our pan-genome comprises more than 3,000 individuals.

A total of 29,870 genes (1,601 additional gene models) were identified, of which 1,582 were to our knowledge novel compared to previously reported genes¹¹. Gene ontology (GO) annotations identified genes that encode response to oxidative stress, response to stimulus, heat shock protein, cellular response to acidic pH and response to cold (Supplementary Data 4 Tables 2, 3), suggesting a possible role in adaptation. The modelling analysis curve eventually reaching saturation suggested that the pan-genome is closed, in concurrence with other plant pan-genomes^{14,16} (Fig. 1a). N50, a widely used metric to assess the quality of an assembly, is the length of the shortest contig for which larger and equal size contigs cover 50% of the total assembly. The N50 values for sequences from de-novo-assembled cultivated and *C. reticulatum* accessions, *C. reticulatum* and the desi genome were 2.61 kb, 1.30 kb, 1.78 kb and 1.76 kb, respectively, whereas the average gene length was 4.72 kb, 1.09 kb, 1.09 kb and 0.98 kb (Supplementary Data 4 Table 1). This pan-genome was further used to assess the effect of presence–absence variations on protein-coding genes (Supplementary Data 4 Table 4, [Supplementary Notes](#)).

Fig. 1: Global chickpea genetic variations.

 [figure1](#)

a, The chickpea pan-genome. Modelling analysis of the pan-genome and core genome shows an increase and decrease in the number of genes with each added genotype, indicating that the pan-genome is a closed pan-genome. The thickness of the curves represents the 99% confidence interval. **b**, Circos diagram illustrating the variation density among chickpea lines. Overall, higher numbers of variations were observed among wild accessions. Tracks indicate SNP density among cultivated (A) and wild (B), insertion density among cultivated (C) and *C. reticulatum* (D), deletion density

among cultivated (E) and *C. reticulatum* (F), and inversion density among cultivated (G) and *C. reticulatum* (H). Links represent inter- and intra-chromosomal translocations. Yellow (cultivated) and purple (*C. reticulatum*) denote intra-chromosomal translocations, whereas orange (cultivated) and green (*C. reticulatum*) represent inter-chromosomal translocations.

Source data

Cultivated (2,258) and *C. reticulatum* (22) accessions with a coverage of greater than 10 \times were analysed to discover structural variations, including insertions (139,483), deletions (47,882), inversions (61,171), intra-chromosomal translocations (417) and inter-chromosomal translocations (2,410) in cultivated and 287,854 insertions, 67,351 deletions, 58,070 inversions, 446 intra-chromosomal translocations and 2,066 inter-chromosomal translocations among *C. reticulatum* accessions as compared to the CDC Frontier genome¹¹ (Fig. 1b, Extended Data Table 1, Supplementary Data 5 Table 1, [Supplementary Notes](#)). More structural variations in the *C. reticulatum* accessions were expected because of their high divergence from cultivated chickpea. We further identified 793 gene-gain copy number variants (CNVs) and 209 gene-loss CNVs in uncultivated accessions, and 643 gene-gain and 247 gene-loss CNVs in *C. reticulatum* accessions (Supplementary Data 5 Tables 2, 3).

Species divergence and migration

To understand speciation and estimate species divergence time in the eight *Cicer* species analysed here, single-copy genes identified using ‘fabales’ genes from the BUSCO¹⁷ database were used to carry out homologue-based gene annotation in preliminary genome assemblies, the CDC Frontier¹¹ and *Medicago truncatula*¹⁸. Using these single-copy genes, *Cicer cuneatum* was estimated to have diverged from other *Cicer* species around 21.4 (19.6–22.8) million years ago (Ma) (Extended Data Fig. 3a, [Supplementary Notes](#)), about the time that Arabia collided with Asia, and a time when ‘Rand Flora’ taxa like *Cicer* may have migrated from Africa into Southwest Asian habitats¹⁹. *C. reticulatum* and *Cicer echinospermum* were estimated to have diverged around 15.3 (14.0 to 16.2) Ma, which is higher than previous estimates and might be influenced by: (i) wild accessions conserved at the International Crops Research Institute for the Semi-Arid Tropics (ICRISAT) representing only some populations of these species, when recent work has shown that only some *C. echinospermum* populations are cross-compatible with *C. arietinum*; and (ii) introgression from *C. echinospermum* into cultivated chickpea, which is widespread in Australian and North American breeding lines, and is also likely to have occurred in International Center for Agricultural Research in the Dry Areas (ICARDA) lines.

Phylogenetic analysis grouped all 195 wild accessions into 6 clusters (Clusters I–VI) (Extended Data Fig. 3b, [Supplementary Notes](#)). Cluster IVa included all *C. reticulatum* and one *C. echinospermum* (ICC 20192; green colour), whereas cluster IVb included all *C. echinospermum* and one *C. reticulatum* (ICC 73071; golden-yellow colour). Similarly, one *Cicer pinnatifidum* (ICC 20168; red colour) was grouped with the *Cicer bijkum* accessions in cluster II, and one *C. bijkum* (ICC 20167; blue colour) was grouped with *C. pinnatifidum* accessions in cluster I. These are two cross-compatible species. Spontaneous hybridization might have occurred in nature. In terms of post-species divergence, a homologue (*Ca_25684*) of *SHATTERPROOF2* (also known as Agamous-like MADS-box protein (*AGL5*)), which is responsible for seed dispersal, was analysed for haplotypic variation ([Supplementary Notes](#)). We found an association of the ‘C’ allele with low or minimal shattering in cultivated species, as seen at the low shattering allele (‘C’) on chromosome 5 at position 1,022,962 of the orthologue in common bean²⁰.

The neighbour-joining tree grouped most South Asian accessions with no distinct clustering for other geographic origins (Extended Data Fig. 4). Our principal component analysis (PCA) of accessions suggests two paths of diffusion or migration of chickpea from the centre of origin in the Fertile Crescent: one path indicates diffusion to South Asia and East Africa, and the other suggests diffusion to the Mediterranean region (probably through Turkey) as well as to the Black Sea and Central Asia (up to Afghanistan) (Fig. 2a–f, Extended Data Fig. 5). This diffusion translated into a pattern of nucleotide diversity (π), among accessions from Central Asia (4.74×10^{-4}) and South Asia (3.62×10^{-4}) (Supplementary Data 6 Table 1), which is consistent with earlier reports². Pairwise fixation index (F_{ST}) estimations further supported these findings (Supplementary Data 6 Table 2, [Supplementary Notes](#)).

Fig. 2: Insights into chickpea migration.



a–f, The PCA based on geographic origin suggests two paths of diffusion (**a, b**). The first path illustrates a diffusion to South Asia (**c**) and East Africa in parallel (**d**). The second path suggests a diffusion to Central Asia (**e**) together with the Mediterranean region (**f**).

Domestication and breeding bottlenecks

Our analysis indicates that chickpea experienced a strong bottleneck beginning around 10,000 years ago. The population size reaching its minimum around 1,000 years ago, followed by a very strong expansion of the population within the last 400 years (Extended Data Fig. 6), suggest a strong recent expansion of chickpea agriculture. One consequence of this bottleneck is shown by the higher π in *C. reticulatum* (2.20×10^{-3}) relative to cultivated accessions (Extended Data Table 1, Supplementary Data 6 Table 1).

Genetic relationship analysis between cultivated and wild chickpea showed that one cultivated accession (ICC 16369) from East Africa was grouped with wild chickpea (Extended Data Fig. 7). This same genotype also showed the presence of the 'T' allele, specific to wild species in *SHATTERPROOF2*, suggesting that ICC 16369 has been mislabelled as belonging to the cultivated chickpea (Supplementary Data 7).

To detect selection sweeps, we pinpointed 18 fragments in cultivated chickpea using the composite likelihood ratio (CLR) (Extended Data Fig. 6, Supplementary Data 6

Tables 8, 9). Combined analysis with reduction of diversity (ROD), F_{ST} and Tajima's D identified genomic regions for *C. reticulatum* (immediate wild species progenitor) versus landraces (2,899; 42,148 kb), landraces versus breeding lines (191; 4,360 kb) and breeding lines versus cultivars (14; 404 kb) that might have undergone selection during domestication and breeding (Supplementary Data 6 Tables 3–6, [Supplementary Notes](#), <https://doi.org/10.6084/m9.figshare.15015327>). We identified 35 regions (222 kb) common between *C. reticulatum* versus landraces and landraces versus breeding lines, and similarly one region (4 kb) between landraces versus breeding lines and breeding lines versus cultivars. Furthermore, we identified a total of 37 unique potential genes in these 36 regions that may have a role in the adaptation of chickpea during migration to different environments by regulating flowering time and plant growth (Supplementary Data 6 Table 7). For example, *FLP2* (flower development and vegetative to reproductive phase transition of meristem), *LRP1* (root growth), *PIP5KL1* (signalling pathways for survival and T cell metabolism) and *MYB12* (flavonoid biosynthesis) are some key genes we pinpointed that are critical for plant growth, metabolic pathways and adaptation in changing environments.

We used genomic evolutionary rate profiling (GERP) analysis to identify 29 Mb (8.36%) genomic regions as evolutionarily constrained (GERP score of greater than 0), indicating purifying selection (Extended Data Fig. 8a). Using constrained genome, sorting intolerant from tolerant²¹ (SIFT) score (less than 0.05) and GERP (greater than 2), 10,616 non-synonymous SNPs were identified as candidate deleterious mutations (Extended Data Fig. 8b). Using the derived allele frequency (DAF) spectrum, we selected 37 non-synonymous deleterious mutations (SIFT < 0.05; GERP > 2; DAF > 0.8) in 36 genes (Supplementary Data 8 Tables 1–4), as fixed that have not been purged through traditional breeding. Detailed analysis indicated a higher (17.88%, $P = 0.01772$) abundance of deleterious alleles in the wild progenitor (*C. reticulatum*) than in cultivated accessions (Extended Data Fig. 8c). Furthermore, the mutation burden for genomic regions under selection suggested that the number of deleterious mutations in landraces was approximately twofold that in breeding lines (206.91%; $P = 2.195676 \times 10^{-60}$) (Extended Data Fig. 8d). To increase the fitness of cultivated chickpea, these deleterious alleles are potential targets for genomics-assisted breeding and genome editing.

Superior haplotypes for key traits

We used 3.94 million SNPs and phenotyping data for 16 traits on 2,980 cultivated genotypes to identify 205 SNPs associated with 11 traits ([Methods](#), Supplementary Data 9 Table 1, [Supplementary Notes](#)). Of the 205 associated SNPs, 152 were present in 79 unique genes with potential roles in controlling seed size and development. Analysis of these genes across cultivated genotypes identified 350 haplotypes (Supplementary Data 9 Tables 2–4, [Supplementary Notes](#)). Using 19.10 million

haplo–pheno combinations, we identified 24 consistent and stable superior haplotypes for 20 genes (Supplementary Data 9 Tables 5–7, Extended Data Fig. 9a). This analysis revealed that the majority of breeding lines (80%) lacked superior haplotypes that are present in the landraces. We validated superior haplotypes by using historical data on 129 chickpea varieties released between 1948 and 2012 (Extended Data Fig. 9b,c). Finally, we identified 56 lines as potential donors for introducing superior haplotypes in breeding (Supplementary Data 9 Tables 8–10).

Enriching the genetic base

We combined OCS²² with a mate allocation method that takes into account genetic gain and genetic diversity as a guide for potential future chickpea pre-breeding programmes or ‘evolving gene banks’^{22,23} ([Supplementary Notes](#)). With a price bonus for earliness and for large seeds, we chose 274 (9.4%) unique genotypes for 325 matings from the 2,898 available genotypes, divided among desi (190), kabuli (120) and intermediate (15), using MateSel²⁴ (Supplementary Data 10 Table 1).

The frequency distribution of predicted progeny index (mean of nine environments) values was bimodal. Higher predicted progeny index values were observed in kabuli as compared with desi. However, marked improvements were predicted in desi and kabuli, from candidate parents to predicted progenies (Extended Data Fig. 10a,b). The frequency distribution of predicted progeny genomic estimated breeding value (GEBV) for yield per plant (YPP) in desi (13.79 g) exceeded kabuli (12.65 g) and a higher response to selection was observed for desi (0.6 g; 4.3%) than for kabuli (0.4 g; 3.5%) (Extended Data Fig. 10c,d). For 100-seed weight (100SW), the mean 100SW of predicted progeny in kabuli (30.6 g) was almost twice that of desi (16.9 g), and the response to selection was three times higher for kabuli (5.7 g; 23%) than for desi (2.0 g; 13%) (Fig. 3a, Extended Data Fig. 10e,f). Kabuli progeny, with a later flowering time, did not respond to selection for earliness (−1.0 day) as rapidly as desi progeny (−3.3 days) (Extended Data Fig. 10g,h). These predicted responses to selection in the next cycle occurred with a relatively small increase in predicted progeny inbreeding in the desi (0.03) and intermediate (0.02), but a large increase in the kabuli (0.17) (Extended Data Fig. 10i, Supplementary Data 10 Table 2, [Supplementary Notes](#)).

Fig. 3: An example of the use of four genomic breeding strategies for improving 100SW.

 **figure3**

a, Mean GEBV and total genetic values predict a 23% increase in one generation for 100SW in kabuli candidates. **b**, Genomic-enabled predictions using Bayesian generalized linear regression (BGLR) on three cross-validation schemes provided the highest mean prediction accuracy with scheme CV0 ($n = 2,980$ cultivated accessions). **c**, A general linear model using the WhoGEM prediction machine provided the highest prediction accuracies for the WhoGEM full model ($n = 1,500$; 300 replicates of a fivefold cross-validation). In each violin plot, the black dot represents the mean. GxE, genotype and environment interaction. **d**, Haplotype-based local GEBVs that are suggested to provide a fivefold improvement in performance over the best accessions with the highest GEBV. The genotypes were classified into three different groups (cultivars (CV, $n = 152$), breeding lines (BL, $n = 396$) and landraces (LR, $n = 2,439$)). Each of the box plots shows the upper and lower whisker (indicated by dashed lines), the 25% and 75% quartiles and the median (as a solid line).

[Source data.](#)

Breeding population improvement

We used different subsets of SNPs and phenotyping data on 16 traits across 12 combinations of year and location, following 3 genomic prediction approaches: (i) interaction of marker and environment covariates ($G \times E$)²⁵; (ii) implementation of the

WhoGEM approach²⁶, and (iii) a haplotype-based approach for estimating local GEBVs²⁷.

In the first approach, 3 genomic relationship matrices with 223,119 (G1), 531,457 (G2) and 754,576 (G3) SNPs, and phenotyping data for 9 traits on 2,980 genotypes, were used to understand the variability explained within the groups and environments (Supplementary Data 10 Table 3). Overall, the environment (E) + genotype (L) + marker effects (G3) model for cross-validation scheme 0 (CV0; see ‘Prediction using the interaction of genomic and environmental covariates’ in Methods) produced the highest average correlation (0.719) for 100SW, and the E + L model returned the lowest value (0.031) for basal secondary branch (Supplementary Data 10 Table 4). For 100SW, genomic prediction accuracy varied from 0.611 (E + L + G3 + G3E) to 0.719 (E + L + G3) for CV1 and CV0, respectively (Fig. 3b).

In the second approach, we used WhoGEM with 276,956 LD-pruned SNPs and phenotyping data for 9 traits on 1,318 genotypes (with GPS data). Prediction accuracies of the full model ranged from 0.25 to 0.91 (Supplementary Data 10 Table 5). Although the highest prediction accuracy was obtained for plot yield (0.914), this method was still efficient in predicting 100SW, with an accuracy of 0.599 (environment-only model) to 0.707 (WhoGEM full model) (Fig. 3c). Evidence for interactions between admixture components and the environment was presented for phenology, plant production and plant architecture traits (Extended Data Fig. 11a–m). The use of admixture components integrates the effects of demography (that is, gene flow and genetic drift) and artificial or natural selection to explain phenotypic variation with reasonable accuracy. This shows considerable potential to detect the accumulation of favourable admixture components from the wider genepool.

In the third approach, 124,833 selected SNPs were used to construct LD blocks, called haplotypes. These SNPs and phenotyping data for 100SW and YPP for 2,980 genotypes were used to estimate local GEBVs for the haplotypes. The local GEBV analysis revealed substantial genetic potential in each subgroup for trait improvement (Extended Data Fig. 12). When comparing the best accessions with the highest GEBVs to the *in silico* genotypes that combined all haplotypes with the highest trait effect across the whole genome, the predicted performance increased by more than threefold for YPP and by more than fivefold for 100SW (Fig. 3d). Our results indicate that capturing novel alleles from landraces through a haplotype-based prediction approach could improve YPP or 100SW by 6–12% (Fig. 3d).

Discussion

Our study reports global polymorphisms in chickpea by sequencing 3,366 germplasm accessions (3,171 cultivated and 195 wild). This analysis brings greater resolution to

our understanding of the within-species diversity of *C. arietinum*. The chickpea pan-genome (592.58 Mb) developed from cultivated draft genomes^{11,12} and the *C. reticulatum* genome¹³, together with WGS data on cultivated and *C. reticulatum* accessions, provided insights into gene content variation across cultivated chickpea and its wild progenitor.

Although some studies based on chloroplast DNA²⁸ and nuclear ribosomal DNA²⁹ have been conducted to investigate the evolution and domestication of *Cicer* species in the past, their resolution was limited. Here, by using WGS data for a large number of individuals, we estimated the divergence time between chickpea and its closest progenitor species. Our study also provides opportunities to rectify misclassifications of accessions to the correct species and to determine whether chickpea seeds preserved in archaeological sites were wild or cultivated.

We identified selective sweeps and candidate genes under domestication and breeding that were responsible for reducing genetic diversity in the cultivated gene pool. Most importantly, our study analysed genetic loads in *Cicer* species. Although selection and recombination have successfully purged many deleterious alleles, the current collection of breeding lines and cultivars still contains substantial genetic loads that affect crop fitness. Here, we have identified deleterious alleles for purging through genome-informed breeding and/or gene editing.

We identified numerous superior haplotypes for improvement-related traits in landraces, and used the concept of superior haplotypes by comparing the yield of the released varieties carrying superior versus regular haplotypes for yield-related traits³⁰. Furthermore, we estimated prediction accuracies for agronomic traits using three genomic prediction approaches and provided a case study for 100SW, demonstrating that genomic prediction approaches have great potential for enhancing crop productivity. We suggest using haplotype mining and genomic prediction approaches in chickpea and other crops to provide climate resilience and improved nutrition to meet future worldwide demand.

Methods

Germplasm sequencing and variant calling

We performed WGS of 2,967 *Cicer* accessions from a global composite collection⁴ using the HiSeq2500 at the Center of Excellence in Genomics and Systems Biology, ICRISAT. By including sequence data of 399 lines from an earlier study², we analysed 3,366 accessions (3,171 cultivated and 195 wild species accessions) altogether ([Supplementary Notes](#)).

We aligned sequencing data from the 3,366 chickpea accessions to the reference genome of CDC Frontier¹¹, using BWA-MEM³¹ v.0.7.15. SNP calling was performed using GATK³² v.3.7 as per GATK best practices for SNP calling, thus creating the base SNP set. We defined two other SNP sets: (i) Set-A: only SNPs with <30% missing call, and biallelic calls, and (ii) Set-B: SNPs with less than 30% missing calls, biallelic calls, and LD-pruned using PLINK³³ v.1.90 (“--indep-pairphase 50 10 0.2” parameter). Set-B SNPs were only used to depict the population genetic structure.

Private and population-enriched SNPs

To determine the private and population-specific SNPs, the frequency of alleles within a given population was determined using VariantsToTable³⁴ of GATK v3.8.1. We defined ‘private alleles’ as those present in at least four accessions within a population and absent in other populations, and ‘population-enriched alleles’ as those present in a given population ($\geq 20\%$) and less frequent in other populations⁵ ($\leq 2\%$).

LD decay, diversity and F_{ST}

LD decay was determined using the software PopLDdecay³⁵ v.3.29 with the parameter “-MaxDist 1000”. Nucleotide diversity (π) was calculated from a 100-kb sliding window with a 10-kb step using VCFtools³⁶ v.0.1.13. The average of all valid windows was considered the population genetic diversity. The fixation index (F_{ST}) was calculated from 100-kb non-overlapping windows using VCFtools. The global weighted F_{ST} was used to measure the differentiation of populations.

Construction of a pan-genome

The chickpea draft genome of CDC Frontier¹¹ (a kabuli variety; considered as the foundation genome) together with ICC 4958^{12,37} (a desi genome sequence), a *C. reticulatum* genome¹³, and de-novo-assembled sequences from 3,171 cultivated and 28 *C. reticulatum* accessions were used to guide the assembly of the chickpea pan-genome using a conservative approach³⁸. Following the alignment of reads from each accession to the reference, unmapped and dangling mapped read pairs were extracted using SAMTools³⁹ v.1.2 based on the FLAG field. The extracted reads were de-novo-assembled using MEGAHIT⁴⁰ v.1.2.9 with default parameters. To identify possible redundancies among assembled contigs that were already present in the foundation genome, the assembled contigs were aligned to the foundation genome using NUCmer⁴¹ v.4.0.0beta2 with the parameters “-l 20 -c 65” and the alignments with length ≥ 500 bp and identity of greater than 80% were extracted to be added into the intermediate pan-genome. The processes were performed one by one: ICC 4958, de-

novo-assembled sequences from 3,171 cultivated accessions, the *C. reticulatum* genome, and de-novo-assembled sequences from 28 *C. reticulatum* accessions. Further, to identify redundancy among the ‘novel’ sequences, all-versus-all alignment was performed using CD-HIT⁴² v.4.81. The same process was performed for the next iteration until no sequence was left. Finally, we removed the potential containments from vectors, bacteria, viruses, animals, fungi and organelle sequences using BLASTN⁴³ v.2.2.31 to the corresponding NT databases and obtained the final pan-genome. As a result, the CDC Frontier genome¹¹ and novel assembled sequences were combined to construct the chickpea pan-genome.

Structural and copy number variations

A total of 2,258 cultivated and 22 *C. reticulatum* accessions (with sequence depth of greater than 10×) were used to identify structural variations against the reference genome of CDC Frontier¹¹, such as large insertions, deletions, inversions, and intra- and inter-chromosomal translocations. The insertions, deletions and inversions were identified using a dual calling strategy through BreakDancer⁴⁴ v.1.1.2 and Pindel⁴⁵ v.0.2.5b9. First, BreakDancer was used to detect structural variations with parameter “-q 20 -y 20 -r 1”. Secondly, the output of BreakDancer was used as an input for Pindel using the parameter “-x 4 -breakdancer” to increase the sensitivity and specificity. To merge the results from BreakDancer and Pindel, two structural variants with a distance between the two breakpoints of less than 100 bp were considered the same structural variation and merged. Owing to the inability of Pindel to detect intra- and inter-chromosomal translocations, only BreakDancer was used for their analysis. Furthermore, a structural variation was considered if it was present in at least 5% of the individuals in a given population.

For CNVs, we first generated a GC-content profile using gcount (<http://bioinfo-out.curie.fr/projects/freec/src/gcount.tar.gz>) with parameter “window = 1000 step = 1000” to normalize non-uniform read coverage of genomic position. Then, Control-FREEC⁴⁶ v.11.0 was used to detect CNVs in 1-kb non-overlapping windows (bins) with parameter “ploidy = 2 window = 1000 step = 1000 mateOrientation=FR” for each high-depth individual (sequencing depth > 10X). Next, the sample-level copy numbers were combined to produce a matrix of copy numbers for each bin at the cohort level. To further reduce false positives, we filtered out the bins with a CNV rate of less than 1%. The affected genes were identified by the presence of overlapping regions with CNVs.

Divergence and phylogenetic relationship

For divergence time estimation, 195 wild species accessions were assembled individually using MEGAHIT⁴⁰ v.1.2.9 with default parameters. Then, the ‘fabales’

genes were downloaded from the BUSCO¹⁷ database (odb10), which contains 5,366 single-copy orthologues to predict the genes for 195 wild species accessions, CDC Frontier genome¹¹ and *M. truncatula* genome¹⁸ (as outgroup) using GeneWise⁴⁷ v.2.4.1 with the parameters “-both -sum -genesf”. On the basis of the gene annotations of 195 wild species accessions, only one sample with the longest average coding sequence (CDS) length was chosen for each wild species. The CDS sequences of single-copy genes in seven wild species, CDC Frontier and *M. truncatula* were extracted. For each single-copy family, multiple sequence alignment was performed using MUSCLE⁴⁸ v.3.8.31 with default parameters and poorly aligned and divergent regions were eliminated using Gblocks⁴⁹ v.0.91b with the parameter “-t=c”. The aligned matrix from each single-copy family was combined to construct the super aligned matrix. The maximum likelihood tree was constructed using RAxML⁵⁰ v.8.2.12 with parameters “-f a -x 12345 -p 12345 -# 1000 -m GTRCATX”. Finally, divergence time was estimated by MCMCTree⁵¹ v.4.4 with three time-calibration points (0.007–0.013 Ma for *C. reticulatum*–*C. arietinum*, 12.2–17.4 Ma for *C. arietinum*–*C. pinnatifidum*, and 30.0–54.0 Ma for *C. arietinum*–*M. truncatula*) from the literature^{52,53,54}.

To assess the relatedness among 195 wild accessions and 3,171 cultivated lines, the genetic distance matrix based on identity by state (IBS) was calculated through PLINK v1.90 with the parameter “--distance 1-ibs” using LD-pruned SNPs (--indep-pairwise 50 10 0.2) present on pseudomolecules. On the basis of the distance matrix, neighbour-joining phylogenetic trees were then constructed using ‘neighbor’ in PHYLIP⁵⁵ v.3.6.

A PCA was undertaken to study the relatedness and clustering among cultivated chickpea accessions. The top 20 principal components (PCs) of the variance-standardized relationship matrix were estimated using EIGENSOFT⁵⁶ v.7.2.0 with default parameters on LD-pruned SNPs present on pseudomolecules. PCA results were plotted using the R package ‘rworldmap’ (ref. ⁵⁷).

Diversity and genetic bottleneck

To characterize variation among populations, population differentiation statistics (F_{ST}) were calculated in a 10-kb/2-kb sliding window using VCFtools v.0.1.13. A range of pairwise F_{ST} was calculated in the same combinations as for the ROD calculations. Tajima’s D was calculated using VCFtools (“--TajimaD 100000”) in 100-kb non-overlapping windows. A window was considered a selection window in the upper 90% of the population’s empirical distribution for ROD and F_{ST} statistics, along with a negative Tajima’s D value (less than –2). Genes located on the selection windows were identified, and functional enrichment of the KEGG pathway (v.87.0) and GO

term for these candidate genes was conducted using the Fisher's exact test with false discovery rate correction using EnrichmentPipeline⁵⁸ (<https://sourceforge.net/projects/enrichmentpipeline/>).

For determining population size histories and split times, the SMC++ programme⁵⁹ v.1.13.1 was used. Individuals with more than 20% missing data were filtered out. We built 20 random datasets of 150 genotypes. For each of the 20 datasets, SMC++ was used with a generation time of one year and a mutation rate of 6.5×10^{-9} (ref. ⁶⁰). To avoid potential bias in the estimates owing to the long run of homozygosity, we filtered out homozygous regions longer than 5 kb in the 150 samples. For each of the 20 estimations, we used 5 different combinations of distinguished lineages, as suggested previously⁵⁹. We then calculated the median of the 20 independent estimates for each time point.

SweeD (v.3.3.1) analysis was performed as previously⁶¹ on chromosomes Ca1 to Ca8. To keep calculation time and resource into reasonable burdens while staying conservative in pointing genomic regions as being likely to be under positive selection, 2 random sub-samples of 251 landraces, proportional to 2,439 landraces for each geographical region, were considered. The analysis computes in each sub-sample a CLR for each SNP along the genome. We used a grid value of 10,000 for each chromosome, corresponding roughly to computing a CLR ratio every 9 kb. We considered the highest 1% CLR values for each sample and kept them as candidate SNPs for positive selection of the positions detected in both samples. Owing to linkage disequilibrium, a high CLR value detected on an SNP can result from selection acting on a nearby gene. Therefore, we computed a list of intervals that are likely to be targeted by selection from the list of SNPs detected under selection, without pointing to particular SNPs but including all SNPs within 10 kb of each other.

Effect of nucleotide variations on protein function was predicted with SIFT 4G²¹ v.2.0.0. Putative deleterious mutations were identified with a SIFT score of less than 0.05. The *Medicago* genome was used as an outgroup to identify the derived alleles in the chickpea genome. Mutation burden was computed by counting the number of derived deleterious alleles present in constrained regions of the genome in each genotype as described before⁸.

Genome-wide association analysis

Genome-wide association study (GWAS) analysis was performed using 3.94 million genome-wide SNPs and phenotypic data generated on 16 traits for 2 seasons and 6 locations. Only biallelic SNPs in cultivated genotypes were used in the GWAS analysis. Furthermore, the filtration was done with a minor allele frequency (MAF) cut-off of 0.05, missing rate cut-off of 0.8 and heterozygosity rate of 0.1. Marker trait

association (MTA) analysis was then performed using a mixed linear model with the filtered HapMap file and phenotyping data. The first three PCs were used to control the population structure. The Manhattan plots and QQ plots were generated from the GWAS results. A *P* value of 3.16×10^{-7} was used to consider the MTA as significant.

Identification of superior haplotypes

For haplotype analysis, we retained a SNP set for 3,171 cultivated chickpea lines according to the following criteria: (i) $\text{MAF} > 0.001$; and (ii) proportion of missing calls per SNP $< 30\%$. The haplotypes present within trait-associated genes were examined and only homozygous calls were considered for haplotype analysis. The identified haplotypes were visualized in Flapjack⁶² v.1.19.09.04.

For the haplo–pheno analysis, haplotypes carrying only one genotype were removed from the analysis. The accessions were categorized on the basis of haplotype groups, and together with phenotypic data, superior haplotypes were identified⁶³. Haplotype-wise means for 100SW, days to flowering (DF) and YPP were compared to define superior haplotypes. Duncan's multiple range test was used for statistical significance.

OCS approach

We used GEBV from the genomic prediction section for key production traits (YPP, 100SW, DF and days to maturity (DM)) to generate a genomic relationship matrix based on 754,576 SNPs. We used the breeding program implementation platform MateSel v.6.3 (<http://matesel.une.edu.au>) to generate an optimized mating design within desi, kabuli and intermediate types. The relative emphasis on the mean index versus co-ancestry was set by choosing the target degrees on the response surface²⁴. We chose a target of 60 degrees to minimize the increase in population co-ancestry (maximize population genetic diversity) while achieving an acceptable rate of genetic gain. As this study aimed to maintain a diverse pre-breeding pool while making economic improvements, we followed the conservative approach for ‘evolving gene banks’ (ref. ²³).

We generated unique economic indices for desi and kabuli chickpea, which were calculated on a US\$ per ha basis and included yield (average GEBV for YPP over 9 sites) with a bonus price for large seeds (when average GEBV for 100SW over 9 sites exceeded the average for kabuli of +5.9 g) and earliness (average GEBV for DF and DM over 9 sites < 0 days). The base price for chickpea was assumed to be US\$400 per tonne, and YPP was converted to an equivalent grain yield value per hectare by assuming that the mean YPP of 18 g per plant is equivalent to 1.8 tonnes per hectare. The index was also adjusted for a price bonus for large seeds and earliness as follows. The starting values for GEBV for 100SW are low in desi candidates (mean -4.0 g) and

high in kabuli candidates (mean +5.9 g). Hence, the starting value for a price bonus for 100SW begins at GEBV + 5.9 g, and there is no bonus below this value. The price bonus per gram (GEBV 100SW > 5.9 g) is US\$35 per gram, which is added to the base price. Similarly, a bonus was provided in price per tonne for GEBV earliness (average of GEBV DF and GEBV DM). The average GEBV earliness in the desi group was -1.6 days, and in the kabuli group was +2.4 days. The starting value for a price bonus for earliness begins at average GEBV 0 days; there is a bonus for negative values of US\$10 per day added to the base price and no bonus for positive values.

Genomic prediction analyses

Prediction using the interaction of genomic and environmental covariates

As described previously²⁵, three models, a basic model (E + L) with main effects of environments (E) and lines (L), a model (E + L + G) including the main effects of markers, and a genomic by environment interaction model (E + L + G + GE) were used. Three different SNP datasets (G1, cultivated accessions; G2, wild accessions; and G3, G1 + G2) were used as a genomic matrix (G), post-conventional quality controls on missing values (<20%) and MAF (>0.05). Phenotyping data for nine traits across 12 different year × location combinations were used. The Pearson's correlation coefficient between observed phenotype and predicted genomic breeding value was used to estimate the accuracy of genomic prediction. Three different random cross-validation (CV) schemes, CV1 (evaluate the prediction accuracy of models when a certain percentage of lines are not observed in any environment), CV2 (estimates the prediction accuracy of models when some lines are evaluated in some environments but not in others) and CV0 (predicts an unobserved environment using the remaining environments as a training set) were used. CV1 and CV2 with fivefold cross-validation were implemented to generate the training and testing sets, and the prediction accuracy was assessed for each testing set. The permutation of the five subsets led to five possible training and validation datasets. This procedure was repeated 20 times, and 100 runs were performed for each trait–environment combination on each population. The same partition was used for the analysis of all the GS models. For CV0, each environment was predicted using the remaining environments. For fitting the GS models, the R package Bayesian Generalized Linear Regression (BGLR)⁶⁴ v.1.0.7 was used.

Prediction using the WhoGEM method

For WhoGEM analysis, 1,318 accessions with the validated geographical location were selected and used as a reference dataset. The SNP dataset was filtered for missing (>0.1) and MAF (<0.01) and used for a detailed search with ADMIXTURE⁶⁵

v.1.3.0 between $K = 19$ and $K = 30$ to identify the most likely number of admixture components. To confirm the admixture value, another method, DAPC (discriminant analysis of principal components), was used. The optimal number of admixture components in the WhoGEM method was obtained by comparing the predicted and recorded locations (ProvenancePredictor algorithm²⁶) and fixed to $K = 23$.

A general linear model explored the relationships between the phenotypes and admixture components, and land types. A forward–backward algorithm was used to reduce the set of predictors to the most significant ones. The model is fitted on the whole dataset, and the significant factors are identified and conserved. A negative control (a model without any genetics (called environment-only)) is also fitted to the data. The models were fitted on the whole dataset, and the significant factors were identified and conserved.

A test of WhoGEM significance is given by a likelihood ratio test comparing the WhoGEM-based model and the environment-only-based model. The performances of the three models (full WhoGEM-based model, additive and environment-only model) are then evaluated using 100–300 replicates of a fivefold cross-validation scheme.

Prediction using a haplotype-based approach

The SNP set was filtered, first by excluding all markers with more than two called alleles, missing (>10%) and MAF (<5%). A subset of 124,833 (20%) of 2.4 million high-quality SNPs were randomly selected to reduce the computational load in further analyses. Those SNPs were used to construct LD blocks and estimate local GEBVs for haplotypes of those LD blocks. Details on the method used to calculate local GEBVs for haplotypes of LD blocks are described in a previous report²⁷.

We also ran a ridge-regression best linear unbiased prediction (BLUP) model in the R-package rrBLUP (ref.⁶⁶) v.4.6.0 to predict marker effects for seven agronomic traits, then summed up the predicted allelic effects of each observed haplotype for all genome-wide LD blocks. Finally, we estimated variances among local GEBVs for haplotypes within each LD block to highlight regions in the genome showing molecular variation linked to observed phenotypic variation for the agronomic traits measured in the field trials.

Reporting summary

Further information on research design is available in the [Nature Research Reporting Summary](#) linked to this paper.

Data availability

The data that support the findings of this study have been deposited in the NCBI under accession code BioProject: [PRJNA657888](#). The chickpea pan-genome assembly and annotations developed in this study are available at <https://doi.org/10.6084/m9.figshare.16592819>. The variant calls for each accession and phenotype data are available to download at <https://cgresources.icrisat.org/cicerseq>. Manhattan and QQ-plots for GWAS analysis are available at <https://doi.org/10.6084/m9.figshare.15015309> and <https://doi.org/10.6084/m9.figshare.15015315>, respectively. [Source data](#) are provided with this paper.

References

1. 1.
McCouch, S. et al. Agriculture: feeding the future. *Nature* **499**, 23–24 (2013).
2. 2.
Varshney, R. K. et al. Resequencing of 429 chickpea accessions from 45 countries provides insights into genome diversity, domestication and agronomic traits. *Nat. Genet.* **51**, 857–864 (2019).
3. 3.
Foyer, C. H. et al. Neglecting legumes has compromised human health and sustainable food production. *Nat. Plants* **2**, 16112 (2016).
4. 4.
Upadhyaya, H. D. et al. Genomic tools and germplasm diversity for chickpea improvement. *Plant Genet. Resour.* **9**, 45–48 (2011).
5. 5.
Wang, W. et al. Genomic variation in 3,010 diverse accessions of Asian cultivated rice. *Nature* **557**, 43–49 (2018).
6. 6.
Bredeson, J. V. et al. Sequencing wild and cultivated cassava and related species reveals extensive interspecific hybridization and genetic diversity. *Nat. Biotechnol.* **32**, 562–570 (2016).

7. 7.

Thudi, M. et al. Recent breeding programs enhanced genetic diversity in both desi and kabuli varieties of chickpea (*Cicer arietinum* L.). *Sci. Rep.* **6**, 38636 (2016).

8. 8.

Ramu, P. et al. Cassava haplotype map highlights fixation of deleterious mutations during clonal propagation. *Nat. Genet.* **49**, 959–963 (2017).

9. 9.

Kremling, K. A. et al. Dysregulation of expression correlates with rare-allele burden and fitness loss in maize. *Nature* **555**, 520–523 (2018).

10. 10.

Milner, S. G. et al. Genebank genomics highlights the diversity of a global barley collection. *Nat. Genet.* **51**, 319–326 (2018).

11. 11.

Varshney, R. K. et al. Draft genome sequence of chickpea (*Cicer arietinum*) provides a resource for trait improvement. *Nat. Biotechnol.* **31**, 240–246 (2013).

12. 12.

Chattopadhyay, D. & Francis, A. A draft genome assembly of *Cicer arietinum* accession ICC4958_v3.0. *Figshare* <https://doi.org/10.6084/m9.figshare.14579274> (2021).

13. 13.

Gupta, S. et al. Draft genome sequence of *Cicer reticulatum* L., the wild progenitor of chickpea provides a resource for agronomic trait improvement. *DNA Res.* **24**, 1–10 (2017).

14. 14.

Zhao, Q. et al. Pan-genome analysis highlights the extent of genomic variation in cultivated and wild rice. *Nat. Genet.* **50**, 278–284 (2018).

15. 15.

Liu, Y. et al. Pan-genome of wild and cultivated soybeans. *Cell* **182**, 162–176 (2020).

16. 16.

Golicz, A. A. et al. The pangenome of an agronomically important crop plant *Brassica oleracea*. *Nat. Commun.* **7**, 13390 (2016).

17. 17.

Simão, F. A., Waterhouse, R. M., Ioannidis, P., Kriventseva, E. V. & Zdobnov, E. M. BUSCO: assessing genome assembly and annotation completeness with single-copy orthologs. *Bioinformatics* **31**, 3210–3212 (2015).

18. 18.

Young, N. et al. The *Medicago* genome provides insight into the evolution of rhizobial symbioses. *Nature* **480**, 520–524 (2011).

19. 19.

Pokorny, L. et al. Living on the edge: timing of Rand Flora disjunctions congruent with ongoing aridification in Africa. *Front. Genet.* **6**, 154 (2015).

20. 20.

Parker, T. A., Berny Miery Teran, J. C., Palkovic, A., Jernstedt, J. & Gepts, P. Pod indehiscence is a domestication and aridity resilience trait in common bean. *New Phytol.* **225**, 558–570 (2020).

21. 21.

Kumar, P., Henikoff, S., & Ng, P. C. Predicting the effects of coding non-synonymous variants on protein function using the SIFT algorithm. *Nat. Protoc.* **4**, 1073–1081 (2009).

22. 22.

Woolliams, J. A., Berg, P., Dagnachew, B. S. & Meuwissen, T. H. E. Genetic contributions and their optimization. *J. Anim. Breed. Genet.* **132**, 89–99 (2015).

23. 23.

Cowling, W. A. et al. Evolving gene banks: improving diverse populations of crop and exotic germplasm with optimal contribution selection. *J. Exp. Bot.* **68**, 1927–1939 (2017).

24. 24.

Kinghorn, B. P. An algorithm for efficient constrained mate selection. *Genet. Sel. Evol.* **43**, 4 (2011).

25. 25.

Jarquín, D. et al. Genotyping by sequencing for genomic prediction in a soybean breeding population. *BMC Genomics* **15**, 740 (2014).

26. 26.

Gentzbittel, L. et al. WhoGEM: an admixture-based prediction machine accurately predicts quantitative functional traits in plants. *Genome Biol.* **20**, 106 (2019).

27. 27.

Voss-Fels, K. P. et al. Breeding improves wheat productivity under contrasting agrochemical input levels. *Nat. Plants* **5**, 706–714 (2019).

28. 28.

Javadi, F., & Yamaguchi, H. Interspecific relationships of the genus *Cicer* L. (Fabaceae) based on trnT-F sequences. *Theor. Appl. Genet.* **109**, 317–322 (2004).

29. 29.

Frediani, M., & Caputo, P. Phylogenetic relationships among annual and perennial species of the genus *Cicer* as inferred from ITS sequences of nuclear ribosomal DNA. *Biol. Plant.* **49**, 47–52 (2005).

30. 30.

Bevan, M. W. et al. Genomic innovation for crop improvement. *Nature* **543**, 346–354 (2017).

31. 31.

Li, H. Aligning sequence reads, clone sequences and assembly contigs with BWA-MEM. Preprint at <http://arxiv.org/abs/1303.3997> (2013).

32. 32.

Poplin, R. et al. Scaling accurate genetic variant discovery to tens of thousands of samples. Preprint at <https://doi.org/10.1101/201178> (2017).

33. 33.

Chang, C. C. et al. Second-generation PLINK: rising to the challenge of larger and richer datasets. *GigaScience* **4**, 7 (2015).

34. 34.

McKenna, A. et al. The Genome Analysis Toolkit: a MapReduce framework for analyzing next-generation DNA sequencing data. *Genome Res.* **20**, 1297–1303 (2010).

35. 35.

Zhang, C., Dong, S. S., Xu, J. Y., He, W. M. & Yang, T. L. PopLDdecay: a fast and effective tool for linkage disequilibrium decay analysis based on variant call format files. *Bioinformatics* **35**, 1786–1788 (2019).

36. 36.

Danecek, P. et al. 1000 Genomes Project Analysis Group, the variant call format and VCFtools. *Bioinformatics* **27**, 2156–2158 (2011).

37. 37.

Chattopadhyay, D. & Francis, A. Structural annotation of the genome assembly of Cicer arietinum accession ICC4958 v3.0. *Figshare* <https://doi.org/10.6084/m9.figshare.14579274> (2021).

38. 38.

Hübner, S. et al. Sunflower pan-genome analysis shows that hybridization altered gene content and disease resistance. *Nat. Plants* **5**, 54–62 (2019).

39. 39.

Li, H. et al. The Sequence Alignment/Map format and SAMtools. *Bioinformatics* **25**, 2078–2079 (2009).

40. 40.

Li, D., Liu, C. M., Luo, R., Sadakane, K. & Lam, T. W. MEGAHIT: an ultra-fast single-node solution for large and complex metagenomics assembly via succinct de Bruijn graph. *Bioinformatics* **31**, 1674–1676 (2015).

41. 41.

Kurtz, S. et al. Versatile and open software for comparing large genomes. *Genome Biol.* **5**, R12 (2004).

42. 42.

Li, W. & Godzik, A. Cd-hit: a fast program for clustering and comparing large sets of protein or nucleotide sequences. *Bioinformatics* **22**, 1658–1659 (2006)

43. 43.

Camacho, C. et al. BLAST+: architecture and applications. *BMC Bioinformatics* **10**, 421 (2009).

44. 44.

Chen, K. et al. BreakDancer: an algorithm for high-resolution mapping of genomic structural variation. *Nat. Methods* **6**, 677–681 (2009).

45. 45.

Ye, K., Schulz, M. H., Long, Q., Apweiler, R. & Ning, Z. Pindel: a pattern growth approach to detect break points of large deletions and medium sized insertions from paired-end short reads. *Bioinformatics* **25**, 2865–2871 (2009).

46. 46.

Boeva, V. et al. Control-FREEC: a tool for assessing copy number and allelic content using next-generation sequencing data. *Bioinformatics* **28**, 423–425 (2011).

47. 47.

Birney, E., Clamp, M. & Durbin, R. GeneWise and genomewise. *Genome Res.* **14**, 988–995 (2004).

48. 48.

Edgar, R. C. MUSCLE: a multiple sequence alignment method with reduced time and space complexity. *BMC Bioinformatics* **5**, 113 (2004).

49. 49.

Castresana, J. Selection of conserved blocks from multiple alignments for their use in phylogenetic analysis. *Mol. Biol. Evol.* **17**, 540–552 (2000).

50. 50.

Stamatakis, A. RAxML-VI-HPC: maximum likelihood-based phylogenetic analyses with thousands of taxa and mixed models. *Bioinformatics* **22**, 2688–2690 (2006).

51. 51.

Yang, Z. PAML 4: phylogenetic analysis by maximum likelihood. *Mol. Biol. Evol.* **24**, 1586–1591 (2007).

52. 52.

Lavin, M., Herendeen, P. S., & Wojciechowski, M. F. Evolutionary rates analysis of Leguminosae implicates a rapid diversification of lineages during the tertiary. *Syst. Biol.* **54**, 575–594 (2005).

53. 53.

Redden, R. J. & Berger, J. D. in *Chickpea Breeding and Management* (eds. Yadav, S. S. et al.) 1–13 (C.A.B. International, 2007).

54. 54.

Kumar, S., Stecher, G., Suleski, M., & Hedges, S. B. TimeTree: a resource for timelines, timetrees, and divergence times. *Mol. Biol. Evol.* **34**, 1812–1819 (2017).

55. 55.

Felsenstein, J. PHYLIP—Phylogeny Inference Package (version 3.2). *Cladistics* **5**, 164–166 (1989).

56. 56.

Price, A. L. et al. Principal components analysis corrects for stratification in genome-wide association studies. *Nat. Genet.* **38**, 904–909 (2006).

57. 57.

South, A. rworldmap: a new r package for mapping global data. *R J.* **3**, 35–43 (2011).

58. 58.

Huang da, W., Sherman, B. T. & Lempicki, R. A. Bioinformatics enrichment tools: paths toward the comprehensive functional analysis of large gene lists. *Nucleic Acids Res.* **37**, 1–13 (2009).

59. 59.

Terhorst, J., Kamm, J. A. & Song, Y. S. Robust and scalable inference of population history from hundreds of unphased whole genomes. *Nat. Genet.* **49**, 303–309 (2017).

60. 60.

Gaut, B. S., Morton, B. R., McCaig, B. C. & Clegg, M. T. Substitution rate comparisons between grasses and palms: synonymous rate differences at the nuclear gene *Adh* parallel rate differences at the plastid gene *rbcL*. *Proc. Natl Acad. Sci. USA* **93**, 10274–10279 (1996).

61. 61.

Pavlidis, P., Živković, D., Stamatakis, A. & Alachiotis, N. SweeD: likelihood-based detection of selective sweeps in thousands of genomes. *Mol. Biol. Evol.* **30**, 2224–2234 (2013).

62. 62.

Milne, I. et al. Flapjack—graphical genotype visualization. *Bioinformatics* **26**, 3133–3134 (2010).

63. 63.

Sinha, P. et al. Superior haplotypes for haplotype based breeding for drought tolerance in pigeonpea (*Cajanus cajan* L.). *Plant Biotechnol. J.* **18**, 2482–2490 (2020).

64. 64.

Pérez, P. & de los Campos, G. Genome-wide regression and prediction with the BGLR statistical package. *Genetics* **198**, 483–495 (2014).

65. 65.

Alexander, D. H. & Lange, K. Enhancements to the ADMIXTURE algorithm for individual ancestry estimation. *BMC Bioinf.* **12**, 246 (2011).

66. 66.

Endelman, J. B. Ridge regression and other kernels for genomic selection with R package rrBLUP. *Plant Genome* **4**, 250–255 (2011).

Acknowledgements

R.K.V. acknowledges funding support in part from the Department of Agriculture and Farmers' Welfare, Ministry of Agriculture and Farmers' Welfare; Department of Biotechnology, Ministry of Science and Technology under the Indo- Australian Biotechnology Fund, Government of India, and the Bill & Melinda Gates Foundation; X.L. acknowledges the National Key R&D Program of China (2019YFC1711000), the Shenzhen Municipal Government of China (JCYJ20170817145512476) and the Guangdong Provincial Key Laboratory of Genome Read and Write (2017B030301011); E.L. thanks the National Science Foundation for funding CyVerse work (DBI-0735191, DBI-1265383 and DBI-1743442); and R.K.V. and W.A.C. thank B. Kinghorn for providing access to MateSel software and for help with OCS in this paper. We also thank S. Abbo and M. W. Bevan for their inputs while we were preparing the manuscript; M. Caccamo for constructive criticism and suggestions to improve the quality of the manuscript; and DivSeek International Network and its members, especially S. McCouch for useful discussions related to ‘The 3000 Chickpea Genome Sequencing Initiative’.

Author information

Affiliations

1. Center of Excellence in Genomics and Systems Biology, International Crops Research Institute for the Semi-Arid Tropics (ICRISAT), Hyderabad, India

Rajeev K. Varshney, Manish Roorkiwal, Prasad Bajaj, Annapurna Chitikineni, Mahendar Thudi, Aamir W. Khan, Vanika Garg, Vinod Kumar Valluri, Pallavi Sinha, Vikas K. Singh, Abhishek Rathore, Muneendra K. Singh & Himabindu Kudapa

2. State Agricultural Biotechnology Centre, Centre for Crop and Food Innovation, Murdoch University, Murdoch, Western Australia, Australia

Rajeev K. Varshney

3. BGI-Qingdao, BGI-Shenzhen, Qingdao, China

Shuai Sun, Xiao Du, Yue Wang & Guangyi Fan

4. China National GeneBank, BGI-Shenzhen, Shenzhen, China

Shuai Sun, Xiao Du, Yue Wang & Guangyi Fan

5. College of Life Sciences, University of Chinese Academy of Sciences, Beijing, China

Shuai Sun

6. Institute of Crop Germplasm Resources, Shandong Academy of Agricultural Sciences (SAAS), Jinan, China

Mahendar Thudi

7. ICAR–Indian Institute of Pulses Research, Kanpur, India

Narendra P. Singh, Khela Ram Soren & Girish Prasad Dixit

8. Genebank, ICRISAT, Hyderabad, India

Hari D. Upadhyaya

9. University of Georgia, Athens, GA, USA

Hari D. Upadhyaya

10. BGI-Shenzhen, Shenzhen, China

Guangyi Fan, Huanming Yang, Xun Xu & Xin Liu

11. State Key Laboratory of Agricultural Genomics, BGI-Shenzhen, Shenzhen, China

Guangyi Fan, Huanming Yang, Jian Wang & Xin Liu

12. The UWA Institute of Agriculture, and School of Agriculture and Environment, The University of Western Australia, Perth, Western Australia, Australia

Wallace A. Cowling, David Edwards & Kadambot H. M. Siddique

13. Biometrics and Statistics Unit, International Maize and Wheat Improvement Center (CIMMYT), Texcoco, Mexico

José Crossa

14. Digital Agriculture Laboratory, Skolkovo Institute of Science and Technology, Moscow, Russia

Laurent Gentzbittel & Cécile Ben

15. Queensland Alliance for Agriculture and Food Innovation, The University of Queensland, St Lucia, Queensland, Australia

Kai Peter Voss-Fels, Lee T. Hickey & Ben J. Hayes

16. International Rice Research Institute (IRRI), South-Asia Hub, ICRISAT, Hyderabad, India

Pallavi Sinha & Vikas K. Singh

17. Laboratoire Ecologie Fonctionnelle et Environnement, Université de Toulouse, CNRS, Toulouse, France

Cécile Ben

18. Institute for Genomic Diversity, Cornell University, Ithaca, NY, USA

Ramu Punna

19. Department of Plant Sciences, University of Saskatchewan, Saskatoon, Saskatchewan, Canada

Bunyamin Tar'an & Amit A. Deokar

20. ICAR–Indian Agricultural Research Institute (IARI), New Delhi, India

Chellapilla Bharadwaj

21. Rajmata Vijayaraje Scindia Krishi Vishwa Vidyalaya, Gwalior, India

Mohammad Yasin

22. Junagadh Agricultural University, Junagadh, India

Motisagar S. Pithia

23. Rajasthan Agricultural Research Institute (RARI), Durgapura, India

Servejeet Singh

24. Department of Agronomy and Horticulture, University of Nebraska–Lincoln, Lincoln, NE, USA

Diego Jarquín

25. DIADE (Diversity-Adaptation-Development of Plants), Université de Montpellier, Institut de Recherche pour le Développement (IRD), Montpellier, France

Philippe Cubry, Anne-Céline Thuillet & Yves Vigouroux

26. International Centre for Agricultural Research in the Dry Areas (ICARDA), Cairo, Egypt

Aladdin Hamwieh

27. International Centre for Agricultural Research in the Dry Areas (ICARDA), Rabat, Morocco

Shiv Kumar

28. Rani Lakshmi Bai Central Agricultural University, Jhansi, India

Sushil K. Chaturvedi

29. National Institute of Plant Genome Research, New Delhi, India

Aleena Francis & Debasis Chattopadhyay

30. Department of Statistics, University of Nebraska–Lincoln, Lincoln, NE, USA

Réka Howard

31. School of Plant Sciences, University of Arizona, Tucson, AZ, USA

Eric Lyons

32. Department of Plant and Soil Science, University of Vermont, Burlington, VT, USA

Eric von Wettberg

33. University of Calcutta, Kolkata, India

Swapan K. Datta

34. Guangdong Provincial Academician Workstation of BGI Synthetic Genomics, BGI-Shenzhen, Shenzhen, China

Huanming Yang

35. Division of Plant Sciences, University of Missouri, Columbia, MO, USA

Henry T. Nguyen

36. James D. Watson Institute of Genome Science, Hangzhou, China

Huanming Yang & Jian Wang

37. Indian Council of Agricultural Research (ICAR), New Delhi, India

Trilochan Mohapatra

38. Department of Genetics, University of Georgia, Athens, USA

Jeffrey L. Bennetzen

39. Guangdong Provincial Key Laboratory of Genome Read and Write, BGI-Shenzhen, Shenzhen, China

Xun Xu

40. BGI-Beijing, BGI-Shenzhen, Beijing, China

Xin Liu

41. BGI-Fuyang, BGI-Shenzhen, Fuyang, China

Xin Liu

Contributions

R.K.V. conceived and designed the experiments. R.K.V. and X.L. coordinated the genome data analysis. R.K.V. and A.C. coordinated the sequencing. M.R., A.C., M.T., N.P.S., H.D.U., M.K.S., M.Y., M.S.P., S. Singh, K.R.S., G.P.D., A.H., S.K. and S.K.C. performed the laboratory and field experiments. R.K.V., M.R., S. Sun., P.B., M.T., N.P.S., X.D., A.W.K., Y.W., V.G., G.F., W.A.C., J.C., L.G., K.P.V.-F., V.K.V., P.S., V.K.S., C. Ben, R.P., C. Bharadwaj, H.K., L.T.H., A.A.D., D.E., Y.V., B.J.H., E.v.W., S.K.D., H.T.N., K.H.M.S., T.M., J.L.B., X.X. and X.L. analysed the data. S. Sun., P.B., X.D., A.W.K., Y.W., V.G., G.F., W.A.C., J.C., L.G., K.P.V.-F., P.S., V.K.S., C. Ben., A.R., D.J., P.C., A.-C.T., R.H., Y.V. and X.L. performed statistical analysis. R.K.V., A.C., N.P.S., H.D.U., B.T., G.P.D., E.L., S.K.D., D.C., A.F., H.Y., J.W., T.M., X.X. and X.L. contributed to the reagents, materials and analysis tools. R.K.V., M.R., P.B., M.T., W.A.C., J.C., L.G., K.P.V.-F., Y.V., K.H.M.S., J.L.B. and X.L. wrote the manuscript. All authors read and approved the manuscript.

Corresponding authors

Correspondence to [Rajeev K. Varshney](#) or [Xin Liu](#).

Ethics declarations

Competing interests

The authors declare no competing interests.

Additional information

Peer review information *Nature* thanks Mario Caccamo and the other, anonymous, reviewers for their contribution to the peer review of this work.

Publisher's note Springer Nature remains neutral with regard to jurisdictional claims in published maps and institutional affiliations.

Extended data figures and tables

Extended Data Fig. 1 Phylogeny-based clustering.

Phylogenetic tree represents clustering of individuals, represented through respective tracks (from inside to outside), Track 1: Biological status; Track 2: Market class; and Track 3: Geographical regions. A clear outgroup of wild accessions is observed.

Extended Data Fig. 2 Linkage disequilibrium decay observed among cultivated chickpea genotypes.

(a) Rapid LD decay was observed in landraces (315 kb) based biological status followed by breeding lines (370 kb) and cultivars (670 kb). (b) Similar LD decay rate was observed among population based on market class, namely desi (340 kb), intermediate (330 kb) and kabuli (330 kb). (c) Among seven geographic populations, genotypes from Black Sea (352 kb) had lowest rate of LD decay followed by Central Asia (330 kb), Middle East (350 kb), South Asia (355 kb), Mediterranean (365 kb) and Americas (370 kb). The population East Africa had much slower LD decay compared to other population based geographic regions. (d) Cultivated accessions from countries Turkey (306.51 kb), Syria (316.22 kb) and Iran (320.61 kb) had more rapid decline of LD decay compared to cultivated accessions from other countries, indicating more recombination events and haplotype diversity/number.

Extended Data Fig. 3 Cicer species evolution.

(a) Speciation and divergence time for eight species in the genus *Cicer*. The maximum likelihood phylogenetic tree showed clear out-grouping of *C. cuneatum* from the other *Cicer* species and *C. reticulatum* being nearest to the cultivated chickpea species (*C. arietinum*). Three time-calibration points (0.007- 0.013 Ma for *C. reticulatum-C. arietinum*, 12.2-17.4 Ma for *C. arietinum-C. pinnatifidum*, and 30.0-54.0 Ma for *C. arietinum-M. truncatula*) were used for estimating divergence time. The nearest wild species (*C. reticulatum* and *C. echinospermum*) related to the cultivated *C. arietinum* were estimated to be diverged from other *Cicer* species around ~15.3 (14.0-16.2) Ma. (b) Genetic diversity among wild species accessions. Phylogenetic tree constructed based on SNPs grouped 195 wild species accessions into six clusters. A clear grouping for accessions of *C. judiacum*, *C. yamashitae* and *C. cuneatum* was observed in Cluster III, Cluster V and Cluster VI, respectively. However, ICC 20168 (one *C. pinnatifidum* accession; red colour) grouped along with *C. bijugum* accessions in Cluster II; similarly, ICC20167 (one *C. bijugum* accession; blue colour) grouped along with *C. pinnatifidum* accessions in Cluster I. Cluster III and Cluster IV were divided into two sub-clusters each, in which both sub-clusters of Cluster III possessed all accessions of *C. judiacum*. In Cluster IVa we observed grouping of all *C. reticulatum* accessions except one *C. echinospermum* accession (ICC 20192; green colour);

similarly, in Cluster IVb one accession of *C. reticulatum* (ICC 73071; golden-yellow colour) grouped along with *C. echinospermum* accessions.

Extended Data Fig. 4 Phylogenetic tree based on *FST*.

Accessions from Mediterranean region, Middle East, Americas and Black Sea regions were clustered together, and South Asia as a separate cluster.

Extended Data Fig. 5 Relationship route of chickpea diffusion and seed morphology.

(a) PCA analysis for landraces. (b) Distance to the most extreme cultivated sample (closest to wild relatives) were plotted on the map. (c, d) For landraces with large seed morphology (kabuli; c) and small seed morphology (desi; d) indicated that small seed was mainly found in East-Asia, South-East Asia and Africa. These suggest large and small seeds were selected independently during chickpea diffusion of agriculture. (e) PCA results summarised a Central Asian diffusion alongside a Mediterranean diffusion, and a South Asian diffusion associated with the diffusion to East Africa.

Extended Data Fig. 6 Composite likelihood ratio values along the chickpea genome and inference of past evolution of effective size.

The composite likelihood ratio for chromosomes 1 to 8 on the x axis is computed for two random subsets of 251 individuals: subset 1 (a) and subset 2 (b). Horizontal grey line shows the threshold above which the highest 1% CLR values are found. (c) Using sequentially markovian coalescent as implemented in SMC++ (Terhorst et al. 2017), we reconstructed the past history of effective size for 20 sets of 150 randomly chosen cultivated genotypes (thin lines). We computed at each time point the median of the estimated histories and plotted it (bold lines). Focus was made for the plotting on timeframe 100 – 20,000 generations ago. Both x and y axes are log-scaled.

Extended Data Fig. 7 Neighbour-joining trees constructed using SNPs present on the pseudomolecules indicates a clear out-grouping of wild species accessions from cultivated accessions.

The cultivated accessions formed three distinct clusters. One landrace from East Africa (ICC 16369) (red arrow) grouped together with wild species accessions.

Extended Data Fig. 8 Genetic loads in chickpea.

a) A snapshot of steps and parameters used to estimate the mutation burden and fixed deleterious alleles. b) Variant annotation using SIFT revealed higher non-synonymous mutations, of which non-synonymous deleterious variants were used to identify deleterious mutations. c) Mutation burden analysis indicated a 17.88% decrease (two-tailed Welch's t-test; $t = 2.525$, $df = 27$, $p = 0.01772$, CI = 95%) in mutation burden in cultivated ($n = 2987$) as compared to progenitor (*C. reticulatum*; $n = 28$). d) Mutation burden for genomic regions under selection showed that landraces ($n = 2439$) contained 206.91% higher (two-tailed Welch's t-test, $t = -17.087$, $df = 1645$, $p = 2.195676 \times 10^{-60}$, CI = 95%) deleterious mutations than breeding lines ($n = 396$). The black solid dots in box plots represent mean values for the respective population. Each of the box plots shows the upper and lower whisker, the 25% and 75% quartiles, the median (as solid line) and the mean (black dot)

[Source data.](#)

Extended Data Fig. 9 Towards developing tailored chickpea with superior haplotypes for yield and related traits.

(a) Representative desi and kabuli chickpea plant (on left) carrying inferior haplotype combination for key traits including 100 seed weight (100SW), days to maturity (DM), plant height (PLHT), pods per plant (PPP), and plot yield (PY). Target desi and kabuli chickpea plant (on right) carrying superior haplotype for 100SW, DM, PLHT, PPP and PY. New breeding lines can be developed by introgressing the superior haplotype combination through haplotype-based breeding. (b) Comparison of average performance among RP1 vs RP2 vs RP3 varieties for 100SW at Patancheru location. An increase in 100SW between the varieties of RP1 vs RP3 was observed, whereas no differences were observed in the case of RP1 vs RP2 and RP2 vs RP3 varieties (datasets of ICRISAT 2014-15 and 2015-16). RP1 indicates chickpea varieties released before 1993, RP2 indicates chickpea varieties released between 1993-2002 and RP3 indicates chickpea varieties released after 2002. (c) Comparison of RP2 and RP3 varieties for 100SW (with and without superior haplotypes) for six locations. A difference between lines carrying the superior haplotypes (RP3+SP) for 100SW was observed in comparison to those which did not (RP3-SP and RP2-SP) except for the Durgapura location. However, marked differences were also observed between the RP3-SP and RP2-SP lines, except for Patancheru and Amlaha locations. RP3+SP indicates RP3 varieties with superior haplotypes, RP3-SP indicates RP3 varieties without 100SW superior haplotype and RP-SP indicates RP2 varieties without 100SW superior haplotype. RP2 indicates chickpea varieties released between 1993-2002 and RP3 indicates chickpea varieties released after 2002.

Extended Data Fig. 10 Response to OCS based on mating allocation for candidate parents and predicted cycle 1 progeny family means in

economic index.

Index increased from parents to cycle 1 progeny in the kabuli group by US\$274/ha, and in the desi group by US\$94/ha, and reflects the high value of large seeds in the kabuli group. Arrows indicate the population mean GEBVs for desi (green), kabuli (orange) and intermediate (blue) groups. (a) Response to selection for candidate parents. (b) Response to selection for predicted cycle 1 progeny family. (c, d) Response to OCS among desi, kabuli and Intermediate accessions is shown for genomic estimated breeding values (GEBVs) for yield per plant (YPP, g). YPP increased by 0.6 g (4.5%) above the average candidate parent YPP (13.2 g) in the desi group, and by 0.4 g (3.3%) above the average candidate parent yield (12.2 g) in the kabuli group. Arrows indicate the population mean GEBVs for desi (green), kabuli (orange) and intermediate (blue) groups. (c) candidate parents. (d) predicted cycle 1 progeny family. (e, f) Response to OCS for GEBVs for 100 seed weight (100SW, g). 100SW increased by 2.0 g (12.7%) above the average candidate parent 100SW (15.0 g) in the desi group, and by 5.7 g (22.9%) above the average candidate parent 100SW (24.9 g) in the kabuli group. Arrows indicate the population mean GEBVs for desi (green), kabuli (orange) and intermediate (blue) groups. (e) candidate parents. (f) predicted cycle 1 progeny family. (g, h) Response to OCS for GEBVs for days to flower (DF). DF decreased by 3.3 d (-4.7%) below the average candidate parent DF (68.6 d) in the desi group, and by 1.0 d (-1.4%) below the average candidate parent DF (72.3 d) in the kabuli group. Arrows indicate the population mean GEBVs for desi (green), kabuli (orange) and intermediate (blue) groups. (g) candidate parents. (h) predicted cycle 1 progeny family. (i) Predicted average inbreeding (F) in cycle 1 progeny in among desi, kabuli and intermediate accessions. Progeny inbreeding increased by 0.170 in the kabuli group, by 0.025 in the desi group, and by 0.015 in intermediate group. Arrows indicate the population mean GEBVs for desi (green), kabuli (orange) and intermediate (blue) groups.

Extended Data Fig. 11 WhoGEM prediction accuracies for different traits in different sites.

A general linear model was used for predicting performance in selected (with a geolocation) 1,318 cultivated chickpea accessions. At each site, 200 replicates of a fivefold cross-validation scheme are applied to estimate the accuracies of WhoGEM model (phenotype as a function of admixture components and market class) compared to environment-only model i.e. a model without genetic effects. Tests of WhoGEM significance are given by likelihood ratio tests between the WhoGEM-based models and the environment-only-based model. Phenology traits: (a) days to flowering (DF), (b) days to maturity (DM), (c) plant height (PLHT) and (d) plant stand (PLST); Production traits: (e) pods per plant (PPP), (f) 100 seed weight (100SW), (g) plot yield (PY) and (h) yield per plant (YPP) and Plant architecture traits: (i) apical primary

branch (APB), (j) apical secondary branch (ASB), (k) basal primary branch (BPB), (l) basal secondary branch (BSB), and (m) tertiary branch (TB). Each of the box plots shows the upper and lower whisker, the 25% and 75% quartiles and the median (as solid line) of the fold change ($n = 1,318$ cultivated accessions).

[Source data.](#)

Extended Data Fig. 12 Assessment of trait improvement potential by stacking the superior haplotypes for target traits.

The genotypes were classified into three different groups (cultivars (CV, $n = 152$); breeding lines (BL, $n = 396$) and landraces (LR, $n = 2,439$)) and these genotypes were grouped in three subgroups s1 (CV), s2 (CV+BL) and s3 (CV+BL+LR). Local GEBVs for haplotypes were calculated by firstly grouping SNP markers based on their pairwise linkage disequilibrium, and then summing up allele effects for each haplotype of each block. The best possible genotype for each trait was generated in silico by adding up the best haplotypes across the whole genome. This in silico genotype was then compared to the accession with the highest GEBV. Each of the box plots shows the upper and lower whisker (indicated by dashed lines), the 25% and 75% quartiles and the median (as solid line)

[Source data.](#)

Extended Data Table 1 Summary of genome diversity features

Supplementary information

Supplementary Information

This file contains Supplementary Notes and References – see contents page for details.

Reporting Summary

Supplementary Data 1

Supplementary Data 2

Supplementary Data 3

Supplementary Data 4

[**Supplementary Data 5**](#)

[**Supplementary Data 6**](#)

[**Supplementary Data 7**](#)

[**Supplementary Data 8**](#)

[**Supplementary Data 9**](#)

[**Supplementary Data 10**](#)

Source data

[**Source Data Fig. 1**](#)

[**Source Data Fig. 3**](#)

[**Source Data Extended Data Fig. 8**](#)

[**Source Data Extended Data Fig. 11**](#)

[**Source Data Extended Data Fig. 12**](#)

Rights and permissions

Open Access This article is licensed under a Creative Commons Attribution 4.0 International License, which permits use, sharing, adaptation, distribution and reproduction in any medium or format, as long as you give appropriate credit to the original author(s) and the source, provide a link to the Creative Commons license, and indicate if changes were made. The images or other third party material in this article are included in the article's Creative Commons license, unless indicated otherwise in a credit line to the material. If material is not included in the article's Creative Commons license and your intended use is not permitted by statutory regulation or exceeds the permitted use, you will need to obtain permission directly from the copyright holder. To view a copy of this license, visit <http://creativecommons.org/licenses/by/4.0/>.

[**Reprints and Permissions**](#)

About this article

Cite this article

Varshney, R.K., Roorkiwal, M., Sun, S. *et al.* A chickpea genetic variation map based on the sequencing of 3,366 genomes. *Nature* **599**, 622–627 (2021).
<https://doi.org/10.1038/s41586-021-04066-1>

- Received: 15 October 2020
- Accepted: 28 September 2021
- Published: 10 November 2021
- Issue Date: 25 November 2021
- DOI: <https://doi.org/10.1038/s41586-021-04066-1>

Share this article

Anyone you share the following link with will be able to read this content:

[Get shareable link](#)

Sorry, a shareable link is not currently available for this article.

[Copy to clipboard](#)

Provided by the Springer Nature SharedIt content-sharing initiative

[A variation map](#)

- Jun Lyu

Research Highlight 10 Nov 2021

This article was downloaded by **calibre** from <https://www.nature.com/articles/s41586-021-04066-1>

- Article
- Open Access
- [Published: 18 October 2021](#)

Exome sequencing and analysis of 454,787 UK Biobank participants

- [Joshua D. Backman](#)¹,
- [Alexander H. Li](#)¹,
- [Anthony Marcketta](#)¹,
- [Dylan Sun](#)¹,
- [Joelle Mbatchou](#)¹,
- [Michael D. Kessler](#)¹,
- [Christian Benner](#)¹,
- [Daren Liu](#)¹,
- [Adam E. Locke](#) ORCID: orcid.org/0000-0001-6227-198X¹,
- [Suganthi Balasubramanian](#)¹,
- [Ashish Yadav](#)¹,
- [Nilanjana Banerjee](#)¹,
- [Christopher E. Gillies](#)¹,
- [Amy Damask](#)¹,
- [Simon Liu](#)¹,
- [Xiaodong Bai](#)¹,
- [Alicia Hawes](#)¹,
- [Evan Maxwell](#)¹,
- [Lauren Gurski](#)¹,
- [Kyoko Watanabe](#) ORCID: orcid.org/0000-0002-3303-8860¹,
- [Jack A. Kosmicki](#)¹,
- [Veera Rajagopal](#)¹,
- [Jason Mighty](#)¹,
- [Regeneron Genetics Center](#),
- [DiscovEHR](#),
- [Marcus Jones](#)¹,
- [Lyndon Mitnaul](#)¹,
- [Eli Stahl](#)¹,

- [Giovanni Coppola](#) [ORCID: orcid.org/0000-0003-2105-1061¹](#),
- [Eric Jorgenson](#) [ORCID: orcid.org/0000-0002-5829-8191¹](#),
- [Lukas Habegger¹](#),
- [William J. Salerno¹](#),
- [Alan R. Shuldiner¹](#),
- [Luca A. Lotta¹](#),
- [John D. Overton¹](#),
- [Michael N. Cantor](#) [ORCID: orcid.org/0000-0002-1074-1203¹](#),
- [Jeffrey G. Reid](#) [ORCID: orcid.org/0000-0001-8645-4713¹](#),
- [George Yancopoulos¹](#),
- [Hyun M. Kang¹](#),
- [Jonathan Marchini](#) [ORCID: orcid.org/0000-0003-0610-8322^{1 na1}](#),
- [Aris Baras](#) [ORCID: orcid.org/0000-0002-6830-3396^{1 na1}](#),
- [Gonçalo R. Abecasis](#) [1 na1](#) &
- [Manuel A. R. Ferreira](#) [ORCID: orcid.org/0000-0001-9059-1825^{1 na1}](#)

Nature volume **599**, pages 628–634 (2021)

- 28k Accesses
- 2 Citations
- 314 Altmetric
- [Metrics details](#)

Subjects

- [Genetics research](#)
- [Genome-wide association studies](#)
- [Rare variants](#)
- [Sequencing](#)

Abstract

A major goal in human genetics is to use natural variation to understand the phenotypic consequences of altering each protein-coding gene in the genome. Here we used exome sequencing¹ to explore protein-altering variants and their consequences in 454,787 participants in the UK Biobank study². We identified 12 million coding variants, including around 1 million loss-of-function and around 1.8 million deleterious missense variants. When these were tested for association with 3,994

health-related traits, we found 564 genes with trait associations at $P \leq 2.18 \times 10^{-11}$. Rare variant associations were enriched in loci from genome-wide association studies (GWAS), but most (91%) were independent of common variant signals. We discovered several risk-increasing associations with traits related to liver disease, eye disease and cancer, among others, as well as risk-lowering associations for hypertension (*SLC9A3R2*), diabetes (*MAP3K15*, *FAM234A*) and asthma (*SLC27A3*). Six genes were associated with brain imaging phenotypes, including two involved in neural development (*GBE1*, *PLD1*). Of the signals available and powered for replication in an independent cohort, 81% were confirmed; furthermore, association signals were generally consistent across individuals of European, Asian and African ancestry. We illustrate the ability of exome sequencing to identify gene–trait associations, elucidate gene function and pinpoint effector genes that underlie GWAS signals at scale.

[Download PDF](#)

Main

A major goal in human genetics is to use natural variation to understand the consequences of altering each protein-coding gene in the genome. Towards that goal, the UK Biobank (UKB) Exome Sequencing Consortium¹ sequenced the exomes of 454,787 UKB participants (Supplementary Table 1), with 95.8% of targeted bases covered at a depth of 20 \times or greater, as previously described^{1,3}. We identified 12.3 million variants in 39 million base pairs across the coding regions of 18,893 genes (Table 1), of which 99.6% were rare variants (minor allele frequency (MAF) < 1% across all ancestries). This catalogue exceeds by about 1.3-fold the coding variation contained in the combined TOPMed⁴ and gnomAD⁵ datasets (9.5 million autosomal variants), and by about 8-fold the coding variation accessible in the UKB through imputation (1.6 million autosomal variants with info score > 0.3; Supplementary Table 2). Among the variants identified were 3,457,173 (median of 10,273 per individual) synonymous, 7,878,586 (9,292 per individual) missense and 915,289 (214 per individual) putative loss-of-function (pLOF) variants (Table 1), of which about half were observed only once in this dataset (singleton variants; Supplementary Fig. 1). About 23% (1,789,828) of missense variants were predicted to be deleterious by 5 prediction algorithms (see [Methods](#); henceforth ‘deleterious missense variants’). This unique catalogue of coding variation, combined with the large sample size and thousands of available phenotypes, provides a unique opportunity to assess gene function at a large scale.

Table 1 Number of coding variants discovered in exome sequencing data from 454,787 participants in the UK Biobank

Association studies of rare variants

GWAS often do not elucidate gene function per se because (i) most protein-coding variants are not accessible through imputation (Supplementary Table 3); and (ii) it is not straightforward to identify the specific genes and mechanisms that underlie associations with common non-coding variants⁶. To illustrate the potential to elucidate gene function through analysis of whole-exome sequencing (WES) data, we tested the association between rare pLOF and deleterious missense variants and 3,994 health-related traits measured in participants in the UKB study (Supplementary Data 1). This included 3,702 binary traits with at least 100 cases and 292 quantitative traits from a variety of domains, including anthropometry, biochemistry and haematology (Supplementary Table 4). About half of the binary traits were uncommon, with a population prevalence between 0.1% and 1% (Supplementary Fig. 2). Association analyses were performed using the whole-genome regression approach implemented in REGENIE⁷, which accounts for relatedness, population structure and polygenicity and uses a fast, approximate Firth regression approach for binary outcomes. Variants were tested individually and on aggregate, through gene burden tests that group protein-altering variants within each gene.

We first analysed WES data from individuals of European ancestry ($n = 430,998$; around 95% of the total sample size), focusing on pLOF (including stop-gain, frameshift, stop-lost, start-lost and essential splice variants) and deleterious missense variants with a MAF of up to 1%. We tested for association between each trait and individual variants in 18,811 genes, as well as with aggregations of variants in each gene, considering either pLOF or pLOF and deleterious missense variants jointly. Overall, we performed a total of around 2.3 billion association tests (Supplementary Table 5), with no evidence for a substantial effect of population structure or unmodelled relatedness on the results (Supplementary Figs. 3, 4). We found 8,865 significant associations—Involving 564 genes, 492 traits and 2,283 gene–trait pairs (Extended Data Fig. 1)—at $P \leq 2.18 \times 10^{-11}$, which corresponds to a Bonferroni correction for multiple testing (that is, $P \leq 0.05/2.3$ billion tests; at this threshold, <0.05 association signals expected by chance across the full result set). As we show later, 8,059 (91%) of these associations could not be explained by linkage disequilibrium (LD) with nearby common variants and, furthermore, 81% of associations available and powered for replication were confirmed in an independent but smaller cohort of $n = 133,370$ individuals (DiscovEHR cohort). All 8,865 associations are provided in Supplementary Data 2, as well as two non-redundant sets that were obtained by retaining only the most significant signals: (i) per gene–trait pair (2,283 signals; filtered view in Supplementary Data 2); or (ii) per gene (564 signals; Supplementary Table 6). Of the 564 lead gene associations, 415 were due to a burden signal (which typically aggregated single-nucleotide polymorphisms (SNPs) and indels) and 149 were due to an individual rare variant. Of these 149, 20 represented

association with an indel variant and 129 represented association with a single-nucleotide variant (SNV) (Supplementary Table 6). Gene targets of drugs approved by the Food and Drug Administration were 3.6-fold more common among the associated genes (36 of 564, or 6.4%; Supplementary Table 6) than in the remaining genes (345 of 18,317, or 1.9%; Fisher's exact test $P = 1.7 \times 10^{-9}$).

The large number of associations identified provides an opportunity to understand the phenotypic consequences of protein-altering variation in humans and identify therapeutic targets. As it is not possible to exhaustively describe all novel gene associations, we instead highlight examples selected from four broad groups of variants: (i) singleton variants; (ii) risk lowering variants; (iii) variants with a beneficial effect on a quantitative trait; and (iv) variants likely to be of somatic origin. These groupings illustrate the value of the UKB exome resource and the potential of our data to power further discovery and analyses.

Associations with singleton variants

We first focused on 69 signals that were discovered when considering a burden of singleton variants, which represent the rarest class of variation and remain well beyond the reach of genotyping arrays and imputation using existing reference panels. Association of a phenotype with the burden of singletons in a gene represents one of the most compelling ways for human genetics to implicate a gene in disease⁸. Each of the 69 genes was associated with an average of 5.7 (mostly correlated) traits, resulting in a total of 393 associations (4.4% of the total; Supplementary Data 2). To our knowledge, 15 of these 69 gene associations have not been previously described (Extended Data Table 1), of which we highlight 2. First, carriers of singleton pLOF variants in the chromatin remodeller *EP400* had lower hand grip strength (96 carriers; effect = -0.55 s.d. units, 95% confidence interval (CI) -0.68 to -0.42 , $P = 8 \times 10^{-16}$), consistent with findings from knock-out mice, which also present peripheral neuropathy and severe hypomyelination of the central nervous system⁹. Second, singleton pLOF variants in *RRBP1*, which encodes an endoplasmic reticulum membrane protein, were associated with lower levels of apolipoprotein B (92 carriers; effect = -0.83 s.d. units, 95% CI -1.0 to -0.64 , $P = 3 \times 10^{-18}$), as well as similar reductions in the levels of low-density lipoprotein and total cholesterol. Consistent with this, silencing of *Rrbp1* in mice altered hepatic lipid homeostasis, resulting in reduced biogenesis of very-low-density lipoprotein¹⁰.

Protective associations with disease outcomes

A major impetus to perform association analyses with rare variants is the identification of genes for which loss-of-function variants are associated with lower disease risk, as these may represent attractive targets for blocking antibodies or other inhibitory

modalities. However, power to identify protective associations with rare variants at $P \leq 2.18 \times 10^{-11}$ was low (Extended Data Fig. 2). Consistent with this, we found only five genes associated with a lower risk of disease outcomes at $P \leq 2.18 \times 10^{-11}$, all previously reported: *PCSK9*, *APOB* and *APOC3* and protection from hyperlipidaemia; *ABCG5* and cholelithiasis; and *IL33* and allergic diseases (Supplementary Table 2).

Of note, however, an additional 11 protective associations were observed at a more liberal significance threshold of $P \leq 10^{-7}$, including 6 previously reported (involving *ANGPTL3*, *IFIH1*, *DBH*, *PDE3B*, *SLC22A12* and *ZNF229*) and 4 that are potentially novel and remain highly associated after accounting for common variant signals (Supplementary Table 2). The first was between *SLC9A3R2* and lower risk of hypertension (5,873 carriers; odds ratio (OR) = 0.81, 95% CI 0.76 to 0.87, $P = 2.2 \times 10^{-10}$). There were also strong associations when systolic blood pressure (SBP; effect = -1.85 mmHg , 95% CI -2.22 to -1.48 , $P = 2.0 \times 10^{-19}$) and diastolic blood pressure (DBP; effect = -1.01 mmHg , 95% CI -1.31 to -0.80 , $P = 4.8 \times 10^{-18}$; Supplementary Data 2) were analysed as quantitative traits, with the SBP association replicating in the DiscovEHR cohort ($P = 2.6 \times 10^{-4}$; Supplementary Table 6). *SLC9A3R2* encodes NHERF-2, a kidney-expressed scaffolding protein that is functionally linked to sodium absorption through interaction with sodium/hydrogen exchanger 3¹¹. An association with a low-frequency missense variant in *SLC9A3R2* (rs139491786, Arg171Trp, MAF = 0.7%) was previously identified in a GWAS of blood pressure¹², but the signal was attributed to a nearby variant in *PKD1* (rs140869992, Arg2200Cys). We show that a burden of rare pLOF and deleterious missense variants in *SLC9A3R2*, as well as Arg171Trp, remain highly associated with SBP, DBP and hypertension after conditioning on Arg2200Cys in *PKD1* (Supplementary Table 8). Overall, the signal is consistent with the well-established role of sodium balance in regulating blood pressure and suggests that blocking *SLC9A3R2* could provide a means for managing blood pressure. Functional and clinical studies that evaluate this possibility are warranted.

The second novel association was between lower risk of childhood asthma and a burden of rare pLOF and deleterious missense variants in *SLC27A3* (3,787 carriers; OR = 0.65, 95% CI 0.55 to 0.76, $P = 8.2 \times 10^{-8}$), which was supported by the following additional observations. First, a burden of rare pLOF and deleterious missense variants was also associated with lower blood eosinophil counts (5,227 carriers; effect = $-0.045 \text{ s.d. units}$, 95% CI -0.070 to -0.020 , $P = 4.4 \times 10^{-4}$), a cell type with critical effector functions in allergic asthma. Second, there were consistent protective associations in the DiscovEHR cohort with both asthma (1,354 carriers; OR = 0.87, 95% CI 0.75 to 1.01, $P = 0.060$) and eosinophil counts (1,755 carriers; effect = $-0.052 \text{ s.d. units}$, 95% CI -0.096 to -0.008 , $P = 0.021$). *SLC27A3* encodes an acyl-

CoA synthetase that activates long-chain fatty acids¹³, is most highly expressed in artery, adipose and lung tissue¹⁴ and is upregulated in lung cancer¹⁵.

The third novel association was between a missense variant in *PIEZ01* (rs61745086, Pro2510Leu, MAF = 0.98%) and reduced risk of varicose veins (7,454 carriers; OR = 0.69, 95% CI 0.61 to 0.79, $P = 2.61 \times 10^{-8}$). *PIEZ01* encodes a mechanosensitive cation channel with a key role in venous and lymphatic valve formation¹⁶. We had previously shown that rare pLOFs in this gene increase the risk of asymptomatic varicose veins of lower extremities by 4.9-fold (162 carriers; 95% CI 2.8 to 8.6, $P = 3.2 \times 10^{-8}$) in the first 49,960 exomes from the UKB³, an association that is now estimated at 2-fold with around 8 times more data (1,355 carriers; OR = 2.08, 95% CI 1.62 to 2.67, $P = 7.4 \times 10^{-9}$). The new protective association with Pro2510Leu, which replicated in the DiscovEHR cohort (2,243 carriers; OR = 0.66, 95% CI 0.47 to 0.93, $P = 0.017$), suggests that this missense variant probably has a gain-of-function effect. This is important because it suggests that activation of *PIEZ01* may provide a therapeutic pathway for a common condition with no available pharmacological interventions.

Finally, the fourth novel association was between *MAP3K15* and protection from type-2 diabetes, which is discussed in greater detail below. Among these four novel protective associations, only two (with *SLC9A3R2* and *PIEZ01*) were observed at $P < 10^{-7}$ when analysing TOPMed imputed data (Supplementary Tables 9, 10).

Protective associations with quantitative traits

The low yield of protective associations with disease traits contrasts with that observed for disease-relevant quantitative traits, such as body mass index, which often provide greater power for genetic studies. Specifically, we found 131 genes for which the direction of effect on a quantitative trait was consistent with a beneficial effect on disease risk (Supplementary Table 11). For example, we found low-frequency protein-altering variants in *ASGR1* associated with lower apolipoprotein B levels (759 carriers; effect = -0.29 s.d. units, 95% CI -0.35 to -0.22, $P = 6.5 \times 10^{-18}$). *ASGR1* haploinsufficiency was previously reported to reduce risk of cardiovascular disease¹⁷, an observation that supported the clinical development of an anti-ASGR1 monoclonal antibody as a lipid-lowering therapeutic agent¹⁸.

As another example, we found an association between lower serum glucose levels and pLOF variants in *FAM234A* (2,439 carriers; effect = -0.14 s.d. units, 95% CI -0.18 to -0.099, $P = 2.0 \times 10^{-12}$), which was independent of associations with common variants (Supplementary Table 11, Supplementary Fig. 5). There was a consistent association in the DiscovEHR cohort with fasting glucose levels (1,132 carriers; effect = -0.046 s.d. units, 95% CI -0.099 to 0.007, $P = 0.09$), albeit not statistically

significant. Of note, a common intronic variant in *FAM234A* was previously reported to associate with a lower risk of type-2 diabetes (rs9940149:A, MAF = 18%, OR = 0.95) and to co-localize with a regulatory variant that lowers the expression of *FAM234A* in multiple tissues¹⁹. Consistent with this, we found that rare pLOFs in *FAM234A* were associated with a 36% reduction in the risk of self-reported diabetes (2,104 carriers; OR = 0.64, 95% CI 0.52 to 0.80, $P = 10^{-4}$). Collectively, results from both rare and common variants implicate *FAM234A*, a gene of unknown function, in the aetiology of diabetes.

We then determined whether there were other examples of genes with both a favourable effect on a quantitative trait and a protective (even if sub-threshold) association with a relevant disease, as observed for *FAM234A*. To this end, for 131 association signals with a quantitative trait, we estimated the genetic correlation (r_g) between the trait and all diseases tested, and then selected the disease with the most significant r_g . We only considered diseases for which the r_g was significant after correcting for multiple testing, if any. For example, eosinophil count was matched to asthma ($r_g = 0.37$), and intra-ocular pressure was matched to glaucoma ($r_g = 0.66$); in total, we found a matching disease for 129 trait associations (Supplementary Table 12). Using this approach, we found that 13 genes had a protective association with a genetically correlated disease that was significant after correcting for multiple testing ($P < 0.05/129 \text{ tests} = 3.8 \times 10^{-4}$; Extended Data Fig. 3). Of these, we highlight the association between a burden of protein-altering variants in *MAP3K15* and both lower levels of haemoglobin A1c (7,551 carriers; effect = $-0.085 \text{ s.d. units}$, 95% CI -0.100 to -0.073 , $P = 7.8 \times 10^{-30}$), lower serum glucose (6,885 carriers; effect = $-0.090 \text{ s.d. units}$, 95% CI -0.110 to -0.073 , $P = 1.7 \times 10^{-25}$) and protection from type-2 diabetes (7,085 carriers; OR = 0.85, 95% CI 0.79 to 0.91, $P = 2.8 \times 10^{-6}$). Furthermore, there was supporting evidence in the DiscovEHR cohort for all three phenotypes: haemoglobin A1c (1,304 carriers; effect = $-0.040 \text{ s.d. units}$, 95% CI -0.079 to -0.002 , $P = 0.038$), glucose (1,754 carriers; effect = $-0.097 \text{ s.d. units}$, 95% CI -0.130 to -0.064 , $P = 1.3 \times 10^{-8}$) and type-2 diabetes (2,455 carriers; OR = 0.91, 95% CI 0.84 to 0.98, $P = 0.018$). *MAP3K15* encodes a ubiquitously expressed, mitogen-activated protein kinase involved in apoptotic cell death²⁰, and has not to our knowledge previously been implicated in type-2 diabetes.

Associations with somatic mutations

Among the 492 traits with at least 1 significant rare variant association, 20 were noteworthy because they involved 2 or more genes with rare variant signals but no common variant signals from GWAS (Extended Data Fig. 4a, b). Notably, for 7 of these 20 traits—myeloid leukaemia (7 genes; Supplementary Fig. 6), sepsis (4 genes) and 5 additional blood related traits—the majority of associated genes were previously

implicated in clonal haematopoiesis of indeterminate potential (CHIP²¹; Supplementary Table 13). The associated variants in these CHIP genes were strongly correlated with age, and the proportion of reads supporting the variant in putative heterozygotes was often less than 35% or greater than 65% (Supplementary Table 14), consistent with these associations being driven by somatic mutations identified through exome sequencing of blood-derived DNA.

Associations in non-European ancestries

We next investigated the extent to which associations identified in the European cohort were shared across other ancestries. To do so, we performed association analyses using WES data for 10,348 individuals of South Asian (SAS), 9,089 individuals of African (AFR) and 2,217 individuals of East Asian (EAS) ancestry from the UKB cohort. When we focused on the 564 non-redundant associations (that is, the strongest association per gene, 484 with a quantitative trait and 80 with a binary trait; Supplementary Table 6), we found that a large fraction of associations was shared across ancestries for quantitative traits but less so for binary traits, probably owing to low power. For quantitative traits, effect sizes were directionally concordant for 83% of associations in individuals of SAS, 73% of associations in individuals of AFR and 74% of associations in individuals of EAS ancestry, increasing to more than 92% when considering associations with $P \leq 0.05$ (Extended Data Fig. 5a). For binary traits, consistent effects were observed for 61% of associations in SAS, 61% in AFR and 64% in EAS (Extended Data Fig. 5b). A similar pattern was observed when considering the full set of 8,865 associations (Supplementary Fig. 7). We then asked whether any new associations were discovered in non-European ancestries (Supplementary Data 3), and found four genes that were not discovered in the European-only analysis (*G6PD*, *HBQ1*, *OR51V1* and *RGS11*), all explained by previous established associations (Supplementary Table 15).

Replication of rare variant associations

We sought to replicate associations using exome sequencing data from the Geisinger DiscovEHR cohort²² ($n = 133,370$ individuals of European ancestry). As above, to facilitate interpretation of results, we focused on the non-redundant set of 564 gene–trait associations discovered in individuals of European ancestry in the UKB cohort (Supplementary Table 6) and determined whether a matching trait could be identified in DiscovEHR. Of the 279 gene–trait associations for which we attempted replication, 193 (69%; 28 with a binary trait, 165 with a quantitative trait) were nominally significant ($P \leq 0.05$) and directionally consistent (Supplementary Table 6), versus around 7 expected by chance ($279 \times 0.05 \times 0.5$). When considering only a subset of 212 gene–trait associations with at least 80% power for replication, the replication rate

was 81% (172 of 212). Supplementary Data 2 provides replication results for all associations available in DiscovEHR (4,083 of 8,865), of which 70% were nominally significant and directionally consistent.

Effect of burden test composition

As noted above, association of a phenotype with the burden of rare coding variants in a gene is a compelling way for human genetics to connect genes and disease⁸. As we show in the [Supplementary Note](#), when we dissected burden associations in greater detail, we found that: (i) most (77% of 7,449) associations could not be detected in single-variant analyses (Supplementary Data 2), demonstrating that they were generally supported by multiple variants; (ii) burden tests that aggregated variants with a MAF of up to 1% identified a larger number of significant associations overall (Supplementary Table 16), but most of these remained significant after excluding variants with a MAF between 0.1% and 1% (Extended Data Fig. 6a), indicating that the greater yield is likely to be explained by the ability to capture in a single test association signals across a wide range of allele frequencies; and (iii) combining pLOFs and deleterious missense variants in the same test became progressively more valuable at more permissive MAF thresholds (Extended Data Fig. 6b). These results demonstrate the utility of performing a variety of burden tests for discovery of genetic associations.

Enrichment of associations in GWAS loci

A major challenge for genetic association studies of complex traits is the identification of effector genes for the thousands of loci identified through GWAS⁶. To address the possibility that rare variant associations might help pinpoint effector genes, we performed a GWAS for each of the 492 traits with a rare variant association ([Methods](#), Supplementary Data 1, Supplementary Fig. 4), and identified a total of 107,276 independent associations with common variants (hereafter ‘GWAS sentinel variants’). As described in greater detail in the [Supplementary Note](#), by combining results from the GWAS and the WES data, we found that: (i) rare variant associations were often within 1 Mb of a GWAS sentinel variant for the same trait (6,564 of 8,865, 74%; Extended Data Fig. 4a); (ii) most rare variant associations (8,059 of 8,865, 91%) remained significant at $P \leq 2.18 \times 10^{-11}$ when we conditioned on GWAS common variant signals (Extended Data Fig. 4c, Supplementary Table 17, Supplementary Data 2); (iii) significant rare variant associations (after conditioning on GWAS signals) were 11.4-fold (95% CI 10.1 to 13.0, $P < 10^{-300}$) more common in genes located within 1 Mb of a GWAS peak, with enrichment reaching 59.4-fold (95% CI 51.8 to 68.2) when we focused only on genes nearest to GWAS sentinel variants (Fig. 1). These results show strong overlap between common variant signals from GWAS and

rare variant signals from exome-wide association studies, suggesting that rare variant burden signals will identify effector genes for thousands of GWAS loci.

Fig. 1: Enrichment of rare variant associations among genes located in GWAS loci.

 figure1

We tested whether genes located in GWAS loci were more likely to have significant associations with a burden of rare variants when compared to genes elsewhere in the genome. We considered four different significance thresholds to define significant burden associations ($P \leq 0.05$, $P \leq 10^{-4}$, $P \leq 10^{-7}$ and $P \leq 2.18 \times 10^{-11}$) and considered 13 different gene-sets, from all genes located within 10 Mb of, to only the nearest gene to, the GWAS sentinel variants. The enrichment of significant associations was greatest when considering the nearest gene to GWAS sentinel variants, reaching 59.3-fold (95% CI 51.8 to 68.2, $P < 10^{-300}$) when considering a significance threshold of $P \leq 2.18 \times 10^{-11}$. Results are based on the analysis of a pruned set of 188 traits (101 binary traits and 87 quantitative traits; see [Methods](#) for details).

Effector genes of GWAS signals

To illustrate the relevance of the findings described above, we highlight 168 genes for which a significant rare variant association ($P \leq 2.18 \times 10^{-11}$ after conditioning on common variants) was observed in the gene nearest to the GWAS sentinel variant (Supplementary Table 18), indicating that these are very likely to be effector genes that underlie the GWAS signal. As an example, we found 82 GWAS signals for serum levels of vitamin D (Extended Data Fig. 7a), and for 5 of these the burden of rare protein-altering variants in the gene nearest the GWAS peak (*DHCR7*, *FLG*, *GC*, *ANGPTL3* and *HAL*) was also associated with vitamin D levels (Extended Data Fig. 7b). Of these, we highlight the association with *HAL*, which has not to our knowledge been previously reported. The first step of vitamin D synthesis occurs in the skin and requires ultraviolet (UV) light. *HAL* is likely to have a role in this step because it encodes an enzyme that converts histidine into trans-urocanic acid, a major UV-absorbing chromophore that accumulates in the stratum corneum²³. Inactivation of *HAL* is therefore expected to decrease the ability of the outermost layer of the epidermis to block UV light. Consistent with this possibility, we found that a burden of rare pLOF and deleterious missense variants in *HAL* was associated with higher levels of vitamin D, greater ease of skin tanning and higher risks of actinic keratosis and non-melanoma skin cancer (Supplementary Table 19). These findings were supported by trait-lowering associations with a common variant (rs10859995:C, 58% frequency) that co-localizes ($\text{LD } r^2 = 0.97$) with an expression quantitative trait locus (rs3819817:T) that increases the expression of *HAL* in skin tissue¹⁴ (Extended Data Fig. 7c). These results implicate *HAL* in both vitamin D levels and skin cancer and highlight an allelic series that includes rare loss-of-function protein-altering variants (trait-increasing) as well as common expression-increasing non-coding variants (trait-lowering).

Associations with brain imaging traits

The brain imaging component of UKB at present includes 2,077 phenotypes derived from magnetic resonance imaging (MRI) for 36,968 individuals. We analysed these data separately given the large number of traits and the relatively smaller sample size, testing the association with rare variants conditional upon GWAS signals as described above. We found 84 associations at $P \leq 2.18 \times 10^{-11}$ with 6 genes (Supplementary Table 20): *AMPD3*, *GBE1*, *PLD1*, *PLEKHG3*, *STAB1* and *TF*. Of these, we highlight the association between lower grey–white matter contrast (GWC) measures across a diffuse set of brain regions and a deleterious missense variant in *PLD1* (rs149535568, Gly237Cys, 196 carriers; effect = −0.49 s.d. units, 95% CI −0.62 to −0.35, $P = 1.4 \times 10^{-12}$), an enzyme that catalyses the hydrolysis of phosphatidylcholine to phosphatidic acid and choline, which has been shown to have a role in synaptogenesis²⁴. GWC is a measure of blurring between the boundaries of grey- and white-matter brain compartments and is thought to be an indicator of local variations in tissue integrity and myelin degradation, increasing water content in the white matter, or iron deposition²⁵. Lower GWC is associated with ageing and lower indices of cognition²⁶, as well as an increased rate of conversion from mild cognitive impairment to dementia²⁷. Related to this finding, among an additional 46 genes with sub-threshold associations with brain imaging phenotypes ($P \leq 10^{-7}$; Supplementary Table 21), 4 genes had large trait-lowering effects on GWC, including 2 that have clear roles in the formation and maintenance of myelin—*GJC2*²⁸ and *UGT8*²⁹—consistent with the association between variants that disrupt the function of these genes and lower GWC. In contrast, the strongest trait-increasing and putatively protective association with GWC was with a deleterious missense variant in *ST6GALNAC5* (rs756654226, Val135Ala, 9 carriers; effect = 1.7 s.d. units, 95% CI 1.1 to 2.4, $P = 8.2 \times 10^{-8}$), a gene that catalyses the biosynthesis of ganglioside from GM1b in the brain³⁰. This aligns with current evidence that the relative abundance of specific gangliosides in the brain changes with age and in common neurological conditions³¹. We discuss notable associations with other genes (*GBE1*, *PLEKHG3*, *STAB1* and *TF*) in the [Supplementary Note](#).

Beyond 500,000 exomes

In our evaluation of the first 49,960 exomes sequenced from UKB participants³, we used a beta-binomial model to predict the number of genes that would contain heterozygous pLOF variants when considering exome data for all 500,000 study participants. At current sample sizes, the observed and predicted numbers match closely (for example, 15,289 observed versus 15,613 predicted genes with at least 50 heterozygous pLOF carriers; Supplementary Table 22). Using our current dataset as a baseline (including all ancestries), we extended our projections to estimate the number of genes containing rare pLOFs (MAF $\leq 1\%$) when exome sequence data become available for 5 million individuals: we predict that 18,035, 17,853 and 8,376 genes will

have at least 50, 100 and 500 heterozygous pLOF carriers, respectively (Supplementary Table 22, Extended Data Fig. 8a). Similarly, we predict that 2,630, 997 and 529 genes will have at least 10, 50 and 100 homozygous pLOF carriers, respectively, when considering 5 million sequenced individuals.

The UKB cohort consists primarily of individuals of European ancestry, and so an important question is whether these projections also apply to populations that are more ancestrally diverse. To address this, we predicted the number of pLOF carriers expected in 5 million individuals on the basis of (i) 46,000 individuals of European ancestry from the UKB; and (ii) 46,000 individuals from the UKB, including 23,000 of European ancestry and 23,000 individuals of other ancestries (10,000 of South Asian, 9,000 of African, 2,000 of East Asian, 1,000 of Hispanic or Latin American and 1,000 of admixed ancestry). We found that projections based on the more diverse set of samples were slightly higher than the estimates from the European-only dataset (Extended Data Fig. 8b).

Whole-genome sequencing and imputation

In the coming years, we expect whole-genome sequence data to be available for all UKB participants, enabling analyses of rare variation to be extended to the remainder of the genome. Our data enable an early assessment of the value of that upcoming resource for genotype imputation, a widely used strategy for increasing the power, completeness and interpretability of array-based association studies³². We phased exome variants onto genotyping array haplotypes for 400,000 individuals, and then used this reference panel to impute exome variants into an array-only target dataset of 50,000 individuals. When reference and target datasets were well matched in ancestry, imputation accuracy remained high ($r^2 \geq 0.5$) for alleles present in at least 5 reference-panel haplotypes, enabling imputation down to an allele frequency of around 0.025%, 0.005% and 0.0005% in panels with around 10,000, 50,000 or 400,000 sequenced individuals (Supplementary Table 23, Fig. 2). As expected, imputation accuracy was lower, but still very good, when reference panel and target samples were less well matched in ancestry (Supplementary Table 23). Using reference panels of different sizes, we observed rapid increases in the ability to impute rare variants with larger panels and thus expect that even rarer variants will be imputable as reference panel sizes grow to 400,000 individuals and beyond (Extended Data Fig. 9, Supplementary Fig. 9).

Fig. 2: Imputation of rare variants from exome sequencing.

 **figure2**

Imputation accuracy (r^2 , y axis) is shown as a function of the variant allele frequency (x axis; minor allele count (MAC) for ultra-rare variants; MAF for variants with $\text{MAF} > 10^{-4}$) and the number of individuals (n) included in the reference panel (different lines). Full results are provided in Supplementary Table [23](#).

Discussion

We report the completion of exome sequencing for 454,787 UKB participants. Our dataset now includes an average of more than 600 coding variants per gene (including around 50 pLOFs per gene on average). In addition to enabling studies of mutation patterns and human demography^{[33](#)}, our dataset represents a major advance towards the goal of understanding the health consequences of modifying each gene in the genome. In our preliminary analyses, we identify associations with health outcomes for pLOF and likely deleterious variation in 564 genes. These findings suggest new biological functions for many genes and potential therapeutic strategies, whether through enzyme replacement, therapeutic blockade or other modalities. All the data we generated are being made available to the UKB scientific community, and the combined creativity and efforts of this community will surely expand on these initial analyses.

The following caveats (expanded in the Supplementary Discussion) should be considered when interpreting our results. First, a small number of potentially low-quality variants may be included in the analysis, but our stringent significant thresholds and demonstrated replicability of most results suggest that this is not a widespread phenomenon. Second, disentangling mechanisms in genes associated with

multiple traits will require careful follow-up analyses to distinguish situations in which a gene affects multiple traits directly from those in which additional signals are shadows of association with one trait. Third, while we focused on burden tests that could identify genes for which all pLOF or deleterious missense variants have a similar effect direction, additional association signals may be identified in genes that contain both trait-increasing and trait-lowering rare variants using alternative approaches such as SKAT³⁴. In addition to these limitations, there are additional challenges that must be addressed with new samples and data: (i) there is limited genetic diversity among UKB participants and we expect that additional insights will become possible as more diverse samples are sequenced, particularly including insights that are relevant to the genetic disease burden specific to non-European individuals; (ii) although self-report questionnaires and electronic health records provide a very scalable way to phenotype hundreds of thousands of individuals, they naturally entail some misclassification—particularly when compared to more laborious and targeted phenotyping protocols; and (iii) given the very limited availability of complete nuclear families, it is not practical to carry out focused analyses of de novo variation, which has been shown to be especially important for several neurodevelopmental traits.

Accomplishing our original goal of understanding the health consequences of genetic variation in each human gene is likely to require sequencing millions of well-characterized and diverse individuals. In our view, our results not only show that this goal is within reach, but also suggest that sequencing 5 million individuals would enable the identification of more than 500 heterozygous LOF carriers for around 15,000 genes—that is, for the great majority of human protein-coding genes. It is our hope that these results and dataset will help provide the impetus and urgency for generating these new datasets that combine health and variation data on millions of individuals.

Methods

Ethical approval and informed consent

Ethical approval for the UK Biobank was previously obtained from the North West Centre for Research Ethics Committee (11/NW/0382). The work described herein was approved by the UK Biobank under application no. 26041. Ethical approval for DiscovEHR analyses was provided by the Geisinger Health System Institutional Review Board under project no. 2006-0258. Informed consent was obtained for all study participants.

Exome sequencing

Sample preparation and sequencing

We have previously described in detail the approach used at the Regeneron Genetics Center to perform exome sequencing in DNA samples from the UK Biobank study³. In brief, genomic DNA samples were transferred to the Regeneron Genetics Center from the UK Biobank and stored in an automated sample biobank at -80°C before sample preparation. DNA libraries were then created by enzymatically shearing DNA to a mean fragment size of 200 base pairs, and a common Y-shaped adapter was ligated to all DNA libraries. Unique, asymmetric 10-base-pair barcodes were added to the DNA fragment during library amplification to facilitate multiplexed exome capture and sequencing. Equal amounts of sample were pooled before overnight exome capture, with a slightly modified version of IDT's xGen probe library. The initial 50,000 samples were processed with IDT 'lot 1' and all other samples with 'lot 2'. The captured DNA was PCR-amplified and quantified by quantitative PCR. The multiplexed samples were pooled and then sequenced using 75-base-pair paired-end reads with two 10-base-pair index reads on the Illumina NovaSeq 6000 platform using S2 (first 50,000 samples) or S4 (all other samples) flow cells. We sequenced all samples delivered to us by the UK Biobank. A portion of samples (about 30,000) could not be delivered because of the COVID-19 pandemic.

Variant calling and quality control

Sample read mapping and variant calling, aggregation and quality control were performed using the SPB protocol described previously³. In brief, for each sample, NovaSeq WES reads are mapped with BWA MEM to the hg38 reference genome. Small variants are identified with WeCall and reported as per-sample gVCFs. These gVCFs are aggregated with GLnexus into a joint-genotyped, multi-sample project-level VCF (pVCF). SNV genotypes with read depth (DP) less than 7 and indel genotypes with read depth less than 10 are changed to no-call genotypes. After the application of the DP genotype filter, a variant-level allele-balance filter is applied, retaining only variants that meet either of the following criteria: (i) at least one homozygous variant carrier; or (ii) at least one heterozygous variant carrier with an allele balance (AB) greater than the cut-off ($\text{AB} \geq 0.15$ for SNVs and $\text{AB} \geq 0.20$ for indels). Samples showing disagreement between genetically determined and reported sex ($n = 279$), high rates of heterozygosity or contamination (estimated with the VerifyBamId tool, specifically with a FREEMIX score $> 5\%$) ($n = 287$), low sequence coverage (less than 80% of targeted bases achieving $20\times$ coverage) ($n = 2$) or genetically identified sample duplicates ($n = 721$ total samples), and WES variants discordant with genotyping chip ($n = 449$), were excluded. A total of 633 samples failed quality control in multiple categories, resulting in 1,105 individuals being excluded. An additional 16 samples were removed for participants who withdrew from

the study. The remaining 454,787 samples were then used to compile a pVCF for downstream analysis, using the GLnexus joint genotyping tool.

Ancestry assignment

We used array data released by the UK Biobank study to determine continental ancestry super-groups (African (AFR), Hispanic or Latin American (HLA, originally referred to as ‘AMR’ by the 1000 Genomes Project), East Asian (EAS), European (EUR) and South Asian (SAS)) by projecting each sample onto reference principal components calculated from the HapMap3 reference panel. In brief, we merged our samples with HapMap3 samples and kept only SNPs in common between the two datasets. We further excluded SNPs with $\text{MAF} < 10\%$, genotype missingness $> 5\%$ or Hardy–Weinberg equilibrium test $P < 10^{-5}$. We calculated principal components (PCs) for the HapMap3 samples and projected each of our samples onto those PCs. To assign a continental ancestry group to each non-HapMap3 sample, we trained a kernel density estimator (KDE) using the HapMap3 PCs and used the KDEs to calculate the likelihood of a given sample belonging to each of the five continental ancestry groups. When the likelihood for a given ancestry group was greater than 0.3, the sample was assigned to that ancestry group. When two ancestry groups had a likelihood of greater than 0.3, we arbitrarily assigned AFR over EUR, HLA over EUR, HLA over EAS, SAS over EUR, and HLA over AFR. Samples were excluded from analysis if no ancestry likelihoods were greater than 0.3, or if more than three ancestry likelihoods were greater than 0.3 ($n = 1,205$).

Generation of analysis-ready files

The following steps were then taken to generate an analysis-ready Plink2 file set. First, we split exome data sample-wise into ancestral groups, defined as described above. Second, within ancestral groups, we excluded variants: (i) with missingness rate > 0.1 ; (ii) with Hardy–Weinberg equilibrium test $P < 10^{-15}$; or (iii) that were monomorphic. We also excluded samples with a missingness rate of greater than 0.1. After applying these filters, we generated ancestry-specific files in Plink2 PGEN format, which were then used for association analyses.

Identification of low-quality variants from exome sequencing using machine learning

In brief, we defined a set of positive control and negative control variants on the basis of: (i) concordance in genotype calls between array and exome sequencing data; (ii) Mendelian inconsistencies in the exome sequencing data; (iii) differences in allele frequencies between exome sequencing batches; (iv) variant loadings on 20 principal

components derived from the analysis of variants with a MAF of less than 1%; (v) transmitted singletons. The model was then trained on up to 30 available WeCall/GLnexus site quality metrics, including, for example, allele balance and depth of coverage. We split the data into training (80%) and test (20%) sets. We performed a grid search with fivefold cross-validation on the training set to identify the hyperparameters that return the highest accuracy during cross-validation, which are then applied to the test set to confirm accuracy. This approach identified as low quality a total of 447,533 coding variants (3.7% of the 12 million total coding variants). These variants were flagged in (not removed from) downstream analyses.

Variant annotation

Variants from WES were annotated as previously described³. In brief, variants were annotated using SnpEff, with the most severe consequence for each variant chosen across all protein-coding transcripts. Gene regions were defined using Ensembl release 85. Variants annotated as stop gained, start lost, splice donor, splice acceptor, stop lost or frameshift, for which the allele of interest is not the ancestral allele, are considered predicted LOF variants. Five annotation resources were used to assign deleteriousness to missense variants: SIFT³⁵; PolyPhen2 HDIV and PolyPhen2 HVAR³⁶; LRT³⁷; and MutationTaster³⁸. Missense variants were considered ‘likely deleterious’ if predicted deleterious by all five algorithms, ‘possibly deleterious’ if predicted deleterious by at least one algorithm and ‘likely benign’ if not predicted deleterious by any algorithm.

Generation of gene burden masks

We aggregated rare variants for gene burden testing as previously described³⁹. In brief, rare variants were collapsed by gene region, such that individuals who are homozygous reference for all variants are considered homozygous reference, heterozygous carriers of any aggregated variant are considered heterozygous, and only minor allele homozygotes for an aggregated variant are considered as minor allele homozygotes. Genotypes were not phased to consider compound heterozygotes in burden testing. For each gene, we considered two categories of masks: a strict burden of rare pLOFs (M1) and a more permissive burden of rare pLOFs and likely deleterious missense variants (M3). For each of these groups, we considered five separate burden masks per gene, based on the frequency of the alternative allele of the variants that were screened in that group: MAF \leq 1%, MAF \leq 0.1%, MAF \leq 0.01%, MAF \leq 0.001%, and singletons only. Thus, overall, up to 10 burden tests were performed for each gene (although for some genes, the rarer burden tests may not have had enough (5) carriers across all samples, in which case the test was not performed). For the purposes of gene burden testing, the singleton mask includes minor allele homozygotes if no other variant carriers are observed in the dataset.

Comparison with other large-scale resources

We compared variant statistics from UKB WES to two large, publicly available resources—gnomAD⁵ v.3.1 and TOPMed⁴ Freeze 8. For both studies, we restricted to ‘PASS’ variants only, and annotated each dataset as described for the UKB WES data. The comparison across datasets was restricted to synonymous, missense and pLOF variants only. We considered data from all ancestries.

Imputation of unmeasured genotypes using the TOPMed reference panel

We used the following approach to generate imputed genotype data in the UKB study for variants discovered by the TOPMed consortium⁴. First, we began with the list of array variants previously used by UKB to perform HRC imputation. We removed all array variants that could not be successfully lifted over to GRCh38, leaving 655,665 variants. Second, we split the array data including 488,374 samples into 20 evenly sized, randomized batches for submission to the TOPMed imputation server. Third, we merged and concatenated the resulting VCF files from the imputation server into one dataset containing nearly 308 million imputed variants. We prepared this dataset for analysis by first splitting into batches of ancestry by continental super-groups, as previously described. We then filtered to variants that were predicted as functional, had a MAF value ≥ 0.0001 in the original TOPMed dataset, or passed the filters of MAF ≥ 0.0001 and INFO ≥ 0.1 within the dataset itself.

Health- and behaviour-related phenotypes

Quantitative measures, clinical outcomes, survey and touch-screen responses, and imaging derived phenotypes were extracted from phenotypes available through the UK Biobank Data Showcase on 1 April 2020. To be considered a case for an ICD10-based phenotype, participants were required to have one or more of the following: (i) one or more diagnosis in inpatient Health Episode Statistics (HES) records; (ii) a cause-of-death diagnosis in death registry; (iii) two or more diagnoses in outpatient data (READ codes mapped to ICD10). Participants who did not meet the case definition for a given ICD10-based phenotype were either (i) excluded from the analysis if they had one diagnosis in the outpatient data; or (ii) included as controls if they had no diagnosis in the outpatient data. In total, data for 4,465 field IDs were downloaded from the UKB repository. We focused primarily on biomarkers, anthropometry and disease outcomes. As such, we excluded from analysis (i) most food and drink intake questions (except for coffee, tea and alcohol intake); (ii) quality control metrics (for example, volume or sample dilution information); (iii) geographic and environmental questions (for example, proximity to coast, pollution index); (iv) most measures pertaining to

lifestyle or socioeconomic status (for example, number of cars owned, total household income); and (v) OPCS traits and any binary traits with fewer than 100 affected individuals. Furthermore, to reduce redundancy among binary traits, we excluded all ‘No’ responses from the analysis (for example, we analysed ‘22127_DD_asthma_1_Yes’ but not ‘22127_DD_asthma_0_No’). In addition to HES and self-report data, we also generated custom phenotype definitions for a select number of diseases of interest, resulting in a total of 3,706 binary traits included in the study. For quantitative traits measured in multiple visits, we calculated the mean value across all visits for each participant and analysed only the resulting phenotype (for example, we analysed average height and not height measured at each visit). Only quantitative traits with data for more than 50,000 individuals, other than brain imaging phenotypes, were included in the analyses. We applied the following additional filters to systematically flag and exclude from analysis traits that were unlikely to be truly quantitative: (i) the mode for the trait was observed in 20% or more of samples (85 traits); (ii) the mode for the trait was observed in 0.5%–20% samples, but the number of unique values was relatively small (less than 100; 58 traits); or (iii) the mode for the trait was observed in 0.5%–20% samples, but the number of unique values was very large (more than 10,000; 9 traits), suggestive of a data error. The remaining 292 traits that passed quality control were normalized using a rank-based inverse-normal transformation.

Brain imaging phenotypes

We analysed 2,158 phenotypes obtained by structural magnetic resonance imaging (MRI), diffusion MRI and task fMRI, downloaded from the UK Biobank Data Showcase on 1 April 2020. The traits were quantile-normalized and a matrix of confounds including age, sex, age-by-sex, head motion, head volume, head position, temporal imaging effects, imaging center and genetic PCs was regressed out of each trait before analysis, as described previously⁴⁰.

Genetic association analyses

Association analyses were performed using the genome-wide regression test implemented in REGENIE⁷, separately for data derived from exome-sequencing and TOPMed imputation. We included in step 1 of REGENIE (that is, prediction of individual trait values based on the genetic data) array variants with MAF > 1%, <10% missingness, Hardy–Weinberg equilibrium test $P > 10^{-15}$ and linkage disequilibrium (LD) pruning (1,000 variant windows, 100 variant sliding windows and $r^2 < 0.9$). We excluded from step 1 any SNPs with high inter-chromosomal LD, in the major histocompatibility (MHC) region, or in regions of low complexity. Of the 454,787 individuals with exome sequencing data, 413 did not have array data after quality control, and so these individuals were excluded from association analyses. For each

trait, the leave-one-chromosome-out predictors obtained with step 1 were then included as covariates in step 2 for both the exome sequencing and TOPMed imputed data. The association model used in step 2 of REGENIE also included as covariates (i) age, age squared², sex, and age-by-sex; (ii) 10 ancestry-informative PCs derived from the analysis of a set of LD-pruned (50 variant windows, 5 variant sliding windows and $r^2 < 0.5$) common variants from the array data generated separately for each ancestry; and (iii) for the analysis of exome data, we additionally included an indicator for exome sequencing batch (6 IDT batches) and 20 PCs derived from the analysis of exome variants with a MAF between 2.6×10^{-5} (roughly corresponding to a minor allele count (MAC) of 20) and 1% also generated separately for each ancestry. We corrected for PCs built from rare variants because previous studies demonstrated that PCs derived from common variants do not adequately correct for fine-scale population structure^{41,42}. We tested associations with genes on chromosome X but not Y. For the non-pseudoautosomal regions of chromosome X, we used a dosage compensation model, with homozygous reference males coded 0, and hemizygous males coded 2.

Association analyses were performed separately for different continental ancestries defined based on the array data, as described above, analysing variants with an MAC of five or greater. Analysis of TOPMed imputed data was only performed for 492 traits that had at least 1 significant rare variant association in the exome sequencing data.

Estimating power to identify risk-lowering and risk-increasing associations

Empirical power calculations

We simulate genotype and phenotype data without population structure or relatedness, using the same sample size as that available for individuals of European ancestry ($n = 430,998$). Markers are simulated independently with alleles drawn from Binomial(2, EAF) based on a given effect allele frequency (EAF) level. We use a logistic model to generate the binary trait:

$$\$ \$ \{ \backslash rm\{l\} \} \{ \backslash rm\{o\} \} \{ \backslash rm\{g\} \} \{ \backslash rm\{i\} \} \{ \backslash rm\{t\} \} (p) = \backslash mu + G \backslash beta \$ \$$$

in which μ is chosen to achieve a desired prevalence level K , G is the genotype vector for the causal marker and $\beta = \log(\text{OR})$ is the effect of the causal marker, and the trait is generated as $Y|p \sim \text{Bernoulli}(p)$. We vary the EAF between 1%, 0.1%, 0.01% and 0.001%, and for each setting generate 10 marker replicates. To simulate a binary trait, we consider the disease prevalence K at 10%, 1% or 0.1% and vary the OR between 1, 0.75, 0.5, 0.35, 0.2 and 0.01 for risk-lowering (protective) variants and 1, 1.5, 2, 5, 10, 20, 30, 40 and 50 for risk-increasing (predisposing) variants. For each simulation setting with 10 marker replicates, we generate 100 phenotypic replicates, which results

in 1,000 replicates, and we perform association testing using REGENIE-FIRTH in which the P value fallback threshold for Firth correction is set to 0.05. Empirical power was then estimated as the proportion of 1,000 simulation replicates with a P value below a significance level α of 2.18×10^{-11} .

Theoretical power

For comparison, we computed theoretical power based on a logistic regression score test as previously described⁴³, where the non-centrality parameter η is

$$\eta = \frac{2N_0(N_1 - p')^2}{N_0 + N_1} \overline{\{p\}}(1 - \overline{\{p\}})$$

where N_1 and N_0 represent the number of cases and controls, respectively, p is the EAF in controls (approximated by the EAF in the population), p' is the EAF in cases and $\overline{\{p\}}$ is the EAF in the study (taken as a weighted average of the EAF in cases and controls).

Leveraging associations with quantitative traits to identify protective associations with relevant diseases

We tested the association between rare variants and 292 quantitative traits, and then leveraged associations with these traits to identify protective associations with relevant diseases. The following four steps were taken to do this. First, for each quantitative trait, we determined whether higher or lower trait levels are associated with a beneficial effect on health. For example, higher bone mineral density is generally accepted to be associated with lower risks of osteoporosis and fractures and, similarly, lower eosinophil counts are associated with lower risks of asthma and atopic dermatitis. Of the 292 quantitative traits tested, for 85 there was consensus among a team of experts in diverse therapeutic areas on the directionality that is associated with beneficial health outcomes.

Second, among all rare variant associations with each of those 85 traits, we identified the subset for which the direction of effect on the trait was beneficial. For example, we identified rare variants that increased (not reduced) bone mineral density, and rare variants that reduced (not increased) eosinophil counts. We found 34 such traits with at least one directionally favourable rare variant association.

Third, we matched each of these 34 quantitative traits to a single relevant disease. We did this by estimating the genetic correlation between each trait and 357 disease outcomes (specifically, 3-digit ICD codes, expert-curated definitions, self-report and doctor-diagnosed diseases; we only considered diseases that had at least 1 rare variant

association at $P < 10^{-7}$), using LD score regression⁴⁴ and association results from the TOPMed-based GWAS described above. We used LD scores calculated for HapMap3 variants in individuals of European ancestry from the 1000 Genomes Project, with variant positions lifted over to genome build GRCh38. For each trait, we then identified any genetic correlations that were significant after correcting for the 357 tests performed ($P < 0.05/357 = 1.4 \times 10^{-4}$) and then, if any, selected the disease that had the most significant genetic correlation for follow-up analysis. In this way, we were able to match 33 of the 34 quantitative traits to a relevant disease.

Finally, for each gene with a significant ($P \leq 2.18 \times 10^{-11}$) and directionally favourable effect on one of these 33 quantitative traits (for example, *IL33* pLOFs and association with lower eosinophil counts), we then determined if there was a consistent protective association with the matched disease (for example, *IL33* pLOFs and protection from asthma).

Determining whether associations were likely to be attributable to somatic mutations

We found a small number of traits with (i) two or more genes with a rare variant association; and (ii) no GWAS common variant signals. For a subset of these traits, we noticed that the associated genes have been implicated in CHIP^{21,45}. Therefore, we addressed the possibility that the observed associations with this small group of traits were explained by somatic mutations identified through exome sequencing of blood-derived DNA. To address this possibility, we (i) estimated the association between each variant (or burden test) and age, because the frequency of somatic (but not germline) mutations typically increases strongly with age; and (ii) counted the number of variant carriers for whom the proportion of sequencing reads supporting the presence of the alternative allele (that is, variant allele fraction) was less than 35% or more than 65%, which would be more consistent with the variant being of somatic than of germline origin.

Replication in the DiscovEHR cohort

The Geisinger Health System (GHS) DiscovEHR cohort has been described previously²². In brief, DiscovEHR is a health-system-based cohort from central and eastern Pennsylvania (USA) with ongoing recruitment since 2006. A subset of 133,370 MyCode participants sequenced as part of the GHS–Regeneron Genetics Center DiscovEHR partnership and confirmed to be of European ancestry were included in this study. We attempted to replicate in DiscovEHR the most significant variant–trait association for each gene, as listed in Supplementary Table 6. We only considered associations for which the trait tested in the UKB cohort could be matched unambiguously to a trait available in the DiscovEHR cohort. To determine whether the

DiscovEHR cohort provided adequate power to replicate an association discovered in the UKB, we carried out a winner's curse-corrected power analysis as described previously⁴⁰. In brief, power to replicate a given trait-variant association in the DiscovEHR cohort at $P < 0.05$ was estimated based on the following parameters: (i) effect size in the UKB cohort (beta), after adjusting for winner's curse; (ii) standard error of the effect size in the DiscovEHR cohort; and (iii) sample size in DiscovEHR cohort. The same approach was used for quantitative and binary traits.

Identification of rare variant associations that were independent of GWAS signals

For each of the 492 traits with at least one rare variant association at $P \leq 2.18 \times 10^{-11}$, we (i) identified common variants independently associated with the trait at $P \leq 10^{-7}$; and (ii) determined whether the rare variant associations remained significant after adjusting for the common variant signals.

To identify common variants independently associated with a given trait, we first performed a GWAS for that trait that included the same individuals used in the analysis of exome-sequencing data and common variants ($\text{MAF} > 1\%$) imputed from TOPMed, as described above. We then identified independent signals (in the autosomes and the X chromosome) using the approximate conditional analysis implemented in GCTA v.1.91.7⁴⁶. To estimate linkage disequilibrium, we randomly sampled 10,000 individuals from the UK Biobank TOPMed imputed dataset, with dosages between 0 and 0.1 considered homozygote for the reference allele (genotype = 0), between 0.9 and 1.1 considered a heterozygote (genotype = 1), and between 1.9 and 2 considered a homozygote for the alternative allele (genotype = 2); all other dosages were assigned a missing genotype. We performed approximate conditional analysis using a window of 10 Mb, collinearity = 0.9 and variants with a $\text{MAF} > 1\%$. We then retained all variants that had an association $P \leq 10^{-7}$ in the GCTA-cojo joint model. These independently associated variants were then included as covariates when analysing rare variants from exome sequencing data, as described below. We used $P \leq 10^{-7}$ to ensure that we included in the subsequent conditional analyses of exome sequencing data any common variant signals that were close to (but did not quite surpass) the more commonly used genome-wide significance threshold of $P \leq 5 \times 10^{-8}$. However, when reporting the number of independent common variant signals for each trait, we consider only the subset that had $P \leq 5 \times 10^{-8}$, to be consistent with previous studies. Overall, of the 492 traits for which we performed a GWAS, 429 had at least 1 common variant with $P \leq 10^{-7}$ and 421 had at least 1 common variant with a $P \leq 5 \times 10^{-8}$.

Having identified independent common variant signals for a given trait, we then tested whether rare variant associations remained significant after adjusting for those common variant signals. To this end, for each trait, we repeated the association analysis in REGENIE (step 2 only; we used the genome-wide predictors that were created in step 1 as part of the original analysis, which did not condition on any common variants) but now including as additional covariates the dosages for all common variants that were found to have an independent association with the trait, as described above. Associations that exceeded $P \leq 2.18 \times 10^{-11}$ in these conditional analyses were determined to be independent of the common variant signals.

Conditional analyses were performed for 429 (out of 492) that had at least one GWAS signal at $P \leq 10^{-7}$. For the remaining 63 traits ($= 492 - 429$), there were no common variants with $P \leq 10^{-7}$ and so for these traits rare variant signals were considered to be independent of GWAS signals.

Number of rare variant associations expected to be found in GWAS loci by chance

We determined whether the number of rare variant associations that were found to be within 1 Mb of a GWAS signal (specifically 6,564 out of 8,865 associations) was greater than that expected by chance. The number expected by chance was estimated as $p \times k$, where p is the proportion of significant associations among all association tests performed across the genome, considering all rare variants (individual variants and burden tests) and the 492 traits with at least one rare variant association; and k is the number of association tests performed across variants located within 1 Mb of a GWAS signal, considering only the rare variant–trait pairs for the matching GWAS common variant–trait pair, as detailed below. Specifically, $p = a / n = 0.0000285$, given that $a = 8,865$; that is, the total number of rare variant associations with $P \leq 2.18 \times 10^{-11}$ across the 492 traits; and $n = 311,080,453$; that is, the total number of rare variant association tests performed across the 492 traits. In turn, k was determined as follows: (i) for each of the 107,276 independent GWAS signals, we identified rare variants that were located within 1 Mb of the GWAS sentinel variant and that were tested for association with the same trait; (ii) for each trait, we then added the number of rare variants tested across all GWAS signals for that trait, removing duplicate entries, if any; and (iii) added the number of rare variant tests performed across all traits. Using this approach, we found that $k = 131,077,005$ tests. Therefore, the number of significant rare variant associations that were expected to be found within 1 Mb of a GWAS signal by chance was $0.0000285 \times 131,077,005 = 3,736$.

Determining the enrichment of rare variant associations among genes in GWAS loci

We used the following approach to determine whether genes located within 1 Mb of GWAS signals were more likely to have a significant rare variant association (specifically, a burden test with $P \leq 2.18 \times 10^{-11}$ after controlling for GWAS signals, to ensure that rare and common variant signals were independent) when compared to other genes in the genome. First, for each trait, we counted the number of genes that (i) were located within 1 Mb of a GWAS sentinel variant and had a significant rare variant association [a]; (ii) were located within 1 Mb of a GWAS sentinel variant and did not have a significant rare variant association [b]; (iii) were not located within 1 Mb of a GWAS sentinel variant and had a significant rare variant association [c]; and (iv) were not located within 1 Mb of a GWAS sentinel variant and did not have a significant rare variant association [d]. For a given trait, the fold-enrichment of significant rare variant associations among genes within 1 Mb of a GWAS signal was estimated as $(a/b)/(c/d)$. Second, to obtain an overall measure of enrichment across all traits, we used the Mantel–Haenszel approach to combine the trait-specific enrichment results (specifically, the 2-by-2 table defined by values a , b , c and d), with significance of the overall estimate being determined by a chi-squared test. The GWAS signals considered in this analysis were located more than 10 Mb apart, to ensure that a given gene could only be matched to a single GWAS signal. We repeated this analysis for different gene sets (for example, genes located within 0.5 Mb of a GWAS signal; 10th nearest gene to a GWAS signal; nearest gene to a GWAS signal; and so on) and different thresholds to define significant rare variant associations ($P \leq 10^{-7}$, $P \leq 10^{-4}$ and $P \leq 0.05$). Of the 421 traits that had at least 1 gene with a significant rare variant association at $P \leq 2.18 \times 10^{-11}$ and also at least one GWAS signal at $P \leq 5 \times 10^{-8}$, we restricted this analysis to a subset of 188 traits (101 binary traits, 87 quantitative traits), obtained after excluding highly redundant traits (for example, there were 20 traits related to body mass, 14 traits related to bone mineral density, both absolute and relative blood cell counts, self-reported and ICD10-based diagnoses).

Imputation of exome variants using a reference panel with array and exome variants

We used SNP array and exome sequencing data from the UK Biobank on 454,378 individuals. For SNP array data, we excluded variants that were not used during a previous round of phasing², resulting in 670,423 SNP array sites. For exome sequencing data, we excluded variants that had an MAC of one or that were flagged as potentially having low quality by the machine learning approach described above, resulting in 15,845,171 exome variants. We then phased these array and exome datasets as follows. First, we built a haplotype scaffold by phasing SNP array data with SHAPEIT4.2.0⁴⁷, phasing whole chromosomes at a time. We then phased the exome sequencing data onto the array scaffold in chunks of 10,000 variants, using 500 SNPs from the array data as a buffer at the beginning and end of each chunk. A

consequence of this process is that when a variant appears in both the array and exome datasets, it is the data from the array dataset that are used.

The phased SNP array and exome sequencing dataset was split into 2 sets: a set of 404,378 reference panel individuals and a target set of 50,000 individuals. To systematically study the effect of reference panel size on imputation accuracy, we generated reference panels by using 2,500, 10,000, 25,000, 50,000, 100,000, 200,000, 300,000 and 400,000 individuals from the set of 404,378 individuals. Each reference panel was then used to impute exome variants using the SNP array data from the 50,000-sample target dataset. The imputation was carried out on chromosome 2 only in chunks of 20 Mb using IMPUTE5⁴⁸, which exhibits sub-linear scaling as reference panel size grows. We examined the sensitivity of these results to ancestry in two ways. First, by measuring imputation accuracy in ancestry-specific subsets of the 50,000 target dataset for the 400,000 reference panel results (for example, only among individuals of South Asian ancestry). Second, we created a single reference panel of 300,000 individuals with principal component analysis (PCA)-derived European ancestry and who self-reported as ‘White British’, and a separate test dataset of 49,926 individuals with PCA-derived European ancestry who did not self-identify as ‘White British’. This testing scenario is denoted 300,000 WB in Supplementary Table [23](#).

We measured imputation accuracy by comparing the imputed dosage genotypes to the true (masked) genotypes at exome variants. Markers were binned according to the MAF of the marker in either the reference panel or the full dataset of 454,374 individuals. In each bin, we report the squared correlation (r^2) between the concatenated vector of all the true (masked) genotypes at markers and the vector of all imputed dosages at the same markers. At the ultra-rare end of the frequency spectrum, we use individual values of MAC for the bins, instead of MAF.

We used imputation accuracy results obtained across different sizes of the reference panel (shown in Supplementary Table [23](#)) to extrapolate performance at larger reference panel sizes. For each MAC or MAF bin we fit logistic curve models to the r^2 values at reference panel sizes $n = 50,000, 100,000, 200,000, 300,000$ and $400,000$ of the form $r^2 \approx c/(1 + \exp(-(a + b \times \log(n))))$. We tried two versions of this model: a two-parameter model with the asymptote (c) fixed at 1, and a three-parameter model that has the restriction that $c \leq 1$. Allowing the logistic curve to be parameterized on $\log(n)$ scale was important. We then used these curves to extrapolate to larger reference panel sizes up to $n = 1,000,000$. The resulting fitted curves from the two- and three-parameter models are shown in Extended Data Fig. [9a](#) and Supplementary Fig. [9a](#), respectively, with associated 95% CI estimated using the delta method. To assess the accuracy of this approach, we repeated the process by excluding the r^2 value for $n = 400,000$, and then used the logistic curve to predict r^2 at $n = 400,000$ (shown by the blue dot on each plot in Extended Data Fig. [9a](#), Supplementary Fig. [9a](#)). We then

aggregated the results into single plots (Extended Data Fig. 9b, Supplementary Fig. 9b) that show both the results of our imputation experiments together with the extrapolated values. The two-parameter logistic model seems to overestimate imputation accuracy in some MAC/MAF bins. This is especially evident when looking at the $n = 400,000$ prediction (Extended Data Fig. 9b). The three-parameter logistic model seems to perform better for the $n = 400,000$ prediction except for the MAC = 2 bin, in which the predictions seem too high and inconsistent with predictions at higher bins.

Prediction of pLOF carriers beyond 500,000 exomes

We estimated the number of pLOF carriers expected to be observed in one and five million sequenced samples using a mixture model of beta-binomial distributions, as previously described³. Model parameters were estimated using heterozygous and homozygous pLOF counts per autosomal gene in 454,787 exomes spanning all ancestries.

Reporting summary

Further information on research design is available in the [Nature Research Reporting Summary](#) linked to this paper.

Data availability

Individual-level sequence data have been deposited with the UK Biobank and are freely available to approved researchers, as has been done with other genetic datasets to date. Individual-level phenotype data are also available to approved researchers for the surveys and health-record datasets from which all of our traits are derived.

Instructions for access to UK Biobank data are available at <https://www.ukbiobank.ac.uk/enable-your-research>. Full details for the significant trait associations with rare variants described in this study are provided in Supplementary Data 2, 3. Summary statistics for the rare variants tested in this study are also available in the GWAS Catalog (accession IDs are in Supplementary Data 4 and are listed separately for single variants and burden tests). The HapMap3 reference panel was downloaded from <ftp://ftp.ncbi.nlm.nih.gov/hapmap/>. GnomAD v3.1 VCFs were obtained from <https://gnomad.broadinstitute.org/downloads>. VCFs for TOPMED Freeze 8 were obtained from <https://bravo.sph.umich.edu/freeze8/hg38/downloads>. LD scores from 1000 Genomes Project were downloaded from <https://data.broadinstitute.org/alkesgroup/LDSCORE/>.

Code availability

The association analysis package used to perform all genetic associations is publicly available at <https://github.com/rgcgithub/regenie>.

References

1. 1. Szustakowski, J. D. et al. Advancing human genetics research and drug discovery through exome sequencing of the UK Biobank. *Nat. Genet.* **53**, 942–948 (2021).
2. 2. Bycroft, C. et al. The UK Biobank resource with deep phenotyping and genomic data. *Nature* **562**, 203–209 (2018).
3. 3. Van Hout, C. V. et al. Exome sequencing and characterization of 49,960 individuals in the UK Biobank. *Nature* **586**, 749–756 (2020).
4. 4. Taliun, D. et al. Sequencing of 53,831 diverse genomes from the NHLBI TOPMed Program. *Nature* **590**, 290–299 (2021).
5. 5. Karczewski, K. J. et al. The mutational constraint spectrum quantified from variation in 141,456 humans. *Nature* **581**, 434–443 (2020).
6. 6. Edwards, S. L., Beesley, J., French, J. D. & Dunning, A. M. Beyond GWASs: illuminating the dark road from association to function. *Am. J. Hum. Genet.* **93**, 779–797 (2013).
7. 7. Mbatchou, J. et al. Computationally efficient whole-genome regression for quantitative and binary traits. *Nat. Genet.* **53**, 1097–1103 (2021).
8. 8.

Zuk, O. et al. Searching for missing heritability: designing rare variant association studies. *Proc. Natl Acad. Sci. USA* **111**, E455–E464 (2014).

9. 9.

Frob, F. et al. Ep400 deficiency in Schwann cells causes persistent expression of early developmental regulators and peripheral neuropathy. *Nat. Commun.* **10**, 2361 (2019).

10. 10.

Anastasia, I. et al. Mitochondria–rough-ER contacts in the liver regulate systemic lipid homeostasis. *Cell Rep.* **34**, 108873 (2021).

11. 11.

He, P., Zhang, H. & Yun, C. C. IRBIT, inositol 1,4,5-triphosphate (IP₃) receptor-binding protein released with IP₃, binds Na⁺/H⁺ exchanger NHE3 and activates NHE3 activity in response to calcium. *J. Biol. Chem.* **283**, 33544–33553 (2008).

12. 12.

Giri, A. et al. Trans-ethnic association study of blood pressure determinants in over 750,000 individuals. *Nat. Genet.* **51**, 51–62 (2019).

13. 13.

Pei, Z. et al. Mouse very long-chain acyl-CoA synthetase 3/fatty acid transport protein 3 catalyzes fatty acid activation but not fatty acid transport in MA-10 cells. *J. Biol. Chem.* **279**, 54454–54462 (2004).

14. 14.

The GTEx Consortium. The GTEx Consortium atlas of genetic regulatory effects across human tissues. *Science* **369**, 1318–1330 (2020).

15. 15.

Pei, Z. et al. Very long-chain acyl-CoA synthetase 3: overexpression and growth dependence in lung cancer. *PLoS ONE* **8**, e69392 (2013).

16. 16.

Li, J. et al. Piezo1 integration of vascular architecture with physiological force. *Nature* **515**, 279–282 (2014).

17. 17.

Nioi, P. et al. Variant *ASGR1* associated with a reduced risk of coronary artery disease. *N. Engl. J. Med.* **374**, 2131–2141 (2016).

18. 18.

Janiszewski, M. et al. A randomized, placebo-controlled, double-blind, ascending single-dose, phase 1 study to evaluate the safety, tolerability, pharmacokinetics, and pharmacodynamics of AMG 529, a novel anti-ASGR1 monoclonal antibody, in healthy subjects. *J. Am. Coll. Cardiol.* **73**, 1755–1755 (2019).

19. 19.

Zhao, W. et al. Identification of new susceptibility loci for type 2 diabetes and shared etiological pathways with coronary heart disease. *Nat. Genet.* **49**, 1450–1457 (2017).

20. 20.

Kaji, T. et al. ASK3, a novel member of the apoptosis signal-regulating kinase family, is essential for stress-induced cell death in HeLa cells. *Biochem. Biophys. Res. Commun.* **395**, 213–218 (2010).

21. 21.

Jaiswal, S. et al. Clonal hematopoiesis and risk of atherosclerotic cardiovascular disease. *N. Engl. J. Med.* **377**, 111–121 (2017).

22. 22.

Dewey, F. E. et al. Distribution and clinical impact of functional variants in 50,726 whole-exome sequences from the DiscovEHR study. *Science* **354**, aaf6814 (2016).

23. 23.

Barresi, C. et al. Increased sensitivity of histidinemic mice to UVB radiation suggests a crucial role of endogenous urocanic acid in photoprotection. *J. Invest. Dermatol.* **131**, 188–194 (2011).

24. 24.

Luo, L. D., Li, G. & Wang, Y. PLD1 promotes dendritic spine development by inhibiting ADAM10-mediated N-cadherin cleavage. *Sci. Rep.* **7**, 6035 (2017).

25. 25.

Uribe, C. et al. Gray/white matter contrast in Parkinson's disease. *Front. Aging Neurosci.* **10**, 89 (2018).

26. 26.

Lewis, J. D. et al. T1 white/gray contrast as a predictor of chronological age, and an index of cognitive performance. *Neuroimage* **173**, 341–350 (2018).

27. 27.

Jefferson, A. L. et al. Gray & white matter tissue contrast differentiates Mild Cognitive Impairment converters from non-converters. *Brain Imaging Behav.* **9**, 141–148 (2015).

28. 28.

Basu, R. & Sarma, J. D. Connexin 43/47 channels are important for astrocyte/oligodendrocyte cross-talk in myelination and demyelination. *J. Biosci.* **43**, 1055–1068 (2018).

29. 29.

Bosio, A., Binczek, E., Le Beau, M. M., Fernald, A. A. & Stoffel, W. The human gene CGT encoding the UDP-galactose ceramide galactosyl transferase (cerebroside synthase): cloning, characterization, and assignment to human chromosome 4, band q26. *Genomics* **34**, 69–75 (1996).

30. 30.

Okajima, T. et al. Molecular cloning of brain-specific GD1 α synthase (ST6GalNAc V) containing CAG/glutamine repeats. *J. Biol. Chem.* **274**, 30557–30562 (1999).

31. 31.

Sipione, S., Monyror, J., Galleguillos, D., Steinberg, N. & Kadam, V. Gangliosides in the brain: physiology, pathophysiology and therapeutic

applications. *Front. Neurosci.* **14**, 572965 (2020).

32. 32.

Howie, B., Fuchsberger, C., Stephens, M., Marchini, J. & Abecasis, G. R. Fast and accurate genotype imputation in genome-wide association studies through pre-phasing. *Nat. Genet.* **44**, 955–959 (2012).

33. 33.

The 1000 Genomes Project Consortium. A global reference for human genetic variation. *Nature* **526**, 68–74 (2015).

34. 34.

Wu, M. C. et al. Rare-variant association testing for sequencing data with the sequence kernel association test. *Am. J. Hum. Genet.* **89**, 82–93 (2011).

35. 35.

Vaser, R., Adusumalli, S., Leng, S. N., Sikic, M. & Ng, P. C. SIFT missense predictions for genomes. *Nat. Protoc.* **11**, 1–9 (2016).

36. 36.

Adzhubei, I., Jordan, D. M. & Sunyaev, S. R. Predicting functional effect of human missense mutations using PolyPhen-2. *Curr. Protoc. Hum. Genet.* **76**, 7.20.1–7.20.41 (2013).

37. 37.

Chun, S. & Fay, J. C. Identification of deleterious mutations within three human genomes. *Genome Res.* **19**, 1553–1561 (2009).

38. 38.

Schwarz, J. M., Rödelsperger, C., Schuelke, M. & Seelow, D. MutationTaster evaluates disease-causing potential of sequence alterations. *Nat. Methods* **7**, 575–576 (2010).

39. 39.

Kosmicki, J. A. et al. Pan-ancestry exome-wide association analyses of COVID-19 outcomes in 586,157 individuals. *Am. J. Hum. Genet.* **108**, 1350–1355 (2021).

40. 40.
Elliott, L. T. et al. Genome-wide association studies of brain imaging phenotypes in UK Biobank. *Nature* **562**, 210–216 (2018).
41. 41.
Mathieson, I. & McVean, G. Differential confounding of rare and common variants in spatially structured populations. *Nat. Genet.* **44**, 243–246 (2012).
42. 42.
Zaidi, A. A. & Mathieson, I. Demographic history mediates the effect of stratification on polygenic scores. *Elife* **9**, e61548 (2020).
43. 43.
Chapman, J. M., Cooper, J. D., Todd, J. A. & Clayton, D. G. Detecting disease associations due to linkage disequilibrium using haplotype tags: a class of tests and the determinants of statistical power. *Hum. Hered.* **56**, 18–31 (2003).
44. 44.
Bulik-Sullivan, B. et al. An atlas of genetic correlations across human diseases and traits. *Nat. Genet.* **47**, 1236–1241 (2015).
45. 45.
Bick, A. G. et al. Inherited causes of clonal haematopoiesis in 97,691 whole genomes. *Nature* **586**, 763–768 (2020).
46. 46.
Yang, J. et al. Conditional and joint multiple-SNP analysis of GWAS summary statistics identifies additional variants influencing complex traits. *Nat. Genet.* **44**, 369–375 (2012).
47. 47.
Delaneau, O., Zagury, J. F., Robinson, M. R., Marchini, J. L. & Dermitzakis, E. T. Accurate, scalable and integrative haplotype estimation. *Nat. Commun.* **10**, 5436 (2019).
48. 48.

Rubinacci, S., Delaneau, O. & Marchini, J. Genotype imputation using the Positional Burrows Wheeler Transform. *PLoS Genet.* **16**, e1009049 (2020).

Acknowledgements

This research has been conducted using the UK Biobank Resource (project 26041). The authors thank everyone who made this work possible, particularly the UK Biobank team, their funders, the professionals from the member institutions who contributed to and supported this work, and most especially the UK Biobank participants, without whom this research would not be possible. The exome sequencing was funded by the UK Biobank Exome Sequencing Consortium (Bristol Myers Squibb, Regeneron, Biogen, Takeda, Abbvie, Alnylam, AstraZeneca and Pfizer). Ethical approval for the UK Biobank was previously obtained from the North West Centre for Research Ethics Committee (11/NW/0382). The work described herein was approved by the UK Biobank under application number 26041. Approval for DiscovEHR analyses was provided by the Geisinger Health System Institutional Review Board under project number 2006-0258. Informed consent was obtained for all study participants.

Author information

Author notes

1. These authors jointly supervised this work: Jonathan Marchini, Aris Baras, Gonçalo R. Abecasis, Manuel A. Ferreira
2. Lists of authors and their affiliations appear in the Supplementary Information

Affiliations

1. Regeneron Genetics Center, Tarrytown, NY, USA

Joshua D. Backman, Alexander H. Li, Anthony Marcketta, Dylan Sun, Joelle Mbatchou, Michael D. Kessler, Christian Benner, Daren Liu, Adam E. Locke, Suganthi Balasubramanian, Ashish Yadav, Nilanjana Banerjee, Christopher E. Gillies, Amy Damask, Simon Liu, Xiaodong Bai, Alicia Hawes, Evan Maxwell, Lauren Gurski, Kyoko Watanabe, Jack A. Kosmicki, Veera Rajagopal, Jason Mighty, Marcus Jones, Lyndon Mitnaul, Eli Stahl, Giovanni Coppola, Eric Jorgenson, Lukas Habegger, William J. Salerno, Alan R. Shuldiner, Luca A. Lotta, John D. Overton, Michael N. Cantor, Jeffrey G. Reid, George Yancopoulos, Hyun M. Kang, Jonathan Marchini, Aris Baras, Gonçalo R. Abecasis & Manuel A. R. Ferreira

Consortia

Regeneron Genetics Center

DiscovEHR

Contributions

Conceptualization: J.D.B., A.H.L., H.M.K., G.C., L.A.L., J. Marchini, G.R.A., A.B. and M.A.R.F. Data curation: A.Y., N.B., V.R., E.S. and M.N.C. Data generation: X.B., A.H., W.J.S., J.G.R. and J.D.O. Formal analysis: J.D.B., A.H.L., A.M., D.S., J. Mbatchou, A.E.L., C.E.G., J.A.K., D.L., M.D.K., A.D., L.G., C.B. and M.A.R.F. Funding acquisition: A.R.S., G.Y., J.D.O., J.G.R., G.R.A. and A.B. Methodology: J. Marchini, H.M.K., G.R.A. and M.A.R.F. Project administration: J. Mighty, M.J. and L.M. Resources: S.B., S.L., E.M., L.H. and J.G.R. Software: J. Mbatchou and J. Marchini. Supervision: E.J., J.D.O., M.N.C., J.G.R., H.M.K., J. Marchini, A.B., G.R.A. and M.A.R.F. Visualization: J.D.B., A.H.L., K.W., M.D.K., C.E.G. and M.A.R.F. Writing (original draft): J.D.B., A.H.L., J. Marchini, G.R.A. and M.A.R.F. Writing (review and editing): E.J., H.M.K., G.Y., A.R.S. and A.B.

Corresponding authors

Correspondence to [Gonçalo R. Abecasis](#) or [Manuel A. R. Ferreira](#).

Ethics declarations

Competing interests

J.D.B., A.H.L., A.M., D.S., J. Mbatchou, C.E.G., D.L., A.E.L., S.B., A.Y., N.B., M.D.K., A.D., S.L., C.B., X.B., A.H., E.M., L.G., K.W., J.A.K., V.R., J. Mighty, M.J., L.M., G.C., E.J., L.H., W.J.S., A.R.S., L.A.L., J.D.O., M.N.C., J.G.R., G.Y., H.M.K., J. Marchini, A.B., G.R.A. and M.A.R.F. are current employees and/or stockholders of Regeneron Genetics Center or Regeneron Pharmaceuticals.

Additional information

Peer review information *Nature* thanks Po-Ru Loh, Yukinori Okada and the other, anonymous, reviewer(s) for their contribution to the peer review of this work. Peer reviewer reports are available.

Publisher's note Springer Nature remains neutral with regard to jurisdictional claims in published maps and institutional affiliations.

Extended data figures and tables

Extended Data Fig. 1 Lead trait associations for 564 genes with a rare variant association at $P \leq 2.18 \times 10^{-11}$.

a, Associations with binary traits. **b**, Associations with quantitative traits. In red (and table): associations with odds ratio >100 for binary traits and $|effect| > 2$ for quantitative traits. Diamonds show associations that were no longer significant after accounting for nearby GWAS signals.

Extended Data Fig. 2 Power to identify associations with rare variants in the analysis of 430,998 participants of European ancestry from the UK Biobank.

a, Protective associations (i.e. with an odds ratio <1). **b**, Predisposing associations (i.e. with an odds ratio >1). Power was estimated using asymptotic theory (broken lines) and also through simulations (solid lines), separately for variants with an effect allele frequency (EAF) of 1% (purple), 0.1% (blue), 0.01% (green) and 0.001% (yellow). Power to identify protective associations was low because identification of rare variants that reduce disease risk typically requires very large numbers of cases, and population cohorts like that ascertained by the UK Biobank study typically include many more unaffected than affected individuals for each disease.

Extended Data Fig. 3 Genes for which a rare variant had a favourable effect on a quantitative trait ($P \leq 2.18 \times 10^{-11}$) and also a protective association with a genetically correlated disease.

a, The x- and y-axes show the effect of the rare variant (listed in Supplementary Table 12) on the quantitative trait and genetically correlated disease, respectively. **b**, Thirteen genes for which the disease association was significant after correcting for multiple testing ($P \leq 0.05/129 = 3.8 \times 10^{-4}$; also shown in red in panel **a**).

Extended Data Fig. 4 Associations with common and rare variants in individuals of European ancestry.

a, Number of traits tested and genetic associations discovered in UKB 450K. An exome-wide association study (ExWAS) was performed for 3,994 traits, of which 492 had at least 1 gene with a rare variant (RV) association at $P \leq 2.18 \times 10^{-11}$. Across all 492 traits, we identified 8,865 significant RV associations, a list that includes redundant associations arising from having tested multiple (often correlated) variants and traits per gene. The 8,865 associations (including 6,564 or 74% located within 1 Mb of a GWAS signal) reduced down to (i) 2,283 associations when selecting only the most significant association per gene per trait (Supplementary Data 2); and (ii) 564 associations when selecting only the most significant association per gene (Supplementary Table 6). For each of the 492 traits with at least 1 RV association, we performed a genome-wide association study (GWAS) using TOPMed data for the same individuals included in the ExWAS. Of the 492 traits, 421 had at least 1 common variant (CV) signal at $P < 5 \times 10^{-8}$. Independent CV associations were identified for each trait using approximate conditional analysis, and then the number of independent associations was summed across all traits, for a total of 107,276 associations (including 7,546 or 7% that were located within 1Mb of an ExWAS signal). **b**, Top half of the figure shows number of independent CV signals ($MAF > 1\%$ and conditionally independent) per trait, from the TOPMed GWAS. Bottom half of the figure shows number of genes with a RV association for the same trait from ExWAS. The x-axis shows all 492 traits that had 1 or more genes with a RV association, sorted by the number of CV signals, with ties in turn sorted by number of genes with a RV association. Traits that did not have RV signals ($3,994 - 492 = 3,506$) are not shown on this plot. Twenty binary traits that had 2 or more genes with a RV association but no CV signals from the GWAS are highlighted by the dashed box and listed in Supplementary Table 13. **c**, This panel shows associations with RV before (x-axis) and after (y-axis) accounting for the effect of CV signals. Of the 8,865 RV associations, 806 (9%) were no longer significant at $P < 2.18 \times 10^{-11}$ after accounting for CV signals (see also Supplementary Table 17). The highlighted association between *HSPG2* and alkaline phosphatase is an example of an association that was greatly attenuated after controlling for the effect of CV signals (regional association plots shown in Supplementary Fig. 8).

Extended Data Fig. 5 Comparison of effect sizes across ancestries for 564 lead associations identified in Europeans.

For each of the 564 genes with at least 1 rare variant association in individuals of European (EUR) ancestry, we selected the most significant association (484 with a quantitative trait, 80 with a binary trait; see Supplementary Table 6) and then compared the effect size estimated in Europeans with that estimated in individuals of South Asian (SAS), African (AFR) and East Asian (EAS) ancestry, if available. **a**, Of the 484 gene associations with a quantitative trait, 355 (83% directionally concordant), 347 (73%) and 210 (74%) were available in SAS, AFR and EAS, respectively. **b**, Of

the 80 gene associations with a binary trait, 31 (61% directionally concordant), 31 (61%) and 11 (64%) were available in SAS, AFR and EAS, respectively. Red circles represent associations with $P \leq 0.05$ in the corresponding non-European ancestry. Numbers in the corner of each quadrant represent the proportion of associations in that quadrant, out of the total number of associations in black, and out of the subset with a $P \leq 0.05$ in red. Triangles: associations between binary traits and variants for which the minor allele count (MAC) was 0 in affected individuals.

Extended Data Fig. 6 Effect of burden mask composition on yield of significant rare variant associations.

a, Comparison of the trait association P -value between burden tests that included pLOF variants with a minor allele frequency (MAF) up to 1% (x-axis) and burden tests that included pLOF variants with a MAF up to 0.1% (y-axis). For a large fraction of associations (64.1% for binary traits, 79.8% for quantitative traits), the association P -value was the same between the 2 burden test strategies, indicating that there were no (or very few) variants with a MAF between 0.1% and 1% included in the burden test. **b**, Comparison of association yield between burden tests that included pLOF variants only and burden tests that included both pLOF and deleterious missense variants. This comparison was performed separately for the 5 different allele frequency thresholds used to determine which variants were aggregated in the burden test. The proportion of trait associations discovered only when considering both pLOF and deleterious missense variants increased steadily with increasing allele frequency, from 19.3% (46/238) when testing only singletons, to 42.6% (655/1,539) when considering variants with a MAF up to 1%.

Extended Data Fig. 7 Illustration of the utility of exome sequencing data to identify likely effector genes of common variant signals from GWAS.

a, GWAS results for serum vitamin D levels, based on TOPMed imputed data for the same individuals with exome sequencing data. There were 82 independent common variant signals (considering only variants with a $\text{MAF} > 1\%$ and $P < 5 \times 10^{-8}$; of these, 62 were located > 10 Mb apart). Analysis of exome sequencing data identified 7 genes with a significant rare variant burden association at $P < 2.18 \times 10^{-11}$ (shown by green circles in the Manhattan plot; up to 10 burden tests performed per gene) after conditioning on GWAS signals. Of these 7 genes (highlighted by the large, green and numbered circles), 5 were the nearest gene to a GWAS signal: *FLG*, *ANGPTL3*, *GC*, *DHCR7* and *HAL*. P-values were capped at $< 10^{-50}$. **b**, Regional association plots are shown for these 7 genes, with green circles showing results from burden tests only, and grey circles showing results from all other variants tested individually, from imputed and exome data. **c**, Association between a sentinel eQTL for *HAL*

(rs3819817) and gene expression in skin tissue (sun exposed – lower leg), estimated by GTEx¹⁴ using linear regression. This variant co-localized ($r^2 = 0.97$) with the peak variant associated with vitamin D levels at the *HAL* locus (rs10859995).

Extended Data Fig. 8 Number of genes with pLOF carriers in exome sequencing data.

a, Predicted number of genes with heterozygote (top-left panel) and homozygote (top-right panel) pLOF carriers in exome sequencing data in datasets of up to 5 million individuals. Bottom panel shows distribution of the observed number of heterozygote pLOF carriers per gene in exome sequencing of 454,787 individuals from the UK Biobank. **b**, Predicted number of genes with heterozygote pLOF carriers in 5 million individuals based on a reference dataset of (i) 46K individuals of European ancestry from the UKB (solid lines); and (ii) 46K individuals from the UKB spanning multiple ancestries (dashed lines), including 23K of European ancestry and 23K individuals of other ancestries (10K of South Asian, 9K of African, 2K of East Asian ancestry, 1K of Hispanic or Latin American ancestry and 1K of admixed ancestry).

Extended Data Fig. 9 Predicted imputation accuracy for variants from exome sequencing as a function of the size of the reference panel using a two-parameter logistic model.

a, Each panel shows the imputation accuracy (r^2 , y-axis) as a function of the number of individuals included in the reference panel (x-axis), for a given allele frequency bin (estimated in the reference panel). Grey dots show the imputation accuracy that was observed when analysing reference panels with up to 400,000 individuals. Red dots show the imputation accuracy that was predicted for reference panels with >400,000 individuals, obtained by fitting a 2-parameter logistic curve to results from reference panels with $\leq 400,000$ individuals. The fit from this logistic curve is shown by the solid line, with associated 95% confidence intervals shown in light red. The blue dot is the extrapolated value for a reference panel of 400,000 individuals obtained by fitting the curve using only reference panels with <400,000 individuals. **b**, Imputation accuracy (r^2 , y-axis) is shown as a function of the variant allele frequency (x-axis; minor allele count [MAC] for ultra-rare variants, minor allele frequency [MAF] for variants with $MAF > 10^{-4}$) and the number of individuals (N) included in the reference panel (different lines). Solid lines show the imputation accuracy that was observed when analysing reference panels with up to 400,000 individuals. Dashed lines show the imputation accuracy that was predicted for reference panels with >400,000 individuals, obtained by fitting a 2-parameter logistic curve to results from reference panels with $\leq 400,000$ individuals.

Extended Data Table 1 Novel gene associations identified through the analysis of a burden of singleton variants

Supplementary information

Supplementary Information

This file contains the Supplementary Discussion, Supplementary Note (including a list of investigators from the Regeneron Genetics Center and a list of investigators from the DiscovEHR cohort), Supplementary Figures 1–10 and the Supplementary References.

Reporting Summary

Peer Review File

Supplementary Tables

This file contains Supplementary Tables 1–23.

Supplementary Data

This file contains Supplementary Data 1–4. Data 1: List of 3,994 traits tested for association with rare variants in individuals of European ancestry from the UK Biobank cohort. Data 2: Summary statistics for 8,865 associations discovered in the analysis of individuals of European ancestry. Data 3: Summary statistics for 376 associations discovered in the analysis of individuals of African, East Asian or South Asian ancestries. Data 4: Summary statistics for the rare variants tested in this study along with GWAS Catalog accession IDs.

Rights and permissions

Open Access This article is licensed under a Creative Commons Attribution 4.0 International License, which permits use, sharing, adaptation, distribution and reproduction in any medium or format, as long as you give appropriate credit to the original author(s) and the source, provide a link to the Creative Commons license, and indicate if changes were made. The images or other third party material in this article are included in the article's Creative Commons license, unless indicated otherwise in a credit line to the material. If material is not included in the article's Creative Commons license and your intended use is not permitted by statutory regulation or exceeds the

permitted use, you will need to obtain permission directly from the copyright holder.
To view a copy of this license, visit <http://creativecommons.org/licenses/by/4.0/>.

[Reprints and Permissions](#)

About this article

Cite this article

Backman, J.D., Li, A.H., Marcketta, A. *et al.* Exome sequencing and analysis of 454,787 UK Biobank participants. *Nature* **599**, 628–634 (2021).
<https://doi.org/10.1038/s41586-021-04103-z>

- Received: 09 July 2021
- Accepted: 06 October 2021
- Published: 18 October 2021
- Issue Date: 25 November 2021
- DOI: <https://doi.org/10.1038/s41586-021-04103-z>

Share this article

Anyone you share the following link with will be able to read this content:

[Get shareable link](#)

Sorry, a shareable link is not currently available for this article.

[Copy to clipboard](#)

Provided by the Springer Nature SharedIt content-sharing initiative

Further reading

- [**A massive effort links protein-coding gene variants to health**](#)
 - Yukinori Okada
 - Qingbo S. Wang

Nature (2021)

A massive effort links protein-coding gene variants to health

- Yukinori Okada
- Qingbo S. Wang

News & Views 25 Oct 2021

This article was downloaded by **calibre** from <https://www.nature.com/articles/s41586-021-04103-z>

| [Section menu](#) | [Main menu](#) |

- Article
- [Published: 20 October 2021](#)

Neural dynamics underlying birdsong practice and performance

- [Jonnathan Singh Alvarado](#) ORCID: [orcid.org/0000-0002-0942-3849¹](https://orcid.org/0000-0002-0942-3849),
- [Jack Goffinet²](#),
- [Valerie Michael¹](#),
- [William Liberti III³](#),
- [Jordan Hatfield](#) ORCID: [orcid.org/0000-0003-3336-7258¹](https://orcid.org/0000-0003-3336-7258),
- [Timothy Gardner](#) ORCID: [orcid.org/0000-0002-1744-3970⁴](https://orcid.org/0000-0002-1744-3970),
- [John Pearson](#) ORCID: [orcid.org/0000-0002-9876-7837^{1,5,6}](https://orcid.org/0000-0002-9876-7837) &
- [Richard Mooney](#) ORCID: [orcid.org/0000-0002-3308-1367¹](https://orcid.org/0000-0002-3308-1367)

Nature volume **599**, pages 635–639 (2021)

- 4722 Accesses
- 93 Altmetric
- [Metrics details](#)

Subjects

- [Basal ganglia](#)
- [Birdsong](#)
- [Social behaviour](#)

Abstract

Musical and athletic skills are learned and maintained through intensive practice to enable precise and reliable performance for an audience. Consequently, understanding such complex behaviours requires insight into how the brain functions during both practice and performance. Male zebra finches learn to produce courtship songs that are more varied when alone and more stereotyped in the presence of females¹. These differences are thought to reflect song practice and performance, respectively^{2,3}, providing a useful system in which to explore how neurons encode and regulate motor variability in these two states. Here we show that calcium signals in ensembles of spiny neurons (SNs) in the basal ganglia are highly variable relative to their cortical afferents during song practice. By contrast, SN calcium signals are strongly suppressed during female-directed performance, and optogenetically suppressing SNs during practice strongly reduces vocal variability. Unsupervised learning methods^{4,5} show that specific SN activity patterns map onto distinct song practice variants. Finally, we establish that noradrenergic signalling reduces vocal variability by directly suppressing SN activity. Thus, SN ensembles encode and drive vocal exploration during practice, and the noradrenergic suppression of SN activity promotes stereotyped and precise song performance for an audience.

Access options

Subscribe to Journal

Get full journal access for 1 year

\$199.00

only \$3.90 per issue

[Subscribe](#)

All prices are NET prices.

VAT will be added later in the checkout.

Tax calculation will be finalised during checkout.

Rent or Buy article

Get time limited or full article access on ReadCube.

from \$8.99

[Rent or Buy](#)

All prices are NET prices.

Additional access options:

- [Log in](#)
- [Access through your institution](#)
- [Learn about institutional subscriptions](#)

Fig. 1: SN ensemble activity is song-specific and variable.

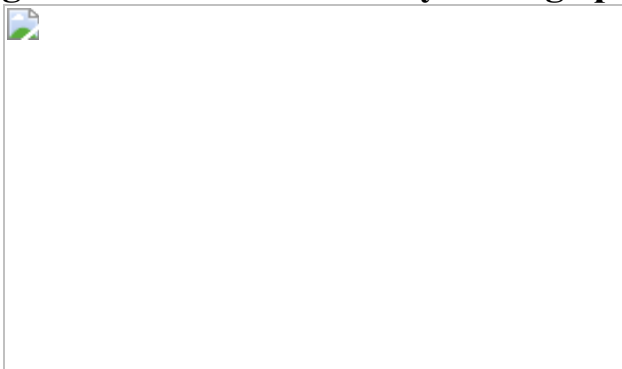


Fig. 2: SN activity drives vocal variability.

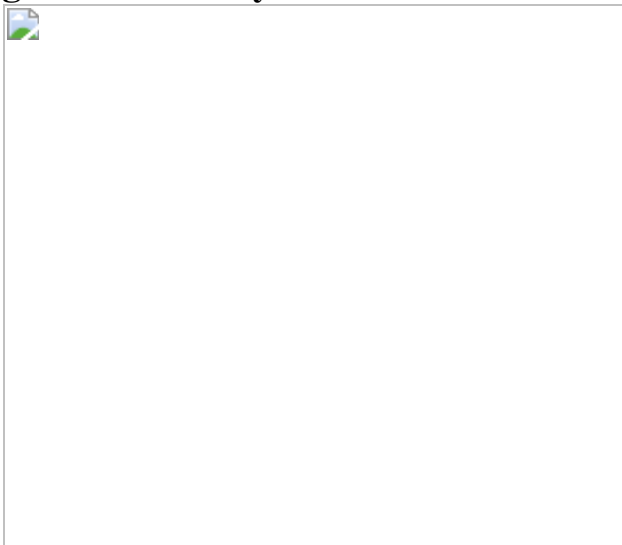
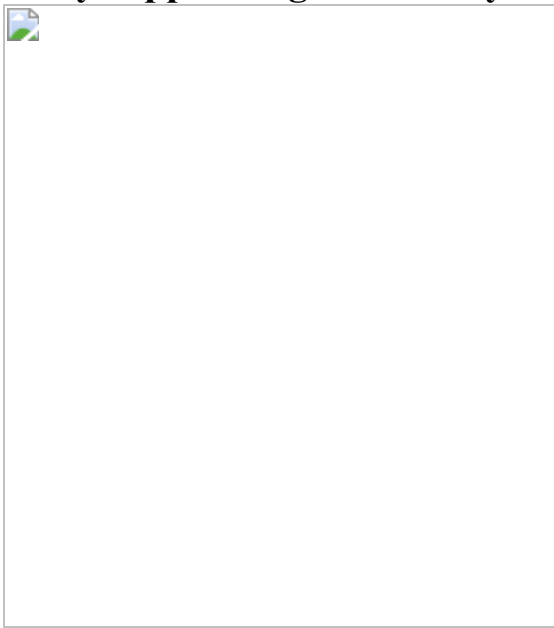


Fig. 3: A joint neural–behavioural modelling approach relates SN population activity and song.



Fig. 4: Noradrenergic signalling in the sBG reduces vocal variability by directly suppressing SN activity.



Data availability

Core datasets have been posted to the Duke University Library Research Data Repository (<https://research.repository.duke.edu>). [Source data](#) are provided with this paper.

Code availability

Custom code and software are available at
<https://github.com/pearsonlab/autoencoded-vocal-analysis> and <https://github.com/pearsonlab/finch-vae>.

References

1. 1.

Sossinka, R. & Böhner, J. Song types in the zebra finch *Poephila guttata castanotis* 1. *Zeitschrift für Tierpsychologie* **53**, 123–132 (1980).

2. 2.

Kao, M. H., Doupe, A. J. & Brainard, M. S. Contributions of an avian basal ganglia–forebrain circuit to real-time modulation of song. *Nature* **433**, 638–643 (2005).

3. 3.

Jarvis, E. D., Scharff, C., Grossman, M. R., Ramos, J. A. & Nottebohm, F. For whom the bird sings: context-dependent gene expression. *Neuron* **21**, 775–788 (1998).

4. 4.

Goffinet, J., Brudner, S., Mooney, R. & Pearson, J. Low-dimensional learned feature spaces quantify individual and group differences in vocal repertoires. *eLife* **10**, e67855 (2021).

5. 5.

Sainburg, T., Thielk, M. & Gentner, T. Q. Finding, visualizing, and quantifying latent structure across diverse animal vocal repertoires. *PLoS Comput. Biol.* **16**, e1008228 (2020).

6. 6.

Woolley, S. C. & Doupe, A. J. Social context-induced song variation affects female behavior and gene expression. *PLoS Biol.* **6**, e62 (2008).

7. 7.

Kao, M. H., Wright, B. D. & Doupe, A. J. Neurons in a forebrain nucleus required for vocal plasticity rapidly switch between precise firing and variable bursting depending on social context. *J. Neurosci.* **28**, 13232–13247 (2008).

8. 8.

Woolley, S. C., Rajan, R., Joshua, M. & Doupe, A. J. Emergence of context-dependent variability across a basal ganglia network. *Neuron* **82**, 208–223 (2014).

9. 9.

Kojima, S., Kao, M. H., Doupe, A. J. & Brainard, M. S. The avian basal ganglia are a source of rapid behavioral variation that enables vocal motor exploration. *J. Neurosci.* **38**, 9635–9647 (2018).

10. 10.

Hein, A. M., Sridharan, A., Nordeen, K. W. & Nordeen, E. J. Characterization of CaMKII-expressing neurons within a striatal region implicated in avian vocal learning. *Brain Res.* **1155**, 125–133 (2007).

11. 11.

Kozhevnikov, A. A. & Fee, M. S. Singing-related activity of identified HVC neurons in the zebra finch. *J. Neurophysiol.* **97**, 4271–4283 (2007).

12. 12.

Hahnloser, R. H. R., Kozhevnikov, A. A. & Fee, M. S. An ultra-sparse code underlies the generation of neural sequences in a songbird.

Nature **419**, 65–70 (2002).

13. 13.

Liberti, W. A. 3rd et al. Unstable neurons underlie a stable learned behavior. *Nat. Neurosci.* **19**, 1665–1671 (2016).

14. 14.

Kingma D. P. & Welling M. Auto-encoding variational Bayes. Preprint at <https://arxiv.org/abs/1312.6114> (2013).

15. 15.

Rezende D. J., Mohamed S. & Wierstra D. Stochastic backpropagation and approximate inference in deep generative models. Preprint at <http://arxiv.org/abs/1401.4082> (2014).

16. 16.

Björklund, A. & Dunnett, S. B. Dopamine neuron systems in the brain: an update. *Trends Neurosci.* **30**, 194–202 (2007).

17. 17.

Zerbi, V. et al. Rapid reconfiguration of the functional connectome after chemogenetic locus coeruleus activation. *Neuron* **103**, 702–718.e5 (2019).

18. 18.

Castelino, C. B., Diekamp, B. & Ball, G. F. Noradrenergic projections to the song control nucleus area X of the medial striatum in male zebra finches (*Taeniopygia guttata*). *J. Comp. Neurol.* **502**, 544–562 (2007).

19. 19.

Person, A. L., Gale, S. D., Farries, M. A. & Perkel, D. J. Organization of the songbird basal ganglia, including area X. *J. Comp. Neurol.* **508**,

840–866 (2008).

20. 20.

Castelino, C. B. & Ball, G. F. A role for norepinephrine in the regulation of context-dependent ZENK expression in male zebra finches (*Taeniopygia guttata*). *Eur. J. Neurosci.* **21**, 1962–1972 (2005).

21. 21.

Leblois, A., Wendel, B. J. & Perkel, D. J. Striatal dopamine modulates basal ganglia output and regulates social context-dependent behavioral variability through D1 receptors. *J. Neurosci.* **30**, 5730–5743 (2010).

22. 22.

Hara, M. et al. Role of adrenoceptors in the regulation of dopamine/DARPP-32 signaling in neostriatal neurons. *J. Neurochem.* **113**, 1046–1059 (2010).

23. 23.

Bharati, I. S. & Goodson, J. L. Fos responses of dopamine neurons to sociosexual stimuli in male zebra finches. *Neuroscience* **143**, 661–670 (2006).

24. 24.

Budzillo, A., Duffy, A., Miller, K. E., Fairhall, A. L. & Perkel, D. J. Dopaminergic modulation of basal ganglia output through coupled excitation-inhibition. *Proc. Natl Acad. Sci. USA* **114**, 5713–5718 (2017).

25. 25.

Aston-Jones, G. & Cohen, J. D. An integrative theory of locus coeruleus-norepinephrine function: adaptive gain and optimal performance. *Annu. Rev. Neurosci.* **28**, 403–450 (2005).

26. 26.

Breton-Provencher, V. & Sur, M. Active control of arousal by a locus coeruleus GABAergic circuit. *Nat. Neurosci.* **22**, 218–228 (2019).

27. 27.

Cooper, B. G. & Goller, F. Physiological insights into the social-context-dependent changes in the rhythm of the song motor program. *J. Neurophysiol.* **95**, 3798–3809 (2006).

28. 28.

Wong, A. L., Lindquist, M. A., Haith, A. M. & Krakauer, J. W. Explicit knowledge enhances motor vigor and performance: motivation versus practice in sequence tasks. *J. Neurophysiol.* **114**, 219–232 (2015).

29. 29.

Pekny, S. E., Izawa, J. & Shadmehr, R. Reward-dependent modulation of movement variability. *J. Neurosci.* **35**, 4015–4024 (2015).

30. 30.

Jaffe, P. I. & Brainard, M. S. Acetylcholine acts on songbird premotor circuitry to invigorate vocal output. *eLife* **9**, e53288 (2020).

31. 31.

Olveczky, B. P., Andalman, A. S. & Fee, M. S. Vocal experimentation in the juvenile songbird requires a basal ganglia circuit. *PLoS Biol.* **3**, e153 (2005).

32. 32.

Sober, S. J., Wohlgemuth, M. J. & Brainard, M. S. Central contributions to acoustic variation in birdsong. *J. Neurosci.* **28**, 10370–10379 (2008).

33. 33.

Sheldon, Z. P. et al. Regulation of vocal precision by noradrenergic modulation of a motor nucleus. *J. Neurophysiol.* **124**, 458–470 (2020).

34. 34.

Fee, M. S. & Goldberg, J. H. A hypothesis for basal ganglia-dependent reinforcement learning in the songbird. *Neuroscience* **198**, 152–170 (2011).

35. 35.

Markowitz, J. E. et al. The striatum organizes 3D behavior via moment-to-moment action selection. *Cell* **174**, 44–58.e17 (2018).

36. 36.

Klaus, A. et al. The spatiotemporal organization of the striatum encodes action space. *Neuron* **95**, 1171–1180.e7 (2017).

37. 37.

Hisey, E., Kearney, M. G. & Mooney, R. A common neural circuit mechanism for internally guided and externally reinforced forms of motor learning. *Nat. Neurosci.* **21**, 589–597 (2018).

38. 38.

Xiao, L. et al. A basal ganglia circuit sufficient to guide birdsong learning. *Neuron* **98**, 208–221.e5 (2018).

39. 39.

Coddington, L. T. & Dudman, J. T. The timing of action determines reward prediction signals in identified midbrain dopamine neurons. *Nat. Neurosci.* **21**, 1563–1573 (2018).

40. 40.

Ghosh, K. K. et al. Miniaturized integration of a fluorescence microscope. *Nat. Methods* **8**, 871–878 (2011).

41. 41.

Zhou, P. et al. Efficient and accurate extraction of in vivo calcium signals from microendoscopic video data. *eLife* **7**, e28728 (2018).

42. 42.

Pisanello, M. et al. Tailoring light delivery for optogenetics by modal demultiplexing in tapered optical fibers. *Sci. Rep.* **8**, 4467 (2018).

43. 43.

Murphy, K. P. *Machine Learning: A Probabilistic Perspective* (MIT Press, 2012).

44. 44.

Wu, M. & Goodman, N. Multimodal generative models for scalable weakly-supervised learning. *Adv. Neural Info. Process. Syst.* **31**, 5575–5585 (2018).

45. 45.

Farries, M. A., Ding, L. & Perkel, D. J. Evidence for “direct” and “indirect” pathways through the song system basal ganglia. *J. Comp. Neurol.* **484**, 93–104 (2005).

Acknowledgements

The authors thank M. Booze for animal husbandry and K. Franks, F. Wang and D. Purves for editorial comments on an earlier version of this manuscript. This work was supported by NIH R01 NS099288 (R.M.), R01 NS118424 (R.M., J.P. and T.G.), the George Barth Geller Fund (R.M.), a Broad Predoctoral Fellowship (J.S.A.) and NIH Predoctoral Fellowship F31 DC017879 (V.M.).

Author information

Affiliations

1. Department of Neurobiology, Duke University, Durham, NC, USA

Jonnathan Singh Alvarado, Valerie Michael, Jordan Hatfield, John Pearson & Richard Mooney

2. Department of Computer Science, Duke University, Durham, NC, USA

Jack Goffinet

3. Department of Electrical Engineering and Computer Science, University of California Berkeley, Berkeley, CA, USA

William Liberti III

4. Phil and Penny Knight Campus for Accelerating Scientific Impact, University of Oregon, Eugene, OR, USA

Timothy Gardner

5. Department of Biostatistics & Bioinformatics, Duke University, Durham, NC, USA

John Pearson

6. Department of Electrical and Computer Engineering, Duke University, Durham, NC, USA

John Pearson

Contributions

J.S.A. and R.M. designed all experiments except the HVC miniscope imaging experiments, which were designed by W.L. and T.G.; J.G. and J.P.

developed VAE methods to analyse acoustic and neural data; J.S.A. performed all in vivo imaging and behavioural experiments and analysed all related data, except for HVC miniscope imaging experiments, which were executed by W.L. and T.G.; V.M. performed in vitro recordings and V.M. and J.S.A. analysed resulting data; J.S.A. and J.H. performed and analysed histological experiments; J.G. analysed acoustic and neural data using VAEs; J.S.A., J.G., J.P. and R.M. wrote the manuscript; J.S.A., J.G., W.L., T.G., J.P. and R.M. edited the manuscript.

Corresponding authors

Correspondence to [John Pearson](#) or [Richard Mooney](#).

Ethics declarations

Competing interests

The authors declare no competing interests.

Additional information

Peer review information *Nature* thanks David Robbe, Kazuhiro Wada and the other, anonymous, reviewer(s) for their contribution to the peer review of this work. Peer reviewer reports are available.

Publisher's note Springer Nature remains neutral with regard to jurisdictional claims in published maps and institutional affiliations.

Extended data figures and tables

[Extended Data Fig. 1 Targeting and characterization of SN activity.](#)

a) CaMKII promoter strategy selectively labels SNs in the sBG. Left: Overlap of CaMKII-GCaMP and the SN marker DARPP-32. Middle:

Superimposed image reveals no overlap between retrogradely labeled globus pallidus internus neurons and CaMKII-GFP (0/41 Tracer(+) neurons were co-labeled with GFP, n = 2 birds). Right: Superimposed images reveal almost no overlap between parvalbumin (PV) and CaMKII-GFP (5/251 PV(+) neurons were co-labeled with GFP, n = 2 birds). Scale bars = 100 μ m.

b) Specificity and sensitivity of HVC PNs and sBG SNs. **c)** Median autocorrelation for all recorded SNs and HVC PNs (median HVC autocorrelation: 0.71, SNs: 0.16). **d)** Shared fraction of active ensemble for SNs and HVC PNs across song renditions (median HVC shared fraction: 0.86, SNs: 0.28). For **(b–d)**, SNs: n = 529 neurons from 7 birds, HVC: n = 165 neurons from 5 birds. **e)** Example of mean SN activity aligned to body velocity; orange shading denotes singing periods. Data are displayed as mean \pm s.e.m. **f)** Detected movement initiations (1311 detected initiations from 1 recording session, top) aligned to SN activity from photometry recordings (bottom). **g)** Group data comparing mean SN activity during singing vs. non-singing locomotion (Student's one-sided paired *t*-test, $t_3=2.464$, *p = 0.0453; n = 4 birds). **h)** Group data comparing mean SN activity during singing vs. playback of the bird's own song (Student's one-sided paired *t*-test; $t_3=3.31$, *p = 0.0226; n = 4 birds). **i)** Disrupted auditory feedback during singing does not acutely affect SN activity. A random 50% of song renditions were targeted for syllable-triggered white noise (top). Participation probability was not affected by the playback of white noise (Student's two-sided paired *t*-test; p = 0.91; n = 184 neurons from 3 birds). **j)** Example traces shown for 4 SNs comparing activity during normal singing and during singing-triggered noise. t = 0 denotes target syllable onset, dashed line is white noise onset. Only song renditions in which the cell participated were included. 0/184 neurons were found to be significantly modulated by white noise (two-sided Mann-Whitney U-test with Hochberg correction, 0/184 significantly modulated neurons from 3 birds). All error bars denote mean \pm s.e.m.

Source data

Extended Data Fig. 2 Example song-related SN activity.

a) Representative motif spectrogram (top) aligned to sample activity traces from the first 6 undirected song renditions for 5 ROIs, aligned to song motif

onset (vertical dashed line; a-g, syllables; i, introductory notes). **b**) Same representative motif as (a), with activity heatmaps for all 171 trials collected throughout the day, along with the corresponding values for all-to-all correlation and sensitivity. Color scale represents z-scored fluorescence. **c**) Fluorescence trace for one neuron showing two example calcium events (top). Event-triggered probability of song syllable for the 5 neurons (bottom, see methods). All detected calcium events in the time series (27.7 minutes of concatenated recordings, 4.9 minutes with vocalizations) were used to generate the average spectrogram, which is visually represented in terms of the probability of occurrence for each syllable.

Extended Data Fig. 3 Supplemental analyses of song, movement, and neural activity during directed and undirected song.

a) Example frequency contours of syllable ‘d’ in undirected (blue) and directed (red) renditions. **b)** Birds with head-mounted miniscopes exhibit typical directed song features in addition to decreased pitch variability, such as faster directed motifs. Left: Cumulative distribution plot for motif durations in 1 bird. Right: group data for 6 birds (Student’s two-sided paired t-test, $t_5 = 1.87$ $p = 0.12$, $n = 6$ birds). **c)** Directed motifs are preceded by more introductory notes than undirected motifs. (Student’s two-sided paired t-test, $t_5 = -7.69$, *** $p = 0.00094$, $n = 6$ birds). **d)** Top: mean activity of 53 ROIs during directed and undirected singing from one bird. Bottom: mean SN population activity aligned to song onset. **e)** Heatmap of mean population activity for interleaved undirected and directed singing. Dashed line = onset of first syllable in motif. **f)** Left: Mean z-scored activity in undirected and directed conditions, plotted for all ROIs that were collected in directed and undirected conditions, averaged across all collected songs Right: Similar to left, but using only trials in which each neuron had a detected event ($n = 215$ neurons from 6 birds). **g)** Relationship between ROI signal (peak of averaged active trials) and the ratio between its directed and undirected activity ($n = 215$ neurons from 6 birds). Dashed line indicates no modulation ($D/U = 1$). **h)** **Photometry** (top) and velocity (bottom) color-matched traces aligned to undirected ($n = 13$) and directed ($n = 11$) songs. Dashed line indicates the onset of the first motif syllable. **i)** R values between average locomotion during song (500 ms time window) and DF/F

for one bird, computed from data in (h) (f). **j**) **Left: Group data showing R values comparing average song-related neural activity to movement in two conditions: averaging locomotion values over a window of 500 ms before motif onset (pre-song) or 500 ms after motif onset (during-song).** **Right: Corresponding p values.** **k**) Representative histology of photometry recordings. Left: Histology of AAV 2/9 AxGCaMP6m.p2a.nls.tdTomato injection into HVC. Middle: HVC axons in sBG from the same bird. Right: Local injection of AAV 2/9.CaMKII.GCaMP6s into sBG. Scale bar = 50 μ m. **l**) Sample recording session for dual recordings from HVC and HVC_{sBG} axons. Undirected singing, (blue) female presentation and directed singing (red) are collected in the same session. **m**) Same as (l), but for SN photometry. All error bars denote mean \pm s.e.m.

Source data

Extended Data Fig. 4 Additional analyses of optogenetic suppression experiments.

- a)** Experimental approach with representative histology from a CAG.ArchT injection into the sBG, both shown in sagittal view. **b)** Optrode recording in a CAG-ArchT bird showing suppressive effect of green light illumination on spontaneous action potential activity of a single sBG unit. **c)** Group data showing suppressive effects of green light illumination across neurons (CamKII, 5 neurons, CAG, 5 neurons). **d)** Sagittal schematic for coinjections of Pan-neuronal (CAG) and SN (CaMKII) fluorescent proteins into the sBG. **e)** CAG-driven expression of TdTomato (magenta) and CaMKII-driven expression of GFP (green) shown superimposed in the sBG (left) and in separate green (middle) and magenta (right) channels in the pallido-recipient thalamic nucleus DLM. Scale bar = 250 μ m.
- f)** Experimental approach for syllable-triggered optogenetic inhibition. **g)** Group data showing pitch variability during directed and laser-stimulated singing normalized to undirected singing for pan-neuronal inhibition. Mixed effects model, 2-sided permutation test. Laser effect size (relative to baseline: -17.8%, ***p = 0.0011, n = 14 syllables from 6 birds. Directed singing effect size: 13.8%, *p = 0.01, n = 12 syllables from 5 birds. **h)** Pitch variability group data (same data as Fig. 2j and Extended

Data Fig. 4g), non-normalized, comparing values during undirected song versus either undirected + laser (L) or directed (D) conditions. **i)** Intrasyllabic variability data normalized to undirected levels. Mixed effects, 2-sided permutation test. Model fit to non-normalized data, comparing undirected and experimental (undirected + laser (green), or directed (red)) conditions (for model output details, see Tables 1 and 2 in Supplementary Information for model details, in all cases significance was assessed using a two-sided permutation test). **Pan-Neuronal:** Estimated laser effect size: -0.00071 (-10.11% of baseline) ± 0.0002 , * $p = 0.015$. Estimated directed singing effect size: -0.0013 (-20.65%) ± 6.94 , ** $p = 0.0098$. **SNs:** Estimated laser effect size: -0.00034 (-4.09%) ± 0.00011 , ** $p = 0.007$. Estimated directed singing effect size: -0.0033 (-22.18%) ± 0.00063 . **GFP:** Estimated laser effect size: -0.000054 (0.60%) ± 0.00043 , $p = 0.80$. Estimated directed singing effect size = -0.0027 (-36.00%) ± 0.00050 , *** $p = 0.000082$. Pan-neuronal Laser n = 14 syllables from 6 birds, directed n = 12 syllables from 5 birds; SNs: Laser n = 16 syllables from 6 birds, directed n = 12 syllables from 5 birds; GFP: Laser n = 15 syllables from 5 birds for laser, directed n = 10 syllables from 4 birds. **j)** Mean syllable frequency group data normalized to undirected levels. **Pan-Neuronal:** Estimated laser effect size: 3.55 ± 3.14 Hz, $p = 0.27$. Estimated directed singing effect size: 9.91 ± 6.94 Hz, $p = 0.17$. **SNs:** Estimated laser effect size: -8.28 ± 4.54 Hz, $p = 0.079$. Estimated directed singing effect size: -13.95 ± 9.13 Hz, $p = 0.14$. **GFP:** Estimated laser effect size: 0.60 ± 0.37 Hz, $p = 0.12$. Estimated directed singing effect size = 3.041 ± 2.46 Hz, $p = 0.23$. Pan-neuronal laser n = 14 syllables from 6 birds, directed n = 12 syllables from 6 birds; SNs: Laser n = 16 syllables from 6 birds, directed n = 12 syllables from 5 birds; GFP: Laser N = 15 syllables from 5 birds for laser, directed n = 10 syllables from 4 birds. **k)** Mean syllable duration group data normalized to undirected levels. **Pan-Neuronal:** Estimated laser effect size: -0.58 ± 0.23 ms, * $p = 0.016$. Estimated directed singing effect size: -0.65 ± 0.28 msec, * $p = 0.035$. **SNs:** Estimated laser effect size: -0.82 ± 0.36 ms, ** $p = 0.029$. Estimated directed singing effect size -2.76 ± 0.62 ms, *** $p = 0.00016$. **GFP:** Estimated laser effect size: -0.84 ± 0.63 ms, $p = 0.19$. Estimated directed singing effect size = -4.37 ± 0.80 ms, *** $p = 0.000030$. Pan-neuronal: Laser N = 14 syllables from 6 birds, directed N = 12 syllables from 6 birds; SNs: Laser N = 16 syllables from 6 birds, directed n = 12 syllables from 5 birds; GFP: Laser n = 15 syllables from 5 birds for laser,

directed n = 10 syllables from 4 birds. Data are displayed as mean \pm sem. All error bars denote mean \pm s.e.m. Pan-neuronal: Laser N = 14 syllables from 6 birds, Directed N = 12 syllables from 6 birds; SNs: Laser N = 16 syllables from 6 birds, Dir N = 12 syllables from 5 birds; GFP: Laser N = 15 syllables from 5 birds for laser, Dir N = 10 syllables from 4 birds. Data are displayed as mean \pm sem. All error bars denote mean \pm s.e.m.

[Source data](#)

Extended Data Fig. 5 Joint encoding model details and comparison to alternate models.

a) Schematic for learning low dimensional latent features of motif spectrograms using a variational autoencoder (VAE) approach. The model learns a compressed representation of the data that is sufficient to reconstruct the original. **b)** Cumulative distribution of pairwise song distances in VAE latent space, grouped by the similarity of the associated neural patterns (neural correlation percentiles, yellow to blue). For more dissimilar neural activity (yellow), songs are farther apart in VAE space, while more highly correlated neural activity (blue) shifts the distribution to the left, implying overall more similar songs, as indicated by smaller VAE vocal latent distances. **c)** Group data showing median VAE distance (relative to the mean) within each neural correlation decile for all 7 sessions from 5 birds; pairs of trials with highly correlated neural activity patterns are closer in VAE latent space. Marker shape denotes bird identity. **d)** Schematic of the joint modeling approach. Acoustic data is modeled using a VAE as before (boxed region) and a second VAE is used to model the neural data. A global latent variable is then used to capture shared variation in the two modalities. **e)** Schematic of model training and validation. VAE models were trained using sevenfold cross-validation. Within each fold, data were partitioned into seven tranches, five for VAE model training (magenta), one for VAE model validation and hyperparameter selection (cyan), and one for assessing model performance (yellow). For the VAE model, average performance on the yellow test set across the seven cross-validation folds is reported. For predictive models trained to predict one set of latents from another, a “leave-one-out” strategy on the yellow data set (right) was used to select predictive model hyperparameters and assess

performance. **f)** Joint encoding outperforms a collection of control models. The shuffle control randomly pairs spectrograms and ROI activity vectors. The time control uses time-in-session to predict the joint encoding model's neural latents (left) and vocal latents (right). The linear model comprises independently trained neural and vocal variational autoencoders (as in Fig. 3a without the global latent), with emission and recognition networks restricted to linear mappings. The separate encoding model comprises independently trained neural and vocal variational autoencoders with emission and recognition models parameterized by deep neural networks. The joint encoding model is the full model as presented in Fig. 3a. For all models, prediction is performed using ridge regression and test performance is evaluated using the cross-validation procedure described in Methods. Average test set performance over 7 cross-validation folds of each of 7 sessions from 5 birds is shown. Each line represents a single bird-session.

g) Model comparison split by experimental session. Performance (measured by R^2) for the task of predicting vocal latents from neural latents (top) and vice versa (bottom) for each of 7 sessions from 5 birds. In addition to the models presented in b, the comparison includes models using motif tempo to predict joint encoding neural latents (top) and vocal latents (bottom); using kernel ridge regression in place of linear ridge regression (with leave-one-out regularization strength and radial basis function bandwidth selection); and a version of the joint encoding model with emission and recognition networks restricted to linear mappings. Joint encoding predictive performance is compared with each control model for each experimental session (one-sided Wilcoxon signed-rank test, * denotes $p < 0.05$). For both imaging sessions of one bird (bird 5, denoted by triangles in panels b–d), both neural latents and vocal latents could be robustly predicted from song tempo. **h)** Left: Predictive performance versus number of song motifs (left) for each of 7 experimental sessions. Poor predictive performance is observed for experimental sessions with fewer than 300 motifs and fewer than 50 ROIs (not shown). Symbols denote birds, as in panels b and c. Right: Similar to left. Opaque markers indicate performance using only first motifs in each bout, faded markers indicate performance using all motifs.

[Source data](#)

Extended Data Fig. 6 Joint encoding model preprocessing and additional examples.

- a)** To minimize time confounders, components of calcium activity vectors (top left) and spectrograms (top middle) that could reliably be predicted by time-of-day were removed (red lines; see Methods). The calcium and spectrogram residuals after prediction are used for further analysis in place of the original data (top right). Positive weights are shown in green and negative weights in magenta. Note that the effects are restricted to regions with vocalization. For two example spectrograms from 10:15 (bottom left) and 10:35 (bottom middle), time-of-day correction makes the resulting syllables more similar to one another. Scale bar for right column: 100 ms.
- b)** Left: Despite time warping, spectrograms show consistent tempo-related changes. Difference plot between the average faster-than-median spectrograms and the average slower-than-median spectrograms (bottom, positive values in green, negative in magenta) for one example bird (Bird 3, squares). The consistent horizontal bands throughout the motif indicate upward pitch shifts associated with faster tempos, which were observed for almost all experimental sessions. Scale bars denote 100 ms. Right: Both ensemble activity and warped spectrograms contain information about tempo. For each experimental session, tempo can be predicted from ensemble activity vectors (blue) and spectrograms (red) after both signals have been corrected for time-of-day. Dotted line denotes chance performance. Scale bars denote 100 ms.
- c)** Spectrograms also show consistent motif-number-related changes. For the same example bird as in b, the average of the first motifs in every bout and the average of all other motifs exhibit clear differences (bottom, positive values in green, negative in magenta). Right: Both ensemble activity and time-warped spectrograms contain information about motif number. For each experimental session, motif number (first motif vs. rest) could be reliably predicted from ensemble activity vectors (blue) and spectrograms (red) using the same procedure described for tempo prediction (reporting test accuracy, weighted by class so that chance performance is 0.5). Dotted line denotes chance performance. Scale bars denote 100 ms.
- d)** Example average ROI activity aligned to the first syllable of bouts consisting of 1, 2, 3 or 4 motifs. Note that ROIs 20 and 21 display qualitatively different activities in bouts of different lengths.
- e)** Weighted average generated spectrograms and ROI

activity pairs, with weights given by their projection along the correlation axis, describe how song spectrograms (middle column) and neural activity (right column) vary together. P-values refer to corresponding correlations of held-out test data, as in Figure 3c. Scale bars for left and middle columns: 100 ms. Scale bars for right column: 250 μ m.

Source data

Extended Data Fig. 7 Effects of adrenergic signaling manipulations on song and neural activity.

- a) Retrograde labelling of dopamine beta hydroxylase (DBH) and tyrosine hydroxylase (TH) positive cell bodies in the locus coeruleus (LC) and ventral tegmental area (VTA), respectively, following retrograde tracer injections into the sBG. Scale bar = xx microns and applies to both panels.
- b) SCH, PHE, and CLON infusion do not significantly affect singing rates (Student's two-tailed paired t-test, CLON: $t_5 = 0.81$, $p = 0.46$, $n = 6$ birds; PHE: $t_7 = 0.97$, $p = 0.28$, $n = 8$ birds; SCH: $t_7 = 1.17$, $p = 0.36$, $n = 8$ birds).
- c) SCH, PHE, and CLON infusion do not significantly affect number of introductory notes per bout (Student's two-tailed paired t-test, CLON: $t_5 = -0.16$, $p = 0.88$, $n = 6$ birds; PHE: $t_7 = 1.05$, $p = 0.33$, $n = 8$ birds; SCH: $t_7 = 0.91$, $p = 0.30$, $n = 8$ birds).
- d) Left: Effects of PHE on pitch variability in directed and undirected song. Mixed effects model, 2-sided permutation test, see Tables 1 and 2 in Supplementary Information for model details. Estimated effect of drug presence on directed: 0.36 (26.1% of baseline) \pm 0.17, * $p = 0.02$. Estimated effect of drug presence on undirected: -0.14 (6.7% of baseline) \pm 0.12, $p = 0.24$. Middle: Effects of CLON on pitch variability in directed and undirected song. Estimated effect of drug presence on DIR: -0.025 (1.5% of baseline) \pm 0.10, $p = 0.1$. Estimated effect of drug presence on UNDIR: -0.36 (14.8% of baseline) \pm 0.12, ** $p = 0.0049$. Right: Effects of SCH on pitch variability in directed and undirected song. Estimated effect of drug presence on directed: 0.081 (4.9% of baseline) \pm 0.22, $p = 0.71$. Estimated effect of drug presence on undirected: 0.048 (2% of baseline) \pm 0.84, $p = 0.57$.
- e) Representative histology showing photometry probe and microdialysis probe placement into sBG for simultaneous drug delivery and photometry. Scale bar = 100

μm . **f**) Representative DF/F measurements during directed and undirected singing for one bird before and after (>1 hour) beginning muscimol infusion. **g**) Muscimol infusion suppresses calcium signals recorded in the sBG during both directed and undirected singing (Student's two-tailed paired t-test; $t_4 = 3.63$, p-values are indicated; $n = 5$ birds). **h**) Sample traces for SN imaging during infusion of SCH23390 into the sBG. **i**) Group data showing mean SN photometry signals during SCH23390 infusion in undirected and directed conditions ($n = 4$ birds). **j**) DARPP32 and $\alpha 2\text{c-AR}$ mRNA co-expression sBG SNs ($n = 3$ birds). Scale bar = $20 \mu\text{m}$. **k**) Low power confocal images showing Fos mRNA expression in a sagittal section of the finch brain across behavioral conditions. Dashed white outlines highlight the sBG and HVC. **l**) Fos intensity levels in HVC and the sBG plotted against motif count (30-minute window) in either directed (red) or undirected (blue) singing conditions. For all immediate early gene experiments, undirected $n = 6$ birds, directed $n = 7$ birds, silent $n = 6$ birds. **m**) Example confocal image z-stack collected in the LC. The intensity and area of Fos puncta (magenta) were quantified within the TH-positive mask (yellow). Scale bar = $50 \mu\text{m}$. **n**) Mean Fos intensity and area within LC TH mask plotted against for directed (red) and undirected (blue) motif counts. **o**) Group data for Fos intensity (left) or area (right) plotted for TH and VGAT masks during either directed (red, $N = 7$ birds) or undirected (blue, $N = 6$ birds) singing conditions. One-way ANOVAs with post hoc Tukey tests were performed separately for TH and VGAT masks under each condition. Post hoc comparisons for significant ANOVAs are displayed. Fos mRNA puncta Intensity: TH mask, $F_{(2,16)} = 7.46$, ** $p = 0.0051$, VGAT mask, $F_{(2,16)} = 7.4$, ** $p = 0.0053$. Fos mRNA Area: TH mask, $F_{(2,16)} = 9.02$, $p = 0.0024$, VGAT mask, $F_{(2,16)} = 3.6$, $p = 0.051$.

Source data

Extended Data Fig. 8 Effects of adrenergic signaling on SN excitability.

a) Rise time, sag, and resting membrane potential can be used to distinguish SNs from non-SNs in the sBG (see Methods). **b)** Three more example SNs recorded during baseline, NA, and PHE. **c)** Effect of NA and PHE on SN

resting membrane potential (One-way repeated measures ANOVA with Greenhouse-Geisser correction. $F_{(1.487, 16.36)} = 0.5950$ p = 0.51; n = 11 cells). **d)** Effect of NA and PHE on SN input resistance (One-way repeated measures ANOVA with Greenhouse-Geisser correction and post-hoc Tukey test. $F_{(1.229, 13.52)} = 7.980$; Baseline vs NA: p = 0.054; NA vs PHE: ***p = 0.0003; n = 11 cells). **e)** 2 example SNs recorded during baseline and PHE, from a different experiment than **a-d**. **f)** F-I curves showing increased action potentials in response to positive current injection for baseline and PHE conditions (n = 12 cells). **g)** Effect of PHE on SN resting membrane potential (Student's two-tailed paired t-test, $t_{10} = 0.55$, p = 0.59; n = 11 cells, separate from those shown in panel **c**). **h)** Effect of PHE on SN input resistance (Student's two-tailed paired t-test, $t_{10} = 5.42$, ***p = 0.0003; n = 11 cells, separate from those shown in panel **d**).

[Source data](#)

Supplementary information

[Supplementary Information](#)

[Reporting Summary](#)

[Peer Review File](#)

[Supplementary Video 1](#)

A movie showing calcium signals recorded with a miniature microscope in the basal ganglia of a male zebra finch singing in social isolation (undirected song).

[Supplementary Video 2](#)

The left frame shows calcium signals recorded with a miniature microscope in the basal ganglia of a male zebra finch singing in social isolation (undirected song). The right frame shows calcium signals recorded with a

miniature microscope in the basal ganglia of a male zebra finch singing to a nearby female (directed song). The two movies are from the same imaging field in the same male finch, collected several minutes apart.

Source data

[Source Data Fig. 1](#)

[Source Data Fig. 2](#)

[Source Data Fig. 3](#)

[Source Data Fig. 4](#)

[Source Data Extended Data Fig. 1](#)

[Source Data Extended Data Fig. 3](#)

[Source Data Extended Data Fig. 4](#)

[Source Data Extended Data Fig. 5](#)

[Source Data Extended Data Fig. 6](#)

[Source Data Extended Data Fig. 7](#)

[Source Data Extended Data Fig. 8](#)

[Source Data Extended Data Fig. 9](#)

Rights and permissions

[Reprints and Permissions](#)

About this article

Cite this article

Singh Alvarado, J., Goffinet, J., Michael, V. *et al.* Neural dynamics underlying birdsong practice and performance. *Nature* **599**, 635–639 (2021). <https://doi.org/10.1038/s41586-021-04004-1>

- Received: 08 December 2020
- Accepted: 07 September 2021
- Published: 20 October 2021
- Issue Date: 25 November 2021
- DOI: <https://doi.org/10.1038/s41586-021-04004-1>

Share this article

Anyone you share the following link with will be able to read this content:

[Get shareable link](#)

Sorry, a shareable link is not currently available for this article.

[Copy to clipboard](#)

Provided by the Springer Nature SharedIt content-sharing initiative

This article was downloaded by **calibre** from <https://www.nature.com/articles/s41586-021-04004-1>

- Article
- [Published: 27 October 2021](#)

A human-specific modifier of cortical connectivity and circuit function

- [Ewoud R. E. Schmidt](#) [ORCID: orcid.org/0000-0003-4654-2377^{1,2 nAff6}](#),
- [Hanzhi T. Zhao](#) [ORCID: orcid.org/0000-0001-6616-7039^{2,3 nAff6}](#),
- [Jung M. Park^{1,2}](#),
- [Mario Dipoppa^{2,4 na1}](#),
- [Mauro M. Monsalve-Mercado^{2,4 na1}](#),
- [Jacob B. Dahan^{1,2}](#),
- [Chris C. Rodgers^{1,2,5}](#),
- [Amélie Lejeune^{1,2}](#),
- [Elizabeth M. C. Hillman](#) [ORCID: orcid.org/0000-0001-5511-1451^{2,3}](#),
- [Kenneth D. Miller^{1,2,4,5}](#),
- [Randy M. Bruno^{1,2,5}](#) &
- [Franck Polleux](#) [ORCID: orcid.org/0000-0003-4313-0481^{1,2,5}](#)

Nature volume **599**, pages 640–644 (2021)

- 9459 Accesses
- 1 Citations
- 287 Altmetric
- [Metrics details](#)

Subjects

- [Genetics of the nervous system](#)
- [Neural circuits](#)

Abstract

The cognitive abilities that characterize humans are thought to emerge from unique features of the cortical circuit architecture of the human brain, which include increased cortico–cortical connectivity. However, the evolutionary origin of these changes in connectivity and how they affected cortical circuit function and behaviour are currently unknown. The human-specific gene duplication *SRGAP2C* emerged in the ancestral genome of the *Homo* lineage before the major phase of increase in brain size^{1,2}. *SRGAP2C* expression in mice increases the density of excitatory and inhibitory synapses received by layer 2/3 pyramidal neurons (PNs)^{3,4,5}. Here we show that the increased number of excitatory synapses received by layer 2/3 PNs induced by *SRGAP2C* expression originates from a specific increase in local and long-range cortico–cortical connections. Mice humanized for *SRGAP2C* expression in all cortical PNs displayed a shift in the fraction of layer 2/3 PNs activated by sensory stimulation and an enhanced ability to learn a cortex-dependent sensory-discrimination task. Computational modelling revealed that the increased layer 4 to layer 2/3 connectivity induced by *SRGAP2C* expression explains some of the key changes in sensory coding properties. These results suggest that the emergence of *SRGAP2C* at the birth of the *Homo* lineage contributed to the evolution of specific structural and functional features of cortical circuits in the human cortex.

Access options

Subscribe to Journal

Get full journal access for 1 year

\$199.00

only \$3.90 per issue

[Subscribe](#)

All prices are NET prices.

VAT will be added later in the checkout.

Tax calculation will be finalised during checkout.

Rent or Buy article

Get time limited or full article access on ReadCube.

from \$8.99

[Rent or Buy](#)

All prices are NET prices.

Additional access options:

- [Log in](#)
- [Access through your institution](#)
- [Learn about institutional subscriptions](#)

Fig. 1: Sparse monosynaptic tracing in layer 2/3 PNs humanized for SRGAP2C expression.

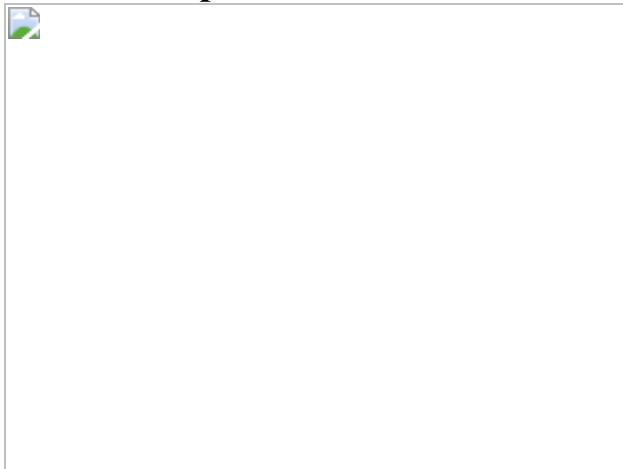


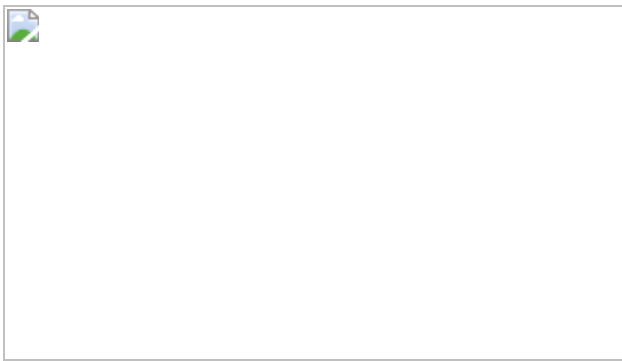
Fig. 2: SRGAP2C expression increases cortical inputs onto layer 2/3 PNs.



Fig. 3: SRGAP2C increases the probability and selectivity of neuronal responses to sensory stimulation.



Fig. 4: Humanized SRGAP2C mice display an increased ability to learn a texture-discrimination task.



Data availability

The reagents, mouse line and datasets generated and/or analysed during the current study are available from the corresponding author upon request.

Code availability

Custom-written Matlab and Python code is available upon request from the corresponding author.

References

1. 1.

Dennis, M. Y. et al. The evolution and population diversity of human-specific segmental duplications. *Nat. Ecol. Evol.* **1**, 0069 (2017).

2. 2.

Ponce de León, M. S. et al. The primitive brain of early *Homo*. *Science* **372**, 165–171 (2021).

3. 3.

Charrier, C. et al. Inhibition of SRGAP2 function by its human-specific paralogs induces neoteny during spine maturation. *Cell* **149**, 923–935 (2012).

4. 4.

Fossati, M. et al. SRGAP2 and its human-specific paralog co-regulate the development of excitatory and inhibitory synapses. *Neuron* **91**, 356–369 (2016).

5. 5.

Schmidt, E. R. E., Kupferman, J. V., Stackmann, M. & Polleux, F. The human-specific paralogs SRGAP2B and SRGAP2C differentially modulate SRGAP2A-dependent synaptic development. *Sci. Rep.* **9**, 18692 (2019).

6. 6.

Sudmant, P. H. et al. Diversity of human copy number variation and multicopy genes. *Science* **330**, 641–646 (2010).

7. 7.

Fortna, A. et al. Lineage-specific gene duplication and loss in human and great ape evolution. *PLoS Biol.* **2**, E207 (2004).

8. 8.

Sporny, M. et al. Structural history of human SRGAP2 proteins. *Mol. Biol. Evol.* **34**, 1463–1478 (2017).

9. 9.

Benavides-Piccione, R., Ballesteros-Yáñez, I., DeFelipe, J. & Yuste, R. Cortical area and species differences in dendritic spine morphology. *J. Neurocytol.* **31**, 337–346 (2002).

10. 10.

Elston, G. N., Benavides-Piccione, R. & DeFelipe, J. The pyramidal cell in cognition: a comparative study in human and monkey. *J. Neurosci.* **21**, RC163 (2001).

11. 11.

Reardon, T. R. et al. Rabies virus CVS-N2cδG strain enhances retrograde synaptic transfer and neuronal viability. *Neuron* **89**, 711–724 (2016).

12. 12.

Wickersham, I. R., Finke, S., Conzelmann, K. K. & Callaway, E. M. Retrograde neuronal tracing with a deletion-mutant rabies virus. *Nat. Methods* **4**, 47–49 (2007).

13. 13.

Allen Mouse Common Coordinate Framework. Technical White Paper (Allen Institute for Brain Science, 2015).

14. 14.

Minamisawa, G., Kwon, S. E., Chevée, M., Brown, S. P. & O'Connor, D. H. A non-canonical feedback circuit for rapid interactions between somatosensory cortices. *Cell Rep.* **23**, 2718–2731.e6 (2018).

15. 15.

Tremblay, R., Lee, S. & Rudy, B. GABAergic interneurons in the neocortex: from cellular properties to circuits. *Neuron* **91**, 260–292 (2016).

16. 16.

Genescu, I. & Garel, S. Being superficial: a developmental viewpoint on cortical layer 1 wiring. *Curr. Opin. Neurobiol.* **66**, 125–134 (2021).

17. 17.

Dana, H. et al. *Thy1*-GCaMP6 transgenic mice for neuronal population imaging in vivo. *PLoS ONE* **9**, e108697 (2014).

18. 18.

Goebbelz, S. et al. Genetic targeting of principal neurons in neocortex and hippocampus of *NEX*-Cre mice. *Genesis* **44**, 611–621 (2006).

19. 19.

Grienberger, C. & Konnerth, A. Imaging calcium in neurons. *Neuron* **73**, 862–885 (2012).

20. 20.

Petersen, C. C. H. Sensorimotor processing in the rodent barrel cortex. *Nat. Rev. Neurosci.* **20**, 533–546 (2019).

21. 21.

Guic-Robles, E., Jenkins, W. M. & Bravo, H. Vibrissal roughness discrimination is barrelcortex-dependent. *Behav. Brain Res.* **48**, 145–152 (1992).

22. 22.

Manita, S. et al. A top-down cortical circuit for accurate sensory perception. *Neuron* **86**, 1304–1316 (2015).

23. 23.

Park, J., Rodgers, C., Hong, Y. K., Dahan, J. & Bruno, R. Primary somatosensory cortex is essential for texture discrimination but not object detection in mice. *IBRO Rep.* **6**, S550 (2019).

24. 24.

Geiller, T. et al. Large-scale 3D two-photon imaging of molecularly identified CA1 interneuron dynamics in behaving mice. *Neuron* **108**, 968–983.e9 (2020).

25. 25.

Rossi, L. F., Harris, K. D. & Carandini, M. Spatial connectivity matches direction selectivity in visual cortex. *Nature* **588**, 648–652 (2020).

26. 26.

Courchet, J. et al. Terminal axon branching is regulated by the LKB1–NUAK1 kinase pathway via presynaptic mitochondrial capture. *Cell* **153**, 1510–1525 (2013).

27. 27.

Hand, R. & Polleux, F. Neurogenin2 regulates the initial axon guidance of cortical pyramidal neurons projecting medially to the corpus callosum. *Neural Dev.* **6**, 30 (2011).

28. 28.

Paxinos, G. & Franklin, K. B. J. *The Mouse Brain in Stereotaxic Coordinates* (Academic, 2001).

29. 29.

Ma, Y. et al. Wide-field optical mapping of neural activity and brain haemodynamics: considerations and novel approaches. *Philos. Trans. R. Soc. B Biol. Sci.* **371**, 20150360 (2016).

30. 30.

Pnevmatikakis, E. A. & Giovannucci, A. NoRMCorre: an online algorithm for piecewise rigid motion correction of calcium imaging data. *J. Neurosci. Methods* **291**, 83–94 (2017).

31. 31.

Peters, A. J., Chen, S. X. & Komiyama, T. Emergence of reproducible spatiotemporal activity during motor learning. *Nature* **510**, 263–267 (2014).

32. 32.

Deneux, T. et al. Accurate spike estimation from noisy calcium signals for ultrafast three-dimensional imaging of large neuronal populations in vivo. *Nat. Commun.* **7**, 12190 (2016).

33. 33.

Hansel, D. & van Vreeswijk, C. How noise contributes to contrast invariance of orientation tuning in cat visual cortex. *J. Neurosci.* **22**, 5118–5128 (2002).

34. 34.

Miller, K. D. & Troyer, T. W. Neural noise can explain expansive, power-law nonlinearities in neural response functions. *J. Neurophysiol.*

87, 653–659 (2002).

35. 35.

Priebe, N. J. & Ferster, D. Inhibition, spike threshold, and stimulus selectivity in primary visual cortex. *Neuron* **57**, 482–497 (2008).

36. 36.

Rubin, D. B., Van Hooser, S. D. & Miller, K. D. The stabilized supralinear network: a unifying circuit motif underlying multi-input integration in sensory cortex. *Neuron* **85**, 402–417 (2015).

37. 37.

Hennequin, G., Ahmadian, Y., Rubin, D. B., Lengyel, M. & Miller, K. D. The dynamical regime of sensory cortex: stable dynamics around a single stimulus-tuned attractor account for patterns of noise variability. *Neuron* **98**, 846–860.e5 (2018).

38. 38.

Keller, A. J. et al. A disinhibitory circuit for contextual modulation in primary visual cortex. *Neuron* **108**, 1181–1193.e8 (2020).

Acknowledgements

The transgenic inducible knock-in mouse model described here was developed in collaboration with genOway (Lyon, France). We thank T. Reardon and S. Fageiray for providing RABV; M. Hirabayashi and Q. Liu for technical help; D. Peterka and the staff at the Zuckerman Institute's Cellular Imaging platform for instrument use and technical advice; and members of the Polleux laboratory and P. Vanderhaeghen for valuable discussions and input. This work was supported by NIH R01 (RO1NS067557) (to F.P.); an award from the Roger De Spoelberch Fondation (to F.P.); an award from the Nomis Foundation (to F.P.); the Netherlands Organization for Scientific Research (NWO Rubicon 825.14.017) (to E.R.E.S.); the European Molecular Biology Organization

(EMBO Long-Term Fellowship ALTF 1055-2014) (to E.R.E.S.); NIH K99 (NS109323) (to E.R.E.S.); NSF GRFP (to J.M.P.); NIH R01 (NS094659) and NIH R01 (NS069679) (to R.M.B.); NIH U19 (U19NS107613) (to M.D., M.M.M.-M. and K.D.M.); a NSF NeuroNex Award (DBI-1707398) (to K.D.M. and M.D.); The Gatsby Charitable Foundation (GAT3708) (to K.D.M. and M.D.); the Simons Collaboration on the Global Brain (543017) (to K.D.M. and M.D.); and R01 NS063226, RF1 MH114276, UF1 NS108213 and U19NS104649 (to E.M.C.H.).

Author information

Author notes

1. Ewoud R. E. Schmidt & Hanzhi T. Zhao

Present address: Department of Neuroscience, Medical University of South Carolina, Charleston, SC, USA

2. These authors contributed equally: Mario Dipoppa, Mauro M. Monsalve-Mercado

Affiliations

1. Department of Neuroscience, Columbia University, New York, NY, USA

Ewoud R. E. Schmidt, Jung M. Park, Jacob B. Dahan, Chris C. Rodgers, Amélie Lejeune, Kenneth D. Miller, Randy M. Bruno & Franck Polleux

2. Mortimer B. Zuckerman Mind Brain Behavior Institute, Columbia University, New York, NY, USA

Ewoud R. E. Schmidt, Hanzhi T. Zhao, Jung M. Park, Mario Dipoppa, Mauro M. Monsalve-Mercado, Jacob B. Dahan, Chris C. Rodgers, Amélie Lejeune, Elizabeth M. C. Hillman, Kenneth D. Miller, Randy M. Bruno & Franck Polleux

3. Department of Biomedical Engineering and Radiology, Columbia University, New York, NY, USA

Hanzhi T. Zhao & Elizabeth M. C. Hillman

4. Center for Theoretical Neuroscience, College of Physicians and Surgeons, Columbia University, New York, NY, USA

Mario Dipoppa, Mauro M. Monsalve-Mercado & Kenneth D. Miller

5. Kavli Institute for Brain Science, Columbia University, New York, NY, USA

Chris C. Rodgers, Kenneth D. Miller, Randy M. Bruno & Franck Polleux

Contributions

E.R.E.S. and F.P. conceived the experiments. E.R.E.S carried out the RABV tracing and synaptic analysis. E.R.E.S. and A.L. performed the spine quantifications, and E.R.E.S. and H.T.Z. performed the two-photon imaging experiments. C.C.R., J.M.P. and R.M.B. developed the texture-discrimination behaviour experiments, and E.R.E.S., J.M.P. and J.B.D. performed these experiments. M.D., M.M.M.-M. and K.D.M. performed the data analysis and computational modelling shown in Extended Data Figs. [8](#) and [9](#). E.R.E.S., H.T.Z. and J.M.P. analysed the data. R.M.B. advised on the behavioural experimental design, and E.M.C.H. and R.M.B. advised on the two-photon data analysis. E.R.E.S. and F.P. wrote the manuscript.

Corresponding author

Correspondence to [Franck Polleux](#).

Ethics declarations

Competing interests

The authors declare no competing interests.

Additional information

Peer review information *Nature* thanks Tatiana Engel and the other, anonymous, reviewer(s) for their contribution to the peer review of this work.

Publisher's note Springer Nature remains neutral with regard to jurisdictional claims in published maps and institutional affiliations.

Extended data figures and tables

Extended Data Fig. 1 Generation of an inducible, humanized SRGAP2C transgenic mouse line.

(a–b) Design strategy for generating SRGAP2C conditional knock in mice. 3x HA tagged *SRGAP2C* was inserted into a *Rosa26* targeting vector (a), which contains a CAG promoter, a floxed STOP-Neomycin cassette, and *Rosa26* homology arms. Image not to scale. Using homologous recombination, the targeting vector was inserted between exon 1 and 2 of the *Rosa26* locus (b). **(c–d)** Verification of SRGAP2C targeting in mouse embryonic stem cells using Southern blot analysis with probes that distinguish the targeted allele (12.2 kb in (c), 13.1 kb in (d)) from the wild-type allele (5.3 kb in (c), 9.2 kb in (d)). **(e)** Mice were genotyped by genomic PCR using the forward and reverse primers indicated that distinguish the WT *Rosa26* allele or the SRGAP2C allele. **(f)** Western blot probed with anti-HA antibody of adult (P30) cortex isolated from SRGAP2C heterozygous conditional knock-in mice crossed with heterozygous *Nex*^{Cre/+} mice (Cre+) or wild-type littermate (Cre-). The presence of Cre induces SRGAP2C-HA expression. Without Cre, no SRGAP2C was detected. Anti-Actin antibody was used as loading control. **(g)** Immunohistochemistry for HA on cortical brain sections from adult SRGAP2C heterozygous conditional knock-in mice crossed with heterozygous *Nex*^{Cre/+} mice (Cre+) or wild-type littermate control (Cre-). Scale bar, 25 μm. **(h)** Same as g, on sections from SRGAP2C heterozygous

conditional knock-in mice in which mRuby-Cre was sparsely expressed using *in utero* cortical electroporation. Scale bar, 10 μ m.

Extended Data Fig. 2 Brain regions containing RABV traced neurons.

(a) Reference brain (top) based on Allen Reference Atlas. Digital reconstruction of RABV traced brain and registration onto reference brain. Black arrow indicates location of starter neurons in barrel field of S1. **(b)** Density plots showing distribution of traced neurons in WT and SRGAP2C mice. Colors in density plot indicate index of connectivity (IOC): number of traced neurons / number of starter neurons). **(c)** IOC for brain regions ipsilateral and contralateral to the injection site. RSP, retrosplenial area, ORB, Orbital cortex, Ai, Agranular Insular cortex, Ect, Ectorhinal cortex, PERI, Perirhinal cortex, ACA, Anterior Cingulate cortex, CP, Caudate-putamen. Bar graphs plotted as mean \pm s.e.m. Open circles in bar graphs indicate individual mice ($n = 10$ for WT and $n = 7$ for SRGAP2C mice).

Extended Data Fig. 3 Distribution of RABV traced neurons.

(a) Index of connectivity (IOC, number of traced neurons / number of starter neurons) for traced neurons in the thalamus. No difference was observed between WT and SRGAP2C mice (two-sided Mann-Whitney test). Left: distribution of traced neurons in WT and SRGAP2C, colors indicate IOC. Right: IOC for Ventralanteriorlateral/medial (VAL/VM), Ventralposterior (VP), and Posterior (PO) thalamic subnuclei. Bar graphs plotted as mean \pm s.e.m. Open circles in bar graphs indicate individual mice ($n = 10$ for WT and $n = 7$ for SRGAP2C mice). **(b-d)** Distribution of traced neurons as a function of their cortical depth. Left: IOC, right: fraction. Shaded area indicates s.e.m.

Extended Data Fig. 4 Connectivity changes are not caused by differences in cortical depth or number of starter neurons.

(a) Anatomical location of starter neurons. **(b)** Cortical depth of starter neurons measured as distance from pial surface is not different between WT

and SRGAP2C mice, two-sided Mann-Whitney test. Data shown as box-and-whisker plots. Center line indicates median, box edges represent first and third quartiles, and whiskers represent minimum and maximum values ($n = 26$ starter neurons from 10 WT mice and $n = 26$ starter neurons from 7 SRGAP2C mice). **(c)** Correlation between number of RABV infected starter neurons and RABV traced neurons (Pearson's correlation coefficient $r = 0.88$, $P = 7 \times 10^{-4}$ for WT, and $r = 0.92$, $P = 3.2 \times 10^{-3}$ for SRGAP2C). **(d)** No correlation was observed between IOC and number of RABV infected starter neurons per brain (Pearson's correlation coefficient $r = -0.5$, $P = 0.14$ for WT, and $r = -0.58$, $P = 0.17$ for SRGAP2C).

Extended Data Fig. 5 Distribution of RABV traced neurons locally in S1.

(a) Distance between RABV traced excitatory neurons in S1 and their closest starter neuron along the medial/lateral (M/L) or rostral/caudal (R/C) plane. No difference was observed between WT and SRGAP2C mice (Kolmogorov-Smirnov test). Data shown as relative frequency distribution. **(b)** Density plots showing distribution of traced excitatory neurons relative to their closest starter neuron for coronal (left, L and M indicate lateral and medial orientation, respectively) and sagittal view (right, R and C indicate rostral and caudal orientation, respectively). Center bins aligned with relative position of starter neuron are indicated by red dashed lines. S, supragranular, G, granular, I, infragranular layers. For coronal, bin size = 50x50 μm . For sagittal, bin size = 50x100 μm . Colors in density plots indicate IOC. **(c)** Cortical layer distribution of RABV traced excitatory neurons in S1 shown as Index of connectivity (IOC, number of traced neurons / number of starter neurons). Shaded area indicates s.e.m. **(d)** Fraction of RABV traced neurons across cortical layers in S1. Dashed lines indicate borders between layers. Roman numbers identify cortical layers. **(e)** Same as (a), for inhibitory neurons. For analysis of interneurons, Parvalbumin-positive and Somatostatin-positive were grouped together. **(f)** Same as (b), for inhibitory neurons. **(g)** Same as in (c), for inhibitory neurons. Shaded area indicates s.e.m. **(h)** RABV traced neurons in layer 1. Left: Coronal section showing location of a layer 1 traced neuron (green arrow) in the barrel field of the primary sensory cortex (S1). Right: IOC for layer 1 traced neurons. No difference was observed between WT and

SRGAP2C mice (Mann-Whitney test). Scale bar, 100 μ m. Bar graphs plotted as mean \pm s.e.m. Open circles in bar graphs indicate individual mice ($n = 10$ for WT and $n = 7$ for SRGAP2C mice).

Extended Data Fig. 6 SRGAP2C expression selectively increases synaptic density on apical dendrites.

(a) Coronal section stained for HA showing sparse labeling of a layer 2/3 cortical pyramidal neuron in the barrel field of the primary somatosensory cortex. Scale bar, 150 μ m. **(b)** Higher magnification of neuron in (a). Red dotted lines indicate approximate location where spine density and size were quantified for distal, apical oblique, and basal dendritic compartments. Panels on right show high magnification images of dendritic segments on which spines can clearly be identified. Left panel scale bar, 50 μ m. Right panel scale bar, 2 μ m. **(c)** Spine density is increased for distal, and apical but not basal dendritic segments. ($P = 1.92 \times 10^{-2}$ for distal, $P = 1.5 \times 10^{-3}$ for apical oblique, $P = 0.3$ for basal; distal: $n = 21$ segments for WT and SRGAP2C, apical oblique: $n = 33$ segments for WT and $n = 24$ segments for SRGAP2C, basal: $n = 32$ segments for WT and $n = 24$ segments for SRGAP2C). Bar graph plotted as mean \pm s.e.m. * $P < 0.05$, ** $P < 0.01$, two-sided Mann-Whitney test. **(d)** Spine size is not significantly changed in adult SRGAP2C expressing layer 2/3 cortical pyramidal neurons. Data shown as box-and-whisker plots. Center line indicates median, box edges represent first and third quartiles, and whiskers represent minimum and maximum values (distal: $n = 1273$ spines for WT and $n = 1083$ spines for SRGAP2C, apical oblique: $n = 2401$ spines for WT and $n = 1650$ spines for SRGAP2C, basal: $n = 2286$ spines for WT and $n = 1448$ spines for SRGAP2C).

Extended Data Fig. 7 Neuronal responses following whisker stimulation.

(a) Left: Coronal section stained for HA showing sparse labeling of a layer 2/3 cortical pyramidal neuron in the barrel field of the primary somatosensory cortex with high magnification (bottom) of dendritic segment in which spines can clearly be identified. Scale bar top, 25 μ m.

Scale bar bottom, 2 μ m. Right: Spine density quantification in SRGAP2C heterozygous conditional knock-in mice crossed with heterozygous $\text{Nex}^{\text{Cre}/+}$ mice. Spine density is increased for distal and apical but not basal dendritic segments ($P = 1.34 \times 10^{-2}$ for distal, $P = 2.47 \times 10^{-2}$ for apical oblique, $P = 0.117$ for basal; distal: $n = 23$ segments for WT and $n = 16$ for SRGAP2C, apical oblique: $n = 22$ segments for WT and $n = 20$ segments for SRGAP2C, basal: $n = 23$ segments for WT and $n = 20$ segments for SRGAP2C). Bar graph plotted as mean \pm s.e.m. * $P < 0.05$, two-sided Mann-Whitney test. (b) Top-down view of placement of stimulating rod (white dashed line, 2mm away from the whisker pad) next to right whisker pad (cyan dashed line). Scale bar, 1mm. (c) Frequency distribution of response fraction for neurons responding to either onset, sustained phase, or offset of the stimulus. (d) Single-trial example responses. Shaded area indicates whisker stimulation. (e) Ten percent of single trial Sustained responses with longest sustained activity converted to Z-scores and sorted by duration of response. ON and OFF dashed lines indicate stimulus onset and offset, respectively (f) Bottom 15 responses shown in (e). (g) Cumulative probability distribution of Sustained response durations (time that Z-score was greater than 1). $P < 1 \times 10^{-4}$, Kolmogorov-Smirnov test. (h) Correlation between behavioral activity and average number of transients ($n = 32$ runs for 8 FOVs from 4 WT mice and $n = 32$ runs for 8 FOVs from 3 SRGAP2C mice). (i) Fraction of time during which behavioral activity was observed ($n = 8$ FOVs from 4 WT and $n = 8$ FOVs from 3 SRGAP2C mice). Bar graph plotted as mean \pm s.e.m., two-sided Mann-Whitney test. (j) Support vector machine (SVM) accuracy in classifying presence or absence of whisker stimulus. Shaded area indicates s.e.m. (k) Normalized SVM prediction accuracy across time from stimulus ON to stimulus OFF for 25 neurons per field of view. Shaded area indicates stimulus time. Multiple t-test with multiple comparison correction using false-discovery rate Benjamini-Hochberg method ($q < 0.05$), * $P < 0.05$, ** $P < 0.01$.

Extended Data Fig. 8 Computational modelling of increased layer 4 to layer 2/3 connectivity explains observed SRGAP2C neuronal response properties.

(a) Stimulus-triggered average fluorescence for all neurons recorded in WT and SRGAP2C mice. Fluorescence has been Z-scored and average activity during the 5 s prior to the stimuli have been subtracted. Horizontal dashed lines correspond to the separation between neurons that significantly increase (top) or decrease (bottom) their activity during evoked activity. Vertical solid lines correspond to stimulus onset and offset. Layer 2/3 PNs have been sorted according to the robustness of their signed response to the stimulus. **(b)** Stimulus-triggered average neural activity (after deconvolving fluorescence) for neurons with high signal-to-noise ratio. Horizontal red lines correspond to the separation between neurons that significantly increase (top) or decrease (bottom) their activity during evoked activity. Neurons between the middle horizontal red lines had an equal average response during spontaneous and evoked activity (typically 0). Neurons have been sorted according to the strength of their signed response to the stimulus. **(c)** The normalized distributions of firing rate differences between whisker stimulation and spontaneous activity. Dashed vertical lines indicate means of the distributions. **(d)** The model considers a population of excitatory neurons in layer 4 (gray) projecting to populations of inhibitory (blue) and excitatory (red, brown) neurons in cortical layer 2/3 of barrel cortex. The strength of the projections targeting layer 2/3 PNs and coming from layer 4 excitatory and layer 2/3 inhibitory neurons is assumed to be larger in SRGAP2C mice than WT mice by a factor ξ , as indicated. All neurons are modelled with a quadratic I/O transfer function. **(e)** The mean rate of simulated excitatory units (μ_e) in SRGAP2C mice (brown) are higher and increase at a higher rate than those in WT mice (red) as a function of the mean excitatory input h from layer 4. This is particularly true for the rates at the input levels we model as spontaneous and evoked activity (left and right gray vertical dashed lines, respectively). A mathematical approximation (black dashed lines; [Supplementary Material](#)) agrees to an excellent degree with the simulations. **(f)** The model ratio of mean excitatory rates between SRGAP2C mice ($\xi = 1.8$, top black curve) or mice with a hypothetical decrease in connection strength ($\xi = 0.2$, bottom black curve) and WT mice. **(g)** The model ratio between the mean excitatory rate during evoked vs. spontaneous activity monotonically increases with the change in connectivity relative to WT mice. **(h)** The model ratio of mean excitatory rates between mice with an arbitrary change in connection strength and WT mice. **(i)** The normalized distributions of

firing rate differences between evoked and spontaneous mean input in the model. As in the experimental data (panel c), both model SRGAP2C and model WT mice contain subgroups of neurons that increase and subgroups that decrease their activity in going from spontaneous to evoked stimulation; and the fraction of neurons increasing their activity is higher in SRGAP2C mice than WT mice. **(j)** As for the mean rates (panel e), the variances of excitatory units in model SRGAP2C mice (brown) are higher, and increase at a higher rate as a function of the mean excitatory input from layer 4, than those in model WT mice (red).

Extended Data Fig. 9 Modelling of layer 2/3 PN response properties in WT and SRGAP2C mice.

(a) Population stimulus-triggered-average neural activity obtained by averaging over all neurons in Extended Data Figure 8b. Vertical dashed lines correspond to stimulus onset and offset. **(b)** Average neural activity computed during the 5 s before the stimulus (Spon.) or during the 5 s of stimulation (evoked; stimulus is applied at time 0) across all selected neurons and trials as a function of the skewness threshold used to select neurons. The threshold in (a) is 1.5. **(c)** Mean and standard deviation of the deconvolved traces in Extended Data Figure 8b during both stimulus conditions. **(d)** The normalized distributions of simulated excitatory rates in both SRGAP2C (brown) and WT (red) mice and during spontaneous and evoked mean input illustrate the increase in the mean and variance discussed in the main text. The shapes of the distributions agree with their mathematical approximations (dashed black line) discussed in [Supplementary Material](#). **(e)** The ratio of the standard deviation of excitatory rates between mice with an arbitrary change in connection strength and WT mice. This demonstrates that the effects are robust to the specific choice of parameters. **(f)** Probability of solutions with $y > 1$ as a function of the number of solutions with a fit error of the firing rates of the wild type mouse below a certain threshold, where $y = [\mu(2c, \text{evoked})/\mu(2c, \text{spont})]/[\mu(\text{wt}, \text{evoked})/\mu(\text{wt}, \text{spont})]$ and μ corresponds to the mean firing rate of the excitatory population.

Extended Data Fig. 10 Whisker-based texture discrimination task.

(a) Example learning curves (lighter shades) of three individual mice. Mean learning curve is shown in darker shade **(b)** Performance (fraction correct) after whiskers facing texture were trimmed dropped to chance level, showing that mice needed their whiskers to perform this task ($n = 11$ for WT and $n = 14$ for SRGAP2C mice). **(c)** Average number of trials per session for pre-training and training phase ($n = 20$ for WT and $n = 18$ for SRGAP2C mice). **(d)** Mean water intake per session ($n = 20$ for WT and $n = 18$ for SRGAP2C mice). Bar graphs plotted as s.e.m. **(e)** Schema showing structure of single trial. Textures rotate and move into position 2 s before opening of the response window (RW). Approximately 1 s before RW opening the texture is within reach of the whiskers, allowing mice to sample the texture while it moves further into position. Upon opening of the RW, correct lick responses lead to a water reward, while incorrect lick responses cause to a time-out. Following RW closure the texture retracts back out of reach of the whiskers. **(f)** Example raster plot of an individual mouse showing the distribution of individual licks (red dot for right licks, blue dot for left licks) relative to opening of the response window before (naïve) and after (expert) learning of the task. Correct licks are either right licks (red) for the R2000 texture, or left licks (blue) for the R200 texture. **(g)** Lick frequency plot for naïve and expert mice. Lick frequency was normalized for each individual mouse to the mean lick frequency before the sampling window. Shaded area around curves indicates s.e.m. **(h)** Average timing of licking onset in expert mice relative to opening of the response window ($P = 4.91 \times 10^{-2}$; $n = 10$ for WT and $n = 15$ for SRGAP2C mice). Bar graph plotted as mean \pm s.e.m. * $P < 0.05$, two-sided Mann-Whitney test. **(i)** Fraction of licks from expert mice that are correct relative to opening of the response window. Shaded area around curves indicates s.e.m., two-sided Mann-Whitney test.

Supplementary information

Supplementary Information

This file contains the Supplementary Methods (a mathematical analysis of the neural network model) and Supplementary Fig. 1 (full blots used in Extended Data Fig. 1c, d).

Reporting Summary

Supplementary Video 1

Three-dimensional reconstruction of a representative RABV-traced brain mapped onto the Allen Reference Atlas. Video of a representative reconstructed RABV-traced brain. The reference brain was adapted from the Allen Institute. Octahedrons represent RABV-traced neurons and are colour coded on the basis of their anatomical location. See text for details.

Supplementary Video 2

Whisker-based texture-discrimination task. Representative movie of a head-fixed mouse performing a whisker-based texture-discrimination task. Textures are rotated into position and subsequently moved towards the whisker pad of the mouse. A water reward is received when the mouse responds by licking the correct left or right lick port. Incorrect responses are punished with a timeout. The task is performed in the dark, and infrared illumination was used for video recording.

Rights and permissions

Reprints and Permissions

About this article

Cite this article

Schmidt, E.R.E., Zhao, H.T., Park, J.M. *et al.* A human-specific modifier of cortical connectivity and circuit function. *Nature* **599**, 640–644 (2021).
<https://doi.org/10.1038/s41586-021-04039-4>

- Received: 22 November 2019
- Accepted: 17 September 2021
- Published: 27 October 2021
- Issue Date: 25 November 2021
- DOI: <https://doi.org/10.1038/s41586-021-04039-4>

Share this article

Anyone you share the following link with will be able to read this content:

[Get shareable link](#)

Sorry, a shareable link is not currently available for this article.

[Copy to clipboard](#)

Provided by the Springer Nature SharedIt content-sharing initiative

This article was downloaded by **calibre** from <https://www.nature.com/articles/s41586-021-04039-4>

| [Section menu](#) | [Main menu](#) |

- Article
- [Published: 03 November 2021](#)

Striatal indirect pathway mediates exploration via collicular competition

- [Jaeeon Lee¹](#) &
- [Bernardo L. Sabatini](#) ORCID: [orcid.org/0000-0003-0095-9177¹](https://orcid.org/0000-0003-0095-9177)

[Nature](#) volume 599, pages 645–649 (2021)

- 6908 Accesses
- 49 Altmetric
- [Metrics details](#)

Subjects

- [Basal ganglia](#)
- [Neural circuits](#)
- [Optogenetics](#)

Abstract

The ability to suppress actions that lead to a negative outcome and explore alternative actions is necessary for optimal decision making. Although the basal ganglia have been implicated in these processes^{1,2,3,4,5}, the circuit mechanisms underlying action selection and exploration remain unclear. Here, using a simple lateralized licking task, we show that indirect striatal

projection neurons (iSPN) in the basal ganglia contribute to these processes through modulation of the superior colliculus (SC). Optogenetic activation of iSPNs suppresses contraversive licking and promotes ipsiversive licking. Activity in lateral superior colliculus (lSC), a region downstream of the basal ganglia, is necessary for task performance and predicts lick direction. Furthermore, iSPN activation suppresses ipsilateral lSC, but surprisingly excites contralateral lSC, explaining the emergence of ipsiversive licking. Optogenetic inactivation reveals inter-collicular competition whereby each hemisphere of the superior colliculus inhibits the other, thus allowing the indirect pathway to disinhibit the contralateral lSC and trigger licking. Finally, inactivating iSPNs impairs suppression of devalued but previously rewarded licking and reduces exploratory licking. Our results reveal that iSPNs engage the competitive interaction between lSC hemispheres to trigger a motor action and suggest a general circuit mechanism for exploration during action selection.

Access options

Subscribe to Journal

Get full journal access for 1 year

\$199.00

only \$3.90 per issue

[Subscribe](#)

All prices are NET prices.

VAT will be added later in the checkout.

Tax calculation will be finalised during checkout.

Rent or Buy article

Get time limited or full article access on ReadCube.

from \$8.99

[Rent or Buy](#)

All prices are NET prices.

Additional access options:

- [Log in](#)
- [Access through your institution](#)
- [Learn about institutional subscriptions](#)

Fig. 1: iSPN activation in ventrolateral striatum induces ipsiversive movements.

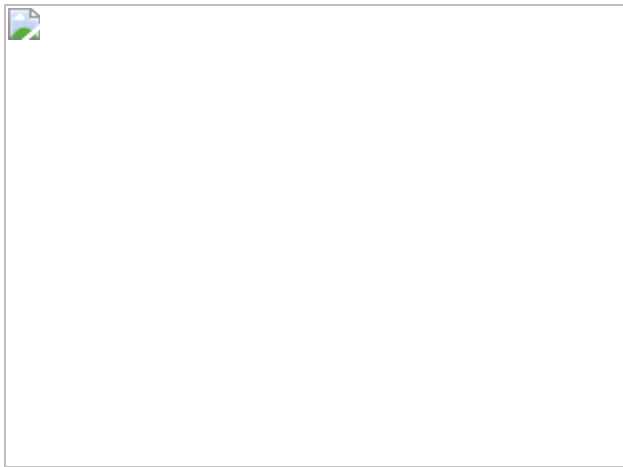


Fig. 2: Bilateral and opposite modulation of ISC hemispheres by iSPN activation.

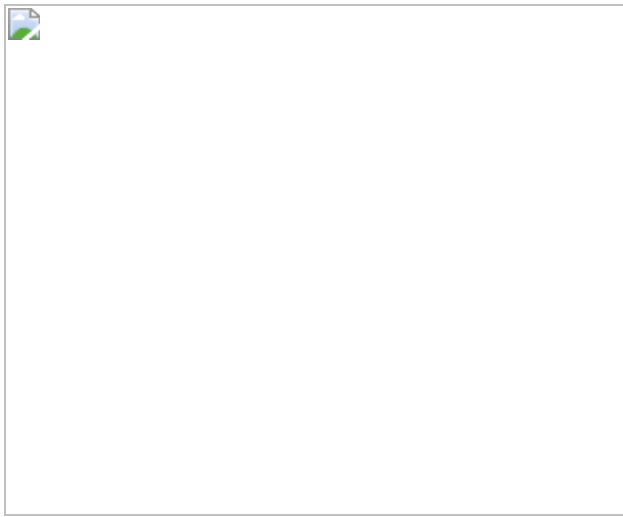


Fig. 3: Unilateral inhibition of ISC mimics iSPN activation.

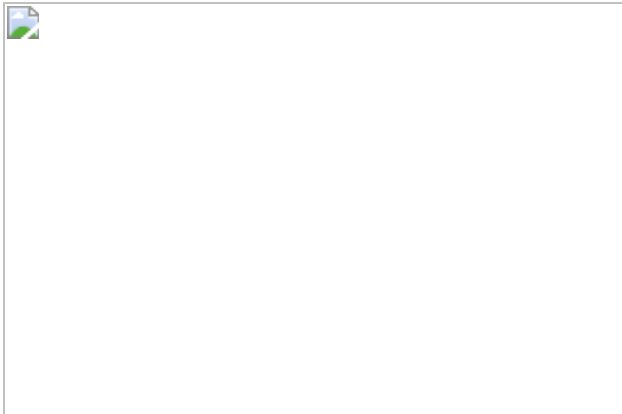
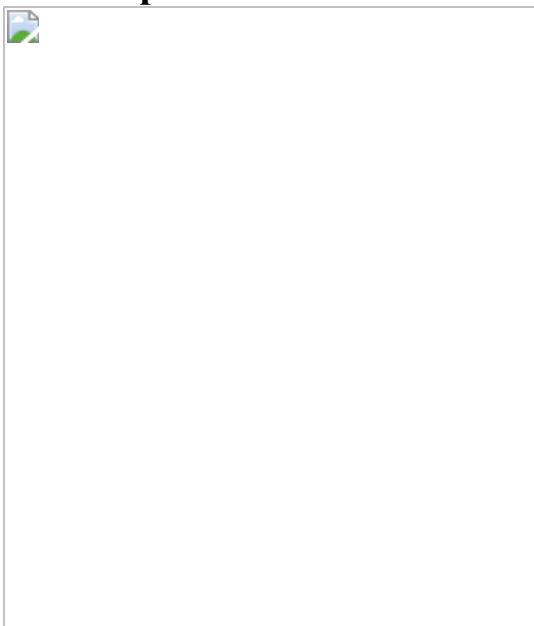


Fig. 4: iSPN activity is necessary for suppression of unrewarded action and for exploration of an alternative action.



Data availability

The data that support the findings of this study are available from the corresponding author upon reasonable request.

Code availability

The code used for analysis (Matlab) is available from the corresponding author upon reasonable request.

References

1. 1.
Amita, H. & Hikosaka, O. Indirect pathway from caudate tail mediates rejection of bad objects in periphery. *Sci. Adv.* **5**, eaaw9297 (2019).
2. 2.
Tai, L.-H., Lee, A. M., Benavidez, N., Bonci, A. & Wilbrecht, L. Transient stimulation of distinct subpopulations of striatal neurons mimics changes in action value. *Nat. Neurosci.* **15**, 1281–1289 (2012).
3. 3.
Nonomura, S. et al. Monitoring and updating of action selection for goal-directed behavior through the striatal direct and indirect pathways. *Neuron* **99**, 1302–1314.e5 (2018).
4. 4.
Parker, N. F. et al. Reward and choice encoding in terminals of midbrain dopamine neurons depends on striatal target. *Nat. Neurosci.* **19**, 845–854 (2016).
5. 5.
Cox, J. & Witten, I. B. Striatal circuits for reward learning and decision-making. *Nat. Rev. Neurosci.* **20**, 482–494 (2019).
6. 6.
Kravitz, A. V. et al. Regulation of parkinsonian motor behaviours by optogenetic control of basal ganglia circuitry. *Nature* **466**, 622–626 (2010).
7. 7.

Kravitz, A. V., Tye, L. D. & Kreitzer, A. C. Distinct roles for direct and indirect pathway striatal neurons in reinforcement. *Nat. Neurosci.* **15**, 816–818 (2012).

8. 8.

Roseberry, T. K. et al. Cell-type-specific control of brainstem locomotor circuits by basal ganglia. *Cell* **164**, 526–537 (2016).

9. 9.

Smith, Y., Bevan, M. D., Shink, E. & Bolam, J. P. Microcircuitry of the direct and indirect pathways of the basal ganglia. *Neuroscience* **86**, 353–387 (1998).

10. 10.

Sheng, M., Lu, D., Shen, Z. & Poo, M. Emergence of stable striatal D1R and D2R neuronal ensembles with distinct firing sequence during motor learning. *Proc. Natl Acad. Sci. USA* **116**, 11038–11047 (2019).

11. 11.

Bakhurin, K. I. et al. Opponent regulation of action performance and timing by striatonigral and striatopallidal pathways. *eLife* **9**, e54831 (2020).

12. 12.

Freeze, B. S., Kravitz, A. V., Hammack, N., Berke, J. D. & Kreitzer, A. C. Control of basal ganglia output by direct and indirect pathway projection neurons. *J. Neurosci.* **33**, 18531–18539 (2013).

13. 13.

Garr, E. & Delamater, A. R. Chemogenetic inhibition in the dorsal striatum reveals regional specificity of direct and indirect pathway control of action sequencing. *Neurobiol. Learn. Mem.* **169**, 107169 (2020).

14. 14.

McPeek, R. M. & Keller, E. L. Deficits in saccade target selection after inactivation of superior colliculus. *Nat. Neurosci.* **7**, 757–763 (2004).

15. 15.

Song, J.-H., Rafal, R. D. & McPeek, R. M. Deficits in reach target selection during inactivation of the midbrain superior colliculus. *Proc. Natl Acad. Sci. USA* **108**, E1433–E1440 (2011).

16. 16.

Mana, S. & Chevalier, G. Honeycomb-like structure of the intermediate layers of the rat superior colliculus: afferent and efferent connections. *Neuroscience* **103**, 673–693 (2001).

17. 17.

Hikosaka, O., Takikawa, Y. & Kawagoe, R. Role of the basal ganglia in the control of purposive saccadic eye movements. *Physiol. Rev.* **80**, 953–978 (2000).

18. 18.

Felsen, G. & Mainen, Z. F. Midbrain contributions to sensorimotor decision making. *J. Neurophysiol.* **108**, 135–147 (2012).

19. 19.

Kopec, C. D., Erlich, J. C., Brunton, B. W., Deisseroth, K. & Brody, C. D. Cortical and subcortical contributions to short-term memory for orienting movements. *Neuron* **88**, 367–377 (2015).

20. 20.

Kaneda, K., Isa, K., Yanagawa, Y. & Isa, T. Nigral inhibition of GABAergic neurons in mouse superior colliculus. *J. Neurosci.* **28**, 11071–11078 (2008).

21. 21.

Rossi, M. A. et al. A GABAergic nigrotectal pathway for coordination of drinking behavior. *Nat. Neurosci.* **19**, 742–748 (2016).

22. 22.

Lee, J., Wang, W. & Sabatini, B. L. Anatomically segregated basal ganglia pathways allow parallel behavioral modulation. *Nat. Neurosci.* **23**, 1388–1398 (2020).

23. 23.

Shin, J. H., Kim, D. & Jung, M. W. Differential coding of reward and movement information in the dorsomedial striatal direct and indirect pathways. *Nat. Commun.* **9**, 404 (2018).

24. 24.

Li, N. et al. Spatiotemporal constraints on optogenetic inactivation in cortical circuits. *eLife* **8**, e48622 (2019).

25. 25.

Essig, J., Hunt, J. B. & Felsen, G. Inhibitory midbrain neurons mediate decision making. Preprint at
<https://doi.org/10.1101/2020.02.25.965699> (2020).

26. 26.

Takahashi, M., Sugiuchi, Y. & Shinoda, Y. Topographic organization of excitatory and inhibitory commissural connections in the superior colliculi and their functional roles in saccade generation. *J. Neurophysiol.* **104**, 3146–3167 (2010).

27. 27.

Sooksawate, T., Isa, K., Behan, M., Yanagawa, Y. & Isa, T. Organization of GABAergic inhibition in the motor output layer of the

superior colliculus. *Eur. J. Neurosci.* **33**, 421–432 (2011).

28. 28.

Takahashi, M., Sugiuchi, Y., Izawa, Y. & Shinoda, Y. Commissural excitation and inhibition by the superior colliculus in tectoreticular neurons projecting to omnipause neuron and inhibitory burst neuron regions. *J. Neurophysiol.* **94**, 1707–1726 (2005).

29. 29.

Doykos, T. K., Gilmer, J. I., Person, A. L. & Felsen, G. Monosynaptic inputs to excitatory and inhibitory neurons of the intermediate and deep layers of the superior colliculus. *J. Comp. Neurol.* **528**, 2254–2268 (2020).

30. 30.

Mysore, S. P. & Knudsen, E. I. A shared inhibitory circuit for both exogenous and endogenous control of stimulus selection. *Nat. Neurosci.* **16**, 473–478 (2013).

31. 31.

Mysore, S. P. & Knudsen, E. I. The role of a midbrain network in competitive stimulus selection. *Curr. Opin. Neurobiol.* **21**, 653–660 (2011).

32. 32.

Jiang, H., Stein, B. E. & McHaffie, J. G. Opposing basal ganglia processes shape midbrain visuomotor activity bilaterally. *Nature* **423**, 982–986 (2003).

33. 33.

Liu, P. & Basso, M. A. Substantia nigra stimulation influences monkey superior colliculus neuronal activity bilaterally. *J. Neurophysiol.* **100**, 1098–1112 (2008).

34. 34.

Geddes, C. E., Li, H. & Jin, X. Optogenetic editing reveals the hierarchical organization of learned action sequences. *Cell* **174**, 32–43.e15 (2018).

35. 35.

Tecuapetla, F., Jin, X., Lima, S. Q. & Costa, R. M. Complementary contributions of striatal projection pathways to action initiation and execution. *Cell* **166**, 703–715 (2016).

36. 36.

Zalocusky, K. A. et al. Nucleus accumbens D2R cells signal prior outcomes and control risky decision-making. *Nature* **531**, 642–646 (2016).

37. 37.

Schultz, W., Dayan, P. & Montague, P. R. A Neural substrate of prediction and reward. *Science* **275**, 1593–1599 (1997).

38. 38.

Cohen, J. Y., Haesler, S., Vong, L., Lowell, B. B. & Uchida, N. Neuron-type-specific signals for reward and punishment in the ventral tegmental area. *Nature* **482**, 85–88 (2012).

39. 39.

Iino, Y. et al. Dopamine D2 receptors in discrimination learning and spine enlargement. *Nature* **579**, 555–560 (2020).

40. 40.

Yamaguchi, T. et al. Role of PKA signaling in D2 receptor-expressing neurons in the core of the nucleus accumbens in aversive learning. *Proc. Natl Acad. Sci. USA* **112**, 11383–11388 (2015).

41. 41.

Lee, S. J. et al. Cell-type-specific asynchronous modulation of PKA by dopamine in learning. *Nature* **590**, 451–456 (2021).

42. 42.

Gerfen, C. R., Paletzki, R. & Heintz, N. GENSAT BAC Cre-recombinase driver lines to study the functional organization of cerebral cortical and basal ganglia circuits. *Neuron* **80**, 1368–1383 (2013).

43. 43.

Guo, Z. V. et al. Flow of cortical activity underlying a tactile decision in mice. *Neuron* **81**, 179–194 (2014).

44. 44.

Mante, V., Sussillo, D., Shenoy, K. V. & Newsome, W. T. Context-dependent computation by recurrent dynamics in prefrontal cortex. *Nature* **503**, 78–84 (2013).

45. 45.

Li, N., Daie, K., Svoboda, K. & Druckmann, S. Robust neuronal dynamics in premotor cortex during motor planning. *Nature* **532**, 459–464 (2016).

46. 46.

Bro, R., Acar, E. & Kolda, T. G. Resolving the sign ambiguity in the singular value decomposition. *J. Chemom.* **22**, 135–140 (2008).

47. 47.

Peron, S. P., Freeman, J., Iyer, V., Guo, C. & Svoboda, K. A cellular resolution map of barrel cortex activity during tactile behavior. *Neuron* **86**, 783–799 (2015).

48. 48.

Franklin, K. B. J. & Paxinos, G. *Paxinos and Franklin's the Mouse Brain in Stereotaxic Coordinates, Compact: The Coronal Plates and Diagrams* (Academic Press, 2019).

Acknowledgements

We thank members of the Sabatini laboratory and W. Regehr, M. Andermann, N. Uchida and S. Gershman for helpful discussions; J. Levasseur for mouse husbandry and genotyping; J. Saulnier and L. Worth for laboratory administration; and W. Kuwamoto, J. Grande, M. Ambrosino, B. Pryor, E. Lubbers and R. Griep for assistance with behavioural experiments and histology. This work was supported by the NIH (NINDS NS103226, U19NS113201), a P30 Core Center Grant (NINDS NS072030), an Iljou Foundation scholarship and a grant from the Simons Collaborative on the Global Brain.

Author information

Affiliations

1. Howard Hughes Medical Institute, Department of Neurobiology, Harvard Medical School, Boston, MA, USA

Jaeeon Lee & Bernardo L. Sabatini

Contributions

J.L. and B.L.S. conceptualized the study, wrote the original draft, and reviewed and edited the manuscript. J.L. performed experiments and analysed the data.

Corresponding author

Correspondence to [Bernardo L. Sabatini](#).

Ethics declarations

Competing interests

B.L.S. is a founder of and holds private equity in Optogenix. Tapered fibres commercially available from Optogenix were used as tools in the research.

Additional information

Peer review information *Nature* thanks the anonymous reviewer(s) for their contribution to the peer review of this work. Peer reviewer reports are available.

Publisher's note Springer Nature remains neutral with regard to jurisdictional claims in published maps and institutional affiliations.

Extended data figures and tables

[Extended Data Fig. 1 Histology, baseline behavior, and effects of iSPN stimulation on the next trial.](#)

a. Example histology (*left*) showing CoChR expression (green) and the tapered fiber location as revealed by glial fibrillary acidic protein (GFAP) staining (magenta). Scale bar: 1 mm. The CoChR expression in striatum averaged across mice is also shown (*right*). **b.** Baseline expert behavior after two weeks of training. Percentages of correct (grey), incorrect (green) and miss (orange) outcomes for left- and right-cued trials ($n = 7$ mice). **c.** *left*, Median lick latency measured from tone onset to spout contact for left- (blue) and right- (red) cued trials. *right*, Mode of inter-trial-interval for licks to the left (blue) and right (red) ports. **d.** Functional map of optogenetic perturbations at 8 striatal sites showing changes in percentages of incorrect (left) and miss (right) outcomes (see Fig. [1e](#)). The color and size of each circle denote the effect size and p-value (bootstrap), respectively ($n = 5$ mice, 9 sessions). **e.** Effect of VLS iSPN stimulation on the next trial ($n+1$ trial) relative to control trials (excluding all $n+1$ trials). For $n+1$ trials, only

those following left-cued trials were included as optogenetic stimulation only affected left-cued trials (i.e. contraversive to the stimulation site in the right striatum) ($n = 7$ mice) (see Fig. 1e; Methods) (n.s.: $P > 0.05$, two-tailed t -test). **f.** Median latency to first lick in no stimulation trials (separated into left vs. right; blue/red) and stimulation trials (sorted into incorrect vs. correct; green/grey). Correct licks during stimulation trials to the left were delayed compared to those during no stimulation trials ($P^* < 0.05$, two-tailed t -test) (left licks: $n = 6$ sessions, right licks: $n = 9$ sessions, see [Methods](#)).

Extended Data Fig. 2 Context-dependent effect of iSPN stimulation.

a, c. Effect of devaluating one motor program by extinction. An example session from one mouse showing the effects of iSPN stimulation on the left (**a**) or right (**c**) hemisphere before (pre-extinction, top) and after (post-extinction, bottom) devaluation of the right port. Each dot represents licking either to the left (blue) or right (red). Trials (rows) are sorted by being no stimulation (black) and stimulation trials (light blue). Only trials with licking cued to the port contralateral to optogenetic stimulation (right in **a**, left in **c**) are shown. **b, d.** Percentages of each outcome type for pre- (black, left) and post- (purple, right) extinction optogenetic stimulation trials (stim, light blue) and control trials (no stim, black). Outcomes are color-coded grey (correct), green (incorrect), and orange (miss) ($n = 5$ mice). The selection of the incorrect port following optogenetic stimulation of iSPN on the right striatum significantly decreased after extinction ($P < 0.0125$, one-tailed t -test), whereas it remained the same for iSPN stimulation on the left ($P = 0.65$, one-tailed t -test). **e.** Effect of bilateral iSPN stimulation. Summary plots for the outcomes for no stimulation (black) and stimulation (light blue) trials, during left- (center) and right- (right) cued trials ($n = 5$ mice). Optogenetic stimulation significantly decreased the correct outcome rate and increased the miss outcome rate but did not change the incorrect outcome rate (** $P < 0.001$, two-tailed t -test; n.s.: $P > 0.05$). **f. left,** We trained a group of mice to only lick to the left spout, while still having access to both spouts. Right iSPN stimulation in these mice failed to induce licking of the right spout, supporting that stimulation-induced licking is not a hardwired motor program. *right*, Stimulation decreased correct outcome rate and increased the miss outcome rate, but failed to increase incorrect

outcome rate (i.e. the rate of licking to the right spout which the mice were never trained to lick) ($**P < 1 \times 10^{-8}$, two-tailed t -test; n.s.: $P > 0.05$). **g.** As in panel **f** for left VLS iSPN stimulation ($*P < 0.05$, two-tailed t -test; n.s.: $P > 0.05$). **h.** In mice trained on the main two-spout task, we also observed that iSPN stimulation during the inter-trial-interval (ITI), when mice rarely licked, induced ipsiversive licking although this effect emerged only after multiple stimulation sessions. Plots showing change in probability of licking after optogenetic stimulation during the ITI relative to control trials ($n = 10$ mice for 1st and 2nd session, $n = 9$ mice for 3rd session). Stimulation caused ipsilateral licking from 2nd session onward, and weakly suppressed contralateral licking relative to baseline ($***P < 1 \times 10^{-4}$, $**P < 0.005$, $*P < 0.05$).

Extended Data Fig. 3 Unilateral inactivation of the direct pathway in VLS suppresses licking on both sides.

a. Schematic showing strategy to inhibit striatal direct pathway. Mice expressing an inhibitory opsin GtACR1 in the direct pathway (*R26-CAG-LNL-GtACR1-ts-FRed-Kv2.1 x Drd1a-Cre*, see [methods](#)) was implanted with a tapered fiber in the right VLS. **b.** Example session during which a mouse underwent direct pathway inactivation similar to the experiment described in Fig.4b (see [Methods](#)). Trials are sorted by trial type similar to that described in Fig.1d. **c.** Percentage trial outcome for contra trials (top) and ipsi trials (bottom). Unilateral direct pathway inactivation lead to a decrease in correct rate and an increase in miss trial rate ($P^{***} < 0.0005$, two-tailed t -test; $n = 5$ mice, power = 2mW). **d.** Change in miss trials percentage for different power levels (0.2, 0.5 and 2mW).

Extended Data Fig. 4 VLS recipient SNr projection, effect of muscimol infusion in ISC, and direction selectivity of activity in ISC.

a-c. AAV1-Cre mediated anterograde tracing of SNr neurons downstream of VLS shows that VLS recipient SNr (^{VLS}SNr) sends bilateral projections to contralateral and ipsilateral ISC. Interestingly, this bilateral projection was largely specific to ISC. **a. left,** Schematic of the AAV1-Cre anterograde

trans-synaptic mapping strategy to reveal the projections of VLS-recipient SNr (^{VLS}SNr). **b.** Example histology of superior colliculus: ^{VLS}SNr (green) projects to both ipsilateral ISC (i-ISC) and contralateral ISC (c-ISC). SNr is outlined with a white dotted line. Scale bars: 1mm (left panel), 100 µm (3 insets in right column). **c. left column,** Schematics of coronal sections and coordinates relative to bregma. VM: ventromedial thalamus; Pf: parafascicular nucleus; SC: superior colliculus; IRt/PCRt: intermediate reticular formation/parvocellular reticular formation. *right column*, histological examples showing SNr axons (green) labelled via anterograde tracing (see Main text, Fig.3b) and DAPI (purple). The left and right columns show contralateral and ipsilateral sides, respectively, relative to the labeled SNr cell bodies (i.e. the injection side). Midline crossing SNr axons were only seen in lateral SC. Similar results were observed in total of n = 3 mice. Scale bars: 200 µm. **d.** Activity in ISC was necessary for the lateralized licking in the task, as muscimol, a GABA_A receptor agonist, infused into ISC unilaterally reduced task performance only on trials in which the correct selection port was contralateral to the infusion site. *left*, Muscimol was infused unilaterally in ISC as the mouse performed the task. *right*, percentages of correct trials before (baseline, grey) and after (muscimol, purple) infusion. Muscimol infusion significantly impaired performance of contralateral cued trials (n = 8 ISC sites, 4 mice, P**<1e-6, two-tailed t-test). **e. left**, Example histological section showing recording probe location (green = Dil). *right*, location of all probe tip location (cross). Each cross depicts one mouse. **f. left**, Each dot shows the average activity of one unit in the first 200 ms after tone onset (spikes/s) during contraversive trials plotted versus that in ipsiversive trials. The directional selectivity of each unit is color-coded (purple: contra; green: ipsi; grey: no preference). Overall population activity was higher during contraversive trials (P<1e-8, two-tailed t-test). *right*, Numbers of cells preferring contraversive or ipsiversive licking trials, or having no preference (contra-preferring: 296/673, ipsi-preferring: 139/673, no preference: 238/673). **g.** Mean firing rate of contraversive preferring (purple), ipsiversive preferring (green) and no preference (grey) units shown aligned to tone onset (dashed line) during contralateral and ipsilateral cued trials (contra: n = 296, ipsi: n = 139; mean ± s.e.m. across units). **h.** Mean firing rate (z-scored relative to firing during the ITI, left) and selectivity (spikes/s, right) of all ISC units. Each row shows data for a single unit, sorted by coding preference (right column for

each panel). For each coding preference, units are sorted by the timing of peak firing relative to baseline. **i.** Selectivity (spikes/s; activity in preferred – anti-preferred trials) aligned to tone onset (left) or 1st lick (right) for contraversive- and ipsiversive-preferring neurons (mean ± s.e.m across units). **j.** Mean firing rate, peak-valley timing and spike width of waveforms of units in each coding group. No significant differences were observed between groups.

Extended Data Fig. 5 Detailed analysis of ISC activity modulation after iSPN stimulation.

a. Example units that were not significantly modulated by stimulation. Peri-stimulus histogram showing no stimulation trials (left) and stimulation trials (right, light blue=laser on) during left- (blue) and right- (red) cued trials. **b.** Changes in firing rate (similar as in Fig.2*i*) but with data separated for contraversive preferring, ipsiversive preferring and no-preference units during left-cued trials (left column) and right-cued trials (right column) in right ISC (top row) and left ISC (bottom row). Only contraversive preferring neurons were significant modulated by iSPN activation in both left and right trials in left and right ISC (p-values for two-tailed *t*-test in the 100ms window after stimulation onset are shown). **c.** Changes in firing rate induced by stimulation (Δ spikes s^{-1} = activity in stim trials – activity in no stim trials) for units in the right (top) and left (bottom) ISC for stimulation trials but including only data from the subset of sessions that had both incorrect and miss outcomes (incorrect: blue, miss: grey; Methods) and separating trials based on outcome. Changes in firing rates in right SC did not differ ($n = 129$, $P = 0.40$, two-tailed *t*-test) but changes were larger in left SC during incorrect licking vs miss trials ($n = 64$, $P = 0.01$, two-tailed *t*-test). Firing rate are show as mean ± s.e.m. across units. **d.** Fractions of neurons that were excited, inhibited, or unchanged by optogenetic stimulation in left- and right-cued trials for contraversive-lick-preferring (*left*), ipsiversive-lick-preferring (*middle*), and untuned (no pref, *right*) groups (similar analysis as Fig.2*g*) recorded in the left or right SC. **e.** iSPN activation during the ITI (e-f). Example units recorded in the left SC (left panel) and right SC (right panel). Peri-stimulus histogram shows trials during which the stimulation did (red/blue) or did not (grey) induce licking. Firing rates are given as mean ± s.e.m across trials. **f.** Average changes in

firing rate after stimulation (Δ spikes s $^{-1}$) in left SC (left panel) and right SC (right panel) grouped by behavioral outcome (red/blue=lick; grey=no lick). Firing rates shown as mean \pm s.e.m across units (left SC: n = 225; right SC: n = 201). **g.** Average firing rates during the 100 ms stimulation window for stimulation trials without (y-axis) vs. with (x-axis) licking. Each dot represents a single unit. P-values show significance of modulation (two-tailed *t*-test).

Extended Data Fig. 6 ISC anatomical projection, IRt inhibition, and analysis of ISC/IRt activity after ISC inactivation.

a. left, Schematic showing strategy to label ISC via anterograde transsynaptic cre (AAV1.Flpo, grey) in tjM1, with injection of anterograde tracer (AAV.fDIO.EYFP, green) in the ISC. **right**, Sagittal section showing the cell bodies around the injection site and the axonal projection on the contralateral ISC. Scale bar, 1 mm (left panel), 200 μ m (2 insets in right column). **b. left**, Coronal section showing expression of Jaws in ISC. Inset shows cell bodies around the injection site. Scale bar, 1 mm (main panel), 50 μ m (inset in top right corner). **right**, optical fiber tip locations. **c.** Coronal section showing expression of Jaws in IRt. Inset shows cell bodies around the injection site. Scale bar, 1 mm (main panel), 50 μ m (inset in top right corner). **d.** Schematic illustrating Jaws expression in right IRt in wild type mice. **e.** Example session showing (as in Fig. 1d) the effect of IRt inhibition on performance in left and right cued trials, as indicated. The purple rectangle shows the time of laser activation (n = 4 mice). **f.** Quantification of trial outcomes (n = 4 mice). Percentages of correct, incorrect and miss outcomes in no stimulation (grey, green and orange) and stimulation trials (purple) in left (left panel) or right (right panel) cued trials. IRt inhibition caused a significant decrease in correct rate ($P^*<0.05$, two-tailed *t*-test) and increase in incorrect and miss rates ($P^*<0.05$, two-tailed *t*-test) in right trials. **g.** Example unit in ISC that was suppressed via red laser stimulation of Jaws expressed in ISC. Laser on period is shown in purple. **h.** Normalized firing rate of all units recorded during left (left panel) and right (right panel) trials with stimulation (blue/red) and without (grey) stimulation. **i.** Quantification of Jaws inhibition for all units during left (blue) and right (red) trials (n = 14 units; $P^*<0.05$, $P^{**}<0.005$, two-tailed *t*-test). **j.** Fraction of cells that were significantly modulated by contralateral

ISC inhibition (similar as in Fig. 3j, but repeated for different coding groups). **k**. Changes in firing rate after contralateral ISC inhibition (Δ spikes s^{-1} = activity in stim trials – activity in no stim trials) for ipsiversive- (green) and contraversive (purple) preferring units during left (left panel) or right (right panel) trials. contraversive preferring but not ipsiversive preferring units were significantly modulated by contralateral ISC inhibition (p-values from two-tailed *t*-test shown for each group). **l**. Same as in **h** but sorted by trial outcome (incorrect=blue, miss=grey). ISC activity after contralateral ISC inhibition differentiated incorrect vs miss trials, with higher excitation during incorrect trials ($P<1e-7$, two-tailed *t*-test).

Extended Data Fig. 7 GtACR1 histology and detailed analysis of effects of iSPN inactivation on task performance and ISC activity.

a. left, Coronal section showing expression of GtACR1 in striatum in an *Adora2a-Cre* mouse crossed with a conditional GtACR1 mouse (see [Methods](#)). **middle**, Inset showing the expression of GtACR1 in iSPN. **right**, Coronal section showing the tapered fiber location as revealed by glial fibrillary acidic protein (GFAP) staining (magenta). Scale bar, 1 mm (left), 50 μ m (middle), 1 mm (right). **b**. similar to Fig. 4c but for ipsiversive trials relative to fiber location (right trials, see main text) during a baseline session (left) and during extinction day1 (right). iSPN inactivation caused a significant decrease in correct rate, and significant increase in correct rate during baseline sessions ($P^*<0.05$, two-tailed *t*-test). **c**. Quantification of percentage trial outcome for contraversive/ipsiversive trials during no stimulation and stimulation trials across session number. **d**. Number of units in each coding group (contra/ipsi/no preference) in left and right SC in mice after left spout extinction. **e**. Fractions of units that were significantly modulated (as in Fig. 2g). There were more excited than inhibited units in right SC (left trial: $P<1e-7$; right trials: $P<1e-99$; two-tailed binomial test), whereas there were more inhibited than excited units in the left SC (left trial: $P<1e-7$; right trials: $P<0.05$; two-tailed binomial test). **f**. As Fig. 4g, but sorted by behavioral outcome (see Main text). Color indicates the behavioral outcome upon iSPN inactivation (blue: left lick; red: right lick; grey: no lick). Change in firing rate in both trial types and both left and right ISC differentiated behavioral outcome (p-values shown for two-tailed

t-test during 100ms window after laser onset). **g**. Schematic diagram summarizing the results shown in panel e. The size of arrow indicates the relative magnitude of modulation (to be compared only across behavioral outcomes and not across recorded location).

Extended Data Fig. 8 Low-dimensional projection of ISC activity reveals logic of iSPNs modulation of ISC.

As the activity of neurons in ISC during the task is complex and heterogenous, we used dimensionality reduction to examine if, as a whole, neuronal population dynamics in ISC could be related to behavior and help explain effects of iSPN activity manipulation. Using only activity from trials without optogenetic stimulation, we projected ISC activity onto an axis (termed coding direction, CD) that best discriminated upcoming lick choice (see [Methods](#)). The projection onto CD represents the linear combination of activity in ISC (as might be calculated by a hypothetical downstream neuron) that allows maximal choice discrimination. As expected, ISC activity along CD discriminated correct trial types (**c**, left panel). Furthermore, optogenetic iSPN activation pushed ISC activity along the CD away from contraversive (left) and towards ipsiversive (right) choice (**c**, middle and right panels), even though activity in the optogenetic trials was not used to calculate the CD. Optogenetic modulation along other dimensions orthogonal to CD (calculated by PCA on the residual non-CD activity) was minimal, indicating that iSPN activity specifically modulates ISC neural population along a trajectory that determines lick choice as opposed to behavioral features, such as lick timing (see Extended Data Fig. [9e,f](#)). After extinction of the left spout, ISC activity no longer moved along the CD towards the left-choice despite delivery of the left cue, consistent with lack of left-port licking in these trials (**d**, left panel). However, after extinction of the left spout, iSPN inactivation pushed ISC activity along the CD towards the left choice (**d**, middle and right panel). Thus, following extinction, activity in VLS iSPN was necessary for suppression of left-choice activity in the ISC. Phrased differently, iSPN activity specifically modulates ISC activity along a choice axis away from an activity space that no longer leads to valuable outcomes. **a**. Schematic showing ISC neural trajectory for left (blue) and right (red) trials. Trajectories maximally diverge along the axis termed coding direction (CD, see [methods](#)). **b**.

Schematic showing lSC units (circle) on each hemispheres projecting onto a hypothetical downstream neuron (grey circle), which controls lick direction. Projection onto CD can be thought of as activity of a hypothetical neuron whose weights achieve maximal lick choice separation (see [methods](#)). **c.** Mean neural trajectories of lSC (both hemispheres combined, see [Methods](#)) projected onto CD during iSPNs activation experiment (see Fig. 2, Main Text). Grey dotted line shows the timing of the tone onset ($t = 0$). *left*, Control trials in which mice either licked left (blue) or right (red) without stimulation. *middle*, Left cued trials during no stim (blue) and stim trials (light blue). *right*, Right cued trials during no stim (red) and stim (light blue) trials. **d.** Mean neural trajectories of lSC (both hemispheres combined, see [Methods](#)) projected onto CD during iSPNs inactivation experiment after extinction (see Fig. 4, Main Text). Traces plotted as panel **c**.

Extended Data Fig. 9 Detailed analysis of low dimensional projection of lSC activity.

a. Activity projections onto PCs, and different coding directions. Left (blue) and right (red) trials are shown relative to tone onset. Coding direction was defined during $-100\sim 0$ ms window relative to tone onset (left, CD^1), $0\sim 100$ ms relative to tone (center, CD^2) and $100\sim 0$ ms relative to first lick (right, CD^3) (see [Methods](#)). CD^1 was used as a control. **b.** PCA on the original data (without first calculating and removing CD^2 information as in Figure 5). Left/right lick (i.e. choice) information is found in PC2 (2nd column). **c.** Left-right choice selectivity measured from the projection of the neural activity along the indicated axes. Selectivity measures how separable the trajectories are along the selected axis. The given P-values are for comparison by one sample two tailed *t*-test ($P^{***} < 0.0005$, $P^* < 0.05$). The trajectories are well-separable along different choice axes. PCs did not reliably discriminate trial type compared to CD (except for PC5). **d.** Explained variance along each dimension (see [Methods](#)). CD explained the most variance in the data ($20.5 \pm 2.3\%$). Explained variances for CD, $CD+PC1+PC2$, and $CD+PC1\sim PC5$ are shown. All error bars show bootstrapped standard error across units. **e.** Projections of neural activity as a function of time relative to the tone onset shown along PC3 (left), PC4 (middle) and PC5 (right). Data are shown for left- (top, blue) and right-

(bottom, red) cued trials. The dotted lines show activity in no stim trials and thick lines that in stim trials. Light blue rectangle shows stimulation on window. **f.** Changes in activity during the stimulation window (100 ms) for each projection after stimulation (Δ project. modulation) along different dimensions during left- (blue) and right- (red) cued trials. Stimulation modulates activity mostly along CD. P-values show significance of modulation (two-tailed t-test). **g.** similar analysis as panel **f** for iSPN inactivation (Main Fig. 4, Extended Data Fig. 8d, see [methods](#)). P-values show significance of modulation (two-tailed t-test).

Extended Data Fig. 10 Circuit mechanism of contra ISC excitation, and model of exploration via iSPNs-Colliculus.

a-d. Potential circuit mechanisms by which iSPN could excite contra ISC. Color indicates the direction of modulation after iSPN activation, and shapes indicate cell type (triangle: excitatory; circle: inhibitory). Note that all these mechanisms are not mutually exclusive and a combination of these might occur together. We provide evidence for model **a** and **b**, in which inhibition ISC in one hemisphere disinhibit ISC on the opposite hemisphere (Fig. 3). **a.** Long-range inhibitory projection crossing the midline could mediate contra ISC excitation. In this scenario, iSPN will cause SNr to be excited, suppressing ipsi ISC, which in turn will disinhibit contra ISC. **b.** Long-range excitatory projection innervating local inhibitory interneurons could mediate this effect. **c.** A region outside SC (grey patch) could mediate the disinhibitory effect (e.g. nucleus isthmus; see main text). **d.** Separate population of SNr neurons could innervate ipsi and contra ISC. In this scenario, iSPN activation would lead to bidirectional modulation of SNr neurons, with ipsi ISC projecting SNr neurons being excited, and contra ISC projecting SNr neurons being inhibited. **e.** Schematic diagram of the exploration model proposed. iSPN integrate information about the outcome of specific action performed in a specific context. The function of iSPN to learn which actions lead to a negative outcome and suppress them in the future. iSPN can then suppress the target action that lead to the negative outcome. Via disinhibition within SC, this leads to a rapid execution of a competing motor program. Although the circuit from specific iSPN to target action is hardwired, competitive interaction within SC is more dynamic and

tunable so the same activation of iSPN can lead to different actions depending on the availability of the competing motor program.

Supplementary information

Peer Review File

Reporting Summary

Rights and permissions

Reprints and Permissions

About this article

Cite this article

Lee, J., Sabatini, B.L. Striatal indirect pathway mediates exploration via collicular competition. *Nature* **599**, 645–649 (2021).
<https://doi.org/10.1038/s41586-021-04055-4>

- Received: 05 October 2020
- Accepted: 27 September 2021
- Published: 03 November 2021
- Issue Date: 25 November 2021
- DOI: <https://doi.org/10.1038/s41586-021-04055-4>

Share this article

Anyone you share the following link with will be able to read this content:

[Get shareable link](#)

Sorry, a shareable link is not currently available for this article.

[Copy to clipboard](#)

Provided by the Springer Nature SharedIt content-sharing initiative

This article was downloaded by **calibre** from <https://www.nature.com/articles/s41586-021-04055-4>

| [Section menu](#) | [Main menu](#) |

- Article
- [Published: 03 November 2021](#)

Disruption of mitochondrial complex I induces progressive parkinsonism

- [Patricia González-Rodríguez](#) ORCID: [orcid.org/0000-0002-2561-3984¹](https://orcid.org/0000-0002-2561-3984),
- [Enrico Zampese](#) ORCID: [orcid.org/0000-0002-8851-2566¹](https://orcid.org/0000-0002-8851-2566),
- [Kristen A. Stout¹](#),
- [Jaime N. Guzman¹](#),
- [Ema Ilijic¹](#),
- [Ben Yang](#) ORCID: [orcid.org/0000-0003-0732-0237¹](https://orcid.org/0000-0003-0732-0237),
- [Tatiana Tkatch¹](#),
- [Mihaela A. Stavarache²](#),
- [David L. Wokosin¹](#),
- [Lin Gao](#) ORCID: [orcid.org/0000-0002-1781-4671³](https://orcid.org/0000-0002-1781-4671),
- [Michael G. Kaplitt²](#),
- [José López-Barneo³](#),
- [Paul T. Schumacker](#) ORCID: [orcid.org/0000-0001-9591-2034⁴](https://orcid.org/0000-0001-9591-2034) &
- [D. James Surmeier](#) ORCID: [orcid.org/0000-0002-6376-5225¹](https://orcid.org/0000-0002-6376-5225)

[Nature](#) volume 599, pages 650–656 (2021)

- 17k Accesses
- 1 Citations
- 695 Altmetric

- [Metrics details](#)

Subjects

- [Parkinson's disease](#)

Abstract

Loss of functional mitochondrial complex I (MCI) in the dopaminergic neurons of the substantia nigra is a hallmark of Parkinson's disease¹. Yet, whether this change contributes to Parkinson's disease pathogenesis is unclear². Here we used intersectional genetics to disrupt the function of MCI in mouse dopaminergic neurons. Disruption of MCI induced a Warburg-like shift in metabolism that enabled neuronal survival, but triggered a progressive loss of the dopaminergic phenotype that was first evident in nigrostriatal axons. This axonal deficit was accompanied by motor learning and fine motor deficits, but not by clear levodopa-responsive parkinsonism—which emerged only after the later loss of dopamine release in the substantia nigra. Thus, MCI dysfunction alone is sufficient to cause progressive, human-like parkinsonism in which the loss of nigral dopamine release makes a critical contribution to motor dysfunction, contrary to the current Parkinson's disease paradigm^{3,4}.

Access options

Subscribe to Journal

Get full journal access for 1 year

\$199.00

only \$3.90 per issue

[Subscribe](#)

All prices are NET prices.
VAT will be added later in the checkout.
Tax calculation will be finalised during checkout.

Rent or Buy article

Get time limited or full article access on ReadCube.

from \$8.99

[Rent or Buy](#)

All prices are NET prices.

Additional access options:

- [Log in](#)
- [Access through your institution](#)
- [Learn about institutional subscriptions](#)

Fig. 1: Loss of NDUFS2 function triggers metabolic adaptations in SN DA neurons.



Fig. 2: Loss of *Ndufs2* induces early axonal dysfunction.

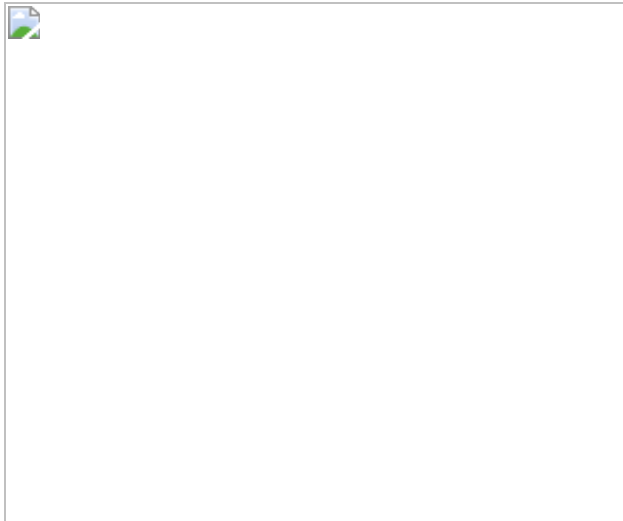


Fig. 3: Progressive loss of the somatodendritic phenotype, but not neuronal death.

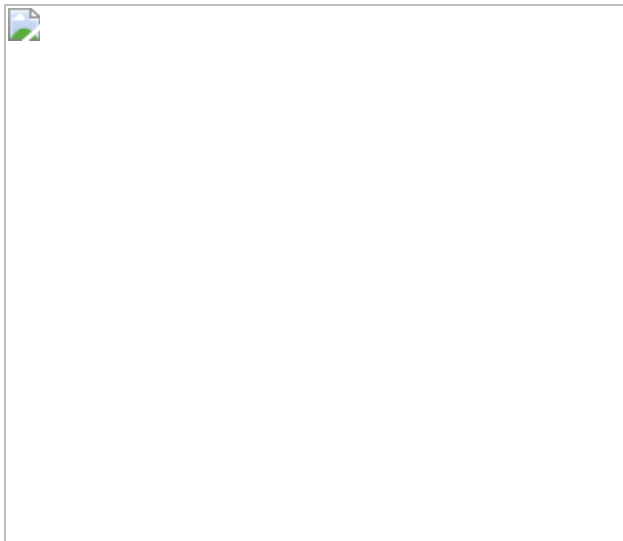


Fig. 4: *cNdufs2*^{-/-} mice present progressive, levodopa-responsive parkinsonism.

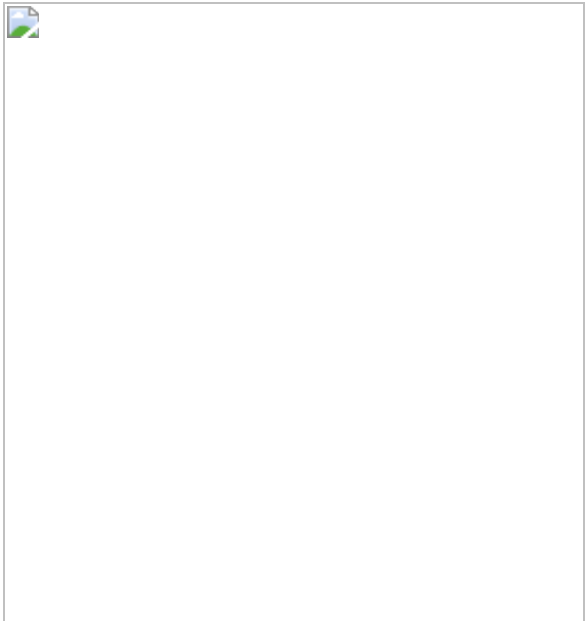
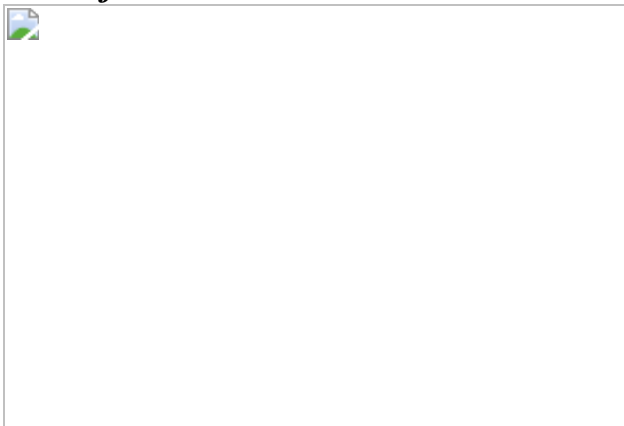


Fig. 5: Boosting mesencephalic dopamine levels reverses motor deficits in *cNdufs2*^{-/-} mice.



Data availability

RNA-seq reads have been deposited at the NCBI Sequence Read Archive under BioProject accession number [PRJNA752682](#). DA release data measured using fast-scan cyclic voltammetry were analysed using custom software that is available at GitHub

(https://github.com/surmeierlab/imagej_macros)⁴². The mouse model will be made available on request. All data generated or analysed in this study are included in this published Article and the [Supplementary Information](#). [Source data](#) are provided with this paper.

References

1. 1.

Surmeier, D. J., Obeso, J. A. & Halliday, G. M. Selective neuronal vulnerability in Parkinson disease. *Nat. Rev. Neurosci.* **18**, 101–113 (2017).

2. 2.

Kim, H. W. et al. Genetic reduction of mitochondrial complex I function does not lead to loss of dopamine neurons in vivo. *Neurobiol. Aging* **36**, 2617–2627 (2015).

3. 3.

Albin, R. L., Young, A. B. & Penney, J. B. The functional anatomy of basal ganglia disorders. *Trends Neurosci.* **12**, 366–375 (1989).

4. 4.

Wichmann, T. Changing views of the pathophysiology of parkinsonism. *Mov. Disord.* **34**, 1130–1143 (2019).

5. 5.

Poewe, W. et al. Parkinson disease. *Nat. Rev. Dis. Primers* **3**, 17013 (2017).

6. 6.

Beilina, A. & Cookson, M. R. Genes associated with Parkinson's disease: regulation of autophagy and beyond. *J. Neurochem.* **139**, 91–107 (2016).

7. 7.

Haelterman, N. A. et al. A mitocentric view of Parkinson's disease. *Annu. Rev. Neurosci.* **37**, 137–159 (2014).

8. 8.

Faustini, G. et al. Mitochondria and α -synuclein: friends or foes in the pathogenesis of Parkinson's disease? *Genes* **8**, 377 (2017).

9. 9.

Bolam, J. P. & Pissadaki, E. K. Living on the edge with too many mouths to feed: why dopamine neurons die. *Mov. Disord.* **27**, 1478–1483 (2012).

10. 10.

Guzman, J. N. et al. Systemic isradipine treatment diminishes calcium-dependent mitochondrial oxidant stress. *J. Clin. Invest.* **128**, 2266–2280 (2018).

11. 11.

Fernández-Agüera, M. C. et al. Oxygen sensing by arterial chemoreceptors depends on mitochondrial complex I signaling. *Cell Metab.* **22**, 825–837 (2015).

12. 12.

Kordower, J. H. & Burke, R. E. Disease modification for Parkinson's disease: axonal regeneration and trophic factors. *Mov. Disord.* **33**, 678–683 (2018).

13. 13.

Sanz, E. et al. Cell-type-specific isolation of ribosome-associated mRNA from complex tissues. *Proc. Natl Acad. Sci. USA* **106**, 13939–13944 (2009).

14. 14.

Fornasiero, E. F. et al. Precisely measured protein lifetimes in the mouse brain reveal differences across tissues and subcellular fractions. *Nat. Commun.* **9**, 4230 (2018).

15. 15.

Narendra, D., Walker, J. E. & Youle, R. Mitochondrial quality control mediated by PINK1 and Parkin: links to parkinsonism. *Cold Spring Harb. Perspect. Biol.* **4**, 11 (2012).

16. 16.

Baker, N., Patel, J. & Khacho, M. Linking mitochondrial dynamics, cristae remodeling and supercomplex formation: how mitochondrial structure can regulate bioenergetics. *Mitochondrion* **49**, 259–268 (2019).

17. 17.

Ekstrand, M. I. et al. Progressive parkinsonism in mice with respiratory-chain-deficient dopamine neurons. *Proc. Natl Acad. Sci. USA* **104**, 1325–1330 (2007).

18. 18.

Tantama, M. et al. Imaging energy status in live cells with a fluorescent biosensor of the intracellular ATP-to-ADP ratio. *Nat. Commun.* **4**, 2550 (2013).

19. 19.

Patriarchi, T. et al. Ultrafast neuronal imaging of dopamine dynamics with designed genetically encoded sensors. *Science* **360**, 6396 (2018).

20. 20.

Paladini, C. A. & Roepke, J. Generating bursts (and pauses) in the dopamine midbrain neurons. *Neuroscience* **282**, 109–121 (2014).

21. 21.

Roeper, J. Dissecting the diversity of midbrain dopamine neurons. *Trends Neurosci.* **36**, 336–342, (2013).

22. 22.

Yu, H. et al. MinK-related peptide 1: a beta subunit for the HCN ion channel subunit family enhances expression and speeds activation. *Circ. Res.* **88**, E84–E87 (2001).

23. 23.

Klaus, A. et al. What, if, and when to move: basal ganglia circuits and self-paced action initiation. *Annu. Rev. Neurosci.* **42**, 459–483 (2019).

24. 24.

Baker, K. A. et al. Simultaneous intrastriatal and intranigral dopaminergic grafts in the Parkinsonian rat model: role of the intranigral graft. *J. Comp. Neurol.* **426**, 106–116 (2000).

25. 25.

Mukhida, K. et al. Enhancement of sensorimotor behavioural recovery in hemiparkinsonian rats with intrastriatal, intranigral, and intrasubthalamic nucleus dopaminergic transplants. *J. Neurosci.* **21**, 3521–3530 (2001).

26. 26.

Robertson, G. S. & Robertson, H. A. D1 and D2 dopamine agonist synergism: separate sites of action? *Trends Pharmacol. Sci.* **8**, 295–299 (1987).

27. 27.

Coune, P. G., Schneider, B. L. & Aebischer, P. Parkinson's disease: gene therapies. *Cold Spring Harb. Perspect. Med.* **2**, a009431 (2012).

28. 28.

Sarre, S. et al. Biotransformation of l-DOPA to dopamine in the substantia nigra of freely moving rats: effect of dopamine receptor agonists and antagonists. *J. Neurochem.* **70**, 1730–1739 (1998).

29. 29.

Diederich, N. J. et al. Parkinson’s disease: is it a consequence of human brain evolution? *Mov. Disord.* **34**, 453–459 (2019).

30. 30.

Pacelli, C. et al. Elevated mitochondrial bioenergetics and axonal arborization size are key contributors to the vulnerability of dopamine neurons. *Curr. Biol.* **25**, 2349–2360 (2015).

31. 31.

Berthet, A. et al. Loss of mitochondrial fission depletes axonal mitochondria in midbrain dopamine neurons. *J. Neurosci.* **34**, 14304–14317 (2014).

32. 32.

Collier, T. J., Kanaan, N. M. & Kordower, J. H. Ageing as a primary risk factor for Parkinson’s disease: evidence from studies of non-human primates. *Nat. Rev. Neurosci.* **12**, 359–366 (2011).

33. 33.

Kordower, J. H. & Bjorklund, A. Trophic factor gene therapy for Parkinson’s disease. *Mov. Disord.* **28**, 96–109 (2013).

34. 34.

Rodriguez, M. C. et al. Subthalamic nucleus-mediated excitotoxicity in Parkinson’s disease: a target for neuroprotection. *Ann. Neurol.* **44**, S175–S188 (1998).

35. 35.

Martínez-Reyes, I. & Chandel, N. S. Mitochondrial TCA cycle metabolites control physiology and disease. *Nat. Commun.* **11**, 102 (2020).

36. 36.

Kordower, J. H. et al. Disease duration and the integrity of the nigrostriatal system in Parkinson's disease. *Brain* **136**, 2419–2431 (2013).

37. 37.

Kovaleski, R. F. et al. Dysregulation of external globus pallidus–subthalamic nucleus network dynamics in Parkinsonian mice during cortical slow-wave activity and activation. *J. Physiol.* **598**, 1897–1927 (2020).

38. 38.

Kravitz, A. V. et al. Regulation of Parkinsonian motor behaviours by optogenetic control of basal ganglia circuitry. *Nature* **466**, 622–626 (2010).

39. 39.

Gerfen, C. R. & Surmeier, D. J. Modulation of striatal projection systems by dopamine. *Annu. Rev. Neurosci.* **34**, 441–466 (2011).

40. 40.

Cheramy, A., Leviel, V. & Glowinski, J. Dendritic release of dopamine in the substantia nigra. *Nature* **289**, 537–542 (1981).

41. 41.

Cáceres-Chávez, V. A. et al. Acute dopamine receptor blockade in substantia nigra pars reticulata: a possible model for drug-induced

parkinsonism. *J. Neurophysiol.* **120**, 2922–2938 (2018).

42. 42.

Galtieri D. J. & Estep, C. M. Neurphysy.
<https://github.com/surmeierlab/neurphys> (2014).

43. 43.

Bouet, V. et al. The adhesive removal test: a sensitive method to assess sensorimotor deficits in mice. *Nat. Protoc.* **4**, 1560–1564 (2009).

44. 44.

Schmued, L. et al. Collateralization and GAD immunoreactivity of descending pallidal efferents. *Brain Res.* **487**, 131–142 (1989)

45. 45.

Heiman, M. et al. Cell type-specific mRNA purification by translating ribosome affinity purification (TRAP). *Nat. Protoc.* **9**, 1282–1291 (2014).

46. 46.

Martin, M. et al. Cutadapt removes adapter sequences from high-throughput sequencing reads. *Embo J.* **17**, 10–12 (2011).

47. 47.

Dobin, A. et al. STAR: ultrafast universal RNA-seq aligner. *Bioinformatics*. **29**, 15–21 (2013).

48. 48.

Anders, S., Pyl, P. T. & Huber, W. HTSeq—a Python framework to work with high-throughput sequencing data. *Bioinformatics* **31**, 166–169 (2015).

49. 49.

Love, M. I. et al. Moderated estimation of fold change and dispersion for RNA-seq data with DESeq2. *Genome Biol.* **15**, 550–558 (2014).

50. 50.

Zhou, Y. et al. Metascape provides a biologist-oriented resource for the analysis of systems-level datasets. *Nat. Commun.* **10**, 1523 (2019).

51. 51.

West, M. J., Slomianka, L. & Gundersen, H. J. G., Unbiased stereological estimation of the total number of neurons in the subdivisions of the rat hippocampus using the optical fractionator. *Anat. Rec.* **231**, 482–497 (1991).

52. 52.

Ilijic, E. et al. The L-type channel antagonist isradipine is neuroprotective in a mouse model of Parkinson’s disease. *Neurobiol Dis.* **43**, 364–371 (2011).

53. 53.

Oorschot, D. E. Total number of neurons in the neostriatal, pallidal, subthalamic, and substantia nigral nuclei of the rat basal ganglia: a stereological study using the cavalieri and optical disector methods. *J. Comp. Neurol.* **366**, 580–599 (1996).

54. 54.

Gundersen, H. J. G. & Jensen, E. B., The efficiency of systematic sampling in stereology and its prediction. *J. Microsc.* **147**, 229–263 (1987).

55. 55.

Zhou, et al. Serotonergic sprouting is induced by dopamine-lesion in substantia nigra of adult rat brain. *Brain Res.* **556**, 108–116 (1991).

Acknowledgements

We thank the staff at the Metabolomic Core Facility at Robert H. Lurie Comprehensive Cancer Center of Northwestern University for HPLC–MS experiments and staff at the NUSeq Core Facility for RNA-seq analysis; D.G. Galtieri for the original scripts in the Surmeier lab GitHub; and G. Yellen for insights on PercevalHR experiments. Electron microscopy tissue processing and imaging was performed at the Northwestern University Center for Advanced Microscopy, supported by NCI CCSG P30 CA060553 awarded to the Robert H. Lurie Comprehensive Cancer Center. This study was supported by grants from the Michael J. Fox Foundation (to D.J.S.), the JPB Foundation (to D.J.S.), the IDP Foundation (to D.J.S.), the Flanagan Fellowship (to P.G.-R.) and the European Research Council ERC Advanced Grant PRJ201502629 (to J.L.-B.).

Author information

Affiliations

1. Department of Neuroscience, Feinberg School of Medicine, Northwestern University, Chicago, IL, USA

Patricia González-Rodríguez, Enrico Zampese, Kristen A. Stout, Jaime N. Guzman, Ema Ilijic, Ben Yang, Tatiana Tkatch, David L. Wokosin & D. James Surmeier

2. Department of Neurological Surgery, Weill Cornell Medical College, New York, NY, USA

Mihaela A. Stavarache & Michael G. Kaplitt

3. Instituto de Biomedicina de Sevilla, Hospital Universitario Virgen del Rocío/CSIC/ Universidad de Sevilla and CIBERNED, Seville, Spain

Lin Gao & José López-Barneo

4. Department of Pediatrics, Northwestern University, Chicago, IL, USA

Paul T. Schumacker

Contributions

Conceptualization: P.G.-R., M.G.K., P.T.S. and D.J.S. Methodology: P.G.-R., E.Z., K.A.S., E.I., J.N.G., B.Y., T.T., L.G., M.A.S., D.L.W., J.L.-B., M.G.K., P.T.S. and D.J.S. Validation: P.G.-R., E.Z., K.A.S., J.N.G., E.I., T.T. and B.Y. Formal analysis: P.G.-R., E.Z., K.A.S., J.N.G., E.I., T.T. and B.Y. Investigation: P.G.-R., E.Z., K.A.S., J.N.G., E.I., T.T., B.Y., L.G., M.A.S., M.G.K., J.L.-B., P.T.S. and D.J.S. Resources: J.L.-B., M.G.K. and D.J.S. Writing: P.G.-R. and D.J.S. Visualization: P.G.-R., P.T.S. and D.J.S. Supervision: D.J.S. Funding acquisition: P.G.-R., J.L.-B. and D.J.S.

Corresponding author

Correspondence to [D. James Surmeier](#).

Ethics declarations

Competing interests

The authors declare no competing interests.

Additional information

Peer review information *Nature* thanks Ken Nakamura and the other, anonymous, reviewer(s) for their contribution to the peer review of this work. Peer reviewer reports are available.

Publisher's note Springer Nature remains neutral with regard to jurisdictional claims in published maps and institutional affiliations.

Extended data figures and tables

Extended Data Fig. 1 Metabolic remodeling in cNdufs2^{-/-} mice.

a, b, *Ndufs2* was ablated specifically in dopaminergic neurons by selective breeding of mice expressing Cre under the control of the dopamine transporter (DAT) promoter with mice containing a floxed allele of the *Ndufs2* gene. **c**, Cartoon representing the activity of the ETC (electron transport chain) and ANT following *Ndufs2* deletion. **d**, Electron micrographs of SN DA neurons. The nucleus and the mitochondria are highlighted in green and red, respectively. Scale bar: 1μm. **e**, Box plots showing no differences in mitochondrial density (wildtype, n=21; c*Ndufs2*^{-/-}, n=21) where n is the number of cells. **f**, Box plots showing mitochondrial morphology in wildtype and MCI-Park SN neurons (wildtype, n=21; c*Ndufs2*^{-/-}, n=21). Insets: representative electron micrographs of mitochondria showing intact (**top**) or abnormal (**bottom**) morphology (wildtype, n=21; c*Ndufs2*^{-/-}, n=21). The percentage of abnormal mitochondria was calculated as the ratio between the area occupied by abnormal mitochondria over the total area occupied by mitochondria for each cell. Scale bar: 0.2μm. **g**, The schematic on top is a sagittal view of the brain, and the red line indicates the position at 3.52mm from bregma, which is shown as a coronal section in the bottom panel (modified from Allen Mouse Brain Atlas, online version 1, 2008). **h**, Box plots indicate that OXPHOS index (OXPHOS/ (OXPHOS + glycolysis)) is lower in *Ndufs2* deficient neurons (wildtype, n=5; c*Ndufs2*^{-/-}, n=7). **i**, Confocal image of dopaminergic terminals in wildtype mice expressing PercevalHR in *ex vivo* brain slice at P40. Scale bar: 20μm. **j**, Box plots show decrease in the OXPHOS index in dopaminergic terminals of c*Ndufs2*^{-/-} mice (wildtype, n=4; c*Ndufs2*^{-/-}, n=5). Wildtype (grey); c*Ndufs2*^{-/-} (black). Two-tailed Mann-Whitney test; (**e**), (**f**), (**h**), (**j**). For the boxplots, the centre line indicates the median, the box limits indicate the first and third quartiles, and the whiskers indicate the data range. *P < 0.05; ***P < 0.0001.

[Source data](#)

Extended Data Fig. 2 Bar graph of enrichment analysis in MCI-Park mice.

Bar graph for viewing top 20 enrichment clusters, one per cluster, using a discrete color scale to represent statistical significance (Metascape).

Wildtype, N=5; *cNdufs2^{-/-}*, N=6 where N is the number of mice. **a**, Enriched Ontology cluster analysis of down-regulated genes. **b**, Gene Ontology biological processes analysis of down-regulated genes. **c**, Enriched Ontology cluster analysis of up-regulated genes. **d**, Gene Ontology biological processes analysis of up-regulated genes.

Extended Data Fig. 3 Enrichment network visualization in MCI-Park mice.

Network of enriched terms colored by cluster identity, where nodes that share the same cluster identity are typically close to each other (Metascape).

Wildtype, N=5; *cNdufs2^{-/-}*, N=6 where N is the number of mice. **a**, Enrichment network visualization in down-regulated genes in MCI-Park mice. **b**, Enrichment network visualization in up-regulated genes in MCI-Park mice.

Extended Data Fig. 4 TH expression in SNc and VTA dopaminergic neurons in wildtype and *cNdufs2^{-/-}* mice.

a, Quantification of TH expression in SNc dopaminergic neurons at P30 and P60 (wildtype, N=5; *cNdufs2^{-/-}*, N=5) where N is the number of mice. **b**, Quantification of TH expression in VTA dopaminergic neurons at P30 and P60 (wildtype, N =5; *cNdufs2^{-/-}*, N =4). **c**, Representative images showing TH-IR in VTA and SN dopaminergic neurons in wildtype mouse at P60. Scale bar: 200 μ m. **d**, Magnified VTA region showing dopaminergic neurons in wildtype at P60. Scale bar: 15 μ m. **e**, Representative images showing TH-IR in VTA and SN dopaminergic neurons in *cNdufs2^{-/-}* mouse at P60. Scale bar: 200 μ m. **f**, Magnified VTA region showing dopaminergic neurons in *cNdufs2^{-/-}* mouse at P60. Scale bar: 15 μ m. Wildtype (grey); *cNdufs2^{-/-}* (black). Two-tailed Mann-Whitney test (**a**) and (**b**). For the

boxplots, the centre line indicates the median, the box limits indicate the first and third quartiles, and the whiskers indicate the data range. * $P < 0.05$; ** $P < 0.01$.

[Source data](#)

Extended Data Fig. 5 Dopamine release is reduced in cNdufs2^{-/-} mice.

Representative images from SN in P30 wildtype (**a**) and cNdufs2^{-/-} (**b**) mice are shown. Scale =5μm. Representative images from dorsal striatum in wildtype (**c**) and cNdufs2^{-/-} (**d**) mice are shown. Scale= 5μm (wildtype, N=5; cNdufs2^{-/-}, N=5) where N is number of mice. Note that at P30, the TH promoter (not TH expression) was effectively driving the expression of a fluorescent reporter (ERtdTomato) in dopaminergic neurons, despite the down-regulation in TH expression in the dorsolateral striatum (shown in Fig. 2c). **e–g**, Dopamine release was measured by fast-scan cyclic voltammetry in wildtype and cNdufs2^{-/-} mice at P20. Representative colorplots (**e**) and traces (**f**) show dramatic reduction in evoked (1p, 350 nA, 2 ms) release in dorsal striatum of cNdufs2^{-/-} mice. Scale: vertical =0.5 μM dopamine, horizontal = 1s. **g**, Summary data demonstrate dopamine release is significantly decreased by P20 (wildtype, N= 12, cNdufs2^{-/-}, N= 4). Striatal dopamine release measured with dLight1.3b at P30 (**h, j, l**) and P60 (**i, k, m**). Traces are ΔF/F₀ over time. Solid lines represent median trace, shaded area is 95% CI. Scale bars: (**h, i**), vertical =200 % ΔF/F₀, horizontal= 500ms. Quantification of dopamine release at P30 (**j, l**) and P60 (**k, m**) in dorsal striatum; striatal dLight1.3b responses were analyzed either by defining 16-pixel-wide line profiles, which provided high temporal resolution measurements of selected regions (**j,k**), or by averaging the entire field of view, with lower temporal resolution but broader sampling area (**l, m**). (**j**, wildtype N=5; cNdufs2^{-/-} N= 5; **k**, wildtype N=6; cNdufs2^{-/-} N= 6; **l**, wildtype N=4; cNdufs2^{-/-} N= 5; **m**, wildtype N=9; cNdufs2^{-/-} N= 4). Wildtype (grey); cNdufs2^{-/-} (black). Two-tailed Mann-Whitney test: (**g**), (**j**), (**k**), (**l**) and (**m**). For the boxplots, the centre line indicates the median,

the box limits indicate the first and third quartiles, and the whiskers indicate the data range. * $P < 0.05$, *** $P \leq 0.0001$.

[Source data](#)

Extended Data Fig. 6 Physiology remodeling in cNdufs2^{-/-} mice.

Dopamine (**a**), DOPAC (**b**), serotonin (**c**), and acetylcholine (**d**) separated from wildtype and cNdufs2^{-/-} striatum tissue lysate (P30 and P60, wildtype, N=4, cNdufs2^{-/-}, N=4) where N is the number of mice. Note that elevation of striatal serotonin was detected at P120. This is a common feature of rodent PD models⁵⁵. **e**, Heat maps illustrating the remodeling of ion channels in cNdufs2^{-/-} mice; repeated samples are grouped horizontally (wildtype, N=5; cNdufs2^{-/-}, N=6). **f**, qPCR analysis of RiboTag harvested mRNA showing a drop in *hcna2* mRNA in cNdufs2^{-/-} neurons (wildtype, N=4; cNdufs2^{-/-}, N=4). **g**, Whole-cell somatic recording showing hyperpolarization-activated, cyclic nucleotide-gated currents from a wildtype and cNdufs2^{-/-} neuron at P30. Scale bars: 100pA, 200ms. **h**, Cumulative probability plot of peak current from wildtype and cNdufs2^{-/-} SN dopaminergic neurons (wildtype, n=12; cNdufs2^{-/-}, n=10) where n is the number of cells. **i**, qPCR analysis of RiboTag harvested mRNA showing a drop in *Cav1.3* mRNA in cNdufs2^{-/-} SN dopaminergic neurons (wildtype, N=4; cNdufs2^{-/-}, N=4). **j**, Cumulative probability plot of peak [Ca²⁺] at proximal dendrite (wildtype, n=8; cNdufs2^{-/-}, n=6). **k**, Whole-cell somatic recordings showing the response to glutamate uncaging in wildtype (left) and cNdufs2^{-/-} (right) mice. Scale bars: 20mV, 1s. Representative SN DA neuron filled with Alexa Flour 594 showing the location for uncaging in blue. Scale bar: 20μm. **l**, Spikes/burst - peak spiking rate plot showing the difference in response to uncaged glutamate between wildtype (n=5) and cNdufs2^{-/-} (n=5). **m**, Representative traces showing spike width in SN neurons from wildtype and cNdufs2^{-/-} at P30. **n**, Box plots indicate AP half width in wildtype and cNdufs2^{-/-} at P30 (wildtype n=6; cNdufs2^{-/-} n=7). Wildtype (grey); cNdufs2^{-/-} (black). Two-tailed Mann-Whitney test: (**a-d**, **f** and **i**). One tailed Mann-Whitney test: (**h**), (**j**), (**l**) and (**n**). For the boxplots,

the centre line indicates the median, the box limits indicate the first and third quartiles, and the whiskers indicate the data range. * $P < 0.05$; ** $P < 0.01$, *** $P < 0.001$.

[Source data](#)

Extended Data Fig. 7 Physiological characterization of SN dopaminergic neurons in *cNdufs2*^{-/-} mice at P60.

a, b, Electron micrographs of SN dopaminergic neurons at P60. The nucleus and the mitochondria are highlighted in green and red, respectively. Scale bar: 2 μ m. **c**, Box plots showing no differences in mitochondrial density (wildtype, n=14; *cNdufs2*^{-/-}, n=23) where n is the number of cells. **d**, Box plots showing abnormal morphology in MCI-Park mitochondria (wildtype, n=14; *cNdufs2*^{-/-}, n=23). **e**, Representative images showing normal (**top**) and abnormal (**bottom**) mitochondria. The percentage of abnormal mitochondria was calculated as the ratio between the area occupied by abnormal mitochondria over the total area occupied by mitochondria for each cell. Scale bar: 500nm. **f**, Schematic diagram of injection site (modified from Allen Mouse Brain Atlas, online version 1, 2008). TH-Fusion Red reporter was bilaterally injected into the SN of *cNdufs2*^{-/-} mouse at P50. Experiments were done at P60 (\pm 4 days). Representative image showing TH-Fusion Red expression in wildtype (**g**) and *cNdufs2*^{-/-} (**h**) mice at P60. Scale bar: 20 μ m (wildtype, N=5; *cNdufs2*^{-/-}, N=5) where N is the number of mice. **i**, Cell attached recordings from identified wildtype and *cNdufs2*^{-/-} SN DA neurons at P60. Scale bars: 10pA, 1s. **j**, Cumulative probability plot of autonomous discharge rates (wildtype n=20; *cNdufs2*^{-/-} n=25 cells). **k**, Whole-cell somatic recordings from a *cNdufs2*^{-/-} SN DA neurons at P60 showing the response to glutamate uncaging. Representative SN DA neuron filled with Alexa Flour 594 is showing the location for uncaging in blue (n=4). Scale bars: 20mV, 2s, 20 μ m. **l**, Spikes/burst - peak spiking rate plot showing the difference in response to uncaged glutamate between wildtype (n=4) and *cNdufs2*^{-/-} (n=5). Wildtype (grey); *cNdufs2*^{-/-} (black). Two-tailed Mann-Whitney test (**c, d**). One-tailed Mann-Whitney test (**j**) and (**l**). For the boxplots, the centre

line indicates the median, the box limits indicate the first and third quartiles, and the whiskers indicate the data range. *P < 0.05.

[Source data](#)

Extended Data Fig. 8 Behavioural phenotypes in *cNdufs2*^{-/-} mice.

a, Schematic diagram of the experimental protocol for Y maze test. The scoring of 2 and 3 was counted as incorrect. **b**, Open-field traces in wildtype and *cNdufs2*^{-/-} mice at P60 and P120 with and without levodopa (3mg/Kg) treatment. **c**, Representative traces showing the effect of levodopa treatment on the speed in wildtype (N=5) and *cNdufs2*^{-/-} (N=5) mice at P120 where N is the number of mice. **d**, Rearing test performance. **e**, Number of rearings in a 3-minute period in wildtype, *cNdufs2*^{-/-} and *cNdufs2*^{-/-} + 3mg/kg levodopa mice at different ages (P20-P120). Number of rearings begin to be impaired at P40. Levodopa did not rescue this deficit (N=11 per group) **f**, Rearing time in wildtype, *cNdufs2*^{-/-} and *cNdufs2*^{-/-} + 3mg/kg levodopa mice at different ages (P20-P120). At P60, *cNdufs2*^{-/-} mice show difficulty transitioning between rearing and landing, spending much more time ‘stuck’ in an elevated posture. Levodopa did not rescue this deficit (N=11 per group). (**g, h**) Body weight was analyzed from P20 to P120. **g**, Body weight development of wildtype (N=10) and *cNdufs2*^{-/-} (N=11) mice in males. **h**, Body weight development of wildtype (N=10) and *cNdufs2*^{-/-} (N=11) mice in females. Wildtype (gray), *cNdufs2*^{-/-} (black), *cNdufs2*^{-/-} plus levodopa (red). One tailed Kruskal-Wallis with Dunn’s correction for multiple comparisons: (**e, f**). One-way ANOVA followed by Tukey’s post hoc test: (**g, h**). Data are presented as median and range (shaded area). *P < 0.05; **P < 0.01.

[Source data](#)

Extended Data Fig. 9 Gait analysis in *cNdufs2*^{-/-} mice.

a, Pictures of wildtype and *cNdufs2^{-/-}* mice footprints: RF (Right Fore), RH (Right Hind), LF (Left Fore) and LH (Left Hind) in yellow. Body length measurements (**b**) and hind limb stance width (**c**) for wildtype (N=7), *cNdufs2^{-/-}* (N=7) and *cNdufs2^{-/-}*+levodopa (N=7) where N is the number of mice. **d**, Representative graph of right hind paw area. Stride length (**e**) and swing duration (**f**) for wildtype N=7, *cNdufs2^{-/-}* N=7 and *cNdufs2^{-/-}*+levodopa N=7. **g**, Step sequence for wildtype (N=7), *cNdufs2^{-/-}* (N=7) and *cNdufs2^{-/-}*+levodopa (N=7). **h**, Stance duration for wildtype (N=7), *cNdufs2^{-/-}* (N=7) and *cNdufs2^{-/-}*+levodopa (N=7). **i**, Brake duration for wildtype (N=7), *cNdufs2^{-/-}* (N=7) and *cNdufs2^{-/-}*+levodopa (N=7). **j**, Paw area for wildtype (N=7), *cNdufs2^{-/-}* (N=7) and *cNdufs2^{-/-}*+levodopa (N=7). **k**, Stride frequency for wildtype (N=7), *cNdufs2^{-/-}* (N=7) and *cNdufs2^{-/-}*+levodopa (N=8). **l**, Propulsion time for wildtype (N=7), *cNdufs2^{-/-}* (N=8) and *cNdufs2^{-/-}*+levodopa (N=7). **m**, Gait symmetry for wildtype (N=7) and *cNdufs2^{-/-}* (N=8) mice. **n**, Fore limb stance width for wildtype (N=7) and *cNdufs2^{-/-}* (N=7) mice. **o**, Box-plots summarizing stereological estimate of the numbers of NeuN-immunopositive neurons in the SNC (**o**) and VTA (**p**), wildtype (N=5) and *cNdufs2^{-/-}* (N=5). **q**, Representative images showing NeuN immunostaining in the midbrain in wildtype (**top panel**) and *cNdufs2^{-/-}* mouse (**bottom panel**) in P120-150 mice. Scale bar: 100µm. Wildtype(grey); *cNdufs2^{-/-}*(black); *cNdufs2^{-/-}*+levodopa (red). One-way ANOVA followed by Tukey's post hoc test: (**b**), (**c**), (**e-n**), two-tailed Mann-Whitney test (**o**, **p**). Data from right hind paw: (**b**), (**c**), (**e-n**). Levodopa dosage: 6mg kg⁻¹. For the boxplots, (**b**), (**c**), (**e**), (**f**), (**o**) and (**p**), the centre line indicates the median, the box limits indicate the first and third quartiles, and the whiskers indicate the data range. (**g-n**): Solid lines represent median trace shaded area is the range. *P < 0.05; **P < 0.01.

[Source data](#)

[Extended Data Fig. 10 SN expression of AADC did not induce DA release in P100 *cNdufs2^{-/-}* mice even after perfusion with dopamine.](#)

a, Schematic diagram of injection site. AAV2-GFP-AADC was bilaterally injected into the striatum of *cNdufs2^{-/-}* mouse at P60. Confocal image of coronal slice containing striatum (**b**) or SN (**c**) from *cNdufs2^{-/-}* mouse. Scale bar: 200 μ m. **d**, Magnified view of SN showing no expression of AADC-GFP. Scale bar: 20 μ m. **e**, Schematic diagram of injection site. AAV2-GFP-AADC was bilaterally injected into the SN of *cNdufs2^{-/-}* mouse at P60. Confocal image of coronal slice containing striatum (**f**) or SN (**g**) from *cNdufs2^{-/-}* mouse. Scale bar: 200 μ m. **h**, Magnified view of SN showing expression of AADC-GFP. Scale bar: 20 μ m. Wildtype (N=5), *cNdufs2^{-/-}* (N=5) where N is the number of mice. **i**, Quantification of dopamine in striatal tissue from wildtype (N=4), *cNdufs2^{-/-}*+low levodopa (1.5mg/kg) with (N=4) or without AADC (N=4) and *cNdufs2^{-/-}*+high levodopa (12mg kg⁻¹) (N=4). **j**, Schematic diagram of the AAV-AADC injection into the SN and AAV-dLight injection into the striatum (P60). **k**, dLight fluorescence (raw in thin lines and average in thick lines) in response to a single electrical stimulus (350 μ A, 2ms). **l**, Summary of dLight responses (wildtype n=16, *cNdufs2^{-/-}*-AADC n=9, *cNdufs2^{-/-}*+AADC n=12 where n is the number of slices). **m**, An example recording of dLight fluorescence response upon bath application of dopamine (100 μ M) followed by washout in a *cNdufs2^{-/-}* mouse injected with AADC in the SN. **n-o**, Example recordings of dLight fluorescence responses (raw in thin lines and average in thick lines) upon single electrical stimulus after dopamine washout. *cNdufs2^{-/-}* mouse injected with AADC (**n**, n=4) or GFP (**o**, n=4) into the SN. Wildtype (grey); *cNdufs2^{-/-}* (black); *cNdufs2^{-/-}*+AADC (red); *cNdufs2^{-/-}*+high levodopa (blue). (**i**), two-way ANOVA followed by Tukey's post hoc test, *P< 0.05; **P< 0.01; (**l**), one-tailed Kruskal-Wallis with Dunn's correction for multiple comparisons, ***P<0.0001. For the boxplots, the centre line indicates the median, the box limits indicate the first and third quartiles, and the whiskers indicate the data range. **p**, Schematic showing the cascade of events following to Ndufs2 deletion in MCI-Park mice. DA (dopamine), DLS (dorsolateral striatum). The schematics in (**a**), (**e**) and (**j**) are modified from the Allen Mouse Brain Atlas, online version 1, 2008 (<http://mouse.brain-map.org>).

[Source data](#)

Supplementary information

Supplementary Tables

This file contains Supplementary Tables 1–8 and their descriptions.

Reporting Summary

Peer Review File

Source data

Source Data Fig. 1

Source Data Fig. 2

Source Data Fig. 3

Source Data Fig. 4

Source Data Fig. 5

Source Data Extended Data Fig. 1

Source Data Extended Data Fig. 4

Source Data Extended Data Fig. 5

Source Data Extended Data Fig. 6

Source Data Extended Data Fig. 7

Source Data Extended Data Fig. 8

[Source Data Extended Data Fig. 9](#)

[Source Data Extended Data Fig. 10](#)

Rights and permissions

[Reprints and Permissions](#)

About this article

Cite this article

González-Rodríguez, P., Zampese, E., Stout, K.A. *et al.* Disruption of mitochondrial complex I induces progressive parkinsonism. *Nature* **599**, 650–656 (2021). <https://doi.org/10.1038/s41586-021-04059-0>

- Received: 11 December 2020
- Accepted: 28 September 2021
- Published: 03 November 2021
- Issue Date: 25 November 2021
- DOI: <https://doi.org/10.1038/s41586-021-04059-0>

Share this article

Anyone you share the following link with will be able to read this content:

[Get shareable link](#)

Sorry, a shareable link is not currently available for this article.

[Copy to clipboard](#)

Provided by the Springer Nature SharedIt content-sharing initiative

Further reading

- [**Mice with disrupted mitochondria used to model Parkinson's disease**](#)

- Zak Doric
- Ken Nakamura

Nature (2021)

[**Mice with disrupted mitochondria used to model Parkinson's disease**](#)

- Zak Doric
- Ken Nakamura

News & Views 03 Nov 2021

This article was downloaded by **calibre** from <https://www.nature.com/articles/s41586-021-04059-0>

| [Section menu](#) | [Main menu](#) |

- Article
- Open Access
- [Published: 03 November 2021](#)

Cold-induced *Arabidopsis* FRIGIDA nuclear condensates for *FLC* repression

- [Pan Zhu](#) [ORCID: orcid.org/0000-0003-0029-3571](#)¹,
- [Clare Lister](#)¹ &
- [Caroline Dean](#) [ORCID: orcid.org/0000-0002-6555-3525](#)¹

Nature volume **599**, pages 657–661 (2021)

- 11k Accesses
- 100 Altmetric
- [Metrics details](#)

Subjects

- [Abiotic](#)
- [Gene silencing](#)
- [Long non-coding RNAs](#)
- [Plant molecular biology](#)
- [Nuclear speckles](#)

Abstract

Plants use seasonal temperature cues to time the transition to reproduction. In *Arabidopsis thaliana*, winter cold epigenetically silences the floral repressor locus *FLOWERING LOCUS C (FLC)* through POLYCOMB REPRESSIVE COMPLEX 2 (PRC2)¹. This vernalization process aligns flowering with spring. A prerequisite for silencing is transcriptional downregulation of *FLC*, but how this occurs in the fluctuating temperature regimes of autumn is unknown^{2,3,4}. Transcriptional repression correlates with decreased local levels of histone H3 trimethylation at K36 (H3K36me3) and H3 trimethylation at K4 (H3K4me3)^{5,6}, which are deposited during

FRIGIDA (FRI)-dependent activation of *FLC*^{7,8,9,10}. Here we show that cold rapidly promotes the formation of FRI nuclear condensates that do not colocalize with an active *FLC* locus. This correlates with reduced FRI occupancy at the *FLC* promoter and *FLC* repression. Warm temperature spikes reverse this process, buffering *FLC* shutdown to prevent premature flowering. The accumulation of condensates in the cold is affected by specific co-transcriptional regulators and cold induction of a specific isoform of the antisense RNA *COOLAIR*^{5,11}. Our work describes the dynamic partitioning of a transcriptional activator conferring plasticity in response to natural temperature fluctuations, thus enabling plants to effectively monitor seasonal progression.

[Download PDF](#)

Main

Plants overwinter before flowering in *Arabidopsis* through FRI-dependent upregulation of *FLC*. This mechanism requires FRIGIDA-LIKE 1 (FRL1), FRIGIDA-ESSENTIAL 1 (FES1), SUPPRESSOR OF FRIGIDA 4 (SUF4) and *FLC* EXPRESSOR (FLX), which associate in a FRI complex⁸. In laboratory conditions of constant cold, *FLC* is transcriptionally repressed in around two to three weeks^{5,6,11}. However, in natural autumnal fluctuating temperatures in field conditions, *FLC* transcriptional shutdown took many months^{3,4}. We therefore investigated whether and how FRI function might change in response to fluctuating temperature.

FRI condensates accumulate in the cold

First, we analysed how cold influences FRI protein interactions. A line carrying a translational *FRI-GFP* fusion, expressed at the same level as endogenous *FRI*, and fully complementing the *fri* early flowering phenotype (Extended Data Fig. 1), was used for immunoprecipitation in combination with mass spectrometry (IP–MS)¹⁰ (Supplementary Table 1). FRI–GFP did not enrich any of the FRI complex components from warm-grown plant extracts, but, counterintuitively, FRI–GFP accumulated in plants that underwent two weeks of cold exposure, and in these conditions FRL1 and FRL2—but not FLX, SUF4 or FES1—were enriched⁸ (Extended Data Table 1). FRI interacted with subunits of the Mediator complex^{12,13}, WDR5a and ATX2 (which promote H3K4me3)^{7,9,14}, the PAF1 complex¹⁵, general transcription factors¹³, RNA-polymerase-II-associated proteins, and many RNA splicing factors and uridine-rich small nuclear ribonucleoproteins (snRNPs)^{16,17,18}, which suggests that FRI has a role in co-transcriptional regulation (Extended Data Table 1). The higher

prevalence of these interactors in extracts from cold-grown plants may reflect the cold-induced accumulation of FRI (Extended Data Table 1).

Second, we analysed the localization of FRI in vivo. Like many other co-transcriptional regulators^{19,20} we found that FRI–GFP forms nuclear condensates, which were increased in size and number after cold exposure (Fig. 1a, Extended Data Fig. 2a–d). A FRI–Myc fusion showed similar condensate formation (Extended Data Fig. 2e,f). Fluorescence recovery after photobleaching (FRAP) revealed relatively slow FRI–GFP dynamics (Fig. 1b,c), like other biomolecular condensates²⁰, but different to FCA–GFP, which have previously been shown to form liquid-like foci (condensates) with a FRAP recovery time of seconds²¹. Formation of the FCA–GFP condensates was not enhanced by cold (Extended Data Fig. 2g–i); thus, FRI and FCA condensates have different biophysical properties.

Fig. 1: Cold-promoted FRI nuclear condensates are linked to *FLC* transcriptional shutdown.

 figure1

a, Confocal microscopic images of FRI–GFP nuclear condensates in root cells in the indicated conditions. For quantitative analysis, see Extended Data Fig. 2c,d. **b, c**, Images (**b**) and quantification (**c**) of FRAP of FRI–GFP nuclear condensates. Time 0 indicates the time of the photobleaching pulse. Red arrows indicate the bleached condensates. Mean \pm s.e.m.; $n = 10$ condensates in 10 cells. **d**, Confocal analysis of subnuclear colocalization of FRI with the co-expressed proteins in tobacco leaf nuclei. Data represent three independent experiments. **e, f**, Representative images (**e**, in the warm; **f**, in the cold) of nuclei expressing FRI–GFP (green) sequentially hybridized with intronic smFISH probes for *FLC* (red). DNA was labelled with DAPI (blue). Three independent experiments gave the same conclusion. **g, h**, Frequency distribution of FRI–GFP condensates (left), non-spliced *FLC* transcript signals (middle) and their

colocalization per nucleus (right) in root cells in the warm (**g**) and in the cold (**h**). Numbers of analysed nuclei are as indicated. Scale bars, 5 µm (**a, b, d**); 10 µm (**e, f**).

Source data

We then analysed whether the FRI interactors co-associate with FRI in the condensates. FRL1–mScarlet I colocalized with FRI–GFP in nuclear condensates after transient co-expression in tobacco leaves (Fig. [1d](#)) but did not form nuclear condensates when transfected alone (Extended Data Fig. [3a–c](#)). Consistently, loss of FRL1 reduced the cold-induced enhancement of the size and number of FRI condensates (Extended Data Fig. [3d–f](#)). By contrast, FRI condensates were less affected in *flx-2* and *suf4* mutants (Extended Data Fig. [3d–f](#)), consistent with FRL1, but not FLX or SUF4, immunoprecipitating with FRI (Extended Data Table [1](#)). Other FRI interactors, GFP–ELF7 and TAF15b–GFP, colocalized with FRI–mScarlet I in condensates (Fig. [1d](#), Extended Data Fig. [3g](#)) and condensates containing the Cajal body marker protein U2B'' (ref. [18](#)) frequently colocalized with FRI–GFP condensates after cold (Extended Data Fig. [3h–j](#)). FRI condensates may therefore share components with Cajal bodies, similar to PML bodies in mammalian cells^{[22](#)}. Overall, these data support the notion that multiple protein interactions enhance the formation of FRI condensates.

We further investigated the domains of FRI that are required for nuclear condensate formation. Consistent with disordered domains having important roles in biomolecular condensation^{[19,21](#)}, a GFP fusion protein with a version of FRI in which the C-terminal disordered domain was deleted no longer formed nuclear condensates (Extended Data Fig. [4](#)). This supports the C terminus being required for FRI function^{[23](#)}. Deletion of the FRI coiled-coil domains^{[10](#)} also led to loss of condensate formation (Extended Data Fig. [4b, c](#)). A naturally occurring 16-base-pair deletion that is found in the loss-of-function FRI allele in Col-0^{[10,23](#)}, which would produce a protein without the C-terminal disordered and coiled-coil domains, prevented condensate formation (Extended Data Fig. [4b, c](#)). Thus, both the C-terminal disordered domain and two coiled-coil domains are required for FRI condensation *in vivo*.

FRI is more stable in the cold

Increased protein concentration is known to promote biomolecular condensation^{[19,20](#)} so we further examined the cold-induced accumulation of FRI. FRI–GFP accumulated after two to four weeks of cold (Extended Data Fig. [5a–c](#)), with no corresponding change in the levels of *FRI* mRNA (Extended Data Fig. [1a](#)). Analysis of nuclear FRI–TAP showed that this stability was not a consequence of the GFP fusion (Extended Data Fig. [5d](#)). The FRI half-life was measured as less than 24 h in the warm, but more

than 24 h in the cold (Extended Data Fig. 5e–h); thus, the cold enhancement of FRI nuclear condensates appears to be a consequence of increased FRI protein stability.

Overexpression using 35S:FRI-GFP (Extended Data Fig. 6a, b) led to a small accumulation of FRI-GFP protein after two weeks of cold exposure and a decrease after four weeks (Extended Data Fig. 6c–e), although FRI is less stable in warm than in cold conditions (Extended Data Fig. 6f). A previous report showed that FRI abundance decreased in the cold²⁴, which may be a consequence of the medium as FRI protein is highly induced by glucose in warm conditions (Extended Data Fig. 6f). Overexpression of FRI-GFP is likely to influence nuclear condensate dynamics²⁵, but one to four weeks of cold still enhanced FRI-GFP condensation even though more FRI condensates were found in warm-grown 35S:FRI-GFP lines compared to FRI-GFP (Extended Data Fig. 6g–i).

Levels of FRI-GFP protein decreased in *frl1-1* and *suf4* mutants, with no concomitant change in *FRI-GFP* mRNA⁸ (Extended Data Fig. 6j–l). By contrast, FRI-GFP protein levels in *flx-2* did not change (Extended Data Fig. 6k, l), despite the disruption to FRI condensation (Extended Data Fig. 3d–f), supporting the notion that increased protein concentration is not sufficient for cold enhancement of FRI condensate formation. Together, these data show that cold stabilization of FRI and increased interaction with multiple factors reciprocally enhance the formation of FRI condensates.

Condensates sequester FRI away from *FLC*

We further addressed the functional consequences of FRI nuclear condensate formation. FRI expanded the zone of *FLC* expression in warm-grown plants and this was antagonized by cold exposure²⁶ (Extended Data Fig. 7a, b). Association of FRI-GFP with the *FLC* 5' region in warm conditions^{8,9} decreased after two weeks of cold exposure (Extended Data Fig. 7c–f), paralleling the decrease in *FLC* transcription^{5,11,26} (Extended Data Fig. 7g) and raising the possibility that condensates are linked to *FLC* transcriptional repression. We used single-molecule RNA fluorescence in situ hybridization (smRNA FISH) and *FLC* intron 1 probes²⁷ to identify nascent *FLC* transcripts that mark transcriptionally active *FLC* loci and investigated whether FRI nuclear condensates associated with an active *FLC* locus. The nascent *FLC* transcripts and the FRI-GFP condensates never colocalized with each other (Fig. 1e–h). Notably, FRI association with the *COOLAIR* promoter increased after two weeks of cold exposure (Extended Data Fig. 7e), consistent with *COOLAIR* upregulation^{5,11,26}. However, despite more cells transcribing *COOLAIR* in the cold²⁶ and more FRI condensates, we did not detect any colocalization between non-spliced *COOLAIR* clouds and FRI-GFP condensates (Extended Data Fig. 7h). FRI and its associated factors may therefore be sequestered into nuclear condensates

away from the *FLC* locus, with nascent transcription dissolving any condensates at the locus²⁸.

Supporting this hypothesis, in the *35S:FRI-GFP* line, in which more FRI nuclear condensates form (Extended Data Fig. [6g–i](#)), *FLC* transcript levels are lower (Extended Data Fig. [7i,j](#)) and a reduction of FRI nuclear condensates in the *frl1-1* mutant (Extended Data Fig. [3d–f](#)) correlates with a slower *FLC* transcriptional shutdown (Extended Data Fig. [7k–m](#)). The low levels of *FLC* transcript in *flx-2* and *suf4* suggest a different mechanism (Extended Data Fig. [7k–m](#)). FLX and SUF4 appear to promote the ability of FRI to transcriptionally activate, but they have less of a role in cold-induced FRI condensation (Extended Data Fig. [3d–f](#)).

FRI condensates track temperature shifts

FLC transcriptional shutdown occurs during autumn as temperatures fluctuate widely over daily and weekly timescales^{3,4}, so we tested whether the cold-induced sequestration of FRI has an important role in fluctuating temperatures. FRI–GFP nuclear condensate dynamics were analysed during a 12-h transient cold exposure (mimicking a cool night in autumn)³. We found that FRI–GFP condensates gradually increased in size and number (Fig. [2a](#), Extended Data Fig. [8a,b](#)), through a process requiring protein synthesis (Extended Data Fig. [5e–h](#)). The accumulation of FRI condensates correlated with downregulation of *FLC* to its lowest expression 12 h after transfer to cold (Fig. [2b](#)), which was further repressed after 2 weeks of cold exposure (Extended Data Fig. [8a–c](#)). Thus, FRI condensation increases rapidly in response to decreasing temperature, correlating with *FLC* transcriptional shutdown.

Fig. 2: Short-term temperature fluctuations influence the formation of FRI nuclear condensates and *FLC* transcription.

 **figure2**

a, c, Confocal microscopic images of FRI–GFP nuclear condensates in wild-type (WT) (top) and *TEX* (bottom) root cells after 0, 6 and 12 h of cold treatment (**a**) and in wild-type plants after they were returned to the warm for 0, 6, 12 and 24 h after a 2-week cold treatment (**c**). Scale bars, 5 μ m. For quantitative analysis, see Extended Data Fig. 8a, b, d, e. **b, d**, Relative transcript level of unspliced *FLC* in the indicated plants within the same time course of changed temperatures in **a, c** by quantitative PCR with reverse transcription (RT–qPCR). Mean \pm s.e.m.; $n = 4$ (**b**) and 3 (**d**) biologically independent experiments.

[Source data](#)

It has previously been observed that a spike of high temperature in autumn slows *FLC* shutdown^{3,4}; thus, we asked whether the cold-induced accumulation of FRI condensates is reversible by warmth. FRI–GFP condensates, monitored at 6-h intervals over the first 24 h after plants were returned to warm temperature, were significantly reduced within the first 6 h and did not recover in either root or leaf cells (Fig. 2c,

Extended Data Fig. 8d–f). This process was not fully blocked by inhibiting proteasome-mediated protein degradation (Extended Data Fig. 8g–j). *FLC* transcription was upregulated in parallel (Fig. 2d) and showed further reactivation after transfer to warm conditions for 10 days (Extended Data Fig. 8k). Therefore, the cold-induced condensation of FRI is easily reversed by warmth, which suggests that the condensates serve as reservoirs allowing a rapid response to warm temperature spikes. These rapid dynamics would buffer the shutdown of *FLC* transcription in the fluctuating temperatures of autumn, contributing to a requirement for the absence of warmth for *FLC* silencing³.

To gain further insight into the dynamics of FRI nuclear condensates in response to temperature shifts, we performed a time-lapse experiment using a temperature-controlled microscope stage. This showed that FRI–GFP nuclear condensates undergo dynamic changes in response to changing temperature, disappearing within five hours of a return to warm conditions (Extended Data Fig. 8l, Supplementary Video 1), but being rescued by cold after a three-hour warm spike (Extended Data Fig. 8m, Supplementary Video 2). In response to the temperature shifts, the FRI condensates fluctuated in number as they grew and fused (Extended Data Fig. 8n,o, Supplementary Video 2)—behaviour typical of biomolecular condensates^{21,28,29}. This induction of FRI condensates did not occur in transient assays in tobacco leaves exposed to cold temperatures (Extended Data Fig. 8p–r).

***COOLAIR* promotes FRI condensates in the cold**

To investigate which other cold-specific factors might contribute to the heterotypic interactions required for condensate formation we tested a role for *COOLAIR*. One *COOLAIR* isoform is differentially induced by the FRI complex after two weeks of cold (Extended Data Fig. 9a–f): class II.ii, a distally polyadenylated transcript that includes an additional exon^{5,11} (Fig. 3a). This change in splicing may involve FRI interacting with splicing factors (Extended Data Fig. 3h–j, Extended Data Table 1) that have previously been shown to have a role in cold-responsive gene regulation^{16,17}. RNA immunoprecipitation (RNA-IP) showed that FRI–GFP specifically enriched *COOLAIR* class II.ii after two weeks of cold (Fig. 3b, Extended Data Fig. 9g,h). In *fri1-1*, in which the FRI condensation is severely attenuated (Extended Data Fig. 3d–f) but *COOLAIR* expression is still relatively high (Extended Data Fig. 9a–c), this enrichment was reduced (Extended Data Fig. 9i). Therefore, the FRI–class II.ii interaction is tightly connected with the cold induction of FRI condensation—a conclusion supported by the rapid changes in class II.ii in response to temperature shifts (Fig. 3c,d) and further induction after two weeks of cold (Extended Data Fig. 9f).

Fig. 3: COOLAIR promotes cold induction of FRI–GFP nuclear condensates and sequestration of FRI from the *FLC* promoter.

 figure3

a, Schematic of *FLC* and *COOLAIR* transcripts at the *FLC* locus. Untranslated regions are indicated by grey boxes and exons by black boxes. kb, kilobase; TSS, transcription start site. **b**, RNA-IP assay of spliced *COOLAIR* enrichment by FRI–GFP with *UBC* as control. Mean \pm s.d.; $n = 4$ replicates over 2 biologically independent experiments. Two-tailed *t*-test. **c**, **d**, Relative transcript level of *COOLAIR* class II.ii in the indicated plants within the same time course of changed temperatures as in Fig. 2 by RT–qPCR. Mean \pm s.e.m.; $n = 4$ (**c**) and 3 (**d**) biologically independent experiments. **e**, Confocal images of wild-type and *TEX* root tip nuclei expressing FRI–GFP. Scale bars, 5 μ m. For quantitative analysis, see Extended Data Fig. 9j,k. **f**, FRI–GFP occupancy on *FLC* promoter region in WT and *TEX* plants by CHIP. Mean \pm s.e.m.; $n = 3$ biologically independent experiments. The exact distance from TSS referred to **a**. Two-way ANOVA adjusted by Sidak’s multiple comparisons test. NS, no significance. **g**, A working model for temperature-controlled FRI nuclear condensation in *FLC* transcriptional regulation. CC, coiled-coil domain; CR, co-transcriptional regulators; DD, disordered domain.

Source data

We next crossed FRI–GFP to a previously described *FLC* terminator exchange (*TEX*) line^{5,26,27}. The *FLC* terminator–*COOLAIR* promoter is exchanged for an *RBCS3B* terminator, which prevents the cold induction of *COOLAIR* transcription^{5,26} (Fig. 3c). There was no increase in the size of FRI condensates within the first 12 h of plants experiencing cold (Fig. 2a, Extended Data Fig. 8a,b), and both the size and the number of FRI condensates were significantly reduced after two weeks of cold (Fig. 3e, Extended Data Fig. 9j,k). This is linked to decreased levels of FRI protein in *TEX*, which might reflect negative feedback from reduction of *COOLAIR* expression (Extended Data Fig. 9l,m). Similarly, the lower cold induction of FRI condensation in

flx-2 and *suf4* mutants (Extended Data Fig. 3d–f) may relate to reduced *COOLAIR* expression (Extended Data Fig. 9a–f). In addition, chromatin immunoprecipitation (ChIP) experiments showed that the cold-induced reduction of FRI occupancy at the *FLC* promoter was less in the *TEX* line compared to the wild type (Fig. 3f), which could account for the inefficient cold-induced *FLC* transcriptional shutdown in *TEX*^{5,26} (Fig. 2b). This mechanism could explain the *COOLAIR*-facilitated removal of H3K36me3 at the *FLC* locus in the early vernalization phase⁵ (Fig. 3g).

Conclusions

Together, our experiments point to a temperature-controlled condensation mechanism that modulates FRI activation of *FLC* transcription; such a mechanism would facilitate *FLC* shutdown in natural fluctuating temperatures. FRI associates with transcriptional co-activators and recruits histone modifiers to the *FLC* promoter, establishing an active transcriptional state at *FLC* in the warm (Fig. 3g). The instability of FRI in the warm enables a fast turnover of these transcriptional complexes (Fig. 3g). After transfer to the cold, FRI protein is stabilized and changes in protein or *COOLAIR* interactions result in the accumulation of nuclear condensates that sequester FRI away from the *FLC* promoter (Fig. 3g). This contrasts with mechanisms in which condensates promote the dwell time of transcriptional regulators at specific genomic loci¹⁹. The combinatorial effect of temperature-specific splicing, and splicing-specific nuclear condensation, gives a wide range of possibilities for *FLC* regulation in different temperature regimes. Given the recognized importance of biological condensates in gene regulation, this type of mechanism may have widespread roles in the plasticity of plant responses to varying environments^{29,30,31}.

Methods

Plant material and growth conditions

All the mutants and transgenic lines were in Columbia-0 (Col-0), except for *FCA-GFP* and *FLC-GUS*, which are in *Landsberg erecta* (Ler). *TEX FRI* (ref. 5), *FCA-GFP* (ref. 21), *fri1-1* (ref. 32), *flx-2* (ref. 33), *suf4* (ref. 34) and *FLC-GUS* with or without *FRI^{JU223}* (ref. 35) have previously been described. *FRI^{JU223}* is a functional transgenic *FRI* allele as described previously¹⁰. *FRI* is Col-0 with an introgressive active *Sf2 FRI* allele and was previously described³⁶. *fri1-1*, *flx-2* and *suf4* were crossed into the *FRI* background to generate *fri1-1 FRI*, *flx-2 FRI* and *suf4 FRI*.

Seeds were surface-sterilized and sown on Murashige and Skoog (MS) agar plates without glucose or sucrose (unless otherwise stated) and kept at 4 °C in the dark for 3

days. For non-vernalization (NV), seedlings were grown in warm conditions (16 h light, 8 h darkness with constant 20 °C) for 10 days unless otherwise stated. For cold treatment, seedlings were pre-grown in warm conditions (16 h light, 8 h darkness with constant 20 °C) for 10 days unless otherwise stated, and then transferred to cold (8 h light, 16 h darkness with constant 5 °C) for a long-term vernalization, such as 2 weeks and 4 weeks (2WV and 4WV). As there is no difference between *FRI* and *fri* in response to photoperiod³⁴ and photoperiod influences flowering in parallel with *FLC*^{37,38}, we use this short-day photoperiod for long-term cold treatment to match natural conditions. For short-term cold treatment (0–12 h), the light conditions were kept the same as in warm conditions. For cold-to-warm transfer experiments, after 1 or 2 weeks of cold treatment, seedlings were moved to warm conditions (16 h light, 8 h darkness with constant 20 °C) for another specified duration, such as 6 h. Plants grow faster in the warm than in the cold (one day growth in the warm is approximately equivalent to seven days in the cold)³⁹, therefore for warm–cold comparisons plants were harvested at the same developmental stage rather than after the same time period.

Plasmid construction and generation of transgenic lines

To generate *pFRI:FRI-GFP* and *pFRI:FRI-Myc* constructs, a 4.56-kb PmII/HpaI fragment containing genomic *FRI* sequence from H51 (ref. 10) was cloned into pBluescript KS (+). This clone spans 0.84 kb upstream of the *FRI* start codon to 1.4 kb downstream of the *FRI* stop codon. *GFP* sequence was amplified and inserted into the XbaI site over the *FRI* stop codon. The *FRI-GFP* fragment was then subcloned into SLJ75515⁴⁰ and transformed into *Agrobacterium tumefaciens* C58 (pGV2260) by triparental mating³⁶. *Myc* sequence was inserted into the XbaI site 6 bp downstream of the *FRI* start codon. The *FRI-Myc* fragment was then subcloned into the EcoRI site of pGreenII 0229 and transformed into *A. tumefaciens* pGV3101 (pMP90). All of the XbaI sites were introduced by site-directed mutagenesis by the oligos listed in Supplementary Table 2. Transgenic *FRI-GFP* and *FRI-Myc* plants in the Col-0 background were generated by floral dipping with *A. tumefaciens*. Transgenic lines with a single insertion were identified in the T₂ generation and segregated 3:1 for Basta resistance. Independent *FRI-GFP* lines showed the same cold-induced condensation.

For the *pFRI:FRI-TAP* and *p35S:FRI-GFP* constructs, *FRI* cDNA was fused with the *TAP* and *GFP* sequences, respectively, and *FRI-TAP* was subcloned into pBluescript KS (+) with the *FRI* promoter, whereas *FRI-GFP* was driven by a CaMV35S promoter. *pFRI:FRI-TAP* and *p35S:FRI-GFP* in the binary vectors were then transferred into *A. tumefaciens*. Transgenic plants were also in the Col-0 background.

The 35S:*GFP-ELF7* (ref. 41), *pTAF15b:TAF15b-GFP* (ref. 42) and *pCsV* (Cassava vein mosaic virus):*TAF15b-GFP* (ref. 42) constructs were previously described.

To generate *pFRI:FRI-mScarlet I*, the same *FRI* genomic sequence from H51 (ref. [10](#)) was used as a template and mScarlet I sequence was inserted to the XbaI site over *FRI* stop codon in pBluescript KS (+). The *FRI-mScarlet I* fragment was then subcloned into SLJ6999^{[40](#)}. For *pFRI:FRI-Col-0-GFP*, an equivalent *FRI* genomic sequence from Col-0 was amplified^{[10](#)} and the GFP sequence was fused before the premature stop codon (after 1,335 bp downstream from ATG, equivalent to 314 amino acids). For *pFRI:FRI-DD-GFP*, the C-terminal disordered domain (DD) from 1,833 bp downstream from ATG to the stop codon (equivalent to 451 to 609 amino acids) was deleted. For *pFRI:FRI-CC-GFP*, two fragments encoding the coiled-coil domains (CC) are deleted: the first spans 118 bp to 300 bp downstream from ATG (equivalent to 40 to 100 amino acids) and the second is from 1,680 bp to 1,832 bp downstream from ATG (equivalent to 400 to 451 amino acids). For *pFRL1:FRL1-mScarlet I*, a 3,972-bp fragment containing *FRL1* genomic sequence from Col-0 was amplified. It includes 1,502 bp upstream from *FRL1* ATG and 1,057 bp downstream from *FRL1* TAG. mScarlet I sequence was inserted before the TAG translational stop codon. *FRI-Col-0-GFP*, *FRI-DD-GFP*, *FRI-CC-GFP* and *FRL1-mScarlet I* DNA fragments were then cloned into the SLJ75515^{[40](#)} destination vector by Gateway Cloning. Plasmids were transformed into *A. tumefaciens* C58 (pGV2260) for infiltration of *Nicotiana benthamiana*^{[21](#)}. All primers used for construction are listed in Supplementary Table [2](#).

IP–MS analyses

The IP–MS analyses were performed as described previously^{[21,36](#)}. For the first experiment (IP1) 2.5 g of seedlings was cross-linked in 1% formaldehyde as previously described^{[43](#)}. For the second (IP2) and third experiment (IP3), the amount of plant material used was doubled. Cross-linked plants were ground into fine powder and lysed in 50 ml of cell lysis buffer (20 mM Tris HCl, pH 7.5, 250 mM sucrose, 25% glycerol, 20 mM KCl, 2.5 mM MgCl₂, 0.1% NP-40, 5 mM DTT). The lysate was filtered through two layers of Miracloth (Merck, D00172956) and pelleted by centrifugation. The pellets were washed twice with 10 ml of nuclear wash buffer (20 mM Tris HCl, pH 7.5, 2.5 mM MgCl₂, 25% glycerol, 0.3% Triton X-100, 5 mM DTT) and resuspended with RIPA buffer (1× PBS, 1% NP-40, 0.5% sodium deoxycholate, 0.1% SDS). All the buffers were supplemented with 0.1 U µl⁻¹ RNaseOUT (Invitrogen, 10777019), 1 mM PMSF and Roche Complete tablets to keep the integrity of any RNA–protein and protein–protein complex. Nuclear lysate was sonicated three times (Diagenode Bioruptor; M level, 30 s ON–30 s OFF, 5 min each time) and nuclear supernatant was obtained after centrifuge. GFP–Trap magnetic agarose beads (25 µl) (Chromotek, GTMA-20) were pre-blocked with 1 mg ml⁻¹ BSA and 1 mg ml⁻¹ yeast total RNA (Sigma) in RIPA buffer for 1 h at 4 °C and incubated with the nuclear supernatant for 2 h at 4 °C. Beads were sequentially washed twice with high-salt wash buffer and low-salt wash buffer (20 mM Tris HCl, pH 7.5, 500 mM (high-salt) or 150

mM NaCl (low-salt), 0.5 mM EDTA, 0.1% SDS and 1% Triton X-100). The beads were finally resuspended in 1× SDS loading buffer and boiled at 95 °C for 15 min to reverse cross-linking. The protein samples were purified from 10% SDS-PAGE gels followed by trypsin digestion. For LCMS analysis, an Orbitrap Fusion Tribrid mass spectrometer (Thermo Fisher Scientific) equipped with an UltiMate 3000 RSLC nano LC system (Thermo Fisher Scientific) was used. Data were searched using Mascot server 2.7 (Matrix Science). Results were imported and evaluated in Scaffold 4.10.0 software (Proteome Software).

RNA expression analysis

RNA was extracted with the hot phenol method^{5,36}. Genomic DNA contamination was removed by TURBO DNA-free kit (Invitrogen, AM1907) following the manufacturer's guidelines. cDNA was synthesized by the SuperScript IV reverse transcriptase (Invitrogen, 18090050) using gene-specific reverse primers. All primers are listed in Supplementary Table 2. The TAIR (The Arabidopsis Information Resource) accession numbers for the genes analysed in this study are *FRI* (AT4G00650), *FLC* (AT5G10140) and *COOLAIR* (AT5G01675). Standard reference genes *PP2A* (AT1G13320) and *UBC* (AT5G25760) for gene expression were used for normalization⁴. Data were analysed using Microsoft Excel (v.2102, 64-bit) and GraphPad Prism 7.

Microscopy and image quantification

The seedlings used for imaging were grown in the following conditions: NV, plants were grown in warm conditions for 7 days; 1WV, plants were grown in warm conditions for 6 days before being transferred to cold conditions for 1 week; 2WV or 4WV, plants were grown in cold conditions for 2 or 4 weeks with a 5-day pre-growth in warm conditions; before a short cold treatment (12 h or shorter), plants were grown in warm conditions for 7 days, so that all of the seedlings imaged are developmentally equivalent to a 7-day-old warm-grown seedling. The warm and cold conditions are the same as described in 'Plant material and growth conditions' unless otherwise stated.

The subcellular localization of FRI-GFP in root tips and first true leaves (Extended Data Figs. 2a, b, 8f) was imaged on a Zeiss LSM780 confocal microscope using a 40×/1.2 water objective and GAsP spectral detector array. The seedlings were kept intact during imaging. GFP was excited at 488 nm (Argon ion laser, laser power: 5.0 %) and detected at wavelengths of 491–695 nm in lambda mode. Linear unmixing projection in ZEN Black (2012) software was applied and the autofluorescence detected at 526–695 nm was unmixed and labelled as background (blue). Images were exported by ZEN Blue (2012).

For quantitative analysis of FRI–GFP and FCA–GFP nuclear condensates, imaging was performed on a Zeiss LSM880 confocal microscope using a $40\times/1.1$ water objective and GAsP spectral detector array. GFP was excited at 488 nm (Argon ion laser, laser power: 5.0 %) and detected at wavelengths of 499–525 nm in lambda mode. An optimal z-step size of 0.61 μm was used over a total depth of 10.37 μm from the upper surface (18 z-slices) and maximum intensity projection was applied for the z-stack. A binary image of just the spots was then created through threshold in Fiji (ImageJ) and the spot area was subsequently measured by Analyze Particles in Fiji (ImageJ). As all images were obtained with a 0.11 μm pixel size, the area of a single pixel is 0.0121 μm^2 . To exclude single pixels, 0.02 μm^2 was set as the minimum size during the analysis. The spot number (with area larger than 0.02 μm^2) per nucleus was gained through displaying the spot outline generated by Analyze Particles in the original image. Violin plots reflecting the data distribution were produced with PlotsOfData⁴⁴. Statistical evaluations with multiple comparisons tests were performed using the GraphPad Prism 7 software.

To compare the fluorescence intensity between roots, imaging was performed with a Zeiss LSM780 confocal microscope using an EC Plan-Neofluar $20\times/0.50$ objective. To allow comparison between treatments, the same settings were used for all images. Measurement of the fluorescence intensity was conducted with Fiji (ImageJ) with the intensity normalized to the background for each image. To collect the total intensity of each root tip, sum slices projections from a z-stack of 16 steps with a step size of 2 μm were applied before analysis.

FRAP

FRAP of FRI–GFP nuclear condensates was performed as described⁴⁵ with a Zeiss LSM780 confocal microscope coupled with a Linkam Heating and Cooling Stage (Meyer instruments). A chamber was created on slides using Grace Bio-Labs Secure Seal adhesive sheets (Sigma, GBL620001) and filled with MS medium. The 2WV *FRI-GFP* seedlings were carefully transferred into the chamber with stage temperature kept at 4 °C. Using a $40\times/1.2$ water objective, the region of an FRI–GFP nuclear condensate was bleached using a laser intensity of 100% at 488 nm. Recovery was recorded for every 2 min for a total of 20 min after bleaching. At each time point, maximum intensity projections from a z-stack of 12 steps with a step size of 1 μm were applied. Analysis of the recovery curves was carried out with Fiji (ImageJ), Microsoft Excel (v.2102, 64-bit) and GraphPad Prism 7.

Time-lapse imaging

The time-lapse microscopy of FRI–GFP nuclear condensates was performed with a Zeiss LSM780 confocal microscope coupled with a Linkam Heating and Cooling

Stage (Meyer instruments). For Supplementary Video 1, 1WV seedlings were transferred into a same chamber as in FRAP experiment and observed under a 40×/1.2 water objective. GFP was excited at 488 nm (Argon ion laser, laser power: 5.0 %) and detected at wavelengths of 490–551 nm. The temperature was first set at 4 °C and images were acquired every 15 or 20 min for 5 h after the temperature rose to 22 °C. At each time point, maximum intensity projections from a z-stack of 12 steps with a step size of 1 μm were applied. For Supplementary Video 2, 1WV seedlings were imaged after being grown in warm conditions (20 °C) for 3 h with the stage temperature kept at 4 °C, and images were acquired every 20 min for 6 h. The same imaging settings were used as in Supplementary Video 1. Images were processed and FRI–GFP nuclear condensates were quantified with Fiji (ImageJ).

Cycloheximide and MG132 treatment

Cycloheximide (CHX) and MG132 treatment were according to a previous study³⁹. Before treatment, plants were grown on MS agar plates as described above. For treatment, seedlings were carefully transferred to new MS agar plates supplemented with either 100 μM CHX (C1988, Sigma-Aldrich) or 100 μM MG132 (474787, Sigma-Aldrich) growing for 24 h. In parallel, the same seedlings were transferred to new MS agar plates supplemented with the same amount of solvent (ethanol for CHX and dimethyl sulfoxide for MG132) as a control. Root tips were then imaged with a Zeiss LSM780 confocal microscope using a 40×/1.2 water objective. GFP was excited at 488 nm (Argon ion laser, laser power: 20.0 %) and detected at wavelengths of 489–530 nm. An optimal z-step size of 0.435 μm was used over a total depth of 11.75 μm from the upper surface (28 z-slices). Images were processed and measurements were conducted with Fiji (ImageJ). Sum slices projection was applied for the z-stack. The whole nuclear intensity was measured and normalized to background in each image before comparison. All images were obtained with a 0.1-μm pixel size and 0.02 μm² was set as the minimum size during the analysis of FRI–GFP nuclear condensates. Statistical evaluations with multiple comparisons tests were performed using the GraphPad Prism software.

smFISH and immunofluorescence

smFISH and immunofluorescence was performed as previously described^{26,46}. Plants were grown in warm conditions for seven days (NV) or in cold conditions for two weeks with a five-day pre-growth in warm conditions (2WV). For FRI–GFP fluorescence microscopy with sequential smFISH, root tips were fixed with 4% paraformaldehyde (PFA) before being squashed. After permeabilization in 70% ethanol for 1 h, the subnuclear localization of FRI–GFP was imaged and the stage positions were saved at the microscope. Next, cover slips were carefully unmounted and *FLC* intron 1 or *COOLAIR* intron probes labelled with Quasar 570 were

hybridized at 37 °C overnight. The probes were the same as previously described^{26,27}. The probe signals were detected using the same stage positions as FRI–GFP. The microscope used was Zeiss Elyra PS with a 100×/1.46 oil-immersion objective and a cooled electron multiplying CCD (charge-coupled device) Andor iXon 897 camera. GFP was exited at 488 nm and detected at wavelengths of 495–550 nm; probes labelled with Quasar 570 were excited at 561 nm and detected at 570–620 nm; DAPI was excited at 405 nm and detected at 420–480 nm. An optimal z-step size of 0.2 μm was used over a total depth of 2.4 μm (23 z-slices) and maximum intensity projection was applied for the z-stack using Fiji (ImageJ).

For FRI–Myc immunofluorescence and colocalization of FRI–GFP and U2B'', squashed root cells were immersed in 70% ethanol overnight at 4 °C for permeabilization. Cell walls were digested with 0.2% Driselase (Sigma, D9515) and 0.15% Macerozyme R-10 (Duchefa Biochemie, M8002) in 1× PBS at 37 °C for 40 min. After being washed three times with 1× PBST, cells were blocked with 2.5% BSA (Thermo Fisher Scientific, AM2616). Primary antibodies: 1: 125 diluted anti-c-Myc (Sigma, M5546), 1: 500 diluted anti-GFP (Abcam, ab290) and 1: 20 diluted anti-U2B'' (4G3, a gift from P. Shaw) were incubated at 37 °C for 3–4 h. Alexa Fluor 488 anti-rabbit secondary antibody (Thermo Fisher Scientific, A-11008, dilution: 1:200) and Alexa Fluor 555 anti-mouse secondary antibody (Thermo Fisher Scientific, A-21424, dilution: 1:200) were incubated for 1 h. After DAPI staining, slides were mounted in Vectashield (Vector Lab, H-1000). Images were acquired on a Zeiss LSM780 confocal microscope using a 63×/1.40 oil objective. For FRI–Myc immunofluorescence, DAPI was excited at 405 nm and detected at 410–513 nm; FRI–Myc–Alexa Fluor 555 was excited at 514 nm and detected at 545–697 nm. For FRI–GFP and U2B'' colocalization, DAPI was excited at 405 nm and detected at 407–489 nm; FRI–GFP–Alexa Fluor 488 was excited at 488 nm and detected at 491–561 nm; U2B''–Alexa Fluor 555 was excited at 561 nm and detected at 562–634 nm.

GUS staining

FLC–GUS staining was performed as previously described³⁵. Whole seedlings were vacuum-infiltrated with GUS staining buffer (1 mM X-gluc (5-bromo-4-chloro-3-indolyl glucuronide), 100 mM phosphate buffer, pH 7.0, 10 mM EDTA, 0.1% Triton X-100, 0.5 mM ferricyanide and ferrocyanide, pH was finally adjusted to 7.0) followed by an overnight or shorter incubation at 37 °C. Whole seedlings and roots were immediately imaged after de-staining with 95% ethanol.

ChIP and quantitative PCR

FRI–GFP ChIP was performed as previously outlined with some modifications^{1,36}. Five grams of NV seedlings and 2.5 g of 2WV seedlings were cross-linked in 1%

formaldehyde and nuclei were purified and lysed as in the IP–MS experiment. Anti-GFP (Abcam, ab290, dilution: 1:400) and protein A agarose beads containing salmon sperm DNA (Millipore, 16-157) were used in the immunoprecipitation. The enriched DNA was purified using the ChIP DNA Clean & Concentrator Kit (Zymo Research, D5205)⁴³. All ChIP experiments were quantified by quantitative PCR (qPCR) with appropriate primers (Supplementary Table 2). The enrichment levels of FRI–GFP at *ACTIN* (*ACT*) and *SHOOT MERISTEMLESS* (*STM*) were used as controls. A transgene carrying a wild-type *FLC* crossed with FRI–GFP was used as control for FRI–GFP ChIP in *TEX*.

Western blot analysis

For checking FRI–GFP enrichment in the ChIP experiment, beads were directly boiled in 1×SDS loading buffer at 95 °C for 15 min after immunoprecipitation. For detecting FRI–GFP and FRI–TAP protein levels in NV, 2WV and 4WV plants, nuclei were purified with the same protocol of IP–MS but from 0.3 g of non-cross-linked seedlings. Whole seedlings were grounded and lysed to get total protein extraction for detecting FRI–GFP protein levels in 35S:*FRI-GFP* plants. ChIP elution and the extracted nuclear and total proteins were separated on NuPAGE 4–12% Bis-Tris protein gel (Invitrogen, NP0321BOX) and transferred to a PVDF membrane (GE Healthcare Life Sciences). Antibodies against GFP (Roche, 11814460001, dilution: 1:2,000), TAP (Thermo Fisher Scientific, CAB1001, dilution: 1:1,000), H3 (Abcam, ab1791, dilution: 1:5,000) and tubulin (Merck Sigma-Aldrich, T5168, dilution: 1:4,000) were used as primary antibodies. Horseradish peroxidase (HRP)-conjugated secondary antibodies: anti-mouse IgG (GE, NA931, dilution: 1:20,000) and anti-rabbit IgG (GE, NA934, dilution: 1:20,000) were used for protein detection with chemiluminescent substrate (Thermo Fisher Scientific, 34095). Western blot signal was captured in ImageQuant LAS 500.

RNA-IP assay

Five grams of NV seedlings and 2.5 g of 2WV seedlings were used for each immunoprecipitation. Nuclei were extracted and purified from cross-linked plant material with the same procedure as in the IP–MS experiment. The pellet was resuspended in 1 ml of nuclear lysis buffer (50 mM Tris HCl, pH 7.5, 100 mM NaCl, 1% Triton X-100, 1 mM MgCl₂ and 0.1 mM CaCl₂) and incubated at 37 °C for 10 min with Turbo DNase (Invitrogen, AM1907)⁴⁷. Then SDS was added to a final concentration of 0.1% and NaCl to 150 mM. Following another hour incubation at 4 °C, nuclear lysate was cleared by centrifugation. A 100-μm quantity of the supernatant was saved as the input. Twenty-five microlitres of pre-blocked GFP–Trap magnetic agarose beads (Chromotek, GTMA-20) were incubated with the nuclear supernatant following the same immunoprecipitation and wash procedure as in IP–MS experiment.

All the buffers used were supplemented with 0.1 U μl^{-1} RNaseOUT (Invitrogen, 10777019), 1 mM PMSF and Roche Complete tablets. Then RNA was eluted and purified as previously described²¹. After another DNA digestion with Turbo DNase, reverse transcription with gene specific primers was performed by SuperScript IV reverse transcriptase. Primers for reverse transcription and qPCR are listed in Supplementary Table 2. RNA enrichment was analysed in Microsoft Excel (v.2102, 64-bit) and GraphPad Prism 7. RNA enriched in NV *FRI-GFP* was normalized to NV *FRI* whereas 2WV *FRI-GFP* was normalized to 2WV *FRI* to reduce any possible influence from *COOLAIR* expression variation.

Reporting summary

Further information on research design is available in the [Nature Research Reporting Summary](#) linked to this paper.

Data availability

Full lists of mass spectrometry are provided as Supplementary Table 1. Raw images of western blots are provided as Supplementary Fig. 1. Other raw images that support the findings of this study are available at <https://doi.org/10.11922/sciencedb.01119>. [Source data](#) are provided with this paper.

References

1. 1.
Yang, H. et al. Distinct phases of Polycomb silencing to hold epigenetic memory of cold in *Arabidopsis*. *Science* **357**, 1142–1145 (2017).
2. 2.
Buzas, D. M., Robertson, M., Finnegan, E. J. & Helliwell, C. A. Transcription-dependence of histone H3 lysine 27 trimethylation at the *Arabidopsis* polycomb target gene *FLC*. *Plant J.* **65**, 872–881 (2011).
3. 3.
Hepworth, J. et al. Absence of warmth permits epigenetic memory of winter in *Arabidopsis*. *Nat. Commun.* **9**, 639–639 (2018).
4. 4.

Antoniou-Kourounioti, R. L. et al. Temperature sensing is distributed throughout the regulatory network that controls *FLC* epigenetic silencing in vernalization. *Cell Syst.* **7**, 643–655 (2018).

5. 5.

Csorba, T., Questa, J. I., Sun, Q. & Dean, C. Antisense *COOLAIR* mediates the coordinated switching of chromatin states at *FLC* during vernalization. *Proc. Natl Acad. Sci. USA* **111**, 16160–16165 (2014).

6. 6.

Yang, H., Howard, M. & Dean, C. Antagonistic roles for H3K36me3 and H3K27me3 in the cold-induced epigenetic switch at *Arabidopsis FLC*. *Curr. Biol.* **24**, 1793–1797 (2014).

7. 7.

Jiang, D., Gu, X. & He, Y. Establishment of the winter-annual growth habit via *FRIGIDA*-mediated histone methylation at *FLOWERING LOCUS C* in *Arabidopsis*. *Plant Cell* **21**, 1733–1746 (2009).

8. 8.

Choi, K. et al. The *FRIGIDA* complex activates transcription of *FLC*, a strong flowering repressor in *Arabidopsis*, by recruiting chromatin modification factors. *Plant Cell* **23**, 289–303 (2011).

9. 9.

Li, Z., Jiang, D. & He, Y. *FRIGIDA* establishes a local chromosomal environment for *FLOWERING LOCUS C* mRNA production. *Nat. Plants* **4**, 836–846 (2018).

10. 10.

Johanson, U. et al. Molecular analysis of *FRIGIDA*, a major determinant of natural variation in *Arabidopsis* flowering time. *Science* **290**, 344–347 (2000).

11. 11.

Swiezewski, S., Liu, F., Magusin, A. & Dean, C. Cold-induced silencing by long antisense transcripts of an *Arabidopsis* Polycomb target. *Nature* **462**, 799–802 (2009).

12. 12.

Hemsley, P. A. et al. The *Arabidopsis* mediator complex subunits MED16, MED14, and MED2 regulate mediator and RNA polymerase II recruitment to CBF-responsive cold-regulated genes. *Plant Cell* **26**, 465–484 (2014).

13. 13.

Yang, Y., Li, L. & Qu, L. J. Plant Mediator complex and its critical functions in transcription regulation. *J. Integr. Plant Biol.* **58**, 106–118 (2016).

14. 14.

Yun, J. Y., Tamada, Y., Kang, Y. E. & Amasino, R. M. *Arabidopsis trithorax-related3/SET domain GROUP2* is required for the winter-annual habit of *Arabidopsis thaliana*. *Plant Cell Physiol.* **53**, 834–846 (2012).

15. 15.

He, Y., Doyle, M. R. & Amasino, R. M. PAF1-complex-mediated histone methylation of *FLOWERING LOCUS C* chromatin is required for the vernalization-responsive, winter-annual habit in *Arabidopsis*. *Gene Dev.* **18**, 2774–2784 (2004).

16. 16.

Guan, Q. et al. A DEAD box RNA helicase is critical for pre-mRNA splicing, cold-responsive gene regulation, and cold tolerance in *Arabidopsis*. *Plant Cell* **25**, 342–356 (2013).

17. 17.

Du, J. L. et al. The splicing factor PRP31 is involved in transcriptional gene silencing and stress response in *Arabidopsis*. *Mol. Plant* **8**, 1053–1068 (2015).

18. 18.

Collier, S. et al. A distant coilin homologue is required for the formation of Cajal bodies in *Arabidopsis*. *Mol. Biol. Cell* **17**, 2942–2951 (2006).

19. 19.

Sabari, B. R., Dall’Agnese, A. & Young, R. A. Biomolecular condensates in the nucleus. *Trends Biochem. Sci.* **45**, 961–977 (2020).

20. 20.

Bienz, M. Head-to-tail polymerization in the assembly of biomolecular condensates. *Cell* **182**, 799–811 (2020).

21. 21.

Fang, X. et al. *Arabidopsis* FLL2 promotes liquid–liquid phase separation of polyadenylation complexes. *Nature* **569**, 265–269 (2019).

22. 22.

Machyna, M., Heyn, P. & Neugebauer, K. M. Cajal bodies: where form meets function. *Wiley Interdiscip. Rev. RNA* **4**, 17–34 (2013).

23. 23.

Risk, J. M., Laurie, R. E., Macknight, R. C. & Day, C. L. FRIGIDA and related proteins have a conserved central domain and family specific N- and C-terminal regions that are functionally important. *Plant Mol. Biol.* **73**, 493–505 (2010).

24. 24.

Hu, X. et al. Proteasome-mediated degradation of FRIGIDA modulates flowering time in *Arabidopsis* during vernalization. *Plant Cell* **26**, 4763–4781 (2014).

25. 25.

Riback, J. A. et al. Composition-dependent thermodynamics of intracellular phase separation. *Nature* **581**, 209–214 (2020).

26. 26.

Rosa, S., Duncan, S. & Dean, C. Mutually exclusive sense–antisense transcription at *FLC* facilitates environmentally induced gene repression. *Nat. Commun.* **7**, 13031–13031 (2016).

27. 27.

Ietswaart, R., Rosa, S., Wu, Z., Dean, C. & Howard, M. Cell-size-dependent transcription of *FLC* and its antisense long non-coding RNA *COOLAIR* explain cell-to-cell expression variation. *Cell Syst.* **4**, 622–635 (2017).

28. 28.

Henninger, J. E. et al. RNA-mediated feedback control of transcriptional condensates. *Cell* **184**, 207–225 (2021).

29. 29.

Zavaliev, R., Mohan, R., Chen, T. & Dong, X. Formation of NPR1 condensates promotes cell survival during the plant immune response. *Cell* **182**, 1093–1108 (2020).

30. 30.

Powers, S. K. et al. Nucleo-cytoplasmic partitioning of ARF proteins controls auxin responses in *Arabidopsis thaliana*. *Mol. Cell* **76**, 177–190 (2019).

31. 31.

Hahm, J., Kim, K., Qiu, Y. & Chen, M. Increasing ambient temperature progressively disassembles *Arabidopsis* phytochrome B from individual photobodies with distinct thermostabilities. *Nat. Commun.* **11**, 1660–1660 (2020).

32. 32.

Michaels, S. D., Bezerra, I. C. & Amasino, R. M. *FRIGIDA*-related genes are required for the winter-annual habit in *Arabidopsis*. *Proc. Natl Acad. Sci. USA* **101**, 3281–3285 (2004).

33. 33.

Andersson, C. R. et al. The *FLX* gene of *Arabidopsis* is required for *FRI*-dependent activation of *FLC* expression. *Plant Cell Physiol.* **49**, 191–200 (2008).

34. 34.

Kim, S., Choi, K., Park, C., Hwang, H. J. & Lee, I. *SUPPRESSOR OF FRIGIDA4*, encoding a C2H2-type zinc finger protein, represses flowering by transcriptional activation of *Arabidopsis FLOWERING LOCUS C*. *Plant Cell* **18**, 2985–2998 (2006).

35. 35.

Angel, A., Song, J., Dean, C. & Howard, M. A Polycomb-based switch underlying quantitative epigenetic memory. *Nature* **476**, 105–108 (2011).

36. 36.

Questa, J. I., Song, J., Geraldo, N., An, H. & Dean, C. *Arabidopsis* transcriptional repressor VAL1 triggers Polycomb silencing at *FLC* during vernalization. *Science* **353**, 485–488 (2016).

37. 37.

Crevillén, P. and Dean, C. Regulation of the floral repressor gene *FLC*: the complexity of transcription in a chromatin context. *Curr. Opin. Plant Biol.* **14**, 38–44 (2011).

38. 38.

He, Y., Chen, T. and Zeng, X. Genetic and epigenetic understanding of the seasonal timing of flowering. *Plant Commun.* **1**, 100008 (2019).

39. 39.

Zhao, Y., Antoniou-Kourounioti, R. L., Calder, G., Dean, C. & Howard, M. Temperature-dependent growth contributes to long-term cold sensing. *Nature* **583**, 825–829 (2020).

40. 40.

Jones, J. D. et al. Effective vectors for transformation, expression of heterologous genes, and assaying transposon excision in transgenic plants. *Transgenic Res.* **1**, 285–297 (1992).

41. 41.

Li, Y. et al. The SNW domain of SKIP is required for its integration into the spliceosome and its interaction with the Pafl complex in *Arabidopsis*. *Mol. Plant* **9**, 1040–1050 (2016).

42. 42.

Eom, H. et al. TAF15b, involved in the autonomous pathway for flowering, represses transcription of *FLOWERING LOCUS C*. *Plant J.* **93**, 79–91 (2018).

43. 43.

Zhu, P. et al. *Arabidopsis* small nucleolar RNA monitors the efficient pre-rRNA processing during ribosome biogenesis. *Proc. Natl Acad. Sci. USA* **113**, 11967–11972 (2016).

44. 44.

Postma, M. & Goedhart, J. PlotsOfData—a web app for visualizing data together with their summaries. *PLoS Biol.* **17**, e3000202 (2019).

45. 45.

Rosa, S. Measuring dynamics of histone proteins by photobleaching in *Arabidopsis* roots. *Methods Mol. Biol.* **1675**, 455–465 (2018).

46. 46.

Duncan, S., Olsson, T. S. G., Hartley, M., Dean, C. & Rosa, S. Single molecule RNA FISH in *Arabidopsis* root cells. *Bio-protocol* **7**, e2240 (2017).

47. 47.

Ariel, F. et al. Noncoding transcription by alternative RNA polymerases dynamically regulates an auxin-driven chromatin loop. *Mol. Cell* **55**, 383–396 (2014).

Acknowledgements

We thank K. Torney for generating the *FRI-Myc* transgenic line; R. Ishikawa and J. Questa for generating the *fri1-1 FRI*, *flx-2 FRI* and *suf4 FRI* genotypes; P. Shaw for the gift of the U2B⁺ antibody; I. Lee and H. Kang for the *TAF15b-GFP* plasmids; L. Ma for the *GFP-ELF7* plasmid; Y. Li for initial observations with FRI-GFP microscopy; G. Calder for image analysis expertise; C. Xu for technical assistance on smRNA FISH and immunostaining; X. Fang for constant discussion; and the laboratories of C.D. and M. Howard for critical input and reading of the manuscript. This work was supported by the UK Biotechnology and Biological Sciences Research Council Institute Strategic Program GEN (BB/P013511/1), a Royal Society Professorship to C.D., an EPSRC Physics of Life grant (EP/T00214X/1) and a European Research Council Advanced Investigator grant (EPISWITCH- 833254).

Author information

Affiliations

1. John Innes Centre, Norwich Research Park, Norwich, UK

Pan Zhu, Clare Lister & Caroline Dean

Contributions

P.Z. and C.D. conceived the study and wrote the manuscript. P.Z. performed most of the experiments and all of the data analysis. C.L. generated the *FRI-GFP*, *FRI-TAP* and 35S: *FRI-GFP* transgenic lines and performed the FLC–GUS staining. C.D. obtained funding and supervised the work.

Corresponding author

Correspondence to [Caroline Dean](#).

Ethics declarations

Competing interests

The authors declare no competing interests.

Additional information

Peer review information *Nature* thanks Chris Helliwell, Salomé Prat and the other, anonymous, reviewers for their contribution to the peer review of this work. Peer reviewer reports are available.

Publisher's note Springer Nature remains neutral with regard to jurisdictional claims in published maps and institutional affiliations.

Extended data figures and tables

[Extended Data Fig. 1 Transgenic *FRI-GFP* is functionally equivalent to endogenous *FRI*.](#)

a–d, Relative expression level of *FRI* mRNA (**a**), unspliced *FLC* (**b**), spliced *FLC* (**c**) and total *COOLAIR* (**d**) in Col-0 plants with introgressive *FRI* (*FRI*) or transgenic *FRI-GFP* with its endogenous promoter, measured by RT–qPCR. Plants were given no cold (non-vernalization, NV) or 2 weeks of cold (2 weeks of vernalization, 2WV). Data are presented as mean \pm s.e.m. of three independent biological replicates. **e, f**, Photographs showing flowering phenotype of Col-0 (*fri*), *FRI-GFP* and *FRI* plants in the warm (NV) or after 5 weeks of cold exposure (5WV). Scale bars, 5 cm.

[Source data](#)

Extended Data Fig. 2 Cold promotes FRI nuclear condensates in both root and leaf cells.

a, Single confocal images of NV and 2WV *Arabidopsis* root tip nuclei expressing FRI–GFP (green) with 2WV non-tagged FRI as a negative control. Data are represented of three independent experiments. **b**, Confocal images of 2WV *Arabidopsis* leaf nuclei expressing FRI–GFP (green). Maximum intensity projections of Z-stacks spanning the entire width of the nucleus were applied. Autofluorescence was unmixed with lambda mode (blue) (see Methods). **a, b**, Scale bars, 10 µm. **c, d**, Quantification of FRI–GFP nuclear condensate area (**c**) and number per nucleus (**d**) in root cells in Fig. 1a. An open circle indicates the median of the data and a vertical bar indicates the 95% confidence interval (CI) determined by bootstrapping. n= 391 (NV), 904 (1WV) and 494 (2WV) condensates (**c**) and n=181 (NV), 144 (1WV) and 130 (2WV) nuclei (**d**). More than 10 plants were analysed. Comparison of mean by two-way ANOVA with adjustment (Sidak's multiple comparisons test). ns, no significance. **e, f**, Representative confocal immunofluorescence images of subnuclear localization of FRI–Myc (red) in NV (**e**) and 2WV (**f**) *Arabidopsis* root cells. Non-tagged FRI was used as a negative control. DNA was stained by DAPI (blue). Scale bars, 5 µm. **g**, Confocal images of *Arabidopsis* root tip nuclei expressing FCA–GFP after 1 week (1WV) and 2 weeks (2WV) of cold treatment. Maximum intensity projections of Z-stacks spanning the entire width of the nucleus were applied. Scale bars, 5 µm. **h, i**, Quantification of FCA–GFP nuclear condensate area (**h**) and number per nucleus (**i**) in root cells. An open circle indicates the median of the data and a vertical bar indicates the 95% confidence interval (CI) determined by bootstrapping. Numbers of nuclear condensates measured in (**h**) were 655 (NV), 839 (1WV) and 613 (2WV). Numbers of nuclei analysed in (**i**) were 163 (NV), 148 (1WV) and 126 (2WV). At least 10 plants in each condition were analysed. Comparison of mean by one-way ANOVA with adjustment (Sidak's multiple comparisons test). ns, no significance.

[Source data](#)

Extended Data Fig. 3 FRI associates with FRL1, TAF15b and U2B'' in nuclear condensates in vivo.

a, Confocal microscopic images of tobacco leaf nuclei with expression of FRI–mScarlet I or FRL1–mScarlet I alone or co-expression of both. Data are representative of 5 independent experiments. **b, c**, Quantification of FRI–mScarlet I nuclear condensate area (**b**) and number per nucleus (**c**) in tobacco leaf with or without FRL1–mScarlet I co-expressed. An open circle indicates the median of the data and a vertical bar indicates the 95% confidence interval (CI) determined by bootstrapping. Numbers of nuclear condensates measured in (**b**) were 204 (FRI), 0 (FRL1) and 320 (FRI+FRL1). Numbers of nuclei analysed in (**c**) were 15 (FRI), 16 (FRL1) and 20

(FRI+FRL1). Comparison of mean by one-way ANOVA with adjustment (Sidak's multiple comparisons test). ns, no significance. **d**, Confocal microscopic images of FRI-GFP nuclear condensates in the indicated mutants. **e, f**, Quantification of FRI-GFP nuclear condensate area (**e**) and number per nucleus (**f**) in the indicated genotypes. An open circle indicates the median of the data and a vertical bar indicates the 95% confidence interval (CI) determined by bootstrapping. Numbers of nuclear condensates measured in (**e**) were (from left to right) 391, 904, 159, 437, 324, 735, 354 and 448. Numbers of nuclei analysed in (**f**) were (from left to right) 181, 144, 96, 105, 132, 177, 142 and 126. At least 10 plants were analysed. Comparison of mean by one-way ANOVA with adjustment (Sidak's multiple comparisons test). ns, no significance. **g**, Confocal microscopic images of tobacco leaf nuclei expressing FRI-mScarlet I and TAF15b-GFP. TAF15b-GFP was driven either by its endogenous protomer or overexpressed with CSV promoter. Data are representative of 3 independent experiments. **h**, Immunostaining images showing relative subnuclear localization of FRI-GFP (green) to U2B'' (red) in root cells in NV and 2WV conditions. DNA was labelled with DAPI (blue). Non-tagged FRI was used a negative control. **i, j**, Quantification of the total number of U2B'' condensates per nucleus (**i**) and those colocalized with FRI-GFP condensates (**j**) in NV and 2WV conditions. An open circle indicates the median of the data and a vertical bar indicates the 95% confidence interval (CI) determined by bootstrapping. n=166 nuclei (NV) and 130 nuclei (2WV). Comparison was via two-tailed *t* test with Welch's correction. ns, no significance. In all the images, scale bars, 5 μ m.

[Source data](#)

Extended Data Fig. 4 The protein domains required for in vivo FRI condensate formation.

a, Prediction of intrinsically disordered regions in FRI protein by IUPred2A. A schematic illustration of FRI domains was shown below. DD, disordered domain, CC, coiled-coil domain and the central domain was in grey. **b**, Schematic illustration of full-length FRI, C-terminal disordered domain deleted FRI (FRI-DD), coiled-coil domain deleted FRI (FRI-CC) and FRI encoded in Col-0 (FRI-Col-0). The mutated amino acids in FRI-Col-0 were indicated¹⁰. **c**, Subnuclear localization of full-length and truncated FRI-GFP in tobacco leaf nuclei. Images are representative of three independent experiments. Scale bars, 5 μ m.

Extended Data Fig. 5 Stability of FRI-GFP is increased in the cold.

a, Nuclear FRI-GFP protein level in NV, 2WV and 4WV FRI-GFP transgenic plants as determined by western blots. Non-tagged FRI was used as a negative control. H3 was used as nuclear protein loading control. Data are representative of two

independent experiments. For gel source data, see Supplementary Fig. 1. **b, c**, Confocal microscopy images of FRI–GFP in root tips of NV, 2WV and 4WV FRI–GFP transgenic plants (**b**) and the quantification of the fluorescence signal (**c**). Scale bars, 50 µm. The fluorescence intensity in cold treated samples is normalized to NV samples. Data are presented as mean ± s.e.m.; n=15 (NV), 12 (2WV) and 13 (4WV) roots. Statistical analysis was via one-way ANOVA with adjustment (Sidak's multiple comparisons test). **d**, Nuclear FRI–TAP protein level in NV, 2WV and 4WV plants expressing FRI–TAP as determined by western blots. Non-tagged FRI was used as a negative control. Asterisks indicate non-specific signals. Data are representative of two independent experiments. For gel source data, see Supplementary Fig. 1. **e**, Confocal microscopy of *Arabidopsis* root tip nuclei expressing FRI–GFP in NV or 2WV plants after treated with cycloheximide (CHX) in the indicated conditions for 24 h. For example, “NV in the cold” means plants grown in NV were kept in the cold for the 24h CHX treatment. Scale bars, 5 µm. **f**, Quantification of nuclear fluorescence intensity in (**e**). The relative intensity of CHX+ to CHX- in each treatment was indicated by percentage on top. n = 136, 122, 95, 107, 144, 153, 141 and 105 root nuclei (from left to right). **g, h**, Box plots showing the distribution of FRI–GFP nuclear condensate area and number in (**e**). Numbers of nuclear condensates measured in (**g**) were 226, 0, 138, 46, 270, 0, 282 and 238 (from left to right) and numbers of nuclei analysed in (**h**) were 113, 127, 66, 80, 94, 185, 95 and 85 (from left to right). **f–h**, At least 10 plants were analysed. Centre lines show median, box edges delineate 25th and 75th percentiles, bars extend to minimum and maximum values and ‘+’ indicates the mean value. Mean was compared by one-way ANOVA with adjustment (Sidak's multiple comparisons test).

Source data

Extended Data Fig. 6 FRI–GFP in 35S: FRI-GFP, fli-1, fix-2 and su fl.

a, Relative transcript level of *FRI* mRNA in the indicated plants measured by RT–qPCR. Data are presented as mean ± s.e.m. of three independent biological replicates. Mean was compared by two-way ANOVA with adjustment (Sidak's multiple comparisons test). ns, no significance. **b, c**, Total FRI–GFP protein level in the indicated plants as determined by western blots. A non-specific band (**b**) or ponceau staining (**c**) was used as loading control. Data are representative of two independent experiments. For gel source data, see Supplementary Fig. 1. **d, e**, Confocal microscopic images (**d**) and quantification of GFP fluorescence signal (**e**) of root tips expressing 35S: *FRI-GFP*. Scale bars, 50 µm. Data are presented as mean ± s.e.m., n = 13 (NV), 12 (1WV), 14 (2WV) and 14 (4WV) roots. **f**, Total FRI–GFP protein level in NV or 2WV 35S: *FRI-GFP* plants after treated with cycloheximide (CHX) in the indicated conditions for 24 h as determined by western blots. For example, “2WV in the warm” means plants after 2 weeks of cold exposure were kept in the warm

condition for the 24h CHX treatment. Plants were initially grown in growth medium without glucose (see Methods) then were transferred to medium without (0%) (top) or with 1% glucose (bottom) for the 24h CHX treatment. Tubulin was used as control. Data are representative of two independent experiments. For gel source data, see Supplementary Fig. 1. **g**, Confocal microscopy of root tip nuclei in 35S: *FRI-GFP* plants (middle) with 35S: *GFP* (right) and NV *FRI-GFP* (left) as control. Maximum intensity projections of Z-stacks spanning the entire width of a nucleus were applied. Scale bars, 5 μm . Images represent 8 independent experiments. **h, i**, Box plots showing the distribution of *FRI-GFP* nuclear condensate area and number in (g). Centre lines show median, box edges delineate 25th and 75th percentiles, bars extend to minimum and maximum values and '+' indicates the mean value. $n = 114, 1185, 1543, 1276$ and 1412 nuclear condensates in (h) and 262, 222, 205, 207 and 216 root nuclei in (i) (from left to right) were analysed. Comparison of mean was via one-way ANOVA with adjustment (Sidak's multiple comparisons test). ns, no significance. **j**, Expression of *FRI-GFP* in NV plants with the indicated genotype, measured by RT-qPCR. Data are presented as mean \pm s.e.m. of three independent biological replicates. One-way ANOVA was used for statistical analysis and P value was adjusted by Sidak's multiple comparisons test. ns, no significance. **k**, Representative confocal microscopic images of *FRI-GFP* root tips in 2WV plants with the indicated backgrounds. Scale bars, 50 μm . **l**, Quantification of the fluorescence intensity in (k). Data are represented as mean \pm s.e.m., $n = 14$ (WT), 13 (*fri1-1*), 13 (*flx-2*) and 12 (*suf4*) roots. One-way ANOVA was used for statistical analysis and P value was adjusted by Dunnett's multiple comparisons test. ns, no significance.

Source data

Extended Data Fig. 7 FRI occupancy on the *FLC* promoter is reduced in the cold and correlates with *FLC* transcriptional shutdown.

a, b, Spatial expression patterns of a translational FLC-GUS reporter in aerial parts (**a**) and root tips (**b**) of NV and 6WV plants in *fri* and *FRI* backgrounds. Scale bars, 1 mm (**a**) and 100 μm (**b**). Data represents two independent experiments. **c**, Schematic illustration of *FLC* and *COOLAIR* transcripts at the *FLC* locus. Untranslated regions (UTR) are indicated by grey boxes and exons by black boxes. kb, kilobase. **d**, *FRI-GFP* was detected after immunoprecipitation by western blots in ChIP experiments. Ponceau staining was used as the loading control. Data are representative of three independent experiments. For gel source data, see Supplementary Fig. 1. **e, f**, *FRI-GFP* ChIP across the *FLC* locus (**e**), *STM* and *ACT* locus (**f**) in plants expressing *FRI-GFP*. Non-tagged *FRI* was used as negative control. The exact distance from TSS referred to (**c**). Data are represented as mean \pm s.d. of three independent biological experiments with two technical repeats. Two-way ANOVA was performed with P values adjusted by Sidak's multiple comparisons test. **g**, Unspliced *FLC* transcript

level in NV and 2WV plants with the indicated backgrounds, measured by RT-qPCR. Data are presented as mean \pm s.e.m. of three biologically independent experiments. **h**, Representative images of nuclei expressing FRI-GFP (green) sequentially hybridized with intronic smFISH probes for *COOLAIR* (red). DNA was labelled with DAPI (blue). n= 327 cells. Scale bars, 5 μ m. **i, j**, Relative transcript level of unspliced *FLC* and spliced *FLC* in the indicated plants measured by RT-qPCR. Data were presented as mean \pm s.e.m. of three independent biological replicates. Two-way ANOVA was performed with P values adjusted by Sidak's multiple comparisons test. **k, l**, Relative transcript level of *FRI* mRNA and unspliced *FLC* in NV and 2WV plants with the indicated genotype, measured by RT-qPCR. Data were presented as mean \pm s.e.m. of three biologically independent experiments (**k**) and with two technical repeats (**l**). Two-way ANOVA was performed with P values adjusted by Sidak's multiple comparisons test. **m**, *FLC* transcriptional shutdown rate indicated by -Slope by Linear Regression of unspliced *FLC* in (**l**). Mean \pm s.e.m., n=6 replicates over 3 biologically independent experiments. P value was through two-tailed t test with Welch's correction.

Source data

Extended Data Fig. 8 FRI-GFP nuclear condensate dynamics change in response to short-term temperature fluctuations.

a, b, Quantification of FRI-GFP nuclear condensate area (**a**) and number per nucleus (**b**) in WT and *TEX* root cells after 0, 6 and 12 h of cold treatment in Fig. [2a](#). Comparisons between 12 h of cold treatment (12H) and 2WV (same data shown in Extended Data Fig. [2c, d](#)) were presented on the right. An open circle indicates the median of the data and a vertical bar indicates the 95% confidence interval (CI) determined by bootstrapping. n = 114, 380, 505, 180, 218, 346, 505 and 494 nuclear condensates in (**a**) and 262, 291, 303, 214, 205, 292, 303 and 130 root nuclei in (**b**) (from left to right). **c**, Fold change on Unspliced *FLC* transcript level in NV plants after transferred in cold for 12 h (12H) and 2 weeks (2WV) compared to NV. **d, e**, Quantification of FRI-GFP nuclear condensate area (**d**) and number per nucleus (**e**) in 2WV wildtype root cells after they were returned to warm for 0, 6, 12 and 24 h in Fig. [2c](#). An open circle indicates the median of the data and a vertical bar indicates the 95% confidence interval (CI) determined by bootstrapping. Numbers of nuclear condensates measured in (**d**) were 494 (0), 223 (6), 228 (12) and 292 (24) and numbers of root nuclei analysed in (**e**) were 130 (0), 109 (6), 152 (12) and 95 (24). At least 10 plants were analysed for each treatment. **a-e**, One-way ANOVA was performed with P values adjusted by Sidak's multiple comparisons test. ns, no significance. **f**, Confocal images of 2WV *Arabidopsis* leaf petiole nuclei expressing FRI-GFP (green) (left) and after transferred to warm conditions for 6 h (right). Maximum intensity projections of Z-stacks spanning the entire width of the nucleus

were applied. Autofluorescence was unmixed with lambda mode (blue) (see Methods). Scale bars, 10 μm . Data are representative of three independent experiments. **g**, Confocal microscopy of *Arabidopsis* root tip nuclei expressing FRI–GFP after treated with MG132 in the indicated conditions for 6 h. Plants were exposed to 1 week of cold before (left). Scale bars, 5 μm . **h**, Quantification of nuclear fluorescence intensity in (g). Fluorescence intensity was normalized to control. n=127, 122 and 166 root nuclei. **i, j**, Box plot showing the distribution of FRI–GFP nuclear condensate area and number in (g). n= 227, 139 and 355 nuclear condensates in (i) and 81, 60 and 116 root nuclei in (j) (from left to right). **h–j**, Centre lines show median, box edges delineate 25th and 75th percentiles, bars extend to minimum and maximum values and ‘+’ indicates the mean value. **k**, Fold change of Unspliced *FLC* expression level in 2WV plants after transferred in warm for 24 h (24H) and 10 days (10D) compared to NV. **h–k**, One-way ANOVA was performed with P values adjusted by Sidak’s multiple comparisons test. ns, no significance. **l, m**, Time-lapse microscopy of 1WV *Arabidopsis* root-tip nuclei expressing FRI–GFP after transfer to warm temperature (**l**) or return to cold temperature after a 3-hour warm spike (**m**). For each microscopic image maximum intensity projections of Z-stacks spanning the entire width of the nucleus were applied. Scale bars, 5 μm . Data are representative of two independent experiments. **n, o**, Quantitative measurement of the area (**n**) and number (**o**) of FRI–GFP nuclear condensates with an area $\geq 0.03 \mu\text{m}^2$ at each time point for the time-lapse experiment related to (**m**) and Supplementary Video 2. Data are represented as mean \pm s.e.m., n = 22 nuclei. **p**, Confocal microscopic images of tobacco leaf nuclei expressing FRI–GFP and FRL1–mScarlet I before and after 24 h cold. Maximum intensity projections of Z-stacks spanning the entire width of the nucleus were applied. Scale bars, 5 μm . Three independent experiments gave similar results. **q, r**, Quantification of FRI–GFP nuclear condensate area (**q**) and number per nucleus (**r**) in tobacco leaf nuclei before and after 24 h of cold exposure. An open circle indicates the median of the data and a vertical bar indicates the 95% confidence interval (CI) determined by bootstrapping. n = 398 (warm) and 353 (cold) nuclear condensates (**q**) and 17 (warm) and 13 (cold) tobacco leaf nuclei (**r**). Two-tailed t test with Welch’s correction. ns, no significance.

Source data

Extended Data Fig. 9 The association of FRI and COOLAIR is disturbed in FRI-complex mutants.

a–c, Relative transcript level of spliced *COOLAIR* isoforms in NV and 2WV plants with the indicated genotype, measured by RT–qPCR. Data are presented as mean \pm s.e.m. of three independent biological replicates. **d–f**, Fold change of spliced *COOLAIR* expression in 2WV plants relative to NV plants in the indicated backgrounds. Fold change of Class II.ii in 12 h cold treated plants (12H) relative to

NV was compared to 2WV on the right in (f). Data are presented as mean \pm s.e.m. of three independent biological replicates. One-way ANOVA was performed with P values adjusted by Sidak's multiple comparisons test. ns, no significance. g, Schematic illustration of *FLC* and *COOLAIR* transcripts at the *FLC* locus. Untranslated regions (UTR) are indicated by grey boxes and exons by black boxes. kb, kilobase. h, RNA-IP assay of unspliced *COOLAIR* enriched by FRI-GFP in NV and 2WV plants.

COOLAIR enrichment in FRI-GFP is normalized to non-tagged FRI. Data are presented as mean \pm s.e.m. of three independent biological replicates. Although there are differences of the fold enrichment between NV and 2WV samples, no statistical significance was detected (two-way ANOVA). Class II.ii was shown as control.

Amplicons for unspliced *COOLAIR* are shown in (g) by blue bars. i, RNA-IP assay of spliced *COOLAIR* enriched by FRI-GFP in 2WV plants in WT and *frl1-1* backgrounds with *UBC* as control. Data are presented as mean \pm s.e.m. of three independent biological replicates. Two-way ANOVA with adjustment by Sidak's multiple comparisons test. ns, no significance. j, k, Quantification of FRI-GFP nuclear condensate area (j) and number per nucleus (k) in root cells in Fig. 3e. An open circle indicates the median of the data and a vertical bar indicates the 95% confidence interval (CI) determined by bootstrapping. Numbers of nuclear condensates measured in (j) were 114 (NV-WT), 142 (NV-*TEX*), 435 (2WV-WT) and 500 (2WV-*TEX*). Numbers of nuclei analysed in (k) were 262 (NV-WT), 214 (NV-*TEX*), 199 (2WV-WT) and 293 (2WV-*TEX*). At least 10 plants were analysed for each treatment. One-way ANOVA with adjustment by Sidak's multiple comparisons test. ns, no significance. l, Representative confocal microscopic images of FRI-GFP root tips in 2WV WT and *TEX* plants. Scale bars, 50 μ m. m, Quantification of the fluorescence intensity in (l). Data are represented as mean \pm s.e.m., n=10 (WT) and 11 (*TEX*) roots. Two-tailed *t* test with Welch's correction.

[Source data](#)

Extended Data Table 1 List of proteins identified by FRI-GFP affinity purification

Supplementary information

[**Supplementary Figure 1**](#)

The original source images for the western blots.

[**Reporting Summary**](#)

[**Supplementary Table 1**](#)

A complete list of proteins identified by IP–MS of FRI–GFP.

[Supplementary Table 2](#)

List of DNA oligos and PCR primers in this study.

[Supplementary Video 1: Response of FRI–GFP nuclear condensates to warm temperature in live cells.](#)

Time-lapse imaging of 1WV *Arabidopsis* root cells expressing FRI–GFP for 5 h after transfer to warm temperature. Time point is indicated on the top left, 00:00 indicates the time when the temperature was raised to 22 °C. Scale bar, 5 μm.

[Supplementary Video 2: Response of FRI–GFP nuclear condensates to cold temperature in live cells.](#)

Time-lapse imaging of 1WV *Arabidopsis* root cells expressing FRI–GFP for 6 h at cold temperature after a 3 h warm spike. Time point is indicated on the top left, 00:00 indicates the time when the temperature was lowered to 4 °C. Scale bar, 5 μm.

[Peer Review File](#)

Source data

[Source Data Fig. 1](#)

[Source Data Fig. 2](#)

[Source Data Fig. 3](#)

[Source Data Extended Data Fig. 1](#)

[Source Data Extended Data Fig. 2](#)

[Source Data Extended Data Fig. 3](#)

[Source Data Extended Data Fig. 5](#)

[Source Data Extended Data Fig. 6](#)

[**Source Data Extended Data Fig. 7**](#)

[**Source Data Extended Data Fig. 8**](#)

[**Source Data Extended Data Fig. 9**](#)

Rights and permissions

Open Access This article is licensed under a Creative Commons Attribution 4.0 International License, which permits use, sharing, adaptation, distribution and reproduction in any medium or format, as long as you give appropriate credit to the original author(s) and the source, provide a link to the Creative Commons license, and indicate if changes were made. The images or other third party material in this article are included in the article's Creative Commons license, unless indicated otherwise in a credit line to the material. If material is not included in the article's Creative Commons license and your intended use is not permitted by statutory regulation or exceeds the permitted use, you will need to obtain permission directly from the copyright holder. To view a copy of this license, visit <http://creativecommons.org/licenses/by/4.0/>.

[Reprints and Permissions](#)

About this article

Cite this article

Zhu, P., Lister, C. & Dean, C. Cold-induced *Arabidopsis* FRIGIDA nuclear condensates for *FLC* repression. *Nature* **599**, 657–661 (2021).
<https://doi.org/10.1038/s41586-021-04062-5>

- Received: 26 January 2021
- Accepted: 27 September 2021
- Published: 03 November 2021
- Issue Date: 25 November 2021
- DOI: <https://doi.org/10.1038/s41586-021-04062-5>

Share this article

Anyone you share the following link with will be able to read this content:

[Get shareable link](#)

Sorry, a shareable link is not currently available for this article.

[Copy to clipboard](#)

Provided by the Springer Nature SharedIt content-sharing initiative

Changing of the seasons — transcriptional buffers against flowering in the cold

- Sara Osman

News & Views 19 Nov 2021

This article was downloaded by **calibre** from <https://www.nature.com/articles/s41586-021-04062-5>

| [Section menu](#) | [Main menu](#) |

- Article
- [Published: 17 November 2021](#)

Herpesviruses assimilate kinesin to produce motorized viral particles

- [Caitlin E. Pegg¹ na1](#),
- [Sofia V. Zaichick¹ na1 nAff7](#),
- [Ewa Bomba-Warczak²](#),
- [Vladimir Jovasevic](#) [ORCID: orcid.org/0000-0001-8963-6758¹ nAff8](#),
- [DongHo Kim¹](#),
- [Himanshu Kharkwal³ nAff9](#),
- [Duncan W. Wilson^{3,4}](#),
- [Derek Walsh](#) [ORCID: orcid.org/0000-0002-8756-4655¹](#),
- [Patricia J. Sollars](#) [ORCID: orcid.org/0000-0002-1731-0502⁵](#),
- [Gary E. Pickard^{5,6}](#),
- [Jeffrey N. Savas](#) [ORCID: orcid.org/0000-0002-8173-5580²](#) &
- [Gregory A. Smith](#) [ORCID: orcid.org/0000-0001-9644-8472¹](#)

[Nature](#) volume **599**, pages 662–666 (2021)

- 5144 Accesses
- 1 Citations
- 239 Altmetric
- [Metrics details](#)

Subjects

- [Cellular neuroscience](#)

- [Herpes virus](#)
- [Kinesin](#)
- [Mechanisms of disease](#)
- [Virus–host interactions](#)

Abstract

Neurotropic alphaherpesviruses initiate infection in exposed mucosal tissues and, unlike most viruses, spread rapidly to sensory and autonomic nerves where life-long latency is established¹. Recurrent infections arise sporadically from the peripheral nervous system throughout the life of the host, and invasion of the central nervous system may occur, with severe outcomes². These viruses directly recruit cellular motors for transport along microtubules in nerve axons, but how the motors are manipulated to deliver the virus to neuronal nuclei is not understood. Here, using herpes simplex virus type I and pseudorabies virus as model alphaherpesviruses, we show that a cellular kinesin motor is captured by virions in epithelial cells, carried between cells, and subsequently used in neurons to traffic to nuclei. Viruses assembled in the absence of kinesin are not neuroinvasive. The findings explain a critical component of the alphaherpesvirus neuroinvasive mechanism and demonstrate that these viruses assimilate a cellular protein as an essential proviral structural component. This principle of viral assimilation may prove relevant to other virus families and offers new strategies to combat infection.

Access options

Subscribe to Journal

Get full journal access for 1 year

\$199.00

only \$3.90 per issue

[Subscribe](#)

All prices are NET prices.
VAT will be added later in the checkout.
Tax calculation will be finalised during checkout.

Rent or Buy article

Get time limited or full article access on ReadCube.

from \$8.99

[Rent or Buy](#)

All prices are NET prices.

Additional access options:

- [Log in](#)
- [Access through your institution](#)
- [Learn about institutional subscriptions](#)

Fig. 1: Kinesin-1 supports initial infection of RPE cells by HSV-1.

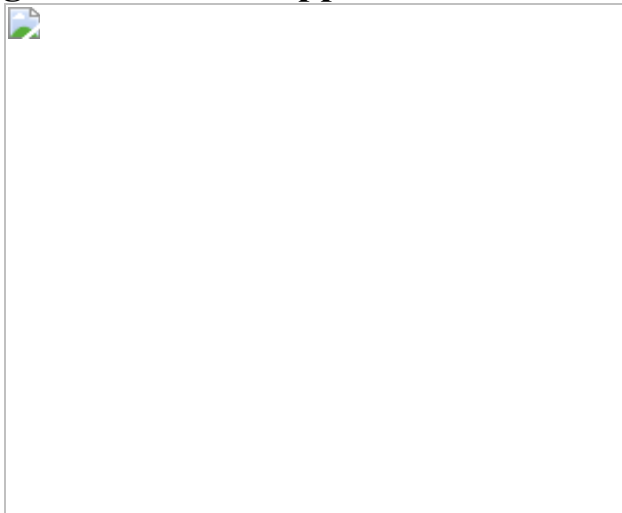


Fig. 2: The presence of kinesin-1 during virus assembly promotes trafficking of capsids to nuclei during subsequent infection.

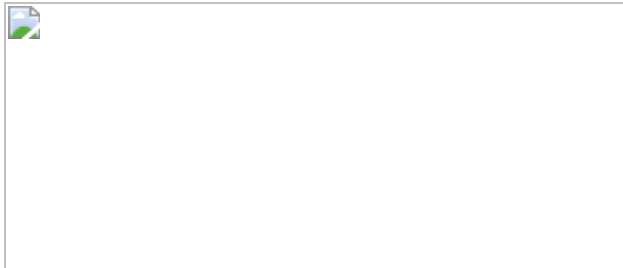


Fig. 3: Kinesin-1 is captured in viral particles and delivered to other cells.

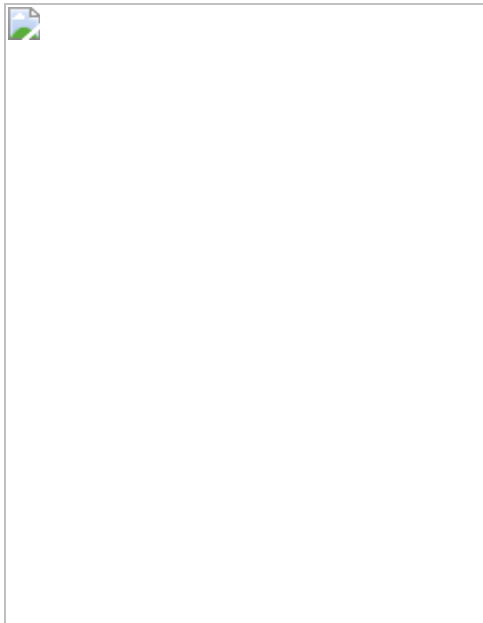
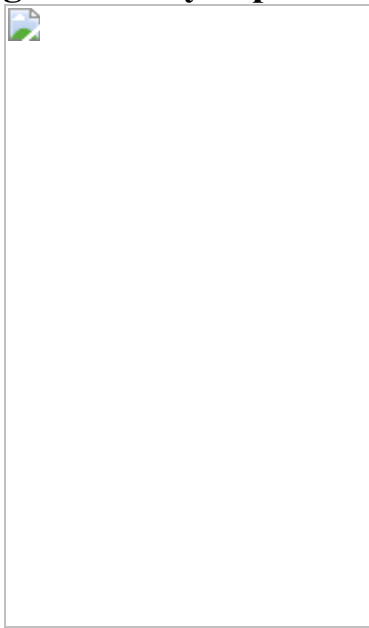


Fig. 4: Virally captured kinesin transports capsids to nuclei.



Data availability

Unfiltered mass spectrometry data, raw microscopy images and plasmid and virus construction details (including primer sequences) are available from the corresponding author upon request.

References

1. 1.

Smith, G. Herpesvirus transport to the nervous system and back again. *Annu. Rev. Microbiol.* **66**, 153–176 (2012).

2. 2.

Lafaille, F. G. et al. Deciphering human cell-autonomous anti-HSV-1 immunity in the central nervous system. *Front. Immunol.* **6**, 208 (2015).

3. 3.

Zaichick, S. V. et al. The herpesvirus VP1/2 protein is an effector of dynein-mediated capsid transport and neuroinvasion. *Cell Host Microbe* **13**, 193–203 (2013).

4. 4.

Smith, G. A., Pomeranz, L., Gross, S. P. & Enquist, L. W. Local modulation of plus-end transport targets herpesvirus entry and egress in sensory axons. *Proc. Natl Acad. Sci. USA* **101**, 16034–16039 (2004).

5. 5.

Antinone, S. E. & Smith, G. A. Retrograde axon transport of herpes simplex virus and pseudorabies virus: a live-cell comparative analysis. *J. Virol.* **84**, 1504–1512 (2010).

6. 6.

Pernigo, S., Lamprecht, A., Steiner, R. A. & Dodding, M. P. Structural basis for kinesin-1:cargo recognition. *Science* **340**, 356–359 (2013).

7. 7.

Robert, A. et al. Kinesin-dependent transport of keratin filaments: a unified mechanism for intermediate filament transport. *FASEB J.* **33**, 388–399 (2019).

8. 8.

Bish, S. E., Song, W. & Stein, D. C. Quantification of bacterial internalization by host cells using a β -lactamase reporter strain: *Neisseria gonorrhoeae* invasion into cervical epithelial cells requires bacterial viability. *Microbes Infect.* **10**, 1182–1191 (2008).

9. 9.

Heine, J. W., Honess, R. W., Cassai, E. & Roizman, B. Proteins specified by herpes simplex virus. XII. The virion polypeptides of type 1 strains. *J Virol* **14**, 640–651 (1974).

10. 10.

Cavrois, M., De Noronha, C. & Greene, W. C. A sensitive and specific enzyme-based assay detecting HIV-1 virion fusion in primary T lymphocytes. *Nat. Biotechnol.* **20**, 1151–1154 (2002).

11. 11.

Lyman, M. G., Feierbach, B., Curanovic, D., Bisher, M. & Enquist, L. W. PRV Us9 directs axonal sorting of viral capsids. *J. Virol.* **81**, 11363–11371 (2007).

12. 12.

Scherer, J. et al. A Kinesin-3 recruitment complex facilitates axonal sorting of enveloped alpha herpesvirus capsids. *PLoS Pathog.* **16**, e1007985 (2020).

13. 13.

Diwaker, D., Murray, J. W., Barnes, J., Wolkoff, A. W. & Wilson, D. W. Deletion of the pseudorabies virus gE/gI-US9p complex disrupts kinesin KIF1A and KIF5C recruitment during egress, and alters the properties of microtubule-dependent transport in vitro. *PLoS Pathog.* **16**, e1008597 (2020).

14. 14.

DuRaine, G., Wisner, T. W., Howard, P., Williams, M. & Johnson, D. C. Herpes simplex virus gE/gI and US9 promote both envelopment and sorting of virus particles in the cytoplasm of neurons, two processes that precede anterograde transport in axons. *J. Virol.* **91**, e00050-17 (2017).

15. 15.

Engelke, M. F. et al. Engineered kinesin motor proteins amenable to small-molecule inhibition. *Nat. Commun.* **7**, 11159 (2016).

16. 16.

Schipke, J. et al. The C terminus of the large tegument protein pUL36 contains multiple capsid binding sites that function differently during assembly and cell entry of herpes simplex virus. *J. Virol.* **86**, 3682–3700 (2012).

17. 17.

Dohner, K. et al. Function of dynein and dynactin in herpes simplex virus capsid transport. *Mol. Biol. Cell.* **13**, 2795–2809 (2002).

18. 18.

DuRaine, G., Wisner, T. W., Howard, P. & Johnson, D. C. Kinesin-1 proteins KIF5A, 5B and 5C promote anterograde transport of herpes simplex virus enveloped virions in axons. *J. Virol.* **92**, e01269-18 (2018).

19. 19.

Radtke, K. et al. Plus- and minus-end directed microtubule motors bind simultaneously to herpes simplex virus capsids using different inner tegument structures. *PLoS Pathog.* **6**, e1000991 (2010).

20. 20.

Diefenbach, R. J. et al. The basic domain of herpes simplex virus 1 pUS9 recruits kinesin-1 to facilitate egress from neurons. *J. Virol.* **90**, 2102–2111 (2016).

21. 21.

Loret, S., Guay, G. & Lippe, R. Comprehensive characterization of extracellular herpes simplex virus type 1 virions. *J. Virol.* **82**, 8605–8618 (2008).

22. 22.

Kramer, T., Greco, T. M., Enquist, L. W. & Cristea, I. M. Proteomic characterization of pseudorabies virus extracellular virions. *J. Virol.* **85**, 6427–6441 (2011).

23. 23.

Miranda-Saksena, M. et al. Herpes simplex virus utilizes the large secretory vesicle pathway for anterograde transport of tegument and envelope proteins and for viral exocytosis from growth cones of human fetal axons. *J. Virol.* **83**, 3187–3199 (2009).

24. 24.

Smith, C. L. *Culturing Nerve Cells* 2nd Edn (eds Banker, G. & Goslin, K.) 261–287 (MIT Press, 1998).

25. 25.

Smith, G. A., Gross, S. P. & Enquist, L. W. Herpesviruses use bidirectional fast-axonal transport to spread in sensory neurons. *Proc. Natl Acad. Sci. USA* **98**, 3466–3470 (2001).

26. 26.

Tanaka, M., Kagawa, H., Yamanashi, Y., Sata, T. & Kawaguchi, Y. Construction of an excisable bacterial artificial chromosome containing a full-length infectious clone of herpes simplex virus type 1: viruses reconstituted from the clone exhibit wild-type properties in vitro and in vivo. *J. Virol.* **77**, 1382–1391 (2003).

27. 27.

Smith, G. A. & Enquist, L. W. Construction and transposon mutagenesis in *Escherichia coli* of a full-length infectious clone of pseudorabies virus, an alphaherpesvirus. *J. Virol.* **73**, 6405–6414 (1999).

28. 28.

Kaufman, H. E., Ellison, E. D. & Waltman, S. R. Double-stranded RNA, an interferon inducer, in herpes simplex keratitis. *Am. J. Ophthalmol.* **68**, 486–491 (1969).

29. 29.

Bohannon, K. P., Sollars, P. J., Pickard, G. E. & Smith, G. A. Fusion of a fluorescent protein to the pUL25 minor capsid protein of pseudorabies virus allows live-cell capsid imaging with negligible impact on infection. *J. Gen. Virol.* **93**, 124–129 (2012).

30. 30.

Huffmaster, N. J., Sollars, P. J., Richards, A. L., Pickard, G. E. & Smith, G. A. Dynamic ubiquitination drives herpesvirus neuroinvasion. *Proc. Natl Acad. Sci. USA* **112**, 12818–12823 (2015).

31. 31.

Richards, A. L. et al. The pUL37 tegument protein guides alpha-herpesvirus retrograde axonal transport to promote neuroinvasion. *PLoS Pathog.* **13**, e1006741 (2017).

32. 32.

Stults, A. M. & Smith, G. A. The herpes simplex virus 1 deamidase enhances propagation but is dispensable for retrograde axonal transport into the nervous system. *J Virol* **93**, e01172-19 (2019).

33. 33.

Tischer, B. K., Smith, G. A. & Osterrieder, N. En passant mutagenesis: a two step markerless red recombination system. *Methods Mol. Biol.* **634**, 421–430 (2010).

34. 34.

Szpara, M. L. et al. A wide extent of inter-strain diversity in virulent and vaccine strains of alphaherpesviruses. *PLoS Pathog.* **7**, e1002282 (2011).

35. 35.

Abramoff, M. D., Magelhaes, P. J. & Ram, S. J. Image processing with ImageJ. *Biophotonics Int.* **11**, 36–42 (2004).

36. 36.

Luxton, G. W. et al. Targeting of herpesvirus capsid transport in axons is coupled to association with specific sets of tegument proteins. *Proc. Natl Acad. Sci. USA* **102**, 5832–5837 (2005).

37. 37.
- Leelawong, M., Lee, J. I. & Smith, G. A. Nuclear egress of pseudorabies virus capsids is enhanced by a subspecies of the large tegument protein that is lost upon cytoplasmic maturation. *J. Virol.* **86**, 6303–6314 (2012).
38. 38.
- Lee, J. I., Luxton, G. W. & Smith, G. A. Identification of an essential domain in the herpesvirus VP1/2 tegument protein: the carboxy terminus directs incorporation into capsid assemblons. *J. Virol.* **80**, 12086–12094 (2006).
39. 39.
- Dodding, M. P., Mitter, R., Humphries, A. C. & Way, M. A kinesin-1 binding motif in vaccinia virus that is widespread throughout the human genome. *EMBO J.* **30**, 4523–4538 (2011).
40. 40.
- Tombacz, D., Toth, J. S., Petrovszki, P. & Boldogkoi, Z. Whole-genome analysis of pseudorabies virus gene expression by real-time quantitative RT-PCR assay. *BMC Genomics* **10**, 491 (2009).
41. 41.
- Lee, G. E., Murray, J. W., Wolkoff, A. W. & Wilson, D. W. Reconstitution of herpes simplex virus microtubule-dependent trafficking in vitro. *J. Virol.* **80**, 4264–4275 (2006).
42. 42.
- Kharkwal, H., Smith, C. G. & Wilson, D. W. Blocking ESCRT-mediated envelopment inhibits microtubule-dependent trafficking of alphaherpesviruses in vitro. *J. Virol.* **88**, 14467–14478 (2014).
43. 43.

Howard, J. & Hyman, A. A. Preparation of marked microtubules for the assay of the polarity of microtubule-based motors by fluorescence microscopy. *Methods Cell. Biol.* **39**, 105–113 (1993).

44. 44.

Shanda, S. K. & Wilson, D. W. UL36p is required for efficient transport of membrane-associated herpes simplex virus type 1 along microtubules. *J. Virol.* **82**, 7388–7394 (2008).

45. 45.

Homa, F. L. et al. Structure of the pseudorabies virus capsid: comparison with herpes simplex virus type 1 and differential binding of essential minor proteins. *J. Mol. Biol.* **425**, 3415–3428 (2013).

46. 46.

Huet, A. et al. Extensive subunit contacts underpin herpesvirus capsid stability and interior-to-exterior allostery. *Nat. Struct. Mol. Biol.* **23**, 531–539 (2016).

47. 47.

Eng, J. K., McCormack, A. L. & Yates, J. R. An approach to correlate tandem mass spectral data of peptides with amino acid sequences in a protein database. *J. Am. Soc. Mass. Spectrom.* **5**, 976–989 (1994).

48. 48.

Xu, T. et al. ProLuCID: An improved SEQUEST-like algorithm with enhanced sensitivity and specificity. *J. Proteomics* **129**, 16–24 (2015).

49. 49.

Cociorva, D., D, L. T. & Yates, J. R. Validation of tandem mass spectrometry database search results using DTASelect. *Curr. Protoc. Bioinformatics Ch.* **13**, Unit 13 14 (2007).

50. 50.

Tabb, D. L., McDonald, W. H. & Yates, J. R., 3rd. DTASelect and Contrast: tools for assembling and comparing protein identifications from shotgun proteomics. *J. Proteome Res.* **1**, 21–26 (2002).

51. 51.

UniProt, C. UniProt: a hub for protein information. *Nucleic Acids Res.* **43**, D204–D212 (2015).

52. 52.

Elias, J. E. & Gygi, S. P. Target-decoy search strategy for increased confidence in large-scale protein identifications by mass spectrometry. *Nat. Methods* **4**, 207–214 (2007).

Acknowledgements

We thank V. Gelfand and K. Verhey for suggestions that helped inform the experimental design and for reagents, and A. Roberts, M. Englke, M. Way, S. Brady and G. Gunderson for reagents. D. Kirchenbuechler of the Northwestern University Cell Imaging Facility, supported by NCI CCSG P30 CA060553, provided invaluable support in the development of the automated image analysis pipeline used in this report. Some confocal imaging was performed on an Andor XDI Revolution microscope purchased through the support of NCRR 1S10 RR031680-01 at the Northwestern University Cell Imaging Facility. Sequencing services were performed at the Northwestern University Genomics Core Facility. In vitro microtubule-dependent motility assays and analyses were performed in the Analytical Imaging Facility of the Albert Einstein College of Medicine, with support from National Cancer Institute cancer center grant P30CA013330. This work was funded by NIH AI056346 (G.A.S., P.J.S. and G.E.P.), AI125244 (D.W.W.), AI141470 (D.W.) and AI148780 (J.N.S.). E.B.W. was supported by NIH NS106812. C.E.P. received support from National Science Foundation DGE-1324585 and NIH Cellular and Molecular Basis of Disease Training Grant T32GM08061.

Author information

Author notes

1. Sofia V. Zaichick

Present address: Gene Therapy Program, Department of Pathology and Laboratory Medicine, University of Pennsylvania Perelman School of Medicine, Philadelphia, PA, USA

2. Vladimir Jovasevic

Present address: Department of Pharmacology, Northwestern University Feinberg School of Medicine, Chicago, IL, USA

3. Himanshu Kharkwal

Present address: Agenus, Lexington, MA, USA

4. These authors contributed equally: Caitlin E. Pegg, Sofia V. Zaichick

Affiliations

1. Department of Microbiology-Immunology, Northwestern University Feinberg School of Medicine, Chicago, IL, USA

Caitlin E. Pegg, Sofia V. Zaichick, Vladimir Jovasevic, DongHo Kim, Derek Walsh & Gregory A. Smith

2. Department of Neurology, Northwestern University Feinberg School of Medicine, Chicago, IL, USA

Ewa Bomba-Warczak & Jeffrey N. Savas

3. Department of Developmental and Molecular Biology, Albert Einstein College of Medicine, Bronx, NY, USA

Himanshu Kharkwal & Duncan W. Wilson

4. Dominick P. Purpura Department of Neuroscience, Albert Einstein College of Medicine, Bronx, NY, USA

Duncan W. Wilson

5. School of Veterinary Medicine and Biomedical Sciences, University of Nebraska-Lincoln, Lincoln, NE, USA

Patricia J. Sollars & Gary E. Pickard

6. Department of Ophthalmology and Visual Sciences, University of Nebraska Medical Center, Omaha, NE, USA

Gary E. Pickard

Contributions

C.E.P., S.V.Z. and G.A.S. conceived the study; C.E.P. performed experiments concerning kinesin-1 assimilation and its discovery, and experiments concerning kinesin-1 involvement in centrosome-to-nucleus trafficking; S.V.Z. performed experiments concerning pUL36 involvement in centrosome-to-nucleus trafficking and kinesin-1 interaction; J.N.S. and E.B.W. performed mass spectrometry and data analysis; D.W. and V.J. performed kinesin siRNA experiments; D.K. and C.E.P. performed nitrocefin experiments; D.W.W. and H.K. performed in vitro motility experiments; P.J.S. and G.E.P. performed mouse infection studies; C.E.P., S.V.Z. and G.A.S. made the figures; C.E.P. and G.A.S. wrote and edited the manuscript; and all authors discussed results and commented on the manuscript.

Corresponding author

Correspondence to [Gregory A. Smith](#).

Ethics declarations

Competing interests

P.J.S., G.E.P. and G.A.S. have disclosed a significant financial interest in Thyreos, Inc. In accordance with their Conflict of Interest policies, the University of Nebraska-Lincoln and Northwestern University Feinberg School of Medicine Conflict of Interest Review Committees have determined that this must be disclosed.

Additional information

Peer review information *Nature* thanks the anonymous reviewer(s) for their contribution to the peer review of this work.

Publisher's note Springer Nature remains neutral with regard to jurisdictional claims in published maps and institutional affiliations.

Extended data figures and tables

[Extended Data Fig. 1 Transiently-expressed PRV pUL36 co-localizes with microtubules and accumulates at the cell periphery.](#)

(A) Schematic representation of seven regions of pUL36. Regions 2 and 6 are proline rich (pink). Position of the capsid binding domain (CBD) consisting of amino acids 3033-3095 is indicated. Amino acid positions are indicated above the schematic. (B) Transiently expressed GFP-pUL36ΔR7, but not GFP-pUL36 (full length), formed small punctae that moved in curvilinear trajectories (also see Supplementary Video 1) and accumulated at the periphery of Vero cells (arrowheads). The 6.9 μm x 2.4 μm boxed region is expanded as a time-lapse montage to the right of the image (n=3 independent experiments). (C) GFP-pUL36ΔR7 decorates microtubules. Vero cells were transiently co-transfected with GFP-pUL36ΔR7 and mCherry-tubulin. The 7.4 μm x 7.4 μm boxed region is expanded below each image. All images were captured between 24-28 h post transfection (hpt) (n=3 independent experiments). Scale bars are 20 μm.

Extended Data Fig. 2 Transiently-expressed PRV pUL36 interacts with components of the Kif5 motor complex.

(A) pUL36 region 7 is dispensable for co-immunoprecipitation (co-IP) with Kif5 heavy chain (KHC) and Kif5 light chain (KLC). HEK293 cells were lysed 16-18 hpt and GFP-pUL36 was immunoprecipitated (IP) with anti-GFP antibody and detected by western blot as indicated. Inputs are 6% of crude lysates (n=3 independent experiments). **(B)** Peripheral accumulations of transiently expressed GFP-pUL36ΔR7 co-localize with endogenous cellular Kif5 components (arrows). Vero cells were fixed and immunostained for KHC or KLC at 20 hpt (n=3 independent experiments). Scale bars are 20 μm. **(C)** GFP-pUL36ΔR7 co-immunoprecipitates with KLC1 and KLC2 isoforms. HEK293 cells transiently expressing GFP or GFP-pUL36ΔR7 were co-transfected with HA-KLC1 and HA-KLC2. Endogenous KHC served as a positive co-immunoprecipitation control (n=3 independent experiments). **(D)** Transient expression mCherry-KLC1 and mCherry-KLC2 in Vero cells. Both fusion proteins show varying degrees of juxtanuclear localization and an absence of peripheral accumulation (n=3 independent experiments). **(E)** mCherry-KLC1 and mCherry-KLC2 redistribute with GFP-pUL36ΔR7 to the cell periphery during transient expression. Vero cells were imaged 24-28 hpt (n=3 independent experiments). Scale bars are 20 μm.

Extended Data Fig. 3 Mapping the PRV pUL36 kinesin-binding region.

(A) Illustration of pUL36 constructs with amino- and carboxyl-terminal GFP fusions indicated (grey circles). Location of a cryptic nuclear localization signal (NLS) at the end of region 2 (vertical grey line in R2) that becomes active when region 6 is deleted is also indicated. Constructs are named for each intact region number with a dash representing deleted regions. In the case of region 6, a subregion consisting of the majority of the sequence was deleted (denoted “s” and consisting of amino acids 2087-2796). **(B)** pUL36 region 5 is required for interaction with the Kif5 complex (KHC, Kif5 heavy chain; KLC, Kif5 light chain; n = 3 independent experiments). **(C)** pUL36 region 6 is required for interaction with the Kif5

complex. Deletion of region 6 also resulted in nuclear localization of the protein due to the NLS in region 2. Mutation of the NLS ($K_{285}RRR > AAAA$) restored protein localization to the cytoplasm (not shown) but did not restore Kif5 interaction ($n = 3$ independent experiments). (D–E) pUL36 regions 5–6, is sufficient for Kif5 binding. Interaction with a dynactin component, p150/glued (p150), was used as a positive co-immunoprecipitation control ($n = 3$ independent experiments each).

Extended Data Fig. 4 PRV pUL36 WD motifs are required for kinesin-1 binding.

(A) Schematic representation of two potential bipartite kinesin-binding motifs (WD1/WD2 and WD3/WD4) in region 5 of pUL36. Corresponding regions from ten different alphaherpesvirinae are aligned. Prospective WD motifs in PRV are highlighted in red. Conserved tryptophans and/or surrounding E, D, N and Q at positions ± 1 and $+2$ in pUL36 orthologs are in blue. The number of amino acids between the WD3 and WD4 tryptophans are indicated only when no other tryptophan was present in between (W-W); otherwise, n.a. is indicated. Table on the right summarizes mutants used for transient expression (RKB, reduced kinesin binding mutant that was subsequently introduced into PRV – see Extended Data Fig. 5 & 6). (B–D) Co-immunoprecipitations of pUL36 proteins and endogenous cellular Kif5 demonstrate that WD3 and WD4 contribute to the pUL36-Kif5 interaction. Interaction with dynactin component, p150/glued (p150) was used as a positive co-immunoprecipitation control ($n = 3$ independent experiments each). (E) Quantitation of cells displaying pUL36 localization at the cell periphery or juxtanuclear between 24–28 hpt. Representative images of cells and scoring are provided at top. Percentile distributions of pUL36 accumulation are illustrated by Venn diagrams (average of $n = 3$ independent experiments >250 cells each). Scale bars are 20 μ m.

Extended Data Fig. 5 The PRV|RKB| mutant is defective for nuclear trafficking and gene expression.

(A) Mutation of WD3 attenuated PRV spread, as measured by plaque size, whereas mutations of WD4 rendered PRV non-viable ($n = 200$ plaques over 3 independent experiments). **(B)** Mutation of the WD4 tryptophan alone also rendered PRV non-viable, whereas mutation of the surrounding acidic residues did not impair viral spread. PRV encoding both the Δ WD3 mutation and WD4(DE>AA) attenuated viral spread but could be propagated and further studied and was designated as the reduced-kinesin binding mutant (RKB; also see Figure S4). Plaque diameters were measured 43 hpt. Data are presented as scatter plots, with each dot representing a single plaque ($n = 200$ plaques over 3 independent experiments). Mean values \pm SD are indicated. (P-values were determined by one-way analysis of variance with a post-hoc Tukey test). **(C)** Incoming capsids of PRV encoding the pUL36 RKB mutant accumulate juxtanuclear in explanted chick dorsal root ganglia (DRG). Representative images of neural soma (transmitted and fluorescent capsid image pairs with nuclei highlighted by dotted lines). Percentile distributions of juxtanuclear capsid accumulation are illustrated at right ($n = 3$ independent experiments > 500 infected cells each). DRG explants were imaged between 2.5-3 hpi. Scale bars are 20 μ m. Mean values \pm SD are indicated. (P values based on two-tailed unpaired t test). **(D)** PRV[RKB] has delayed viral gene expression. PK15 cells were infected at MOI 10 and total RNA was collected at 4 hpi. Relative IE180 mRNA levels were measured by RT-PCR first-strand DNA synthesis and qPCR amplification using primers specific for PRV IE180 and the swine ribosomal S28 rRNA (loading control). Data was normalized to S28 rRNA levels and depicted as a fold change with respect to IE180 mRNA levels during WT infection ($n = 3$ independent experiments). Mean values \pm SD are indicated. (P values based on two-tailed unpaired t test).

Extended Data Fig. 6 PRV[RKB] is impaired for kinesin-based transport.

Viral particles were harvested from the cytoplasm of infected RK13 cells and allowed to bind to fluorescent microtubules *in vitro*. **(A)** Numbers of bound fluorescent viral particles were counted and are represented as a percentage of those initially added to the imaging chamber. Four independent chambers containing a total of 1204 and 805 bound particles were counted for wild-type PRV (WT) and PRV encoding the reduced

kinesin binding mutant pUL36 allele [RKB]. **(B)** Motility was measured after addition of ATP supplemented with: no inhibitor (light grey bars), 5 μ M sodium orthovanadate (a dynein inhibitor; medium grey bars) or 1 mM AMP-PNP (a kinesin inhibitor; dark grey bars). Numbers of motile virions were determined from triplicate motility chambers, and motility plotted as a percentage of the number of motile particles seen in the absence of inhibitor. For WT and RKB respectively, the numbers of individual viral particles examined for each set of conditions were as follows: no inhibitor (658, 706), sodium orthovanadate (776, 714), AMP-PNP (776, 714). Mean values \pm SD are indicated ($n = 3$ independent experiments). (P values based on two-tailed unpaired t test).

[Extended Data Fig. 7 Kinesin-1 knockdown impairs HSV-1 infection in primary human fibroblasts.](#)

(A) Normal human dermal fibroblasts (NHDF) cells were depleted of Kif5 isoforms by siRNA knockdown. Kif5 expression profile in SK-N-SH cells as a standard that expresses all three Kif5 isoforms ($n = 1$ independent experiment). **(B)** Control and Kif5B-depleted NHDF cells were infected with HSV-1 in the presence of 100 μ M cycloheximide ($n = 1$ independent experiment). At 8 hpi, cells were fixed and immunofluorescence was performed. Scale bar is 20 μ m.

[Extended Data Fig. 8 Kif5B and Kif5C function interchangeably to rescue pUL36 peripheral accumulation in RPE \$\Delta\$ Kif5B \(KO\) cells.](#)

Quantitation of transiently-transfected cells displaying GFP-pUL36 Δ R7 localization at the cell periphery ($n = 3$ independent experiments > 150 each). Scoring methodology is provided in Extended Data Fig. 4. Mean values \pm SD are indicated. (P values based on two-tailed unpaired t test).

[Extended Data Fig. 9 Model of viral assimilation of kinesin-1.](#)

Neuroinvasive herpesviruses capture Kif5 (conventional kinesin; kinesin-1) into the tegument of newly formed virions during infection of epithelial

cells. The captured epithelial kinesin-1 is carried between cells as a structural virion component and is deposited into cells (epithelia and neurons) upon the subsequent round of infection (first blue panel). Upon entry, cytosolic capsids engage in retrograde axonal transport effected by the cytoplasmic dynein/dynactin microtubule motor. The assimilated kinesin is presumably carried in an inactive state during this step of infection (second blue panel). Dynein/dynactin-based transport directs the capsid ‘minus-ended’ along microtubules ending at the centrosome, where the virus uses assimilated kinesin to transport to nuclei (third blue panel). When viruses are attenuated for assimilated-kinesin binding (e.g., PRV[RKB]) or are produced in the absence of Kif5, capsids predominately accumulate at the centrosome and do not progress toward the nucleus despite the presence of endogenous neuronal kinesin-1 (pink panel). Nevertheless, endogenous kinesin also supports nuclear trafficking of capsids.

Extended Data Table 1 Description of recombinant viruses and mammalian expression plasmids used in this study

Supplementary information

Supplementary Information

This file contains Supplementary Data 1 and 2, legends for Supplementary Data 3 and 4, legends for Supplementary Videos 1 and 2 and Supplementary Fig. 1.

Reporting Summary

Supplementary Video 1

See Supplementary Information for description.

Supplementary Video 2

See Supplementary Information for description.

Supplementary Data 3

Data derived from automated analysis of capsid localization that support Fig. 1c. The spreadsheet includes all formula for post-analysis of automated data pipeline.

Supplementary Data 4

Data derived from automated analysis of capsid localization that support Fig. 2d. This spreadsheet includes all formulae for post-analysis of the automated data pipeline.

Rights and permissions

Reprints and Permissions

About this article

Cite this article

Pegg, C.E., Zaichick, S.V., Bomba-Warczak, E. *et al.* Herpesviruses assimilate kinesin to produce motorized viral particles. *Nature* **599**, 662–666 (2021). <https://doi.org/10.1038/s41586-021-04106-w>

- Received: 09 November 2020
- Accepted: 07 October 2021
- Published: 17 November 2021
- Issue Date: 25 November 2021
- DOI: <https://doi.org/10.1038/s41586-021-04106-w>

Share this article

Anyone you share the following link with will be able to read this content:

[Get shareable link](#)

Sorry, a shareable link is not currently available for this article.

[Copy to clipboard](#)

Provided by the Springer Nature SharedIt content-sharing initiative

Further reading

- **Motor-powered trafficking**

- Andrea Du Toit

Nature Reviews Microbiology (2021)

This article was downloaded by **calibre** from <https://www.nature.com/articles/s41586-021-04106-w>

| [Section menu](#) | [Main menu](#) |

- Article
- [Published: 27 October 2021](#)

Early-life inflammation primes a T helper 2 cell–fibroblast niche in skin

- [Ian C. Boothby](#) [ORCID: orcid.org/0000-0002-1112-2834](#)^{1,2},
- [Maxime J. Kinet](#)³,
- [Devi P. Boda](#)¹,
- [Elaine Y. Kwan](#)^{1,4},
- [Sean Clancy](#)¹,
- [Jarish N. Cohen](#)⁵,
- [Ireneusz Habrylo](#)^{1,2},
- [Margaret M. Lowe](#)¹,
- [Mariela Pauli](#)¹,
- [Ashley E. Yates](#)¹,
- [Jamie D. Chan](#)⁵,
- [Hobart W. Harris](#)⁶,
- [Isaac M. Neuhaus](#)¹,
- [Timothy H. McCalmont](#)^{1,5},
- [Ari B. Molofsky](#) [ORCID: orcid.org/0000-0003-0764-3175](#)⁷ &
- [Michael D. Rosenblum](#) [ORCID: orcid.org/0000-0002-0462-5732](#)¹

[Nature](#) volume **599**, pages 667–672 (2021)

- 6380 Accesses
- 1 Citations
- 78 Altmetric

- [Metrics details](#)

Subjects

- [Mucosal immunology](#)
- [T-helper 2 cells](#)

Abstract

Inflammation early in life can prime the local immune milieu of peripheral tissues, which can cause lasting changes in immunological tone that confer disease protection or susceptibility¹. The cellular and molecular mechanisms that prompt changes in immune tone in many nonlymphoid tissues remain largely unknown. Here we find that time-limited neonatal inflammation induced by a transient reduction in neonatal regulatory T cells causes a dysregulation of subcutaneous tissue in mouse skin. This is accompanied by the selective accumulation of type 2 helper T ($T_{H}2$) cells within a distinct microanatomical niche. $T_{H}2$ cells are maintained into adulthood through interactions with a fibroblast population in skin fascia that we refer to as $T_{H}2$ -interacting fascial fibroblasts (TIFFs), which expand in response to $T_{H}2$ cytokines to form subcutaneous fibrous bands.

Activation of the $T_{H}2$ –TIFF niche due to neonatal inflammation primes the skin for altered reparative responses to wounding. Furthermore, we identify fibroblasts in healthy human skin that express the TIFF transcriptional signature and detect these cells at high levels in eosinophilic fasciitis, an orphan disease characterized by inflammation and fibrosis of the skin fascia. Taken together, these data define a previously unidentified $T_{H}2$ cell niche in skin and functionally characterize a disease-associated fibroblast population. The results also suggest a mechanism of immunological priming whereby inflammation early in life creates networks between adaptive immune cells and stromal cells to establish an immunological set-point in tissues that is maintained throughout life.

Access options

Subscribe to Journal

Get full journal access for 1 year

\$199.00

only \$3.90 per issue

[Subscribe](#)

All prices are NET prices.

VAT will be added later in the checkout.

Tax calculation will be finalised during checkout.

Rent or Buy article

Get time limited or full article access on ReadCube.

from \$8.99

[Rent or Buy](#)

All prices are NET prices.

Additional access options:

- [Log in](#)
- [Access through your institution](#)
- [Learn about institutional subscriptions](#)

Fig. 1: Transient neoT_{reg} cell reduction causes temporary derangement of stromal architecture and lasting T_H2 cell accumulation in the skin subcutis.

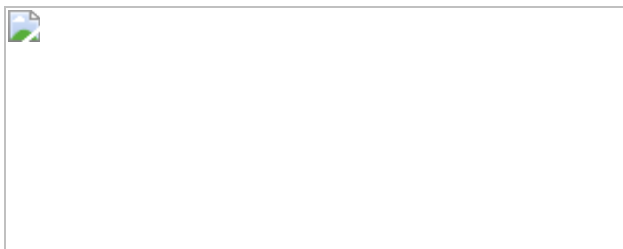


Fig. 2: neoT_{reg} cell reduction causes outgrowth of an *Il13ra1*⁺ fibroblast population in skin fascia.



Fig. 3: Reciprocal interactions between skin T_H2 cells and *Il13ra1*⁺ fibroblasts (TIFFs) drive fascial expansion and T_H2 cell maintenance.

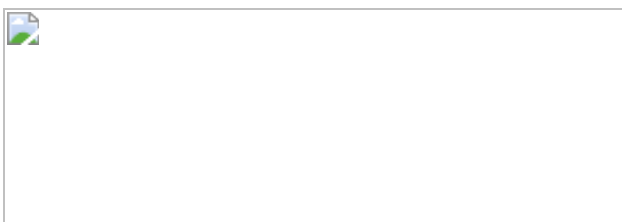
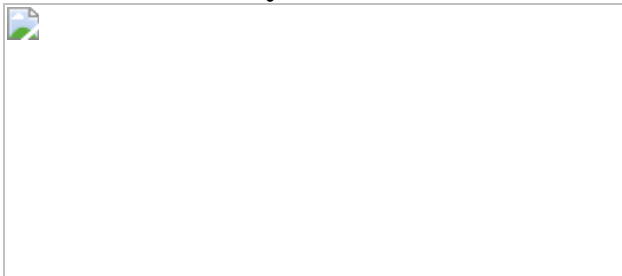


Fig. 4: TIFF-like cells are present in healthy human skin and in a fibroinflammatory disease of the fascia.



Data availability

Sequencing data are publicly available at the Gene Expression Omnibus under accession number [GSE183031](#). Cross-tissue fibroblast atlas data⁹ were downloaded from <https://www.fibroxplorer.com/download>. Additional data presented here are available upon request from the corresponding author. [Source data](#) are provided with this paper.

Code availability

Code used for analysis of scRNA-seq data is available upon request from the corresponding author.

References

1. 1.

Al Nabhani, Z. & Eberl, G. Imprinting of the immune system by the microbiota early in life. *Mucosal Immunol.* **13**, 183–189 (2020).

2. 2.

Schärschmidt, T. C. et al. A wave of regulatory T cells into neonatal skin mediates tolerance to commensal microbes. *Immunity* **43**, 1011–1021 (2015).

3. 3.

Schärschmidt, T. C. et al. Commensal microbes and hair follicle morphogenesis coordinately drive T_{reg} migration into neonatal skin. *Cell Host Microbe* **21**, 467–477 (2017).

4. 4.

Kim, J. M., Rasmussen, J. P. & Rudensky, A. Y. Regulatory T cells prevent catastrophic autoimmunity throughout the lifespan of mice. *Nat. Immunol.* **8**, 191–197 (2007).

5. 5.

Nussbaum, J. C. et al. Type 2 innate lymphoid cells control eosinophil homeostasis. *Nature* **502**, 245–248 (2013).

6. 6.

Collins, N. et al. Skin CD4⁺ memory T cells exhibit combined cluster-mediated retention and equilibration with the circulation. *Nat. Commun.* **7**, 11514 (2016).

7. 7.

Kobayashi, T. et al. Homeostatic control of sebaceous glands by innate lymphoid cells regulates commensal bacteria equilibrium. *Cell* **176**, 982–997.e16 (2019).

8. 8.

Ali, N. et al. Regulatory T cells in skin facilitate epithelial stem cell differentiation. *Cell* **169**, 1119–1129.e11 (2017).

9. 9.

Buechler, M. B. et al. Cross-tissue organization of the fibroblast lineage. *Nature* **593**, 575–579 (2021).

10. 10.

Joost, S. et al. The molecular anatomy of mouse skin during hair growth and rest. *Cell Stem Cell* **26**, 441–457.e7 (2020).

11. 11.

Zhang, L. et al. Diet-induced obesity promotes infection by impairment of the innate antimicrobial defense function of dermal adipocyte progenitors. *Sci. Transl. Med.* **13**, eabb5280 (2021).

12. 12.

Driskell, R. R. et al. Distinct fibroblast lineages determine dermal architecture in skin development and repair. *Nature* **504**, 277–281 (2013).

13. 13.

Kimura-Ueki, M. et al. Hair cycle resting phase is regulated by cyclic epithelial FGF18 signaling. *J. Invest. Dermatol.* **132**, 1338–1345 (2012).

14. 14.

Kim, B. S. et al. TSLP elicits IL-33-independent innate lymphoid cell responses to promote skin inflammation. *Sci. Transl. Med.* **5**, 170ra16 (2013).

15. 15.

Salimi, M. et al. A role for IL-25 and IL-33-driven type-2 innate lymphoid cells in atopic dermatitis. *J. Exp. Med.* **210**, 2939–2950 (2013).

16. 16.

Ricardo-Gonzalez, R. R. et al. Tissue signals imprint ILC2 identity with anticipatory function. *Nat. Immunol.* **19**, 1093–1099 (2018).

17. 17.

Obata-Ninomiya, K. et al. The skin is an important bulwark of acquired immunity against intestinal helminths. *J. Exp. Med.* **210**, 2583–2595 (2013).

18. 18.

Boothby, I. C., Cohen, J. N. & Rosenblum, M. D. Regulatory T cells in skin injury: at the crossroads of tolerance and tissue repair. *Sci. Immunol.* **5**, eaaz9631 (2020).

19. 19.

Correa-Gallegos, D. et al. Patch repair of deep wounds by mobilized fascia. *Nature* **576**, 287–292 (2019).

20. 20.

Naik, S. et al. Inflammatory memory sensitizes skin epithelial stem cells to tissue damage. *Nature* **550**, 475–480 (2017).

21. 21.

Findley, T. W., Chaitow, L. & Huijing, P. (eds) *Fascia: The Tensional Network of the Human Body* (Churchill Livingstone, 2012).

22. 22.

Stuart, T. et al. Comprehensive integration of single-cell data. *Cell* **177**, 1888–1902 (2019).

23. 23.

Ramachandran, P. et al. Resolving the fibrotic niche of human liver cirrhosis at single-cell level. *Nature* **575**, 512–518 (2019).

24. 24.

Chan, K. K. et al. Eosinophilic fasciitis following checkpoint inhibitor therapy: four cases and a review of literature. *Oncologist* **25**, 140–149 (2020).

25. 25.

Mortezaei, M., Barrett, M. & Edrissian, M. Successful treatment of refractory eosinophilic fasciitis with reslizumab. *JAAD Case Rep.* **6**, 951–953 (2020).

26. 26.

Merrick, D. et al. Identification of a mesenchymal progenitor cell hierarchy in adipose tissue. *Science* **364**, eaav2501 (2019).

27. 27.

Dahlgren, M. W. et al. Adventitial stromal cells define group 2 innate lymphoid cell tissue niches. *Immunity* **50**, 707–722.e6 (2019).

28. 28.

Spallanzani, R. G. et al. Distinct immunocyte-promoting and adipocyte-generating stromal components coordinate adipose tissue

immune and metabolic tenors. *Sci. Immunol.* **4**, eaaw3658 (2019).

29. 29.

Schwalie, P. C. et al. A stromal cell population that inhibits adipogenesis in mammalian fat depots. *Nature* **559**, 103–108 (2018).

30. 30.

Scott, R. W., Arostegui, M., Schweitzer, R., Rossi, F. M. V. & Underhill, T. M. *Hic1* defines quiescent mesenchymal progenitor subpopulations with distinct functions and fates in skeletal muscle regeneration. *Cell Stem Cell* **25**, 797–813.e9 (2019).

31. 31.

Dahlgren, M. W. & Molofsky, A. B. Adventitial cuffs: regional hubs for tissue immunity. *Trends Immunol.* **40**, 877–887 (2019).

32. 32.

Vainchtein, I. D. et al. Astrocyte-derived interleukin-33 promotes microglial synapse engulfment and neural circuit development. *Science* **359**, 1269–1273 (2018).

33. 33.

Hagan, A. S., Zhang, B. & Ornitz, D. M. Identification of a FGF18-expressing alveolar myofibroblast that is developmentally cleared during alveologenesis. *Development* **147**, dev181032 (2020).

34. 34.

Camberis, M. et al. Evaluating the in vivo Th2 priming potential among common allergens. *J. Immunol. Methods* **394**, 62–72 (2013).

35. 35.

Bankhead, P. et al. QuPath: open source software for digital pathology image analysis. *Sci. Rep.* **7**, 16878 (2017).

36. 36.

Yang, B. et al. Single-cell phenotyping within transparent intact tissue through whole-body clearing. *Cell* **158**, 945–958 (2014).

37. 37.

Korotkevich, G. et al. Fast gene set enrichment analysis. Preprint at *bioRxiv* <https://doi.org/10.1101/060012> (2021).

Acknowledgements

We thank the staff at the UCSF Parnassus Flow Cytometry Core (RRID:SCR_018206) for assistance with flow cytometry analysis and cell sorting (supported in part by NIH P30 DK063720 and by the NIH S10 instrumentation grant 1S10OD021822-01); the UCSF Biological Imaging and Development Core for confocal microscopy and analysis; the UCSF Genomics CoLab and Institute for Human Genetics for scRNA-seq and the UCSF Mouse Pathology Core for histology; and T. Scharschmidt, C. Lowell, J. Cyster, M. Ansel, T. Peng and A. Abbas for comments and discussion; D. Ornitz and A. Hagan for the donation of *Fgf18^{CreERT2}* tissue; and R. Locksley and H.-E. Liang for *N. brasiliensis* larvae. Figs. 1a, b and Extended Data Figs. 8a, g, 9a, e, o and v were created using BioRender.com. I.C.B. was supported by NIH F30AI147364, NIH T32GM007618 and NIH T32AI007334. M.D.R. is supported by NIH R01AR077553 and R01AR071944.

Author information

Affiliations

1. Department of Dermatology, University of California at San Francisco, San Francisco, CA, USA

Ian C. Boothby, Devi P. Boda, Elaine Y. Kwan, Sean Clancy, Ireneusz Habrylo, Margaret M. Lowe, Mariela Pauli, Ashley E. Yates, Isaac M. Neuhaus, Timothy H. McCalmont & Michael D. Rosenblum

2. Medical Scientist Training Program, University of California at San Francisco, San Francisco, CA, USA

Ian C. Boothby & Ireneusz Habrylo

3. Division of Rheumatology, Department of Medicine, University of California at San Francisco, San Francisco, CA, USA

Maxime J. Kinet

4. California Institute of Regenerative Medicine, San Francisco State University, San Francisco, CA, USA

Elaine Y. Kwan

5. Department of Pathology, University of California at San Francisco, San Francisco, CA, USA

Jarish N. Cohen, Jamie D. Chan & Timothy H. McCalmont

6. Department of Surgery, University of California at San Francisco, San Francisco, CA, USA

Hobart W. Harris

7. Department of Laboratory Medicine, University of California at San Francisco, San Francisco, CA, USA

Ari B. Molofsky

Contributions

Conceptualization: I.C.B. and M.D.R. Methodology: I.C.B. and M.D.R.

Investigation: I.C.B., M.J.K., D.P.B., S.C., E.Y.K., I.H. and J.N.C.

Resources: M.D.R. and A.B.M. Data curation: I.C.B. Writing (original

(draft): I.C.B. Writing (editing and revision): I.C.B., A.B.M. and M.D.R. Supervision: M.D.R. Human sample procurement coordination: M.M.L., M.P., A.E.Y., J.D.C., H.W.H., I.M.N., T.H.M. and M.D.R. Data analysis of Extended Data Fig. 5: S.C. Design and analyses of all other experiments: I.C.B. (executed with assistance from M.J.K., D.P.B., E.Y.K., I.H. and J.N.C.).

Corresponding author

Correspondence to [Michael D. Rosenblum](#).

Ethics declarations

Competing interests

Funding for scRNA-seq studies of healthy human skin was provided by LEO Pharmaceuticals. M.D.R. is a founder and consultant for TRex Bio., Sitryx Bio. and Mozart Therapeutics.

Additional information

Peer review information *Nature* thanks Christopher Buckley, Laura Mackay and the other, anonymous, reviewer(s) for their contribution to the peer review of this work. Peer reviewer reports are available.

Publisher's note Springer Nature remains neutral with regard to jurisdictional claims in published maps and institutional affiliations.

Extended data figures and tables

[Extended Data Fig. 1 Characteristics of cutaneous inflammation induced by neonatal Treg reduction.](#)

(a) Weights of PBS- and DT-treated *FoxP3^{DTR}* mice from the time of treatment to adulthood. $n = 3\text{--}7$ mice per data point, 51 total. **(b)**

Quantification of Tregs in skin and skin-draining lymph nodes (sdLN) following neoTreg depletion. $n = 3$ -9 animals per data point (60 total), 1 experiment per time point. (c–f) Representative flow cytometry and quantifications of immune cell populations in skin and skin-draining lymph nodes during the inflammatory phase of neonatal Treg depletion at P25 and adult Treg depletion at P67 (both 10 days after DT). *Gating:* CD8 T cells ($CD3^+ CD8^+$); CD4 Teffs ($CD3^+ CD4^+ FoxP3^-$); Ly6C monocytes (Ly6G $^-$ Siglec F $^-$ CD64 $^+$ CD11c $^-$ CD11b $^+$ Ly6C $^+$). $n = 18$ animals. (g) Representative histology of wildtype neonatal mice treated with PBS or DT and sacrificed 10 days post-injection. (h) Histology of selected organs in Δ neoTreg and control mice at P25. gWAT – perigonadal white adipose tissue. Data are displayed as mean +/- SD from one independent experiment, representative of 2-3 repeats. * $p < 0.05$, ** $p < 0.01$, *** $p < 0.001$ (all two-sided); repeated measures two-way ANOVA (a); two-way ANOVA with Šídák multiple comparison test (b-c); one-way ANOVA with Tukey's multiple comparisons test (c-f).

[Source data](#)

[Extended Data Fig. 2 Resolution of inflammation and return to homeostasis following neonatal Treg reduction.](#)

(a) Representative skin histology of control and neonatal Treg-depleted $FoxP3^{DTR}$ mice at P25, P35, and P50 (10, 20, and 35 days post-DT treatment). Fibrous bands are outlined with dotted lines and regenerating adipocytes are marked by arrows. (b) Abundance of selected inflammatory immune cell populations in skin 0-90 days after neoTreg depletion. $n = 3$ -9 animals per data point (60 total), 1 experiment per time point. (c) T helper and CD8 $^+$ T cell cytokine production 0-35 days after neoTreg depletion, quantified by intracellular cytokine staining. $n = 3$ -9 animals per data point (51 total), 1 experiment per time point. (d–f) Sample gating and quantification of dermal $\gamma\delta$ T cells, ILC2s, and Tc2 cells 0-90 days after neoTreg depletion in $Il5^{Red5/+}$; $FoxP3^{DTR}$ mice. $n = 3$ -9 animals per data point (51 total, d-e); 3-6 animals per data point, (19 total, f), 1 experiment per time point. Data are displayed as mean +/- SD from one independent experiment, representative of 2-3 repeats. * $p < 0.05$, ** $p < 0.01$, *** $p <$

0.001 (all two-sided); Student's t test at selected time points during adulthood (b-e); two-way ANOVA with Šídák multiple comparison test (f) . All results were reproduced over 2-3 independent experiments.

[Source data](#)

Extended Data Fig. 3 CD49d marks subcutis-resident Th2 cells that are associated with subdermal eosinophilia and age-specific fibrous band formation.

(a-c) Expression of CD69, CD103 (α_E integrin), and CD49d (α_4 integrin) on skin lymphocytes in Δ neoTreg mice aged to adulthood. Bulk Teff defined as IL5^{Red5-} FoxP3⁻ CD4⁺ T cells. $n=4$ animals. **(d-f)** Δ neoTreg mice were aged to adulthood, subcutis was separated from the dermis/epidermis, and the two skin fractions were analyzed separately by flow cytometry. Th2 localization over time (d), lymphocyte localization at P50 (e), and CD49d expression in dermal vs. subdermal lymphocytes (f) is shown. $n=4-5$ animals per data point, 14 total (d); 4 animals (e); 5 animals (f). **(g-i)** Quantification of CD49d⁺ Th2 cells (g) and eosinophils (h) in Δ neoTreg and Δ adTreg mice during the inflammatory phase of Treg reduction at 10 days post-DT. Myeloid cell localization in Δ neoTreg mice (i) was quantified by flow cytometry of dissected skin layers. $n=19$ animals (g-h); 5 animals (i). **(j-l)** Δ neoTreg mice were treated every other day with FTY720 or vehicle from P8 to P25. Histology (j), Th2 numbers (k), and eosinophil numbers (l) are shown at P25. $n=7$ animals. **(m-n)** CD49d expression on IL5-Red5⁺ Th2 cells and frequency of CD49d⁺ Th2 cells in Δ neoTreg and Δ adTreg mice during (D10 / P25) and after (D35 / P50) inflammation. $n=23$ animals. Data are displayed as mean +/- SD from one independent experiment, representative of 2-3 repeats. * $p < 0.05$, ** $p < 0.01$, *** $p < 0.001$ (all two-sided); repeated-measures ANOVA with Dunnett's multiple comparison test (a-c, e); 2-way repeated-measures ANOVA with Sidak multiple comparison test (f); Welch's ANOVA with Dunnett's multiple comparison test (g-h); Student's t-test (k-n) . All results were reproduced over 2-3 independent experiments.

[Source data](#)

Extended Data Fig. 4 Single-cell transcriptomic characterization of skin stroma in control and ΔneoTreg mice.

(a) Expression of marker genes for skin stromal clusters in control mice. **(b)** Expression of fibroblast markers and ECM genes in control mouse skin stroma. **(c)** Expression of immune-related genes in mouse skin stroma, split by control (PBS) and ΔneoTreg (DT) sample. **(d)** Differential gene expression analysis of *Il13ra1*⁺ FBs (TIFFs) in ΔneoTreg vs. control mice. **(e)** Expression of MHC class II-related transcripts in skin stromal clusters (ctrl and ΔneoTreg samples combined). **(f)** Expression of cell surface markers used to design the *Il13ra1*⁺ FB flow cytometry gating strategy in main figure [2d](#). **(g)** Representative flow cytometry of fibroblast markers PDPN and PDGFR α within subsets of Lin⁻ skin stromal cells from P25 control mice.

Extended Data Fig. 5 *Il13ra1*⁺ FBs / TIFFs are transcriptomically similar to *Pi16*⁺ fibroblasts found across mouse organs.

Published data were downloaded from a mouse cross-tissue fibroblast atlas, containing twenty-eight 10X scRNASeq datasets across 16 murine tissues that were aligned, filtered, and analyzed with a standardized methodology to minimize batch effects.⁹ **(a)** Steady-state atlas of all 16 tissues was re-plotted, demonstrating similar clustering to published meta-analysis. **(b)** Expression of TIFF markers from control skin in cross-tissue clusters defined by the atlas. **(c)** Expression of the top 50 TIFF markers (ranked by log-fold change) in cross-tissue atlas clusters. **(d)** Cross-tissue atlas cluster representation in selected tissues. SAT – subcutaneous adipose tissue; VAT – visceral adipose tissue. **(e)** Enrichment of all skin TIFF markers with logFC > 0.25 (n = 313) among cross-tissue fibroblast atlas clusters, calculated using the Seurat AddModuleScore function. **(f)** Geneset enrichment analysis of the skin TIFF gene set among cross-tissue fibroblast atlas clusters.

Extended Data Fig. 6 Anatomic characterization of *Il13ra1*⁺ fibroblasts (TIFFs).

(a) IF microscopy of mouse back, ear, and tail skin to identify fascia (CD26), adipocytes (PLIN1), and skeletal muscle (MyoIV). **(b)** Variable layering of fascia, adipocytes, and skeletal muscle at two different back skin locations at in P22 control mice. **(c)** Control skin was dissected from P22 mice and the subcutis was manually separated from the dermis and epidermis. *Il13ra1*⁺ FBs (TIFFs) were quantified in each fraction. **(d)** *Fgf18* expression by scRNAseq in control Lin⁻ skin stromal cells. **(e)** Confocal microscopy of adult skin from *Fgf18*^{CreRET2}; *Rosa26*^{tdTomato} mice injected with tamoxifen for five days prior to harvest. *Top row*: Z-projection with tdTomato signal thresholded for visualization. *Bottom row*: inset of fascia with original tdTomato fluorescence. All results were reproduced over 2-3 independent experiments.

Extended Data Fig. 7 Further characterization of Th2-TIFF interactions in the subdermal niche.

(a) IF microscopy of skin from wildtype mice injected for five days with IL-13 or IL-33 starting at P21 with quantification of fascial proliferation by Ki67. $n = 9$ animals. **(b)** Skin histology from ΔneoTreg mice crossed to IL4/13- or IL33-deficient strains at P25 (10 days post-DT). **(c)** Expression of IL4RA on TIFFs from wildtype neonate (P25) and adult (P50) mice. $n = 10$ animals. **(d-f)** Adult mice were injected for 7 days with type 2 cytokines and the indicated cell populations in skin were quantified by flow cytometry. $n = 13$ animals (d); 7 animals (e-f). **(g-h)** TIFFs and dermal fibroblasts were sorted from P21 mouse skin and co-cultured with sorted IL-5^{Red5+} skin Th2 cells from ΔneoTreg mice for four days. $n = 12$ samples (h). **(i-j)** IL-18R1 and ST2 expression in skin lymphocyte subsets with quantification of IL-18R1 expression (see main fig. 3g for ST2). $n = 4$ animals. **(k-l)** ΔneoTreg mice were aged to adulthood, the subcutis was separated from the dermis/epidermis, and expression of alarmin receptors was quantified across lymphocyte subsets. $n = 5$ animals. Data are displayed as mean +/- SD from one independent experiment, representative of 2-3 repeats. * $p < 0.05$, ** $p < 0.01$, *** $p < 0.001$ (all two-sided); Welch's

ANOVA with Dunnett Multiple Comparisons Test (a, d, h, j); Student's t-test (c, e-f); two-way ANOVA with Šídák multiple comparison test (l).

[Source data](#)

Extended Data Fig. 8 Th2-TIFF interactions and niche priming across multiple models of early life subcutaneous inflammation.

(a-d) Mice were immunized subcutaneously (s.c.) with ovalbumin (OVA) and papain. CD49d⁺ Th2 cells (b, c) and TIFFs (d) were quantified at indicated timepoints. $n = 25$ animals I; 10 animals (d). **(e-f)** *Pdgfra*^{Cre}; *Il4ra*^{ff} mice and Cre⁻ controls were injected with OVA-papain at P8 and P15. IL4RA expression (e) and TIFF frequency (f) were quantified at P25. $n = 13$ mice. **(g-j)** Mice were infected s.c. with *Nippostrongylus brasiliensis* at P8 and boosted with s.c. *N. brasiliensis* allergen at P15. CD49d⁺ Th2 cells (g, i) and TIFFs (j) were quantified at indicated timepoints. $n = 13$ mice (h); 12 mice (j). Data are displayed as mean +/- SD from one independent experiment; each experiment was reproduced 2-3 times. * $p < 0.05$, ** $p < 0.01$, *** $p < 0.001$ (all two-sided); Student's t-test (c-d, f, i-j); two-way ANOVA with Šídák multiple comparison test (e).

[Source data](#)

Extended Data Fig. 9 Neonatal Treg reduction primes skin for Th2-driven tissue reparative responses during adulthood.

(a-b) Control and ΔneoTreg mice were aged to adulthood and then treated with two shots DT (identical to neonatal dosing regimen). Representative histology is shown with fibrous bands outlined. **(c)** Th2 and ILC2 cell numbers in adult ctrl (*Il5*^{Red5/+}; *FoxP3*^{DTR} + PBS), ΔneoTreg (*Il5*^{Red5/+}; *FoxP3*^{DTR} + DT), and ΔneoTreg/ΔTh2 (*Il5*^{Red5/+}; *Rosa26*^{DTA/+}; *FoxP3*^{DTR}) mice. $n = 16$ animals. **(d)** Wound bed ILC2 numbers (gated as CD45⁺ CD3⁻ CD4⁻ CD8⁻ Thy1⁺ IL5^{Red5+}). $n = 7-10$ animals per data point in 2 pooled experiments per time point (108 total). **(e-n)** Control, ΔneoTreg, and ΔneoTreg/ΔTh2 mice were aged to adulthood and subjected to full-thickness cutaneous wounding. **(f)** Th2 numbers in skin 0 – 10 days post

wounding (dpw). $n = 4$ -11 animals per data point in 2 pooled experiments per time point (89 total). (g) Th2 frequency in paired skin biopsies taken at dpw0 and dpw7. $n = 22$ animals in one experiment. (h-i) Wound area was quantified daily, fit to a one-phase exponential decay model, and tested for equivalence of the rate constant (h). Rate constants of curves fit to each biological replicate are shown in (i). (j-k) Alternatively activated macrophage (AAM) and eosinophil frequency in dpw10 wounded skin. $n = 42$ animals in 2 pooled experiments. (l) TIFF abundance in wound beds at 0 –10 dpw. $n = 4$ -16 animals in 2 pooled experiments (97 total). (m-n) Flow cytometric quantification (m) and IF microscopy (n) of CD26^{hi} TIFFs in wounds at dpw10. $n = 39$ animals in 2 pooled experiments. (o-u) ΔneoTreg mice were aged to adulthood, wounded, and treated with FTY720 every other day. Wound closure (p-q) and flow cytometric quantifications of Th2 cells, alternatively activated macrophages (AAMs), eosinophils, and TIFFs are shown (r-u) are shown. $n = 11$ animals. (v-ab) Neonatal mice were immunized with OVA/papain, aged to adulthood, and wounded. Wound closure (w-x) and flow cytometric quantifications of Th2 cells, alternatively activated macrophages (AAMs), eosinophils, and TIFFs are shown (y-ab). $n = 22$ animals. Data are displayed as mean +/- SD (c-d, f, i-m, q-u, x-ab) or SEM (h, p, w). Results were reproduced over 2 independent experiments (a-d; o-ab) or 4 independent experiments pooled into two separate analyses (e-n). * $p < 0.05$, ** $p < 0.01$, *** $p < 0.001$ (all two-sided); ANOVA with Dunnett Multiple Comparisons Test (c, i-k, m, x-ab); least-squares quadratic regression with extra sum-of-squares F test (f, l); mixed-effects analysis with Šídák multiple comparison test (g); nonlinear one-phase exponential decay regression (h, p, w); Student's t-test (q-u).

[Source data](#)

[Extended Data Fig. 10 Characterization of human skin stroma.](#)

- (a) Gating strategy used to FACS-purify human Lin⁻ stromal cells (CD45⁻ CD31⁻ Ecad⁻, CD235a⁻). (b) Expression of top 50 murine TIFF (mTIFF) orthologs in human skin stroma, ranked by fold-change. (c) Expression of mouse TIFFs and Thbs4+ FB markers in healthy human stromal clusters. (d) Human and ortholog-converted mouse scRNAseq data were integrated and co-clustered. Cluster identities from single-species analyses (main

fig. 4a-b) are shown projected onto the cross-species UMAP. (e) Sample histology of healthy and eosinophilic fasciitis lesional skin with IHC staining for GATA3 and CD4.

Supplementary information

Supplementary Fig. 1

Representative flow cytometry gating.

Reporting Summary

Peer Review File

Supplementary Table 1

Metadata and cell counts by cluster for all human and mouse scRNA-seq experiments.

Supplementary Table 2

List of marker genes for each cluster of murine stromal cells (control and Δ neoT_{reg} cell integrated analysis).

Supplementary Table 3

List of marker genes for each cluster of human stromal cells (analysis of healthy samples only).

Supplementary Table 4

Orthologues of mTIFF signature genes used for enrichment analyses of human data.

Supplementary Table 5

Patient characteristics for skin samples used in immunohistochemistry analysis.

Source data

[Source Data Fig. 1](#)

[Source Data Fig. 2](#)

[Source Data Fig. 3](#)

[Source Data Fig. 4](#)

[Source Data Extended Data Fig. 1](#)

[Source Data Extended Data Fig. 2](#)

[Source Data Extended Data Fig. 3](#)

[Source Data Extended Data Fig. 7](#)

[Source Data Extended Data Fig. 8](#)

[Source Data Extended Data Fig. 9](#)

Rights and permissions

[Reprints and Permissions](#)

About this article

[Cite this article](#)

Boothby, I.C., Kinet, M.J., Boda, D.P. *et al.* Early-life inflammation primes a T helper 2 cell–fibroblast niche in skin. *Nature* **599**, 667–672 (2021). <https://doi.org/10.1038/s41586-021-04044-7>

- Received: 20 January 2021
- Accepted: 20 September 2021
- Published: 27 October 2021
- Issue Date: 25 November 2021
- DOI: <https://doi.org/10.1038/s41586-021-04044-7>

Share this article

Anyone you share the following link with will be able to read this content:

[Get shareable link](#)

Sorry, a shareable link is not currently available for this article.

[Copy to clipboard](#)

Provided by the Springer Nature SharedIt content-sharing initiative

Further reading

- [**Fibroblast niche sets TH2 skin tone in early life**](#)
 - Lucy Bird

Nature Reviews Immunology (2021)

This article was downloaded by **calibre** from <https://www.nature.com/articles/s41586-021-04044-7>

- Article
- [Published: 03 November 2021](#)

Tumour DDR1 promotes collagen fibre alignment to instigate immune exclusion

- [Xuijie Sun¹](#),
^{na1},
- [Bogang Wu](#) [ORCID: orcid.org/0000-0003-1654-198X¹](#),
^{na1},
- [Huai-Chin Chiang](#) [ORCID: orcid.org/0000-0002-7616-3362¹](#),
^{na1},
- [Hui Deng²](#),
- [Xiaowen Zhang¹](#),
- [Wei Xiong²](#),
- [Junquan Liu²](#),
- [Aaron M. Rozeboom³](#),
- [Brent T. Harris³](#),
- [Eline Blommaert](#) [ORCID: orcid.org/0000-0003-0040-5158⁴](#),
- [Antonio Gomez](#) [ORCID: orcid.org/0000-0001-5308-981X⁵](#),
- [Roderic Espin Garcia](#) [ORCID: orcid.org/0000-0003-2494-0964⁴](#),
- [Yufan Zhou](#) [ORCID: orcid.org/0000-0002-8385-433X⁶](#),
- [Payal Mitra⁷](#),
- [Madeleine Prevost¹](#),
- [Deyi Zhang⁸](#),
- [Debarati Banik¹](#),
- [Claudine Isaacs³](#),
- [Deborah Berry³](#),
- [Catherine Lai³](#),
- [Krysta Chaldekas³](#),
- [Patricia S. Latham](#) [ORCID: orcid.org/0000-0003-2782-9444⁹](#),
- [Christine A. Brantner¹⁰](#),

- [Anastas Popratiloff¹⁰](#),
- [Victor X. Jin ORCID: orcid.org/0000-0002-8765-3471⁶](#),
- [Ningyan Zhang ORCID: orcid.org/0000-0002-4348-2180²](#),
- [Yanfen Hu⁷](#),
- [Miguel Angel Pujana ORCID: orcid.org/0000-0003-3222-4044⁴](#),
- [Tyler J. Curiel ORCID: orcid.org/0000-0001-6962-9411⁸](#),
- [Zhiqiang An ORCID: orcid.org/0000-0001-9309-2335²](#) &
- [Rong Li ORCID: orcid.org/0000-0002-6471-6580¹](#)

Nature volume **599**, pages 673–678 (2021)

- 11k Accesses
- 167 Altmetric
- [Metrics details](#)

Subjects

- [Breast cancer](#)
- [Cancer microenvironment](#)

Abstract

Immune exclusion predicts poor patient outcomes in multiple malignancies, including triple-negative breast cancer (TNBC)¹. The extracellular matrix (ECM) contributes to immune exclusion². However, strategies to reduce ECM abundance are largely ineffective or generate undesired outcomes^{3,4}. Here we show that discoidin domain receptor 1 (DDR1), a collagen receptor with tyrosine kinase activity⁵, instigates immune exclusion by promoting collagen fibre alignment. Ablation of *Ddr1* in tumours promotes the intratumoral penetration of T cells and obliterates tumour growth in mouse models of TNBC. Supporting this finding, in human TNBC the expression of DDR1 negatively correlates with the intratumoral abundance of anti-tumour T cells. The DDR1 extracellular domain (DDR1-ECD), but not its intracellular kinase domain, is required for immune exclusion. Membrane-

untethered DDR1-ECD is sufficient to rescue the growth of *Ddr1*-knockout tumours in immunocompetent hosts. Mechanistically, the binding of DDR1-ECD to collagen enforces aligned collagen fibres and obstructs immune infiltration. ECD-neutralizing antibodies disrupt collagen fibre alignment, mitigate immune exclusion and inhibit tumour growth in immunocompetent hosts. Together, our findings identify a mechanism for immune exclusion and suggest an immunotherapeutic target for increasing immune accessibility through reconfiguration of the tumour ECM.

Access options

Subscribe to Journal

Get full journal access for 1 year

\$199.00

only \$3.90 per issue

[Subscribe](#)

All prices are NET prices.

VAT will be added later in the checkout.

Tax calculation will be finalised during checkout.

Rent or Buy article

Get time limited or full article access on ReadCube.

from \$8.99

[Rent or Buy](#)

All prices are NET prices.

Additional access options:

- [Log in](#)

- [Access through your institution](#)
- [Learn about institutional subscriptions](#)

Fig. 1: DDR1 promotes mammary tumour growth in immunocompetent hosts.



Fig. 2: DDR1 inhibits the infiltration of anti-tumour immune cells.



Fig. 3: DDR1-dependent ECM remodelling inhibits anti-tumour immune infiltration.

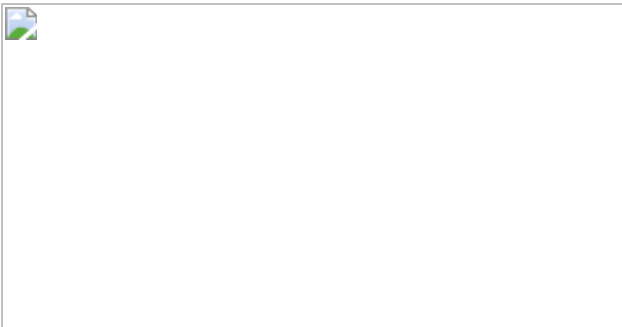
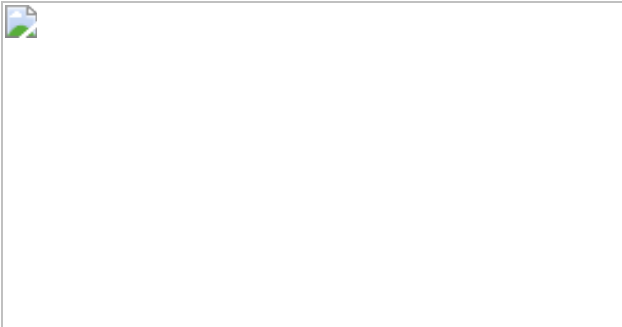


Fig. 4: DDR1 as a therapeutic target for tumour immunotherapy.



Data availability

DDR1 protein expression correlation scatter plots were drawn with data obtained from the CPTAC (<https://cptac-data-portal.georgetown.edu/study-summary/S015>) (Fig. 2e, Extended Data Fig. 3p). The correlation between *DDR1* mRNA levels and patient survival was performed with data acquired from the Kaplan–Meier Plotter database (<https://kmplot.com/analysis/>) (Extended Data Fig. 3f,g). Correlations between the mRNA levels of *DDR1* and immune markers were performed with data extracted from [GSE88847](#) (Extended Data Fig. 3k–n) and the TCGA project (https://www.cbiportal.org/study/summary?id=brca_tcga_pan_can_atlas_2018) (Fig. 2d, Extended Data Figs. 3h–j, o, 10e). Disease-specific survival Kaplan–Meier curves were drawn with data obtained from the TCGA project (<https://gdc.cancer.gov/>) (Extended Data Fig 10a–d). All data generated and analysed during this study, except the RNA-seq dataset, are included in this published Article and its supplementary files. The RNA-seq dataset has been deposited to the NCBI Gene Expression Omnibus database and the accession number is [GSE139239](#). [Source data](#) are provided with this paper.

References

1. 1.
Gruoso, T. et al. Spatially distinct tumor immune microenvironments stratify triple-negative breast cancers. *J. Clin. Invest.* **129**, 1785–1800 (2019).
2. 2.
Cox, T. R. The matrix in cancer. *Nat. Rev. Cancer* **21**, 217–238 (2021).
3. 3.
Bejarano, L., Jordao, M. J. C. & Joyce, J. A. Therapeutic targeting of the tumor microenvironment. *Cancer Discov.* **11**, 933–959 (2021).

4. 4.

Chen, Y. et al. Type I collagen deletion in α SMA⁺ myofibroblasts augments immune suppression and accelerates progression of pancreatic cancer. *Cancer Cell* **39**, 548–565 (2021).

5. 5.

Leitinger, B. Discoidin domain receptor functions in physiological and pathological conditions. *Int. Rev. Cell Mol. Biol.* **310**, 39–87 (2014).

6. 6.

Valiathan, R. R., Marco, M., Leitinger, B., Kleer, C. G. & Fridman, R. Discoidin domain receptor tyrosine kinases: new players in cancer progression. *Cancer Metastasis Rev.* **31**, 295–321 (2012).

7. 7.

Hidalgo-Carcedo, C. et al. Collective cell migration requires suppression of actomyosin at cell-cell contacts mediated by DDR1 and the cell polarity regulators Par3 and Par6. *Nat. Cell Biol.* **13**, 49–58 (2011).

8. 8.

Gao, H. et al. Multi-organ site metastatic reactivation mediated by non-canonical discoidin domain receptor 1 signaling. *Cell* **166**, 47–62 (2016).

9. 9.

Edwards, D. N. et al. Selective glutamine metabolism inhibition in tumor cells improves anti-tumor T lymphocyte activity in triple-negative breast cancer. *J Clin. Invest.* **131**, e140100 (2021).

10. 10.

Jiang, P. et al. Signatures of T cell dysfunction and exclusion predict cancer immunotherapy response. *Nat. Med.* **24**, 1550–1558 (2018).

11. 11.

Jimenez-Sanchez, A., Cast, O. & Miller, M. L. Comprehensive benchmarking and integration of tumor microenvironment cell estimation methods. *Cancer Res.* **79**, 6238–6246 (2019).

12. 12.

Vogel, W. F., Aszodi, A., Alves, F. & Pawson, T. Discoidin domain receptor 1 tyrosine kinase has an essential role in mammary gland development. *Mol. Cell. Biol.* **21**, 2906–2917 (2001).

13. 13.

Takai, K. et al. Discoidin domain receptor 1 (DDR1) ablation promotes tissue fibrosis and hypoxia to induce aggressive basal-like breast cancers. *Genes Dev.* **32**, 244–257 (2018).

14. 14.

Carafoli, F. et al. Structure of the discoidin domain receptor 1 extracellular region bound to an inhibitory Fab fragment reveals features important for signaling. *Structure* **20**, 688–697 (2012).

15. 15.

Vogel, W. F. Ligand-induced shedding of discoidin domain receptor 1. *FEBS Lett.* **514**, 175–180 (2002).

16. 16.

Agarwal, G., Mihai, C. & Iscrum, D. F. Interaction of discoidin domain receptor 1 with collagen type 1. *J. Mol. Biol.* **367**, 443–455 (2007).

17. 17.

Ruggeri, J. M. et al. Discoidin domain receptor 1 (DDR1) is necessary for tissue homeostasis in pancreatic injury and pathogenesis of pancreatic ductal adenocarcinoma. *Am. J. Pathol.* **190**, 1735–1751 (2020).

18. 18.

Ambrogio, C. et al. Combined inhibition of DDR1 and Notch signaling is a therapeutic strategy for KRAS-driven lung adenocarcinoma. *Nat. Med.* **22**, 270–277 (2016).

19. 19.

Salmon, H. et al. Matrix architecture defines the preferential localization and migration of T cells into the stroma of human lung tumors. *J. Cell. Invest.* **122**, 899–910 (2021).

20. 20.

Kaur, A. et al. Remodeling of the collagen matrix in aging skin promotes melanoma metastasis and affects immune cell motility. *Cancer Discov.* **9**, 64–81 (2019).

21. 21.

Ray, A. & Provenzano, P. P. Aligned forces: Origins and mechanisms of cancer dissemination guided by extracellular matrix architecture. *Curr. Opin. Cell Biol.* **72**, 63–71 (2021).

22. 22.

Tomko, L. A. et al. Targeted matrisome analysis identifies thrombospondin-2 and tenascin-C in aligned collagen stroma from invasive breast carcinoma. *Sci. Rep.* **8**, 12941 (2018).

23. 23.

Dunlap, S. M. et al. Dietary energy balance modulates epithelial-to-mesenchymal transition and tumor progression in murine claudin-low

and basal-like mammary tumor models. *Cancer Prev. Res.* **5**, 930–942 (2012).

24. 24.

Mertins, P. et al. Proteogenomics connects somatic mutations to signalling in breast cancer. *Nature* **534**, 55–62 (2016).

25. 25.

Hanzelmann, S., Castelo, R. & Guinney, J. GSVA: gene set variation analysis for microarray and RNA-seq data. *BMC Bioinformatics* **14**, 7 (2013).

26. 26.

Fougner, C., Bergholtz, H., Norum, J. H. & Sorlie, T. Re-definition of claudin-low as a breast cancer phenotype. *Nat. Commun.* **11**, 1787 (2020).

27. 27.

Kim, D. et al. TopHat2: accurate alignment of transcriptomes in the presence of insertions, deletions and gene fusions. *Genome Biol.* **14**, R36 (2013).

28. 28.

Love, M. I., Huber, W. & Anders, S. Moderated estimation of fold change and dispersion for RNA-seq data with DESeq2. *Genome Biol.* **15**, 550 (2014).

29. 29.

Ashburner, M. et al. Gene ontology: tool for the unification of biology. *Nat. Genet.* **25**, 25–29 (2000).

30. 30.

Suzuki, R. & Shimodaira, H. Pvclust: an R package for assessing the uncertainty in hierarchical clustering. *Bioinformatics* **22**, 1540–1542 (2006).

31. 31.

Raudvere, U. et al. gProfiler: a web server for functional enrichment analysis and conversions of gene lists. *Nucleic Acids Res.* **47**, W191–W198 (2019).

32. 32.

Li, T. et al. TIMER2.0 for analysis of tumor-infiltrating immune cells. *Nucleic Acids Res.* **48**, W509–W514 (2020).

33. 33.

Newman, A. M. et al. Determining cell type abundance and expression from bulk tissues with digital cytometry. *Nat. Biotechnol.* **37**, 773–782 (2019).

34. 34.

Erikson, A., Ortegren, J., Hompland, T., de Lange Davies, C. & Lindgren, M. Quantification of the second-order nonlinear susceptibility of collagen I using a laser scanning microscope. *J. Biomed. Opt.* **12**, 044002 (2007).

35. 35.

Wu, B. et al. PPAR γ inhibition boosts efficacy of immune checkpoint immunotherapy against murine melanoma in a sexually dimorphic manner. *Int. J. Biol. Sci.* **16**, 1526–1535 (2020).

36. 36.

Meng, W. et al. Efficient generation of monoclonal antibodies from single rhesus macaque antibody secreting cells. *MAbs* **7**, 707–718 (2015).

37. 37.

Gui, X. et al. Disrupting LILRB4/APOE interaction by an efficacious humanized antibody reverses T-cell suppression and blocks AML development. *Cancer Immunol. Res.* 7, 1244–1257 (2019).

Acknowledgements

We thank S. Hursting for M-Wnt cells, S. Abrams for AT-3 cells, L. Sun for HCC1937 cells, and John R Hawse and Thomas C. Spelsberg for Hs578T cells. We also thank L. Lin for technical assistance in plasmid construction, L. Audoly for discussion, G. T. Salazar for editing the manuscript and X. Zhang for technical assistance with oestrogen receptor and progesterone receptor (ER and PR) immunohistochemistry. The work was supported by grants to R.L. and T.J.C. from the National Institutes of Health (NIH) (CA206529); to R.L. from NIH (CA246707) and the Walter G. Ross Foundation; to T.J.C. from NIH (CA205965) and the Owens Foundation and the Skinner Endowment; to Y.H. from NIH (CA212674); the Congressionally Directed Medical Research Program (W81XWH-17-1-0008); to V.X.J from NIH (GM114142); and to Z.A. from the Cancer Prevention and Research Institute of Texas (RP150551 and RP190561) and the Welch Foundation (AU-0042-20030616). The Genome Sequencing Facility at the UT Health San Antonio is supported by NIH-NCI P30 CA054174 (Mays Cancer Center at UT Health San Antonio), NIH Shared Instrument grant 1S10OD021805-01 (S10 grant), and CPRIT Core Facility Award (RP160732). Georgetown University Medical Center Shared Resources are supported in part by P30 CA051008 (Lombardi Comprehensive Cancer Center Support Grant; Principal Investigator L. Weiner). The ICO-IDIBELL research was supported by the Generalitat de Catalunya (SGR 2017-449; PFI-Salut SLT017-20-000076; and CERCA program) and the Carlos III Institute of Health (ISCIII), funded by FEDER funds ('A way to build Europe'), grants PI18/01029 and PI21/01306.

Author information

Author notes

1. These authors contributed equally: Xiujie Sun, Bogang Wu, Huai-Chin Chiang

Affiliations

1. Department of Biochemistry and Molecular Medicine, School of Medicine and Health Sciences, The George Washington University, Washington, DC, USA

Xiujie Sun, Bogang Wu, Huai-Chin Chiang, Xiaowen Zhang, Madeleine Prevost, Debarati Banik & Rong Li

2. Texas Therapeutics Institute, Brown Foundation Institute of Molecular Medicine, The University of Texas Health Science Center at Houston, Houston, TX, USA

Hui Deng, Wei Xiong, Junquan Liu, Ningyan Zhang & Zhiqiang An

3. Lombardi Comprehensive Cancer Center, Georgetown University Medical Center, Washington, DC, USA

Aaron M. Rozeboom, Brent T. Harris, Claudine Isaacs, Deborah Berry, Catherine Lai & Krysta Chaldekas

4. ProCURE, Catalan Institute of Oncology, Oncobell, Bellvitge Institute for Biomedical Research (IDIBELL), L'Hospitalet del Llobregat, Barcelona, Spain

Eline Blommaert, Roderic Espin Garcia & Miguel Angel Pujana

5. Rheumatology Department and Rheumatology Research Group, Vall d'Hebron Hospital Research Institute, Barcelona, Spain

Antonio Gomez

6. Department of Molecular Medicine, University of Texas Health San Antonio, San Antonio, TX, USA

Yufan Zhou & Victor X. Jin

7. Department of Anatomy and Cell Biology, School of Medicine and Health Sciences, The George Washington University, Washington, DC, USA

Payal Mitra & Yanfen Hu

8. Department of Medicine, The Mays Cancer Center, University of Texas Health San Antonio, San Antonio, TX, USA

Deyi Zhang & Tyler J. Curiel

9. Department of Pathology, School of Medicine and Health Sciences, The George Washington University, Washington, DC, USA

Patricia S. Latham

10. GW Nanofabrication and Imaging Center, The George Washington University, Washington, DC, USA

Christine A. Brantner & Anastas Popratiloff

Contributions

R.L. managed and oversaw the overall project. R.L., X.S., Z.A., T.J.C. and N.Z. designed the experiments and wrote the manuscript. X.S., B.W., H.D., X.Z., H.-C.C., D.Z., W.X., J.L., P.M., D.B., C.I., A.M.R., M.P., D.B., B.H., C.L., K.C., P.S.L., C.A.B. and A.P. performed the experiments. X.S., B.W., M.A.P., E.B., A.G., R.E.G., D.B., C.A.B., X.Z., P.S.L., Y.Z., V.X.J., A.P., Y.H., N.Z., T.J.C., Z.A. and R.L. analysed the data.

Corresponding authors

Correspondence to [Miguel Angel Pujana](#), [Tyler J. Curiel](#), [Zhiqiang An](#) or [Rong Li](#).

Ethics declarations

Competing interests

X.S., H.D., N.Z., Z.A. and R.L. are co-inventors of a pending patent application (62/949,300) filed by the University of Texas Health Science Center at Houston on the anti-DDR1 antibodies described in this manuscript. The University of Texas System and The George Washington University have licensed the patent to Parthenon Therapeutics for drug development. R.L. receives stock option and financial compensation for his role as a member on the Scientific Advisory Board of Parthenon Therapeutics.

Additional information

Peer review information *Nature* thanks Joan Brugge, Shannon Turley and the other, anonymous, reviewers for their contribution to the peer review of this work.

Publisher's note Springer Nature remains neutral with regard to jurisdictional claims in published maps and institutional affiliations.

Extended data figures and tables

[Extended Data Fig. 1 Differential effects of tumour *Ddr1*-KO on tumour growth in vitro and in vivo.](#)

(a) Immunoblotting of DDR1, DDR2 and loading control β-ACTIN in M-Wnt and AT-3 *Ddr1*-WT/KO tumour cells. Images are representatives of three independent experiments. **(b–d)** In vitro cell proliferation of E0771 (WT: n = 3, KO: n = 5, b), M-Wnt (WT: n = 3, KO: n = 5, c) and AT-3 (WT: n = 6, KO: n = 4, d) tumour cells, n indicate technical repeats. Out of three biological repeats. **(e–f)** M-Wnt (n = 4 tumours/group, e) and AT-3 (n = 5 tumours/group, f) tumour growth in immunodeficient mice. **(g–h)** M-Wnt (n = 7 tumours/group, g) and AT-3 (n = 7 tumours/group, h) tumour growth

in immunocompetent C57BL/6 mice. (i–j) M-Wnt and AT-3 tumours were grown firstly in *Rag1*^{−/−} hosts. Approximately 60 mg of tumour pieces were transplanted to C57BL/6 mice. Tumour volume of M-Wnt (WT⁺ n = 9 tumours, KO: n = 10 tumours, i) and AT-3 (WT: n = 10 tumours, KO: n = 9 tumours, j). (k) Percentage of CD8⁺ in CD3⁺ T cells in blood, n = 5 mice/group. (l) Tumour volumes in C57BL/6 hosts with prior treatment of anti-IgG or anti-CD8 antibody (n = 5 tumours/group). (m) CD8⁺ TILs normalized by tumour weight in *Rag1*^{−/−} mice after adoptive transfer of CD8⁺ T cells or medium (sham), n = 6 tumours/group. (n) Tumour volumes in *Rag1*^{−/−} mice after adoptive transfer of CD8⁺ T cells or medium (sham). n = 6 tumours/group. Arrow indicates transfer of CD8⁺ T cells on day 17. (o) Tumour weight from rechallenged mice (n = 6 tumours/group). Values represent mean ± SEM. *p* value and n as indicated, all tests used two-way ANOVA except for CD8⁺ quantification, which used two-tailed Student's t-test.

[Source data](#)

Extended Data Fig. 2 Immunophenotyping of *Ddr1*-WT and *Ddr1*-KO tumours.

(a–d) TIL number normalized by E0771 *Ddr1*-WT/KO tumour weight/gram. Cell number of CD44^{hi} CD62L^{lo} CD8⁺ (a) and CD44^{hi} CD62L^{lo} CD4⁺ (b) IFN γ ⁺ CD8⁺ (c) and IFN γ ⁺ CD4⁺ (d) T cells. WT/KO: n = 5 tumours/group. (e–p) TIL numbers normalized by tumour weight of M-Wnt (n = 4 tumours/group, e–j) and AT-3 tumours (n = 5 tumours/group, k–p). (q–t) Percentages of T cells from E0771 *Ddr1*-WT and KO tumours (n = 5 tumours/group) positive for Ki67 (CD4⁺ in q and CD8⁺ in r), IFN γ (CD8⁺ in s) or GZMB (CD8⁺ in t). n.s. not significant. Values represent mean ± SEM. *p* value as indicated, two-tailed Student's t-test.

[Source data](#)

Extended Data Fig. 3 Correlation between DDR1 and immune markers in human breast cancer.

(a) Representative images of CD8⁺ T cell staining at E0771 tumour margin and in the tumour core (bottom panels). **(b, c)** Representative images (b) and quantification (c) of CD8⁺ T cell IHC at M-Wnt tumour margin and core (WT: n = 8 tumours, KO: n = 4 tumours). **(d, e)** Representative images (d) and quantification (e) of CD8⁺ T cell IHC at AT-3 tumour margin and core (n = 5 tumours/group). Images in (a), (b), and (d) showing tumour margin at top panel (tumour boarder denoted by red dash lines) and tumour core at bottom panel. Box areas at higher magnification are shown in the upper right inlets. Red arrow heads indicate CD8⁺ cells. The y-axis in (c) and (e) refers to percent of CD8⁺ cells over total cells in a given field. Scale bar: 100 μm and 10 μm in inlets. Two-tailed Student's t-test. **(f–g)** Correlation between DDR1 mRNA levels and overall survival of all patients with breast cancer (f) and patients with TNBC (g) in the Kaplan-Meier Plotter database (<https://kmplot.com/analysis/>). **(h–j)** Scatter plots showing the negative gene expression (Z-score) correlation between *DDR1* mRNA levels and *GZMB* (h), *IFNG* (i), and *PRF1* (j) in TCGA TNBC tumours (n = 162). The corresponding Spearman's correlation coefficients and p values are shown. **(k–n)** Correlation of *DDR1* mRNA levels and anti-tumour immune markers in 37 samples from patients with TNBC (GSE88847). **(o)** Scatter plot showing the negative gene expression correlation between *DDR1* mRNA levels and signature for accumulation of T cells in tumours using TCGA TNBC tumour data. **(p)** Scatter plots showing the negative expression correlation between DDR1 protein expression and cytolytic effector pathway in CPTAC BRCA. **(q)** Correlation between percentages of CD8⁺ immune cells and DDR1⁺ tumour cells in a TNBC cohort (n = 12). **(r)** Correlation between percentages of CD8⁺ immune cells and DDR1⁺ tumour cells in a DDR1^{high} (n = 7) and DDR1^{low} (n = 5) TNBC samples. **(s)** Patient numbers of immune-excluded (n = 4) and non-immune-excluded (n = 6) in DDR1^{high} and DDR1^{low} group. Only the 10 patient samples with paired margin and core information were used for the immune exclusion calculation in Extended Data Fig. 3s, two-sided Chi-square test.

[Source data](#)

[**Extended Data Fig. 4 DDR1 dependent transcriptomic changes.**](#)

(a) Quantification of αCD31 IHC of WT and KO tumours transplanted from *Rag1*^{-/-} to C57BL/6 hosts (n = 6 tumours; n.s., not significant). Data are presented as mean values +/- SEM. Two-tailed Student's t-test **(b)** Comparison of non-synonymous tumour mutational burden between *Ddr1*-WT (n = 4 tumours) and KO tumours (n = 5 tumours, n.s., not significant). Data are presented as mean values +/- SEM. Two-tailed Student's t-test **(c)** Venn diagram showing the numbers of DEGs in each *Ddr1*-KO-WT comparison and the identity overlaps between them. The pairwise overlap significance is indicated. The GO terms overrepresented (FDR-adjusted $p < 0.05$ relative to mouse genome background) in the overlapping sets are shown; the genes corresponding to each annotation are also indicated.

Source data

Extended Data Fig. 5 Mutational and biochemical analysis of DDR1-ECD in vitro and in vivo.

(a) Diagram of full-length (FL) DDR1 (top) and tumour curves of either E0771 *Ddr1*-WT or KO tumour cells carrying various DDR1 expression vectors: empty vector (EV), FL, deletion of the kinase domain (ΔKD), and extracellular domain (ECD) only. All p values were compared to KO + EV group. TM: transmembrane domain. WT: n = 9 tumours, KO+EV: n = 10 tumours, KO+FL: n = 10 tumours, KO+ ΔKD: n = 6 tumours, KO+ECD: n = 5 tumours. **(b)** Crystal structure of mouse DDR1 collagen-binding domain, generated by Jmol software (<http://www.jmol.org/>). Amino acid residues targeted in the mutational analysis are shown. **(c)** Immunoblots of Flag-tagged mouse WT DDR1-ECD and point mutants ectopically expressed in M-Wnt tumour cells, with GAPDH as the loading control. Images are representatives from three independent experiments. **(d)** Immunoblots of Flag-tagged mouse WT DDR1-ECD and point mutants ectopically expressed in AT-3 tumour cells, with GAPDH as the loading control. Images are representatives from three independent experiments. **(e-f)** Growth curves of M-Wnt (e) and AT-3 (f) *Ddr1*-KO tumours with ectopically expressed mouse WT DDR1-ECD or collagen-binding point mutants. The numbers in parenthesis indicate outgrowing tumours (larger than 100 mm³) versus total injected. **(g, h)** Immunoblots of full-length DDR1 in cells and soluble ECD in conditioned medium from various

mouse (g) and triple-negative human breast cancer cell lines plus ER-positive MCF7 (h). Images are representatives from three independent experiments. (i) Coomassie staining of recombinant Fc-ECD under non-reducing and reducing conditions. (j) Rescue of *Ddr1*-KO E0771 tumour growth in immunocompetent hosts by recombinant Fc-ECD versus PBS vehicle (n = 6 tumours/group). (k) Diagram of the Transwell assay for CD8⁺ T cell migration. Primary CD8⁺ T cells were loaded in the upper chamber that had been pre-seeded with decellularized ECM derived from tumour cells. The lower chamber contained medium with or without CCL21. (l) CD8⁺ T cells in vitro migration activity was abrogated by decellularized ECM from AT-3 tumour cells in a DDR1-dependent manner. Value of migrated CD8⁺ T cell number without ECM and CCL12 is set at “1” (lanes 1 and 2: n = 3; lanes 3 and 4: n = 7), n refers to technical repeats. Values represent mean ± SEM. *p* value as indicated, two-tailed Student’s t-test for all tests except for tumour volumes, which were done by two-way ANOVA.

[Source data](#)

[Extended Data Fig. 6 SHG microscopy of *Ddr1*-WT and *Ddr1*-KO tumours.](#)

(a) E0771 *Ddr1*-WT/KO tumours transplanted from *Rag1*^{−/−} to C57BL/6 hosts were analysed by SHG, To-pro-3 staining for all nuclei, and collagen fibre individualization. Scale bar: 50 μm. (b, c) M-Wnt (WT n = 8 tumours, KO n = 4 tumours) and AT-3 (n = 5 tumours/group) *Ddr1*-WT/KO tumours transplanted from *Rag1*^{−/−} to C57BL/6 hosts were analysed for infiltrating CD3⁺ T cells normalized by total cells via IHC. (d–g) M-Wnt and AT-3 *Ddr1*-WT/KO tumours transplanted from *Rag1*^{−/−} to C57BL/6 hosts were analysed for collagen fibre alignment (d, e) and fibre length (f, g), n = 4 tumours/group. (h–j) E0771, n = 5 tumours/group (h), M-Wnt, n = 4 tumours/group (i) and AT-3, n = 4/group (j) *Ddr1*-WT/KO tumours transplanted from *Rag1*^{−/−} to C57BL/6 hosts were analysed for fibre numbers by the CT-Fire software. (k–m) E0771 *Ddr1*-WT/KO tumours (WT n = 10 tumours, KO n = 8 tumours) from immunodeficient *Rag1*^{−/−} hosts were analysed for collagen fibre alignment (k), fibre length (l) and

fibre numbers (m) by the CT-Fire software. **(n)** Growth curves of E0771 *Ddr1*-KO tumours in immunocompetent hosts that were intratumorally injected with recombinant WT and mutant Fc-ECD (WT: n = 10 tumours, W54A: n = 9 tumours). **(o)** Representative images of E0771 *Ddr1*-KO tumours treated with recombinant WT or mutant Fc-ECD in C57BL/6 hosts as analysed by SHG, To-pro-3 staining, and collagen fibre individualization. Scale bar: 50 µm. **(p)** Quantification of collagen fibre alignment in WT and mutant Fc-ECD treated tumours (n = 5 tumours/group). **(q)** Enumeration of infiltrating CD3⁺ T cells normalized by total cells via IHC (WT: n = 4 tumours, KO: n = 3 tumours). Values represent mean ± SEM. *p* value as indicated, two-tailed Student's t-test for all tests except for tumour volumes, which were done by two-way ANOVA.

[Source data](#)

[Extended Data Fig. 7 Screening for huDDR1-neutralizing antibodies.](#)

(a) Immunoblots of ectopic human (hu) DDR1 and endogenous mouse DDR1 in cell lysates and medium of E0771-derived cells. **(b)** Tumour growth curve of E0771-derived *Ddr1*-WT, KO+EV, KO+huDDR1 cells (n = 7 tumours/group). **(c)** Transwell migration assay for purified CD8⁺ T cells in the presence of conditioned medium from E0771 cells containing endogenous WT DDR1, *Ddr1*-KO, or *Ddr1*-KO and ectopic expression of huDDR1 (n = 3 technical repeats). Value of migrated CD8⁺ T cell number with parental E0771-conditioned medium is set at “1”. **(d)** Quantification of CD8⁺ T cell migration in the presence of DDR1-neutralizing antibodies, using conditioned medium from E0771 *Ddr1*-KO or KO+huDDR1 cells (IgG: n = 4, #3, #9, #14, #33; n = 2, technical repeats). Control: isotype IgG; anti-DDR1 antibody: #3, #9, #14, and #33. Value of migrated CD8⁺ T cell number in the far-left column is set at “1”. **(e)** Tumour curves treated with control IgG, #3, #9, #14, and #33 (n = 8 tumours/group). Antibody administration started when tumour volume reached approximately 100 mm³. All *p* values were compared to the control IgG group and *p* value as indicated. **(f)** Tumours host survival curves of E0771 *Ddr1*-KO tumour cells with ectopically expressed human (hu) DDR1 in C57BL/6 hosts

treated intratumorally with isotype IgG (Ctrl, n = 17, tumours) or anti-DDR1 antibody #9 (n = 18, tumours). (g) Host body weight treated with control IgG, #3, #9, #14, and #33 (Ctrl n = 4 mice, #3, #9, #14, and #33 n = 4 mice/group). Antibody administration started when tumour volume reached approximately 100 mm³. Data are presented as mean values +/– SEM. (h, i) E0771 KO+huDDR1 tumours in C57BL/6 (n = 8 tumours/group, h) and *Rag1*^{−/−} hosts (n = 6 tumours/group, i) treated with either isotype IgG or anti-DDR1 #33 antibody. (j, k) Tumour volume (j) and survival curve (k) of M-Wnt KO+huDDR1 tumours in C57BL/6 mice treated with isotype IgG and anti-DDR1 antibody #9 (n = 10, tumours/group). (l, m) Tumour growth (l) and survival percentage (m) of AT-3 KO+huDDR1 tumours in C57BL/6 mice treated with isotype IgG and anti-DDR1 antibody #3 (n = 10, tumours/group). Values represent mean ± SEM. *p* value as indicated. Tumour volumes were examined by two-way ANOVA; survival analysis was examined by log-rank (Mantel–Cox) test, and migration assay were examined by two-tailed Student’s t-test.

[Source data](#)

[Extended Data Fig. 8 DDR1 antibody treatment inhibits spontaneous mammary tumour growth.](#)

(a–b) Binding affinity of all four anti-ECD antibody clones for human (a) and mouse (b) DDR1. (c–d) Spontaneous MMTV-PyMT body weight of C57BL/6 hosts treated with control or #9 in the pre-tumour (from 11 weeks old, control: n = 7 mice, #9: n = 8 mice, c) and post-tumour groups (control n = 7 mice, #9 n = 8 mice, d). Data are presented as mean values +/– SEM. (e) Tumour incidence (percentage of tumour-bearing mammary glands per mouse, in MMTV-PyMT spontaneous mammary tumour model of C57BL/6 genetic background, treated in a “post-tumour” scheme with Ctrl (n = 7 mice) or anti-DDR1 #9 antibody (n = 8 mice). Data are presented as mean values + SEM. (f, g) Spontaneous MMTV-PyMT tumour growth in C57BL/6 hosts (accumulative tumour volume per mouse, f) and incidence percentage (per mouse, g) with pre-tumour treatment (control: n = 7 mice, #9: n = 8 mice). Data are presented as mean values +/– SEM. (h, i) Spontaneous MMTV-PyMT tumour growth (accumulative tumour volume per mouse) in FVB hosts treated with control or #9 before tumour growth

(from 5 to 7 weeks old, h) and post-tumour groups (i). control: n = 7 mice, #9: n = 8 mice, n.s. not significant. Two-way ANOVA were used for all tests.

[Source data](#)

Extended Data Fig. 9 DDR1 antibody boosts the infiltration of anti-tumour immune cells.

(a–d) Indicated TIL numbers normalized by tumour weight in E0771 KO+huDDR1 tumours from C57BL/6 mice treated with control and anti-DDR1 antibody #9 (n = 4 tumours/group). **(e–h)** Percentage of Ki67-positive cells in CD4⁺, CD8⁺ T cells and percentage of IFN γ - or GZMB-positive cells in CD8⁺ T cells from the same antibody-treated mice as in **(a–d)** (n = 4 tumours/group). n.s. not significant. **(i)** Representative images of transplanted mammary tumours treated with Ctrl or anti-DDR1 #9 antibody, analysed by SHG, To-pro-3 staining, and collagen fibre individualization. Scale bar: 50 μ m. **(j)** Quantification of CD8⁺ T cells in tumour margin and core in control and anti-DDR1 antibody-treated E0771 KO+huDDR1 tumours (Ctrl: n = 8 tumours, #9: n = 9 tumours). **(k, l)** TILs from spontaneous mammary tumours (C57B/6) treated with Ctrl or anti-DDR1 #9 antibody under the pre-tumour **(k)** and post-tumour **(l)** conditions. n = 6 tumours/group. **(m, n)** Representative IHC images of CD3⁺ and CD8⁺ T cells in tumour margin and core in control and anti-DDR1 antibody-treated E0771 KO+huDDR1 tumours. Tumour boarder denoted by red dash lines. Box areas at higher magnification are shown in the inlets. Red arrow heads indicate CD8⁺ cells. Scale bar: 100 μ m and 10 μ m in inlet. **(o)** Representative images of tumours from the post-tumour treatment group, analysed by SHG, To-pro-3 staining, and collagen fibre individualization. Scale bar: 50 μ m. **(p)** Quantification of tumour fibre alignment in pre- and post-tumour treatment in C57BL/6 hosts (n = 5 tumours/group). Values represent mean \pm SEM. *p* value as indicated, two-tailed Student's t-test.

[Source data](#)

Extended Data Fig. 10 DDR1-related clinical correlation in cancers.

(a–d) Kaplan–Meier curves showing disease specific survival (DSS) rates for TCGA patients with breast cancer divided by major tumour subtypes: basal-like **(a)**, HER2 positive **(b)**, luminal A **(c)**, and luminal B **(d)**. Each subtype is further divided in four patient groups according to the tumour expression levels of the *DDR1* gene and collagen-alignment signature. The gene/signature classification in high and low expression was based on their corresponding average expression values. The log-rank test *p* value and the number of individuals at risk at different follow-up times are shown in each tumour subtype analysis. **(e)** Correlation between human *DDR1* and *GZMB* mRNA expression in various cancer types.

Supplementary information

Supplementary Information

This file contains Supplementary Figures 1–14 and their accompanying legends.

Reporting Summary

Supplementary Table 1

Most variable gene expression and associated GO terms.

Supplementary Table 2

DEGs between *Ddr1*-KO and *Ddr1*-WT tumours.

Supplementary Table 3

Cell types and differences between *Ddr1*-KO and *Ddr1*-WT tumours in immunocompetent host.

Source data

[**Source Data Fig. 1**](#)

[**Source Data Fig. 2**](#)

[**Source Data Fig. 3**](#)

[**Source Data Fig. 4**](#)

[**Source Data Extended Data Fig. 1**](#)

[**Source Data Extended Data Fig. 2**](#)

[**Source Data Extended Data Fig. 3**](#)

[**Source Data Extended Data Fig. 4**](#)

[**Source Data Extended Data Fig. 5**](#)

[**Source Data Extended Data Fig. 6**](#)

[**Source Data Extended Data Fig. 7**](#)

[**Source Data Extended Data Fig. 8**](#)

[**Source Data Extended Data Fig. 9**](#)

Rights and permissions

[**Reprints and Permissions**](#)

About this article

Cite this article

Sun, X., Wu, B., Chiang, HC. *et al.* Tumour DDR1 promotes collagen fibre alignment to instigate immune exclusion. *Nature* **599**, 673–678 (2021). <https://doi.org/10.1038/s41586-021-04057-2>

- Received: 18 October 2019
- Accepted: 22 September 2021
- Published: 03 November 2021
- Issue Date: 25 November 2021
- DOI: <https://doi.org/10.1038/s41586-021-04057-2>

Share this article

Anyone you share the following link with will be able to read this content:

[Get shareable link](#)

Sorry, a shareable link is not currently available for this article.

[Copy to clipboard](#)

Provided by the Springer Nature SharedIt content-sharing initiative

This article was downloaded by **calibre** from <https://www.nature.com/articles/s41586-021-04057-2>

- Article
- [Published: 10 November 2021](#)

Diverse alterations associated with resistance to KRAS(G12C) inhibition

- [Yulei Zhao¹](#)^{nal},
- [Yonina R. Murciano-Goroff²](#)^{nal},
- [Jenny Y. Xue^{1,3}](#)^{nal},
- [Agnes Ang⁴](#)^{nal},
- [Jessica Lucas](#) [ORCID: orcid.org/0000-0002-6462-7975¹](#),
- [Trang T. Mai¹](#),
- [Arnaud F. Da Cruz Paula⁵](#),
- [Anne Y. Saiki](#) [ORCID: orcid.org/0000-0003-3913-1860⁴](#),
- [Deanna Mohn⁴](#),
- [Pragathi Achanta⁴](#),
- [Ann E. Sisk²](#),
- [Kanika S. Arora^{5,6}](#),
- [Rohan S. Roy³](#),
- [Dongsung Kim¹](#),
- [Chuanchuan Li¹](#),
- [Lee P. Lim⁷](#),
- [Mark Li⁷](#),
- [Amber Bahr⁸](#),
- [Brian R. Loomis](#) [ORCID: orcid.org/0000-0002-1863-1199^{5,6}](#),
- [Elisa de Stanchina⁸](#),
- [Jorge S. Reis-Filho](#) [ORCID: orcid.org/0000-0001-9927-1270⁵](#),
- [Britta Weigelt](#) [ORCID: orcid.org/0000-0003-2969-3173⁵](#),
- [Michael Berger](#) [ORCID: orcid.org/0000-0003-3882-5000^{5,6}](#),

- [Gregory Riely²](#),
- [Kathryn C. Arbour²](#),
- [J. Russell Lipford^{4 na2}](#),
- [Bob T. Li](#) [ORCID: orcid.org/0000-0001-6661-8733^{2 na2}](#) &
- [Piro Lito](#) [ORCID: orcid.org/0000-0003-2196-3503^{1,2,3,9 na2}](#)

[Nature](#) volume **599**, pages 679–683 (2021)

- 10k Accesses
- 398 Altmetric
- [Metrics details](#)

Subjects

- [Cancer therapeutic resistance](#)
- [Non-small-cell lung cancer](#)
- [Targeted therapies](#)

Abstract

Inactive state-selective KRAS(G12C) inhibitors^{1,2,3,4,5,6,7,8} demonstrate a 30–40% response rate and result in approximately 6-month median progression-free survival in patients with lung cancer⁹. The genetic basis for resistance to these first-in-class mutant GTPase inhibitors remains under investigation. Here we evaluated matched pre-treatment and post-treatment specimens from 43 patients treated with the KRAS(G12C) inhibitor sotorasib. Multiple treatment-emergent alterations were observed across 27 patients, including alterations in *KRAS*, *NRAS*, *BRAF*, *EGFR*, *FGFR2*, *MYC* and other genes. In preclinical patient-derived xenograft and cell line models, resistance to KRAS(G12C) inhibition was associated with low allele frequency hotspot mutations in KRAS(G12V or G13D), NRAS(Q61K or G13R), MRAS(Q71R) and/or BRAF(G596R), mirroring observations in patients. Single-cell sequencing in an isogenic lineage identified secondary RAS and/or BRAF mutations in the same cells as

KRAS(G12C), where they bypassed inhibition without affecting target inactivation. Genetic or pharmacological targeting of ERK signalling intermediates enhanced the antiproliferative effect of G12C inhibitor treatment in models with acquired RAS or BRAF mutations. Our study thus suggests a heterogenous pattern of resistance with multiple subclonal events emerging during G12C inhibitor treatment. A subset of patients in our cohort acquired oncogenic KRAS, NRAS or BRAF mutations, and resistance in this setting may be delayed by co-targeting of ERK signalling intermediates. These findings merit broader evaluation in prospective clinical trials.

Access options

Subscribe to Journal

Get full journal access for 1 year

\$199.00

only \$3.90 per issue

[Subscribe](#)

All prices are NET prices.

VAT will be added later in the checkout.

Tax calculation will be finalised during checkout.

Rent or Buy article

Get time limited or full article access on ReadCube.

from \$8.99

[Rent or Buy](#)

All prices are NET prices.

Additional access options:

- [Log in](#)
- [Access through your institution](#)
- [Learn about institutional subscriptions](#)

Fig. 1: Genetic alterations associated with resistance to sotorasib treatment.



Fig. 2: Treatment-emergent alterations in preclinical models.

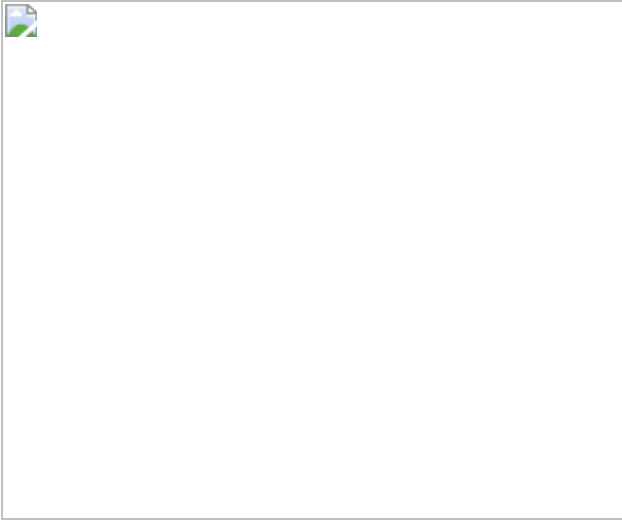


Fig. 3: Temporal tracking of treatment-emergent alterations.



Fig. 4: Effect of co-targeting ERK signalling intermediates.





Data availability

The data supporting the findings of this study are available within the paper and its supplementary information files. The data have been deposited in the Sequence Read Archive ([PRJNA756044](#)). Genomic and associated clinical data for patients are available in cBioPortal for Cancer Genomics at <http://cbioportal.org/msk-impact> and/or may be requested by qualified researchers from Amgen clinical studies. Complete details are available at: <http://www.amgen.com/datasharing>. Materials, reagents or other experimental data are available upon reasonable request from the corresponding author. [Source data](#) are provided with this paper.

Code availability

The analysis was performed using standard protocols with previously described computational tools. No custom code was used in this study.

References

1. 1.

Ostrem, J. M., Peters, U., Sos, M. L., Wells, J. A. & Shokat, K. M. K-Ras(G12C) inhibitors allosterically control GTP affinity and effector interactions. *Nature* **503**, 548–551 (2013).

2. 2.

Lito, P., Solomon, M., Li, L. S., Hansen, R. & Rosen, N. Allele-specific inhibitors inactivate mutant KRAS G12C by a trapping mechanism. *Science* **351**, 604–608 (2016).

3. 3.

Patricelli, M. P. et al. Selective inhibition of oncogenic KRAS output with small molecules targeting the inactive state. *Cancer Discov.* **6**, 316–329 (2016).

4. 4.

Janes, M. R. et al. Targeting KRAS mutant cancers with a covalent G12C-specific inhibitor. *Cell* **172**, 578–589.e17 (2018).

5. 5.

Canon, J. et al. The clinical KRAS(G12C) inhibitor AMG 510 drives anti-tumour immunity. *Nature* **575**, 217–223 (2019).

6. 6.

Hallin, J. et al. The KRAS(G12C) inhibitor MRTX849 provides insight toward therapeutic susceptibility of KRAS-mutant cancers in mouse models and patients. *Cancer Discov.* **10**, 54–71 (2020).

7. 7.

Kim, D., Xue, J. Y. & Lito, P. Targeting KRAS(G12C): from inhibitory mechanism to modulation of antitumor effects in patients. *Cell* **183**, 850–859 (2020).

8. 8.

Xue, J. Y. et al. Rapid non-uniform adaptation to conformation-specific KRAS(G12C) inhibition. *Nature* **577**, 421–425 (2020).

9. 9.

Hong, D. S. et al. KRAS(G12C) inhibition with sotorasib in advanced solid tumors. *N. Engl. J. Med.* **383**, 1207–1217 (2020).

10. 10.

Pylayeva-Gupta, Y., Grabocka, E. & Bar-Sagi, D. RAS oncogenes: weaving a tumorigenic web. *Nat. Rev. Cancer* **11**, 761–774 (2011).

11. 11.

Simanshu, D. K., Nissley, D. V. & McCormick, F. RAS proteins and their regulators in human disease. *Cell* **170**, 17–33 (2017).

12. 12.

Karoulia, Z., Gavathiotis, E. & Poulikakos, P. I. New perspectives for targeting RAF kinase in human cancer. *Nat. Rev. Cancer* **17**, 676–691 (2017).

13. 13.

Riely, G. J. et al. Frequency and distinctive spectrum of KRAS mutations in never smokers with lung adenocarcinoma. *Clin. Cancer Res.* **14**, 5731–5734 (2008).

14. 14.

Cancer Genome Atlas Research Network. Comprehensive molecular profiling of lung adenocarcinoma. *Nature* **511**, 543-550 (2014).

15. 15.

Riely, G. J. et al. 99O_PR KRYSTAL-1: activity and preliminary pharmacodynamic (PD) analysis of adagrasib (MRTX849) in patients (Pts) with advanced non-small cell lung cancer (NSCLC) harboring KRASG12C mutation. *J. Thoracic Oncol.* **16**, S751–S752 (2020).

16. 16.

Misale, S. et al. KRAS G12C NSCLC models are sensitive to direct targeting of KRAS in combination with PI3K inhibition. *Clin. Cancer Res.* **25**, 796–807 (2019).

17. 17.

Boned Del Rio, I. et al. SHOC2 complex-driven RAF dimerization selectively contributes to ERK pathway dynamics. *Proc. Natl Acad. Sci. USA* **116**, 13330–13339 (2019).

18. 18.

Jones, G. G. et al. SHOC2 phosphatase-dependent RAF dimerization mediates resistance to MEK inhibition in RAS-mutant cancers. *Nat. Commun.* **10**, 2532 (2019).

19. 19.

Wohlhieter, C. A. et al. Concurrent mutations in STK11 and KEAP1 promote ferroptosis protection and SCD1 dependence in lung cancer. *Cell Rep.* **33**, 108444 (2020).

20. 20.

Gao, Y. et al. V211D mutation in MEK1 causes resistance to MEK inhibitors in colon cancer. *Cancer Discov.* **9**, 1182–1191 (2019).

21. 21.

Miles, L. A. et al. Single-cell mutation analysis of clonal evolution in myeloid malignancies. *Nature* **587**, 477–482 (2020).

22. 22.

Pellegrino, M. et al. High-throughput single-cell DNA sequencing of acute myeloid leukemia tumors with droplet microfluidics. *Genome Res.* **28**, 1345–1352 (2018).

23. 23.

Bolger, A. M., Lohse, M. & Usadel, B. Trimmomatic: a flexible trimmer for Illumina sequence data. *Bioinformatics* **30**, 2114–2120 (2014).

24. 24.

Langmead, B., Trapnell, C., Pop, M. & Salzberg, S. L. Ultrafast and memory-efficient alignment of short DNA sequences to the human genome. *Genome Biol.* **10**, R25 (2009).

25. 25.

Kim, D. et al. TopHat2: accurate alignment of transcriptomes in the presence of insertions, deletions and gene fusions. *Genome Biol.* **14**, R36 (2013).

26. 26.

Li, H. et al. The Sequence Alignment/Map format and SAMtools. *Bioinformatics* **25**, 2078–2079 (2009).

27. 27.

McKenna, A. et al. The Genome Analysis Toolkit: a MapReduce framework for analyzing next-generation DNA sequencing data. *Genome Res.* **20**, 1297–1303 (2010).

28. 28.

Cheng, D. T. et al. Memorial Sloan Kettering-Integrated Mutation Profiling of Actionable Cancer Targets (MSK-IMPACT): a hybridization capture-based next-generation sequencing clinical assay for solid tumor molecular oncology. *J. Mol. Diagn.* **17**, 251–264 (2015).

29. 29.

Zehir, A. et al. Mutational landscape of metastatic cancer revealed from prospective clinical sequencing of 10,000 patients. *Nat. Med.* **23**, 703–713 (2017).

30. 30.

Xue, Y. et al. An approach to suppress the evolution of resistance in BRAF(V600E)-mutant cancer. *Nat. Med.* **23**, 929–937 (2017).

Acknowledgements

We thank M. Mroczkowski for her insight on the manuscript. We also thank C. Rudin for providing *STK11* and *KEAP1* knockout cells and G. Caponigro for providing LXH254. P.L. is supported in part by the NIH/NCI (1R01CA23074501 and 1R01CA23026701A1), the Pew Charitable Trusts, the Damon Runyon Cancer Research Foundation and the American Lung Association. Y.Z. is supported in part by the Charles H. Revson Senior Fellowship in Biomedical Science (21-31). J.Y.X. is supported in part by the NRSA F30 program (1F30CA232549-01). E.d.S. is supported in part by the MSKCC Pilot Center for Precision Disease Modeling program (U54 OD020355). K.C.A. is supported in part by a Career Development Award from the LUNGevity foundation. J.S.R.-F. is supported in part by the Breast Cancer Research Foundation and Gerald Leigh Charitable Trust. B.W. is supported in part by Cycle for Survival and Breast Cancer Research Foundation grants. J.R.-F. and B.W. are supported in part by the NIH/NCI P50 CA247749 01 grant. Y.R.M.-G. is supported by a Young Investigator Award from Conquer Cancer from the ASCO Foundation and has received training through an institutional K30 grant (CTSA UL1TR00457). We acknowledge the Josie Robertson Investigator Program at MSKCC, a Medical Scientist Training Program grant to the Weill Cornell–Rockefeller–Sloan Kettering Tri-Institutional MD-PhD Program (T32GM007739) and the MSKCC Support Grant-Core Grant program (P30 CA008748). We also acknowledge the use of the Integrated Genomics Operation Core, funded by the NCI Cancer Center Support Grant (P30 CA08748), Cycle for Survival, and the Marie-Josée and Henry R. Kravis Center for Molecular Oncology. Clinical study funding was provided by Amgen Inc.

Author information

Author notes

1. These authors contributed equally: Yulei Zhao, Yonina R. Murciano-Goroff, Jenny Y. Xue, Agnes Ang

2. These authors jointly supervised this work: J. Russell Lipford, Bob T. Li, Piro Lito

Affiliations

1. Human Oncology and Pathogenesis Program, Memorial Sloan Kettering Cancer, New York, NY, USA

Yulei Zhao, Jenny Y. Xue, Jessica Lucas, Trang T. Mai, Dongsung Kim, Chuanchuan Li & Piro Lito

2. Department of Medicine, Memorial Sloan Kettering Cancer Center, New York, NY, USA

Yonina R. Murciano-Goroff, Ann E. Sisk, Gregory Riely, Kathryn C. Arbour, Bob T. Li & Piro Lito

3. Weill Cornell–Rockefeller–Sloan Kettering Tri-Institutional MD-PhD Program, New York, NY, USA

Jenny Y. Xue, Rohan S. Roy & Piro Lito

4. Amgen, Thousand Oaks, CA, USA

Agnes Ang, Anne Y. Saiki, Deanna Mohn, Pragathi Achanta & J. Russell Lipford

5. Department of Pathology, Memorial Sloan Kettering Cancer Center, New York, NY, USA

Arnaud F. Da Cruz Paula, Kanika S. Arora, Brian R. Loomis, Jorge S. Reis-Filho, Britta Weigelt & Michael Berger

6. Center for Molecular Oncology, Memorial Sloan Kettering Cancer Center, New York, NY, USA

Kanika S. Arora, Brian R. Loomis & Michael Berger

7. Resolution Bioscience, Kirkland, WA, USA

Lee P. Lim & Mark Li

8. Antitumor Assessment Core Facility, Memorial Sloan Kettering Cancer Center, New York, NY, USA

Amber Bahr & Elisa de Stanchina

9. Department of Medicine, Weill Cornell Medical College, New York, NY, USA

Piro Lito

Contributions

Y.Z., Y.R.M.-G., J.Y.X., A.A., J.R.L., B.T.L. and P.L. designed the study and analysed the data. Y.Z., J.Y.X, J.L., T.T.M., R.S.R., D.K. and C.L. performed the experiments and/or provided key scientific input. A.B. and E.d.S. helped perform in vivo studies. Y.R.M.-G., K.C.A., A.E.S., G.R. and B.T.L. helped to identify clinical specimens and carried out chart review for emergent alterations. A.A. and J.R.L. helped to carry out review of the clinical trial repository to identify emergent alterations. A.Y.S., D.M., P.A. and J.R.L. performed data collection and analysis. A.F.D.C.P., B.W. and J.S.R.-F. helped to carry out single-cell DNA sequencing. K.S.A., B.R.L. and M.B. helped to carry out bulk sequencing studies and data analysis. Y.Z., Y.R.M.-G., J.Y.X., A.A. and P.L. were the main writers of the manuscript. All other authors reviewed the manuscript and contributed to writing it.

Corresponding author

Correspondence to [Piro Lito](#).

Ethics declarations

Competing interests

P.L. reports grants to his institution from Amgen, Mirati, Revolution Medicines, Boehringer Ingelheim and Virtec Pharmaceuticals; is listed as an inventor on patents filed by MSKCC on the treatment of BRAF-mutant or KRAS-mutant cancers; and reports consulting fees from Black Diamond Therapeutics, AmMax Bio, Repare Therapeutics and compensated scientific advisory board activity in Revolution Medicines and Boehringer Ingelheim. J.S.R.-F. reports receiving personal/consultancy fees from Goldman Sachs, REPARSE Therapeutics, Paige.AI and Eli Lilly; holds membership of the scientific advisory boards of VolitionRx, REPARSE Therapeutics and Paige.AI, membership of the Board of Directors of Grupo Oncoclinicas, and ad hoc membership of the scientific advisory boards of Roche Tissue Diagnostics, Ventana Medical Systems, Novartis, Genentech and InVicro, outside the scope of this study; and owns Paige.AI and REPARSE Therapeutic stocks. Y.R.M.-G. received support for travel, accommodation and expenses from AstraZeneca. M.B. reports consulting fees from Roche and Eli Lilly. A.A., A.S., D.M., P.A. and J.R.L. are employees and shareholders of Amgen Inc. All other authors declare no competing interests.

Additional information

Peer review information *Nature* thanks the anonymous reviewers for their contribution to the peer review of this work.

Publisher's note Springer Nature remains neutral with regard to jurisdictional claims in published maps and institutional affiliations.

Extended data figures and tables

[Extended Data Fig. 1 Characteristics of patients with lung cancer with an exceptional response to sotorasib treatment.](#)

a, Percent of patients with baseline alterations in the indicated genes. No significant differences by Fisher exact test. **b**, *KRAS(G12C)* allele frequency in baseline plasma specimens. **c**, As in **b** but only patients with available archival/baseline tissue are plotted. **d**, Baseline tumour burden, as

determined by the sum of the longest diameter in RECIST target lesions. Two tailed p values from Mann-Whitney tests are shown in **b–d**. The lines denote median values. In **a**, **b** and **d**: n = 8 (CR/LTR) and n = 28 (Other) patients, whereas in **c**: n = 5 (CR/LTR) and n = 8 (Other) patients.

[Source data](#)

Extended Data Fig. 2 Treatment-emergent alterations in patient-derived xenograft models.

a, PDX-bearing mice were treated with sotorasib (100 mpk, Lu1, Lu10), adagrasib (100 mpk, Lu3, Lu7, Re1, Co1) or MRTX1257 (50 mpk, Lu36, Lu69). The dotted line represents a tumour size of ~500 mm³, which was used to determine latency (n = 4, mean ± s.e.m.). **b**, Characteristics of patient derived xenograft models. **c**, **d**, VAFs or estimated copy numbers for the indicated variants (**c**) or genes (**d**). A large number of mutations were identified in Lu36, including several BRAF alterations. Re1 had a baseline *BRAF(E26D)* variant, which has been reported as germline. See Supplementary Data [3](#) for a complete list of alterations.

[Source data](#)

Extended Data Fig. 3 Characterization of cell lines with acquired G12Ci resistance.

a, G12Ci-sensitive lung cancer cells (H358) were selected in the absence (H358T) or in the presence of G12Ci-treatment (see [Methods](#)), either in cell-culture (1M) or in athymic mice followed by cell-culture (R1, R2). **b**, The indicated cell lines were treated with sotorasib (left) or adagrasib (right) for 72h to determine the effect on cell proliferation (n = 3, mean ± s.e.m.). **c**, **d**, Resistant (1M, R1, R2) or parental (P) cells were treated with the indicated inhibitors for two weeks to determine the effect of cell viability by crystal violet staining. A representative of two independent experiments is shown. **e**, Athymic mice bearing parental (H358T, Par) or resistant (R1, R2) cell line xenografts were treated with vehicle or MRTX1257 (50 mpk) to determine the effect on tumour growth (n = 5, mean ± s.e.m.). **f**, **g**, The indicated cell lines were treated with increasing

concentrations of sotorasib for 2 h (**f**) or with 1 μ M over time (**g**). The effect on KRAS signalling was determined by immunoblotting. A representative of at least two independent experiments for each cell line is shown. For gel source data, see Supplementary Fig. [1](#).

[Source data](#)

Extended Data Fig. 4 Single-cell modelling of G12Ci-resistant models.

a, Boxplots (median, upper and lower quartiles, and outliers) showing the distribution of the allele frequency (VAF) for the indicated variants across subclonal populations in G12Ci-resistant models. **b**, A neighbour-joining tree showing the relationship of the single-cells originating from the indicated parental or resistant models. The circular heat map indicates the presence (blue) or absence (white) of the indicated variants in each single cell.

[Source data](#)

Extended Data Fig 5 Secondary RAS mutations in the absence of KRAS-directed therapy.

a, Heat map of 304 KRAS-mutant biopsy specimens harbouring multiple RAS variants. **b**, Alluvial plot showing the pairings of mutations across samples. Residues with cancer-associated hotspot mutations are labelled. **c**, As in **a** but only KRAS(G12C) mutant samples are shown. **d**, Frequency of 2°RAS mutations in samples with KRAS(G12C) (left) or any KRAS mutation (right). All specimens were sequenced using MSK-IMPACT.

[Source data](#)

Extended Data Fig. 6 Propensity of treatment-emerging alterations to attenuate KRAS(G12C) inhibition.

a–g, H358 cells expressing the indicated variants under dox-inducible promoters (**a–f**) or H358 cells with CRISPR/CAS9 mediated deletion of KEAP1 or STK11 (**g**, ref. [19](#).), were treated as shown to determine the effect on signalling intermediates by immunoblotting (**a**) or cell viability (**b–g**) using cell titre glow. In **b–f**, n = 3, in **g**, n = 4. Mean ± s.e.m. are shown. A representative of at least two independent experiments is shown. For gel source data of **a**, see Supplementary Fig. [1](#).

[Source data](#)

[Extended Data Fig. 7 Progressive attenuation of KRAS\(G12C\) singling inhibition during drug selection.](#)

a, b, KRAS(G12C) mutant cells were expanded in the presence of G12Ci-treatment to establish isogenic lineages (1M, R1 and R2) with acquired resistance. Serial passages (p) from the indicated lineages were assayed to determine the magnitude and duration of ERK inhibition (**a**) or cleaved PARP induction (**b**) after drug re-challenge for 0–72h. In the 1M series, p15 and p25 denote passages when the selection drug concentration was increased. The experiment was carried out several passages later. p0 denotes parental cells. pERK and cPARP immunoblots were quantified with imageJ and their expression level was normalized to time 0. **c**, Unlabelled parental (H358) cells and BFP-labelled derivatives expressing dox-inducible NRAS(Q61K) were co-cultured in the presence of dox and/or sotorasib for 72h (n = 4, mean ± s.e.m.). **d**, Parental H358 cells or their derivatives expressing NRAS(Q61K) (100%) were treated in the presence of sotorasib in the presence or absence of dox for 72h (n = 4, mean ± s.e.m.). Norm: min-max normalization. **e, f**, RFP-labelled parental (H358) cells and GFP-labelled derivatives expressing dox-inducible NRAS(Q61K) were co-cultured in the presence of dox and/or sotorasib for 72h to determine the distribution of subpopulations (**e**) by FACS (n = 20,000 independent single cells) and the effect of the minor 2^oNRAS subclone on the major KRAS(G12C)-mutant parental subpopulation (**f**). A representative of two independent experiments is shown in **e, f**.

[Source data](#)

Extended Data Fig. 8 Selective vulnerabilities in resistant cells harbouring KRAS and NRAS mutations.

a, Parental H358 (sensitive) and R1 (resistant) cells expressing CAS9 were transfected with a genome-wide sgRNA library. The cells were treated in triplicate with either DMSO or G12Ci (sotorasib, 1 μ M) for 14 days. The scaled mean expression of four independent sgRNAs targeting the indicate genes is shown. **b, c**, Parental or resistant cells expressing control (sgNT) or SHOC2-specific sgRNAs were subjected to immunoblotting to determine the expression of SHOC2 (**b**) or the effect on the indicated signalling intermediates (**c**). **d–f**, Parental (**d**), R1 (**e**) and R2 (**f**) cells were treated with either DMSO or sotorasib for 10 days to determine the effect on cell number ($n = 4$, mean \pm s.e.m). **g–h**, R1 cells expressing NRAS-specific siRNAs were treated with sotorasib for the indicated times to determine the effect on signalling intermediates (**g**) or proliferation (**h**, $n = 6$, mean \pm s.e.m). A representative of at least two independent experiments is shown. For gel source data, see Supplementary Fig. 1.

Source data

Extended Data Fig. 9 Co-targeting ERK-signalling enhances KRAS(G12C) inhibition in models harbouring secondary RAS/BRAF mutations.

a, b, The indicated models were treated with sotorasib (1 μ M) in combination with trametinib (25 nM, **a**) or LXH254 (2 μ M; **b**) to determine the effect on ERK signalling intermediates. For gel source data, see Supplementary Fig. 1. **c**, Resistant and parental cell lines were treated with G12Ci (sotorasib, 1 μ M; adagrasib, 200 nM or MRTX1257, 200 nM) in combination with a RAFdi (LXH254, 2 μ M), MEKi (trametinib, 50 nM) or ERKi (SCH984, 500 nM) to determine the effect on cell viability. **d–f**, H358 cells expressing the dox-induced variants shown were treated with sotorasib (1 μ M) alone or in combination with the noted inhibitors to determine the effect on cell viability over time, using cell titre glow (**d**, $n = 4$ and **e**, $n = 6$; mean is shown) or crystal violet staining (**f**, 10 days). A representative of two independent repeats is shown.

[Source data](#)

Extended Data Fig. 10 Targeting KRAS(G12C) in combination with MAPK intermediates in vivo.

Mice bearing the indicated cell line (**a**, n = 5, mean ± s.e.m.) or patient-derived xenograft (**b**, n = 4, mean ± s.e.m.) were treated with the inhibitors shown to determine the effect on tumour growth. Fractional differences in tumour volume over time are shown.

[Source data](#)

Supplementary information

Supplementary Information

A merged PDF containing: Supplementary Discussion; Supplementary References (31–43); Supplementary Table 1 (primers for amplicon sequencing); Supplementary Fig. 1 (images of western blots).

Reporting Summary

Supplementary Data 1

Additional clinical information on patients treated with sotorasib.

Supplementary Data 2

Single-cell sequencing data of parental H358 and G12Ci resistant cell lines.

Supplementary Data 3

Bulk targeted exome sequencing of PDX models.

Supplementary Data 4

Bulk sequencing data for parental H358 and G12Ci resistant cell lines.

Supplementary Data 5

Raw counts and analysed data from sgRNA screens in parental H358 and R1 resistant cells.

Source data

[**Source Data Fig. 1**](#)

[**Source Data Fig. 2**](#)

[**Source Data Fig. 3**](#)

[**Source Data Fig. 4**](#)

[**Source Data Extended Data Fig. 1**](#)

[**Source Data Extended Data Fig. 2**](#)

[**Source Data Extended Data Fig. 3**](#)

[**Source Data Extended Data Fig. 4**](#)

[**Source Data Extended Data Fig. 5**](#)

[**Source Data Extended Data Fig. 6**](#)

[**Source Data Extended Data Fig. 7**](#)

[**Source Data Extended Data Fig. 8**](#)

[**Source Data Extended Data Fig. 9**](#)

Source Data Extended Data Fig. 10

Rights and permissions

Reprints and Permissions

About this article

Cite this article

Zhao, Y., Murciano-Goroff, Y.R., Xue, J.Y. *et al.* Diverse alterations associated with resistance to KRAS(G12C) inhibition. *Nature* **599**, 679–683 (2021). <https://doi.org/10.1038/s41586-021-04065-2>

- Received: 01 March 2021
- Accepted: 27 September 2021
- Published: 10 November 2021
- Issue Date: 25 November 2021
- DOI: <https://doi.org/10.1038/s41586-021-04065-2>

Share this article

Anyone you share the following link with will be able to read this content:

[Get shareable link](#)

Sorry, a shareable link is not currently available for this article.

[Copy to clipboard](#)

Provided by the Springer Nature SharedIt content-sharing initiative

This article was downloaded by **calibre** from <https://www.nature.com/articles/s41586-021-04065-2>

| [Section menu](#) | [Main menu](#) |

- Article
- Open Access
- [Published: 17 November 2021](#)

Cell-type specialization is encoded by specific chromatin topologies

- [Warren Winick-Ng](#) [ORCID: orcid.org/0000-0002-8716-5558¹](#)^{na1},
- [Alexander Kukalev](#)¹^{na1},
- [Izabela Harabula](#)^{1,2}^{na1},
- [Luna Zea-Redondo](#)^{1,2}^{na1},
- [Dominik Szabó](#)^{1,2}^{na1},
- [Mandy Meijer](#) [ORCID: orcid.org/0000-0003-3314-1224³](#),
- [Leonid Serebreni](#)¹^{nAff16},
- [Yingnan Zhang](#)⁴,
- [Simona Bianco](#) [ORCID: orcid.org/0000-0001-5819-060X⁵](#),
- [Andrea M. Chiariello](#) [ORCID: orcid.org/0000-0002-6112-0167⁵](#),
- [Ibai Irastorza-Azcarate](#)¹,
- [Christoph J. Thieme](#) [ORCID: orcid.org/0000-0002-1566-0971¹](#),
- [Thomas M. Sparks](#)¹,
- [Silvia Carvalho](#)^{1,6,7,8},
- [Luca Fiorillo](#) [ORCID: orcid.org/0000-0003-2967-0123⁵](#),
- [Francesco Musella](#)⁵,
- [Ehsan Irani](#)^{1,9},
- [Elena Torlai Triglia](#) [ORCID: orcid.org/0000-0002-6059-0116¹](#)^{nAff17},
- [Aleksandra A. Kolodziejczyk](#)^{10,11}^{nAff18},
- [Andreas Abentung](#)¹²^{nAff19},
- [Galina Apostolova](#)¹²,
- [Eleanor J. Paul](#) [ORCID: orcid.org/0000-0003-1183-9285¹³](#)^{nAff20}^{nAff21},
- [Vedran Franke](#) [ORCID: orcid.org/0000-0003-3606-6792¹⁴](#),
- [Rieke Kempfer](#)^{1,2},
- [Altuna Akalin](#) [ORCID: orcid.org/0000-0002-0468-0117¹⁴](#),
- [Sarah A. Teichmann](#) [ORCID: orcid.org/0000-0002-6294-6366^{10,11}](#),
- [Georg Dechant](#)¹²,
- [Mark A. Ungless](#)¹³,

- [Mario Nicodemi](#)^{5,9},
- [Lonnie Welch](#)⁴,
- [Gonçalo Castelo-Branco](#) ORCID: orcid.org/0000-0003-2247-9393^{3,15} &
- [Ana Pombo](#) ORCID: orcid.org/0000-0002-7493-6288^{1,2,9}

Nature volume **599**, pages 684–691 (2021)

- 13k Accesses
- 216 Altmetric
- [Metrics details](#)

Subjects

- [Data integration](#)
- [Gene regulation](#)
- [Genetics of the nervous system](#)
- [Nuclear organization](#)
- [Regulatory networks](#)

Abstract

The three-dimensional (3D) structure of chromatin is intrinsically associated with gene regulation and cell function^{1,2,3}. Methods based on chromatin conformation capture have mapped chromatin structures in neuronal systems such as in vitro differentiated neurons, neurons isolated through fluorescence-activated cell sorting from cortical tissues pooled from different animals and from dissociated whole hippocampi^{4,5,6}. However, changes in chromatin organization captured by imaging, such as the relocation of *Bdnf* away from the nuclear periphery after activation⁷, are invisible with such approaches⁸. Here we developed immunoGAM, an extension of genome architecture mapping (GAM)^{2,9}, to map 3D chromatin topology genome-wide in specific brain cell types, without tissue disruption, from single animals. GAM is a ligation-free technology that maps genome topology by sequencing the DNA content from thin (about 220 nm) nuclear cryosections. Chromatin interactions are identified from the increased probability of co-segregation of contacting loci across a collection of nuclear slices. ImmunoGAM expands the scope of GAM to enable the selection of specific cell types using low cell numbers (approximately 1,000 cells) within a complex tissue and avoids tissue dissociation^{2,10}. We report cell-type specialized 3D chromatin structures at multiple genomic scales that relate to patterns of gene expression. We discover extensive ‘melting’ of long genes when they are highly

expressed and/or have high chromatin accessibility. The contacts most specific of neuron subtypes contain genes associated with specialized processes, such as addiction and synaptic plasticity, which harbour putative binding sites for neuronal transcription factors within accessible chromatin regions. Moreover, sensory receptor genes are preferentially found in heterochromatic compartments in brain cells, which establish strong contacts across tens of megabases. Our results demonstrate that highly specific chromatin conformations in brain cells are tightly related to gene regulation mechanisms and specialized functions.

[Download PDF](#)

Main

To explore how genome folding is related to cell specialization, we applied immunoGAM to mouse brain tissue slices and analysed three cell types with diverse functions (Fig. 1a): oligodendroglia (oligodendrocytes and their precursors (OLGs)) from the somatosensory cortex; pyramidal glutamatergic neurons (PGNs) from the cornu ammonis 1 (CA1) of the dorsal hippocampus; and dopaminergic neurons (DNs) from the ventral tegmental area (VTA) of the midbrain. OLGs are important for neuronal myelination and circuit formation¹¹, whereas PGNs are important for temporal and spatial memory formation and consolidation¹², and DNs are activated during cue-guided reward-based learning¹³. Publicly available GAM data from mouse embryonic stem (mES) cells⁹ were used for comparison (Supplementary Table 1).

Fig. 1: ImmunoGAM captures cell-type-specific chromatin contacts in the mouse brain.

 figure1



a, ImmunoGAM was applied to three brain cell types: OLGs, DNs and PGNs (one independent biological replicate for OLGs and two replicates for DNs and PGNs). **b**, Schematic of the ImmunoGAM workflow. OLGs were selected by immunolabelling with GFP, DNs with tyrosine hydroxylase and PGNs using tissue morphology. Nuclear profiles were laser microdissected, each from a single cell, with three collected together, as described for multiplex-GAM⁹. **c**, Example of cell-type-specific contact differences at the *Pcdh* locus (chromosome 18: 36–39 Mb). GAM matrices represent co-segregation frequencies of 50-kb genomic windows using normalized pointwise mutual information (NPMI). Dashed lines illustrate cell-type differences. NPMI scales range between 0 and 99th percentile per cell type. Contact density heatmaps represent insulation scores using 100–1,000 kb square sizes. RNA-seq and ATAC-seq tracks represent normalized pseudobulk reads from scRNA-seq and scATAC-seq, respectively, except for bulk ATAC-seq from mES cells. **d**, Strong contacts between *Vmn* and *Olfr* receptor gene clusters on chromosome 17 (0–60 Mb) within B compartments (Comp.), separated by ~35 Mb, are observed in brain cells but not in mES cells. Compartments A and B were classified using normalized PCA eigenvectors².

Source data

We selected cell types from brain tissue slices by immunofluorescence with cell marker antibodies before genomic extraction (Fig. 1b). A detailed flowchart of immunoGAM quality control (QC) measures and normalization is shown in Extended Data Fig. 1a–d and Supplementary Table 2. GAM contact matrices, each from about 850 cells, had low biases in GC content and mappability (Extended Data Fig. 2a–c). We calculated local contact densities and topological domains using the insulation square method¹⁴, and calculated compartments associated with open chromatin (compartment A) and closed chromatin (compartment B) using principal component analysis (PCA)² (Supplementary Tables 3–5).

As an example of cell-type-specific organization, we considered the *Pcdh* locus, which contains three clusters of cell adhesion genes (*Pcdha*, *Pcdhb* and *Pcdhg*) and occupies two topologically associating domains (TADs) in mES cells, as previously described¹⁵ (Fig. 1c, see Extended Data Fig. 3a for replicates). Mapping contact densities using 100–1,000 kb insulation squares showed that the locus is generally open above 500 kb. Higher expression of *Pcdha* and *Pcdhb* coincides with increased long-range contacts between the three clusters in neurons¹⁶ and OLGs¹⁷ and with additional long-range contacts with the highly expressed *Fgfl* gene in OLGs. We also discovered contacts spanning tens of megabases in brain cells. For example, strong contacts connected two regions approximately 3- and 5-Mb wide, separated by 35 Mb, which contained clusters of vomeronasal (*Vmn*) and olfactory (*Olfr*) receptor genes (Fig. 1d, see Extended Data Fig. 3b for replicates). Thus, the application of immunoGAM in

specific brain cell types reveals large rearrangements in 3D chromatin architecture at short-range and long-range genomic lengths.

To further investigate how cell-type-specific 3D genome topologies relate to gene expression and chromatin accessibility, we produced or collected published single-cell RNA sequencing (scRNA-seq) data and single-cell assay for transposase-accessible chromatin with high-throughput sequencing (ATAC-seq) data from mES cells, the cortex, the hippocampus and the midbrain ([Methods](#), Extended Data Fig. 4, Supplementary Table 6). After selecting cell populations equivalent to those captured by immunoGAM, we compiled cell-type-specific pseudobulk RNA-seq and ATAC-seq datasets.

TADs extensively rearrange between cell types

Complex and extensive cell-type-specific changes in TAD-level contacts were frequent, for example, at a 4-Mb region that contains *Scn* genes that encode sodium voltage-gated channel subunits (Fig. 2a, see Extended Data Fig. 5a for replicates). We obtained a total of approximately 2,300 TADs across cell types, with a median length of about 1 Mb, which is in line with previous reports⁶ (Extended Data Fig. 5b). Although pairwise comparisons of TAD border positions confirmed previous levels of conservation^{4,6} (78–89%; Extended Data Fig. 5c), multiway comparisons showed high cell-type specificity (Fig. 2b, see Extended Data Fig. 5d for sparser combinations). One-third of the borders were unique and significantly more insulated in other cell types (Extended Data Fig. 5e), with some variability noted between biological replicates (59–65%) (Extended Data Fig. 5f). By contrast, only 8% of the total set of borders was shared by brain cells and 14% by all cell types. Shared borders showed significantly stronger insulation in brain cells than in mES cells (Extended Data Fig. 5g), which suggests that there is structural stabilization after terminal differentiation. Unique boundaries often contained expressed genes (52–55% in brain cells, 38% in mES cells) (Extended Data Fig. 5h) and genes with enriched Gene Ontology (GO) terms relevant to the specialized cell type (Fig. 2c, Supplementary Table 7), such as ‘membrane depolarization’ and ‘cognition’ in PGNs or genes important for dopaminergic differentiation and dopamine synthesis in DNs.

Fig. 2: Chromatin domains rearrange extensively in brain cells, notably at long genes that undergo melting events.

 **figure2**

a, Example of cell-type-specific contacts at genomic regions (chromosome 2: 64.3–67.3 Mb) with differential expression. Dashed boxes represent 500 kb insulation scores used to determine TAD boundaries (indicated with coloured boxes below). Replicate 1 is shown for brain cells. **b**, UpSet plots representing multiway TAD boundary comparisons show extensive cell-type specificity. Boundaries were defined as 150 kb genomic regions centred on the lowest insulation score windows and were considered different when separated by >50 kb edge-to-edge. **c**, Cell-type-specific borders contain genes with GO terms relevant for cell functions. The top four GO terms were the most enriched, and the fifth was selected (over-representation measured by Z-score; one-sided Fisher's exact permuted P values < 0.01). Asterisk indicates multiple *Hist1* genes. **d**, **e**, *Grik2* and *Dscam* overlap with cell-type-specific TAD borders and extensively decondense, or ‘melt’, in PGNs and DNs, respectively. **f**, The MELTRON pipeline was applied at long genes (>300 kb, 479 genes) to determine melting scores from contact density maps that represent insulation score values using 100–1,000 kb squares. Genes were considered to melt if the melting score computed across their coding region was >5 ($P < 1 \times 10^{-5}$; one-sided Kolmogorov–Smirnov testing using maximum distances between distributions). **g**, Melting associates with higher expression, especially in PGNs and DNs (two-sided Wilcoxon rank-sum test; $**P < 0.01$, $****P < 0.0001$; P values from left to right, $P = 3.5 \times 10^{-3}$, $P = 1.8 \times 10^{-8}$, $P = 8.3 \times 10^{-6}$). lsRRPM, length-scaled RNA reads per million; RPM, reads per million.

[Source data](#)

Long neuronal genes melt in brain cells

Many neuronal genes involved in specialized functions are long (>300 kb) and produce many isoforms owing to complex RNA processing¹⁸. Chromatin reorganization was most apparent at long genes in both PGNs and DNs (Fig. [2d,e](#)). For example, *Grik2* loses contact density in PGNs compared to mES cells, especially around the transcription start site (TSS) and transcription end site (TES) (Fig. [2d](#)). By contrast, *Dscam* decondenses across its entire gene body in DNs (Fig. [2e](#)). To assess whether decondensation relates to the expression of long genes, we compared the insulation of the most and least expressed long genes (Extended Data Fig. [5i](#)). Highly expressed genes were significantly less insulated at TSSs and TESs and throughout gene bodies in both DNs and PGNs, but not in OLGs or mES cells. The general contact loss at highly expressed long neuronal genes is reminiscent of the decondensation, or ‘melting’, observed by microscopy at polytene chromosome puffs¹⁹ or tandem gene arrays²⁰.

To detect melting genome-wide in an unbiased manner, we devised the MELTRON pipeline. MELTRON calculates a ‘melting score’ as the significant difference between cumulative probabilities of insulation scores across a range of genomic scales (100–1,000 kb) between two cell types and within regions of interest, here defined as all (479) long genes (Fig. [2f](#)). We found 120–180 melting genes with melting scores of >5 (Kolmogorov–Smirnov test, $P < 1 \times 10^{-5}$) between brain cells and mES cells (Fig. [2g](#), Supplementary Table [8](#)). *Grik2* had melting scores of 12 and 26 in PGNs (replicates 1 and 2, respectively), whereas *Dscam* had scores of 38 and 50 in DNs (replicates 1 and 2, respectively) and *Magi2* had a score of 73 in OLGs (Extended Data Fig. [6a,b](#)). Melting scores in the PGN and DN replicates correlated well (Extended Data Fig. [6c](#)).

Melting genes were significantly more transcribed and showed higher chromatin accessibility than non-melting long genes, especially in PGNs and DNs (Fig. [2g](#), Extended Data Fig. [6d–f](#)). Of interest, many top (3%) melting genes (24 out of 44) are sensitive to topoisomerase I inhibition in ex vivo neuronal cultures²¹, which was in contrast to 16% (42 out of 261) with intermediate melting scores or 16% of non-melting genes (Extended Data Fig. [6g](#)). This result suggests that extensive melting of long genes is associated with the resolution of topological constraints²¹. Melting genes often belonged to compartment A in both mES cells and the corresponding brain cell (43–58%), especially when highly transcribed in both cell types (Extended Data Fig. [6h](#)). Genes melting in OLGs and DNs were less likely to be lamina-associated or nucleolus-associated in mES cells, whereas PGNs did not show any preferred association (Extended Data Fig. [6i,j](#)). Therefore, melting of long genes is not trivially associated with a transition from a heterochromatic state in mES cells to open

chromatin in brain cells, although such events can occur (for example, *Magi2* in OLGs or *Dscam* in DNs) (Supplementary Table 8).

We next examined in more detail melting in neurexin 3 (*Nrxn3*) and RNA binding Fox 1 homologue 1 (*Rbfox1*) genes, both of which are highly sensitive to topoisomerase I inhibition²¹. *Nrxn3* encodes a membrane protein involved in synaptic connections and plasticity. In mES cells, *Nrxn3* spans two TADs with high contact density, localizes in compartment B and associates with the nuclear lamina and the nucleolus. In DNs, *Nrxn3* extensively melts (replicate scores of 48 and 49), is highly transcribed and accessible and belongs to compartment A (Fig. 3a, see Extended Data Fig. 7a for all cell types and replicates). *Rbfox1* encodes a RNA-binding protein that regulates alternative splicing. In mES cells, *Rbfox1* lies within a dense contact domain in compartment A, has very low expression and low chromatin accessibility. It also has nucleolar-associated domain and partial lamina-associated domain memberships. *Rbfox1* extensively melts in PGNs (scores of 65 and 39), which coincides with its highest expression and high accessibility in these cells (Fig. 3b, Extended Data Fig. 7b).

Fig. 3: Extensive decondensation and relocalization of highly expressed long neuronal genes.

 **figure3**

a, b, Examples of two melting genes. *Nrxn3* occupies two dense TADs in mES cells but melts in DNs where it is most highly expressed and accessible (**a**; chromosome 12: 87.6–92.4 Mb). *Rbfox1* is highly condensed in mES cells and melts in PGNs where it is highly expressed and accessible (**b**; chromosome 16: 4.8–9.8 Mb). Compartment

tracks are shown for each cell type, and published lamina-associated domains (LADs⁴⁷) and nucleolus-associated domains (NADs⁴⁸) for mES cells. **c**, Polymer models show extensive *Nrxn3* melting in DNs compared to mES cells. Colour bars shows DN domain positions. **d**, Gyration radii of green melting domains are significantly higher in DNs than in mES cells ($****P = 1.1 \times 10^{-92}$; two-sided Mann–Whitney test, $n = 450$). Arrows indicate positions of exemplar models. **e**, Genomic regions covered by cryo-FISH probes across the entire *Rbfox1* gene, or targeting the gene TSS, middle of the coding region (Mid) or TES (Supplementary Table 11 contains the probe list). **f**, *Rbfox1* (pseudocoloured green) occupies small, rounded foci in mES cells, often at the nucleolus periphery (immunostained for nucleophosmin 1, ref. 49; pseudocoloured purple). In PGNs, *Rbfox1* occupies larger, decondensed foci away from nucleoli. Arrows indicate *Rbfox1* foci in mES cells (orange) and PGNs (blue). Scale bars, 3 μm . **g**, *Rbfox1* occupies significantly larger areas in PGNs than in mES cells ($**P = 0.008$; two-sided Mann–Whitney test; two experimental replicates (Repl. 1 and Repl. 2) with $n = 13, 39$ and $38, 25$ respectively). Most *Rbfox1* foci localize at the nucleolar periphery in mES cells, but away from the nucleolus in PGNs. **h**, Cryo-FISH experiments that target TSS, Mid and TES regions of *Rbfox1* (pseudocoloured cyan, green, purple) show extensive separation in PGNs compared with mES cells. Arrows indicate *Rbfox1* foci in mES cells (orange) and PGNs (blue). Scale bars, 3 μm . **i**, The TSS and TES regions of *Rbfox1* are significantly more separated in PGNs than mES cells (two-sided Mann–Whitney test; $**P < 0.01$; from left to right, $P = 0.003$, $P = 0.179$, $P = 0.331$; NS, not significant). **j**, Schematics summarizing the melting of long genes in neurons, which is accompanied by locus relocalization away from repressive nuclear landmarks.

Source data

To further understand the melting process in the *Nrxn3* region, we used a polymer-physics-based approach²² to generate ensembles of 3D models in mES cells and DNs from GAM matrices (Fig. 3c, Supplementary Tables 9 and 10). 3D models were validated by reconstructing in silico GAM matrices (Extended Data Fig. 7c). mES cell models showed intermingled globular domains, including the green and red domains that contain *Nrxn3* (Supplementary Video 1, see Extended Data Fig. 7d for additional examples). In DNs, the melted green domain becomes highly extended and has high gyration radii (Fig. 3c,d, Supplementary Video 2), while the upstream (grey) and downstream (blue) domains condense (Fig. 3a, Extended Data Fig. 7e).

Next, we applied fluorescence *in situ* hybridization on cryosections (cryo-FISH)^{2,23} to visualize *Rbfox1* in mES cells and PGNs (Fig. 3e, Supplementary Table 11). In mES cells, a fluorescence-labelled probe across *Rbfox1* revealed circular foci (average area of $0.44 \pm 0.17 \mu\text{m}^2$, mean \pm s.d.) often localized at the nucleolar surface (59%) or the nuclear periphery (27%; Fig. 3f,g, Extended Data Fig. 7f). In PGNs, *Rbfox1*

decondensed and elongated with significantly high areas ($0.59 \pm 0.31 \mu\text{m}^2$; Mann–Whitney test, $P < 0.01$) and localized to the nucleoplasm interior (77%). Using specific probes for the TSS, the middle and the TES of *Rbfox1* revealed increased separation between the TSS and the TES in PGNs compared to mES cells (Fig. 3*h,i*; $0.65 \pm 0.41 \mu\text{m}$ and $0.37 \pm 0.22 \mu\text{m}$, respectively; Mann–Whitney test $P < 0.01$; Extended Data Fig. 7*g*).

The extensive changes in *Rbfox1* localization and condensation led us to ask whether melting is generally related to changes in intrachromosomal and interchromosomal contacts. We assessed this by comparing their *trans–cis* contact ratios (Methods). Melted genes had significantly lower *trans–cis* values (higher intrachromosomal contacts) in DNs and PGNs than in mES cells (Extended Data Fig. 8*a–c*), but not in OLGs or in non-melting long genes (Extended Data Fig. 8*a,d*). Of note, *Rbfox1* had a higher *trans–cis* ratio in PGNs, whereas *Nrxn3* had a lower *trans–cis* ratio in DNs (Extended Data Fig. 8*e,f*). Decreased *trans–cis* ratios of melting genes in DNs or PGNs were independent of NAD association in mES cells (Extended Data Fig. 8*g*), whereas non-melting genes with low *trans–cis* values were generally associated with NADs in mES cells (Extended Data Fig. 8*h*).

Together, polymer modelling from GAM data and single-cell imaging highlight that domain melting is a previously unappreciated topological feature of very long genes. Domain melting occurs when genes are highly expressed, or highly accessible, in brain cell types, and the process is robustly captured by immunoGAM (Fig. 3*j*). The decondensation of long genes in brain cells relative to mES cells often coincides with extensive reorganization of their chromosomal contacts, preferentially alongside increased intrachromosomal contacts.

Differential hubs of expressed genes

To explore how extensive chromatin rearrangements relate to changes in *cis*-regulatory elements and expressed genes, we extracted the top (5%) most differential contacts between PGNs and DNs within 5 Mb (ref. 9) (Fig. 4*a*, a detailed pipeline is provided in Extended Data Fig. 9*a*). We searched for binding motifs in accessible regions, which typically cover about 1.3 kb of the 50-kb contacting windows (Extended Data Fig. 9*b*), from differentially expressed transcription factors (TFs) that covered >5% of differential contacts (16 DN-specific and 32 PGN-specific TFs; Extended Data Fig. 9*c,d*, Supplementary Table 12). Out of 1,275 possible combinations of TF motif pairs, we prioritized 19 pairs (combinations of 14 TF motifs) that were most enriched in contacts of a given cell type or with a high ability to distinguish cell types (information gain; a full pipeline and criteria are provided in Extended Data Fig. 9*e,f*, and see Supplementary Table 13 for all TF pairs).

Fig. 4: Neuron-specific genes establish specific contacts rich in putative TF-binding sites.

 figure4

a, GAM contacts from PGNs and DNs (mouse replicate 1) were normalized (Z-score) and subtracted to produce differential contacts matrices. The top 5% most differential contacts (top 5% diff.) ranged from 0.05 to 5 Mb. Contacts containing TF motifs within accessible chromatin on each contacting window were selected in the most (top five) enriched in PGNs or DNs or with the highest discriminatory power (information gain; Extended Data Fig. 9f). **b**, Multiple TF pairs coincide in the same PGN (left) or DN (right) differential contacts. The most abundant groups of contacts are shown for each cell type. **c**, Differential contacts with the most enriched combination TF feature pairs contain expressed genes in both windows. **d**, Differential contacts with the most abundant TF feature pairs in PGNs contain differentially expressed genes (top), with PGN-specific roles (middle; one-sided Fisher's exact permuted $P < 0.01$). The top enriched GO terms show that differential contacts between PGN upregulated genes (bottom) contain genes upregulated in PGNs (blue) and other expressed genes. **e**, Differential contacts with the most abundant TF feature pairs in DNs contain differentially expressed genes (top) with DN-specific functions (middle; one-sided Fisher's exact permuted $P < 0.01$). The top enriched GO terms show that differential contacts between DN upregulated genes (bottom) contain genes upregulated in DNs

(green) and other expressed genes. **f**, Left, *Egr1* is highly expressed (chromosome 18: 33.7–36.0 Mb) and contacts with its downstream domain in PGNs compared with DNs. Right, the differential contact matrix shows increased PGN-specific contacts in the entire region surrounding *Egr1* (right). The *Egr1*-containing TAD (inset; chromosome 18: 34.65–35.85 Mb) has multiple putative TF-binding sites found within PGN-accessible regions, most notably surrounding the *Egr1* gene (grey dashed box), not found in DNs. **g**, Schematics summarizing the presence of genes related to synaptic plasticity in PGN-specific contacts and to drug addiction in DN-specific contacts, with accessible chromatin harbouring binding sites for differentially expressed TFs.

Source data

We searched for differential contacts containing the most common TF-pair combinations (Fig. 4b, a full list is shown in Extended Data Fig. 9g). In PGNs, homodimers and heterodimers for *Neurod1* and/or *Neurod2* putative binding sites characterized the most abundant contacts, together with *Egr1*, *Etv5*, *Lhx2*, *Maz*, *Nr3c1*, *Pou3f2* and *Ubp1* (*Neurod* group; 5,572 contacts). In DNs, contacts containing *Neurod1* and *Neurod2* appeared as heterodimers (660 contacts). The most frequent TF-motif pair in DNs, and the second most in PGNs, is a *Ctcf* homodimer (892 and 781 contacts, respectively). The next most abundant DN-specific contacts contained *Foxa1* combined with *Ctcf*, *Nr2f1* or *Nr4a1* (*Foxa1*-TF group; 1,612 contacts). All groups spanned 0.05–5 Mb and captured strong contacts (Extended Data Fig. 10a,b). The selected differential contacts rarely coincided with two TAD borders (Extended Data Fig. 10c) and often involved compartment A windows (Extended Data Fig. 10d). Networks of differential contacts, built on the basis of motif co-occurrence using all 50 differentially expressed TFs, confirmed connectivity between multiple TF motifs in PGNs, and between *Foxa1* or *Neurod* and specific TFs in DNs (Extended Data Fig. 10e,f, Supplementary Table 14).

Many contacts in each TF-motif group contained expressed genes in both contacting windows (30–45% in DNs, 40–50% in PGNs) that were significantly above the genome-wide or top 5% contact frequencies (10–16%; Fig. 4c, Extended Data Fig. 10g). Many of these genes were differentially expressed between PGNs and DNs (1,490 and 975, respectively, out of 3,537 differentially expressed genes; Extended Data Fig. 10h). In PGN-specific contacts, both the *Neurod* and *Ctcf*-*Ctcf* groups contained PGN upregulated genes with GO terms related to synaptic plasticity (Fig. 4d). Two PGN upregulated genes, *Dlg4* (which is important for long-term potentiation²⁴) and *Shisa6* (which prevents desensitization of AMPA receptors during plasticity²⁵) were present within a hub of *Neurod* contacts that contained other activity-related genes, including *Map2k4* and *Dnah9* (see Extended Data Fig. 10i for the differential contact matrix). DN upregulated genes found with the *Foxa1*-TF (139

out of 1,844), the *Neurod*-TF (87) or the *Ctcf*-*Ctcf* (80) pair are involved in synaptic organization and addiction pathways (Fig. 4e). For example, *Dnm3* has altered protein expression in an alcohol-dependence paradigm²⁶ and makes contacts containing the *Foxa1*-TF pair with *Mrps14* (downregulated after nicotine exposure²⁷), *Cacynp* (upregulated following alcohol exposure²⁸) and *Pou2fl* (a co-factor associated with alcohol dependence²⁹) (see Extended Data Fig. 10j for the differential contact matrix). Of note, *Egr1*, an immediate early gene upregulated in activated neurons³⁰, establishes PGN-specific contacts containing accessible regions covered by *Egr1* and *Neurod* motifs (Fig. 4f, see Extended Data Fig. 10k for replicate data). *Egr1* was highly upregulated in PGNs ($\log_2(\text{fold-change}) = 3$, PGNs compared to DNs) and gained contacts with its adjacent TAD. It also contained accessible chromatin peaks rich in TF motifs belonging to the *Neurod* group that are not seen in DNs. Binding of EGR1 protein to its own promoter is confirmed in published chromatin immunoprecipitation with sequencing (ChIP-seq) data from the cortex³¹.

Together, our strategy identifies hubs of chromatin contacts specific for different neuron types that contain putative binding sites for differentially expressed TFs (Fig. 4g). These interconnected hubs bring together distal genes with specialized neuronal functions, such as synaptic plasticity in PGNs or drug addiction in DNs.

Extensive A/B compartment reorganization

Last, we found broad changes in A/B compartmentalization between all cell types (Extended Data Fig. 11a,b), with lowest Pearson's correlations of compartment eigenvector values between brain cells and mES cells and highest correlations between neuronal replicates (Extended Data Fig. 11c). Only 12% of genomic windows changed from compartment B in mES cells to compartment A in brain cells or between compartment A in mES cells to compartment B in brain cells (7%; see Extended Data Fig. 11d,e for per-chromosome transitions). Similar mean and total genomic lengths occupied contiguously by A or B compartments characterized all cell types (Extended Data Fig. 11f). B-to-A transitions from mES cells to brain cells contained 335 genes more strongly expressed in brain cells than in mES cells (Extended Data Fig. 12a). Their enriched GO terms included ‘behaviour’ and ‘gated ion channel activity’ (Fig. 5a). A-to-B transitions in mES cells to brain cells contained mostly silent genes in all cell types (572 out of 715 genes), except 50 transcriptional regulation genes highly expressed in mES cells (Fig. 5a, Extended Data Fig. 12b).

Fig. 5: Sensory receptor gene clusters preferentially belong to B compartments in brain cells and form megabase-range interactions.

 **figure5**

a, Selected top enriched GO terms for genes that increase expression in all brain cells relative to mES cells and move from compartment B in mES cells to compartment A in brain cells (pink box), and for genes that decrease expression in brain cells and move to compartment B compared to mES cells (blue box). All enriched GO terms had one-sided Fisher's exact permuted $P = 0$. **b**, Top enriched GO terms for genes silent in all cell types that gain membership to compartment B in brain cells. Most genes are *Olfr* and *Vmn* sensory receptor cluster genes. All enriched GO terms had one-sided Fisher's exact permuted $P = 0$. **c**, GAM contact matrices containing *Vmn* and orphan receptor genes (chromosome 7: 35–55 Mb) show large clusters of strong

interactions between B compartments in OLGs, PGNs and DNs, but not mES cells. Dashed boxes indicate interacting regions.

Source data

We found that A-to-B transitions were enriched for sensory receptor genes such as *Vmn* (149 genes out of 572 silent genes in the group) and *Olf* (179 genes), and these were often found in clusters^{32,33} (Fig. 5b). Although silent, only 35% of *Vmn* and 66% of *Olf* genes belonged to compartment B in mES cells compared with 82–96% and 72–85%, respectively, in brain cells (Extended Data Fig. 12c). *Vmn* and *Olf* genes were often involved in strong clusters of contacts in brain cells that spanned up to 50 Mb (Fig. 5c, additional examples in Fig. 1d, Extended Data Fig. 12d,e). Long-range contacts in brain cells were significantly stronger when B compartments contained *Vmn* or, to a lesser extent, *Olf* genes (at distances >3 Mb) (Extended Data Fig. 12f). This result suggests that sensory genes are not only more likely to belong to heterochromatic B compartments but also to more strongly contact other B compartments in brain cells.

Discussion

Here we introduced immunoGAM to capture genome-wide chromatin conformation states of specialized cell populations in the mouse brain. We discovered extensive reorganization of chromatin topology across genomic scales, including cell-type-specific TAD reorganization that involves genes relevant to brain cell specialization (Extended Data Fig. 12g).

We reported melting of long genes (>300 kb) with highest expression levels and/or accessible chromatin in brain cells. Single-cell imaging of *Rbfox1* in PGNs showed that the most prominent decondensation occurred between TSSs and TESs. Many long genes have specialized regulation in brain cells, for example, by topoisomerase activity²¹ or DNA methylation³⁴, by long stretches of H3K27ac or H3K4me1 acting as enhancer-like domains³⁵ or by large transcription loops³⁶. Their regulation is further complicated by intricate RNA processing dynamics¹⁸, which are required for adaptive responses based on activation state. Many of the highlighted genes, including *Nrxn3*, *Rbfox1*, *Grik2* and *Dscam*, have genetic variants associated with or directly causal of neuronal diseases^{37,38,39,40}. Thus, understanding how gene melting relates to regulation will become important to understanding the mechanisms of neurological disease.

Cell-type-specific networks of contacts were enriched for putative binding sites of differentially expressed TFs and connected hubs of differentially expressed genes with specialized functions^{24,25,30}, which is reminiscent of transcription factories⁴¹. DN-

specific loops contained genes related to drug-exposure response and addiction paradigms. Midbrain VTA DNs are the first brain cells that respond to addictive substances, including amphetamines, nicotine and cocaine^{42,43}. Future studies can explore the relationship between DN-specific chromatin landscapes and the regulation of these critical genes, with potential implications for the onset of addiction. PGN-specific contacts connected hubs of synaptic plasticity genes. Of note, PGN-specific contacts at the *Egr1* gene, which is involved in the activation of long-term potentiation, contained *Egr1* binding motifs, which suggests that there may be self-activation mechanisms. Together with reports that de novo chromatin looping can accompany transcriptional activation⁵, our work suggests that coordinated TF binding at distant locations in the linear genome, but in close contact due to the 3D chromatin landscape, may be critical for the induction of long-term potentiation.

Our results also highlighted the specialization of repressive long-range contacts in brain cells. Repressed *Olf* genes form a large interchromosomal hub in mature olfactory sensory neurons to regulate specificity of single *Olf* gene activation⁴⁴. We showed that sensory genes also form strong *cis*-contacts in brain cells not directly involved in sensory processes, a result confirmed in adult cortical neurons⁴⁵. Tight 3D compartmentalization of *Vmn* and *Olf* genes may be important for their repression in brain cells, as *Olf* genes can be stochastically activated and mis-expressed in neurodegenerative diseases⁴⁶.

Finally, we showed that immunoGAM requires low cell numbers (approximately 1,000 cells) from single individuals while retaining the spatial organization of cells within brain tissues. This highlights its potential to provide insights into the aetiology and progression of neurological disease. Collectively, our work showed that cell specialization in the brain and chromatin structure are intimately linked at multiple genomic scales.

Methods

Randomization, blinding, and sample size

Randomization and blinding were not relevant for the current study. The experiments and the subsequent analyses were performed on wild-type animals or cell lines, for which no clinical trial, treatment or disease comparison was performed. Samples were processed in different laboratories by different people, and there was no selection criteria for the wild-type mice used in the study. The appropriate number of samples for a GAM dataset varies and depends on multiple parameters such as nuclear volume, level of chromatin compaction, quality of DNA extraction, and so on. Because most of these parameters can be assessed only after the data have been collected and

processed, we recommend that the optimal resolution is defined during the collection of each GAM dataset, rather than trying to estimate optimal sample size before data collection. GAM data can be collected in multiple batches from the same starting material, therefore the sample size can be increased until the desired resolution is achieved. For scRNA-seq experiments in mES cells, no statistical method was used to predetermine sample size. Libraries were generated twice, from mES cells from different biological replicates, to account for experimental variability. For scATAC-seq experiments, no statistical method was used to predetermine sample size.

Animal maintenance

Collection of GAM data from DNs was performed using one C57Bl/6NCrl (RRID: IMSR_CR:027; WT) mouse, which was purchased from Charles River, and from one tyrosine hydroxylase–green fluorescent protein (TH–GFP; B6.Cg-Tg(TH-GFP)21-31/C57B6) mouse, obtained as previously described^{50,51}. All procedures involving WT and TH–GFP animals were approved by the Imperial College London’s Animal Welfare and Ethics Review Body. Adult male mice aged 2–3 months were used. All mice had access to food and water ad libitum and were kept on a 12-h light/12-h dark cycle at 20–23 °C and 45 ± 5% humidity. WT and TH–GFP mice received an intraperitoneal injection of saline 14 days or 24 h, respectively, before tissue collection, and they were part of a larger experiment for a different study. Collection of single-nucleus ATAC-seq (snATAC-seq) data from the midbrain VTA was performed using male C57Bl/6Nl (RRID: IMSR_CR:027; WT) mice, aged 7 and 9 weeks, which were a gift from M. Gotthardt. Mice for snATAC-seq were housed in a temperature-controlled room at 22 ± 2 °C with humidity of 55 ± 10% in individually ventilated cages with 12-h light/12-h dark cycles and with access to food and water ad libitum. All experiments involving snATAC-seq animals were carried out following institutional guidelines as approved by LaGeSo Berlin and following the Directive 2010/63/EU of the European Parliament on the protection of animals used for scientific purposes. Organ preparation was done under license X9014/11.

Collection of GAM data from somatosensory oligodendrocyte cells was performed using *Sox10::cre-RCE::loxP-EGFP* animals⁵², which were obtained by crossing *Sox10::cre* animals⁵³ on a C57BL/6j genetic background with *RCE::loxP-EGFP* animals⁵⁴ on a C57BL/6×CD1 mixed genetic background, both available from The Jackson Laboratory. The *cre* allele was maintained in hemizygosity, whereas the reporter allele was maintained in hemizygosity or homozygosity. Experimental procedures for *Sox10::cre-RCE::loxP-EGFP* animals were performed following the European directive 2010/63/EU, local Swedish directive L150/SJVFS/2019:9, Saknr L150 and Karolinska Institutet complementary guidelines for the procurement and use of laboratory animals, Dnr 1937/03-640. The procedures described were approved by the local committee for ethical experiments on laboratory animals in Sweden

(Stockholms Norra Djurförsöksetiska nämnd), licence number 130/15. One male mouse was killed at post-natal day 21 (P21). Mice were housed to a maximum number of 5 per cage in individually ventilated cages with the following light/dark cycle: dawn 6:00–7:00, daylight 7:00–18:00, dusk 18:00–19:00, night 19:00–6:00. All mice had access to food and water ad libitum and were housed at 22 °C and 50% humidity.

Collection of GAM data from hippocampal CA1 PGNs was performed using two 19-week-old male *Satb2*^{fl/fl} mice. C57Bl/6NCrl (RRID: IMSR_CR:027; WT) mice were purchased from Charles River, *Satb2*^{fl/fl} mice that carry the *loxP* flanked exon 4 have been previously described⁵⁵. The experimental procedures were done according to the Austrian Animal Experimentation Ethics Board (Bundesministerium für Wissenschaft und Verkehr, Kommission für Tierversuchsangelegenheiten). All mice had access to food and water ad libitum and were kept on a 12-h light/12-h dark cycle at 22.5 °C and 55 ± 10% humidity.

Tissue fixation and preparation

WT, TH-GFP and *Satb2*^{fl/fl} mice were anaesthetised under isoflurane (4%), given a lethal intraperitoneal injection of pentobarbital (0.08 µl, 100 mg ml⁻¹ Euthatal) and transcardially perfused with 50 ml ice-cold PBS followed by 50–100 ml 4% depolymerized paraformaldehyde (PFA; electron microscopy grade, methanol-free) in 250 mM HEPES–NaOH (pH 7.4–7.6). *Sox10::cre-RCE::loxP-EGFP* animals were killed using an intraperitoneal injection of ketaminol and xylazine followed by transcardial perfusion with 20 ml PBS and 20 ml 4% PFA in 250 mM HEPES (pH 7.4–7.6). Brains from WT or TH-GFP mice were removed, and the tissue containing the VTA was dissected from each hemisphere at room temperature and rapidly transferred to fixative. For *Satb2*^{fl/fl} mice, the CA1 field hippocampus was dissected from each hemisphere at room temperature. For *Sox10*^{cre/RCE} mice, brain tissue containing the somatosensory cortex was dissected at room temperature. Following dissection, tissue blocks were placed in 4% PFA in 250 mM HEPES–NaOH (pH 7.4–7.6) for post-fixation at 4 °C for 1 h. Brains were then placed in 8% PFA in 250 mM HEPES and incubated at 4 °C for 2–3 h. Tissue blocks were then placed in 1% PFA in 250 mM HEPES and kept at 4 °C until tissue was prepared for cryopreservation (up to 5 days, with daily solution changes).

Cryoblock preparation and cryosectioning

Fixed tissue samples from different brain regions were further dissected to produce about 1.5 × 3 mm tissue samples suitable for Tokuyasu cryosectioning² (Extended Data Fig. 1a) at room temperature in 1% PFA in 250 mM HEPES. For the hippocampus, the dorsal CA1 region was further isolated. Approximately 1–3 × 1–3

mm blocks were dissected from all brain regions and were further incubated in 4% PFA in 250 mM HEPES at 4 °C for 1 h. The fixed tissue was transferred to 2.1 M sucrose in PBS and embedded for 16–24 h at 4 °C, before being positioned at the top of copper stub holders suitable for ultracryomicrotomy and frozen in liquid nitrogen. Cryopreserved tissue samples are kept indefinitely immersed under liquid nitrogen.

Frozen tissue blocks were cryosectioned with an Ultracryomicrotome (Leica Biosystems, EM UC7), with an approximate 220–230 nm thickness². Cryosections were captured in drops of 2.1 M sucrose in PBS solution suspended in a copper wire loop and transferred to 10-mm glass coverslips for confocal imaging or onto a 4.0-μm polyethylene naphthalate (PEN; Leica Microsystems, 11600289) membrane on metal framed slides for laser microdissection.

Immunofluorescence detection of GAM samples for confocal microscopy

For confocal imaging, cryosections were incubated in sheep anti-TH (1:500; Pel Freez Arkansas, P60101-0), mouse anti-pan-histone H11-4 (1:500; Merck, MAB3422) or chicken anti-GFP (1:500; Abcam, ab13970) followed by donkey anti-sheep or goat anti-chicken IgG conjugated with Alexa Fluor-488 (for TH and GFP; Abcam) or donkey anti-mouse IgG conjugated with Alexa Fluor-555 or Alexa Fluor-488 (for pan-histone; Invitrogen).

For PGNs, cryosections were washed (3 times, 30 min in total) in PBS, permeabilized (5 min) in 0.3% Triton X-100 in PBS (v/v) and incubated (2 h, room temperature) in blocking solution (1% BSA (w/v), 5% fetal bovine serum (FBS (w/v), Gibco, 10270), 0.05% Triton X-100 (v/v) in PBS). After incubation (overnight, 4 °C) with primary antibody in blocking solution, the cryosections were washed (3–5 times, 30 min) in 0.025% Triton X-100 in PBS (v/v) and immunolabelled (1 h, room temperature) with secondary antibodies in blocking solution followed by 3 washes (15 min) in PBS. Cryosections were then counterstained (5 min) with 0.5 μg ml⁻¹ 4',6'-diamino-2-phenylindole (DAPI; Sigma-Aldrich, D9542) in PBS, and then rinsed in PBS and water. Coverslips were mounted in Mowiol 4-88 solution in 5% glycerol, 0.1 M Tris-HCl (pH 8.5).

The number of SATB2-positive cells present in the hippocampal CA1 area of the *Satb2*^{flox/flox} control mice was determined by counting nuclei positive for SATB2 immunostaining (1:100; Abcam, ab10563678). To avoid counting the same nuclei, only every 30th ultrathin section cut through the tissue was collected, and the remaining sections discarded. Twenty-five nuclei were identified in the pyramidal neuron layer per image in the DAPI channel, and only SATB2-positive cells were counted. We confirmed that most cells (96%) within the CA1 layer were PGNs (data not shown).

For DNs and OLGs, cryosections were washed (3 times, 30 min in total) in PBS, quenched (20 min) in PBS containing 20 mM glycine, then permeabilized (15 min) in 0.1% Triton X-100 in PBS (v/v). Cryosections were then incubated (1 h, room temperature) in blocking solution (1% BSA (w/v), 0.2% fish-skin gelatin (w/v), 0.05% casein (w/v) and 0.05% Tween-20 (v/v) in PBS). After incubation (overnight, 4 °C) with the antibody in blocking solution, the cryosections were washed (3–5 times, 1 h) in blocking solution and immunolabelled (1 h, room temperature) with secondary antibodies in blocking solution, followed by 3 washes (15 min) in 0.5% Tween-20 in PBS (v/v). Cryosections were then counterstained with 0.5 µg ml⁻¹ DAPI in PBS, then rinsed in PBS. Coverslips were mounted in Mowiol 4-88.

Digital images were acquired with a Leica TCS SP8-STED confocal microscope (Leica Microsystems) using a ×63 oil-immersion objective (numerical aperture of 1.4) or a ×2 oil-immersion objective, using a pinhole equivalent to 1 Airy disk. Images were acquired using 405-nm excitation and 420–480-nm emission for DAPI, 488-nm excitation and 505–530-nm emission for TH or GFP, and 555-nm excitation and 560-nm emission using a long-pass filter at 1,024 × 1,024 pixel resolution. Images were processed using Fiji (v.2.0.0-rc-69/1.52p), and adjustments included the optimization of the dynamic signal range with contrast stretching.

Immunofluorescence detection of GAM samples for laser microdissection

For laser microdissection, cryosections on PEN membranes were washed, permeabilized and blocked as for confocal microscopy, and incubated with primary and secondary antibodies as indicated above except for the use of higher concentrations of primary antibodies, as follows: anti-TH (1:50), anti-pan-histone (1:50) or anti-GFP (1:50). Secondary antibodies were used at the same concentration. Cell staining was visualized using a Leica laser microdissection microscope (Leica Microsystems, LMD7000) using a ×3 dry objective. Following detection of cellular sections of the cell types of choice containing nuclear slices (nuclear profiles (NPs)), individual NPs were laser microdissected from the PEN membrane and collected into PCR adhesive caps (AdhesiveStrip 8C opaque, Carl Zeiss, 415190-9161-000). We used multiplex-GAM⁹, for which three NPs were collected into each adhesive cap and the presence of NPs in each lid was confirmed with a ×5 objective using a 420–480-nm emission filter. Control lids not containing NPs (water controls) were included for each dataset collection to keep track of contamination and noise amplification of whole-genome amplification (WGA) and library reactions, and can be found in Supplementary Table 2.

WGA of NPs

WGA was performed using an in-house protocol. In brief, NPs were lysed directly in the PCR adhesive caps for 4 h (or 24 h for 160 out of 585 GAM samples from DN replicate 1) at 60 °C in 1.2× lysis buffer (30 mM Tris-HCl pH 8.0, 2 mM EDTA pH 8.0, 800 mM guanidinium-HCl, 5 % (v/v) Tween 20, 0.5 % (v/v) Triton X-100) containing 2.116 units ml⁻¹ Qiagen protease (Qiagen, 19155). After protease inactivation at 75 °C for 30 min, the extracted DNA was amplified using random hexamer primers with an adaptor sequence. The pre-amplification step was done using 2× DeepVent mix (2× Thermo polymerase buffer (10×), 400 μM dNTPs, 4 mM MgSO₄ in ultrapure water), 0.5 μM GAT-7N primers (5'-GTG AGT GAT GAT GGT TGA GGT AGT GTG GAG NNN NNN N) and 2 units μl⁻¹ DeepVent (exo-) DNA polymerase (New England Biolabs, M0259L) in the programmable thermal cycler for 11 cycles. Primers that annealed to the general adaptor sequence were then used in a second exponential amplification reaction to increase the amount of product. The exponential amplification was done using 2× DeepVent mix, 10 mM dNTPs, 100 μM GAM-COM primers (5'-GTGAGTGATGGTTGAGGTAGTGTGGAG) and 2 units μl⁻¹ DeepVent (exo-) DNA polymerase in the programmable thermal cycler for 26 cycles. For a small number of NPs from DNs (Supplementary Table 2), WGA was performed using a WGA4 kit (Sigma-Aldrich) using the manufacturer's instructions; the recent formulation of this kit is no longer suitable for GAM data production from subcellular nuclear slices.

GAM library preparation and high-throughput sequencing

Following WGA, the samples were purified using SPRI beads (0.725 or 1.7 ratio of beads per sample volume). The DNA concentration of each purified sample was measured using a Quant-iT Pico Green dsDNA assay kit (Invitrogen, P7589) according to the manufacturer's instructions. GAM libraries were prepared using an Illumina Nextera XT library preparation kit (Illumina, FC-131-1096) following the manufacturer's instructions with an 80% reduced volume of reagents. Following library preparation, the DNA was purified using SPRI beads (1.7 ratio of beads per sample volume) and the concentration for each sample was measured using a Quant-iT PicoGreen dsDNA assay. An equal amount of DNA from each sample was pooled together (up to 196 samples), and the final pool was additionally purified three times using the SPRI beads (1.7 ratio of beads per sample volume). The final pool of libraries was analysed using DNA High Sensitivity on-chip electrophoresis on an Agilent 2100 Bioanalyzer to confirm the removal of primer dimers and to estimate the average size and DNA fragment size distribution in the pool. NGS libraries were sequenced on an Illumina NextSeq 500 machine according to the manufacturer's instructions using single-end 75 bp reads. The number of sequenced reads for each sample can be found in Supplementary Table 2.

Tn5-based libraries are preferred for GAM data sequencing to increase fragment sequence variation, which helps avoid the need for dark cycles in the current Illumina machines. This choice greatly reduces the cost of sequencing and decreases the frequency of noise reads from absent windows seen with the previous protocol³.

GAM data sequence alignment

Sequenced reads from each GAM library were mapped to the mouse genome assembly GRCm38 (December 2011, mm10) with Bowtie2 (v.2.3.4.3) using default settings⁵⁶. All non-uniquely mapped reads, reads with mapping quality <20 and PCR duplicates were excluded from further analyses.

GAM data window calling and sample QC

Positive genomic windows present within ultrathin nuclear slices were identified for each GAM library. In brief, the genome was split into equal-sized windows (50 kb), and the number of nucleotides sequenced in each bin was calculated for each GAM sample with bedtools⁵⁷. Next, we determined the percentage of orphan windows (that is, positive windows that were flanked by two adjacent negative windows) for every percentile of the nucleotide coverage distribution and we identified the percentile with the lowest percentage of orphan windows for each GAM sample in the dataset. The number of nucleotides that corresponds to the percentile with the lowest percentage of orphan windows in each sample was used as an optimal coverage threshold for window identification in each sample. Windows were called positive if the number of nucleotides sequenced in each bin was greater than the determined optimal threshold.

Each dataset was assessed for QC by determining the percentage of orphan windows in each sample, the number of uniquely mapped reads to the mouse genome and the correlations from cross-well contamination for every sample (Supplementary Table 2). Most GAM libraries passed the QC analyses (86–96% in each dataset; Extended Data Fig. 1b,c). To assess the quality of sampling in each GAM dataset, we measured the frequency with which all possible intrachromosomal pairs of genomic windows are found in the same GAM sample; we found that 98.8–99.9% of all mappable pairs of windows were sampled at least once at resolution 50 kb at all genomic distances. Each sample was considered to be of good quality if they had <70% orphan windows, >50,000 uniquely mapped reads and a cross-well contamination score determined per collection plate of <0.4 (Jaccard index). The number of samples in each cell type that passed QC is summarized in Extended Data Fig. 2a. Following QC analysis, we noted that the 160 (out of 585) DN replicate 1 samples incubated with lysis buffer for 24 h had decreases in orphan windows (median = 26% and 36% for 24 h and 4 h, respectively) and increases in total genome coverage (median = 9% and 6% for 24 h

and 4 h, respectively). Although these differences were minor, we recommend 24 h lysis for future work.

Publicly available GAM datasets from mES cells

For mES cells, GAM datasets were downloaded from the 4D Nucleome portal (<https://data.4dnucleome.org/>). We used 249×3 NP GAM datasets from mES cells (clone 46C), which were grown at 37°C in a 5% CO_2 incubator in Glasgow modified Eagle's medium (MEM), supplemented with 10% FBS, 2 ng ml^{-1} leukaemia inhibitory factor (LIF) and 1 mM 2-mercaptoethanol, on 0.1% gelatin-coated dishes. Cells were passaged every other day. After the last passage, 24 h before collection, mES cells were re-plated in serum-free ESGRO Complete Clonal Grade medium (Merck, SF001-B). The list of 4DN sample identity numbers is provided in Supplementary Table 1.

Visualization of pairwise chromatin contact matrices

To visualize GAM data, contact matrices were calculated using pointwise mutual information (PMI) for all pairs of windows genome-wide. PMI describes the difference between the probability of a pair of genomic windows being found in the same NP given both their joint distribution and their individual distributions across all NPs. PMI was calculated using the following formula, where $p(x)$ and $p(y)$ are the individual distributions of genomic windows x and y , respectively, and $p(x,y)$ are their joint distribution:

$$\text{PMI} = \log(p(x,y)/p(x)p(y)) \quad (1)$$

PMI can be bounded between -1 and 1 to produce a normalized PMI (NPMI) value given by the following formula:

$$\text{NPMI} = \text{PMI} / (-\log(p(x,y))) \quad (2)$$

For visualization of the contact matrices, scale bars are adjusted in each genomic region displayed to a range between 0 and the 99th percentile of NPMI values for each cell type.

Insulation score and topological domain boundary calling

TAD calling was performed by calculating insulation scores in NPMI GAM contact matrices at 50-kb resolution, as previously described^{2,9}. The insulation square method was chosen as it was previously shown that the domain borders detected in GAM data

are also found in Hi-C, for which they are the most robust (most insulated)^{2,9}. The insulation score was computed individually for each cell type and biological replicate, with insulation square sizes ranging from 100 to 1,000 kb. TAD boundaries were called using a 500-kb insulation square size and based on local minima of the insulation score. This approach does not detect meta-TADs or sub-TADs, and results in numbers and lengths of domains were similar to previous reports^{6,58}. Future work with higher resolution GAM datasets will enable further analyses of the reorganization of domains at finer genomic scales to investigate changes in sub-TADs, which have been previously shown to occur following cell commitment to neuronal lineages⁵⁹.

Within each dataset, boundaries that were touching or overlapping by at least one nucleotide were merged. Boundaries were further refined to consider only the minimum insulation score within the boundary and one window on each side, to produce a 3-bin ‘minimum insulation score’ boundary. In comparisons of boundaries between different datasets, 150-kb boundaries were considered different when separated by at least one 50-kb genomic bin, that is, if the centre of the boundaries are separated by at least 200 kb (note chromosome Y was excluded from the analysis). In Fig. 2b, we considered the boundary coordinate as the genomic window within a boundary with the lowest insulation value. TAD border coordinates for all cell types can be found in Supplementary Table 3, and the full range of insulation scores (100–1,000 kb) for all cell types can be found in Supplementary Table 4. UpSet plots for TAD border overlaps, compartments and TF motif analyses were generated using either custom Python or R scripts or using the UpSetR package (v.1.4.0)⁶⁰.

Identification of compartments A and B

For compartment analysis, matrices of co-segregation frequency were determined using the ratio of independent occurrence of a single positive window in each sample over the pairwise co-occurrence of pairs of positive windows in a given pair of genomic windows². GAM co-segregation matrices at 250-kb resolution were assigned to either A or B compartments, as previously described². In brief, each chromosome was represented as a matrix of observed interactions $O(i,j)$ between locus i and locus j (co-segregation) and separately for $E(i,j)$, whereby each pair of genomic window is the mean number of contacts with the same distance between i and j . A matrix of observed over expected values $O/E(i,j)$ was produced by dividing O by E . A correlation matrix $C(i,j)$ was produced between column i and column j of the O/E matrix. PCA was performed for the first three components on matrix C before extracting the component with the best correlation to GC content. Loci with PCA eigenvector values with the same sign that correlate best with GC content were called A compartments, whereas regions with the opposite sign were B compartments. For visualizations and Pearson’s correlations between datasets, eigenvector values on the same chromosome in compartment A were normalized from 0 to 1, whereas values on the same

chromosome in compartment B were normalized from -1 to 0 . Compartments were considered common if they had the same compartment definition within the same genomic bin. Compartment changes between cell types were computed after considering compartments that were common between biological replicates unless otherwise indicated.

To identify and visualize gene expression differences among genes in changing compartments, k -means clustering was performed on triplicate pseudo-replicates of each cell type using a custom Python script (Extended Data Fig. 12a, b). The number of clusters were determined using the elbow method, with k -means = 6 for genes in compartment B in mES cells and compartment A in brain cells, and k -means = 5 for compartment A in mES cells and compartment B in brain cells.

mES cell culture for scRNA-seq and scATAC-seq

mES cells from the 46C clone, derived from E14tg2a and expressing GFP under the *Sox1* promoter⁶¹, were a gift from D. Henrique (Instituto de Medicina Molecular, Faculdade Medicina Lisboa, Lisbon, Portugal). mES cells were cultured as previously described⁶². In brief, cells were routinely grown at $37\text{ }^{\circ}\text{C}$, 5% (v/v) CO_2 , on gelatine-coated (0.1% v/v) Nunc T25 flasks in Gibco Glasgow's MEM (Invitrogen, 21710082), supplemented with 10% (v/v) fetal calf serum (BioScience LifeSciences, 7.01, batch number 110006) for scRNA-seq or Gibco FBS (Invitrogen, 10270-106, batch number 41F8126K) for ATAC-seq, $2,000$ units ml^{-1} LIF (Millipore, ESG1107), 0.1 mM β -mercaptoethanol (Invitrogen, 31350-010), 2 mM l-glutamine (Invitrogen, 25030-024), 1 mM sodium pyruvate (Invitrogen, 11360070), 1% penicillin-streptomycin (Invitrogen, 15140122) and 1% MEM non-essential amino acids (Invitrogen, 11140035). Medium was changed every day and cells were split every other day. mES cell batches tested negative for *Mycoplasma* infection, which was performed according to the manufacturer's instructions (AppliChem, A3744,0020). Before collecting material for scRNA-seq or ATAC-seq, cells were grown for 48 h in serum-free ESGRO Complete Clonal Grade medium (Merck, SF001- B), supplemented with $1,000$ units ml^{-1} LIF, on gelatine -coated (Sigma, G1393-100 ml, 0.1% v/v) Nunc 10-cm dishes, with a change in medium after 24 h .

46C E14tg2 mES cells are not listed in the ICLAC Register of Misidentified Cell Lines. The 46C E14tg2 mES cell line was generated by insertion of an eGFP cassette under the control of the *Sox1* promoter in E14tg2 cells. Reads aligned with the GFP sequence were identified in the GAM sequencing data from mES cells. In addition, genome sequencing data from GAM mES cell samples was mined for single nucleotide polymorphisms (SNPs). Although GAM sequencing reads are sparsely distributed across the genome, there was a 64% overlap of GAM mES cell SNPs with

SNPs identified from the parental E14tg2 genome sequencing data (<https://www.ncbi.nlm.nih.gov/sra?term=SRX389523>; data not shown).

Single-cell mRNA library preparation

Two batches (denoted batch A and B) of single-cell mRNA-seq libraries were prepared according to the Fluidigm manual “Using the C1 Single-Cell Auto Prep System to Generate mRNA from Single Cells and Libraries for Sequencing”. Cell suspension was loaded on 10–17 µm C1 Single-Cell Auto Prep IFCs (Fluidigm, 100-5760, kit 100-6201). After loading, the chip was observed under the microscope to score cells as singlets, doublets, multiplets, debris or other. The chip was then loaded again on Fluidigm C1 IFCs, and cDNA was synthesized and pre-amplified in the chip using a Clontech SMARTer kit (Takara Clontech, 634833). In batch B, we included Spike-In Mix 1 (1:1,000; Life Technologies, 4456740) as per the Fluidigm manual. Illumina sequencing libraries were prepared using a Nextera XT kit (Illumina, FC-131-1096) and a Nextera Index kit (Illumina, FC-131-1002), as previously described⁶³. Libraries from each microfluidic chip (96 cells) were pooled and sequenced on 4 lanes on Illumina HiSeq 2000, 2×100-bp paired-end (batch A) or 1 lane on Illumina HiSeq 2000, 2×125-bp paired-end (batch B) at the Wellcome Trust Sanger Institute Sequencing Facility (Supplementary Table 15).

scRNA-seq data processing, mapping and expression estimates

To calculate expression estimates, mRNA-seq reads were mapped with STAR (spliced transcripts alignment to a reference, v.2.4.2a)⁶⁴ and processed with RSEM using the ‘single-cell-prior’ option (RNA-seq by expectation-maximization, v.1.2.25)⁶⁵. The references provided to STAR and RSEM were the GTF annotation from UCSC Known Genes (mm10, v.6) and the associated isoform–gene relationship information from the Known Isoforms table (UCSC), adding information for ERCC sequences in samples from batch B. Tables were downloaded from the UCSC Table browser (<http://genome.ucsc.edu/cgi-bin/hgTables>) and for ERCCs, from the ThermoFisher website (<http://www.thermofisher.com/order/catalog/product/4456739>). Gene-level expression estimates in ‘Expected Counts’ from RSEM were used for the analysis.

scRNA-seq data processing QC

Cells scored as doublets, multiplets or debris during visual inspection of the C1 chip were excluded from the analysis. Datasets were also excluded if any of the following conditions were met: <500,000 reads (calculated using sam-stats from ea-utils.1.1.2-537)⁶⁶; <60% of reads mapped (calculated with sam-stats); <50% reads mapped to mRNA (picard-tools-2.5.0, <http://broadinstitute.github.io/picard/>); >15% of reads mapped to chrM (sam-stats); if present, >20% of reads mapped to ERCCs (sam-stats).

Following processing, 98 single cells passed quality thresholds in the final dataset. Correlations between previously published mES cells (clone 46C) mRNA-seq bulk⁶² and the scRNA-seq mES cell transcriptomes were performed to assess the quality of the single-cell data. Correlations were performed as previously described⁶⁷. Average single-cell expression was highly correlated with bulk RNA-seq data (Extended Data Fig. 4c).

scRNA-seq analysis

To utilize published single-cell transcriptomes from brain cell types of interest, we selected P21–22 OLGs⁶⁸, P22–32 CA1 PGNs⁶⁹ and P21–26 VTA DNs⁷⁰ on the basis of the cell type and subtype definitions provided in the respective publications. The matrices of counts provided in each publication, along with the single-cell mES cell transcriptomes produced that passed QC, were combined with no prior batch correction due to the lack of equivalent cell types across all single-cell datasets. The combined matrix of counts was normalized by applying the LogNormalize method and scaled using Seurat (v.3.1.4)⁷¹. The scaled data were used for a PCA, followed by processing through dimensionality reduction using uniform manifold approximation and projection (UMAP)⁷² for visualization purposes using the Seurat R package⁷¹, with default parameters. Visualization of known cell-type-specific marker genes confirmed that the different transcriptomes are grouped into cell-type-specific clusters (Extended Data Fig. 4e). Single mES cell transcriptomes from batch A and B clustered together, and were pooled for further analyses. Genes that could not be mapped to the chosen reference GTF were removed (UCSC; accessed from iGenomes July 17, 2015; https://support.illumina.com/sequencing/sequencing_software/igenome.html).

To generate bigwig tracks for visualization, raw fastq files from each single cell within the same cell type were pooled into one fastq file. Reads were mapped to the mouse genome (mm10) using STAR with default parameters but—outFilterMultimapNmax 10. BAM files were sorted and indexed using Samtools (v.1.3.1)⁷³ and normalized (reads per kilobase of transcript per million (RPKM)) bigwigs were generated using DeepTools (v.3.1.3)⁷⁴ bamCoverage. To account for differences in the number of technical replicates in OLG samples, cells were divided into groups by the number of runs (1, 2 and 6). The median of the reads for the group with the lowest sequencing depth was used as a threshold to normalize the other groups (that is, the rest of the fastq files were randomly downsampled to that number of reads). The three groups of raw reads were pooled together and processed by applying the same method as for the other cell types. Pseudobulk expression was determined using the regularized log (R-log) value for each gene (Extended Data Fig. 4f,g). In each cell type, only the genes with R-log values of ≥ 2.5 in all pseudobulk replicates were considered expressed.

Differential gene expression analysis

For differential expression analysis for all cell types, pseudobulk replicate samples were obtained by randomly partitioning the total number of single cells per dataset into three groups and pooling all unique molecular identifiers (UMIs) per gene of cells belonging to the same replicate. To determine differentially expressed genes, all six possible pairwise comparisons between samples were performed using DEseq2 (v.1.24.0) with default parameters⁷⁵. In addition, shrunken \log_2 fold-changes were added with the lfcShrink function, using default parameters. Genes classified as differentially expressed in at least one comparison were considered for further analysis (adjusted P value < 0.05 ; Benjamini–Hochberg multiple testing correction method). A summary table for the differential expression analysis of all cell types can be found in Supplementary Table 12. For the TF motif analysis, only the differentially expressed genes obtained from the comparison between DNs and PGNs were considered for further analysis (Extended Data Fig. 9c, d).

Tn5 purification

The pTXB1 plasmid carrying the Tn5-intein-CBD fusion construct with the hyperactive Tn5 protein containing the E54K and L372P mutations was obtained from Addgene (plasmid 60240). Tn5 expression and purification was performed as previously described⁷⁶, except that the final storage buffer was 50 mM HEPES-KOH pH 7.2, 0.8 M NaCl, 0.1 mM EDTA, 1 mM dithiothreitol and 55% glycerol.

Tn5 adapter mix preparation

To generate 100 μM adapter mix, 200 μM Tn5MErev (5'-[phos]CTGTCTCTTATACACATC) was mixed with of 200 μM Tn5ME-A (5'-TCGTCGGCAGCGTCAGATGTGTATAAGAGACAG; Adapter_mixA, 1:1 ratio). Separately, 200 μM Tn5MErev was mixed with 1 volume of 200 μM Tn5ME-B (5'-GTCTCGTGGGCTCGGAGATGTGTATAAGAGACAG; Adapter_mixB, 1:1 ratio). The two mixtures were incubated for 5 min at 95 °C and gradually cooled to 25 °C at a ramp rate of 0.1 °C s⁻¹. Finally, the Adapter_mixA was mixed with Adapter_mixB at a 1:1 ratio for a final 100 μM adapter mix.

mES cell ATAC-seq library preparation

ATAC-seq libraries were generated from approximately 75,000 mES cell nuclei following the Omni ATAC protocol⁷⁷ with a modified transposition reaction: TAPS-DMF buffer (50 mM TAPS-NaOH, pH 8.5, 25 mM MgCl₂, 50% DMF), 0.1% Tween-20, 0.1% digitonin, in 0.25x PBS. A total of 3 μl of the Tn5 mix (5.6 μg Tn5 and 0.143 volume of 100 μM adapter mix) was added to the transposition reaction mix. Libraries were prepared as described in the Omni ATAC protocol. The final library was sequenced with an Illumina NextSeq 500 machine according to manufacturer's instructions, using paired-end 75 bp reads (150 cycles).

Isolation of the VTA for snATAC-seq

Male C57Bl/6Nl (RRID: IMSR_CR:027; WT) mice, aged 7 and 9 weeks, were killed by cervical dislocation. Brains were removed and the tissue containing the midbrain VTA was dissected from each hemisphere at room temperature and rapidly frozen on dry ice. Frozen midbrain samples were kept at -80°C until further processing.

DN snATAC-seq library preparation

Two 10X Genomics scATAC-seq libraries from the midbrain VTA, VTA-1 and VTA-2 (from mice aged 7 or 9 weeks, respectively), were generated from midbrain VTA samples according to the 10X Genomics manual “Nuclei Isolation from Mouse Brain Tissue for Single Cell ATAC Sequencing Rev B” for flash-frozen tissue with minor adjustments. In brief, 500 μl 0.1 \times lysis buffer (10 mM Tris-HCl, pH 7.4, 10 mM NaCl, 3 mM MgCl₂, 1% BSA, 0.01% Tween-20, 0.01% Nonidet P40 substitute, 0.001% digitonin, and 1 \times complete Mini, EDTA-free protease inhibitor cocktail, Millipore-Sigma, 11836170001) was added to the frozen samples and immediately homogenized using a pellet pestle (15 times), followed by 5 min incubation on ice. The lysate was pipette mixed 10 times, then incubated 10 min on ice. Finally, 500 μl of chilled wash buffer (10 mM Tris-HCl, pH 7.4, 10 mM NaCl, 2 mM MgCl₂, 1% BSA, 0.1% Tween-20) was added to the lysed cells, and the suspension was passed through a 30- μm CellTrics strainers (Th Geyer, 7648779). The final approximately 500 μl nuclei suspension was stained with DAPI (final concentration 0.03 $\mu\text{g ml}^{-1}$) for about 5 min.

Around 200,000 DAPI-positive events were sorted using a BD FACSAria III flow cytometer with 70- μm nozzle configuration with sample and sort collection device cooling set to 4 $^{\circ}\text{C}$ into 300 μl Diluted Nuclei buffer (commercial buffer from 10X Genomics) in a 1.5-ml Eppendorf tube. A first gate excluded debris in a forward scatter/side scatter plot (see examples in Extended Data Fig. 4*h, i*). A consecutive, second gate in a DAPI-A/DAPI-H plot was used to exclude doublets and nuclei with incomplete DNA content (BD FACSDiva software, v.8.0.2). The collected nuclei were centrifuged at 500g for 5 min at 4 $^{\circ}\text{C}$ and resuspended in 20 μl Diluted Nuclei buffer. The nucleus concentration was determined using a Countess II FL Automated Cell Counter in DAPI fluorescence mode. snATAC-seq

libraries were prepared per the Chromium Next GEM Single Cell ATAC Reagent kits v.1.1 User Guide. In brief, nuclei were loaded on a microfluidics chip together with transposition reagents, transposase enzyme, beads with oligo-dT tags and oil to create an emulsion. Afterwards, the transposase reaction takes place inside the droplets. The barcoded cDNA is recovered from the emulsion, amplified and cleaned using a bead purification process. The cDNA is then used for library construction, including enzymatic fragmentation, adapter ligation and sample index PCR. Libraries were sequenced with either an Illumina NextSeq 500 machine using paired-end 75 bp reads (for VTA-1, 150 cycles) or a NovaSeq 6000 using paired-end 75 bp reads (for VTA-2, 100 cycles).

ATAC-seq data processing, mapping, processing and QC

For bulk mES cell ATAC-seq, paired-end reads were mapped to the mouse genome (mm10) using Bowtie with the following parameters:–minins 25–maxins 2000–no-discordant–dovetail–soft-clipped-unmapped-tlen. Low-quality mapped reads ($\text{MQ} < 30$) and mitochondrial reads were removed. Duplicated reads were removed with Sambamba⁷⁸ (v.0.6.8). Reads passing quality checks were converted to BAM format for further analyses.

For VTA snATAC-seq, paired-end reads were demultiplexed and mapped to the mouse genome (mm10) using the 10X Genomics Cellranger software (version cellranger-atac-1.2.0). The two VTA snATAC-seq libraries were analysed using ArchR software (v.0.9.1)⁷⁹. Doublets were removed following default parameters in ArchR. Next, low-quality cells (identified as TSS enrichment score <4 and $<2,500$ unique fragments per cell) were removed for further analyses.

Next, dimensionality reduction was performed using the Latent semantic indexing (LSI) dimensionality reduction method from ArchR, with default parameters (except iterations = 10, resolution = 0.2, varFeatures = 60,000). The ArchR addHarmony function was used to run the Harmony algorithm for batch correction with default parameters, followed by clusters calling. Gene scores were determined as specified by ArchR⁷⁹. DNs were identified as the cluster with higher gene scores for *Th*, a well-known DN marker, and confirmed by additional DN marker expression (for example, *Lmx1b*,

Foxa2, *Foxa1* and *Slc6a3*). The DN cluster is composed of 216 cells in total (113 from VTA-1 and 103 from the VTA-2). UMI duplicates were collapsed to one fragment. To visualize an approximation for gene expression, gene scores were calculated using the createArrowFiles (addGeneScoreMat = TRUE) function in ArchR.

Processing of published OLG and PGN scATAC-seq

scATAC-seq BAM files for OLGs were downloaded from the sciATAC-seq in vivo atlas of the mouse brain⁸⁰. Next, reads were extracted from the BAM file that corresponded to cells from the cluster identified as oligodendrocytes from the prefrontal cortex (458 cells), to produce a pseudobulk ATAC BAM file. The original data, mapped to the mm9 genome, were converted to mm10 using the liftOver tool from UCSC utilities (<https://genome.ucsc.edu/cgi-bin/hgLiftOver>).

scATAC-seq datasets were obtained from hippocampal PGNs⁸¹. A BAM file containing all cell types was supplied by A. Adey (Molecular and Medical Genetics, Oregon Health & Science University, Portland, OR, USA). Reads were extracted from the BAM file that corresponded to the NR1 PGN population (270 cells) to produce a pseudobulk ATAC BAM file.

Generation of normalized ATAC-seq bigwig tracks

A size factor normalization was applied to generate ATAC-seq bigwig tracks comparable between mES cells, OLGs, PGNs and DNs. First, a count matrix was generated for all TSS regions (± 250 bp), which contained reads from at least two of the four cell types. The TSS list was extracted from the genes.gtf file included in the cell ranger reference data (refdata-cellranger-atac-mm10-1.2.01; <https://support.10xgenomics.com/single-cell-atac/software/pipelines/latest/advanced/references>). To calculate size factors, the TSS count matrix was processed through DESeqDataSetFromMatrix and estimateSizeFactors from the DESeq2 package⁷⁵. For all cell types, the scale factor (SF) = (cell type size factor) $\times -1$.

Each pseudobulk ATAC-seq BAM file from mES cells, PGNs and OLGs was converted to the bedGraph format using the genomeCoverageBed function from bedtools⁵⁷ with the following parameters: -pc -bg -scale SF. For DNs, ATAC-seq fragment files were converted to the bedGraph format using the genomeCoverageBed function from bedtools⁵⁷ with the following parameters: -g chrom.sizes -bg -scale SF. The mm10 chrom.sizes file was downloaded from UCSC using fetchChromSize from UCSC utilities (<http://hgdownload.soe.ucsc.edu/admin/exe/>). The bedGraph files were then converted to bigwig using the bedGraphToBigWig function from UCSC utilities.

DN and PGN ATAC-seq peak calling

ATAC-seq peaks were called in DNs following the iterative overlap peak merging procedure described in the ArchR package⁷⁹. First, two pseudobulk replicates were generated by running the addGroupCovariates function and then reproducible peaks were called using the addReproduciblePeakSet function. For PGNs, peaks for the NR1 cluster were obtained from Sinnamon et al.⁸¹. For further analyses, peaks were considered positive if they were found in at least 10% of single nuclei (>10 nuclei in DNs; >13 cells in PGNs).

RNA and ATAC-seq length-scaled ATAC reads per million

To calculate length-scaled RNA reads per million (lsRRPM) for 479 long genes (>300 kb), the mES cell BAM file (paired-end) was read using the readGAlignmentPairs function from the GenomicAlignments function from the GenomicAlignments package in R (v.1.20.1; <https://bioconductor.org/packages/release/bioc/html/GenomicAlignments.html>). For published single-cell datasets (OLGs, PGNs, DNs; single-end libraries), BAM files were loaded using the readGAlignments function from the GenomicAlignment package. Owing to the very long length of some reads, all BAM fragments were resized to the 5' end base pair to avoid overlapping with multiple features. Next, the following formula was used to compute lsRRPM values for each cell type and per gene:

```
$$\{\rm{l}\} \{\rm{s}\} \{\rm{R}\} \{\rm{R}\} \{\rm{P}\} \{\rm{M}\} = \{\rm{n}\}
\{\rm{u}\} \{\rm{m}\} \{\rm{b}\} \{\rm{e}\} \{\rm{r}\} \{\rm{o}\} \{\rm{f}\} \},
\{\rm{o}\} \{\rm{v}\} \{\rm{e}\} \{\rm{r}\} \{\rm{l}\} \{\rm{a}\} \{\rm{p}\} \{\rm{s}\} \},
\{\rm{b}\} \{\rm{e}\} \{\rm{t}\} \{\rm{w}\} \{\rm{e}\} \{\rm{e}\} \{\rm{n}\} \},
\{\rm{R}\} \{\rm{N}\} \{\rm{A}\} \{\rm{f}\} \{\rm{r}\} \{\rm{a}\} \{\rm{g}\}
\{\rm{m}\} \{\rm{e}\} \{\rm{n}\} \{\rm{t}\} \{\rm{s}\} \{\rm{a}\} \{\rm{n}\}
\{\rm{d}\}, \{\rm{l}\} \{\rm{o}\} \{\rm{n}\} \{\rm{g}\}, \{\rm{g}\} \{\rm{e}\}
\{\rm{n}\} \{\rm{e}\}, \{\rm{b}\} \{\rm{o}\} \{\rm{d}\} \{\rm{y}\} \{\rm{g}\}
\{\rm{e}\} \{\rm{n}\} \{\rm{e}\}, \{\rm{l}\} \{\rm{e}\} \{\rm{n}\} \{\rm{g}\} \{\rm{g}\} \{\rm{t}\}
\{\rm{h}\}, \{(10)^{-6}\} \times \{\rm{t}\} \{\rm{o}\} \{\rm{t}\} \{\rm{a}\}
\{\rm{l}\}, \{\rm{n}\} \{\rm{u}\} \{\rm{m}\} \{\rm{b}\} \{\rm{e}\} \{\rm{r}\} \},
\{\rm{o}\} \{\rm{f}\}, \{\rm{R}\} \{\rm{N}\} \{\rm{A}\}, \{\rm{f}\} \{\rm{r}\}
\{\rm{a}\} \{\rm{g}\} \{\rm{m}\} \{\rm{e}\} \{\rm{n}\} \{\rm{t}\} \{\rm{s}\},
\{(10)^{-6}\} $$
```

To calculate length-scaled ATAC reads per million (lsARPM) for 479 long genes (>300 kb), concordant paired-end fragments were extracted for all cell types using the `readGAlignmentPairs` function from the GenomicAlignments package in R with the following total number of fragments: 37,261,746 (mES cells), 2,121,258 (OLGs), 4,594,229 (PGNs) and 8,939,526 (DNs). Next, the following formula was used to compute lsARPM values for each cell-type and per gene:

```
$$\{\rm{l}\} \{\rm{s}\} \{\rm{A}\} \{\rm{R}\} \{\rm{P}\} \{\rm{M}\} = \{\rm{n}\}
\{\rm{u}\} \{\rm{m}\} \{\rm{b}\} \{\rm{e}\} \{\rm{r}\} \{\rm{o}\} \{\rm{f}\} \},
\{\rm{o}\} \{\rm{v}\} \{\rm{e}\} \{\rm{r}\} \{\rm{l}\} \{\rm{a}\} \{\rm{p}\} \{\rm{s}\} \},
\{\rm{b}\} \{\rm{e}\} \{\rm{t}\} \{\rm{w}\} \{\rm{e}\} \{\rm{e}\} \{\rm{n}\} \},
\{\rm{A}\} \{\rm{T}\} \{\rm{A}\} \{\rm{C}\}, \{\rm{f}\} \{\rm{r}\} \{\rm{a}\}
\{\rm{g}\} \{\rm{m}\} \{\rm{e}\} \{\rm{n}\} \{\rm{t}\} \{\rm{s}\} \{\rm{a}\}
\{\rm{n}\} \{\rm{d}\}, \{\rm{l}\} \{\rm{o}\} \{\rm{n}\} \{\rm{g}\}, \{\rm{g}\}
\{\rm{e}\} \{\rm{n}\} \{\rm{e}\}, \{\rm{b}\} \{\rm{o}\} \{\rm{d}\} \{\rm{y}\}
\{\rm{g}\} \{\rm{e}\} \{\rm{n}\} \{\rm{e}\}, \{\rm{l}\} \{\rm{e}\} \{\rm{n}\}
\{\rm{g}\} \{\rm{t}\} \{\rm{h}\}, \{(10)^{-6}\} \times \{\rm{t}\} \{\rm{o}\}
\{\rm{t}\} \{\rm{a}\} \{\rm{l}\}, \{\rm{n}\} \{\rm{u}\} \{\rm{m}\} \{\rm{b}\}
\{\rm{e}\} \{\rm{r}\}, \{\rm{o}\} \{\rm{f}\}, \{\rm{A}\} \{\rm{T}\} \{\rm{A}\}
\{\rm{C}\}, \{\rm{f}\} \{\rm{r}\} \{\rm{a}\} \{\rm{g}\} \{\rm{m}\} \{\rm{e}\}
\{\rm{n}\} \{\rm{t}\} \{\rm{s}\}, \{(10)^{-6}\} $$
```

GO analysis

GO term enrichment analysis was performed using GOElite (v.1.2.4)⁸². In Extended Data Fig. 4n, DN snATAC-seq marker genes were extracted with the getMarkerFeatures function from ArchR with default parameters. Marker genes were selected as genes with \log_2 fold change values of >1 and false discovery rate of <0.01 in the DN cluster compared with all clusters from the VTA (total of 973 genes). All unique genes were used as the background GO dataset. In Fig. 2c, all genes expressed in at least one cell type, annotated to mm10, were used as the background dataset. In Fig. 4d, e, all genes expressed in PGNs or DNs were used as the background dataset, and in Fig. 5a, b, all unique genes were used. Default parameters were used for the GO enrichment: GO terms that were enriched above the background (significant permuted P values of <0.05 , 2,000 permutations) were pruned to select the terms with the largest Z-score (>1.96) relative to all corresponding child or parent paths in a network of related terms (genes changed >2). GO terms which had a permuted P value of ≥ 0.01 , contained fewer than 6 genes per GO term or from the ‘cellular_component’ ontology, were not reported in the main figures. A full list of unfiltered GO terms can be found in Supplementary Table 7.

MELTRON pipeline

To assess gene insulation differences, insulation square values at 10 length scales (100–1,000 kb) were calculated for genes >300 kb in length ($n = 479$; calculated for a minimum 8×50 -kb bins, that is, 400 kb minimum length). Cumulative probability distributions of insulation square values were calculated for each dataset, and the brain cells were compared to mES cell probability distributions for each gene by computing the maximum distance between the distributions and applying a Kolmogorov–Smirnov test. P values were corrected for multiple testing using the Bonferroni method, and $-\log_{10}$ transformed to obtain a domain melting score. Domain melting scores for each gene in each comparison can be found in Supplementary Table 8. For visualization, empirical cumulative probabilities and insulation score values were smoothed using a Gaussian kernel density estimate (adjust = 0.3).

Calculation of the *trans–cis* contact ratio

To determine the interaction strength of contacts to all (*trans*) somatic chromosomes relative to interaction strength to their own (*cis*) chromosome, *cis* and *trans* NPMI-normalized matrices were calculated at 250-kb resolution. Bins detected in less than 3%, or more than 75%, of 3 NP samples were removed from the analysis. To be sensitive to outliers, NPMI values of both *cis* (NPMI_C) and *trans* (NPMI_T) contacts for every bin were summarized with the arithmetic mean. The *trans–cis* contact ratio was then obtained using the following formula:

$$\begin{aligned} & \text{\$\$trans\mbox{--}cis\,}\{\text{\rm c}\}\,\{\text{\rm o}\}\,\{\text{\rm n}\}\,\{\text{\rm t}\}\,\{\text{\rm a}\}\} \\ & \{\text{\rm c}\}\,\{\text{\rm t}\}\},\{\text{\rm r}\}\,\{\text{\rm a}\}\,\{\text{\rm t}\}\,\{\text{\rm i}\}\} \\ & \{\text{\rm o}\}\}=\text{frac}\{\sum\{\text{\rm N}\}\,\{\text{\rm P}\}\,\{\text{\rm M}\}\} \\ & \{\text{\rm I}\}\}\}_{\text{\rm T}}\}\backslash\text{div}\{\text{\rm g}\}\,\{\text{\rm e}\}\,\{\text{\rm n}\}\,\{\text{\rm o}\}\,\{\text{\rm m}\}\} \\ & \{\text{\rm i}\}\,\{\text{\rm c}\}\},\{\text{\rm b}\}\,\{\text{\rm i}\}\,\{\text{\rm n}\}\,\{\text{\rm s}\}\} \\ & (\{\text{\rm n}\}_{\{\text{\rm T}\}})\}\{\sum\{\text{\rm N}\}\,\{\text{\rm P}\}\,\{\text{\rm M}\}\} \\ & \{\text{\rm I}\}\}_{\{\text{\rm C}\}}\}\backslash\text{div}\{\text{\rm g}\}\,\{\text{\rm e}\}\,\{\text{\rm n}\}\,\{\text{\rm o}\}\,\{\text{\rm m}\}\} \\ & \{\text{\rm i}\}\,\{\text{\rm c}\}\},\{\text{\rm b}\}\,\{\text{\rm i}\}\,\{\text{\rm n}\}\,\{\text{\rm s}\}\} \\ & (\{\text{\rm n}\}_{\{\text{\rm C}\}})\}\}\$\$ \end{aligned}$$

Trans–cis values of bins spanning long genes were summarized with the median.

Modelling and in silico GAM

To reconstruct 3D conformations of the *Nrxn3* locus, we employed the Strings & Binders Switch (SBS) polymer model of chromatin^{83,84}. In the SBS model, a chromatin region is modelled as a self-avoiding chain of beads, including different binding sites for diffusing, cognate, molecular binders. Binding sites of the same type can be bridged by their cognate binders, which then drives polymer folding. The optimal SBS polymers for the *Nrxn3* locus in mES cells and DNs were inferred using PRISMR, a machine-learning-based procedure that finds the minimal arrangement of the polymer binding sites that best describe input pairwise contact data, such as Hi-C²² or GAM⁸⁵. Here, PRISMR was applied to the GAM experimental data by considering the NPMI normalization on a 4.8 Mb

region around the *Nrxn3* gene (chromosome 12: 87,600,000–92,400,000; mm10) at 50-kb resolution in mES cells and DNs. The procedure returned optimal SBS polymer chains made of 1,440 beads, including 7 different types of binding sites, in both cell types. A full list of *x*, *y* and *z* coordinates for mES cell and DN polymer model structures can be found in Supplementary Tables 9 and 10, respectively.

Next, to generate thermodynamic ensembles of 3D conformations of the locus, molecular dynamics simulations were run of the optimal polymers, using the freely available LAMMPS software (v.5june2019)⁸⁶. In these simulations, the system evolves according to the Langevin equation, with dynamics parameters derived from classical polymer physics studies⁸⁷. Polymers are first initialized in self-avoiding conformations and then left to evolve to reach their equilibrium globular phase⁸³. Beads and binders have the same diameter $\sigma = 1$, expressed in dimensionless units, and experience a hard-core repulsion by use of a truncated Lennard–Jones potential. Analogously, attractive interactions are modelled with short-ranged Lennard–Jones potentials⁸³. A range of affinities between beads and cognate binders were sampled in the weak biochemical range, from $3.0 K_B T$ to $8.0 K_B T$ (where K_B is the Boltzmann constant and T the system temperature). In addition, binders interact nonspecifically with the polymer with a lower affinity, sampled from $0 K_B T$ to $2.7 K_B T$. For the sake of simplicity, the same affinity strengths were used for all different binding site types. The total binder concentration was taken above the polymer coil–globule transition threshold⁸³. For each of the considered cases, ensembles of up to 450 distinct equilibrium configurations were derived. Full details about the model and simulations are discussed in Barbieri et al.⁸³ and Chiariello et al.⁸⁴.

In silico GAM NPMI matrices were obtained from the ensemble of 3D structures by applying the in silico GAM algorithm¹⁰, here generalized to simulate the GAM protocol with 3 NPs per GAM sample and to perform NPMI normalization. In silico GAM NPMI matrices can be obtained using previously published algorithms¹⁰, by aggregating the content of three in silico slices into one tube, and then applying the NPMI normalization formula (see the section ‘Visualization of pairwise chromatin contact

matrices', therein¹⁰). Specifically, the same number of slices were used as in the GAM experiments, 249×3 NPs for mES cellCs and 585×3 NPs for DNs. Pearson's correlation coefficients were used to compare the in silico and experimental NPMI GAM matrices.

Example of single 3D conformations were rendered by a third-order spline of the polymer bead positions, with regions of interest highlighted in different colours. To quantify the size and variability of the 3D structures in mES cells and DNs, the average gyration radius (R_g) was measured from the selected domains encompassing and surrounding the *Nrxn3* gene, expressed in dimensionless units σ in Fig. 3d, Extended Data Fig. 7e. Analyses and plots were produced with the Anaconda package v.4.7.12, and 3D structure visualizations were produced with POV Ray, v.3.7 (<http://www.povray.org/download/>).

Cryosections for FISH experiments

Fixed and cryopreserved hippocampal CA1 tissue and mES cells were cryosectioned as previously described (see 'Cryoblock preparation and cryosectioning' above) with an approximate thickness of 400 nm and transferred to glass coverslips (thickness number 1.5, diameter 10 mm) coated with laminin (Sigma-Aldrich, P8920) according to the manufacturer's instructions for the three-colour FISH experiment (TSS, middle and TES), or washed in 100% ethanol and autoclaved for the immunofluorescence whole-gene FISH experiment (nucleolus, *Rbfox1*).

BAC probes labelling and precipitation

BACs targeting the *Rbfox1* locus (Supplementary Table 11) were obtained from the BACPAC Resources Center (<https://bacpacresources.org>) and amplified from glycerol stocks using a MIDIPrep kit (NucleoBond Xtra BAC purification kit, Machery-Nagel, 740436). Purified BACs were labelled using a nick translation kit (Abbott Molecular, 7J0001) according to the manufacturer's instructions and the following fluorophores (all Invitrogen, Thermo Fisher Scientific): ChromaTide Alexa Fluor 488-5-dUTP (C11397), ChromaTide Alexa Fluor 568-5-dUTP (C11399) and Alexa Fluor 647-aha-dUTP (A32763). Labelled BAC probes were co-

precipitated with yeast tRNA ($20\text{ }\mu\text{g }\mu\text{l}^{-1}$ final concentration; Invitrogen, AM7119) and mouse *Cot-1* DNA ($3\text{ }\mu\text{g }\mu\text{l}^{-1}$ final concentration; Invitrogen, 18440-016) overnight at $-20\text{ }^\circ\text{C}$. After clean up in 70% ethanol, the probes were dissolved in 100% deionized formamide (for 1 h; Sigma, F9037) before adding (1:1) a $2\times$ hybridization mix (20% dextran sulfate, 0.1 M phosphate buffer in $4\times$ saline-sodium citrate (SSC); mixing for 1 h), denatured (10 min, $80\text{ }^\circ\text{C}$), and reannealed (30 min, $37\text{ }^\circ\text{C}$) before hybridization.

Immunolabelling before FISH

Immunofluorescence labelling of the nucleolus was performed as described above ('Immunofluorescence detection for confocal microscopy') by incubating the cryosections overnight (at $4\text{ }^\circ\text{C}$) with a mouse monoclonal antibody anti-nucleophosmin B23 (a gift from H. Busch⁴⁹), followed by incubation (1 h) with donkey antibodies raised against mouse IgG conjugated with Alexa Fluor-555 (Invitrogen). Before cryo-FISH, the bound antibodies were fixed (1 h, $4\text{ }^\circ\text{C}$) in 8% depolymerized PFA (EM-grade) in 250 mM HEPES–NaOH (pH 7.6) and rinsed in PBS.

Cryo-FISH

Cryo-FISH was performed as previously described^{2,23} with a few modifications. In brief, cryosections were washed (30 min) in $1\times$ PBS, rinsed with $2\times$ SSC (Sigma, S6639) and incubated (2 h, $37\text{ }^\circ\text{C}$) in $250\text{ }\mu\text{g ml}^{-1}$ RNase A (Sigma, R4642) in $2\times$ SSC. After washing in $2\times$ SSC, cryosections were treated (10 min) with 0.1 M HCl, dehydrated in ethanol (30%, 50%, 70%, 90%, 100% series, 3 min each on ice) and denatured (10 min) at $80\text{ }^\circ\text{C}$ in 70% formamide, $2\times$ SSC, 0.05 M phosphate buffer (pH 7.4). Cryosections were dehydrated as described above, and overlaid on hybridization mixture on HybriSlip (Invitrogen, H18202). After sealing with rubber cement and incubation (48 h, $37\text{ }^\circ\text{C}$) in a moist chamber, cryosections were washed (25 min, $42\text{ }^\circ\text{C}$) in 50% formamide in $2\times$ SSC, (30 min, $60\text{ }^\circ\text{C}$) in $0.1\times$ SSC and (10 min, $42\text{ }^\circ\text{C}$) in 0.1% Triton X-100 in $4\times$ SSC. After rinsing with $1\times$ PBS, coverslips were mounted in Vectashield mounting medium (anti-Fading) with DAPI (Vector Laboratories, H-1200).

Cryo-FISH microscopy

Cryo-FISH images were collected sequentially with a Leica TCS SP8-STED confocal microscope (Leica Microsystems DMI6000B-CS) using Leica Application Suite X v.3.5.5.19976 and a HC PL APO CS2 $\times 63/1.40$ oil objective (numerical aperture of 1.4, Plan Apochromat) (see ‘Immunofluorescence detection for confocal microscopy’) using the following settings: 405-nm excitation and 420–500-nm emission (for DAPI), 488-nm excitation and 510–535-nm emission (for probes labelled with ChromaTide Alexa Fluor-488 and for nucleophosmin), 568-nm excitation and 586–620-nm emission (for probes labelled with ChromaTide Alexa Fluor-568), 647-nm excitation and 657–700-nm emission (for probes labelled with Alexa Fluor-647), and 555-nm excitation and 586–640-nm emission (for immunofluorescence labelling of nucleophosmin with Alexa Fluor-555). All images were collected with a $\times 4$ zoom at $1,024 \times 1,024$ pixel resolution (pixel size of $0.0451 \mu\text{m}$, resolution of $22.1760 \text{ pixels } \mu\text{m}^{-1}$).

Cryo-FISH image analysis

Images were analysed using Fiji software (v.2.0.0-rc-69/1.52p)⁸⁸. All images were pre-processed as previously described²³. Genomic foci were visually identified, and areas of the manually defined objects were measured using the Fiji-Area tool. For the cryo-FISH experiment combined with immunofluorescence, the location of genomic loci in relation to the nuclear lamina or nucleolus was assessed on the basis of the overlap of foci with the nucleolus (identified by nucleophosmin immunolabelling) or the nuclear lamina (as defined by the periphery of the DAPI staining) by at least three pixels. To determine the distance between the TSS, middle and TES genomic foci, we took the centre of mass of the selected objects, as defined by Fiji-Center of mass function (the brightness-weighted average of the x and y coordinates of all pixels within the selected areas). Distances between the objects were measured using the Fiji-Line tool between the centres of mass defined for each object. Images for visualization in figure panels were processed using Fiji or Adobe Photoshop CS6, for which

adjustments included the optimization of the dynamic signal range with contrast stretching.

Determination of differential contacts between GAM datasets

Significant differences in pairwise contacts between a pair of GAM datasets were determined as previously described with modifications⁹. In brief, genomic windows with low detection, defined as less than 2% of the distribution of all detected genomic windows for each chromosome, were removed from both datasets to be compared. Contacts were filtered to be within 0.5–5 Mb distance and above 0.15 NPMI, and NPMI contact frequencies at each genomic distance of each chromosome were normalized by computing a Z-score transformation, and a differential matrix (D) was derived by subtracting the two Z-score normalized matrices⁹.

TF-binding site analysis

To find TF-binding motifs present within specific contacts, significant differential contacts were determined for DNs and PGNs. Accessible regions within the differential contacts were determined using scATAC-seq for PGNs⁸¹ and DNs. To account for methodological differences, including lower sequencing depth in PGN scATAC-seq data (Extended Data Fig. 41), we considered only the peaks that occurred in >10% of cells (>10 cells in DNs; >13 in PGNs). Motif finding within accessible regions in significant contacts was performed using the Regulatory Genomics Toolbox (v.0.12.3; <https://www.regulatory-genomics.org/motif-analysis/introduction/>) with TF motifs (from the HOCOMOCO database, v.11)⁸⁹ obtained for TFs expressed in either DNs or PGNs ($R\text{-log} \geq 2.5$) to determine the percentage of windows containing each TF motif. Next, TF motifs were filtered based on (1) the percentage of windows containing the motif (>5%) and (2) the differential expression in either PGNs or DNs ($-\log_{10}(\text{adjusted } P \text{ value}) > 3$, see ‘Differential gene expression analysis’ above), which resulted in 50 TF motifs for feature pair analysis (33 TF motifs from PGNs and 17 from DNs; Extended Data Fig. 9c,d).

Feature pairs associated with specific contacts were determined as previously described⁹ and testing the 1,275 combinations of motif pairs (1,225 heterotypic motif pairs and 50 homotypic motif pairs). The number of contacts containing each pair of selected TF motifs (PGN_{TF} and DN_{TF}), together with the percentage of total significant differential contacts in PGNs and DNs (PGN and DN), were used to determine the enrichment score for all TF feature pair interactions (that is, the ratio between frequencies of contacts in PGNs or DNs, $(\text{PGN}_{\text{TF}}/\text{PGN})/(\text{DN}_{\text{TF}}/\text{DN})$). The effectiveness of a TF pair for discriminating between contacts from PGNs and DNs was assessed by using the information gain measure⁹⁰. Enrichment and information gain for all TF feature pair interactions, as well as differential expression values for TFs (DNs compared to PGNs), can be found in Supplementary Table 13. The top feature pairs were extracted on basis of the highest information gain (ten feature pairs), PGN enrichment (five feature pairs) and DN enrichment (five feature pairs) scores. Contact overlaps for top feature pairs were visualized using UpSet plots.

Network and community detection analysis of TF-binding sites in significant differential contacts

To determine the interconnectivity between different TF motifs found in accessible regions of significant differential contacts, the number of contacts for each pair of TF motifs (1,275 pairs) was determined. After filtering pairs of TF motifs involved in less than 20% of the total contacts (15,833 and 5,400 contacts minimum in PGNs and DNs, respectively), a network was built for each cell type with TF motifs as nodes and number of contacts as weighted edges. The Leiden algorithm was used to detect communities of strongly interconnected nodes, using the leiden package in R^{91,92}, with a resolution of 1.01 for both PGNs and DNs (Extended Data Fig. 10f, Supplementary Table 14).

GAM aggregated contact plots

To visualize the average contact intensity for a set of genomic contacts, NPMI contact frequencies at each genomic distance of each chromosome were first normalized by computing a Z-score transformation. The resulting

Z-score values were determined for each contact and for each contact in a 4-bin radius (50-kb bins). For each chromosome, Z-score values for each set of contacts and for the surrounding bins were summarized by the arithmetic mean. Mean values computed for each chromosome were added together and divided by the number of chromosomes.

Reporting summary

Further information on research design is available in the [Nature Research Reporting Summary](#) linked to this paper.

Data availability

Raw fastq sequencing files for all samples from DN, PGN and OLG GAM datasets, together with non-normalized co-segregation matrices, normalized pair-wised chromatin contacts maps and raw GAM segregation tables are available from the GEO repository under accession number [GSE148792](#). Raw fastq sequencing files for mES cell GAM datasets are available from 4DN data portal (<https://data.4dnucleome.org/>). The 4DN sample IDs for all samples used in the study are available in Supplementary Table 1. All polymer model 3D structures produced for the analyses of this work are available in Supplementary Tables 9 and 10. Raw confocal and laser microdissection images, as well as images and ROIs for cryo-FISH experiments are available at: https://github.com/pombo-lab/WinickNg_Kukalev_Harabula_Nature_2021/tree/main/microscopy_images/.

Raw single cell mES cell transcriptome data are available from ENA data portal (<https://www.ebi.ac.uk/ena/browser/home>). The ENA sample IDs for all samples used in the study are available in Supplementary Table 15. Position sorted BAM files for ATAC-seq data from mES cells and DNs are available from the GEO repository under accession number [GSE174024](#), together with processed bigwig files. A public UCSC session with all data produced, as well as all published data utilized in this study is available at http://genome-euro.ucsc.edu/s/Kjmorris/Winick_Ng_2021_GAMbrainpublicsession. Source data are provided with this paper.

Code availability

Processing and plotting scripts for MELTRON and insulation scores are available at: <https://github.com/pombo-lab/Meltron/>. Processing and plotting scripts for the *trans–cis* contact ratios are available at https://github.com/pombo-lab/GAM_trans_cis_ratio/. Custom python and R scripts for GAM window calling, GAM quality control, GAM genome sampling quality and resolution, production of NPMI matrices, aggregated maps, *k*-means clustering, calculation of insulation scores and compartment calling were deposited in https://github.com/pombo-lab/WinickNg_Kukalev_Harabula_Nature_2021/tree/main/code/.

References

1. 1. Jung, I. et al. A compendium of promoter-centered long-range chromatin interactions in the human genome. *Nat. Genet.* **51**, 1442–1449 (2019).
2. 2. Beagrie, R. A. et al. Complex multi-enhancer contacts captured by genome architecture mapping. *Nature* **543**, 519–524 (2017).
3. 3. Quinodoz, S. A. et al. Higher-order inter-chromosomal hubs shape 3D genome organization in the nucleus. *Cell* **174**, 744–757 (2018).
4. 4. Fraser, J. et al. Hierarchical folding and reorganization of chromosomes are linked to transcriptional changes in cellular differentiation. *Mol. Syst. Biol.* **11**, 852 (2015).
5. 5.

Beagan, J. A. et al. Three-dimensional genome restructuring across timescales of activity-induced neuronal gene expression. *Nat. Neurosci.* **23**, 707–717 (2020).

6. 6.

Bonev, B. et al. Multiscale 3D genome rewiring during mouse neural development. *Cell* **171**, 557–572 (2017).

7. 7.

Walczak, A. et al. Novel higher-order epigenetic regulation of the *Bdnf* gene upon seizures. *J. Neurosci.* **33**, 2507–2511 (2013).

8. 8.

Harabula, A. & Pombo, A. The dynamics of chromatin architecture in brain development and function. *Curr. Opin. Genet. Dev.* **67**, 84–93 (2021).

9. 9.

Beagrie, R. A. et al. Multiplex-GAM: genome-wide identification of chromatin contacts yields insights not captured by Hi-C. Preprint at *bioRxiv* <https://doi.org/10.1101/2020.07.31.230284> (2021).

10. 10.

Fiorillo, L. et al. Comparison of the Hi-C, GAM and SPRITE methods by use of polymer models of chromatin. *Nat. Methods* **18**, 482–490 (2021).

11. 11.

Huges, E. G., Orthmann-Murphy, J. L., Langseth, A. J. & Bergles, D. E. Myelin remodeling through experience-dependent oligodendrogenesis in the adult somatosensory cortex. *Nat. Neurosci.* **21**, 696–706 (2018).

12. 12.

Stackman, Jr, R. W., Cohen, S. J., Lora, J. C. & Rios, L. M. Temporal inactivation reveals that the CA1 region of the mouse dorsal hippocampus plays an equivalent role in the retrieval of long-term object memory and spatial memory. *Neurobiol. Learn. Mem.* **133**, 118–128 (2016).

13. 13.

Keiflin, R. & Janak, P. H. Dopamine prediction errors in reward learning and addiction: from theory to neural circuitry. *Neuron* **88**, 247–263 (2015).

14. 14.

Crane, E. et al. Condensin-driven remodeling of X-chromosome topology during dosage compensation. *Nature* **523**, 240–244 (2015).

15. 15.

Monahan, K. et al. Role of CCCTC binding factor (CTCF) and cohesin in the generation of single-cell diversity of protocadherin- α gene expression. *Proc. Natl Acad. Sci. USA* **23**, 9125–9130 (2012).

16. 16.

Hirayama, T., Tarusawa, E., Yoshimura, Y., Galjart, N. & Takeshi, Y. CTCF is required for neural development and stochastic expression of clustered *Pcdh* genes in neurons. *Cell Rep.* **2**, 345–357 (2012).

17. 17.

Yu, Y., Suo, L. & Wu, Q. Protocadherin α gene cluster is required for myelination and oligodendrocyte development. *Zoolog. Res.* **33**, 362–366 (2012).

18. 18.

Ray, T. A. et al. Comprehensive identification of mRNA isoforms reveals the diversity of neural cell-surface molecules with roles in retinal development and disease. *Nat. Commun.* **11**, 3328 (2020).

19. 19.

Zuckerkandl, E. Gene control in eukaryotes and the *c*-value paradox "excess" DNA as an impediment to transcription of coding sequences. *J. Mol. Evol.* **9**, 73–104 (1976).

20. 20.

Müller, W. G., Walker, D., Hafer, G. L. & McNally, J. G. Large-scale chromatin decondensation and recondensation regulated by transcription from a natural promoter. *J. Cell Biol.* **154**, 33–48 (2001).

21. 21.

King, I. F. et al. Topoisomerases facilitate transcription of long genes linked to autism. *Nature* **501**, 58–62 (2013).

22. 22.

Bianco, S. et al. Polymer physics predicts the effects of structural variants on chromatin architecture. *Nat. Genet.* **50**, 662–667 (2018).

23. 23.

Branco, M. R. & Pombo, A. Intermingling of chromosome territories in interphase suggests role in translocations and transcription-dependent associations. *PLoS Biol.* **4**, e138 (2006).

24. 24.

Bustos, F. J. et al. Epigenetic editing of the *Dlg4/PSD95* gene improves cognition in aged and Alzheimer's disease mice. *Brain* **140**, 3252–3268 (2017).

25. 25.

Klaassen, R. V. et al. Shisa6 traps AMPA receptors at postsynaptic sites and prevents their desensitization during synaptic activity. *Nat. Commun.* **7**, 10682 (2016).

26. 26.

Gorini, G., Roberts, A. J. & Mayfield, R. D. Neurobiological signatures of alcohol dependence revealed by protein profiling. *PLoS ONE* **8**, e82656 (2013).

27. 27.

Wang, J. et al. Genome-wide expression analysis reveals diverse effects of acute nicotine exposure on neuronal function-related genes and pathways. *Front. Psychiatry* **2**, 5 (2011).

28. 28.

Bell, R. L. et al. Gene expression changes in the nucleus accumbens of alcohol-preferring rats following chronic ethanol consumption. *Pharmacol. Biochem. Behav.* **94**, 131–147 (2010).

29. 29.

Repunte-Canonigo, V. et al. Identifying candidate drivers of alcohol dependence-induced excessive drinking by assembly and interrogation of brain-specific regulatory networks. *Genome Biol.* **16**, 68 (2015).

30. 30.

Duclot, F. & Kabbaj, M. The role of early growth response 1 (EGR1) in brain plasticity and neuropsychiatric disorders. *Front. Behav. Neurosci.* **11**, 35 (2017).

31. 31.

Sun, Z. et al. EGR1 recruits TET1 to shape the brain methylome during development and upon neuronal activity. *Nat. Commun.* **10**, 3892 (2019).

32. 32.

Magklara, A. et al. An epigenetic signature for monoallelic olfactory receptor expression. *Cell* **145**, 555–570 (2011).

33. 33.

Kambere, M. B. & Lane, R. P. Co-regulation of a large and rapidly evolving repertoire of odorant receptor genes. *BMC Neurosci.* **8**, S2 (2007).

34. 34.

Gabel, H. W. et al. Disruption of DNA-methylation-dependent long gene repression in Rett syndrome. *Nature* **522**, 89–93 (2015).

35. 35.

Zhao, Y. T. et al. Long genes linked to autism spectrum disorders harbor broad enhancer-like chromatin domains. *Genome Res.* **28**, 933–942 (2018).

36. 36.

Leidescher, S. et al. Spatial organisation of transcribed eukaryotic genes. Preprint at *bioRxiv* <https://doi.org/10.1101/2020.05.20.106591> (2021).

37. 37.

Vaags, A. K. et al. Rare deletions at the neurexin 3 locus in autism spectrum disorder. *Am. J. Hum. Genet.* **90**, 133–141 (2012).

38. 38.

Lee, J.-A. et al. Cytoplasmic Rbfox1 regulates the expression of synaptic and autism-related genes. *Neuron* **89**, 113–128 (2016).

39. 39.

Guzmán, Y. F. et al. A gain-of-function mutation in the *GRIK2* gene causes neurodevelopmental deficits. *Neurol. Genet.* **3**, e129 (2017).

40. 40.

Guidi, S. et al. Neurogenesis impairment and increased cell death reduce total neuron number in the hippocampal region of fetuses with Down syndrome. *Brain Pathol.* **18**, 180–197 (2008).

41. 41.

Brackley, C. A., Johnson, J., Kelly, S., Cook, P. R. & Marenduzzo, D. Simulated binding of transcription factors to active and inactive regions folds human chromosomes into loops, rosettes and topological domains. *Nucleic Acids Res.* **44**, 3503–3512 (2016).

42. 42.

Lüscher, C. & Malenka, R. C. Drug-evoked synaptic plasticity in addiction: from molecular changes to circuit remodeling. *Neuron* **69**, 650–663 (2011).

43. 43.

Lüscher, C. & Ungless, M. The mechanistic classification of addictive drugs. *PLoS Med.* **3**, e437 (2006).

44. 44.

Monahan, K., Horta, A. & Lomvardas, S. LHX2- and LDB1-mediated trans interactions regulate olfactory receptor choice. *Nature* **565**, 448–453 (2018).

45. 45.

Tan, L. et al. Changes in genome architecture and transcriptional dynamics progress independently of sensory experience during postnatal brain development. *Cell* **184**, 741–758 (2021).

46. 46.

Ansoleaga, B. et al. Dysregulation of brain olfactory and taste receptors in AD, PSP and CJD, and AD-related model. *Neuroscience* **248**, 369–382 (2013).

47. 47.

Peric-Hupkes, D. et al. Molecular maps of the reorganization of genome–nuclear lamina interactions during differentiation. *Mol. Cell* **38**, 603–613 (2010).

48. 48.

Bizhanova, A., Yan, A., Yu, J., Zhu, L. J. & Kaufman, P. D. Distinct features of nucleolus-associated domains in mouse embryonic stem cells. *Chromosoma* **129**, 121–139 (2020).

49. 49.

Valdez, B. C. et al. Identification of the nuclear and nucleolar localization signals of the protein p120. *J. Biol. Chem.* **269**, 23776–23783 (1994).

50. 50.

Sawamoto, K. et al. Generation of dopaminergic neurons in the adult brain from mesencephalic precursor cells labeled with a nestin–GFP transgene. *J. Neurosci.* **21**, 3895–3903 (2001).

51. 51.

Matsushita, N. et al. Dynamics of tyrosine hydroxylase promoter activity during midbrain dopaminergic neuron development. *J. Neurochem.* **82**, 295–304 (2002).

52. 52.

Falcão, A. M. et al. Disease-specific oligodendrocyte lineage cells arise in multiple sclerosis. *Nat. Med.* **24**, 1837–1844 (2018).

53. 53.

Matsuoka, T. et al. Neural crest origins of the neck and shoulder. *Nature* **436**, 347–355 (2005).

54. 54.

Sousa, V. H. et al. Characterization of Nkx6-2-derived neocortical interneuron lineages. *Cereb. Cortex* **19**, i1–i10 (2009).

55. 55.

Jaitner, C. et al. Satb2 determines miRNA expression and long-term memory in the adult central nervous system. *eLife* **5**, e17361 (2016).

56. 56.

Langmead, B. & Salzberg, S. L. Fast gapped-read alignment with Bowtie 2. *Nat. Methods* **9**, 357–359 (2012).

57. 57.

Quinlan, A. R. & Hall, I. M. BEDTools: a flexible suite of utilities for comparing genomic features. *Bioinformatics* **26**, 841–842 (2010).

58. 58.

Dixon, J. R. et al. Chromatin architecture reorganization during stem cell differentiation. *Nature* **518**, 331–336 (2015).

59. 59.

Phillips-Cremins, J. E. et al. Architectural protein subclasses shape 3-D organization of genomes during lineage commitment. *Cell* **153**, 1281–1295 (2013).

60. 60.

Lex, A. et al. UpSet: visualization of intersecting sets. *IEEE Trans. Vis. Comput. Graph.* **20**, 1983–1992 (2014).

61. 61.

Ying, Q. L., Stavridis, M., Griffiths, D., Li, M. & Smith, A. Conversion of embryonic stem cells into neuroectodermal precursors in adherent monoculture. *Nat. Biotechnol.* **21**, 183–186 (2003).

62. 62.

Ferrai, C. et al. RNA polymerase II primes Polycomb-repressed developmental genes throughout terminal neuronal differentiation. *Mol. Syst. Biol.* **13**, 946 (2017).

63. 63.

Kolodziejczyk, A. A. et al. Single cell RNA-sequencing of pluripotent states unlocks modular transcriptional variation. *Cell Stem Cell* **17**, 471–485 (2015).

64. 64.

Dobin, A. et al. STAR: ultrafast universal RNA-seq aligner. *Bioinformatics* **29**, 15–21 (2013).

65. 65.

Li, B. & Dewey, C. N. RSEM: accurate transcript quantification from RNA-seq data with or without a reference genome. *BMC Bioinformatics* **12**, 323 (2011).

66. 66.

Aronesty, E. ea-utils: Command-line tools for processing biological sequencing data. <https://expressionanalysis.github.io/ea-utils/> (2011).

67. 67.

Kar, G. et al. Flipping between Polycomb repressed and active transcriptional states introduces noise in gene expression. *Nat. Commun.* **8**, 36 (2017).

68. 68.

Marques, S. et al. Oligodendrocyte heterogeneity in the mouse juvenile and adult central nervous system. *Science* **352**, 1326–1329 (2016).

69. 69.

Zeisel, A. et al. Brain structure. Cell types in the mouse cortex and hippocampus revealed by single-cell RNA-seq. *Science* **347**, 1138–1142 (2015).

70. 70.

La Manno, G. et al. Molecular diversity of midbrain development in mouse, human, and stem cells. *Cell* **167**, 566–580 (2016).

71. 71.

Macosko, E. Z. et al. Highly parallel genome-wide expression profiling of individual cells using nanoliter droplets. *Cell* **161**, 1202–1214 (2015).

72. 72.

McInnes, L., Healy, J., Saul, N. & Großberger, L. UMAP: uniform manifold approximation and projection. *J. Open Source Softw.* <https://doi.org/10.21105/joss.00861> (2018).

73. 73.

Li, H. et al. The sequence alignment/map format and SAMtools. *Bioinformatics* **25**, 2078–2079 (2009).

74. 74.

Ramirez, F. et al. deepTools2: a next generation web server for deep-sequencing data analysis. *Nucleic Acids Res.* **44**, W160–W165 (2016).

75. 75.

Love, M. I., Huber, W. & Anders, S. Moderated estimation of fold change and dispersion for RNA-seq data with DESeq2. *Genome Biol.* **15**, 550 (2014).

76. 76.

Picelli, S. et al. Tn5 transposase and tagmentation procedures for massively scaled sequencing projects. *Genome Res.* **24**, 2033–2040 (2014).

77. 77.

Corces, M. R. et al. An improved ATAC-seq protocol reduces background and enables interrogation of frozen tissues. *Nat. Methods* **14**, 959–962 (2017).

78. 78.

Tarasov, A., Vilella, A. J., Cuppen, E., Nijman, I. J. & Prins, P. Sambamba: fast processing of NGS alignment formats. *Bioinformatics* **31**, 2032–2034 (2015).

79. 79.

Granja, J. M. et al. ArchR is a scalable software package for integrative single-cell chromatin accessibility analysis. *Nat. Genet.* **53**, 403–411 (2021).

80. 80.

Cusanovich, D. A. et al. A single-cell atlas of in vivo mammalian chromatin accessibility. *Cell* **174**, 1309–1324 (2018).

81. 81. Sinnamon, J. R. et al. The accessible chromatin landscape of the murine hippocampus at single-cell resolution. *Genome Res.* **29**, 857–869 (2019).
82. 82. Zambon, A. C. et al. GO-Elite: a flexible solution for pathway and ontology over-representation. *Bioinformatics* **28**, 2209–2210 (2012).
83. 83. Barbieri, M. et al. Complexity of chromatin folding is captured by the strings and binders switch model. *Proc. Natl Acad. Sci. USA* **109**, 16173–16178 (2012).
84. 84. Chiariello, A. M., Annunziatella, C., Bianco, S., Esposito, A. & Nicodemi, M. Polymer physics of chromosome large-scale 3D organisation. *Sci. Rep.* **6**, 29775 (2016).
85. 85. Fiorillo, L. et al. Inference of chromosome 3D structures from GAM data by a physics computational approach. *Methods* **181–182**, 70-79 (2020).
86. 86. Plimpton, S. Fast parallel algorithms for short-range molecular dynamics. *J. Comput. Phys.* **117**, 1–19 (1995).
87. 87. Kremer, K. & Grest, G. S. Dynamics of entangled linear polymer melts: a molecular-dynamics simulation. *J. Chem. Phys.* **92**, 5057–5086 (1990).

88. 88.

Schindelin, J. et al. Fiji: an open-source platform for biological-image analysis. *Nat. Methods* **9**, 676–682 (2012).

89. 89.

Kulakovskiy, I. V. et al. HOCOMOCO: towards a complete collection of transcription factor binding models for human and mouse via large-scale ChIP-seq analysis. *Nucleic Acids Res.* **46**, D252–D259 (2018).

90. 90.

Larose, D. T. & Larose, C. D. Discovering Knowledge in Data. An Introduction to Data Mining 2nd edn (Wiley, 2014).

91. 91.

Traag, V. A., Waltmann, L. & van Eck, N. J. From Louvain to Leiden: guaranteeing well-connected communities. *Sci. Rep.* **9**, 5233 (2019).

92. 92.

Kelly, S. T. leiden: R implementation of the Leiden algorithm. R version 0.3.3 <https://github.com/TomKellyGenetics/leiden> (2019).

93. 93.

Pombo, A., Edwards, P. A. W., Nicodemi, M., Scialdone, A. & Beagrie, R. A. Genome architecture mapping. International patent PCT/EP2015/079413 (2015).

Acknowledgements

The authors thank S. Q. Xie and A. Ashraf for help processing midbrain samples; R. A. Beagrie for sharing access to the mES cell GAM data before publication and discussions; M. Bartosovic for help with manuscript rebuttal; E. Espel for help optimizing the whole-genome amplification

protocol; M. Gotthardt for providing animals and R. Jüttner for help with midbrain dissections for snATAC-seq; C. Baugher for help developing the TF motif analysis pipeline; members of the Pombo laboratory for discussions; C. Braeuning of the Scientific Genomics Platform for scientific and technical support, and A. Schütz and her team of the Protein Production and Characterization Platform, both at the Max Delbrück Center for Molecular Medicine in the Helmholtz Association, Berlin; A. Adey for providing a BAM file of the published PGN scATAC-seq analysis; and the David Garfield group for sharing an optimized protocol for the bulk ATAC-seq fragmentation reaction. A.P. and A. Akalin acknowledge support from the Helmholtz Association (Germany). A.P. and M.N. acknowledge support from the National Institutes of Health Common Fund 4D Nucleome Program grants U54DK107977 and 1UM1HG011585, and the Berlin Institute of Health (BIH). A.P. and L.Z.-R. acknowledge support by the Deutsche Forschungsgemeinschaft (DFG; German Research Foundation) International Research Training Group (IRTG2403). A.P. acknowledges support from the DFG under Germany's Excellence Strategy—EXC-2049—390688087. G.C.-B. acknowledges European Union Horizon 2020/European Research Council Consolidator Grant (EPIScOPE no. 681893), Swedish Research Council (no. 2015-03558; 2019-01360), Swedish Brain Foundation (no. FO2017-0075), Knut and Alice Wallenberg Foundation (grant 2019-0107), The Swedish Society for Medical Research (SSMF, grant JUB2019), Ming Wai Lau Centre for Reparative Medicine and Karolinska Institutet. G.D. and G.A. acknowledge support from the Austrian FWF through DK W1206 ‘Signal Processing in Neurons’ and SFB F44 ‘Cell Signaling in Chronic CNS Disorders’, P25014-B24. M.A.U. acknowledges funding by the Medical Research Council (UK) (U120085816) and a Royal Society University Research Fellowship. M.N. thanks support from CINECA ISCRA Grant HP10CYFPS5 and HP10CRTY8P, by computer resources at INFN and Scope at the University of Naples (M.N.). L.W. acknowledges the support of Ohio University’s GERB program. I.H. was supported by a Boehringer Ingelheim Fonds PhD fellowship, E.T.T. by an EMBO short-term fellowship (ASTF 336-2015), and I.I.-A. by a Long-Term Fellowship from the Federation of European Biochemical Societies (FEBS). S.C. is a GABBA PhD fellow supported by the FCT (Fundação para a Ciência e Tecnologia; PD/BD/135453/2017).

Author information

Author notes

1. Leonid Serebreni

Present address: Research Institute of Molecular Pathology (IMP), Vienna Biocenter (VBC), Vienna, Austria

2. Elena Torlai Triglia

Present address: Broad Institute of MIT and Harvard, Cambridge, MA, USA

3. Aleksandra A. Kolodziejczyk

Present address: Immunology Department, Weizmann Institute of Science, Rehovot, Israel

4. Andreas Abentung

Present address: Department of Clinical and Molecular Medicine, Norwegian University of Science and Technology, Trondheim, Norway

5. Eleanor J. Paul

Present address: Center for Developmental Neurobiology, Institute of Psychiatry, Psychology and Neuroscience, King's College London, London, UK

6. Eleanor J. Paul

Present address: MRC Center for Neurodevelopmental Disorders, King's College London, London, UK

7. These authors contributed equally: Warren Winick-Ng, Alexander Kukalev, Izabela Harabula, Luna Zea-Redondo and Dominik Szabó

Affiliations

1. Max-Delbrück Centre for Molecular Medicine, Berlin Institute for Medical Systems Biology, Epigenetic Regulation and Chromatin Architecture Group, Berlin, Germany

Warren Winick-Ng, Alexander Kukalev, Izabela Harabula, Luna Zea-Redondo, Dominik Szabó, Leonid Serebreni, Ibai Irastorza-Azcarate, Christoph J. Thieme, Thomas M. Sparks, Sílvia Carvalho, Ehsan Irani, Elena Torlai Triglia, Rieke Kempfer & Ana Pombo

2. Institute of Biology, Humboldt-Universität zu Berlin, Berlin, Germany

Izabela Harabula, Luna Zea-Redondo, Dominik Szabó, Rieke Kempfer & Ana Pombo

3. Laboratory of Molecular Neurobiology, Department of Medical Biochemistry and Biophysics, Karolinska Institutet, Stockholm, Sweden

Mandy Meijer & Gonçalo Castelo-Branco

4. School of Electrical Engineering and Computer Science, Ohio University, Athens, OH, USA

Yingnan Zhang & Lonnie Welch

5. Dipartimento di Fisica, Università di Napoli Federico II, and INFN Napoli, Complesso Universitario di Monte Sant'Angelo, Naples, Italy

Simona Bianco, Andrea M. Chiariello, Luca Fiorillo, Francesco Musella & Mario Nicodemi

6. UCIBIO, Department of Life Sciences, NOVA School of Science and Technology, Universidade NOVA de Lisboa, Caparica, Portugal

Sílvia Carvalho

7. Instituto de Ciências Biomédicas Abel Salazar, Universidade do Porto, Porto, Portugal

Sílvia Carvalho

8. Graduate Program in Areas of Basic and Applied Biology, Universidade do Porto, Porto, Portugal

Sílvia Carvalho

9. Berlin Institute of Health, Berlin, Germany

Ehsan Irani, Mario Nicodemi & Ana Pombo

10. Cavendish Laboratory, University of Cambridge, Cambridge, UK

Aleksandra A. Kolodziejczyk & Sarah A. Teichmann

11. Wellcome Sanger Institute, Wellcome Genome Campus, Hinxton, Cambridge, UK

Aleksandra A. Kolodziejczyk & Sarah A. Teichmann

12. Institute for Neuroscience, Medical University of Innsbruck, Innsbruck, Austria

Andreas Abentung, Galina Apostolova & Georg Dechant

13. Institute of Clinical Sciences, Imperial College London, London, UK

Eleanor J. Paul & Mark A. Ungless

14. Max-Delbrück Centre for Molecular Medicine, Berlin Institute for Medical Systems Biology, Bioinformatics and Omics Data Science Platform, Berlin, Germany

Vedran Franke & Altuna Akalin

15. Ming Wai Lau Centre for Reparative Medicine, Stockholm node,
Karolinska Institutet, Stockholm, Sweden

Gonçalo Castelo-Branco

Contributions

The authors consider the joint first authors to have extensively contributed to this work and consider that A.K. and I.H. contributed equally. A.P. designed the concept for this work. W.W.-N., M.M., A. Abentung, E.J.P. and A.P. collected animal tissue samples. I.H., W.W.-N., L.S., A.K., M.M. and R.K. produced the GAM datasets. I.H., L.S., A.K., W.W.-N. and M.M. optimized the experimental immunoGAM protocol. W.W.-N., A.K., C.J.T., I.I.-A., E.I. and T.M.S. developed the computational pipelines for bioinformatics and QC analyses of the GAM data. A.K. and I.I.-A. performed the QC analyses of the GAM data. T.M.S. and C.J.T. developed the NPMI normalization of the GAM data. T.M.S. performed the bias analysis of the GAM data. W.W.-N., A.K. and D.S. performed the bioinformatics analyses of the GAM data. D.S. developed the domain melting analysis, with consultation from C.J.T. D.S. devised the MELTRON pipeline and performed the domain melting analysis of the GAM data. D.S. developed the *trans–cis* ratio analysis. C.J.T. initially developed the differential contact approach⁹, and W.W.-N. and C.J.T. further developed and adapted this analysis for the current study. W.W.-N. performed the differential contact analysis. Y.Z. performed the TF motif finding enrichment, network and community analyses in differential contacts. W.W.-N. performed the post-hoc analyses of TF motif enrichment in differential contacts. E.T.T. performed the mES cell culture experiments. E.T.T. and A.A.K. produced the scRNA-seq data. L.Z.-R. and D.S. performed the RNA-seq analysis. L.Z.-R. performed the differential gene expression analysis. L.Z.-R. optimized the snATAC-seq protocol, produced and analysed the bulk and scATAC-seq data. S.B. optimized the polymer modelling method and performed PRISM analysis. S.B. and A.M.C. produced models for polymer modelling. A.M.C. performed the statistical analyses of polymer models. L.F. and F.M. performed the in silico GAM experiments. I.H. and S.C. performed and analysed the FISH experiments. W.W.-N., D.S., I.H., L.Z.-R., Y.Z., A.K., T.M.S., S.B., A.M.C. and M.M.

produced the final data plots. S.A.T. supervised the scRNA-seq experiments. M.M., G.A., G.D., M.A.U. and G.C.-B. supervised the animal tissue collection and provided animal samples. A.P. and S.C. supervised the cryo-FISH experiments. A.P., A.K. and W.W.-N. supervised the GAM experiments. A.P. and W.W.-N. supervised the ATAC-seq. V.F. and A. Akalin supervised the RNA-seq. M.N. supervised the polymer modelling and in silico GAM. L.W. supervised the TF motif and network analyses. W.W.-N., A.P., A.K., I.H., D.S., L.Z.-R., L.W., Y.Z., G.C.-B., M.M., S.B., A.M.C. and M.N. contributed to the interpretation of the results. W.W.-N. wrote the first draft of the manuscript. W.W.-N. designed the figures and illustrations, with contributions from A.P., D.S. and I.H. W.W.-N., A.P., A.K., I.H., D.S., L.Z.-R., Y.Z., L.W., G.C.-B., S.C., S.B. and A.M.C. wrote the manuscript. All authors provided critical feedback and helped revise the manuscript.

Corresponding authors

Correspondence to [Warren Winick-Ng](#) or [Ana Pombo](#).

Ethics declarations

Competing interests

In the past 3 years, S.A.T. has acted as a consultant for Genentech and Roche, and is a remunerated member of Scientific Advisory Boards of Biogen, GlaxoSmithKline and Foresite Labs. A.P. and M.N. hold a patent on GAM⁹³.

Additional information

Peer review information Peer review statement: *Nature* thanks Chongyuan Luo and the other, anonymous, reviewer(s) for their contribution to the peer review of this work. Peer reviewer reports are available.

Publisher's note Springer Nature remains neutral with regard to jurisdictional claims in published maps and institutional affiliations.

Extended data figures and tables

Extended Data Fig. 1 ImmunoGAM experimental pipeline and GAM data quality control.

a, ImmunoGAM experimental pipeline. VTA and CA1 dissections and cryoblock preparations are shown as examples. After fixation, brain tissue is dissected and cryopreserved in sucrose/PBS solution, before sectioning on an ultracryomicrotome (~220nm thick tissue slices; -100 °C). For confocal imaging, DAPI staining labels nuclear slices and helps to morphologically identify the CA1 PGN layer in the hippocampus, or was combined with TH immunolabelling to identify DNs in the midbrain, or with GFP immunolabelling to identify OLG lineage cells in the cortex (scale bars = 10 µm for OLGs and DNs, 100 µm for PGNs). For laser microdissection, nuclei were identified by indirect immunofluorescence using anti-pan-histone antibodies to morphologically select PGNs of the pyramidal neuron layer, or were combined with immunofluorescence detection of TH for DNs or GFP for OLGs. Laser microdissection images are shown as examples (scale bars = 30 µm for DNs, 200 µm for PGNs). Three nuclear slices were selected and laser microdissected from the tissue to fall into the same PCR lid, as described for multiplex-GAM⁹ (scale bars = 30 µm for panels a and b, 400 µm for panels c-e). Genomic DNA content was extracted from each sample and amplified using whole-genome amplification, followed by Illumina NextSeq sequencing. **b**, Quality control parameters (uniquely mapped reads, genome coverage of positive windows, and percentage of orphan windows; see [Methods](#)) for all combined GAM samples collected from brain cell types. Each data point represents a GAM sample. Samples passing QC are shown in green, samples not passing QC in red. **c**, Percentages of uniquely mapped reads and orphan windows per GAM sample, shown separately for each dataset produced in this study. Samples not passing QC are shown in red, water control samples (laser-microdissected material not containing a nuclear profile) are shown in black. **d**, Normalized point-wise mutual information (NPMI) normalization corrects for differences in the co-segregation matrix caused by changes in the window detection frequency (WDF; see [Methods](#)). Example shown for PGNs replicate 1 (R1; chr7:60,000,000-80,000,000).

Source data

Extended Data Fig. 2 Normalization of immunoGAM data.

a, Summary of GAM datasets used in this study. VTA DNs were collected from two animals, an 8-week old wild-type mouse and a 10-week old mouse carrying a TH-GFP reporter. PGNs were collected from two 8-week old wildtype littermate mice. Cortical OLGs were collected based on detection of GFP expression from a 3-week old Sox10-cre-LoxP-GFP mouse. GAM data from mES cell (clone 46C) was previously published¹¹, and available from the 4DNucleome portal after quality control (<https://data.4dnucleome.org/>; Supplementary Table 1). **b**, 50-kb windows for PGNs R1 were divided into equally sized groups depending on their GC content, mappability, window detection frequency (WDF) or *DpnII* restriction density. Heatmaps of mean observed/expected bias (represented as a fold change) are shown for co-segregation, D-prime (used for previous GAM normalizations³), PMI and NPMI normalizations. NPMI normalization results in the lowest absolute bias percentage for all tested categories (box plots on right). Box plot definitions were as follows: 25th percentile lower limit, 75th percentile upper limit, and center line as the median; interquartile range (IQR) was 25th to 75th percentile; upper whisker was (75th percentile + (IQR*1.5)), lower whisker was (25th percentile – (IQR*1.5)) or zero if negative; outliers outside the whiskers were indicated with open circles. n = 100 for each bias tested, representing all combinations of deciles in PGNs R1. **c**, Absolute bias analysis for remaining immunoGAM datasets. Box plot definitions were as in panel b.

Source data

Extended Data Fig. 3 ImmunoGAM contact matrices from replicate mice.

a, GAM contact matrices centered on the *Pcdh* gene cluster for mESC, CA1 PGN replicate 2, and VTA DN replicate 2 (Chr18: 36,000,000-39,000,000; 50-kb resolution). ChIP-seq peaks for CTCF¹⁵ are shown below the mES cell matrix, showing extensive binding at the *Pcdh* locus. Dashed lines

illustrate differences in contacts between *Pcdh-α*, - β and - γ genes for different cell types. Scale bars are adjusted to a range between the 0 value and the 99th percentile of NPMI values for each cell type. **b**, Example matrices for replicate 2 of CA1 PGN and VTA DN, for Chr17: 0–60,000,000 at 50-kb resolution. Dashed lines illustrate vomeronasal (*Vmn*) and olfactory (*Olfr*) receptor gene clusters within B compartments, separated by ~35 Mb, are observed in brain cells but not in mES cells. Compartments A/B were classified using normalized PCA eigenvectors².

Source data

Extended Data Fig. 4 Curation of scRNA-seq and snATAC-seq data from published datasets and datasets produced for the present study.

a, Schematic representation of scRNA-seq datasets used in this study. We collected published scRNA-seq datasets from cortex and hippocampus, and produced scRNA-seq from midbrain. From each of the brain tissues, we select the specific cell types that were matched with those collected for the presented GAM data. The selected datasets from each cell type were combined and visualized through UMAP embedding, coloured by expression of each marker gene: *Sox10* for OLGs, *Camk2a* for PGNs and *Th* for DNs. Cluster contours are drawn to highlight separation between cell types. All marker genes were found highly expressed in their respective cell types. **b**, scRNA-seq datasets were also generated from mES cells. UMAP clustering is coloured by the expression of *Nanog*. **c**, Pearson's correlation plot of gene expression in mES cells (clone 46C) between published bulk²⁶ versus single-cell RNA-seq. Average single-cell expression is highly correlated with bulk RNA-seq (two-sided Pearson's R product-moment correlation; $R = 0.93$, $p < 2.2 \times 10^{-16}$). Only genes common to both datasets are represented (total genes in bulk dataset = 22822, total genes in single cell dataset = 23208, common to both = 22045). **d**, Single cell expression of *Rbfox3*, a pan-neuronal marker, overlaid on the UMAP of single cell transcriptomes. **e**, Additional examples of UMAPs for single cell transcriptomes of cell-type markers. *Pou5f1* and *Sox2* were used as markers for mES cells, *Olig2* and *Pdgfra* for OLGs, *Wfs1* and *Satb2* for PGNs, and

Slc6a3 and *Calb1* for DNs. All markers show higher expression in their respective cell types. **f**, Distribution of regularized log (R-log) values for pseudobulk scRNA-seq datasets. For each cell type, cells were randomly partitioned into 3 pseudobulk replicates before pooling and normalizing reads. The distribution of R-log values is bi-modal for all cell types and pseudobulk replicates. To consider expressed genes for downstream analysis, a 2.5 R-log threshold (dashed red lines) was applied in all datasets. Genes with R-log ≥ 2.5 in all three pseudobulk replicates are considered expressed for that cell type. **g**, Example scRNA-seq pseudobulk tracks of sequenced reads for marker genes in each cell type. Tracks were RPKM normalized to allow for cell-type comparisons. Markers were: *Esrrb* for mES cells, *Pdgfra* for OLGs, *Wfs1* for PGNs and *Slc6a3* for DNs. All markers are specifically expressed in their respective cell types. **h**, Exemplar plots of fluorescence-activated cell sorting (FACS) and gating strategy in midbrain VTA samples. Two biological replicate samples from independent mice, VTA-1 (*top*) and VTA-2 (*bottom*) were sorted to determine percentage of intact nuclei. Debris was excluded with a first gate (*left*; SSC/FSC plots, n = 10000 for VTA-1 and VTA-2, a total of n = 200000 DAPI positive events were sorted) and damaged nuclei with a second gate using DAPI (*right*; DAPI-H/DAPI-A plots, n=8687 and 8748 for VTA-1 and VTA-2, respectively). The frequencies of parent populations are indicated by circles within the plots, and the target intact nuclei are indicated by the boxed area. **i**, Table indicating the total number of recorded events for VTA-1 and VTA-2 exemplar FACS gating as shown in Extended Data Fig. 4h, as well as the number and percentage of intact nuclei. **j**, Distribution of fragment sizes for (sc)ATAC-seq data used in this study. Bulk ATAC-seq data was generated from mES cells. snATAC-seq was generated from midbrain VTA, from which 216 nuclei were classified as DNs (see [Methods](#)). OLG and PGN scATAC-seq was collected from published data (see [Methods](#), Supplementary Table 6). **k**, Aggregated sequencing reads at 2kb genomic regions centered on transcription start sites (TSSs). Nucleosome-free regions (NFRs; < 147 bp) were extracted from the ATAC alignment BAM files in each cell type (i.e. fragments). NFRs are enriched at the TSS for all ATAC-seq datasets. **l**, Number of fragments per cell/nucleus for sc/snATAC-seq datasets. The number of unique fragments per nucleus was highest for DNs. **m**, Single-cell accessibility maps for DNs generated in the present study were visualized

together by UMAP embedding, and coloured by expression of DN marker genes or marker genes for OLGs and PGNs. Per-cell gene scores were calculated for each DNs marker gene (see [Methods](#)). DNs expressed DN-specific markers *Pitx3*, *Foxa2*, *Lmx1b* and *Th*, while not expressing OLG and PGN markers *Olig2* and *Camk2a*, respectively. **n**, Top four enriched gene ontologies (GO) for DN marker genes (973 genes; over-representation as measured by Z-Score; see [Methods](#) for marker selection), containing terms relevant for dopamine metabolism, synaptic transmission and behaviour. All enriched GOs were highly significantly enriched (one-sided Fisher's exact permuted p-values = 0).

[Source data](#)

[Extended Data Fig. 5 Identification of contact density changes, TAD borders, and differences in contacts between cell types.](#)

a, GAM contact matrices for replicates 2 obtained from PGNs and DNs, within a 2-Mb region (50-kb resolution; Chr2:64,800,000-66,800,000). Contact density maps, TAD borders, pseudobulk scRNA-seq, and pseudobulk scATAC-seq tracks are indicated for each cell type below matrices. **b**, Distributions of TAD lengths in each GAM dataset. TAD length was calculated as the distance between two boundary points (defined as lowest insulation score point within a boundary). **c**, Pairwise comparisons of TAD boundary overlap between cell types. TAD boundaries were determined using insulation square method, using square size of 500kb, and the minimum score considered +1 bin on either side, giving a constant total of 150-kb TAD boundaries. The matrix of percentages of common TAD boundaries is not symmetrical as the percentage of overlap between boundaries varies with the direction of the comparison. The first dataset in the comparison is specified on the y axis, and the second on the x-axis. **d**, Four-way comparison of TAD boundary overlap between all cell types is shown as an UpSet plot. TAD boundaries were defined as in 5c. **e**, Average insulation score profiles centered on cell-type specific TAD borders show low average insulation scores in the cell type where the borders are detected, with highly significant differences at central border window with all other cell types (two-sided Mann-Whitney U test for central TAD border window in unique cell-type border and compared to all

other cell types; *** $p < 0.0001$; $p = 1.1 \times 10^{-20}$, 1.2×10^{-17} , and 1.0×10^{-17} for mES cells compared to OLGs, PGNs and DNs, respectively; $p = 6.0 \times 10^{-18}$, 2.4×10^{-12} , and 4.1×10^{-11} for OLGs compared to mES cells, PGNs and DNs, respectively; $p = 1.0 \times 10^{-10}$, 2.0×10^{-07} , and 1.3×10^{-09} for PGNs compared to mES cells, OLGs and DNs, respectively; and $p = 6.7 \times 10^{-10}$, 1.8×10^{-12} , and 8.5×10^{-08} for DNs compared to mES cells, OLGs and PGNs, respectively). **f**, Venn plots show overlap between TAD boundaries in PGN or DN replicates 1 and 2. Overlaps were performed by comparing replicate 1 (R1) to replicate 2 (R2), and conversely R2 to R1. **g**, Average insulation score profiles of common TAD borders (first UpSet plot group) centered on the lowest insulation point within each TAD border are shown for each cell type (two-sided Mann-Whitney test for central TAD border window in mES cell border and compared to each brain cell-type; *** $p < 0.0001$; $p = 8.6 \times 10^{-10}$, 1.5×10^{-18} , and 1.0×10^{-18} for mES cells compared to OLGs, PGNs and DNs, respectively). **h**, Percentage of TAD borders containing expressed genes ($R - \log_{10}(ge) \geq 2.5$) in each cell type for the groups shown in **d**. Higher percentage of borders contain expressed genes in groups with shared borders in two or more cell types. In all groups, brain cells have a higher percentage of borders with expressed genes compared to mES cells. **i**, Average insulation score profiles at the gene TSS or TES for genes $>300\text{kb}$ in length, using insulation square size 500kb . The top and bottom 20% expressing genes were determined using the length-normalized number of reads covering the gene body (length-scaled RNA Reads per Million; lsRRPM). The top expressing long genes have significantly lower insulation scores compared to the lowest expressed genes, at both the TSS and TES, in DNs and PGNs, while mES cells are lower at the TSS only, and OLGs show no detectable difference (two-sided Mann-Whitney test at TSS or TES windows; * $p < 0.05$, ** $p < 0.01$, *** $p < 0.001$, **** $p < 0.0001$; p-values at the TSS, $p = 0.02$, 0.009 , 0.328 , 0.027 for DNs, PGNs, OLGs and mES cells, respectively; p-values at the TES, $p = 7.2 \times 10^{-6}$, 1.8×10^{-8} , 0.323 , 0.177 for DNs, PGNs, OLGs and mES cells, respectively).

[Source data](#)

Extended Data Fig. 6 Identification of domain melting in long expressed genes.

a, Cumulative probability of insulation square scores ranging from 100 – 1000 kb for *Grik2* in all cell types and replicates (*left*). Comparison between PGNs replicates 1 and 2 and mES cells, with maximum distance (d) and TAD melting scores (*right*). Cumulative probability distributions of insulation scores and domain melting scores for *Grik2* in PGNs, *Dscam* in PGNs, and *Magi2* in OLGs (*right*). All genes were compared to mES cells, with maximum distance (d) indicated for each comparison. **b**, Example of domain melting for *Magi2* in OLGs. **c**, Correlation of replicate domain melting scores for replicates 1 and 2 in PGNs and DNs (two-sided Pearson’s R product-moment correlation was calculated for all 479 long genes; *** $p < 2.2 \times 10^{-16}$ for both PGNs and DNs). **d**, Domain melting scores for each gene (n = 479) in PGNs R2 and DNs R2, compared to mES cells. Genes with melting scores > 5 are coloured in each cell type. Density estimates of length-scaled RNA reads per million (lsRRPM) transcription levels are shown for genes with melting scores > 5 (coloured by cell type) compared to non-melting genes (grey; two-sided Wilcoxon rank-sum test; *** $p = 5.4 \times 10^{-9}$ and 6.5×10^{-11} in PGNs and DNs, respectively). **e**, Melting genes have higher density of open chromatin regions throughout their gene bodies (length-scaled ATAC-seq RPM values; lsARPM), especially in PGNs and DNs, and to a minor extent in OLGs (two-sided Wilcoxon rank-sum test; * $p < 0.05$, *** $p < 0.0001$; p-values from left to right, $p = 0.015$, 4.0×10^{-10} , 1.3×10^{-7}). **f**, Domain melting scores compared to length-scaled ATAC-seq reads per million (lsARPM) transcription levels for each gene (n = 479) in PGNs R2 and DNs R2. Density estimates of lsARPM open chromatin levels are shown for genes with melting scores > 5 (coloured by cell type) compared to non-melting genes (grey; two-sided Wilcoxon rank-sum test; *** $p = 2.6 \times 10^{-6}$ and 2.2×10^{-16} in PGNs and DNs, respectively). **g**, Long genes within the top 3% melting scores in any cell-type (24 of 44 genes) have a higher likelihood of sensitivity to topoisomerase inhibition⁴⁵ compared to genes with intermediate melting scores (42 of 261) and genes with no domain melting (27 of 174; two-sided χ^2 test; *** p -value = 5.0e-9). **h**, Heatmaps of genes with domain melting in OLGs, and with domain melting in at least

1 replicate for PGNs and DNs, clustered by change in transcription level (length-scaled RNA RPM; lsRRPM) from mES cells to brain cell type. ATAC-seq (length-scaled ATAC RPM; lsARPM), compartments in each cell-type, and percentage of mES cell lamina- and nucleolus-associated domain (LAD⁴⁷ and NAD⁴⁸, respectively) in mES cells are shown for comparison. The density of the change in lsRRPM, lsARPM, and melting scores are shown for each cluster (violin plots on *right*). Compartment changes are shown as bar plots (*lower right*). **i**, mES cell LAD association (defined as > 50% of gene body with feature) for genes with or without melting domains in brain cell types and replicates. For DNs and OLGs, genes with domain melting were less likely to be LAD associated in mES cells, compared to non-melting genes (Two-sided Fisher's exact test; **p < 0.01, ***p < 0.001; p-values from left to right, p = 0.001, 0.272, 0.209, 0.003, 0.0001). **j**, mES cell NAD association (defined as > 50% of gene body with feature) for genes with or without melting domains in brain cell-types and replicates. For DNs and OLGs, genes with domain melting were less likely to be NAD associated in mES cells, compared to non-melting genes (Two-sided Fisher's exact test; *p < 0.05, **p < 0.01; p-values from left to right, p = 0.003, 0.272, 0.209, 0.055, 0.008).

Source data

Extended Data Fig. 7 Characteristics and mechanisms of domain melting in long expressed genes.

a, Contact density maps for each cell type and replicate, at the *Nrxn3* locus, calculated using insulation square sizes ranging from 100 – 1000 kb. Contact density is reduced in PGNs and DNs replicate 2 (R2), similar to R1 but occurring in slightly differing regions of the gene. **b**, Contact density maps for each cell type and replicate, at the *Rbfox1* locus. Contact density is reduced in OLGs and PGNs R2, in the same region as R1. **c**, Ensembles of polymer models were produced for the *Nrxn3* locus in mES cells and in DNs from experimental GAM data using PRISMR modelling (n= 450). The quality of the models was verified by applying *in-silico* GAM to the ensemble of polymers and comparison between NPMI-normalized contact matrices from *in-silico* and experimental immunoGAM (Pearson r = 0.72 and 0.79 for mES cells and DNs, respectively). Colour bars below *in-silico*

matrices highlight the position of domains in DNs and are used to colour the polymer examples shown in Fig. 3c and Extended Data Fig. 7d. d, Additional examples of polymer models for the *Nrxn3* locus in mES cells and DNs. The *Nrxn3* melted TAD is represented by the green coloured region and is more decondensed in DNs than mES cells. See Fig. 3c for location and colouring of the domains. e, Distribution of gyration radii of all domains in polymer models for mES cells and DNs (see Fig. 3c for location and colouring of the domains; n= 450, two-sided Mann-Whitney test between mES cells and DNs; dashed lines indicate quartiles; ***p<0.0001; domains from left to right p= 3.0e-151, 0.0005, 1.1e-92, 2.0e-147, 7.3e-40, 2.5e-67). f, Exemplar images of whole gene cryo-FISH for *Rbfox1* (green) in mES cells and PGNs, using probes that label the whole gene. Nucleoli (purple) were detected by an anti-nucleophosmin 1 antibody. Yellow inset of the ~400 nm section shows a single nucleus. Inset on nuclear section (yellow box) with *Rbfox1* FISH signal and each imaging channel. Yellow outline indicates region of *Rbfox1* signal used for area measurement and localization to nuclear landmarks. g, Exemplar images of tri-colour cryo-FISH for *Rbfox1* TSS (teal), Mid (green) and TES (purple) in mES cells and PGNs (see Fig. 3e for schematic). Yellow inset of the 400 nm section shows a single nucleus. Inset on nuclear section (yellow box) is shown for all three FISH signals, and each imaging channel separately. Yellow outline indicates region of *Rbfox1* signal used for center of mass distance measurements.

Source data

Extended Data Fig. 8 Melting genes often show increased contacts with their own chromosome.

a, Melting genes are more likely to gain intra-chromosomal contacts in PGNs and DNs R1, but not OLGs, compared to mES cells (two-sided Wilcoxon rank-sum test; **p<0.01, ***p<0.001; p-values from left to right, p = 0.003, 0.0003, 0.329). Median *trans-cis* contact ratios were calculated for each gene with domain melting in DNs, PGNs, or OLGs, and compared to mES cells. b, Median *trans-cis* contact ratios were calculated for each gene with domain melting in PGNs R2 or DNs R2. Median *trans-cis* ratios were significantly lower for PGNs and DNs R2 melting genes when

compared to mES cells (two-sided Wilcoxon rank-sum test; *p<0.05, ***p<0.0001; p-values were p = 0.037 and 0.0003 for PGNs and DNs, respectively). **c**, Correlation of median *trans-cis* ratios for all long genes (> 300kb) in R1 and R2 for PGNs or DNs. In PGNs, median *trans-cis* ratios were significantly correlated between replicates, with a high correlation value (Two-sided Pearson's R product-moment correlation; R=0.9, ****p < 2.2x10⁻¹⁶). DNs had a lower correlation, though the correlation was still significant (R=0.16, ***p = 0.0005). **d**, Median *trans-cis* contact ratios were calculated for each gene without domain melting. Non-melting genes show no preference for changes in *trans-cis* contact ratios between brain cells and mES cells (two-sided Wilcoxon rank-sum test). **e**, The *Rbfox1* locus gains contacts with other chromosomes in PGNs, compared to mES cells. *Trans-cis* contact ratios were determined by the mean ratio between trans NPMI scores and cis NPMI scores (250kb genomic bins), and normalizing each ratio as a percentile for each chromosome. Inset (grey shaded region) shows a 7Mb region (Chr16: 3,000,000-10,000,000) containing the *Rbfox1* gene (blue shaded region). **f**, *Trans-cis* contact ratios are shown for chromosome 12 in mES cells and DNs. Inset (grey shaded region) shows a 7Mb region (Chr12: 85,000,000-92,000,000) containing the *Nrxn3* gene (green shaded region). **g**, Median *trans-cis* ratios for genes with melting domains, separated by association with NAD association (defined as > 50% of gene body with feature). For DNs, median *trans-cis* ratios were significantly decreased when compared to mES cells, regardless of association with NADs (two-sided Wilcoxon rank-sum test; *p<0.05, **p<0.01; p-values from left to right, p = 0.927, 0.233, 0.100, 0.010, 0.044, 0.003). For PGNs, median *trans-cis* ratios were significantly decreased for non-NAD associated genes (**p<0.01), and trending toward significance for NAD-associated genes, when compared to mES cells (p=0.1). OLGs had no significant differences in median *trans-cis* values for both NAD associated and non-associated genes, when compared to mES cells. **h**, Median *trans-cis* ratios for genes without melting domains, separated by association with NAD association (defined as > 50% of gene body with feature). NAD-associated genes had significantly lower *trans-cis* values in all brain cell types when compared to mES cells (two-sided Wilcoxon rank-sum test; **p<0.01; p-values from left to right, p = 0.002, 0.205, 0.013, 0.147, 0.002, 0.911). For all brain cell types, non-melting genes that were

not associated with NADs had no significant differences in median *trans-cis* values when compared to mES cells.

[Source data](#)

Extended Data Fig. 9 Analysis of transcription factor binding sites and differentially expressed genes in GAM differential contacts between DNs and PGNs.

a, GAM contacts from PGNs and DNs (mouse replicate 1) were normalized (Z-Score) and subtracted to produce differential contacts matrices. Top 5% differential contacts ranged 0.05-5 Mb. Contacts containing TF motifs within accessible chromatin on each contacting window were selected in most (top 5) enriched in PGNs or DNs or with highest discriminatory power (information gain). **b**, Distribution of the number of ATAC-seq peaks per 50kb GAM window in DNs and PGNs (*upper panel*; mean(μ) = 2.6 and 2.0 in DNs and PGNs, respectively). Number of base pairs covered by ATAC-seq peaks per 50kb GAM window in DNs and PGNs (*lower panel*; μ = 1270 and 1326 in DNs and PGNs, respectively). **c**, Correlation plot of cell type and replicates for differential gene expression analysis. Pseudobulk replicates correlate most highly with one another, followed by brain cell types. *Right*, heatmap of differentially expressed (DE) genes between PGNs and DNs, clustered by cell type. **d**, Selection of TF motifs based on percentage of TF motifs in accessible regions within unique windows (> 5%) and differential expression between PGNs (Benjamini-Hochberg corrected two-sided Wald test; $\log_{10}(p. \text{adj.}) < 3$) and DNs (- $\log_{10}(p. \text{adj.}) > 3$). PGN-selected TFs (33) are shown in blue, DN-selected TFs (17) are shown in green. A list of selected TFs are shown below, with TF motifs continuing after the TF enrichment analysis in **(f)** coloured in blue (PGNs) or green (DNs). **e**, Full pipeline to determine pairs of genomic windows in GAM differential contacts containing transcription factor binding sites⁹. GAM contacts from PGNs and DNs were normalized and compared to produce a differential Z-Score matrix with a 0.05-5 Mb distance range. The top 5% differential contacts with > 0.15 NPMI values for each dataset were extracted from the differential matrices. Accessible chromatin regions were mapped to the top differential contacts. Next, TF motifs were filtered based on expression in at least one cell type. Accessible regions in differential

contacts were used to determine the percentage of TF motifs within unique windows. To find TFs with the potential to drive contact specificity between DNs and PGNs, we chose for further analyses the TF motifs that were found in DN or PGN accessible regions within differential contacts which (1) were present in at least 5% of contacts, and (2) the TFs were differentially expressed between DNs and PGNs ($-\log_{10}(p.\text{adj.}) > 3$). The 50 TFs which met the requirements were further investigated to determine the frequency of each motif pair (TF feature pair) in PGN and DN differential contacts. The top-20 TF feature pairs were selected for further analyses based: (a) on Information gain score (top 10 feature pairs selected), and (b) on enrichment in either PGNs (top 5 selected) or DNs (top 5 selected). **f**, TF motif pairs selected by enrichment scores in DNs or PGNs, or by the highest Information gain scores. **g**, Overlaps of top 20 TF feature pair contacts for PGN and DN significant differential contacts. The top 40 groups with overlapping TF features are shown for each cell type.

[Source data](#)

Extended Data Fig. 10 Features of top differential contacts containing pairs of TF binding sites.

a, Percentage of contacts at each genomic distance for top differential contacts found in TF feature pair groups. Contacts in all groups are enriched at distances > 2 Mb. **b**, Aggregated maps of average Z-scores for TF-containing contact groups in PGNs and DNs. The Z-Score was determined for each contact and a 200kb (4 genomic bin) radius. For each group, chromosome- and distance-matched contacts were randomly sampled three times from the genome-wide distribution (one exemplar is shown for each group). **c**, Percentage of contacts (< 2 Mb) that fall within a TAD border in both windows, one window or no windows. For both cell types, most contacts do not overlap with TAD borders, with a slight no differences detected for top differential contacts found in TF feature pair groups, except a modest increase for contacts that have both windows with a border for *Ctcf-Ctcf* containing contacts in both PGNs and DNs. **d**, Overlap of TF-containing contact groups with compartment identity in each contacting window. For both cell types, TF-containing contact groups were more likely to be in A-compartment in both contacting windows, compared to the

genome-wide average and all top differential contacts. **e**, TF motif network and community analysis. After determining the number of contacts for each TF pair, only pairs involved in > 20% of total TF-containing contacts were considered. A network was built with each TF as a node and contacts as the edge weight. Community detection was performed using a Leiden algorithm, before visualizing the network. **f**, Network analysis and community detection for TF motifs found within DN or PGN differential contacts. **g**, Overlap of TF-pair containing contacts with 1000 random circular permutations of PGN and DN expressed gene regions shows that the observed enrichments of contacts with genes in both windows are significantly higher than the expected distribution (two-sided t-test; ***empirical p = 0.001 for all observed values tested). The enrichments were also seen, to smaller degree than for the TF-pair containing contacts, for all contacts between A-compartment windows. **h**, Number of PGN or DN differentially expressed (DE) genes found in differential contacts according to sets of TF feature pairs. **i**, Differential Z-Score matrix showing PGN-upregulated genes that form contacts across a ~4.5-Mb linear genomic distance (pink box; Chr11: 65,400,000-70,400,000). *Upper right* inset shows PGN significant differential contacts containing the *Neurod* group (contacts are shown in pink). Genes highlighted in blue are upregulated in PGNs. **j**, Differential Z-Score matrix showing DN-upregulated genes that form contacts across a ~5-Mb linear genomic distance (pink boxes; Chr1: 160,000,000-166,000,000). *Upper right* inset shows DN significant differential contacts containing the *Foxal1*-TF group (contacts are shown in orange). Genes highlighted in green are upregulated in DNs. **k**, GAM contact matrices showing a 2.3-Mb region surrounding the *Egr1* gene for PGNs R1 and R2 (Chr18: 33,700,000-36,000,000).

[Source data](#)

[Extended Data Fig. 11 Identification of compartments and differences between cell types.](#)

a, Open and closed chromatin compartments (A and B, respectively) display different genomic distributions in mES cells, OLGs, PGNs and DNs. Mouse replicates 1 and 2 (R1 and R2, respectively) are shown. Purple, compartment A; orange, compartment B. **b**, Comparison of

compartment A/B membership in GAM datasets from PGNs and DNs and their replicates. Compartment changes show good overlap between replicates. Purple, compartment A; orange, compartment B. **c**, Pearson's correlation of eigenvectors shows the largest differences between mES cells and brain cell types. **d**, UpSet plot showing all combinations of compartments changes. Most genomic windows share membership to compartments A, followed by B, in all cell types. The most frequent compartment changes occur from compartment B in mES cells to A in all brain cells (pink box), followed by changes from A in mES cells to B in all brain cells (blue box). **e**, Compartment changes for each cell type comparison in each chromosome. Only compartments common to both replicates were used in the comparison. Brain cell types have higher overlap with each other as compared to mES cells. PGNs and DNs had the most overlap for most chromosomes. **f**, Violin plots of the distribution of compartment lengths show similar lengths between cell types. *Right*, percentage of the genome covered by A or B compartments in each cell type shows similar distribution between cell types.

[Source data](#)

[Extended Data Fig. 12 Genomic regions involved in strong long-range contacts in brain cells regions contain sensory receptor clusters in B compartments.](#)

a, Heatmap of gene expression for genes that change compartments between compartment B in mES cells to compartment A in all brain cells. Clustering of genes by expression shows six distinct clusters where clusters 3 and 4 contain genes that increase their expression between mES cells and all brain cell types. Gene ontology (GO) in Fig. [5a](#) was done on genes from clusters 3 and 4 combined (pink box). Expression is calculated as the R-log value for each cell type (see [Methods](#)). **b**, Heatmap of gene expression for genes that change from compartment A in mES cells to compartment B in brain cells. Clustering of genes by expression identifies five clusters. Genes in cluster 4 are expressed in mES cells and show lower expression in the brain cell types; they were used for GO analysis presented in Fig. [5a](#) (light blue box). Genes in clusters 2 and 3 are not expressed in mES cells nor brain cells; they were combined and used for GO analyses presented in Fig.

5b (dark blue box). Expression is calculated as the R-log value for each cell-type. **c**, A higher proportion of *Olfr* and *Vmn* genes are found in B compartments in brain cells, compared to mES cells. **d**, GAM contact matrices show interactions between an *Olfr/Vmn* gene cluster and a second *Olfr* cluster (dashed boxes) separated by 25 Mb (Chr7: 80,000,000-110,000,000). The contacts between the two receptor clusters are strongest in OLGs, where the B compartment is strongest. **e**, GAM contact matrices show strong interactions that span a 30Mb distance between compartment B regions in OLGs, PGNs and DNs (purple circle), but not mES cells (Chr7: 52,000,000-95,000,000). Dashed boxes indicate contacts containing *Olfr* and *Vmn* gene clusters. **f**, Distribution of the top 20% of Z-Score normalized contacts for each genomic window at distances > 3 Mb (Two-sided Mann-Whitney U test; exact p-values are indicated on the plot). **g**, Summary diagram. The 3D genome is extensively reorganized in brain cells to reflect its gene expression specialization. (i) Contacts are rearranged at multiple scales, where formation of new TAD borders can coincide with genes important for cell specialization in all cell types. (ii) Domain melting occurs at very long genes which are highly transcribed and with high chromatin accessibility in brain cells. (iii) The most specific contacts in neurons contain complex networks of binding sites of neuron-specific transcription factors. Contacts bridge genes expressed in the neurons where the contacts are observed, with specialized functions, such as in synaptic plasticity (PGNs) and addiction (DNs). (iv) Finally, B compartments contain clusters of sensory receptor genes silent in all cell types which form strong contacts across tens of megabases.

[Source data](#)

Supplementary information

[Reporting Summary](#)

[Peer Review File](#)

[locus PRISMIR model mES cells](#)

Supplementary Video 1 ***Nrxn3* locus PRISM model mES cells.** Example polymer model for mES cells in the *Nrxn3* locus (chr12:87,600,000–92,400,000).

locus PRISM model DNs

Supplementary Video 2 ***Nrxn3* locus PRISM model DNs.** Example polymer model for DNs in the *Nrxn3* locus (chr12:87,600,000–92,400,000).

4DN sample IDs for mES cell GAM samples

Supplementary Table 1 . List of ID numbers from the 4DN portal (<https://data.4dnucleome.org/>) for multiplex-GAM mES cell samples.

Experimental, sequencing and QC metrics

Supplementary Table 2 . Details of the sequencing datasets generated for this study (number of nuclear slices, negative controls) including sequencing depth, experimental batch and QC measurements.

TAD border coordinates

Supplementary Table 3 . List of TAD border coordinates for each cell type and replicate.

Insulation scores

Supplementary Table 4 . List of insulation scores (range 100–1,000 kb) for each cell type and replicate.

Compartment EV and classification

Supplementary Table 5 . List of compartment eigenvector value scores and A/B classification for each cell type and replicate.

Details of published datasets and scRNA/ATAC-seq

Supplementary Table 6 . Details of published datasets and types of data accessed for this study, including accession numbers. An overview of RNA/ATAC-seq generated in this study is also included.

Full GO terms and associated genes

Supplementary Table 7 . Full GO terms for all analyses (genes tested, background genes) performed in this study, including unfiltered GO terms that were enriched above background (see Methods).

Domain melting score analysis

Supplementary Table 8 . Details of genes tested in the domain melting score analysis, including gene length, length-scaled RPM values and melting score.

3D polymer coordinates for the

Supplementary Table 9 ***Nrxn3* locus in mES cells**. List of x , y , z coordinates for each polymer structure derived from GAM mES cells for the *Nrxn3* locus.

3D polymer coordinates for the

Supplementary Table 10 ***Nrxn3* locus in DNs**. List of x , y , z coordinates for each polymer structure derived from GAM DNs for the *Nrxn3* locus.

BAC details for cryo-FISH experiments

Supplementary Table 11 . Details of BAC probes used for the *Rbfox1* cryo-FISH experiments, including BAC IDs and genomic coordinates.

Cell-type-specific differential expression analysis

Supplementary Table 12 . Details of the differential gene expression analysis for scRNA-seq datasets used in this study, including replicate

expression values, fold-change and adjusted *P* values.

TF motif feature pair analysis

Supplementary Table 13 . Details of all 1,275 TF motif feature pairs tested in the TF motif analysis, including number of significant differential contacts in PGNs or DNs, info gain and enrichment score metrics, and PGN versus DN differential expression values.

TF motif network and community analysis

Supplementary Table 14 . List of TF motifs in the network detection and community analysis. For each motif, the total number of connections and community assignment are listed.

ENA accession numbers for mES cell scRNA-seq samples

Supplementary Table 15 . List of ENA accession numbers (<https://www.ebi.ac.uk/ena/browser/home>) and experimental batch for mESC cell transcriptomes generated in this study.

Source data

Source Data Fig. 1

Source Data Fig. 2

Source Data Fig. 3

Source Data Fig. 4

Source Data Fig. 5

Source Data Extended Data Fig. 1

[**Source Data Extended Data Fig. 2**](#)

[**Source Data Extended Data Fig. 3**](#)

[**Source Data Extended Data Fig. 4**](#)

[**Source Data Extended Data Fig. 5**](#)

[**Source Data Extended Data Fig. 6**](#)

[**Source Data Extended Data Fig. 7**](#)

[**Source Data Extended Data Fig. 8**](#)

[**Source Data Extended Data Fig. 9**](#)

[**Source Data Extended Data Fig. 10**](#)

[**Source Data Extended Data Fig. 11**](#)

[**Source Data Extended Data Fig. 12**](#)

Rights and permissions

Open Access This article is licensed under a Creative Commons Attribution 4.0 International License, which permits use, sharing, adaptation, distribution and reproduction in any medium or format, as long as you give appropriate credit to the original author(s) and the source, provide a link to the Creative Commons license, and indicate if changes were made. The images or other third party material in this article are included in the article's Creative Commons license, unless indicated otherwise in a credit line to the material. If material is not included in the article's Creative Commons license and your intended use is not permitted by statutory regulation or exceeds the permitted use, you will need to obtain

permission directly from the copyright holder. To view a copy of this license, visit <http://creativecommons.org/licenses/by/4.0/>.

[Reprints and Permissions](#)

About this article

Cite this article

Winick-Ng, W., Kukalev, A., Harabula, I. *et al.* Cell-type specialization is encoded by specific chromatin topologies. *Nature* **599**, 684–691 (2021). <https://doi.org/10.1038/s41586-021-04081-2>

- Received: 04 August 2020
- Accepted: 30 September 2021
- Published: 17 November 2021
- Issue Date: 25 November 2021
- DOI: <https://doi.org/10.1038/s41586-021-04081-2>

Share this article

Anyone you share the following link with will be able to read this content:

[Get shareable link](#)

Sorry, a shareable link is not currently available for this article.

[Copy to clipboard](#)

Provided by the Springer Nature SharedIt content-sharing initiative

| [Section menu](#) | [Main menu](#) |

- Article
- Open Access
- [Published: 07 October 2021](#)

Transposon-associated TnpB is a programmable RNA-guided DNA endonuclease

- [Tautvydas Karvelis](#) ORCID: [orcid.org/0000-0002-0685-2947](#)¹,
- [Gytis Druteika](#) ORCID: [orcid.org/0000-0003-3370-7734](#)¹,
- [Greta Bigelyte](#) ORCID: [orcid.org/0000-0002-1432-1433](#)¹,
- [Karolina Budre](#)¹,
- [Rimante Zedaveinyte](#) ORCID: [orcid.org/0000-0002-0738-6976](#)¹,
- [Arunas Silanskas](#)¹,
- [Darius Kazlauskas](#)¹,
- [Česlovas Venclovas](#) ORCID: [orcid.org/0000-0002-4215-0213](#)¹ &
- [Virginijus Siksnys](#) ORCID: [orcid.org/0000-0003-1983-2096](#)¹

[Nature](#) volume 599, pages 692–696 (2021)

- 13k Accesses
- 1 Citations
- 66 Altmetric
- [Metrics details](#)

Subjects

- [DNA](#)
- [Transposition](#)

Abstract

Transposition has a key role in reshaping genomes of all living organisms¹. Insertion sequences of IS200/IS605 and IS607 families² are among the simplest mobile genetic elements and contain only the genes that are required for their transposition and its regulation. These elements encode *tnpA* transposase, which is essential for mobilization, and often carry an accessory *tnpB* gene, which is dispensable for transposition. Although the role of TnpA in transposon mobilization of IS200/IS605 is well documented, the function of TnpB has remained largely unknown. It had been suggested that TnpB has a role in the regulation of transposition, although no mechanism for this has been established^{3,4,5}. A bioinformatic analysis indicated that TnpB might be a predecessor of the CRISPR–Cas9/Cas12 nucleases^{6,7,8}. However, no biochemical activities have been ascribed to TnpB. Here we show that TnpB of *Deinococcus radiodurans* ISDra2 is an RNA-directed nuclease that is guided by an RNA, derived from the right-end element of a transposon, to cleave DNA next to the 5'-TTGAT transposon-associated motif. We also show that TnpB could be reprogrammed to cleave DNA target sites in human cells. Together, this study expands our understanding of transposition mechanisms by highlighting the role of TnpB in transposition, experimentally confirms that TnpB is a functional progenitor of CRISPR–Cas nucleases and establishes TnpB as a prototype of a new system for genome editing.

[Download PDF](#)

Main

Insertion sequences are widespread mobile genetic elements (MGEs) that only contain genes that are required for transposition and its regulation. Insertion sequences from the IS200/IS605 and IS607 families are among the simplest and most ancient MGEs². Typically, they carry subterminal left end (LE) and right end (RE) palindromic elements at MGE ends and encode either *tnpA* and *tnpB* genes in various configurations, or isolated *tnpA* or *tnpB* genes (ISfinder database)⁹. The well-characterized *D. radiodurans* ISDra2 of the IS200/IS605 family consists of partially overlapping *tnpA* and *tnpB* genes flanked by LE and RE elements^{10,11,12} (Fig. 1a). The transposon mobilization occurs through a single-strand ‘peel and paste’ mechanism¹³ (Fig. 1b). ISDra2 TnpA, an extremely small (140 amino acids) Y1 transposase of the HUH family, excises a specific DNA strand near the 5'-TTGAT sequence to form a single-stranded transposon circle that is then integrated 3' to the TTGAT target in a new location to complete the transposition cycle without duplication of the target site^{10,12}. Another well-studied MGE, IS608 from *Helicobacter pylori*, follows the same mechanism but using a 5'-TTAC tetranucleotide sequence instead of the 5'-TTGAT pentanucleotide targeted by ISDra2 (refs.^{4,14,15}). In both cases, excision or insertion of a single-stranded transposon circle occurs on the lagging DNA strand at

the replication fork, coupling the transposition with the DNA replication cycle of the host¹⁶.

Fig. 1: ISDra2 MGE of the IS200/IS605 family.

 figure1

a, Schematic representation of the *D. radiodurans* ISDra2 locus. The MGE consists of the *tnpA* and *tnpB* genes flanked by left end (LE) and right end (RE) partially palindromic elements (shown in red and blue, respectively). Amino acid residues at the predicted RuvC nuclease active site are indicated above the *tnpB* gene. **b**, TnpA-mediated ‘peel and paste’ transposition mechanism for ISDra2. The TnpA dimer catalyses transposon excision from the lagging strand during DNA replication forming a circular single-stranded DNA intermediate and a donor joint. The excised transposon circle inserts at the acceptor joint into the lagging DNA strand 3' to the TTGAT sequence, completing the transposition cycle. Transposon excision/insertion sites are marked by red triangles. **c**, Experimental workflow of the expression and purification of the TnpB complex from *E. coli* cells and bound RNA extraction. sRNA-seq, small RNA sequencing. **d**, Alignment of sRNA sequenced reads to the ISDra2 locus. The blue colour shows the RNA sequences derived from the RE element, and the green marks the last 16 nt at the sequenced RNA 3' ends, which align with the transposon flanking DNA.

Although the function of TnpA in transposition is well established, the role of TnpB remains elusive. ISDra2 TnpB (408 amino acids) is not essential for transposition and is thought to regulate excision and insertion of transposons^{3,4,5}, although a regulatory mechanism has yet to be established. Bioinformatic prediction of the conserved RuvC-

like active site in the TnpB sequence led to speculations that TnpB could be an ancestor of Cas9 and Cas12 nucleases adopted by CRISPR–Cas systems^{6,7,8}. However, neither the role of the RuvC motif in transposition nor the nuclease activity of TnpB have been experimentally demonstrated.

TnpB forms an RNP complex with reRNA

To establish the biochemical function of TnpB in the *D. radiodurans* ISDra2 element, we aimed to isolate and biochemically characterize the TnpB protein. Initially, we expressed *tnpB* fused to the sequence encoding the 10×His-maltose-binding protein (MBP) tag in *Escherichia coli* but failed to isolate the intact TnpB protein from cell extracts by Ni²⁺-affinity chromatography due to low yield (Extended Data Fig. 1a). However, co-expression of *tnpB* with a full ISDra2 transposon (with inactivated *tnpA*) resulted in a substantially increased TnpB yield, suggesting that additional transposon elements are required for stable expression of TnpB (Extended Data Fig. 1b, c). Subsequent biochemical analysis of TnpB samples revealed that RNA co-purified with the TnpB protein (Extended Data Fig. 1d). To characterize TnpB-bound RNAs, we performed small RNA sequencing that revealed the enrichment of non-coding RNAs approximately 150 nucleotides (nt) long derived from ISDra2 transposon RE element that we termed right end element RNAs (reRNAs) (Fig. 1c, d). The reRNA co-purified with TnpB fully matched to the 3' end of the *tnpB* gene and RE sequence, except for the last approximately 16 nt at the 3' end, which were derived from the DNA sequence flanking the IS200/IS605 transposon (Fig. 1d). The enrichment of non-coding RNAs associated with *tnpB*-encoding transposons from the IS200/IS605 family has been previously reported; however, their function remains elusive^{17,18}. Here we provide experimental evidence that TnpB forms a ribonucleoprotein (RNP) complex with reRNA derived from the 3' end of the transposon .

TnpB RNP cleaves DNA in vitro

Guided by the similarities of TnpB to the CRISPR–Cas12f effector complexes that function as RNA-guided double-stranded DNA (dsDNA) nucleases¹⁹, we hypothesized that the approximately 16-nt 3' terminal of reRNA, which are derived from the DNA adjacent to the transposon and would be variable per se (Fig. 1d), might function as a guide sequence that directs TnpB to its target and activates DNA cleavage. To test this hypothesis, we adopted the previously developed protospacer adjacent motif (PAM) identification assay for Cas9/Cas12 nucleases¹⁹. First, we engineered the plasmids encoding TnpB and reRNA, where the 3'-terminal reRNA 16-nt sequence was replaced by 16-nt (Fig. 2a) or 20-nt (Extended Data Fig. 2a) sequences that matched the target next to the 7-nt (7N) randomized region in the plasmid library. Next, following *E. coli* transformation and expression, cell lysates

containing TnpB RNP complexes were used for plasmid library cleavage. The DNA ends that would result from the plasmid cleavage were repaired by T4 DNA polymerase, subjected to adapter ligation, PCR amplified and sequenced. Sequencing of the adapter-ligated fragments revealed enrichment of the products having adapters at the target site 20–21 bp (targeted strand) and 15 bp (non-targeted strand) from the randomized region, indicating cleavage of the plasmid library by the TnpB RNP complex (Fig. 2b, Extended Data Fig. 2b). The positions of the adapter ligation for the targeted strand and non-targeted strand suggested a staggered cleavage pattern generating 5' overhangs. Further analysis of DNA fragments revealed enrichment of TTGAT sequences in the randomized 7N region 5' upstream of the target sequence (Fig. 2c, Extended Data Figs. 2c,d, 3). Notably, the TTGAT sequence that licensed cleavage of the plasmid library by TnpB matched the target site sequence that is required for TnpA-mediated ISDra2 transposon excision and insertion¹¹. Because this sequence was equivalent to the PAM sequence that is required for initiation of DNA cleavage by Cas9 or Cas12 nucleases, we termed it transposon-associated motif (TAM).

Fig. 2: TnpB protein is an RNA-guided dsDNA nuclease.

 **figure2**

a, Experimental workflow for the establishment of dsDNA cleavage requirements by the TnpB–reRNA complex. *E. coli* cells were transformed with a plasmid expressing TnpB and HDV ribozyme-terminated reRNA, containing the 16-nt sequence that matched the target in the plasmid DNA library, flanked by the randomized 7-nt sequence (7N). Cell lysate was used for library digestion followed by double-stranded break (DSB) capture. F, forward primer, annealing to the ligated adapter; R1 and R2, reverse primers, annealing to the target plasmid backbone. **b**, Determination of adapter ligation positions indicate the formation of DSBs in the targeted sequence. ‘–TnpB’ represents the cleavage reactions using lysates obtained from the cells that do not express TnpB. The blue and red triangles indicate the positions of F + R1-enriched and F + R2-enriched adapter ligated reads, respectively. **c**, WebLogo representation of

motifs identified in the 7N randomized region at 20–21-bp F + R1-enriched adapter ligated reads. **d**, Experimental workflow of the expression and purification of the TnpB RNP complex. *E. coli* cells were transformed with a plasmid expressing TnpB and a separate plasmid expressing HDV ribozyme-terminated reRNA. The reRNA-encoding construct contained the 16-nt guide sequence, which was different from the guide sequence used in the plasmid library cleavage experiment. **e**, The TnpB RNP complex cleaves supercoiled and linearized target plasmid *in vitro*. Cleavage is blocked by the D191A mutation at the RuvC-like active site. **f**, Target plasmid cleavage (TAM+/Target+, TAM-/Target+ and TAM+/Target-) by the TnpB RNP complex *in vitro*. TAM and the target complementary to the reRNA 3'-end sequence are required for plasmid DNA cleavage. **g**, Sanger sequencing of the TnpB-cleaved plasmid products reveals multiple cleavage positions at the non-targeted strand (NTS) and a single cleavage site at the target strand (TS) (marked with red triangles). For uncropped gel images, see Supplementary Fig. 1.

Next, to validate the requirements for dsDNA cleavage established on the plasmid DNA library, we purified the TnpB–reRNA complex with 1:1 stoichiometry (Fig. 2d, Extended Data Fig. 4) and tested its ability to cleave dsDNA substrates (Fig. 2e,f, Extended Data Fig. 5). First, incubation of the TnpB complex with the plasmid (both supercoiled and linearized), containing the target next to the TAM sequence, converted the supercoiled plasmid into its linear form or yielded linear DNA cleavage products of expected size, respectively (Fig. 2e). Mutation of the conserved D191 residue in the RuvC-like active site compromised cleavage, indicating that the RuvC motif is responsible for cleavage of dsDNA (Fig. 2e). DNA cleavage required both TAM and the target-matching sequence at the 3' end of reRNA (Fig. 2f). Last, run-off sequencing of the cleavage products confirmed a staggered cleavage pattern at 15–21 bp from the TAM that resulted in 5' overhangs (Fig. 2g). Data for the synthetic oligonucleotide cleavage (Extended Data Fig. 5) were consistent with the plasmid DNA cleavage experiments (Fig. 2e,f). TnpB RNP also cleaved a matching single-stranded DNA in a TAM-independent manner (Extended Data Fig. 6). Together, these results demonstrate that TnpB functions as a TAM-dependent RNA-guided dsDNA nuclease.

TnpB ensures DNA interference in *E. coli*

To probe whether TnpB is able to cleave its target in the cells, we adopted a plasmid interference assay (Fig. 3a). In brief, *E. coli* cells expressing the TnpB complex were transformed with a plasmid containing the TAM-flanked target and carrying the kanamycin resistance gene that enable growth on kanamycin-supplemented agar plates (Fig. 3a). Serial dilutions of the transformants revealed plasmid interference in the cells containing the native TnpB variant but not TnpB with the mutated RuvC motif (Fig. 3b). Together, these results confirm that TnpB can cleave dsDNA target *in vivo*.

The dsDNA cleavage activity of TnpB and the target site requirements established here allow us to propose the role of TnpB in the transposition of IS200/IS605 MGEs (Fig. 3c). We suggest that TnpB guided by reRNA makes a double-stranded break (DSB) at the 5'-TTGAT flanked donor joint site that is formed in DNA when the transposon circle is excised during replication. A TnpB-induced DSB could then facilitate homology-directed repair to reinstate the transposon at the donor joint using its intact copy on the sister chromatid, ensuring that both DNA copies secured a transposon copy before cell division (Fig. 3c).

Fig. 3: TnpB-mediated plasmid interference in vivo.

 figure3

a, Experimental workflow of the plasmid interference assay in *E. coli*. The cleavage of a target plasmid results in loss of kanamycin (Kn) resistance. The reRNA-encoding construct contained the 16-nt guide sequence. AmpR, ampicillin/carbenicillin (Ap/Cb) resistance gene; KanR, kanamycin resistance gene. **b**, Plasmid interference assay. *E. coli* culture samples were serially diluted ($10\times$) and the *E. coli* transformants were grown on the media supplemented with Cb and Kn at 25 °C for 44 h. Interference is compromised for the catalytically dead D191A and E278A TnpB variants. Target '+' or '-' indicates the plasmids with or without the target, respectively. For the uncropped plate image, see Supplementary Fig. 1. **c**, Proposed role of TnpB in transposition. The IS200/IS605 transposon circle is excised from the lagging strand during DNA replication resulting in two DNA copies: one copy that originates from the leading strand and carries an intact transposon, and another copy that originates from the lagging strand and lacks the transposon at the original site due to the strand-

specific transposon excision. However, the latter DNA copy still carries the transposon ‘footprint’ in the form of the donor joint, comprised of the 5'-TTGAT sequence and the 3'-flanking DNA sequence that becomes a target to the TnpB-reRNA complex. In this case, the 5'-TTGAT sequence serves as a TAM that initiates the binding of the reRNA sequence to the matching DNA sequence followed by dsDNA cleavage. TnpB-induced DSB could facilitate homology-directed repair to reinstate the transposon at the donor joint using its intact copy on the sister chromatid, ensuring that both DNA copies have a transposon-coding gene before cell division. Red triangles indicate DNA cleavage sites.

TnpB cleaves genomic DNA in human cells

Finally, after demonstrating RNA-guided dsDNA cleavage both in vitro and in *E. coli*, we tested whether TnpB can be adopted for genome editing of human cells (HEK293T). Plasmids encoding the TnpB protein fused with a nuclear localization sequence and reRNA constructs targeting five 20-nt sites next to the 5'-TTGAT TAM sequence in human genomic DNA (gDNA) were transiently transfected into HEK293T cells (Fig. 4a). After 72 h, gDNA was extracted and analysed by sequencing for the presence of insertions and deletions (indels) at the targeted cleavage sites, indicating DSB repair events and genome editing. At the two tested sites (*AGBL1-2* and *EMX1-1*), TnpB introduced mutations at frequencies of 10–20% (Fig. 4b), similar to the levels observed for CRISPR–Cas9 and Cas12-based editing^{20,21,22,23,24,25}. *AGBL1-1* and *EMX1-2* sites were moderately (1–5%) modified, whereas no indels were detected at the *HPRT1* site. Further analysis of the obtained indels revealed a domination of deletions at the cleavage site over insertions (Fig. 4c), similar to the mutational profiles observed after Cas12 cleavage^{23,25}. Therefore, these results indicate that compact RNA-guided TnpB nucleases can cleave eukaryotic gDNA and may be adopted as tools for genome editing.

Fig. 4: TnpB nuclease is a novel genome editor.

 **figure4**

a, The experimental workflow of the human cell line (HEK293T) genome-editing experiment. NLS, nuclear localization sequence. **b**, Detection of indel activity in the five tested targets of 20 nt in length in human gDNA (represented as the mean of three biologically independent experiments (shown in dots) \pm standard deviation). The TnpB (non-targeting) expression plasmid used as a negative control encodes the rRNA-containing guide sequence that does not match any target in the human gDNA. **c**, Indel profile distribution within the target sequence in the *EMX1-1* site showing the distribution of deletions (blue line) and insertions (red line) across the cleavage site (dotted line). The profile was obtained by aligning all reads at the *EMX1-1* site and counting deletions and insertions at each position.

Discussion

Overall, in this study, we identified the functional activity of the TnpB protein from the ISDra2 system by demonstrating TAM-dependent RNA-guided dsDNA cleavage. This observation expands our understanding of the transposition mechanisms of MGEs in the large IS200/IS605 family. Although TnpA has been widely studied, revealing the TnpA-mediated ‘peel and paste’ transposition mechanism, TnpB is not essential for transposition but may have a role in its regulation as it has been suggested for ISDra2 TnpB, although no mechanism for this has been established⁵. The inhibitory effect of TnpB on the excision and integration steps of ISDra2 transposition reported previously⁵ should be revisited, taking into consideration the RNA-guided TnpB nuclease activity demonstrated in this work.

Here we show that both in vitro (Fig. 2e,f) and in *E. coli* cells (Fig. 3b), TnpB cleaves the donor joint that would be generated after transposon excision and propose that TnpB-mediated DSB triggers homology-directed repair to reinstate the transposon into its original site. This process would be analogous to the group I intron homing promoted by intron encoded endonucleases²⁶. We propose that in MGEs containing both *tnpA* and *tnpB*, two types of transposition will occur: (1) excision of the transposon and insertion of it at a new site (catalysed by TnpA) (Fig. 1b); and (2) transposon ‘homing’, a process in which TnpB cuts DNA in a transposon-less allele, triggering recombination that copies the transposon into the same position (Fig. 3c). TnpB thus provides a backup mechanism that prevents the possible loss of MGEs if the integration step of the excised transposon is unsuccessful and ensures that both daughter cells will acquire identical DNA copies. In this case, the ‘peel and paste’ mechanism, which was proposed for TnpA, in the presence of TnpB is transformed into a ‘peel, paste and copy’ mechanism. The RNA-guided DNA cleavage activity of TnpB could also enable transposon integration into ectopic sites flanked by homologous sequences containing the TAM and matching guide RNA, thus providing an additional mechanism for transposon propagation.

Recently, the evolution of CRISPR–Cas9 nucleases from IscB proteins of the distinct IS200/IS605 transposon family has been reconstructed and RNA-guided DNA cleavage activity of the TnpB protein has been reported; however, the role of TnpB in transposition has not been discussed in detail²⁷. The demonstration of the RNA-guided dsDNA cleavage activity of TnpB provides a direct experimental confirmation of an evolutionary scenario for class 2 CRISPR–Cas systems, pinpointing MGEs as predecessors of Cas9 and Cas12 effectors^{6,7,8}. Sequence comparisons of TnpB and Cas12 family proteins show similar domain organizations, including a conserved RuvC endonuclease-like motif (Extended Data Fig. 7). The closest TnpB neighbours on the evolutionary tree are the miniature Cas12f nucleases^{8,19,28}. However, there are important differences between TnpB and the Cas12f nucleases. First, whereas Cas12f nucleases use a guide RNA that originates from the CRISPR array, TnpB uses right transposon element-derived rRNA as a guide. Next, TnpB is a monomer and requires a single rRNA molecule (Extended Data Fig. 3c), whereas Cas12f nucleases are dimers that bind to a single copy of a crRNA (CRISPR RNA)–tracrRNA (trans-activating crRNA) duplex^{29,30}. Last, although the TAM sequence required for TnpB cleavage seems to be equivalent to the PAM sequence that licenses Cas12f cleavage, Cas12f proteins show distinct PAM requirements¹⁹. It would be interesting to see whether the PAM diversity of Cas12f nucleases correlate with the distinct TAM sequence requirements of TnpB proteins, reflecting evolutionary relationships between Cas12 nucleases and MGEs of the IS200/IS605/IS607 families. RNA-guided DNA insertion by CRISPR-associated Tn7-like transposons provides another example of the interplay between MGEs and CRISPR–Cas systems^{31,32}.

Finally, we show that TnpB also cleaves dsDNA in human cells and expands the genome-editing toolbox by providing a new class of extremely compact non-Cas nucleases with different biochemical requirements for genome-editing applications (Extended Data Table 1). The natural diversity of TnpB orthologues, including eukaryotic variants that remain to be characterized³³, and their miniature size suitable for adeno-associated virus-based delivery open new horizons for human therapeutic applications.

Methods

Engineering of TnpB expression vectors

The IS200/IS605 ISDra2 system from *D. radiodurans* R1 (GenBank AE000513.1) was ordered as a synthetic sequence cloned into the pTwist vector under the T7 promoter (pTWIST-ISDra2; Twist Biosciences). To obtain the ISDra2 variant with a deletion within the *tnpA* gene (pGD3), the pTWIST-ISDra2 plasmid was pre-cleaved with NdeI (Thermo Fisher Scientific), 5' overhangs filled-in using T4 DNA polymerase (Thermo Fisher Scientific) and self-circularized with T4 DNA ligase (Thermo Fisher Scientific). For TnpB purification, two pBAD-derived expression vectors were constructed: the *tnpB*-encoding sequence was fused to N-terminal 10×His-TwinStrep-MBP (pTK120-ISDra2-TnpB) or N-terminal 6×His-MBP and C-terminal StrepTag II (pTK151) protein purification tags and cloned under arabinose-inducible promoters using the NEBuilder HiFi DNA Assembly Kit (New England Biolabs). To obtain the reRNA expression vector (pGB71) for TnpB RNP complex purification, the reRNA-encoding sequence with the T7 promoter at the 5' end and hepatitis delta virus (HDV) ribozyme with the T7 terminator at the 3' end (assembled by PCR from synthetic oligonucleotides) was cloned into the pACYC184 vector between HindIII and BclI restriction sites (Thermo Fisher Scientific). The self-cleaving HDV ribozyme ensured fixed 16-nt guide RNA length at the 3' end of reRNA. pGB74-78, containing reRNA-encoding and *tnpB*-encoding sequences under T7 and T7lac promoters, respectively, used for TnpB complex expression in 7N plasmid library cleavage and plasmid interference assays, were obtained by cloning the reRNA-encoding construct between Bsu15I and EcoRI, and *tnpB* between NdeI and XhoI (Thermo Fisher Scientific) restriction sites into the pETDuet-1 vector (Novagen). For genome-editing experiments in human HEK293T cells, reRNA (targeting 20-bp sites in human gDNA) and TnpB (fused at the 3' end with SV40 nuclear localization sequence (NLS)-T2A-GFP) encoding constructs were cloned into the pX458-derived plasmid (a gift from F. Zhang, Addgene plasmid #48138) under U6 and CAG promoters, respectively (pRZ122-127), using the NEBuilder HiFi DNA Assembly Kit (New England Biolabs). The Phusion Site-Directed Mutagenesis Kit (Thermo Fisher Scientific) was used to obtain plasmid variants with a mutated RuvC

active site. The description of the TnpB expression plasmids and links to the sequences are provided in Supplementary Table 1.

Expression and purification of the TnpB RNP complex

For the initial TnpB protein expression and purification, *E. coli* BL21-AI cells were transformed with pTK120-ISDra2-TnpB or pTK120-ISDra2-TnpB with pGD3 (plasmid encoding ISDra2 transposon with a deletion within the *tnpA* gene) and grown in LB medium, supplemented with ampicillin (100 µg/ml) or ampicillin (100 µg/ml) and chloramphenicol (50 µg/ml), respectively, at 37 °C. After culturing to an OD₆₀₀ of 0.6–0.8, protein expression was induced with 0.2% arabinose and the cells were grown for an additional 16 h at 16 °C. Next, the cells were pelleted by centrifugation, resuspended in 20 mM Tris-HCl (pH 8.0 at 25 °C), 250 mM NaCl, 5 mM 2-mercaptoethanol, 25 mM imidazole, 2 mM PMSF and 5% (v/v) glycerol containing buffer and disrupted by sonication. After removing cell debris by centrifugation, the supernatant was loaded onto the Ni²⁺-charged HiTrap chelating HP column (GE Healthcare) and proteins were eluted with a linear gradient of increasing imidazole concentration from 25 mM to 500 mM in 20 mM Tris-HCl (pH 8.0 at 25 °C), 500 mM NaCl, 5 mM 2-mercaptoethanol and 5% (v/v) glycerol buffer. The fractions containing TnpB were pooled, dialysed against 20 mM Tris-HCl (pH 8.0 at 25 °C), 250 mM NaCl, 2 mM DTT and 50% (v/v) glycerol-containing buffer and stored at –20 °C. The obtained purified TnpB samples were used for nucleic acid extraction and analysis.

For increased expression and yield of the TnpB RNP complex, *E. coli* BL21-AI cells were transformed with reRNA (pGB71) and TnpB (pTK151) or TnpB^{D191A} (pTK152) expression vectors and grown in LB medium, supplemented with ampicillin (100 µg/ml) and chloramphenicol (50 µg/ml) at 37 °C. After culturing to an OD₆₀₀ of 0.6–0.8, protein expression was induced with 0.2% arabinose and cells were grown for additional 16 h at 16 °C. Next, the cells were pelleted by centrifugation, resuspended in 20 mM Tris-HCl (pH 8.0 at 25 °C), 500 mM NaCl, 5 mM 2-mercaptoethanol, 25 mM imidazole, 2 mM PMSF and 5% (v/v) glycerol-containing buffer and disrupted by sonication. The supernatant obtained after centrifugation was loaded onto the Ni²⁺-charged HiTrap chelating HP column (GE Healthcare) and bound proteins were eluted with a linear gradient of increasing imidazole concentration from 25 mM to 500 mM in 20 mM Tris-HCl (pH 8.0 at 25 °C), 500 mM NaCl, 5 mM 2-mercaptoethanol and 5% (v/v) glycerol buffer. The fractions containing TnpB RNP complexes were pooled and the 6×His-MBP tag was cleaved by overnight incubation with TEV protease at 8 °C. Next, the reaction mixture was loaded onto the StrepTrap column (GE Healthcare), washed with 20 mM Tris-HCl (pH 8.0 at 25 °C), 150 mM NaCl, 5 mM 2-mercaptoethanol and 5% (v/v) glycerol buffer and bound TnpB complex eluted with 2.5 mM *d*-desthiobiotin solution. Fractions containing TnpB RNP were pooled, loaded on a HiTrap heparin HP column (GE Healthcare) and eluted using a linear gradient of

increasing NaCl concentration from 0.15 M to 1.0 M. Obtained TnpB RNP complex fractions were pooled, concentrated up to 0.5 ml using the Amicon Ultra-15 centrifugal filter unit (Merck Millipore) and loaded on a Superdex 200 10/300 GL (GE Healthcare) gel filtration column equilibrated with 20 mM Tris-HCl (pH 8.0 at 25 °C), 250 mM NaCl and 5 mM 2-mercaptoethanol buffer. Peak fractions containing TnpB RNP complexes were pooled and dialysed against 20 mM Tris-HCl (pH 8.0 at 25 °C), 250 mM NaCl, 2 mM DTT and 50% (v/v) glycerol-containing buffer and stored at -20 °C. The concentration of the TnpB RNP complex was determined by quantifying the intensity of protein bands in SDS-PAGE gels and comparing them to the protein standard of known concentration. The sequences of TnpB protein constructs are listed in Supplementary Table 2.

Molecular mass measurements by mass photometry

Measurement coverslips (no. 1.5 H, 24 × 50 mm; Marienfeld) were cleaned by sequential sonication for 5 min in MilliQ water, isopropanol and MilliQ water and then dried using a clean stream of nitrogen gas. A prepared coverslip was mounted onto the OneMP mass photometer (Refeyn) and a CultureWell Reusable Gasket (Grace Bio-Labs) was placed on top. A gasket well was filled with 10 µl of 20 mM Tris-HCl (pH 8.0 at 25 °C) and 250 mM NaCl buffer, 10 µl of the diluted TnpB RNP complex sample (approximately 60 nM) was added and the adsorption of biomolecules was monitored for 120 s using the AcquireMP software (Refeyn). For converting the measured ratiometric contrast into molecular mass, Un1Cas12f1 protein¹⁹ and its oligomers ranging from 60 kDa to 250 kDa (monomer to tetramer) were used for calibration. Samples were measured in triplicates. Mass photometry movies were analysed using DiscoverMP (Refeyn).

Extraction and analysis of TnpB-bound nucleic acids

To extract TnpB-bound nucleic acids, 100 µl of purified TnpB samples was incubated with 5 µl (20 mg/ml) of proteinase K (Thermo Fisher Scientific) for 45 min at 37 °C in 1 ml of 10 mM Tris-HCl (pH 7.5 at 37 °C), 5 mM MgCl₂, 100 mM NaCl, 1 mM DTT and 1 mM EDTA reaction buffer. Next, the mixtures were treated with phenol:chloroform:isoamyl alcohol (25:24:1) solution and the aqueous phase was subsequently mixed with chloroform to remove any remaining phenol. The solution with nucleic acids was split into fresh tubes (198 µl into each) and incubated with 2 µl of RNase I (10 U/µl) (Thermo Fisher Scientific) or DNase I (10 U/µl) (Thermo Fisher Scientific) for 45 min at 37 °C. Reaction products were mixed with 2× RNA loading dye (Thermo Fisher Scientific), separated on TBE-Urea (8 M) 15% denaturing polyacrylamide gel using 0.5× TBE electrophoresis buffer (Thermo Fisher Scientific) and visualized with SYBR Gold (Thermo Fisher Scientific).

RNA isolation from the TnpB RNP complex

For TnpB-bound RNA extraction, 100 µl of purified TnpB complex was incubated with 5 µl (20 mg/ml) of proteinase K (Thermo Fisher Scientific) for 45 min at 37 °C in 1 ml of 10 mM Tris-HCl (pH 7.5 at 37 °C), 5 mM MgCl₂, 100 mM NaCl, 1 mM DTT and 1 mM EDTA reaction buffer. DNA was removed by adding 10 µl of DNase I (10 U/µl) (Thermo Fisher Scientific) and incubating for an additional 45 min at 37 °C, and the reaction mixture was purified with a GeneJET RNA Cleanup and Concentration Micro Kit (Thermo Fisher Scientific). Next, 3 µg of purified RNAs was phosphorylated at 37 °C for 30 min using 1 µl (10 U/µl) of PNK (Thermo Fisher Scientific) in 1× reaction buffer A (Thermo Fisher Scientific) supplemented with 1 mM ATP (20 µl reaction volume). Reaction products were purified using a GeneJET RNA Cleanup and Concentration Micro Kit (Thermo Fisher Scientific).

RNA sequencing and analysis

RNA libraries were prepared using Collibri Stranded RNA Library Prep Kit for Illumina Systems (Thermo Fisher Scientific) according to the manufacturer's instructions for small RNAs (protocol MAN0025359), pooled in an equimolar ratio and pair-end sequenced (2 × 75 bp) using MiSeq Reagent Kit v2, 300 cycles (Illumina) on a MiSeq System (Illumina). The pair-end reads shorter than 20 bp were filtered with Cutadapt³⁴. The remaining reads were mapped to the transposon-encoding plasmid (pTWIST-ISDra2; Supplementary Table 1) using BWA³⁵ and converted to the BAM file format with SAMtools³⁶. The resulting coverage data were visualized using Integrative Genomics Viewer³⁷.

TnpB cleavage of plasmid DNA library

For dsDNA cleavage detection and TAM characterization, the previously developed PAM determination assay for Cas9 and Cas12 effectors was adopted^{19,38,39}. In brief, the *tnpB* gene and reRNA constructs, targeting 16-bp or 20-bp sequences in the plasmid library pTZ57 (Supplementary Table 1), adjacent to a 7N randomized region (Supplementary Table 2), were cloned into a pETDuet-1 (Millipore Sigma) vector (pGB77-78; Supplementary Table 1). Next, *E. coli* ArcticExpress (DE3) cells were transformed with TnpB RNP components encoding plasmids and the cells were grown in LB medium supplemented with ampicillin (100 µg/ml) and gentamicin (10 µg/ml). After reaching an OD₆₀₀ of 0.5, TnpB expression was induced with 0.5 mM IPTG and the culture was incubated overnight at 16 °C. The cells from 10 ml of overnight culture were collected by centrifugation, resuspended in 1 ml of lysis buffer (20 mM phosphate (pH 7.0), 0.5 M NaCl, 5% (v/v) glycerol and 2 mM PMSF) and lysed by sonication. Cell debris was removed by centrifugation, and 10 µl of the obtained TnpB

RNPs containing supernatant were used directly in the digestion experiments. In brief, lysate was mixed with 1 µg of the 7N randomized plasmid library (approximately 20 M fold coverage of all 7N TAM sequences) in 100 µl of reaction buffer (10 mM Tris-HCl (pH 7.5 at 37 °C), 100 mM NaCl, 1 mM DTT and 10 mM MgCl₂) and incubated for 1 h at 37 °C. Cleaved DNA ends were repaired by adding 1 µl of T4 DNA polymerase (Thermo Fisher Scientific), 1 µl of 10 mM dNTP mix (Thermo Fisher Scientific) and incubating at 11 °C for 20 min, followed by heating the mix up to 75 °C for 10 min. Next, 3'-dA overhangs were added by incubating the reaction mixture with 1 µl of DreamTaq polymerase (Thermo Fisher Scientific) and 1 µl of 10 mM dATP (Thermo Fisher Scientific) for 30 min at 72 °C. In addition, RNA was removed by incubating for 15 min at 37 °C with 1 µl of RNase A (Thermo Fisher Scientific) and the DNA was purified using the GeneJet PCR Purification Kit (Thermo Fisher Scientific). The purified cleavage products (100 ng) were ligated with a dsDNA adapter containing a 3'-dT overhang (100 ng) for 1 h at 22 °C using 1 µl of T4 DNA ligase (Thermo Fisher Scientific) in 20 µl reaction volume. Next, the adapter-bearing cleavage products were PCR amplified and gel purified using the GeneJet Gel Purification Kit (Thermo Fisher Scientific). DNA libraries were prepared using the Collibri PS DNA Library Prep Kit for Illumina Systems (Thermo Fisher Scientific) according to the manufacturer's instructions, pooled in an equimolar ratio and pair-end sequenced (2 × 150 bp) using MiSeq Reagent Kit v2, 300 cycles (Illumina) on a MiSeq System (Illumina).

dsDNA target cleavage by the TnpB RNP complex was evaluated by examining the adapter ligation at the targeted sequence in the 7N plasmid library. This was accomplished by extracting and counting all reads containing the adapter ligated at the 0–30 bp target positions next to the 7N region and identifying 10 bp of perfectly matching sequences derived from the adapter and the plasmid backbone. The analysis revealed that 1–5% of total reads have the adapter ligated at the 0–30-bp target positions. The reads exhibiting elevated frequency of adapter ligation in the target region (20–21 bp from the 7N randomized sequence) were used for 7N sequence (TAM) extraction and representation in WebLogo⁴⁰ and position frequency matrix (PFM) formats. The Python scripts used in the cleavage position identifications and TAM characterization are provided in the GitHub repository (https://github.com/tkarvelis/Nuclease_manuscript).

DNA substrates

Plasmid DNA substrates used in in vitro cleavage assays (pGB72-73) were obtained by cloning oligoduplexes assembled after annealing complementary synthetic oligonucleotides (Thermo Fisher Scientific) into the pSG4K5 plasmid (a gift from X. Wang, Addgene plasmid #74492) pre-cleaved with EcoRI and NheI restriction endonucleases (Thermo Fisher Scientific). The links to the plasmid sequences are

provided in Supplementary Table 1 and the targeted sequences are provided in Supplementary Table 3.

Synthetic DNA substrates were 5' end labelled by incubating 1 μ M of oligonucleotide (Thermo Fisher Scientific) with 1 μ l (10 U/ μ l) of PNK (Thermo Fisher Scientific) and 32 P- γ -ATP (PerkinElmer) at 37 °C for 30 min in 7.5 μ l of 1 \times reaction buffer A (Thermo Fisher Scientific). Oligoduplexes (100 nM) were obtained by combining 32 P-labelled and unlabelled complementary oligonucleotides (1:1.5 molar ratio) followed by heating to 95 °C and slow cooling to room temperature. The sequences of the substrates are provided in Supplementary Table 2.

DNA cleavage assays

Plasmid DNA cleavage reactions were initiated by mixing 100 nM of TnpB RNP complex with 3 nM of plasmid DNA (pGB72-73; Supplementary Table 1) in 10 mM Tris-HCl (pH 7.5 at 37 °C), 10 mM MgCl₂, 1 mM DTT, 1 mM EDTA and 100 mM NaCl reaction buffer and incubating at 37 °C for 60 min. The reactions were quenched by adding 3 \times loading dye solution (0.03% bromophenol blue, 0.3% SDS and 75 mM EDTA in 30% (v/v) glycerol) and analysed by agarose gel electrophoresis and ethidium bromide staining. The linearized plasmid substrate was obtained by pre-cleaving target plasmid with NdeI endonuclease (Thermo Fisher Scientific).

Cleavage reactions with synthetic oligoduplexes (Supplementary Table 4) were initiated by combining 100 nM TnpB RNP complex with 1 nM radiolabelled substrate in 100 μ l of 10 mM Tris-HCl (pH 7.5 at 37 °C), 10 mM MgCl₂, 1 mM DTT, 1 mM EDTA and 100 mM NaCl reaction buffer at 37 °C. Aliquots of 10 μ l were removed from the reaction mixture at timed intervals (0 min, 1 min, 5 min, 15 min and 60 min), quenched with 1.8 \times volume of a loading dye (95% (v/v) formamide, 0.01% bromophenol blue and 25 mM EDTA) and subjected to denaturing gel electrophoresis (20% polyacrylamide containing 8.5 M urea in 0.5 \times TBE buffer).

Plasmid interference assay

Plasmid interference assays were performed in the *E. coli* Arctic Express (DE3) strain bearing TnpB and reRNA encoding plasmids (pGB74-76) (Supplementary Table 1). The cells were grown at 37 °C to an OD₆₀₀ of approximately 0.5 and electroporated with 100 ng of a target-containing plasmid engineered from pSG4K5 (a gift from X. Wang, Addgene plasmid 74492) (pGB72; Supplementary Table 1). After 1 h, co-transformed cells were further diluted by serial of 10 \times fold dilutions and grown at 25 °C on plates containing IPTG (0.1 mM), gentamicin (10 μ g/ml), carbenicillin (100 μ g/ml) and kanamycin (50 μ g/ml) for 44 h.

HEK293T cell culturing and genome editing

HEK293T cells purchased from the American Type Culture Collection (catalogue number CRL-3216) were cultivated in DMEM (Gibco) supplemented with 10% FBS (Gibco), penicillin (100 U/ml) and streptomycin (100 µg/ml) (Thermo Fisher Scientific). The cell line was not further authenticated and was not tested for mycoplasma contamination. A day before transfection, the cells were plated in a 24-well plate at a density of 1.4×10^5 cells per well. The transfection mixture was prepared by mixing 1 µg of plasmid encoding NLS-tagged TnpB and its reRNA (pRZ122-127; Supplementary Table 1) with 2 µl of TurboFect transfection reagent (Thermo Fisher Scientific) in 100 µl of serum-free DMEM. After 15 min of incubation at room temperature, the transfection mix was added dropwise to the cells. The cells were then grown for 72 h at 37 °C and 5% CO₂.

Indel characterization

Transfected HEK293T cells were trypsinized, washed and resuspended in 100 µl of PBS (approximately 6×10^5 cells were collected from each well), and 10 µl of the obtained suspension was lysed using 50 µl of QuickExtract solution (Lucigen). Next, two rounds of PCR were performed: first to amplify the DNA region surrounding each target site, and second to add the sequences required for Illumina sequencing and indexing. In brief, 1–4 µl of cell lysate was used in the primary PCR with primers specific to the targeted genomic locus that were 5' tailed with Illumina Read1 and Read2 sequences, in a final volume of 20 µl, using Hot Start Phusion Polymerase (Thermo Fisher Scientific). The thermocycler setting consisted of initial denaturation at 98 °C for 30 s, 15 cycles of 98 °C for 15 s, 56.8 °C for 15 s, 72 °C for 30 s, and final incubation at 72 °C for 5 min. The resulting amplicons were cleaned using 1.8× volume of magnetic beads (Lexogen) and eluted in 30 µl of elution buffer. Of the eluted mixture, 6 µl was used as a template for the second round of PCR, in a final volume of 30 µl, to index and add P5 and P7 adapters required for Illumina sequencing, using the Lexogen PCR Add on Kit (Lexogen) with the i7 6 nt Index Set (Lexogen). The thermocycler setting consisted of initial denaturation at 98 °C for 30 s, 15 cycles of 98 °C for 10 s, 65 °C for 20 s, 72 °C for 30 s and final incubation at 72 °C for 1 min. To ensure the purity of the PCR products, an additional cleanup with 0.9× volume of magnetic beads (Lexogen) was performed. Barcoded and purified DNA samples were quantified by Qubit 4 Fluorometer (Thermo Fisher Scientific), analysed using BioAnalyzer (Agilent), pooled in an equimolar ratio and pair-end sequenced (2 × 75 bp) using the MiniSeq High Output Reagent Kit, 150 cycles (Illumina) on a MiniSeq System (Illumina). Indels were analysed using CRISPResso2 with the following parameters: minimum of 70% homology for alignment to the amplicon sequence, quantification window of 10 bp, ignoring substitutions to avoid false positives and phred33 score of more than 10 for average read and single base pair

quality⁴¹. The primers and target sequences are provided in Supplementary Tables 5 and 6, respectively.

ISDra2 TnpB modelling and structure comparison

To gain insight into the structure of TnpB, we submitted separately N-terminal and C-terminal regions to the well-performing publicly available structure prediction servers trRosetta⁴², tFOLD (<https://drug.ai.tencent.com>) and RaptorX⁴³, as established by CASP (Critical Assessment of Protein Structure Prediction). All three methods returned very similar structures for either N-terminal or C-terminal region. As expected, the C-terminal region features the RuvC domain with the inserted zinc-finger domain. The structure of the modelled N-terminal region corresponded to a β -barrel domain with the inserted three-helix bundle. A search with the trRosetta model of the N-terminal region of TnpB against the Protein Data Bank using Dali⁴⁴ identified N-terminal lobes of other Cas12 proteins as the closest matches. The TnpB β -barrel matched a similar domain in Cas12, often referred to as the ‘Wedge’ domain, whereas the inserted helical bundle matched a part of the ‘Rec’ domain. More detailed structural comparison with available different Cas12 groups revealed that the N-terminal region of TnpB corresponds to the minimal common structural elements present in Cas12. The TnpB RuvC region also represents a streamlined version of Cas12 RuvC domain variants. Most recently, as the highly accurate AlphaFold2 structure prediction method⁴⁵ became publicly available, we sought further investigation of the TnpB structure. AlphaFold2 produced TnpB models that were very similar to those obtained previously, suggesting that the predicted TnpB structure might be fairly accurate.

Statistics and reproducibility

All experiments represented without replicates (for example, gels for qualitative characterization of proteins and nucleic acids) have been reproduced at least three times independently (except for the small RNA sequencing and plasmid library cleavage experiments, which were performed once).

Reporting summary

Further information on research design is available in the [Nature Research Reporting Summary](#) linked to this paper.

Data availability

All data are available in the paper and the supplementary material. In addition, small RNA and plasmid library cleavage sequencing data are available on the NCBI Sequence Read Archive under BioProject ID [PRJNA723137](#). The ISfinder database was accessed at <https://isfinder.biotoul.fr>.

Code availability

The Python scripts used for identification of the plasmid library cleavage positions and characterization of TAMs are available in a GitHub repository found at https://github.com/tkaryelis/Nuclease_manuscript.

References

1. 1.
Koonin, E. V. Viruses and mobile elements as drivers of evolutionary transitions. *Phil. Trans. R. Soc. B* **371**, 20150442 (2016).
2. 2.
Siguier, P., Gourbeyre, E. & Chandler, M. Bacterial insertion sequences: their genomic impact and diversity. *FEMS Microbiol. Rev.* **38**, 865–891 (2014).
3. 3.
Kersulyte, D., Mukhopadhyay, A. K., Shirai, M., Nakazawa, T. & Berg, D. E. Functional organization and insertion specificity of IS607, a chimeric element of *Helicobacter pylori*. *J. Bacteriol.* **182**, 5300–5308 (2000).
4. 4.
Kersulyte, D. et al. Transposable element ISHp608 of *Helicobacter pylori*: nonrandom geographic distribution, functional organization, and insertion specificity. *J. Bacteriol.* **184**, 992–1002 (2002).
5. 5.
Pasternak, C. et al. ISDra2 transposition in *Deinococcus radiodurans* is downregulated by TnpB. *Mol. Microbiol.* **88**, 443–455 (2013).
6. 6.

Kapitonov, V. V., Makarova, K. S. & Koonin, E. V. ISC, a novel group of bacterial and archaeal DNA transposons that encode Cas9 homologs. *J. Bacteriol.* **198**, 797–807 (2016).

7. 7.

Shmakov, S. et al. Diversity and evolution of class 2 CRISPR–Cas systems. *Nat. Rev. Microbiol.* **15**, 169–182 (2017).

8. 8.

Makarova, K. S. et al. Evolutionary classification of CRISPR–Cas systems: a burst of class 2 and derived variants. *Nat. Rev. Microbiol.* **18**, 67–83 (2020).

9. 9.

Siguier, P., Perochon, J., Lestrade, L., Mahillon, J. & Chandler, M. ISfinder: the reference centre for bacterial insertion sequences. *Nucleic Acids Res.* **34**, D32–D36 (2006).

10. 10.

Hickman, A. B. et al. DNA recognition and the precleavage state during single-stranded DNA transposition in *D. radiodurans*. *EMBO J.* **29**, 3840–3852 (2010).

11. 11.

Islam, M. S. et al. Characterization and distribution of IS8301 in the radioresistant bacterium *Deinococcus radiodurans*. *Genes Genet. Syst.* **78**, 319–327 (2003).

12. 12.

Pasternak, C. et al. Irradiation-induced *Deinococcus radiodurans* genome fragmentation triggers transposition of a single resident insertion sequence. *PLoS Genet.* **6**, e1000799 (2010).

13. 13.

He, S. et al. The IS200/IS605 family and “peel and paste” single-strand transposition mechanism. *Microbiol. Spectr.* **3**, 3.4.02 (2015).

14. 14.

Barabas, O. et al. Mechanism of IS200/IS605 family DNA transposases: activation and transposon-directed target site selection. *Cell* **132**, 208–220 (2008).

15. 15.

Guynet, C. et al. In vitro reconstitution of a single-stranded transposition mechanism of IS608. *Mol. Cell* **29**, 302–312 (2008).

16. 16.

Hoang, B. T. et al. Single-stranded DNA transposition is coupled to host replication. *Cell* **142**, 398–408 (2010).

17. 17.

Gomes-Filho, J. V. et al. Sense overlapping transcripts in IS1341-type transposase genes are functional non-coding RNAs in archaea. *RNA Biol.* **12**, 490–500 (2015).

18. 18.

Jäger, D., Förstner, K. U., Sharma, C. M., Santangelo, T. J. & Reeve, J. N. Primary transcriptome map of the hyperthermophilic archaeon *Thermococcus kodakarensis*. *BMC Genomics* **15**, 684 (2014).

19. 19.

Karvelis, T. et al. PAM recognition by miniature CRISPR–Cas12f nucleases triggers programmable double-stranded DNA target cleavage. *Nucleic Acids Res.* **48**, 5016–5023 (2020).

20. 20.

Cong, L. et al. Multiplex genome engineering using CRISPR/Cas systems. *Science* **339**, 819–823 (2013).

21. 21.

Jinek, M. et al. RNA-programmed genome editing in human cells. *eLife* **2**, e00471 (2013).

22. 22.

Mali, P. et al. RNA-guided human genome engineering via Cas9. *Science* **339**, 823–826 (2013).

23. 23.

Zetsche, B. et al. Cpf1 is a single RNA-guided endonuclease of a class 2 CRISPR–Cas system. *Cell* **163**, 759–771 (2015).

24. 24.

Liu, J.-J. et al. CasX enzymes comprise a distinct family of RNA-guided genome editors. *Nature* **566**, 218–223 (2019).

25. 25.

Pausch, P. et al. CRISPR–CasΦ from huge phages is a hypercompact genome editor. *Science* **369**, 333–337 (2020).

26. 26.

Stoddard, B. L. Homing endonucleases from mobile group I introns: discovery to genome engineering. *Mob. DNA* **5**, 7 (2014).

27. 27.

Altae-Tran, H. et al. The widespread IS200/605 transposon family encodes diverse programmable RNA-guided endonucleases. *Science* **374**, 57–65 (2021).

28. 28.

Harrington, L. B. et al. Programmed DNA destruction by miniature CRISPR–Cas14 enzymes. *Science* **362**, 839–842 (2018).

29. 29.

Takeda, S. N. et al. Structure of the miniature type V-F CRISPR–Cas effector enzyme. *Mol. Cell* **81**, 558–570.e3 (2021).

30. 30.

Xiao, R., Li, Z., Wang, S., Han, R. & Chang, L. Structural basis for substrate recognition and cleavage by the dimerization-dependent CRISPR–Cas12f nuclease. *Nucleic Acids Res.* **49**, 4120–4128 (2021).

31. 31.

Klompe, S. E., Vo, P. L. H., Halpin-Healy, T. S. & Sternberg, S. H. Transposon-encoded CRISPR–Cas systems direct RNA-guided DNA integration. *Nature* **571**, 219–225 (2019).

32. 32.

Strecker, J. et al. RNA-guided DNA insertion with CRISPR-associated transposases. *Science* **365**, 48–53 (2019).

33. 33.

Bao, W. & Jurka, J. Homologues of bacterial TnpB_IS605 are widespread in diverse eukaryotic transposable elements. *Mob. DNA* **4**, 12 (2013).

34. 34.

Martin, M. Cutadapt removes adapter sequences from high-throughput sequencing reads. *EMBnet.journal* **17**, 10–12 (2011).

35. 35.

Li, H. & Durbin, R. Fast and accurate long-read alignment with Burrows–Wheeler transform. *Bioinformatics* **26**, 589–595 (2010).

36. 36.

Li, H. et al. The Sequence Alignment/Map format and SAMtools. *Bioinformatics* **25**, 2078–2079 (2009).

37. 37.

Robinson, J. T. et al. Integrative genomics viewer. *Nat. Biotechnol.* **29**, 24–26 (2011).

38. 38.

Karvelis, T. et al. Rapid characterization of CRISPR–Cas9 protospacer adjacent motif sequence elements. *Genome Biol.* **16**, 253 (2015).

39. 39.

Karvelis, T., Young, J. K. & Siksnys, V. A pipeline for characterization of novel Cas9 orthologs. *Methods Enzymol.* **616**, 219–240 (2019).

40. 40.

Crooks, G. E. WebLogo: a sequence logo generator. *Genome Res.* **14**, 1188–1190 (2004).

41. 41.

Clement, K. et al. CRISPResso2 provides accurate and rapid genome editing sequence analysis. *Nat. Biotechnol.* **37**, 224–226 (2019).

42. 42.

Yang, J. et al. Improved protein structure prediction using predicted interresidue orientations. *Proc. Natl Acad. Sci. USA* **117**, 1496–1503 (2020).

43. 43.

Xu, J. Distance-based protein folding powered by deep learning. *Proc. Natl Acad. Sci. USA* **116**, 16856–16865 (2019).

44. 44.

Holm, L. in *Structural Bioinformatics: Methods and Protocols* (ed. Gáspári, Z.) 29–42 (Springer US, 2020).

45. 45.

Jumper, J. et al. Highly accurate protein structure prediction with AlphaFold. *Nature* **96**, 583–589 (2021).

Acknowledgements

We thank Ž. Kapustina for small RNA sequencing, S. Henkel-Heinecke and R. Seidel for performing mass photometry experiments, and S. Halford for the comments and critical reading of the manuscript. Research was supported by a Novozyme Prize grant to V.S.

Author information

Affiliations

1. Institute of Biotechnology, Life Sciences Center, Vilnius University, Vilnius, Lithuania

Tautvydas Karvelis, Gytis Druteika, Greta Bigelyte, Karolina Budre, Rimante Zedaveinyte, Arunas Silanskas, Darius Kazlauskas, Česlovas Venclovas & Virginijus Siksny

Contributions

T.K. and V.S. designed the research. T.K., G.D., G.B. and A.S. performed the protein purifications. T.K. and K.B. carried out RNA purification for small RNA sequencing, plasmid library cleavage and DNA interference in *E. coli* experiments. G.D. and G.B. performed the DNA cleavage experiments in vitro. T.K., G.B. and R.Z. performed the genome editing experiments. D.K. and C.V. were involved in sequence and structure analyses. T.K. and V.S. wrote the manuscript with input from all authors. All authors read and approved the final manuscript.

Corresponding authors

Correspondence to [Tautvydas Karvelis](#) or [Virginijus Siksny](#).

Ethics declarations

Competing interests

T.K. and V.S. are co-inventors on a patent application (PCT/IB2021/055958) filed by Vilnius University relating to the work described in this paper. V.S. is a chairman of and has financial interest in CasZyme.

Additional information

Peer review information *Nature* thanks Martin Jinek and the other, anonymous, reviewer(s) for their contribution to the peer review of this work.

Publisher's note Springer Nature remains neutral with regard to jurisdictional claims in published maps and institutional affiliations.

Extended data figures and tables

[Extended Data Fig. 1 Purification of ISDra2 TnpB.](#)

a, b, Experimental workflow for expression and purification of a single TnpB (**a**) and TnpB co-expressed with ISDra2 (Δ TnpA) (**b**) in *E. coli* cells. SDS-PAGE gels show elution fractions of proteins bound to HisTrap chelating column. Red boxes denote bands corresponding to an intact 10 \times MBP-TnpB protein (95.4 kDa). **c**, SDS-PAGE gel of pooled fractions indicated in **a** and **b**. **d**, Detection and analysis of nucleic acids co-purifying with TnpB protein. For uncropped gel images, see Supplementary Fig. 2.

Extended Data Fig. 2 TnpB RNP complex cleaves dsDNA in a TAM dependent manner.

a, Experimental workflow of double-stranded (ds) DNA cleavage activity detection. The reRNA encoding construct contained 20 nt guide sequence. F – forward primer, annealing to ligated adapter. R1 and R2 – reverse primers, annealing to the plasmid backbone. 7N represents the randomized region in the plasmid library next to the targeted sequence. **b**, Adapter ligation position determination indicating double-stranded break (DSB) formation in the targeted sequence. “-TnpB” represents the cleavage reactions using lysates obtained from the cells that do not express TnpB. **c, d**, WebLogo representation of motifs identified in 7N randomized region at 20–21 bp F + R1 and F + R1 (-TnpB) enriched adapter ligated reads, respectively. No substantial enrichment is observed at 7N region for “-TnpB” reactions.

Extended Data Fig. 3 Position frequency matrix (PFM) of the nucleotides at 7N region obtained after plasmid library cleavage using *E. coli* lysates.

a, b, PFM representation of nucleotides distribution identified in 7N randomized region at 20–21 bp F + R1 enriched adapter ligated reads obtained from *E. coli* cells expressing TnpB and reRNA constructs with 16 nt and 20 nt guide sequences, respectively. **c**, the cleavage reaction using lysate obtained from the cells that do not express TnpB demonstrates no substantial enrichment of motifs at 7N region.

Extended Data Fig. 4 TnpB RNP complex purification.

a, Experimental workflow of TnpB RNP complex expression and multi-step purification. The reRNA encoding construct contained a 16 nt guide sequence and carried an HDV ribozyme sequence at the 3'-end, which enabled production of the reRNA with fixed 16 nt length guide sequence. **b**, SDS-PAGE analysis of the purified TnpB and TnpB (D191A) RNP complexes. For uncropped gel image, see Supplementary Fig. 2. **c**, Molecular mass of TnpB and reRNA RNP complex determined by mass photometry. Experimentally established molecular mass

corresponds to TnpB RNP complex consisting of a TnpB protein monomer bound to a ~150 nt long reRNA in a 1:1 molar ratio.

Extended Data Fig. 5 Synthetic dsDNA cleavage by TnpB RNP complex.

a, b, Cleavage of dsDNA substrates containing a target (represented in green colour) with TAM (red colour) (**a**) or without TAM sequence (**b**). TnpB RNP complex cleaves dsDNA in a TAM-dependent manner. Cleavage is blocked by D191A mutation at the RuvC-like active site (lane D). NTS and TS represent non-target and target strand, respectively. M – DNA marker lane. For uncropped gel images, see Supplementary Fig. 2.

Extended Data Fig. 6 Synthetic ssDNA cleavage by TnpB RNP complex.

a, b, Cleavage of ssDNA substrates containing a target (represented in green colour) with TAM (red colour) (**a**) or without TAM sequence (**b**). TnpB RNP complex cleaves ssDNA in a TAM-independent manner. Cleavage is blocked by D191A mutation at the RuvC-like active site (lane D). NTS and TS represent non-target and target strand, respectively. M – DNA marker lane. For uncropped gel images, see Supplementary Fig. 2.

Extended Data Fig. 7 Comparison of a TnpB model with experimentally determined representative structures of different Cas12 groups.

a, Schematic representation of common structural domains/motifs (coloured) and unique structural regions (grey) along the sequence; WED – wedge domain, corresponding to the β -barrel, REC – helical bundle, RuvC – RuvC domain with the inserted helical hairpin (HH) and either the zinc-finger domain (ZnF), or analogous domain inserted in the same relative position. Length of all sequences are approximately to scale. TnpB represents a minimal domain organization also present in Cas12 groups. **b**, Comparison of N-terminal regions between TnpB and other Cas12 proteins; the N-terminal WED and REC domains are involved in PAM recognition in Cas12f and are expected to participate in TAM recognition in TnpB. **c**, Comparison of corresponding RuvC regions.

Extended Data Table 1 Comparison of biochemical features of RNA-guided nucleases adopted for genome editing

Supplementary information

Supplementary Information

This file contains Supplementary Fig. 1 (unprocessed gel images for the Main text Figs), Supplementary Fig. 2 (unprocessed gel images for the Extended Data Figs), and Supplementary Tables 1–6.

Reporting Summary

Rights and permissions

Open Access This article is licensed under a Creative Commons Attribution 4.0 International License, which permits use, sharing, adaptation, distribution and reproduction in any medium or format, as long as you give appropriate credit to the original author(s) and the source, provide a link to the Creative Commons license, and indicate if changes were made. The images or other third party material in this article are included in the article's Creative Commons license, unless indicated otherwise in a credit line to the material. If material is not included in the article's Creative Commons license and your intended use is not permitted by statutory regulation or exceeds the permitted use, you will need to obtain permission directly from the copyright holder. To view a copy of this license, visit <http://creativecommons.org/licenses/by/4.0/>.

Reprints and Permissions

About this article

Cite this article

Karvelis, T., Druteika, G., Bigelyte, G. *et al.* Transposon-associated TnpB is a programmable RNA-guided DNA endonuclease. *Nature* **599**, 692–696 (2021). <https://doi.org/10.1038/s41586-021-04058-1>

- Received: 30 July 2021
- Accepted: 27 September 2021
- Published: 07 October 2021
- Issue Date: 25 November 2021
- DOI: <https://doi.org/10.1038/s41586-021-04058-1>

Share this article

Anyone you share the following link with will be able to read this content:

[Get shareable link](#)

Sorry, a shareable link is not currently available for this article.

[Copy to clipboard](#)

Provided by the Springer Nature SharedIt content-sharing initiative

Further reading

- [**A vast potential genome editor toolbox**](#)

- Grant Otto

Nature Reviews Genetics (2021)

This article was downloaded by **calibre** from <https://www.nature.com/articles/s41586-021-04058-1>

| [Section menu](#) | [Main menu](#) |

- Article
- [Published: 03 November 2021](#)

Few-fs resolution of a photoactive protein traversing a conical intersection

- [A. Hosseiniزاده¹](#),
- [N. Breckwoldt ORCID: orcid.org/0000-0003-4307-6833^{2,3,4}](#),
- [R. Fung ORCID: orcid.org/0000-0001-6886-9915¹](#),
- [R. Sepehr¹](#),
- [M. Schmidt ORCID: orcid.org/0000-0002-0962-9468¹](#),
- [P. Schwander ORCID: orcid.org/0000-0003-2350-8838¹](#),
- [R. Santra ORCID: orcid.org/0000-0002-1442-9815^{2,3,4}](#) &
- [A. Ourmazd ORCID: orcid.org/0000-0001-9946-3889¹](#)

[Nature](#) volume 599, pages 697–701 (2021)

- 3103 Accesses
- 126 Altmetric
- [Metrics details](#)

Subjects

- [Biophysical chemistry](#)
- [Computational models](#)

Abstract

The structural dynamics of a molecule are determined by the underlying potential energy landscape. Conical intersections are funnels connecting otherwise separate potential energy surfaces. Posited almost a century ago¹, conical intersections remain the subject of intense scientific interest^{2,3,4,5}. In biology, they have a pivotal role in vision, photosynthesis and DNA stability⁶. Accurate theoretical methods for examining conical intersections are at present limited to small molecules. Experimental investigations are challenged by the required time resolution and sensitivity. Current structure-dynamical understanding of conical intersections is thus limited to simple molecules with around ten atoms, on timescales of about 100 fs or longer⁷. Spectroscopy can achieve better time resolutions⁸, but provides indirect structural information. Here we present few-femtosecond, atomic-resolution videos of photoactive yellow protein, a 2,000-atom protein, passing through a conical intersection. These videos, extracted from experimental data by machine learning, reveal the dynamical trajectories of de-excitation via a conical intersection, yield the key parameters of the conical intersection controlling the de-excitation process and elucidate the topography of the electronic potential energy surfaces involved.

Access options

Subscribe to Journal

Get full journal access for 1 year

\$199.00

only \$3.90 per issue

[Subscribe](#)

All prices are NET prices.

VAT will be added later in the checkout.

Tax calculation will be finalised during checkout.

Rent or Buy article

Get time limited or full article access on ReadCube.

from \$8.99

[Rent or Buy](#)

All prices are NET prices.

Additional access options:

- [Log in](#)
- [Access through your institution](#)
- [Learn about institutional subscriptions](#)

Fig. 1: Evolution of dynamical modes as a function of pump–probe delay time.

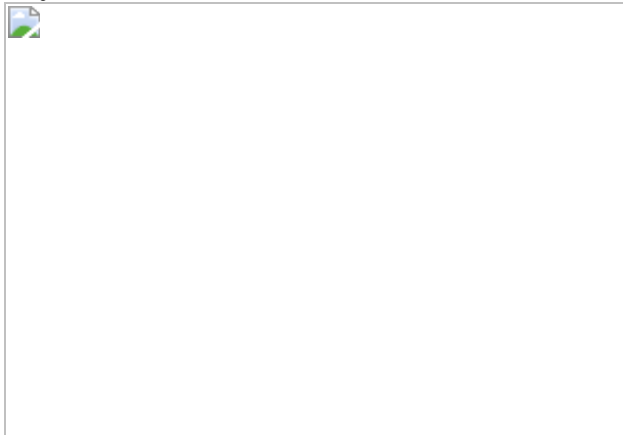


Fig. 2: Topography of the conical intersection and the associated population dynamics in PYP, as deduced from five experimental dynamic trajectories.



Data availability

The structures have been deposited in the Protein Data Bank, together with their respective weighted difference structure factor amplitudes, under accession codes [5HD3](#), [5HDC](#), [5HDD](#), [5HDS](#) and [5HD5](#). [Source data](#) are provided with this paper.

Code availability

The code will be made available on request.

References

1. 1.

von Neumann, J. & Wigner, E. P. *Über das Verhalten von Eigenwerten bei adiabatischen Prozessen* Vol. A1 (Springer, 1993).

2. 2.

Chang, K. F. et al. Revealing electronic state-switching at conical intersections in alkyl iodides by ultrafast XUV transient absorption spectroscopy. *Nat. Commun.* **11**, 4042 (2020).

3. 3.

Cerullo, G. & Garavelli, M. A novel spectroscopic window on conical intersections in biomolecules. *Proc. Natl Acad. Sci. USA* **117**, 26553–26555 (2020).

4. 4.

Yang, J. et al. Imaging CF₃I conical intersection and photodissociation dynamics with ultrafast electron diffraction. *Science* **361**, 64–67 (2018).

5. 5.

Tenboer, J. et al. Time-resolved serial crystallography captures high-resolution intermediates of photoactive yellow protein. *Science* **346**, 1242–1246 (2014).

6. 6.

Nogly, P. et al. Retinal isomerization in bacteriorhodopsin captured by a femtosecond X-ray laser. *Science* **361**, eaat0094 (2018).

7. 7.

Yang, J. et al. Simultaneous observation of nuclear and electronic dynamics by ultrafast electron diffraction. *Science* **368**, 885–889 (2020).

8. 8.

Zinchenko, K. S. et al. Sub-7-femtosecond conical-intersection dynamics probed at the carbon K-edge. *Science* **371**, 489–494 (2021).

9. 9.

Perman, B. et al. Energy transduction on the nanosecond time scale: early structural events in a xanthopsin photocycle. *Science* **279**, 1946–1950 (1998).

10. 10.

Pande, K. et al. Femtosecond structural dynamics drives the *trans/cis* isomerization in photoactive yellow protein. *Science* **352**, 725–729 (2016).

11. 11.

Polli, D. et al. Conical intersection dynamics of the primary photoisomerization event in vision. *Nature* **467**, 440–443 (2010).

12. 12.

Van Beeumen, J. J. et al. Primary structure of a photoactive yellow protein from the phototrophic bacterium *Ectothiorhodospira halophila*, with evidence for the mass and the binding site of the chromophore. *Protein Sci.* **2**, 1114–1125 (1993).

13. 13.

Jones, R. O. Density functional theory: its origins, rise to prominence, and future. *Rev. Mod. Phys.* **87**, 897–923 (2015).

14. 14.

Calegari, F., Sansone, G., Stagira, S., Vozzi, C. & Nisoli, M. Advances in attosecond science. *J. Phys. B* **49**, 062001 (2016).

15. 15.

Wolf, T. J. A. et al. The photochemical ring-opening of 1,3-cyclohexadiene imaged by ultrafast electron diffraction. *Nat. Chem.* **11**, 504–509 (2019).

16. 16.

Fung, R. et al. Dynamics from noisy data with extreme timing uncertainty. *Nature* **532**, 471–475 (2016).

17. 17.

Coifman, R. R. et al. Geometric diffusions as a tool for harmonic analysis and structure definition of data: diffusion maps. *Proc. Natl Acad. Sci. USA* **102**, 7426–7431 (2005).

18. 18.

Giannakis, D., Schwander, P. & Ourmazd, A. The symmetries of image formation by scattering. I. Theoretical framework. *Opt. Express* **20**, 12799–12826 (2012).

19. 19.

Giannakis, D. & Majda, A. J. Nonlinear Laplacian spectral analysis for time series with intermittency and low-frequency variability. *Proc. Natl Acad. Sci. USA* **109**, 2222–2227 (2012).

20. 20.

Sauer, T., Yorke, J. A. & Casdagli, M. Embedology. *J. Stat. Phys.* **65**, 579–616 (1991).

21. 21.

Takens, F. in *Lecture Notes in Mathematics* Vol. 898 (ed. Warwick) 366–381 (Springer-Verlag, 1981).

22. 22.

Packard, N., Crutchfield, J., Farmer, J. & Shaw, R. Geometry from a time series. *Phys. Rev. Lett.* **45**, 712–716 (1980).

23. 23.

Fung, R. et al. Achieving accurate estimates of fetal gestational age and personalised predictions of fetal growth based on data from an international prospective cohort study: a population-based machine learning study. *Lancet Digit. Health* **2**, e368–e375 (2020).

24. 24.

Dashti, A. et al. Retrieving functional pathways of biomolecules from single-particle snapshots. *Nat. Commun.* **11**, 4734 (2020).

25. 25.

Moffat, K. The frontiers of time-resolved macromolecular crystallography: movies and chirped X-ray pulses. *Faraday Discuss.* **122**, 65–77; discussion 79–88 (2003).

26. 26.

Schmidt, M., Rajagopal, S., Ren, Z. & Moffat, K. Application of singular value decomposition to the analysis of time-resolved macromolecular X-ray data. *Biophys. J.* **84**, 2112–2129 (2003).

27. 27.

Prieto, G. A., Parker, R. L. & Vernon Iii, F. L. A Fortran 90 library for multitaper spectrum analysis. *Comput. Geosci.* **35**, 1701–1710 (2009).

28. 28.

Mitra, P. & Bokil, H. *Observed Brain Dynamics* (Oxford Univ. Press, 2008).

29. 29.

Jerri, A. J. The Shannon sampling theorem—its various extensions and applications: a tutorial review. *Proc. IEEE* **65**, 1565–1596 (1977).

30. 30.

Grunbein, M. L. et al. Illumination guidelines for ultrafast pump-probe experiments by serial femtosecond crystallography. *Nat. Methods* **17**, 681–684 (2020).

31. 31.

Barty, A. et al. Self-terminating diffraction gates femtosecond X-ray nanocrystallography measurements. *Nat. Photonics* **6**, 35–40 (2012).

32. 32.

Kuramochi, H. et al. Probing the early stages of photoreception in photoactive yellow protein with ultrafast time-domain Raman spectroscopy. *Nat. Chem.* **9**, 660–666 (2017).

33. 33.

Socratese, G. *Infrared and Raman Characteristic Group Frequencies: Tables and Charts* 3rd edn (Wiiley, 2004).

34. 34.

Pandey, S. et al. Time-resolved serial femtosecond crystallography at the European XFEL. *Nat. Methods* **17**, 73–78 (2020).

35. 35.

Henry, E. & Hofrichter, J. Singular value decomposition: application to analysis of experimental data. *Methods Enzymol.* **210**, 129–192 (1992).

36. 36.

Fung, R. et al. Dynamics from noisy data with extreme timing uncertainty. *Nature* **532**, 471–475 (2016).

37. 37.

Schwander, P., Giannakis, D., Yoon, C. H. & Ourmazd, A. The symmetries of image formation by scattering. II. Applications. *Opt. Express* **20**, 12827–12849 (2012).

38. 38.

Winn, M. D. et al. Overview of the CCP4 suite and current developments. *Acta Crystallogr. D* **67**, 235–242 (2011).

39. 39.

Emsley, P., Lohkamp, B., Scott, W. G. & Cowtan, K. Features and development of Coot. *Acta Crystallogr. D* **66**, 486-501 (2010).

40. 40.

Köppel, H., Domcke, W. & Cederbaum, L. S. in *Advances in Chemical Physics* (eds Rice, S. et al.) 59–246 (2007).

41. 41.

Domcke, W., Yarkony, D. R. & Köppel, H. *Conical Intersections* (WorldScientific, 2004).

42. 42.

Gromov, E. V. et al. Theoretical study of excitations in furan: spectra and molecular dynamics. *J. Chem. Phys.* **121**, 4585–4598 (2004).

43. 43.

Faraji, S., Meyer, H. D. & Koppel, H. Multistate vibronic interactions in difluorobenzene radical cations. II. Quantum dynamical simulations. *J. Chem. Phys.* **129**, 074311 (2008).

44. 44.

Arnold, C., Vendrell, O., Welsch, R. & Santra, R. Control of nuclear dynamics through conical intersections and electronic coherences. *Phys. Rev. Lett.* **120**, 123001 (2018).

45. 45.

The MCTDH package v.8.4.18 (2019).

46. 46.

Beck, M. The multiconfiguration time-dependent Hartree (MCTDH) method: a highly efficient algorithm for propagating wavepackets. *Phys. Rep.* **324**, 1–105 (2000).

47. 47.

Meyer, H. D., Manthe, U. & Cederbaum, L. S. The multi-configurational time-dependent Hartree approach. *Chem. Phys. Lett.* **165**, 73–78 (1990).

Acknowledgements

We acknowledge valuable discussions with E. Lattman, K. Moffat, T. Martinez and past and present members of the UWM data science group. The development of underlying techniques was supported by the US Department of Energy, Office of Science, Basic Energy Sciences, under award DE-SC0002164 (underlying dynamical techniques) and by the US National Science Foundation under awards STC-1231306 (underlying data analytical techniques) and DBI-2029533 (underlying analytical models). N.B. and R. Santra were supported by the Cluster of Excellence ‘CUI: Advanced Imaging of Matter’ of Deutsche Forschungsgemeinschaft (DFG)–EXC 2056–project no. 390715994.

Author information

Affiliations

1. University of Wisconsin Milwaukee, Milwaukee, WI, USA
A. Hosseiniزاده, R. Fung, R. Sepehr, M. Schmidt, P. Schwander & A. Ourmazd
2. Center for Free-Electron Laser Science, Deutsches Elektronen-Synchrotron (DESY), Hamburg, Germany
N. Breckwoldt & R. Santra
3. Department of Physics, Universität Hamburg, Hamburg, Germany
N. Breckwoldt & R. Santra
4. The Hamburg Centre for Ultrafast Imaging, Hamburg, Germany
N. Breckwoldt & R. Santra

Contributions

A.O. designed this study. A.O., A.H., P.S., R.F. and R. Sepehr co-defined the algorithm and the data-analytical pipeline. A.H. and R.F. performed analytical and computational work, and tested and validated the algorithm with participation by A.O. N.B. and R. Santra performed the quantum-dynamics simulations. M.S. provided experimental data and expertise in crystallographic data analysis. All authors contributed to the manuscript.

Corresponding author

Correspondence to [A. Ourmazd](#).

Ethics declarations

Competing interests

The authors declare no competing interests.

Additional information

Peer review information *Nature* thanks the anonymous reviewer(s) for their contribution to the peer review of this work. Peer reviewer reports are available.

Publisher's note Springer Nature remains neutral with regard to jurisdictional claims in published maps and institutional affiliations.

Extended data figures and tables

[Extended Data Fig. 1 PYP chromophore in trans configuration and structure dynamical modes obtained by our approach.](#)

a, The PYP chromophore in the trans configuration. The oval contains the primary structure-dynamically active region, with the numbered atoms and aromatic structures identified. C: carbon, N: nitrogen, O: oxygen, S: sulfur.

b, c, The structure dynamical modes obtained by our approach can be

combined to yield the more intuitive torsional angle, which is commonly chosen as the primary reaction coordinate for isomerization in PYP. Changes in the torsional angle and the bend of the chromophore axis relative to equilibrium values necessarily increase the energy of the ground state structure. Near the CI the structure on the ground state PES and that on the excited state PES are essentially identical with very similar energies. The structure on the excited state PES determined at 615 fs is therefore an excellent model for the electronic ground state structure near the PYP conical intersection.

[Extended Data Fig. 2](#) Dynamical trajectories near the conical intersection.

Unless otherwise stated, arbitrary units. **a, b**, Time evolutions (chronos) of modes 3 and 4, respectively. **c**, The experimental dynamical trajectory (in black) obtained from modes 3 and 4 as collective variables x and y , respectively, and the best-fit simulated trajectory, with color showing the passage of time (see color bar). The red dot indicates the position of the conical intersection. For additional trajectories, see [Supplementary Information](#). **d**, The calculated de-excitation dynamics as reflected in the electronic state population for the trajectory shown in Panel c above. The brown and blue curves represent the populations of the upper and the lower adiabatic electronic states, respectively.

[Source data](#)

[Extended Data Fig. 3](#) Frequency content of a typical chrono, in this case chrono-4.

a, Fourier power spectrum. **b**, Multi-taper analysis. The vertical axis of the latter essentially represents the signal-to-noise ratio. Each chrono displays a characteristic frequency spectrum.

[Source data](#)

Extended Data Fig. 4 Dynamical trajectories near the conical intersection.

Unless otherwise stated, arbitrary units. **a, b**, Time evolutions (chronos) of modes 2 and 3, respectively. **c**, The experimental dynamical trajectory (in black) obtained from modes 2 and 3 as collective variables x and y , respectively, and the best-fit simulated trajectory, with color showing the passage of time (see color bar). The red dot indicates the position of the conical intersection. **d**, The calculated de-excitation dynamics as reflected in the electronic state population for the trajectory shown in Panel c above. The brown and blue curves represent the populations of the upper and the lower adiabatic electronic states, respectively.

[Source data](#)

Extended Data Fig. 5 Dynamical trajectories near the conical intersection.

Unless otherwise stated, arbitrary units. **a, b**, Time evolutions (chronos) of modes 2 and 4, respectively. **c**, The experimental dynamical trajectory (in black) obtained from modes 2 and 4 as collective variables x and y , respectively, and the best-fit simulated trajectory, with color showing the passage of time (see color bar). The red dot indicates the position of the conical intersection. **d**, The calculated de-excitation dynamics as reflected in the electronic state population for the trajectory shown in Panel c. The brown and blue curves represent the populations of the upper and the lower adiabatic electronic states, respectively.

[Source data](#)

Extended Data Fig. 6 Dynamical trajectories near the conical intersection.

Unless otherwise stated, arbitrary units. **a, b**, Time evolutions (chronos) of modes 2 and 5, respectively. **c**, The experimental dynamical trajectory (in black) obtained from modes 2 and 5 as collective variables x and y ,

respectively, and the best-fit simulated trajectory, with color showing the passage of time (see color bar). The red dot indicates the position of the conical intersection. **d**, The calculated de-excitation dynamics as reflected in the electronic state population for the trajectory shown in Panel c above. The brown and blue curves represent the populations of the upper and the lower adiabatic electronic states, respectively.

[Source data](#)

[Extended Data Fig. 7 Dynamical trajectories near the conical intersection.](#)

Unless otherwise stated, arbitrary units. **a, b**, Time evolutions (chronos) of modes 4 and 5, respectively. **c**, The experimental dynamical trajectory (in black) obtained from modes 4 and 5 as collective variables x and y , respectively, and the best-fit simulated trajectory, with color showing the passage of time (see color bar). The red dot indicates the position of the conical intersection. **d**, The calculated de-excitation dynamics as reflected in the electronic state population for the trajectory shown in Panel c above. The brown and blue curves represent the populations of the upper and the lower adiabatic electronic states, respectively.

[Source data](#)

[Extended Data Fig. 8 Comparing modes from light and dark data.](#)

a, The first five chronos obtained from light data ordered according to pump-probe delay. **b**, The first five chronos obtained from dark data lexicographically sorted according to run numbers followed by event numbers. The first two chronos are identical, except for scale. This is a hallmark of a one-parameter process. Correlation analysis shows the single-parameter process correlates with the integrated Bragg spot intensity (Pearson correlation: 0.93), most likely pertaining to drift in the incident beam intensity. The subsequent chronos represent noise.

[Source data](#)

Extended Data Table 1 Peak positions obtained from multi-taper Fourier analysis of the chronos before the encounter with the conical intersection vs. peak positions obtained from time-resolved Raman spectra of PYP, all in THz

Extended Data Table 2 Parameters of the potential energy surface and parametric grid of simulated trajectories near the conical intersection

Supplementary information

Supplementary Information

This file contains Supplementary Information sections 1–4 and Supplementary Figs. 1–5.

Reporting Summary

Supplementary Data

This file contains source data for Supplementary Figs. 1, 3, 4 and 5.

Peer Review File

Supplementary Video 1

Difference electron density video along mode 2

Supplementary Video 2

Difference electron density video along mode 3

Supplementary Video 3

Difference electron density video along mode 4

Supplementary Video 4

Difference electron density video along mode 5

Supplementary Video 5

Difference electron density video along trajectory of mode 2/mode 3

Supplementary Video 6

Difference electron density video along trajectory of mode 2/mode 4

Supplementary Video 7

Difference electron density video along trajectory of mode 2/mode 5

Supplementary Video 8

Difference electron density video along trajectory of mode 3/mode 4

Supplementary Video 9

Difference electron density video along trajectory of mode 4/mode 5

Source data

Source Data Fig. 1

Source Data Fig. 2

Source Data Extended Data Fig. 2

Source Data Extended Data Fig. 3

Source Data Extended Data Fig. 4

Source Data Extended Data Fig. 5

[**Source Data Extended Data Fig. 6**](#)

[**Source Data Extended Data Fig. 7**](#)

[**Source Data Extended Data Fig. 8**](#)

Rights and permissions

[Reprints and Permissions](#)

About this article

Cite this article

HosseiniZadeh, A., Breckwoldt, N., Fung, R. *et al.* Few-fs resolution of a photoactive protein traversing a conical intersection. *Nature* **599**, 697–701 (2021). <https://doi.org/10.1038/s41586-021-04050-9>

- Received: 12 November 2020
- Accepted: 23 September 2021
- Published: 03 November 2021
- Issue Date: 25 November 2021
- DOI: <https://doi.org/10.1038/s41586-021-04050-9>

Share this article

Anyone you share the following link with will be able to read this content:

[Get shareable link](#)

Sorry, a shareable link is not currently available for this article.

[Copy to clipboard](#)

Provided by the Springer Nature SharedIt content-sharing initiative

This article was downloaded by **calibre** from <https://www.nature.com/articles/s41586-021-04050-9>

| [Section menu](#) | [Main menu](#) |

- Matters Arising
- [Published: 24 November 2021](#)

Spatial scale and the synchrony of ecological disruption

- [Robert K. Colwell](#) ORCID: [orcid.org/0000-0002-1384-0354^{1,2,3,4}](https://orcid.org/0000-0002-1384-0354)

[Nature](#) volume 599, pages E8–E10 (2021)

- 762 Accesses
- 7 Altmetric
- [Metrics details](#)

Subjects

- [Biogeography](#)
- [Climate-change ecology](#)

[Matters Arising](#) to this article was published on 24 November 2021

The [Original Article](#) was published on 08 April 2020

arising from C. H. Trisos et al. *Nature* <https://doi.org/10.1038/s41586-020-2189-9> (2020)

Access options

[Subscribe to Journal](#)

Get full journal access for 1 year

\$199.00

only \$3.90 per issue

[Subscribe](#)

All prices are NET prices.

VAT will be added later in the checkout.

Tax calculation will be finalised during checkout.

Rent or Buy article

Get time limited or full article access on ReadCube.

from \$8.99

[Rent or Buy](#)

All prices are NET prices.

Additional access options:

- [Log in](#)
- [Access through your institution](#)
- [Learn about institutional subscriptions](#)

Fig. 1: Spatial scale of terrestrial ecosystems and biogeography.

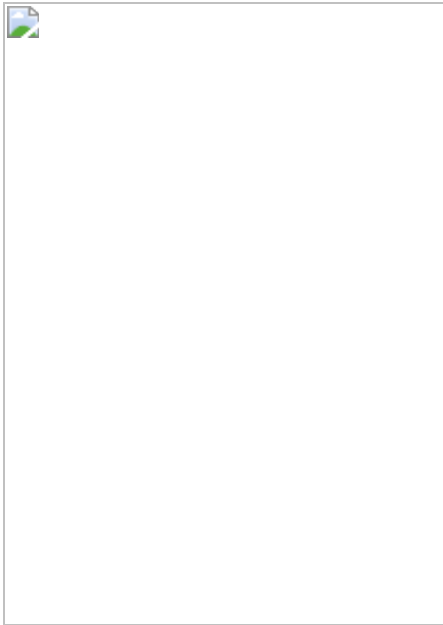
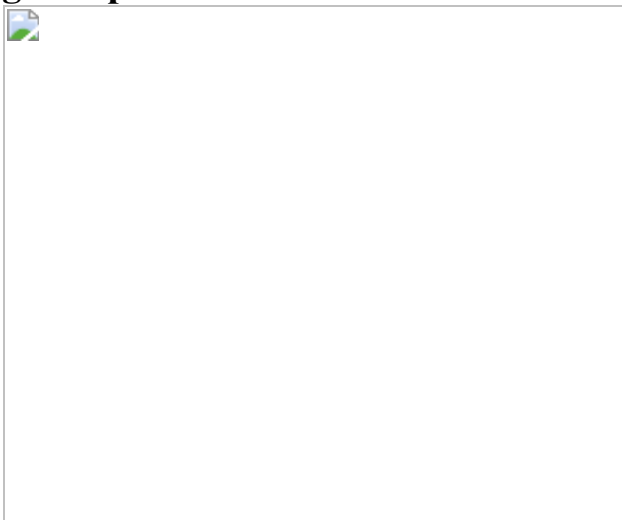


Fig. 2: Spatial scale of marine habitats and biotas.



References

1. 1.

Trisos, C. H., Merow, C. & Pigot, A. L. The projected timing of abrupt ecological disruption from climate change. *Nature* **580**, 496–501 (2020).

2. 2.

Pecl, G. T. et al. Biodiversity redistribution under climate change: impacts on ecosystems and human well-being. *Science* **355**, eaai9214 (2017).

3. 3.

Sih, T. L., Cappo, M. & Kingsford, M. Deep-reef fish assemblages of the Great Barrier Reef shelf-break (Australia). *Sci. Rep.* **7**, 10886 (2017).

4. 4.

Rahbek, C. et al. Humboldt's enigma: what causes global patterns of mountain biodiversity? *Science* **365**, 1108–1113 (2019).

5. 5.

Rahbek, C. et al. Building mountain biodiversity: geological and evolutionary processes. *Science* **365**, 1114–1119 (2019).

6. 6.

Morato, T., Hoyle, S. D., Allain, V. & Nicol, S. J. Seamounts are hotspots of pelagic biodiversity in the open ocean. *Proc. Natl Acad. Sci. USA* **107**, 9707–9711 (2010).

7. 7.

Colwell, R. K., Brehm, G., Cardelús, C. L., Gilman, A. C. & Longino, J. T. Global warming, elevational range shifts, and lowland biotic attrition in the wet tropics. *Science* **322**, 258–261 (2008).

8. 8.

Stroud, J. T. et al. Is a community still a community? Reviewing definitions of key terms in community ecology. *Ecol. Evol.* **5**, 4757–4765 (2015).

9. 9.

Lima, F. P. et al. Loss of thermal refugia near equatorial range limits. *Glob. Change Biol.* **22**, 254–263 (2016).

10. 10.

Lenoir, J. & Svenning, J. C. Climate-related range shifts—a global multidimensional synthesis and new research directions. *Ecography* **38**, 15–28 (2014).

11. 11.

Bell, G. Evolutionary rescue. *Annu. Rev. Ecol. Evol. Syst.* **48**, 605–627 (2017).

12. 12.

Ackerly, D. D. Community assembly, niche conservatism, and adaptive evolution in changing environments. *Int. J. Plant Sci.* **164**, S165–S184 (2003).

13. 13.

Valladares, F. et al. The effects of phenotypic plasticity and local adaptation on forecasts of species range shifts under climate change. *Ecol. Lett.* **17**, 1351–1364 (2014).

14. 14.

Rangel, T. F. et al. Modeling the ecology and evolution of biodiversity: biogeographical cradles, museums, and graves. *Science* **361**, eaar5452 (2018).

15. 15.

Desbruyères, D., McDonagh, E. L., King, B. A. & Thierry, V. Global and full-depth ocean temperature trends during the early twenty-first century from Argo and repeat hydrography. *J. Clim.* **30**, 1985–1997 (2017).

Author information

Affiliations

1. Department of Ecology and Evolutionary Biology, University of Connecticut, Storrs, CT, USA

Robert K. Colwell

2. University of Colorado Museum of Natural History, Boulder, CO, USA

Robert K. Colwell

3. Departamento de Ecologia, Universidade Federal de Goiás, Goiânia, Goiás, Brazil

Robert K. Colwell

4. Center for Macroecology, Evolution and Climate, GLOBE Institute, University of Copenhagen, Copenhagen O, Denmark

Robert K. Colwell

Contributions

R.K.C. developed the ideas, wrote the manuscript, and prepared the figures.

Corresponding author

Correspondence to [Robert K. Colwell](#).

Ethics declarations

Competing interests

The author declares no competing interests.

Additional information

Publisher's note Springer Nature remains neutral with regard to jurisdictional claims in published maps and institutional affiliations.

Rights and permissions

[Reprints and Permissions](#)

About this article

Cite this article

Colwell, R.K. Spatial scale and the synchrony of ecological disruption. *Nature* **599**, E8–E10 (2021). <https://doi.org/10.1038/s41586-021-03759-x>

- Received: 04 May 2020
- Accepted: 22 June 2021
- Published: 24 November 2021
- Issue Date: 25 November 2021
- DOI: <https://doi.org/10.1038/s41586-021-03759-x>

Share this article

Anyone you share the following link with will be able to read this content:

[Get shareable link](#)

Sorry, a shareable link is not currently available for this article.

[Copy to clipboard](#)

Provided by the Springer Nature SharedIt content-sharing initiative

This article was downloaded by **calibre** from <https://www.nature.com/articles/s41586-021-03759-x>

| [Section menu](#) | [Main menu](#) |

- Matters Arising
- [Published: 24 November 2021](#)

Reply to: Spatial scale and the synchrony of ecological disruption

- [Christopher H. Trisos^{1,2,3}](#),
- [Cory Merow⁴](#) &
- [Alex L. Pigot](#) [ORCID: orcid.org/0000-0002-6490-6261⁵](#)

Nature volume **599**, pages E11–E13 (2021)

- 347 Accesses
- 1 Citations
- 1 Altmetric
- [Metrics details](#)

Subjects

- [Climate-change ecology](#)
- [Community ecology](#)

The [Original Article](#) was published on 24 November 2021

replying to R. K. Colwell. *Nature* <https://doi.org/10.1038/s41586-021-03760-4> (2021)

Access options

[Subscribe to Journal](#)

Get full journal access for 1 year

\$199.00

only \$3.90 per issue

[Subscribe](#)

All prices are NET prices.

VAT will be added later in the checkout.

Tax calculation will be finalised during checkout.

Rent or Buy article

Get time limited or full article access on ReadCube.

from \$8.99

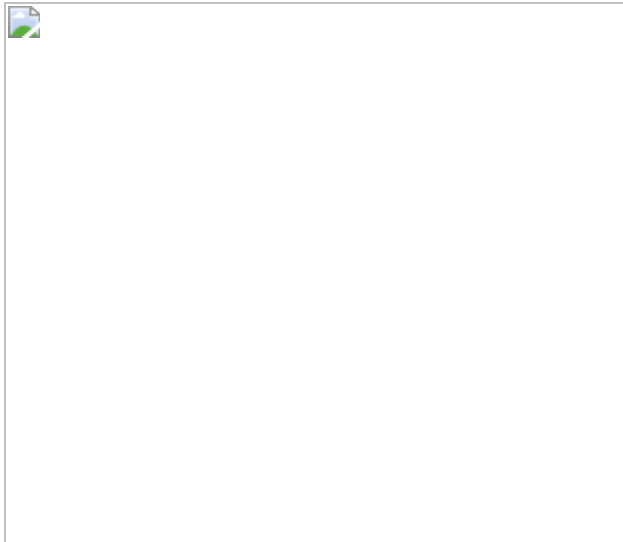
[Rent or Buy](#)

All prices are NET prices.

Additional access options:

- [Log in](#)
- [Access through your institution](#)
- [Learn about institutional subscriptions](#)

Fig. 1: Abrupt exposure is a general pattern and not an artefact of homogenizing mountain regions.



Data availability

Elevation data are publicly available from <https://www.ngdc.noaa.gov/mgg/global/>. Code and data to reproduce Fig. 1 are available at Figshare (<https://doi.org/10.6084/m9.figshare.14730501>).

References

1. 1.

Colwell, R. K. Spatial scale and the synchrony of ecological disruption. *Nature* <https://doi.org/10.1038/s41586-021-03760-4> (2021).

2. 2.

Trisos, C. H., Merow, C. & Pigot, A. L. The projected timing of abrupt ecological disruption from climate change. *Nature* **580**, 496–501 (2020).

3. 3.

Jorda, G. et al. Ocean warming compresses the three-dimensional habitat of marine life. *Nat. Ecol. Evol.* **4**, 109–114 (2020).

4. 4.

Hughes, T. P. et al. Global warming transforms coral reef assemblages. *Nature* **556**, 492–496 (2018).

5. 5.

Ricklefs, R. E. Disintegration of the ecological community. *Am. Nat.* **172**, 741–750 (2008).

6. 6.

Hurlbert, A. H. & Jetz, W. Species richness, hotspots, and the scale dependence of range maps in ecology and conservation. *Proc. Natl Acad. Sci. USA* **104**, 13384–13389 (2007).

7. 7.

Nadeau, C. P., Urban, M. C. & Bridle, J. R. Coarse climate change projections for species living in a fine-scaled world. *Glob. Change Biol.* **23**, 12–24 (2017).

8. 8.

Stewart, S. B. et al. Climate extreme variables generated using monthly time-series data improve predicted distributions of plant species. *Ecography* **44**, 626–639 (2021).

9. 9.

Harris, R. M. B. et al. Biological responses to the press and pulse of climate trends and extreme events. *Nat. Clim. Change* **8**, 579–587 (2018).

10. 10.

McKechnie, A. E. & Wolf, B. O. The Physiology of Heat Tolerance in Small Endotherms. *Physiology* **34**, 302–313 (2019).

11. 11.

Valladares, F. et al. The effects of phenotypic plasticity and local adaptation on forecasts of species range shifts under climate change. *Ecol. Lett.* **17**, 1351–1364 (2014).

12. 12.

Mahony, C. R. & Cannon, A. J. Wetter summers can intensify departures from natural variability in a warming climate. *Nat. Commun.* **9**, 783 (2018).

13. 13.

Molnár, P. K., Derocher, A. E., Thiemann, G. W. & Lewis, M. A. Predicting survival, reproduction and abundance of polar bears under climate change. *Biol. Conserv.* **143**, 1612–1622 (2010).

14. 14.

Lister, B. C. & Garcia, A. Climate-driven declines in arthropod abundance restructure a rainforest food web. *Proc. Natl Acad. Sci. USA* **115**, E10397–E10406 (2018).

15. 15.

Vergés, A. et al. Long-term empirical evidence of ocean warming leading to tropicalization of fish communities, increased herbivory, and loss of kelp. *Proc. Natl Acad. Sci. USA* **113**, 13791–13796 (2016).

16. 16.

Genin, A., Levy, L., Sharon, G., Raitsos, D. E. & Diamant, A. Rapid onsets of warming events trigger mass mortality of coral reef fish. *Proc. Natl Acad. Sci. USA* **117**, 25378–25385 (2020).

17. 17.

Poloczanska, E. S. et al. Global imprint of climate change on marine life. *Nat. Clim. Change* **3**, 919–925 (2013).

18. 18.

Ruthrof, K. X. et al. Subcontinental heat wave triggers terrestrial and marine, multi-taxa responses. *Sci. Rep.* **8**, 13094 (2018).

19. 19.

Wernberg, T. et al. Climate-driven regime shift of a temperate marine ecosystem. *Science* **353**, 169–172 (2016).

20. 20.

Hughes, T. P. et al. Spatial and temporal patterns of mass bleaching of corals in the Anthropocene. *Science* **359**, 80–83 (2018).

21. 21.

Spooner, F. E. B., Pearson, R. G. & Freeman, R. Rapid warming is associated with population decline among terrestrial birds and mammals globally. *Glob. Change Biol.* **24**, 4521–4531 (2018).

22. 22.

Wiens, J. J. Climate-related local extinctions are already widespread among plant and animal species. *PLoS Biol.* **14**, e2001104 (2016).

23. 23.

Sinervo, B. et al. Erosion of lizard diversity by climate change and altered thermal niches. *Science* **328**, 894–899 (2010).

24. 24.

Soroye, P., Newbold, T. & Kerr, J. Climate change contributes to widespread declines among bumble bees across continents. *Science* **367**, 685–688 (2020).

25. 25.

Williams, J. W., Ordonez, A. & Svenning, J. C. A unifying framework for studying and managing climate-driven rates of ecological change. *Nat. Ecol. Evol.* **5**, 17–26 (2021).

26. 26.

NOAA National Geophysical Data Center. 2009: ETOPO1 1 Arc-Minute Global Relief Model. NOAA National Centers for Environmental Information. Accessed 10.05.2021.

Author information

Affiliations

1. African Climate and Development Initiative, University of Cape Town, Cape Town, South Africa

Christopher H. Trisos

2. National Socio-Environmental Synthesis Center (SESYNC), Annapolis, MD, USA

Christopher H. Trisos

3. Centre for Statistics in Ecology, the Environment, and Conservation, University of Cape Town, Cape Town, South Africa

Christopher H. Trisos

4. Eversource Energy Center and Ecology and Evolutionary Biology, University of Connecticut, Storrs, CT, USA

Cory Merow

5. Centre for Biodiversity and Environment Research, Department of Genetics, Evolution and Environment, University College London,

London, UK

Alex L. Pigot

Contributions

A.L.P., C.H.T. and C.M. contributed to writing the manuscript.

Corresponding author

Correspondence to [Alex L. Pigot](#).

Ethics declarations

Competing interests

The authors declare no competing interests.

Additional information

Publisher's note Springer Nature remains neutral with regard to jurisdictional claims in published maps and institutional affiliations.

Supplementary information

[Reporting Summary](#)

Rights and permissions

[Reprints and Permissions](#)

About this article

Cite this article

Trisos, C.H., Merow, C. & Pigot, A.L. Reply to: Spatial scale and the synchrony of ecological disruption. *Nature* **599**, E11–E13 (2021). <https://doi.org/10.1038/s41586-021-03760-4>

- Published: 24 November 2021
- Issue Date: 25 November 2021
- DOI: <https://doi.org/10.1038/s41586-021-03760-4>

Share this article

Anyone you share the following link with will be able to read this content:

[Get shareable link](#)

Sorry, a shareable link is not currently available for this article.

[Copy to clipboard](#)

Provided by the Springer Nature SharedIt content-sharing initiative

Further reading

- [Reply to: Spatial scale and the synchrony of ecological disruption](#)
 - Christopher H. Trisos
 - Cory Merow
 - Alex L. Pigot

Nature (2021)

[The projected timing of abrupt ecological disruption from climate change](#)

- Christopher H. Trisos

- Cory Merow
- Alex L. Pigot

Article 08 Apr 2020

This article was downloaded by **calibre** from <https://www.nature.com/articles/s41586-021-03760-4>

| [Section menu](#) | [Main menu](#) |

Amendments & Corrections

- [**Author Correction: Codon-specific translation reprogramming promotes resistance to targeted therapy**](#)

[11 November 2021]

Author Correction •

- Author Correction
- [Published: 11 November 2021](#)

Author Correction: Codon-specific translation reprogramming promotes resistance to targeted therapy

- [Francesca Rapino](#)^{1,2},
- [Sylvain Delaunay](#)^{1,2},
- [Florian Rambow](#)^{3,4},
- [Zhaoli Zhou](#)^{1,2},
- [Lars Tharun](#)⁵,
- [Pascal De Tullio](#)⁶,
- [Olga Sin](#)^{7,8,9},
- [Kateryna Shostak](#)^{2,10},
- [Sebastian Schmitz](#)^{1,2},
- [Jolanda Piepers](#)¹¹,
- [Bart Ghesquière](#)¹²,
- [Latifa Karim](#)^{2,13},
- [Benoit Charlotteaux](#)^{2,13},
- [Diane Jamart](#)^{1,2},
- [Alexandra Florin](#)⁵,
- [Charles Lambert](#)²,
- [Andrée Rorive](#)¹⁴,
- [Guy Jerusalem](#)¹⁴,
- [Eleonora Leucci](#)^{3,4},
- [Michael Dewaele](#)^{3,4},
- [Marc Vooijs](#)¹¹,

- [Sebastian A. Leidel](#)^{7,8,9},
- [Michel Georges](#)^{2,13},
- [Marianne Voz](#)²,
- [Bernard Peers](#)²,
- [Reinhard Büttner](#)⁵,
- [Jean-Christophe Marine](#)^{3,4},
- [Alain Chariot](#)^{2,10,15} &
- [Pierre Close](#) ORCID: orcid.org/0000-0002-8844-9616^{1,2,15}

Nature volume **599**, page E14 (2021)

- 655 Accesses
- 1 Altmetric
- [Metrics details](#)

Subjects

- [Cancer therapeutic resistance](#)
- [Mechanisms of disease](#)
- [Melanoma](#)
- [tRNAs](#)

The [Original Article](#) was published on 20 June 2018

[Download PDF](#)

Correction to: *Nature* <https://doi.org/10.1038/s41586-018-0243-7> Published online 20 June 2018

In the version of this Letter initially published, not all the raw source data used to generate the graphs in the figures were presented at time of publication; they are hereby provided. Further, there are various corrections to the Figures and Extended Data Figures, as described below.

1. 1.

Some dots and error bars were unintentionally misplaced in the final formatting of some of the graphs, which could lead to data misinterpretation. Therefore, we provide corrected graphs for the following: Fig. 3f and Extended Data Figs. 1b, 1k, 2k, 2m, 4a, 6b, 8e and 9g. All stated statistics and conclusions remain correct.

2. 2.

In Extended Data Fig. 10i, the y-axis was wrongly labeled during the formatting of the figure. This has now been corrected.

3. 3.

In Fig. 4a, the Elp1 and Elp3 blots provided in the source data files did not correspond to those shown in the main figure. The correct source data files are now provided.

4. 4.

In Fig. 4c, the Elp3 and a-tubulin blots were provided in the source data file and wrongly referenced in the figure.

5. 5.

In Extended Data Fig. 3f, the original GLUT1 blot was provided in the source data file and wrongly referenced in the figure.

6. 6.

In Extended Data Fig. 9b, the ELP1 and ELP3 blots for SK-MEL-5 and A2058 lines were swapped in the main figure. The source date files were correct, and a corrected figure panel is here provided.

7. 7.

For Extended Data Figs. 1e, 4e, 8a and 8b, we correct mistakes in the labeling of the blots in the source data files.

8. 8.

For Fig. 3a source data files, we correct mistakes in the labeling in the legend of the table.

Finally, a question was raised to us regarding the specificity of the ELP1 signal in the RPL26 immunoprecipitation experiments shown in the Extended Data Fig. 10b. Therefore, to confirm that the ELP1 signal is specific in the anti-RPL26 immunoprecipitation, we reproduced the co-immunoprecipitation experiment using A2058 cells and the protocol provided in our manuscript. The antibody used in the manuscript was no longer commercially available, therefore in order to detect ELP1, we used the anti-ELP1 antibody (sc-100765; fully validated in our lab). This additional experiment shows that ELP1 binds RPL26 in A2058 cells, fully confirming and validating the results published in the manuscript in Extended Data Fig. 10b.

We thank the scientists who brought to our attention these unintentional inaccuracies. We are certain that the corrections and the raw source data now provided should fully clarify the conclusions published in the original manuscript.

Supplementary information is available in the online version of this Amendment.

Author information

Affiliations

1. Laboratory of Cancer Signaling, University of Liège, Liège, Belgium

Francesca Rapino, Sylvain Delaunay, Zhaoli Zhou, Sebastian Schmitz, Diane Jamart & Pierre Close

2. GIGA-institute, University of Liège, Liège, Belgium

Francesca Rapino, Sylvain Delaunay, Zhaoli Zhou, Kateryna Shostak, Sebastian Schmitz, Latifa Karim, Benoit Charlotteaux, Diane Jamart, Charles Lambert, Michel Georges, Marianne Voz, Bernard Peers, Alain Chariot & Pierre Close

3. Laboratory for Molecular Cancer Biology, Department of Oncology, KU Leuven, Leuven, Belgium

Florian Rambow, Eleonora Leucci, Michael Dewaele & Jean-Christophe Marine

4. Center for Cancer Biology, VIB, Leuven, Belgium

Florian Rambow, Eleonora Leucci, Michael Dewaele & Jean-Christophe Marine

5. Institute for Pathology, University Hospital Cologne, Cologne, Germany

Lars Tharun, Alexandra Florin & Reinhard Büttner

6. Centre for Interdisciplinary Research on Medicines (CIRM), University of Liège, Liège, Belgium

Pascal De Tullio

7. Max Planck Research Group for RNA Biology, Max Planck Institute for Molecular Biomedicine, Münster, Germany

Olga Sin & Sebastian A. Leidel

8. Faculty of Medicine, University of Münster, Münster, Germany

Olga Sin & Sebastian A. Leidel

9. Cells-in-Motion Cluster of Excellence, University of Münster, Münster, Germany

Olga Sin & Sebastian A. Leidel

10. Laboratory of Medical Chemistry, University of Liège, Liège, Belgium

Kateryna Shostak & Alain Chariot

11. Department of Radiotherapy (MAASTRO)/GROW, School for Developmental Biology and Oncology, Maastricht University, Maastricht, The Netherlands

Jolanda Piepers & Marc Vooijs

12. Metabolomics Core Facility, Center for Cancer Biology, VIB, Leuven, Belgium

Bart Ghesquière

13. Unit of Animal Genomics, University of Liège, Liège, Belgium

Latifa Karim, Benoit Charlotteaux & Michel Georges

14. Medical Oncology, CHU Sart Tilman Liège, University of Liège, Liège, Belgium

Andrée Rorive & Guy Jerusalem

15. WELBIO, University of Liège, Liège, Belgium

Alain Chariot & Pierre Close

Corresponding author

Correspondence to [Pierre Close](#).

Supplementary information

Supplementary Data 1

Corrected graphs, Figs. 3, 4 and Extended Data Figs. 1–4, 6, 8–10.

Supplementary Data 2

Comparison and explanation of differences, Figs. 3,4 and Extended Data Figs. 1–4, 6, 8–10.

Supplementary Data 3

Blots and xenographs, Figs. 1–4, Extended Data Figs. 1–5, 8–10.

Supplementary Data 4

Raw source data, Figs. 1–4, Extended Data Figs. 1–5, 7–10.

Rights and permissions

Reprints and Permissions

About this article

Cite this article

Rapino, F., Delaunay, S., Rambow, F. *et al.* Author Correction: Codon-specific translation reprogramming promotes resistance to targeted therapy. *Nature* **599**, E14 (2021). <https://doi.org/10.1038/s41586-021-04074-1>

- Published: 11 November 2021
- Issue Date: 25 November 2021
- DOI: <https://doi.org/10.1038/s41586-021-04074-1>

Share this article

Anyone you share the following link with will be able to read this content:

[Get shareable link](#)

Sorry, a shareable link is not currently available for this article.

[Copy to clipboard](#)

Provided by the Springer Nature SharedIt content-sharing initiative

This article was downloaded by **calibre** from <https://www.nature.com/articles/s41586-021-04074-1>

| [Section menu](#) | [Main menu](#) |

Nature Outline